



BIBLIOTHÈQUE

CÉGEP DE L'ABITIBI-TÉMISCAMINGUE
UNIVERSITÉ DU QUÉBEC EN ABITIBI-TÉMISCAMINGUE

Mise en garde

La bibliothèque du Cégep de l'Abitibi-Témiscamingue et de l'Université du Québec en Abitibi-Témiscamingue (UQAT) a obtenu l'autorisation de l'auteur de ce document afin de diffuser, dans un but non lucratif, une copie de son œuvre dans [Depositum](#), site d'archives numériques, gratuit et accessible à tous. L'auteur conserve néanmoins ses droits de propriété intellectuelle, dont son droit d'auteur, sur cette œuvre.

Warning

The library of the Cégep de l'Abitibi-Témiscamingue and the Université du Québec en Abitibi-Témiscamingue (UQAT) obtained the permission of the author to use a copy of this document for nonprofit purposes in order to put it in the open archives [Depositum](#), which is free and accessible to all. The author retains ownership of the copyright on this document.

POLYTECHNIQUE MONTRÉAL

affiliée à l'Université de Montréal

et

l'Université du Québec en Abitibi-Témiscamingue

Stabilization of arsenic trioxide roaster waste dust in cemented paste backfill

AMIRHOSSEIN MOHAMMADI

Département des génies civil, géologique et des mines

Thèse présentée en vue de l'obtention du diplôme de *Philosophiæ Doctor*

Génie minéral

Novembre 2024

POLYTECHNIQUE MONTRÉAL

affiliée à l'Université de Montréal

et

l'Université du Québec en Abitibi-Témiscamingue

Cette thèse intitulée :

Stabilization of arsenic trioxide roaster waste dust in cemented paste backfill

présentée par **Amirhossein MOHAMMADI**

en vue de l'obtention du diplôme de *Philosophiæ Doctor*

a été dûment acceptée par le jury d'examen constitué de :

Li LI, président

Isabelle DEMERS, membre et directrice de recherche

Nicholas A BEIER, membre et codirecteur de recherche

Mostafa BENZAAZOUA, membre et codirecteur de recherche

Yassine TAHA, membre

Samuel COUSSY, membre externe

DEDICATION

To my wife, Hoda, whose patience, love, and understanding have been my source of strength

and

To my beloved son, Aryo!

ACKNOWLEDGEMENTS

First and foremost, I would like to extend my sincere thanks to my supervisor, Professor Isabelle Demers, for her invaluable guidance, support, and encouragement throughout this research. I also wish to thank my co-supervisors, Professor Nicholas A. Beier and Professor Mostafa Benzaazoua, for their support and valuable advice. I am grateful to Professor Li Li, Professor Yassine Taha, and Dr. Samuel Coussy for evaluating this thesis. My thanks also go to Dr. Valerie Schoepfer for her contributions and support.

I would like to acknowledge the UQAT Institut de Recherche en Mines et Environnement (IRME), the Giant Mine Oversight Board (GMOB), and the Natural Sciences and Engineering Research Council (NSERC) of Canada (Alliance grant) for their financial support and for enabling me to carry out this project.

Special thanks are due to the University of Alberta Permafrost Archives Science Laboratory for their assistance with CT scanning and image processing, and to the Canadian Light Source, supported by the Canada Foundation for Innovation, NSERC, the University of Saskatchewan, the Government of Saskatchewan, Western Economic Diversification Canada, the National Research Council Canada, and the Canadian Institutes of Health Research, for their contribution to the XAS analysis.

I would like to thank the Unité de recherche et de service en technologie minérale (URSTM) technical team for their help during this project. Special thanks to Sylvette, Elvin, Jean-Christophe, Guillaume, Alain, Pierre-Alain, and Joël for their assistance, good humor, and ingenuity. I also thank the administrative team of UQAT/IRME for their support throughout my journey.

I am grateful to Oumou Bah, the intern who assisted with this project, as well as all my friends and fellow students. Special thanks go to Jonathan Tremblay, Jordan Harvey, Joel Pumple, and Asma Khouaja for their assistance and collaboration in performing various analyses that enriched my research experience. Their expertise has been a source of inspiration.

I also thank my entire family—my mother, father, and sisters—for their support throughout my academic journey. Their encouragement and belief in my abilities have been a constant source of motivation. Finally, a big thank you to my wife, Hoda, for her support and help throughout this work. I would also like to express my deepest gratitude to my son, Aryo, who has recently entered

my life. His arrival has been a source of immense joy and inspiration. Although he may not fully understand the journey I have undertaken, his presence has been a constant reminder of what truly matters and has given me renewed strength and motivation throughout this process.

RÉSUMÉ

L'ancienne mine Giant située à environ cinq kilomètres au nord de Yellowknife sur le Grand lac des Esclaves dans les Territoires du Nord-Ouest (TNO), au Canada, a été exploitée de 1948 à 2004. Au cours de son exploitation, la mine a traité du minerai d'or, une partie du minerai étant envoyée hors site pour traitement entre 1999 et 2004. Le processus d'extraction de l'or impliquait le grillage de minéraux contenant de l'arsenic, qui produisait des poussières de grillage contenant du trioxyde d'arsenic (ATRW). Environ 237 000 tonnes de ces poussières ont été générées et stockées sous terre dans quinze chambres spécialement construites et des chantiers exploités. De plus, plus de 17 millions de tonnes de résidus ont été produites et stockées dans des parcs à résidus miniers. La poussière d'ATRW, contenant environ 60 % d'arsenic, présente des risques importants pour la santé et l'environnement en raison de sa forte toxicité et de ses propriétés cancérigènes. La gestion de la quantité importante de poussières ATRW est un défi en raison de la nature de ses particules fines et de ses conditions de stockage. Pour résoudre ce problème, une approche intégrée a évalué plus de 50 technologies ou méthodes, identifiant la méthode « de congélation en bloc » comme étant la solution la plus viable. Cette méthode stabilise la poussière en gelant le sol autour des chambres de stockage et des chantiers. Initialement considérée comme une mesure temporaire avec une durée de vie allant jusqu'à 100 ans, cette méthode n'élimine pas l'arsenic, le laissant chimiquement instable et soluble, ce qui pourrait entraîner une contamination potentielle si le bloc gelé dégèle en raison d'un entretien négligé. Les changements climatiques et le réchauffement de la planète ont encore compliqué la situation, posant des défis importants sur le plan environnemental, économique et politique, en particulier pour les résidents des TNO. La présence d'exploitations minières à ciel ouvert et de vastes chantiers souterrains a également perturbé le pergélisol discontinu de la région. Par conséquent, les autorités minières suggèrent qu'une combinaison de méthodes pourrait être nécessaire pour la gestion permanente des poussières ATRW.

Diverses technologies ont été utilisées pour gérer les déchets contenant de l'arsenic et les sols et sédiments contaminés par l'arsenic. Parmi celles-ci, la solidification et la stabilisation sont des techniques prometteuses qui utilisent des agents liants pour encapsuler les déchets dangereux, réduisant ainsi leur mobilité et leur lessivage. Une méthode notable de solidification et de stabilisation est la technologie de remblai en pâte cimenté (RPC). Cette méthode consiste à créer une pâte à haute densité à partir de résidus filtrés, de liants et d'eau, qui est épaissie pour empêcher la décantation et est ensuite transportée dans des cavités minières. Le RPC offre des avantages

environnementaux en déposant en toute sécurité les résidus d'usine dangereux, tels que les résidus sulfurés, et d'autres déchets miniers contaminés, dans des ouvertures souterraines. Cette approche atténue les impacts environnementaux et réduit les coûts d'élimination et de remise en état des surfaces. Les liants hydrauliques utilisés dans le RPC peuvent réagir lors de l'hydratation avec les métaux et métalloïdes, notamment l'arsenic, conduisant à la formation de composés stables par précipitation.

Les recherches antérieures sur la fixation de l'arsenic dans les RPC sont limitées et l'utilisation de l'ATRW dans les RPC n'a pas été explorée auparavant. L'objectif principal de cette étude est d'évaluer la faisabilité de l'incorporation des poussières d'ATRW dans les RPC pour stabiliser l'arsenic et réduire sa lixiviation. Pour atteindre cet objectif, la sélection du ou des liants appropriés et des conditions de mélanges est cruciale pour produire des échantillons de RPC avec une lixiviation minimale et une résistance mécanique adéquate. Dans cette étude, divers matériaux ont été utilisés, notamment des résidus et de la poussière d'ATRW de la mine Giant, cinq liants différents (ciment à usage général (GU) et mélanges de GU avec des cendres volantes (FA), des scories, de la chaux (LI) et des poussières de four à chaux (LKD) selon différents pourcentages), de la silice pure imitant les résidus, du trioxyde d'arsenic pur et de l'eau déionisée (DI). Les résidus et la poussière ATRW de la mine Giant ont été transportés au laboratoire, préparés et homogénéisés pour être caractérisés et utilisés dans les tests. Avant de déterminer les liants et les mélanges appropriés, les caractéristiques physiques, chimiques et minéralogiques des poussières ATRW et des résidus de la mine Giant, ainsi que les liants potentiels et autres matériaux, ont été évalués. Ces caractéristiques ont un impact significatif sur les propriétés mécaniques, les propriétés géochimiques, la conductivité hydraulique et la microstructure des échantillons de RPC.

Dans le cadre de la phase initiale de cette étude, des analyses préliminaires ont été menées pour examiner les effets de l'incorporation de trioxyde d'arsenic pur sur les propriétés géomécaniques et géochimiques des RPC. Les échantillons préliminaires de RPC ont été préparés en deux lots. Dans le premier lot, trois liants (ciment GU, GU/FA et GU/scorie) ont été utilisés avec 10 % de liant et 15 % d'As₂O₃ pur de qualité réactif, ainsi que de la silice pure broyée (Sil-Co-Sil[®]), résidus de la mine Giant et eau DI. Ces échantillons ont été préparés dans des conditions non drainées et durcis jusqu'à 96 jours. Sur la base des résultats de résistance à la compression uniaxiale non confinée (UCS) du premier lot, le deuxième lot d'échantillons a été préparée en utilisant du Sil-Co-Sil[®] comme résidus, du ciment GU à 5 % comme liant, de l'eau DI et des pourcentages variables d'As₂O₃

(0, 5, 10 et 15 %) dans des conditions drainées. Ces échantillons ont été durcis jusqu'à 28 jours, les tests UCS étant effectués après 7 et 28 jours. Pour évaluer le comportement géochimique des pâtes, des mélanges de ciment GU, d' As_2O_3 pur (0 à 15 %) et d'eau DI ont été préparés dans les mêmes proportions que les échantillons RPC et mélangés pendant 28 jours maximum. Le pH, la conductivité électrique (EC) et la composition chimique des mélanges ont ensuite été évalués. De plus, la microstructure des mélanges RPC et As_2O_3 -ciment a été analysée par microscopie électronique à balayage (MEB). Les résultats du premier lot d'échantillons préliminaires ont révélé que l'UCS des échantillons contenant de l' As_2O_3 pur était significativement inférieure à celle des échantillons sans As_2O_3 , en particulier pour le liant GU/scorie. Alors que les échantillons de GU/scories sans As_2O_3 présentaient la résistance la plus élevée, ceux contenant de l' As_2O_3 présentaient des résistances nettement plus faibles, sans aucune prise observée même après 96 jours. Les échantillons avec un liant GU pur contenant l' As_2O_3 présentaient l'UCS le plus élevé, suivis par les échantillons GU/FA. Dans la plupart des cas, l'allongement du temps de durcissement de 28 à 96 jours a entraîné une UCS plus élevée. Pour les échantillons sans As_2O_3 , les échantillons GU et GU/FA contenant de la silice pure présentaient un UCS plus élevé que ceux contenant des résidus, tandis que les échantillons GU/scorie avec des résidus présentaient un UCS significativement plus élevé. Les résultats du deuxième lot ont indiqué que l'ajout d' As_2O_3 pur (en remplacement partiel de la silice pure) diminuait considérablement la résistance mécanique des échantillons de RPC, la réduction la plus significative étant observée à une teneur en arsenic de 5 %. La résistance des échantillons contenant de l' As_2O_3 ne s'est pas améliorée de manière significative après 7 jours de durcissement, principalement en raison d'une baisse du pH (inférieure à 10,5) et probablement en raison de retards et d'une inhibition du durcissement au début de la phase de durcissement. L'analyse MEB a confirmé la formation de certains gels de calcium-silicate-hydrate (C-S-H) contenant de l'arsenic, ainsi que des mélanges complexes d'oxydes dans les mélanges As_2O_3 -ciment.

Dans la deuxième phase de cette étude, des échantillons RPC avec des proportions de mélange variables ont été préparés pour identifier les paramètres clés influençant la résistance, en utilisant la méthodologie de surface de réponse (RSM). La stabilité physique du RPC a été évaluée à l'aide du test UCS, tandis que les analyses de conductivité hydraulique saturée et de tomographie (CT) ont fourni une évaluation de la microstructure du CPB. Dans un premier temps, de petits échantillons de RPC ont été préparés pour identifier les liants les plus efficaces et le pourcentage

optimal de poussières ATRW. Ces échantillons utilisaient 5 % de quatre liants différents (GU, GU/FA, GU/LI et GU/LKD) avec diverses teneurs en poussières ATRW (4 % à 14 %), des résidus de la mine Giant et de l'eau DI. Après durcissement et test de compression de ces échantillons à 7 et 28 jours, deux liants (GU et GU/LKD) et 10 % de poussière ATRW ont été identifiés comme les meilleures conditions pour préparer les échantillons principaux de RPC. Ces échantillons principaux ont été préparés avec différentes formulations de mélanges (pourcentage de solides, pourcentage de liant, temps de durcissement) et leur résistance mécanique a été évaluée. Les résultats ont indiqué que les échantillons RPC préparés avec du ciment GU avaient une résistance significativement plus élevée que ceux avec le mélange GU/LKD. Pour les deux types de liants, la résistance la plus élevée a été obtenue dans les échantillons contenant 6 % de liant et 76 % de solides, avec des valeurs d'environ 491 kPa et 531 kPa pour GU, et 214 kPa et 213 kPa pour GU/LKD, après 28 et 90 jours, respectivement. L'étude des interactions entre les variables indépendantes a permis de mieux comprendre comment ces variables affectent les variables dépendantes. Les pourcentages de liant et de solides se sont révélées être les plus importantes, tandis que le temps de durcissement a eu un effet négligeable. Des pourcentages plus élevés de liant et de solides étaient associées à des valeurs UCS plus élevées dans les échantillons RPC. L'ajout de 10 % d'ATRW aux résidus a réduit l'UCS des échantillons RPC de plus de 30 %, en particulier dans les échantillons contenant moins de liant et de matières solides. Bien que les différences de microstructure n'aient pas été détectables par les expériences de conductivité hydraulique saturée, les observations par tomographie ont révélé que la formation de matériaux contenant de l'arsenic à haute densité était significativement plus importante dans les échantillons présentant l'UCS le plus élevé, en particulier ceux préparés avec le liant GU.

Dans la troisième phase de cette étude, six recettes d'échantillons RPC ont été sélectionnées pour des tests de lixiviation monolithique (TLT) : deux recettes avec l'UCS le plus élevé et quatre recettes avec un UCS de milieu de gamme. Des analyses microstructurales, notamment la thermogravimétrie (TG), la spectroscopie d'absorption des rayons X (XAS), la spectroscopie infrarouge à transformée de Fourier (FTIR) et la tomographie, ont été réalisées pour examiner la microstructure de ces échantillons RPC. L'objectif était d'étudier la relation entre leur résistance, leur comportement géochimique et les caractéristiques de leurs pores. Lors des tests TLT, seuls les échantillons à haute résistance ont subi l'intégralité du processus de lixiviation; les autres se sont désintégrés. Le pH des lixiviats collectés pendant le TLT est resté inférieur à 10, ce qui indique

que la dissolution de l'ATRW a abaissé le pH de la pâte et a empêché la formation de produits d'hydratation tels que la portlandite, l'ettringite et le gypse. La lixiviation de l'arsenic, du calcium et du sulfate n'a pas atteint un plateau et pourrait se poursuivre au-delà de la période de lixiviation de 64 jours. Le principal mécanisme de lixiviation de l'arsenic dans les échantillons de RPC étudiés a été identifié comme étant le lessivage de surface, avec un certain degré d'épuisement. Les résultats des tests UCS et de lixiviation ont indiqué que l'inclusion d'ATRW pourrait apporter une certaine résistance, en particulier dans les échantillons ayant des teneurs en liant et en solides plus élevées. Cependant, la libération d'arsenic, principalement à partir de la surface des RPC, pourraient être importants, même dans les échantillons à haute résistance. Le principal produit d'hydratation identifié était des gels de C-S-H à teneur réduite, attribués au pH plus faible de la pâte. De plus, aucune liaison chimique entre l'arsenic et le calcium n'a été observée dans les échantillons à haute résistance, qui présentaient des volumes de pores plus élevés et des sphéricités plus faibles. Sur la base de ces résultats, il a été conclu que l'incorporation d'ATRW dans le RPC nécessite des modifications préliminaires pour réduire la solubilité de l'arsenic et minimiser les surfaces exposées du RPC sujettes au lessivage.

ABSTRACT

The former Giant Mine located approximately five kilometers north of Yellowknife on Great Slave Lake in the Northwest Territories (NWT), Canada, operated from 1948 until 2004. During its operation, the mine processed gold ore, with some ore sent off-site for processing between 1999 and 2004. The gold extraction process involved roasting arsenic-bearing minerals, which produced arsenic trioxide roaster waste (ATRW) dust. Approximately 237,000 tonnes of this dust were generated and stored underground in fifteen purpose-built chambers and mined-out stopes. Additionally, more than 17 million tonnes of tailings were produced and stored in tailings ponds. The ATRW dust, containing around 60% arsenic, poses significant health and environmental hazards due to its high toxicity and carcinogenic properties. Managing the substantial quantity of ATRW dust is challenging due to its fine particulate nature and storage conditions. To address this, an integrated approach assessed over 50 technologies or methods, identified the "Frozen Block" method as the most viable solution. This method stabilizes the dust by freezing the ground around the storage chambers and stopes. Initially considered a temporary measure with a lifespan of up to 100 years, this method does not remove the arsenic, leaving it chemically unstable and soluble, which could lead to potential release if the frozen block thaws due to neglected maintenance. Climate change and global warming further complicated the situation, presenting significant challenges to the environment, economy, and politics, particularly for residents of NWT. The presence of open-pit mining and extensive underground workings in the area has also disrupted the region's discontinuous permafrost. Consequently, mine authorities suggest that a combination of methods may be necessary for the permanent management of the ATRW dust.

Various technologies have been employed to manage arsenic-bearing wastes and soils and sediments contaminated with arsenic. Among these, solidification and stabilization are promising techniques that use binding agents to encapsulate hazardous waste, reducing its mobility and leaching. One notable solidification and stabilization method is the cemented paste backfill (CPB) technology. This method involves creating a high-density paste from dewatered tailings, binding agents, and water, which is thickened to prevent settling and is then transported into mined cavities. CPB offers environmental benefits by safely depositing hazardous mill tailings, such as sulfide tailings, and other contaminated mine wastes into underground openings. This approach mitigates environmental impacts and reduces surface disposal and reclamation costs. The hydraulic binders

used in CPB can react during hydration with metals and metalloids, particularly arsenic, leading to the formation of stable compounds through precipitation.

Previous research on arsenic fixation within CPBs is limited, and the use of ATRW in CPBs had not been explored before. The primary objective of this study was to assess the feasibility of incorporating ATRW dust into CPBs to stabilize arsenic and reduce its leachability. To achieve this goal, selecting the appropriate binder(s) and mixing ratios was crucial to produce CPB samples with minimal leachability and adequate mechanical strength. In this study, various materials were used, including tailings and ATRW dust from Giant Mine, five different binders (general use (GU) cement, and mixtures of GU with fly ash (FA), slag, lime (LI), and lime kiln dust (LKD) in different percentages), pure silica mimicking tailings, pure arsenic trioxide, and deionized (DI) water. The tailings and ATRW dust from Giant Mine were transported to the laboratory, prepared, and homogenized for characterization and use in the tests. Before determining the suitable binders and mixing ratios, the physical, chemical, and mineralogical characteristics of the ATRW dust and tailings from Giant Mine, as well as the potential binders and other materials, were evaluated. These characteristics significantly impact the mechanical properties, leachability, hydraulic conductivity, and microstructure of the CPB samples.

As the initial phase of this study, preliminary analyses were conducted to examine the effects of incorporating pure arsenic trioxide on the geomechanical and geochemical properties of CPBs. The preliminary CPB samples were prepared in two batches. In the first batch, three binding agents (GU cement, GU/FA, and GU/slag) were used with 10% binder and 15% reagent-grade pure As_2O_3 , along with pure ground silica (Sil-Co-Sil[®]), Giant Mine tailings, and DI water. These samples were prepared under undrained conditions and cured for up to 96 days. Based on the unconfined compressive strength (UCS) results from the first batch, the second batch of samples were prepared using Sil-Co-Sil[®] as tailings, 5% GU cement as binder, DI water, and varying As_2O_3 percentages (0, 5, 10, and 15%) under drained conditions. These samples were cured for up to 28 days, with UCS tests performed after 7 and 28 days. To evaluate the geochemical behavior of the pastes, mixtures of GU cement, pure As_2O_3 (0 to 15%), and DI water were prepared in the same proportions as the CPB samples and mixed for up to 28 days. The pH, electrical conductivity (EC), and chemical composition of the mixtures were then assessed. Additionally, the microstructure of the CPBs and As_2O_3 -cement mixtures was analyzed using scanning electron microscopy (SEM). Results of the first batch of the preliminary samples revealed that UCS of samples containing pure

As_2O_3 was significantly lower compared to samples without As_2O_3 , especially for the GU/slag binder. While GU/slag samples without As_2O_3 exhibited the highest strength, those with As_2O_3 showed notably weaker strengths, with no setting observed even after 96 days. Samples with pure GU binder containing As_2O_3 displayed the highest UCS, followed by GU/FA samples. In most cases, extending the curing time from 28 to 96 days resulted in higher UCS for the samples. For samples without As_2O_3 , GU and GU/FA samples with pure silica exhibited higher UCS than those with tailings, whereas GU/Slag samples with tailings showed significantly higher UCS. Results from the second batch indicated that adding pure As_2O_3 (as a partial substitution for pure silica) substantially decreased the mechanical strength of the CPB samples, with the most significant reduction observed at 5% arsenic content. The strength of As_2O_3 -containing samples did not improve significantly after 7 days of curing, primarily due to a drop in pH (below 10.5) and likely due to delays and inhibition in hardening during the early curing stage. SEM analysis confirmed the formation of some calcium-silicate-hydrate (C-S-H) gels containing arsenic, as well as complex mixtures of oxides in the As_2O_3 -cement mixtures.

In the second phase of this study, CPB samples with varying mixing proportions were prepared to identify the key parameters influencing strength, utilizing response surface methodology (RSM). The physical stability of the CPB was assessed using UCS test, while saturated hydraulic conductivity and computed tomography (CT) analyses provided a detailed evaluation of the CPB microstructure. Initially, small CPB samples were prepared to identify the most effective binders and the optimal percentage of ATRW dust. These samples used 5% of four different binding agents (GU, GU/FA, GU/LI, and GU/LKD) with various ATRW dust contents (4% to 14%), Giant Mine tailings, and DI water. After curing and testing these samples at 7 and 28 days, two binding agents (GU and GU/LKD) and 10% ATRW dust were identified as the best conditions for preparing the main CPB samples. These main samples were cast with various mix designs (differing in solid content, binder content, and curing times) and their mechanical strength was evaluated. The results indicated that CPB samples prepared with GU cement had significantly greater strength compared to those with the GU/LKD mixture. For both binder types, the highest strength was achieved in samples containing 6% binder and 76% solids, with values of approximately 491 kPa and 531 kPa for GU, and 214 kPa and 213 kPa for GU/LKD, after 28 and 90 days, respectively. Investigating the interactions among the independent variables provided deeper insight into how these variables affected the dependent ones. Binder content and solid content were found to be the most significant,

while curing time had a negligible effect. Higher binder and solid contents were associated with higher UCS values in the CPB samples. Adding 10% ATRW to the tailings reduced the UCS of CPB samples by more than 30%, particularly in samples with lower binder and solid contents. While microstructure differences were not detectable through saturated hydraulic conductivity experiments, CT scan observations revealed that the formation of high-density arsenic-containing materials was significantly greater in samples with the highest UCS, especially those prepared with GU binder.

In the third phase of this study, six CPB recipes were selected for monolithic tank leaching (TLT) tests: two recipes with the highest UCS and four recipes with mid-range UCS. Microstructural analyses, including thermogravimetry (TG), X-ray absorption spectroscopy (XAS), Fourier-transform infrared spectroscopy (FTIR), and computed tomography, were conducted to examine the microstructure of these CPB samples. The goal was to investigate the relationship between their strength, leaching behavior, and pore characteristics. During the TLT tests, only the high-strength samples endured the entire leaching process, while the others disintegrated. The pH of the leachates collected during TLT remained below 10, indicating that ATRW dissolution lowered the paste's pH and hindered the formation of hydration products such as portlandite, ettringite, and gypsum. The leaching of arsenic, calcium, and sulfate did not reach a plateau and could continue beyond the 64-day leaching period. The primary leaching mechanism for arsenic in the CPB samples studied was identified as surface wash-off, with some extent of depletion. Results from UCS and leaching tests indicated that including ATRW could provide some strength, particularly in samples with higher binder and solid contents. However, arsenic release, primarily from the surface of CPBs, could be substantial, even in high-strength samples. The main hydration product identified was C-S-H gels at a relatively low content, attributed to the low pH of the paste. Furthermore, no chemical bonding between arsenic and calcium was observed in the high-strength samples, which exhibited higher pore volumes and lower sphericities. Based on these findings, it was concluded that incorporating ATRW into CPBs requires preliminary modifications to reduce arsenic solubility and minimize exposed CPB surfaces prone to leaching.

TABLE OF CONTENTS

DEDICATION	III
ACKNOWLEDGEMENTS	IV
RÉSUMÉ.....	VI
ABSTRACT	XI
TABLE OF CONTENTS	XV
LIST OF TABLES	XIX
LIST OF FIGURES.....	XXII
LISTE OF SYMBOLS AND ABBREVIATIONS	III
LIST OF APPENDICES	IX
CHAPTER 1 INTRODUCTION.....	1
1.1 Context	1
1.2 Research background	2
1.3 Objectives of the study	3
1.4 Hypothesis of the study.....	3
1.5 Structure of the document	4
CHAPTER 2 THEORY OF THE PROJECT AND LITERATURE REVIEW	5
2.1 Introduction.....	5
2.2 Gold mining.....	6
2.3 Ore processing and dust production at the Giant Mine.....	7
2.3.1 Ore processing.....	7
2.3.2 ATRW dust production and management.....	12
2.4 Closure options for ATRW dust at the Giant Mine	15
2.5 Previous work on ATRW dust stabilization at the Giant Mine.....	18

2.5.1	Cement-encapsulated samples.....	18
2.5.2	Bitumen-encapsulated samples.....	20
2.6	Arsenic geochemistry related to roaster waste.....	21
2.7	Solidification and stabilization process.....	24
2.7.1	Solidification and stabilization mechanisms.....	25
2.7.2	Arsenic solidification and stabilization.....	29
2.8	Cemented paste backfilling of arsenic-bearing materials.....	34
2.8.1	The quality criteria of CPBs.....	37
2.8.2	Arsenic stabilization in cemented paste backfills.....	50
2.9	Design of Experiments (DOE).....	55
2.9.1	Factorial design.....	56
2.9.2	Response surface methodology (RSM).....	57
2.9.3	Applicability of the RSM in cemented paste backfills.....	65
2.10	Research needs.....	66
CHAPTER 3 EXPERIMENTAL PROCEDURE.....		67
3.1	Cemented paste backfilling of ATRW dust.....	67
3.1.1	Preparation, homogenization, and sampling of ATRW dust and tailings.....	67
3.1.2	Other materials (binding agents, pure silica and pure As ₂ O ₃).....	74
3.2.1	Physical characteristics.....	75
3.2.2	Chemical Analyses.....	76
3.2.3	Mineralogical analysis.....	76
3.2.4	Cemented paste backfill preparation and curing.....	77
3.2.5	Slump measurement.....	83
3.2.6	Strength of the CPB samples.....	85

3.2.7	Hydraulic conductivity of the CPB samples	86
3.2.8	Monolithic Tank leaching test.....	86
3.2.9	Arsenic trioxide solubility in cement buffering solution	88
3.3	Parallel extraction tests on synthetic CPB samples, ATRW dust and tailings of the Giant Mine 89	
3.3.1	Characterization of the stabilized arsenic compounds	91
CHAPTER 4 RESULTS.....		97
4.1	Characterization results	97
4.1.1	Physical characteristics	97
4.1.2	Chemical characterization.....	98
4.1.3	Mineralogical composition.....	99
4.2.1	Binder selection.....	99
4.2.2	Behaviour of simplified CPB: silica as tailings, and pure As ₂ O ₃ as ATRW (Article 1) 102	
4.2.3	Arsenic trioxide solubility in cement buffering solution	109
4.3	Studies using Giant mine ATRW and tailings	114
4.3.1	Determination of optimal ATRW content in CPB	114
4.3.2	Strength development in CPB samples prepared with Giant Mine ATRW and tailings (Article 2)	115
4.4	Pore structure of CPBs	131
4.4.1	Saturated hydraulic conductivity.....	131
4.4.2	CT scanning.....	132
4.5	Leaching analysis (Article 3)	141
4.6	Characterisation of bonds within CPB	151
4.6.1	Thermogravimetric analysis.....	151

4.6.2	FTIR analysis	153
4.6.3	XAS analysis	155
4.7	Parallel extraction tests on synthetic CPB samples, ATRW dust and tailings of the Giant Mine 157	
CHAPTER 5	DISCUSSIONS	160
CHAPTER 6	CONCLUSIONS AND RECOMMENDATIONS	165
6.1	Conclusions	165
6.2	Recommendations for future works	168
REFERENCES	170
APPENDIX A	COMPLEMENTARY LITERATURE REVIEWS	207
APPENDIX B	ARTICLE 1: THE EFFECTS OF ARSENIC TRIOXIDE ADDITION ON THE MECHANICAL AND GEOCHEMICAL PROPERTIES OF THE CEMENTED PASTE BACKFILL	252
APPENDIX C	ARTICLE 2: GEOMECHANICAL ASPECTS OF STABILIZING ARSENIC TRIOXIDE ROASTER WASTE IN CEMENTED PASTE BACKFILL AT THE GIANT MINE, CANADA	279
APPENDIX D	ARTICLE 3: STUDY ON THE LEACHING BEHAVIOR OF CEMENTED PASTE BACKFILL CONTAINING ARSENIC TRIOXIDE ROASTER WASTE (ATRW) ...	325
APPENDIX E	ARTICLE 4: STUDY OF THE EFFECTS OF ARSENIC TRIOXIDE ROASTER WASTE DUSTS ON THE MECHANICAL BEHAVIOUR OF CEMENTED PASTE BACKFILLS	367
APPENDIX F	ARTICLE 5: ARSENIC SPECIATION IN CEMENTED PASTE BACKFILL USING PARALLEL EXTRACTION	381
APPENDIX G	XAS PARAMETERS	384

LIST OF TABLES

Table 2.1 Solubility of arsenic trioxide dust (SRK, 2002).....	15
Table 2.2 Different categories and their alternatives for long-term arsenic trioxide dust management (Arcadis, 2017)	16
Table 2.3 Unconfined compressive strength and leachate analysis of cement-encapsulated arsenic trioxide dust samples (SRK, 2002)	19
Table 2.4 Leachate results from bitumen encapsulated arsenic trioxide dust samples (SRK, 2002)	20
Table 2.5 Chemical formulae and cement nomenclature for major constituents of Portland cement (Taylor, 1997).....	27
Table 2.6 A summary of studies on the incorporation of arsenic-contaminated materials into the cemented paste backfills.....	52
Table 2.7 Determination of α for rotability.....	63
Table 2.8 Number of runs required by Central Composite and Box-Behnken designs	64
Table 3.1 The identification and amounts of the dust samples	68
Table 3.2 The specifications of the first batch of the preliminary CPB samples	79
Table 3.3 The specifications of the second batch of the preliminary CPB samples	80
Table 3.4 Independent factors and levels of RSM experiments.....	81
Table 3.5 Central composite design in the form of coded and actual values	82
Table 3.6 The specifications of each extraction analysis	90
Table 4.1 Particle size parameters, specific gravity, and specific surface area of ATRW, tailings, pure silica (Sil-Co-Sil [®] 106), and pure As ₂ O ₃	98
Table 4.2 The results of the XRF analysis of the ATRW dusts and tailings samples.....	98
Table 4.3 Chemical analysis results of the dusts and tailings samples by ICP-AES and ICP-MS methods	99
Table 4.4 Chemical analysis of pure silica (Sil-Co-Sil [®] 106).....	99

Table 4.5 Mineral composition determined by XRD for ATRW and tailings samples	100
Table 4.6 Mass of ingredients used for the preparation of the second batch of preliminary CPB samples (Mohammadi, Demers, Benzaazoua, et al., 2023a).....	102
Table 4.7 Slump results for the CPB samples (Mohammadi, Demers, Benzaazoua, et al., 2023a)	103
Table 4.8 Results of the UCS tests on the CPB samples prepared with GU cement and mixture of GU/LKD	116
Table 4.9 Fit summary results of the UCS (response) for the GU and GU/LKD samples	117
Table 4.10 Model summary statistics for the UCS (response) of GU and GU/LKD samples	117
Table 4.11 Coefficients for the quadratic model of UCS for GU and GU/LKD samples	118
Table 4.12 ANOVA results for ATRW dust containing CPB samples prepared using GU and GU/LKD	119
Table 4.13 The UCS of CPB samples without ATRW prepared using GU and GU/LKD binders	127
Table 4.14 Coefficients for the modified quadratic model of UCS for GU and GU/LKD samples	128
Table 4.15 Saturated hydraulic conductivity of CPB samples	131
Table 4.16 The statistical parameters related to the main scalars of the pores in ROI of the CPB samples	138
Table 4.17 Calculated leached mass of each component (E^*_i) during each leaching period	143
Table 4.18 The calculated values encompass the slopes of the regression lines (r_c), their corresponding standard deviations (Sd_{rc}), concentration factors (CF), and the leaching mechanisms for As, Ca, and SO_4^{2-} in the four main samples, based on EA NEN 7375 (EA NEN 7375, 2004)	150
Table 4.19 The observed peaks and their corresponding normalized absorbances	154
Table 4.20 The pH of the solutions before and after extraction using different reagents	158

Table 4.21 Concentration of each arsenic species (As^{3+} and As^{5+}) in the extracted leachates using various reagents.....	159
Table 4.22 Various arsenic-containing minerals in the extracted solutions and their saturation indices based on geochemical modeling.....	159

LIST OF FIGURES

Figure 2.1 Schematic products and waste streams at a metal mine. Figure taken from (Lottermoser, 2010).....	6
Figure 2.2 Giant mine location and layout. Figure taken from (SRK, 2002).....	8
Figure 2.3 A schematic diagram of a fluid-bed roaster. Figure taken from (Thomas & Cole, 2016).....	9
Figure 2.4 Roaster and gas cleaning circuits of Giant mine. Figure taken from (SRK, 2002).....	11
Figure 2.5 Timeline depicting when chambers were filled with arsenic trioxide dust at the Giant Mine. Green bars represent chambers sampled in 2004 SRK drilling program and grey bars represent chambers from which archive samples are not currently available. Figure taken from (SRK, 2002).....	14
Figure 2.6 Illustration of Frozen Block method. Figure taken from (Keeling & Sandlos, 2017).....	17
Figure 2.7 Eh-pH digram for the system As-O-H at 25 °C, 1 bar, and $\sum As = 10^{-6}$ M. Gray shaded area shows the solid phase. Figure taken from (Craw & Bowell, 2014).....	23
Figure 2.8 A SEM image of hardened Portland cement paste. Figure taken from (Soler, 2007).....	28
Figure 2.9 History of mine backfilling technology. Figure taken from (Hustrulid & Bullock, 2001).....	35
Figure 2.10 Schematic diagram illustrating the different components of paste backfill. Figure taken with modifications from (Benzaazoua et al., 2002).....	36
Figure 2.11 A schematic of a typical underground stope filling process. Figure taken from (N. J. F. Koupouli et al., 2016).....	37
Figure 2.12 Intrinsic and extrinsic factors affect the quality of cement tailings backfill. Figure taken from (S. Yin et al., 2018).....	38
Figure 2.13 Schematic diagram of components of CPB and their associated characteristics that affect CPB strength. Figure taken from (Deb et al., 2017).....	39
Figure 2.14 Typical flow curves for different types of non-Newtonian fluids. Figure taken from (Chhabra, 2010).....	43

Figure 2.15 Second-order system displaying contour plot and response surface for a) a maximum, b) a minimum, and c) a saddle point. Figure taken from (Myers, Montgomery, & Anderson-cook, 2016).....	62
Figure 2.16 Central composite design for a) $k = 2$, $\alpha = 1.414$; b) $k = 3$, $\alpha = 1.682$	62
Figure 2.17 Comparison between Box Behnken Design and Central Composite Design with three factors ($k = 3$). Figure taken from (NIST/SEMATECH, 2012)	64
Figure 3.1 A plan of the different steps of the project	68
Figure 3.2 Dust samples preparation and homogenization flowchart.....	69
Figure 3.3 The planetary ball mill with 4 cylinders	69
Figure 3.4 Horizontal roller mill, a) top view, b) front view	70
Figure 3.5 Dust sample B233-P9, a) before, b) after grinding with roller mill.....	70
Figure 3.6 Different steps of homogenization, preparation, and sampling of ATRW dusts, a) rolling at different directions, b) the final row of material, c) sampling from the right end, d) sampling from the left end, e) sampling from the center of the mass.....	71
Figure 3.7 Rotary sample splitter, a) side view that shows the controller, b) front view	72
Figure 3.8 Two representative subsamples for the dust samples, left: a subsample of the odd dust sample, right: a subsample of other eight dust samples	73
Figure 3.9 Excavation and sampling of the tailings at the Giant Mine tailings impoundment.....	73
Figure 3.10 A view of a) two barrels of tailings of the Giant Mine, b) sampling from the whole height of each barrel, c) a view of the hand auger and the collected sample	74
Figure 3.11 Process of the preparation of the preliminary/main CPB samples	78
Figure 3.12 The plan of the preliminary and main CPB samples	79
Figure 3.13 A schematic view of the original Abrams cone and the mini cone. Figure taken from (Jia et al., 2016).....	84
Figure 3.14 The relationship between Abrams cone and mini cone slump measurements	85
Figure 3.15 A view of the UCS test apparatus and data acquisition system.....	85

Figure 3.16 The process of preparation and testing of samples in saturated hydraulic conductivity analysis	86
Figure 4.1 Particle size distribution of ATRW, tailings, pure silica, and pure As ₂ O ₃	97
Figure 4.2 UCS of the first batch of preliminary CPB samples, prepared with both a) Sil-Co-Sil® and b) Giant Mine tailings, with and without pure arsenic trioxide.....	101
Figure 4.3 CPB sample prepared with GU/Slag binder, Sil-Co-Sil® as tailings, and subjected to a 96-day curing process.....	102
Figure 4.4 UCS tests results on the CPB samples with various As ₂ O ₃ contents after 7 and 28 days of curing (Mohammadi, Demers, Benzaazoua, et al., 2023a).....	104
Figure 4.5 Effect of As ₂ O ₃ content on the stress-strain (deformation) behavior of CPB cured for (a) 7 and (b) 28 days (Mohammadi, Demers, Benzaazoua, et al., 2023a)	106
Figure 4.6 Relationship between UCS and modulus of elasticity after (a) 7 days, (b) 28 days (Mohammadi, Demers, Benzaazoua, et al., 2023a)	106
Figure 4.7 Relationship between modulus of elasticity and inverse of strain at break (a) 7 days, (b) 28 days (Mohammadi, Demers, Benzaazoua, et al., 2023a).....	107
Figure 4.8 Variations of (a) EC and (b) pH of the cement-As ₂ O ₃ mixtures versus time for the mixtures with various As ₂ O ₃ contents (Mohammadi, Demers, Benzaazoua, et al., 2023a).....	108
Figure 4.9 Variations of the dissolved elements (As, Sb, Ca, and S) in the cement-As ₂ O ₃ mixtures containing different percentages of arsenic trioxide versus time (Mohammadi, Demers, Benzaazoua, et al., 2023a).....	109
Figure 4.10 Variations of pH and EC of the mixtures with time	110
Figure 4.11 Variations of the concentrations of major elements (As, Ca, S, and Sb) in As ₂ O ₃ and tailings mixtures	111
Figure 4.12 BSE image (a) and semi-quantitative EDS analyses (b) of the various silicate and arsenioferous oxides observed in CPB-5% sample (Mohammadi, Demers, Benzaazoua, et al., 2023a).....	113

Figure 4.13 BSE image (a) and semi-quantitative EDS analyses (b) of the various silicate and arsenioferous oxides observed in 15% As_2O_3 -cement mixture polished section	114
Figure 4.14 The UCS of small CPB samples prepared using various binders after a) 7 days and b) 28 days of curing	115
Figure 4.15 Normal plot of residuals for c) GU and d) GU/LKD samples; and predicted vs. externally studentized residuals of e) GU and f) GU/LKD samples in CCD experiments. .	121
Figure 4.16 Surface plots for the UCS of GU and GU/LKD samples at different curing times: a) GU-28 days, b) GU/LKD-28 days, c) GU-59 days, d) GU/LKD-59 days, e) GU-90 days, and f) GU/LKD-90 days	124
Figure 4.17 Surface plots for the UCS of GU and GU/LKD samples at different binder content: a) GU-4%, b) GU/LKD-4%, c) GU-5%, d) GU/LKD-5%, e) GU-6%, and f) GU/LKD-6%. .	125
Figure 4.18 Surface plots for the UCS of U and GU/LKD samples at different solid contents: a) GU-72%, b) GU/LKD-72%, c) GU-74%, d) GU/LKD-74%, e) GU-76%, and f) GU/LKD-76%.....	126
Figure 4.19 The optimization (prediction and desirability) of a) GU and b) GU/LKD samples for the scenario of all parameters in their initial ranges.....	129
Figure 4.20 The optimization (prediction and desirability) of a) GU and b) GU/LKD samples for the scenario of minimized binder content	130
Figure 4.21 2D greyscale images along the center of each core in both longitudinal and transverse profiles containing the segmented regions (black: pores, white: high-density materials, and gray: CPB matrix) and the location of ROIs	133
Figure 4.22 3D model of each core cut in half lengthwise, displaying each segmented region (blue: pores, yellow: high-density materials, and gray: CPB matrix)	135
Figure 4.23 3D model of each ROI cut in half lengthwise, displaying each segmented region individually (gray: sediment matrix, yellow: high-density materials, blue: pores)	137
Figure 4.24 Pore volume histograms of the ROIs of CPB samples	138
Figure 4.25 Mean Feret diameter histograms of the ROIs of CPB samples	139

Figure 4.26 Sphericity histograms of the ROIs of CPB samples	139
Figure 4.27 The number of different volumes of pores (left) and the distribution of the sphericity of the pores (right).....	140
Figure 4.28 Relationship between sphericity and pore volume	141
Figure 4.29 A view of the samples (with a diameter of 5.2 cm and a length of about 5 cm) after various time intervals (start of the analysis and after 6 hr, 24 hr, and 64 days).....	142
Figure 4.30 Variations in released mass of arsenic, calcium, and sulfate in relation to pH and EC during each TLT extraction.....	145
Figure 4.31 Cumulative released contents of components during TLT; a) arsenic, b) calcium, and c) sulfate	147
Figure 4.32 Depletion curves of As and Ca from the leached samples	149
Figure 4.33 TG and DTG curves of two main CPB samples.....	152
Figure 4.34 FTIR spectra of two CPB samples (dashed lines indicate positions of the observed peaks)	154
Figure 4.35 (a) Normalized As K-edge XANES spectra for four CPB samples and reference compounds; (b) Measured (solid red lines) and modelled (black dashed lines) $\chi(k)$ EXAFS spectra (c) Measured (solid red lines) and modelled (black dashed lines) magnitudes of Fourier transformed EXAFS spectra.....	156
Figure 4.36 Arsenic leached during the parallel extraction experiment using various reagents.	158

LISTE OF SYMBOLS AND ABBREVIATIONS

2D	Two-dimensional
3D	Three-dimensional
A	Area
AAS	Alkali-activated slag
AFm	Alumina-ferric oxide-mono
AFt	Alumina-ferric oxide-tri
AMD	Acid mine drainage
ANOVA	Analysis of variance
ATRW	Arsenic trioxide roaster waste
BA	Bottom ash
BBD	Box-Behnken design
BFS	Blast furnace slag
BOFSS	Basic oxygen furnace steel slag
BSE	Backscattered electron
B _w	Binder percentage
C-(A)-S-H	Calcium-(aluminate)-silicate-hydrate
C2S	Dicalcium silicate
C3A	Tricalcium aluminate

C3S	Tricalcium silicate
C4AF	Calcium aluminoferrite
C_c	Coefficient of curvature
CCD	Central composite design
CF	Concentration factor
C_i	Concentration
CKD	Cement kiln dust
CN	Coordination number
CPB	Cemented paste backfill
CT	Computed tomography
C_u	Coefficient of uniformity
CV	Coefficient of variation
C_w	Solid percentage
DI	Deionized
DOE	Design of experiment
DTG	Derivative thermogravimetry
D_w	Dust percentage
E	Elastic modulus
E^*_i	Leached mass

EC	Electrical conductivity
Eh	Oxidation-reduction potential
EXAFS	Extended X-ray absorption fine structure
FA	Fly ash
FE-SEM	Field emission scanning electron microscopes
FGBFS	Finely-ground blast furnace slag
FGDG	Flue gas desulfurization gypsum
FTIR	Fourier transform infrared spectroscopy
GGBFS	Ground granulated blast-furnace slag
G _s	Specific gravity
GU	General use
HDPE	High density poly ethylene
IC	Ion chromatography
ICP-AES	Inductively coupled plasma atomic emission spectroscopy
ICP-MS	Inductively coupled plasma mass spectrometry
k _{sat}	Saturated hydraulic conductivity
LI	Lime
LKD	Lime kiln dust
MCL	Maximum contaminant level

MIP	Mercury intrusion porosimetry
NMR	Nuclear magnetic resonance
OPC	Ordinary Portland cement
PAS	Polyaluminium sulfate
pH	Power of Hydrogen
ppm	Part per million
PSD	Particle size distribution
r	Interatomic distance
R ²	Coefficient of determination
r _c	slope of the regression line
ROI	Region of interest
RSM	Response surface methodology
S	Sphericity
S/S	Solidification and stabilization
S ₀ ²	Amplitude reduction factor
SAFA	Silico-aluminous fly ash
SCM	Supplementary cementitious materials
SD	Standard deviation
SD _{rc}	Standard deviation in TLT test

SEM	Scanning electron microscopy
SEM-EDS	Scanning electron microscopy energy dispersive X-ray spectroscopy
SF	Silica fume
SRPC	Sulfate-resistant Portland cement
TCLP	Toxicity characteristic leaching procedure
TERRE-NET	Toward environmentally responsible resource extraction
TG	Thermogravimetry
TLT	Tank leaching test
T_w	Tailings percentage
UCS	Unconfined compressive strength
V	Volume
W/C	Water to cement ratio
WHO	World health organization
XANES	X-ray absorption near edge structure
XAS	X-ray absorption spectroscopy
XRD	X-ray diffraction
XRF	X-ray fluorescence
γ	Shear rate
ΔE_0	Energy shifts

ϵ	Strain
ϵ_n^*	Cumulative leached mass
ϵ_n	Derived cumulative leached mass
η	Dynamic viscosity
σ	Normal stress
σ^2	Debye–Waller factor
τ	Shear stress
τ_0	Shear yield stress

LIST OF APPENDICES

APPENDIX A COMPLEMENTARY LITERATURE REVIEWS.....	207
APPENDIX B ARTICLE 1: THE EFFECTS OF ARSENIC TRIOXIDE ADDITION ON THE MECHANICAL AND GEOCHEMICAL PROPERTIES OF THE CEMENTED PASTE BACKFILL	252
APPENDIX C ARTICLE 2: GEOMECHANICAL ASPECTS OF STABILIZING ARSENIC TRIOXIDE ROASTER WASTE IN CEMENTED PASTE BACKFILL AT THE GIANT MINE, CANADA.....	279
APPENDIX D ARTICLE 3: STUDY ON THE LEACHING BEHAVIOR OF CEMENTED PASTE BACKFILL CONTAINING ARSENIC TRIOXIDE ROASTER WASTE (ATRW)...	325
APPENDIX E ARTICLE 4: STUDY OF THE EFFECTS OF ARSENIC TRIOXIDE ROASTER WASTE DUSTS ON THE MECHANICAL BEHAVIOUR OF CEMENTED PASTE BACKFILLS.....	367
APPENDIX F ARTICLE 5: ARSENIC SPECIATION IN CEMENTED PASTE BACKFILL USING PARALLEL EXTRACTION.....	381
APPENDIX G XAS PARAMETERS.....	384

CHAPTER 1 INTRODUCTION

1.1 Context

In numerous countries, the exploitation of mineral resources holds substantial significance for economic growth, employment, and infrastructure development. Following the extraction of resources from the Earth, the material undergoes processing to extract its valuable components. Mining operations generate a substantial volume of mine wastes, including tailings and dust, constituting the most substantial portion of waste produced by industrial activities. The term "mine waste" suggests that the material lacks current economic value and is an undesired by-product of mining. Nonetheless, it is acknowledged that certain mine wastes can be beneficial, a realization dating back to the early stages of mining and smelting. The properties of wastes generated at different mines vary significantly. Each mine produces its distinct waste, necessitating individual characterization, prediction, monitoring, treatment, and secure disposal. Mine wastes are commonly classified based on their physical and chemical properties, as well as their source (Lottermoser, 2010).

Mine wastes typically contain metals and metalloids, and their release can have impacts on soil, sediment, water quality, as well as ecosystem and human health (Williams et al., 2006). Therefore, the surface disposal of these wastes is not only a significant expense but can also lead to potential long-term environmental issues, such as acid mine drainage (AMD) (Ghirian & Fall, 2016; Tariq & Yanful, 2013). Mining activities can also induce distinct alterations in the topography, hydrology, and stability of a landscape. Upon the end of mining operations, both the mined land and its waste deposits require rehabilitation. The rehabilitation of mine sites should be seamlessly integrated throughout the entire mining process, encompassing planning, development, and final closure stages.

Cementitious solidification and stabilization (S/S) is one of the employed methods for treating and ultimately disposing of hazardous wastes from mining. Cementitious materials are favored due to their cost-effectiveness, compatibility with various disposal scenarios, and capacity to meet stringent processing and performance standards (USEPA, 1996). This treatment plays a crucial role in safeguarding human health and the environment by immobilizing contaminants within the treated material, thus preventing their migration to human, animal, and plant receptors (Wilk, 2004).

The conventional storage of tailings in tailings impoundments has led to significant issues, including dam breakage accidents and environmental contamination. In reaction to these challenges, tailings and other mine wastes are commonly employed as backfill materials to fill underground stopes (D. Wu, 2020). This disposal method has been a staple in the mining industry for over a century (Lottermoser, 2010).

Cemented paste backfill (CPB) is a carefully engineered mixture comprising dewatered tailings (typically consisting of fine silt-size particles) from the milling or processing operation of the mine, water, and hydraulic binders, containing between 70% and 85% solids by weight. Hydraulic binders, such as Portland cements, lime, pulverized fly ash, and blast furnace slag, act as binding agents, creating cohesive strength within the CPB. This allows exposed fill faces to become self-supporting when adjacent stopes are extracted (Belem & Benzaazoua, 2008). Over the past few decades, CPB technology has gained increasing application in revitalizing mined cavities in underground mine operations due to its cost-effectiveness and superior mechanical performance compared to other backfilling methods, such as rock fills and hydraulic fills (Fall et al., 2010; Yue Zhao, Soltani, et al., 2019). Some researchers have recognized CPB as a method to manage or restrict the development of acid rock drainage and the migration of metals, metalloids, and other contaminants (Arcadis, 2017; Hamberg et al., 2015b; MEND, 2006). In this project, the effectiveness of this method in managing arsenic trioxide roaster waste (ATRW) dust was evaluated.

1.2 Research background

The Giant Mine, situated in Yellowknife, Northwest Territories, was a gold producer from 1948 until 1999. Following this period, the mine continued operating until 2004, during which the gold ore was shipped offsite for processing. When operations ended, the Government of Canada took over as the site custodian. The processing of Giant Mine ore resulted in a substantial production of ATRW dust as a by-product. Roughly 237,000 tonnes of this dust were generated and stored underground in fifteen purpose-built chambers and mined-out stopes. The dust contains approximately 60% arsenic. To prevent the release of arsenic into the groundwater surrounding the mine, the ATRW dust and the rock surrounding each chamber and stope are kept frozen (SRK, 2007). However, concerns about the long-term effectiveness of this method, the risks associated with storing such toxic waste, and the significant impact of global warming on permafrost have

compelled mine authorities (the Government of Canada, through Crown-Indigenous Relations and Northern Affairs Canada, CIRNAC) to explore more permanent solutions. The Giant Mine Oversight Board (GMOB) was established as an independent organisation that manages research funds to provide insights on the remediation of the Giant Mine. Previous studies on the treatability of arsenic compounds through cement stabilization have indicated that it is possible to effectively stabilize high arsenic-containing material using cement stabilization and solidification. The CPB method combines the physical and chemical encapsulation of cement stabilization, while offering a means for emplacement within the subsurface (Arcadis, 2017). Existing studies on immobilizing ATRW dust from the Giant Mine had not thoroughly explored the application of cemented paste backfill. While this method has demonstrated good performance in stabilizing arsenic compounds, its applicability for stabilizing ATRW dust specifically has not been thoroughly investigated. Additionally, there is limited research on the initial release or washout of arsenic from the cemented paste backfills, and its long-term performance requires evaluation.

1.3 Objectives of the study

The primary goal of this research project was to evaluate the efficacy of stabilizing arsenic by incorporating ATRW into cemented paste backfill, offering a potentially effective solution for safely and permanently managing ATRW dust. The specific objectives of this project were as follows: i) identifying the most effective binders and optimizing their proportions for the long-term stabilization of ATRW dust, ii) optimizing the content of dust and tailings within the CPB samples, and iii) elucidating the arsenic speciation and stabilization mechanisms occurring during the cement hardening and curing processes, along with their respective impacts on leaching properties.

1.4 Hypothesis of the study

The main hypothesis of this research suggested that adding ATRW dust to cemented paste backfill could securely stabilize the dust permanently, ensuring mechanical stability for the stopes and minimizing arsenic leaching into nearby waters. While some studies have explored the stabilization of arsenic compounds within cemented paste backfills, the specific stabilization mechanisms of ATRW dust have not been previously investigated. Furthermore, given that the ATRW dusts from the Giant Mine are not comprised solely of arsenic trioxide, the presence of other constituents and impurities may influence the solubility and stabilization efficacy of the arsenic trioxide.

1.5 Structure of the document

This thesis comprises six chapters. Chapter one provides introductory information, including the project's objectives, hypothesis, and overall structure. Chapter two delves into the theoretical framework and literature reviews, covering various aspects of mine waste production and management, particularly in gold mines, the production process of ATRW dust at the Giant Mine and previous management practices for this hazardous material. It explores processes related to arsenic management in mine wastes, mechanisms of solidification and stabilization for contaminants, and their applicability to arsenic-containing materials. Additionally, this chapter examines cemented paste backfill technology, the influence of different parameters on its quality, and previous studies on arsenic stabilization within CPB. Chapter three focuses on the processes of preparing and characterizing Giant Mine wastes (ATRW dust and tailings) and other materials for CPB sample preparation. It also details the procedures for preliminary and main prepared CPB samples and outlines the required mechanical, leaching, hydraulic conductivity, microstructural, and environmental characterization tests on the CPB samples and other ATRW dust-containing mixtures. In chapter four, the results of initial characterization, mechanical, geochemical, hydraulic conductivity, and microstructural analyses on the prepared CPB samples and ATRW dust-containing mixtures are presented and discussed. Complementary tests conducted to study the behavior of ATRW dust and Giant Mine tailings in various environmental conditions are covered at the end of chapter four. The findings of the thesis are then integrated and discussed in chapter five to address all project objectives. Finally, chapter six provides concluding remarks and recommendations for future projects. Appendices contain a summary of the literature review and published and submitted articles based on the project findings as well as a summary of the XAS statistical analysis results.

CHAPTER 2 Theory of the project and literature review

2.1 Introduction

The mining industry plays a significant role in the global economy by offering a wide range of mineral products to industrial consumers. This industry encompasses mining, mineral processing, and metallurgical extraction operations. Mining involves the commercial exploitation of minerals or energy resources, characterized by extracting material from the ground to recover one or more mined material components. Mineral processing aims to separate and concentrate the ore mineral(s), while metallurgical extraction is employed to break the crystallographic bonds of ore minerals to recover the desired element or compound. Various forms of mineral processing, such as crushing, grinding, gravity, magnetic or electrostatic separation, and flotation, are typically associated with mining operations at mine sites. These processes may also be accompanied by metallurgical extraction techniques for materials like gold, copper, nickel, uranium, or phosphate, including roasting, heap leaching, or in situ leaching (Lottermoser, 2010).

The mining and mineral processing industry generates a substantial volume of processed materials and produces numerous wastes. Managing solid wastes and wastewaters produced and disposed of at modern mine sites is challenging due to their hazardous nature, containing materials such as heavy metals, metalloids, radioactive substances, acids, and process chemicals. These materials necessitate monitoring, treatment, and secure disposal, as they accumulate in large volumes at mine sites. The physical and chemical characteristics of mining wastes depend on factors such as mineralogy, geochemistry, type of mining equipment, particle size of mined material, and water content. Similarly, the physical and chemical properties of processing wastes vary based on the mineralogy and geochemistry of the treated material, type of processing technology, particle size of crushed material, and process chemicals involved. However, not all mine wastes are problematic or require monitoring or treatment. Many of them do not contain or release contaminants, are inert or benign, and pose no environmental threat (Lottermoser, 2010). Figure 2.1 illustrates a schematic of the product and waste stream in a metal mine.

The mining and milling of sulfide ores result in the generation of significant quantities of sulfide-rich mine wastes and mill tailings. These wastes/tailings are typically abundant in pyrite and pyrrhotite and contain toxic metals and metalloids such as arsenic (As), copper (Cu), and zinc (Zn) (Ercikdi, Cihangir, et al., 2009). When exposed to the atmosphere or oxygenated groundwater, the

sulfides undergo oxidation, leading to the production of acidic water containing sulfate, heavy metals, and metalloids. Pyrite (FeS_2) is often the predominant sulfide mineral present, and its weathering at mine sites gives rise to the most substantial environmental challenge faced by the industry today – acid mine drainage (Lottermoser, 2010). The production of AMD releases a significant amount of acid and other hazardous constituents, such as sulfate and heavy metals, which have severe impacts on the ecosystem (Genty et al., 2012; Yılmaz et al., 2020). Consequently, finding effective and economically viable ways to mitigate the environmental impacts of AMD has always been a primary concern for all mining operations (Abdul-Hussain & Fall, 2011; Orejarena & Fall, 2008).

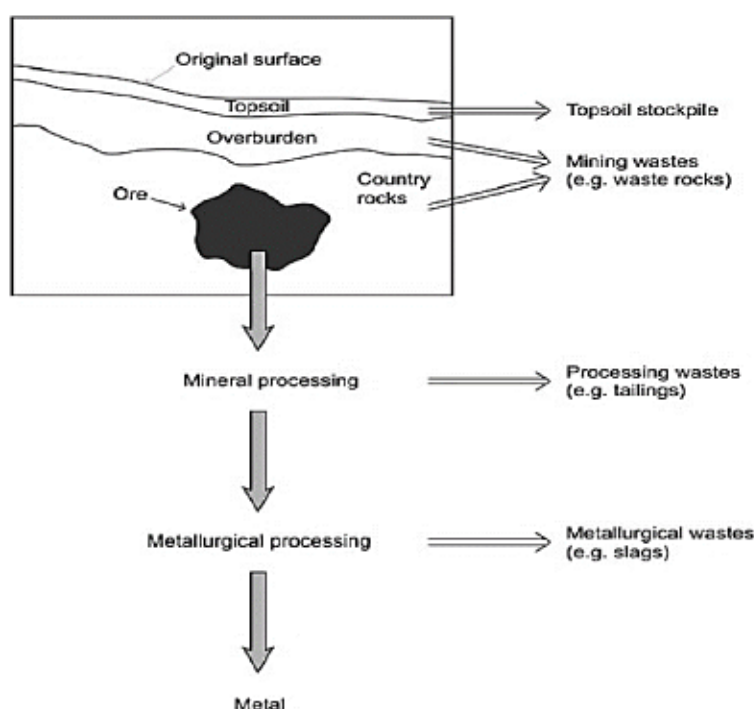


Figure 2.1 Schematic products and waste streams at a metal mine. Figure taken from (Lottermoser, 2010)

2.2 Gold mining

Gold mining and extraction boast a history spanning over 3000 years. In centuries past, a significant portion of gold was extracted through physical concentration of gold particles and mercury usage. However, since the late 19th century, mercury has ceased industrial use due to the development of cyanide leaching, which facilitated large-scale gold mining operations (Lottermoser, 2010). Gold is found in various geological environments, with estimates suggesting an average content in the

Earth's crust ranging from 0.003 to 0.004 parts per million (ppm). Economically recoverable deposits, determined by factors such as total reserve, mining method, and the geological setting of the deposit, may contain concentrations ranging from 0.69 to 1.37 ppm (equivalent to 0.02 to 0.04 troy ounces of gold per tonne of rock). Geological processes play a crucial role in concentrating gold into minable ore deposits. With the exception of placer deposits, all other gold deposits are formed through hydrothermal processes (USEPA, 1994). Combinations of different types of hydrothermal systems within various host rocks lead to variations in deposit morphology, grade ranges (variations in gold content), and alteration of wall rocks. The mineral composition of a deposit is determined by reactions between hydrothermal solutions and the surrounding wall rock. The chemistry of the wall rock, solution, temperature, and pressure are the most significant factors influencing this process. Most gold ores contain some sulfur-bearing minerals, while carbonate deposits may also contain carbonaceous material (USEPA, 1994).

2.3 Ore processing and dust production at the Giant Mine

2.3.1 Ore processing

The former Giant Mine is situated on Great Slave Lake, approximately five kilometers north of Yellowknife, in the Northwest Territories, Canada (Figure 2.2). Gold in the ore was closely associated with arsenic-bearing minerals, and the extraction process involved roasting, which also generated arsenic trioxide dust (SRK, 2002). The Giant Mine is located within altered metavolcanic rocks of the Archean Yellowknife greenstone belt. Mineralization occurs as disseminated wall-rock and subordinate vein deposits, extending 6.5 km along strike. Unlike typical mesothermal deposits, it has a limited vertical extent of approximately 600 m and unusually high concentrations of Sb and As (Van Hees et al., 1999). The ore had a complex mineral composition, with the majority of gold contained within arsenopyrite (FeAsS) and arsenian pyrite (FeS_2), necessitating an oxidation process to expose the gold for cyanide leaching solutions. The primary method for processing refractory arsenical gold ores, including those at Giant Mine, involved high-temperature roasting followed by conventional cyanidation and Merrill Crowe precipitation (Northwest Consulting Limited, 2003). Over the years, the processing plant at Giant Mine underwent various modifications and upgrades, with treatment methods including amalgamation, flotation, cyanidation, fluo-solids roasting, and activated carbon. From 1962 until closure in 1999, the milling

process remained largely unchanged, with only minor adjustments made to accommodate ore chemistry variations (Silke, 2013).

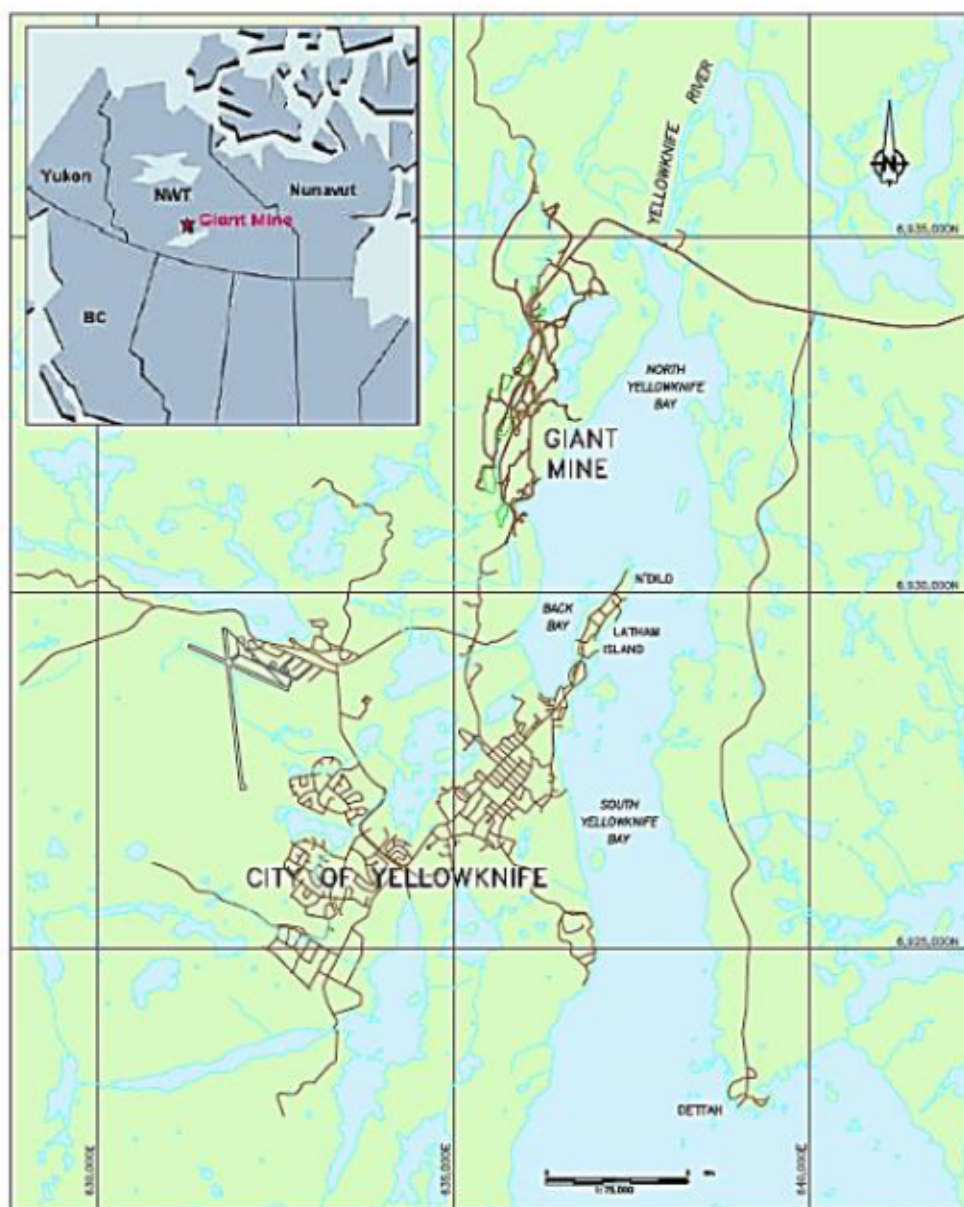


Figure 2.2 Giant mine location and layout. Figure taken from (SRK, 2002)

Following the crushing and grinding of the ore to around 80% -200 mesh, the ore sulfides were concentrated through flotation to approximately 10% of the original ore weight. This concentration ratio was regulated to achieve a sulfur concentration of approximately 17%, which was necessary to sustain autogenous roasting conditions (Northwest Consulting Limited, 2003).

Before cyanidation of the flotation concentrate, it was imperative to undergo physical and chemical breakdown of the sulfide minerals. This was achieved through a two-stage fluo-solids roasting process conducted at high temperatures. The primary objective of the roasting process was to generate porous particles by volatilizing arsenic, sulfur, and antimony, thereby exposing the fine gold (Silke, 2013). The roasting of Fe-sulfide-rich flotation concentrate led to the oxidation of the Fe-sulfides into nanocrystalline, micro-porous Fe-oxides, predominantly maghemite ($\gamma\text{Fe}_2\text{O}_3$) and hematite (Bromstad et al., 2017a).

Two-stage roasters are typically utilized for arsenopyrite ores, while one-stage roasters are preferred for pyritic ores (Thomas & Cole, 2016). A cross-section of a fluidized-bed roaster, such as the one at the Giant Mine, is depicted in Figure 2.3.

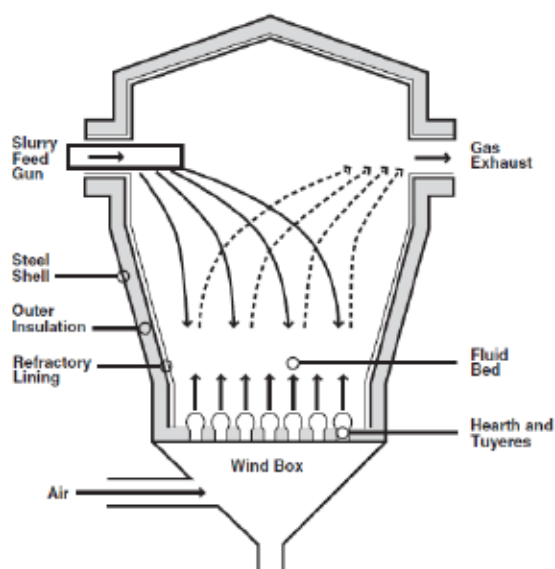


Figure 2.3 A schematic diagram of a fluid-bed roaster. Figure taken from (Thomas & Cole, 2016)

The rationale for employing two-stage roasters can be elucidated by examining process chemistry. Initially, arsenic is volatilized, diffusing through the expanded, heated arsenopyrite lattice. Subsequently, a blend of hematite and magnetite is generated:



In the presence of oxygen, the volatilized arsenic undergoes rapid oxidation, resulting in the formation of arsenic trioxide:



It is imperative to prevent the formation of arsenic pentoxide (As_2O_5). If the reaction between hematite and arsenic pentoxide takes place, it results in the formation of a nonporous ferric arsenate. This compound tends to trap the gold in the calcine, hindering subsequent gold recovery through cyanidation:



The calcine, which is the product of the roasting process, ideally should exhibit a chocolate brown color to facilitate cyanidation. This color can be attained by producing a calcine composed of approximately 80% hematite (Fe_2O_3) and 20% magnetite (Fe_3O_4). This indicates that complete or near-complete sulfide oxidation has been achieved (Thomas & Cole, 2016):



As depicted in Figure 2.4, following the flotation process, the roasting of the bulk arsenopyrite concentrate occurred in two stages: the initial stage involved partial oxidizing conditions aimed at volatilizing the arsenic at 500 °C, while the subsequent stage, also at 500 °C, constituted an almost complete oxidizing roast to oxidize sulfur and produce a porous calcine conducive to cyanidation (Thomas & Cole, 2016). The first stage reactor, commonly referred to as the arsenic elimination stage (Equations 2.1 to 2.4), facilitated the partial oxidation of arsenic in the arsenopyrite at elevated temperature (500 °C), leading to the release of sulfur as gaseous sulfur dioxide (Silke, 2013). The dust-laden gas from this stage exited through a fluo-seal and airlift arrangement into the second stage roaster compartment, known as the oxidation stage. Both stages operated in an autogenous manner, deriving fuel from the sulfur present in the concentrate. Air was injected into the second stage roaster through tuyeres, creating a complete oxidizing atmosphere to promote the formation of volatile arsenic oxide and convert magnetite to hematite. The dust-laden roaster gases

were directed to cyclones, where underflows were water-quenched and merged with the bed calcine. The remaining calcine dust and gas exited the cyclones at 470 °C and underwent air tempering to 370 °C before entering the Cottrell precipitator for dust collection (Silke, 2013).

The calcines were gathered from the discharge of the roaster bed and from cyclones designed for dust collection situated along the roaster exhaust ducting. Following water quenching and subsequent ball milling, the calcines underwent washing with fresh water before being routed to the three-stage cyanidation circuit, which was succeeded by Merrill Crowe precipitation and refining processes (Northwest Consulting Limited, 2003).

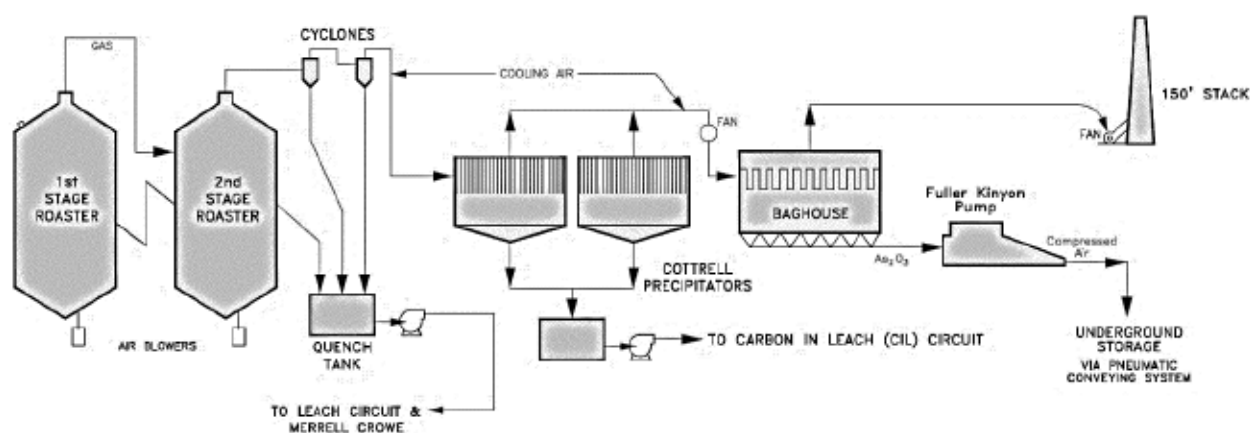


Figure 2.4 Roaster and gas cleaning circuits of Giant mine. Figure taken from (SRK, 2002)

An essential drawback of roasting is the elevated antimony content in the ore. Concentrates with antimony levels exceeding 0.5% fed into the roaster at Giant Mine could result in clinkering, necessitating a costly shutdown for roaster-bed cleaning. This issue stems from the oxidation of the mineral stibnite (Sb_2S_3), which readily transforms into antimony trioxide, leading to concentrate clinkering due to its low melting point (Thomas, 1988; Thomas & Cole, 2016):



Therefore, stringent control measures were necessary at the Giant Mine operation to monitor sulfide and antimony levels closely. A standard flotation concentrate analysis typically consisted of Au - 57 g/t; S - 20%; Sb - 0.3%; and As - 9%.

2.3.2 ATRW dust production and management

To address the need for arsenic collection and gold recovery from the roaster gases, various technologies were implemented at the Giant Mine over the years. Initially, the off-gases from the roasting stages were released directly into the atmosphere without arsenic recovery. However, starting from October 1951, multiple iterations of gas cleaning methods were introduced, resulting in the generation and disposal of arsenic trioxide dust as a waste by-product (SRK, 2002). The off-gases underwent initial filtration through cyclones to remove coarse dust particles, followed by passage through a cold electrostatic precipitator known as the Cottrell, where arsenic trioxide dust was collected and subsequently pumped underground into sealed chambers. However, the efficiency of this system was deemed insufficient. To enhance dust collection, a parallel Hot Cottrell plant was installed in 1955, and in 1958, a Dracco baghouse was added to meet standards set by the Department of National Health and Welfare (Silke, 2013). The off-gases were cleaned of gold-bearing dust by passing through the Cottrell electrostatic precipitator, and gold recovery was achieved using a carbon-in-pulp method (Thomas & Cole, 2016). Over time, experimentation led to the adoption of hot precipitation (at 370 °C) as a more effective method for dust recovery. Commercial treatment of the Hot Cottrell dust was initiated through a carbon-leach circuit starting in 1961 (Silke, 2013). The new Cottrell installation significantly improved the recovery of gold-bearing dust that had previously been lost. Operating at 50,000 volts, the Cottrell employed electrical energy to charge the fine particles of entrained dust in the roaster off-gases, subsequently collecting them on oppositely charged rods. Time-controlled rapping hammers were employed to dislodge dust from the collecting and discharged electrodes. The collected Cottrell calcine dust was directed into V-shaped hoppers and conveyed to quench tanks. Meanwhile, the tail gas from the Cottrell was cooled to 90 °C by blending the off-gas with large volumes of outside air, leading to the formation of solid arsenic trioxide. This arsenic trioxide was then filtered from the gas stream in the baghouse. The remaining gas stream, consisting of a diluted mixture of sulfur dioxide and air, passed through the baghouse fabric dust filter before being exhausted into the atmosphere through a 150-foot high brick stack (Silke, 2013). It's noteworthy that none of the gas cleaning circuits installed resulted in reduced sulfur dioxide emissions (as depicted in Figure 2.4). By 1962, following further modifications, the arsenic trioxide dust collection efficiency reached 98%, successfully preventing approximately 17 tons of arsenic per day from being released into the

atmosphere from a roaster feed rate of 40 tons/day (Northwest Consulting Limited, 2003; Silke, 2013).

Between 1951 and 1999, mine operators at Giant Mine stored the arsenic trioxide dust underground in purpose-built chambers and mined-out ore stopes (SRK, 2002). The ore treatment plant operated from 1948 to 1999, processing 18 million tons of ore with a grade of 0.49 ounces per ton and recovering 7 million ounces of gold, achieving an average recovery rate of 85.5%. During this period, more than 17 million tonnes of tailings were generated, along with over 237,000 metric tonnes of arsenic trioxide as a by-product of roasting (Silke, 2009, 2013). Presently, this substantial quantity of dust is stored underground in ten chambers and five mined-out stopes. The chambers feature regular block-like shapes, while the stopes exhibit irregular shapes. Situated between depths of 20 to 75 meters below the ground surface, all storage areas are segregated from the rest of the mine by concrete bulkheads. Additionally, any escaped arsenic is captured by a water collection system within the mine, and the collected water undergoes treatment to remove arsenic before being discharged into the environment (SRK, 2002).

Between 1981 and 1987, an opportunity emerged to sell a portion of the crude arsenic trioxide product to the wood preservative industry. During this period, over 7400 tons of arsenic trioxide were gathered and transported to southern markets for inclusion in wood preservative formulations. To facilitate this endeavor, a dedicated transfer and loading facility was constructed. However, shipments ceased when buyers opted for higher-quality alternatives, prompting the discontinuation of this arrangement (Northwest Consulting Limited, 2003; Silke, 2013).

The ATRW dust contains approximately 60% arsenic, posing significant hazards to both human health and the environment. If this arsenic trioxide were to dissolve in water, it would pose a risk to both people and the environment if it were to reach Great Slave Lake and Baker Creek, which flows through the mine site (SRK, 2002). Arsenic emissions from the Giant Mine during its early operations posed a health hazard to the community until stricter environmental controls were implemented. There is documented evidence of a two-year-old boy's death in April 1951, along with several anecdotal reports of deaths in the Dene population around the same time (Silke, 2013). A previous study of soil samples from the Yellowknife area beyond the mine property found varying concentrations of arsenic (As) in mineral soils, humus, and leaf litter, ranging from up to 30 mg/kg near unmineralized bedrock to 300 mg/kg over mineralized bedrock (Kerr, 2006). In

contrast, the average arsenic content in soils for all of Canada is 6.6 mg/kg (Reimann et al., 2009). Naturally occurring arsenic in the Yellowknife Greenstone Belt is derived from arsenopyrite-bearing bedrock and its weathering products (Kerr, 2006; Wrye, 2008). The presence of As_2O_3 derived from the roaster and roaster Fe-oxides in soils on the Giant Mine property has been confirmed (Wrye, 2008).

The chemical properties of the ATRW dust have undergone changes over time due to alterations in the processing and dust collection systems. The most significant transformation occurred in 1964 with the implementation of the final dust collection system at the site. Chambers B230, B233, B234, B235, B236, and B208 are classified as "old" deposits, as they were deposited before 1964. In contrast, dusts in other stopes and chambers are categorized as "new" dusts, produced since 1964 (Figure 2.5). This age differentiation is reflected in the chemical analysis and solubility data. Materials produced before the modifications have a lower arsenic content and higher gold content, while those produced after the changes exhibit higher arsenic content and lower gold content (SRK, 2007).

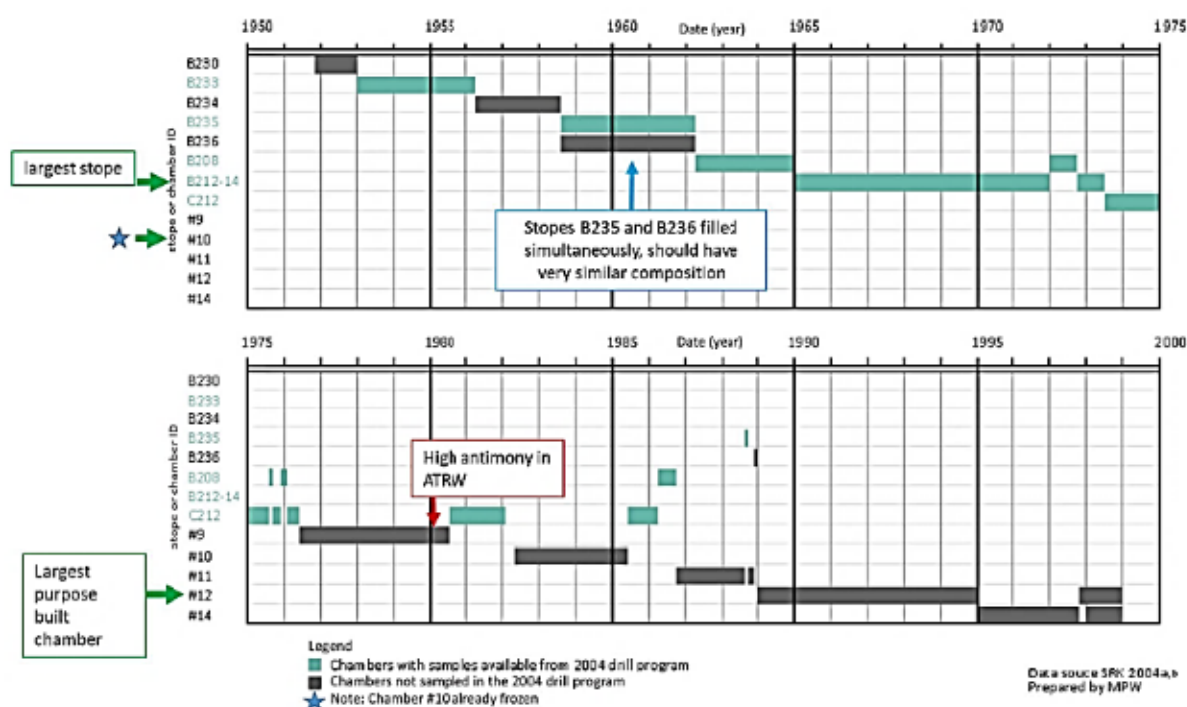


Figure 2.5 Timeline depicting when chambers were filled with arsenic trioxide dust at the Giant Mine. Green bars represent chambers sampled in 2004 SRK drilling program and grey bars represent chambers from which archive samples are not currently available. Figure taken from (SRK, 2002)

Table 2.1 summarizes the solubility of ATRW in water at two different temperatures. The ranges in the table indicate the variability in arsenic solubility, which appears to be at least partially dependant on the antimony content of the samples. Samples with a higher antimony content, which is generally typical of the “old” material, tend to show a lower arsenic solubility (SRK, 2002).

Table 2.1 Solubility of arsenic trioxide dust (SRK, 2002)

Solution concentration	5 °C	10 °C
g As ₂ O ₃ /L	6.2 – 11.9	7.4 – 12.7
g As/L	4.7 – 9.0	5.6 – 9.6

2.4 Closure options for ATRW dust at the Giant Mine

The long-term management of the ATRW dust located at Giant Mine poses challenges due to its substantial quantity (237,000 tonnes), fine particulate nature, and current storage conditions in subsurface chambers and stopes. Given this complexity, an integrated approach involving multiple technologies or methods will likely be necessary to ensure effective treatment (Arcadis, 2017). In addition to the ATRW dust, approximately 17 million tonnes of tailings are stored in ponds constructed on the site. The South, Central, North, and Northwest tailings impoundments cover a total area of about 95 hectares. Moreover, water treatment sludges are stored in settling and polishing ponds, adding an additional nine hectares to the storage area. Both the tailings and the sludge contain moderate levels of arsenic and are susceptible to wind erosion when dry, posing potential risks of environmental contamination. Additionally, they could be ingested by animals seeking salt (SRK, 2007).

After the closure of the mine in 2000, the Giant Mine Remediation Project Team commenced the evaluation of approaches for managing the arsenic trioxide dust. Various potential treatment solutions were scrutinized, with over 50 technologies assessed to identify the most promising option. These methods underwent initial evaluation against threshold criteria to assess their technological advancements, technical maturity, and associated risks. In the subsequent stage of assessment, methods that met the initial screening criteria were further evaluated against a comprehensive set of criteria and assigned an overall ranking (Arcadis, 2017). These potential methodologies were categorized into four groups: in-situ management, dust extraction, ex-situ waste stabilization/processing, and physical isolation, and disposal. Table 2.2 outlines the alternatives within each category. Several factors, including effectiveness, compatibility with cold

climates, short- and long-term health and safety risks, operation and maintenance requirements, technical maturity, and associated costs, were taken into consideration. Priority was given to factors such as long-term effectiveness, safety for people and the environment, and operation and maintenance measures (Arcadis, 2017). Teams comprising experts from government agencies, research organizations, universities, and businesses evaluated different solutions, assigning scores based on their expertise and insights.

Table 2.2 Different categories and their alternatives for long-term arsenic trioxide dust management (Arcadis, 2017)

#	Category	Alternatives
1	In-situ management	Frozen block Nano-scale zero-valent iron
2	Dust extraction	Remote mechanical mining methods Hydraulic borehole mining
3	Ex-situ waste stabilization/processing	Cement stabilization Cemented paste backfills Vitrification Mineral precipitation Biologically-mediated reductive arsenic precipitation Biologically-mediated oxidative arsenic precipitation
4	Physical isolation and disposal	Sand-shell purpose-built vault

The "Frozen Block" method emerged as the most suitable management approach available at that time for addressing the arsenic trioxide dust issue at the Giant Mine. This remedial method involves stabilizing the dust by freezing the ground surrounding the dust chambers and stopes (Figure 2.6). Water in contact with the frozen ground freezes, forming a capsule that restricts groundwater exposure to the waste. This approach combines active and passive freezing methods. Active freezing entails circulating a cold liquid through pipes installed in the ground. Once the dust and surrounding rock are completely frozen, the system transitions to passive freezing using thermosyphons. However, a small amount of ATRW remained dispersed throughout other underground mine workings. Continuous water treatment and monitoring efforts was implemented to prevent this arsenic from leaving the site.

Given the perpetual maintenance of the thermosyphons, there is a strong probability of achieving long-term stability for the arsenic. However, as the arsenic remains chemically unstable and is not removed from the vicinity, it retains its inherent solubility, which could lead to a release if maintenance is neglected and the frozen block thaws (Arcadis, 2017). Climate change and global warming pose significant challenges to the environment, economy, and politics, making them pressing concerns for residents of the Northwest Territories (NWT). With temperatures in the North rising at a rate three times faster than the global average, NWT residents are concerned about the repercussions of climate change (Government of Northwest Territories, 2019). Furthermore, the presence of open-pit mining and extensive underground workings in the chamber areas has affected the discontinuous permafrost in the region. Decreasing permafrost stability, coupled with changes in the permeability of the host rock, has prompted a re-evaluation of the mine reflow rate and a reassessment of more permanent underground storage methods (N. Thompson et al., 2002).

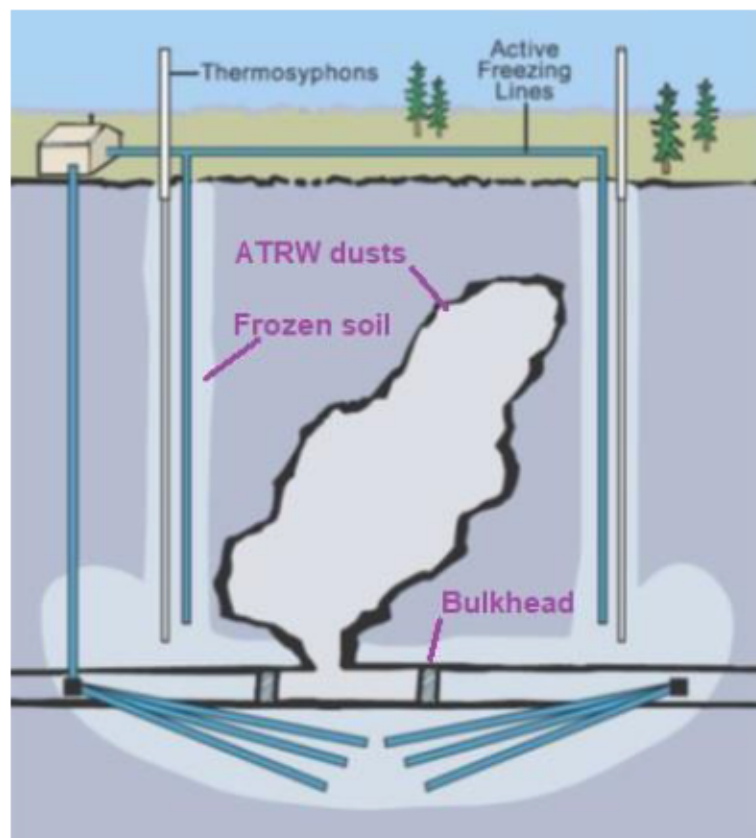


Figure 2.6 Illustration of Frozen Block method. Figure taken from (Keeling & Sandlos, 2017)

Mine authorities have proposed that a variety of methods may be necessary for the permanent management of the ATRW dust. Efforts have been made to identify a more effective long-term

management solution, including regular evaluations of arsenic management technologies and the allocation of funds to support arsenic management research. In 2015, the Giant Mine Oversight Board (GMOB) was established as an independent entity to ensure the implementation of these measures and to oversee the remediation efforts at the Giant Mine site in an environmentally sound, socially responsible, and culturally appropriate manner (Arcadis, 2017). Additionally, other research projects, such as the "Examination of arsenic trioxide dust composition and solubility", "Sulfidation of As_2O_3 to low-solubility arsenic sulfide (As_2S_3)", and "Leaching behavior and geochemical stability of vitrified arsenical glass," have been conducted to enhance understanding of the physical and geochemical properties of the roaster waste and to explore potentially viable remediation alternatives that may require further research ((GMOB), 2021).

2.5 Previous work on ATRW dust stabilization at the Giant Mine

Giant Mine authorities explored methods for stabilizing the ATRW dust while maintaining its chemical form. These methods aimed to incorporate the material into a stable matrix comprising cement, bitumen, or glass. The goal was to control the interaction between arsenic trioxide and water within a disposal facility and mitigate the release of arsenic from the facility (Arcadis, 2017).

Stabilization tests were carried out in 2002 on a sample of ATRW dust obtained from the Giant Mine, which contained approximately 69% As_2O_3 . The primary objective of these tests involving cement/bitumen stabilization was to investigate the relationship between the proportion of ATRW dust in the cement/bitumen mixture and its physical and chemical stability. Ultimately, the aim was to develop a mixture capable of stabilizing ATRW dust, thereby enabling its safe disposal in a secure surface waste containment facility. The application of cement/bitumen to the Giant Mine ATRW dust was initially assessed as part of the Giant Mine Arsenic Trioxide Management Alternatives (SRK, 2002).

2.5.1 Cement-encapsulated samples

Nine cylinders were prepared with a cement content of 20.5%, each containing amounts of ATRW dust from 0% (control sample) to 68% on a dry weight basis. Cement cylinders underwent UCS testing at both 14 and 28 days. Cylinders containing 0% to 45% dust exhibited sufficient strength and were subjected to leaching tests using a standard tank leaching procedure, with each cylinder submerged in deionized water. Additionally, freeze/thaw tests were conducted on three cement

cylinders containing 0%, 17%, and 34% ATRW dust. The results of the 28-day UCS tests are presented in Table 2.3, indicating that cylinders reached full strength within two weeks of curing. However, strength decreased with increasing ATRW dust content, attributed to the rising water-to-cement ratio, which reduced the strength of cement mixtures (Arcadis, 2017). Despite maintaining the cement content at 20.5% of the dry weight of materials, a higher amount of water was necessary to achieve a workable stabilized ATRW dust mixture. Leachate analysis revealed alkaline leachates for all samples, with pH decreasing as the ATRW dust content increased. As expected, arsenic concentrations in the leachate rose with higher dust percentages in the cylinders (Arcadis, 2017; SRK, 2002).

Table 2.3 Unconfined compressive strength and leachate analysis of cement-encapsulated arsenic trioxide dust samples (SRK, 2002)

% As ₂ O ₃ dust	Water/cement ratio	28-day strength (MPa)	90-day leachate analysis	
			pH	Dissolved As (mg/L)
0%	0.48	28.8	9.86	<0.05
11%	1.1	11.8	11.00	25.6
17%	1.25	9	11.41	47.2
22%	1.41	4.8	10.92	182
28%	1.6	2.3	10.82	318
34%	1.7	1.3	10.12	491
45%	1.96	0.6	9.86	893
57%	2.3	0.16	-	-
68%	3.5	0.07	-	-

The freeze/thaw test was conducted on the cement-encapsulated dust samples, with a maximum of twelve cycles specified by the test procedure. The findings revealed that samples containing 17% and 28% dust could endure only two and one freeze/thaw cycles, respectively, before disintegrating. The results suggested that the presence of ATRW dust had an adverse impact on the durability of the cement/dust mixtures. A likely contributing factor to these outcomes was the higher water-to-cement ratios in the cylinders containing ATRW dust. A leachate collection and treatment system would be necessary for landfills containing cement-encapsulated ATRW (Arcadis, 2017; SRK, 2002). Additionally, the results suggested that bitumen could be effective in encapsulating ATRW dust. Therefore, it was recommended to use a bitumen mix containing a

maximum of 40% ATRW dust for encapsulation by bitumen. Samples containing up to 60% arsenic trioxide dust exhibited favorable leaching characteristics (Arcadis, 2017).

2.5.2 Bitumen-encapsulated samples

Nine bitumen-encapsulated (include bitumen ratio) ATRW dust samples underwent leaching tests exclusively, as standard strength tests were deemed unsuitable for the bitumen samples produced in that study. Freeze/thaw testing was not conducted due to the inadequacy of existing testing protocols. Arsenic concentrations measured in the leach tests are detailed in Table 2.4. The results indicated that arsenic release from bitumen-encapsulated ATRW dust was minimal, and arsenic concentrations remained relatively constant over time and across varying dust content levels (Arcadis, 2017; SRK, 2002). However, bitumen samples containing 50% and 60% ATRW dust were highly viscous and required manual manipulation.

Table 2.4 Leachate results from bitumen encapsulated arsenic trioxide dust samples (SRK, 2002)

% As ₂ O ₃ dust	90-day leachate analysis	
	pH	Dissolved As (mg/L)
0%	6.27	<0.05
10%	5.96	<0.05
15%	5.79	<0.05
20%	5.78	<0.05
25%	5.71	0.05
30%	5.73	0.14
40%	5.81	0.35
50%	5.79	0.13
60%	5.75	0.17

These methods were ultimately abandoned due to several reasons, including data gaps concerning the long-term stability of the processed cement/bitumen monoliths, uncertainties surrounding cement/bitumen and arsenic stabilization chemistry, and health and safety concerns associated with ATRW dust extraction and processing (Arcadis, 2017; SRK, 2007). However, recent studies have made significant progress in characterizing the chemical behavior of arsenic stabilized by cement, and the mechanism of arsenic stabilization is now better understood, which provided additional insight into the behavior of arsenic-containing dust within the cement matrix (Camacho et al.,

2009b; Choi et al., 2009; Clancey et al., 2015; B.-J. Kim et al., 2016; J. S. Li, Beiyuan, et al., 2017; J. S. Li, Wang, et al., 2017; D. G. Liu et al., 2018; Mohammad Eisa et al., 2020; Moon et al., 2010; Randall, 2012; Tsang et al., 2014; Yoon et al., 2010; H. Zhao et al., 2010).

2.6 Arsenic geochemistry related to roaster waste

Arsenic ranks as the 53rd most abundant element and constitutes approximately 1.5 ppm of the Earth's crust. It naturally occurs in the environment in various minerals, commonly in association with sulfur, metals, and occasionally in pure elemental crystal form (Mohammad Eisa et al., 2020). The chemical variability of arsenic arises from its electronic structure and bonding properties, leading to a range of forms in solid, aqueous, and gaseous states. As a metalloid belonging to the third row of group V elements, arsenic has just one stable isotope, ⁷⁵As (Davis et al., 2003). It is positioned beneath nitrogen and phosphorus in the periodic table and possesses an excess of electrons and unfilled orbitals, allowing for stable formal oxidation states ranging from +5 to -3 (O'Day, 2006). Inorganic arsenic typically occurs in valence states of -3, 0, +3 (as arsenite), and +5 (as arsenate); however, valence states of -3 and 0 are rare in natural environments (Choi et al., 2009).

Arsenic is an extremely toxic element and a known carcinogen to humans, even in trace quantities (Moon et al., 2004). The toxicity, bioavailability, and mobility of arsenic compounds in soils and sediments are influenced by factors such as the type and quantity of adsorbing constituents, pH value, and redox potential (Choi et al., 2009). Among the various forms of arsenic, As (III) and As (V) are the most prevalent in nature, with As (III) being both more mobile and more toxic.

Arsenic ferrihydrides and other arsenic compounds exhibit very low solubility in neutral to acidic environments (pH between 4 and 8), a characteristic highly dependent on formation conditions (Joussemet et al., 2001). Calcium arsenates, particularly in the presence of excess lime and at pH values above 10, tend to be more stable, forming alkaline arsenites such as $\text{Ca}(\text{AsO}_2) \cdot \text{Ca}(\text{OH})_2$, alkaline arsenates like $\text{Ca}_3(\text{AsO}_4)_2 \cdot \text{Ca}(\text{OH})_2$, and gypsum ($\text{CaSO}_4 \cdot 2\text{H}_2\text{O}$). However, at lower pH values or in the presence of carbonation (resulting in calcite formation, CaCO_3), highly soluble intermediate compounds (e.g., $\text{Ca}_3(\text{AsO}_4)_2$ and $\text{Ca}_2(\text{AsO}_4)_2$) may form. The decalcification of calcium arsenates leads to the release of soluble AsO_4^{3-} anions (Benzaazoua, Marion, et al., 2004). Under acidic conditions (e.g., the release of H^+ ions following sulfide oxidation) and minimal presence of neutralizing agents in infiltrating water (e.g., carbonates or cement hydrates), arsenic

tends to be relatively mobile and can leach into solution. Conversely, under weakly acidic or alkaline conditions, arsenic exhibits relative immobility due to hydrolysis and coprecipitation phenomena, particularly with iron oxyhydroxides like goethite. The presence of certain elements such as Fe, Co, Ni, Pb, and Zn in the solution, and their interaction with soluble arsenate anions, can lead to the formation of stable arsenates such as scorodite ($\text{FeAsO}_4 \cdot 2\text{H}_2\text{O}$), erythrite ($((\text{Co},\text{Ni})_3(\text{AsO}_4)_2 \cdot 8\text{H}_2\text{O})$), annabergite ($\text{Ni}_3(\text{AsO}_4)_2 \cdot 8\text{H}_2\text{O}$), beudantite ($\text{PbFe}_3(\text{AsO}_4)(\text{SO}_4)(\text{OH})_6$) and adamite ($\text{Zn}_2(\text{AsO}_4)(\text{OH})$). These secondary compounds remain stable under near-neutral to slightly basic pH conditions (Benzaazoua, Marion, et al., 2004; Joussemet et al., 2001).

The oxidation states of arsenic in various environments, including rainwater, surface water, groundwater, soils, and sediments, are subject to variation based on factors such as the source of arsenic input, oxygen availability (oxic or anoxic conditions), redox conditions, pH levels, biological processes, the presence of iron, and other elemental constituents, as well as seasonal fluctuations. The oxide phases of arsenic encompass arsenites, characterized by As (III), arsenio-arsenates, a combination of As (III) and As (V), and arsenates, where arsenic typically exists as As(V) (Cesbron, 2001). The oxidation states of arsenite and arsenate species fluctuate depending on factors such as redox potential (Eh), pH levels, the chemical composition of the environment, and the extent of biological transformations (Randall, 2012). Figure 2.7 illustrates the Eh-pH diagram of arsenic for the As-O-H system. Arsenite exists as a neutral hydroxide (H_3AsO_3^0) until $\text{pH} > 9$, beyond which the ionized form H_2AsO_3^- becomes prevalent. In circum-neutral pH waters with high salinity, arsenite solubility can exceed 10 g/l. Arsenate can be present in two forms: H_2AsO_4^- (below pH 6.8) or HAsO_4^{2-} (pH 6.8 – 11.5) (Clark & Raven, 2004). Anionic arsenic compounds have an affinity for binding to soils, clays, organic matter, and various metal hydroxides/oxides, including those of iron, manganese, and aluminum (Randall, 2012).

H_3AsO_4 and AsO_4^{3-} may be present under extremely acidic and alkaline conditions, respectively. Conversely, under reducing conditions where the pH is below 9.2, the uncharged arsenite species (H_3AsO_3) is predominant. In such environments, native arsenic remains stable under strongly reducing conditions (Davis et al., 2003). Typically, As (V) species predominate in oxygenated conditions, while As (III) typically dominates in strongly reducing environments where Fe (III) and sulfate reduction processes occur. In oxic waters, As (III) may persist due to biological reduction of As (V), especially during warmer months. Rivers near sources of industrial effluents rich in As (III) often exhibit higher proportions of As (III) (Davis et al., 2003).

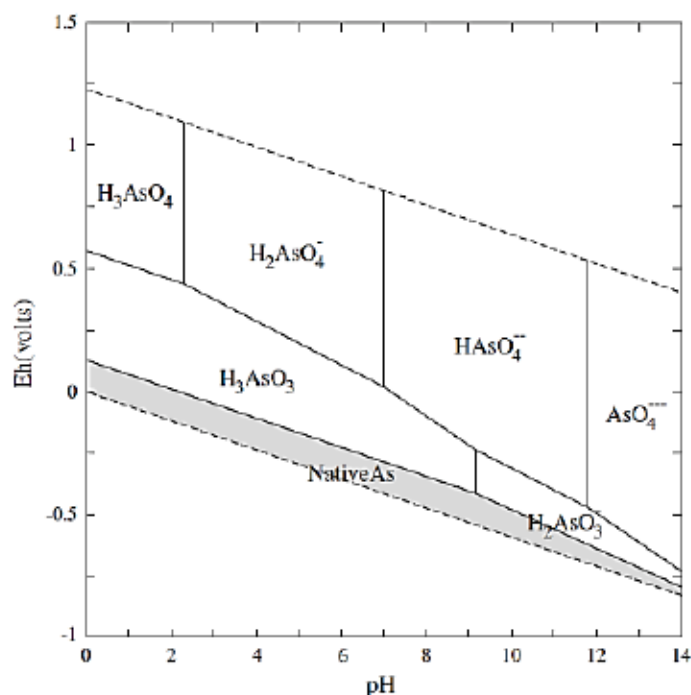
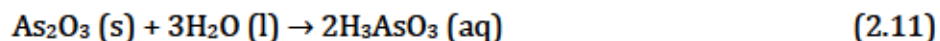


Figure 2.7 Eh-pH diagram for the system As-O-H at 25 °C, 1 bar, and $\Sigma\text{As} = 10^{-6}$ M. Gray shaded area shows the solid phase. Figure taken from (Craw & Bowell, 2014)

Anthropogenic emissions of As oxides include arsenic trioxide (As_2O_3), which is among the most bioaccessible and toxic forms of arsenic. In nature, arsenic trioxide exists in two allotropic modifications. The most common cubic form, arsenolite, is a secondary mineral formed from the oxidation of native As, arsenopyrite, löllingite, and the weathering of scorodite. The monoclinic dimorph of As trioxide, claudetite, often accompanies arsenolite closely. The stabilities of arsenolite and claudetite are quite similar, given their nearly identical free energies of formation (i.e., arsenolite -576.34 kJ/mol and claudetite -576.53 kJ/mol). However, claudetite is slightly more stable than arsenolite under ambient conditions (with a difference of -0.19 kJ/mol). Arsenolite and claudetite dissolve at $\text{pH} < 8$ and temperatures up to 90 °C, as shown in Equation (2.11); they remain stable when in equilibrium with high-pH waters (Drahota & Filippi, 2009):



When water reaches equilibrium with arsenolite, it can contain up to $10 - 16$ g/L As. Arsenolite derived from roasted sulfide ore remains stable in alkaline, reduced environments (Craw & Bowell, 2014).

The valence state and morphology of arsenic in the environment are not static, and arsenic species undergo changes over time (Blanchard et al., 2017). In more detail, the physicochemical conditions that favor arsenic mobilization in aquifers are variable, complex, and poorly understood, although some key factors leading to high groundwater arsenic concentrations have recently been identified. Mobilization can occur under strongly reducing conditions, where arsenic, primarily as As (III), is released through desorption from, and/or dissolution of iron oxides. Immobilization under reducing conditions is also possible. Certain sulfate-reducing microorganisms can respire As (V), resulting in the formation of an As_2S_3 precipitate. Some immobilization of arsenic may also occur if iron sulfides are formed (Davis et al., 2003). In the following section, some main methodologies for the stabilization and immobilization of different arsenic species are briefly discussed. It is worth mentioning that most previous studies in the field of arsenic stabilization have focused on stabilizing arsenates and arsenites, as these species, along with some secondary minerals, are typically the final forms in most environments.

2.7 Solidification and stabilization process

Various technologies are utilized for cleaning up arsenic-bearing wastes or soils and sediments contaminated with arsenic. Cleanup methods encompass site isolation, physical separation, bioremediation, phytoremediation, washing, heating, electrokinetics, permeable reactive barriers, solidification and stabilization, or in some cases, in-situ vitrification. Often, the most cost-effective solution for land remediation involves solidification and stabilization (S/S) technologies, which alter arsenic both physically and chemically, encapsulating it into a less mobile and less toxic form (Randall, 2012). Undoubtedly, the most sustainable approach for managing As-containing materials is to convert As into its least mobile or stabilized form and then sequester the stabilized material from the environment using a solidification/encapsulation process (Sullivan et al., 2010). S/S technologies have a well-documented history and have been the most widely used method for reducing arsenic mobility and treating other heavy-metal-containing wastes in soils and other solids using materials such as Portland cement, fly ashes (FA), slags, lime, limestone, cement kiln dust (CKD), lime kiln dust (LKD), gypsum and phosphate mixtures, ferrous sulfates, pozzolanic materials, geopolymers, and certain specific reagents (Wilk, 2004). S/S techniques have been extensively employed for managing and disposing of low-level radioactive and hazardous wastes, as well as for remediating contaminated sites (Mohammad Eisa et al., 2020).

Solidification entails processes that encase waste to produce a solid material and restrict the migration of contaminants by reducing the available surface area exposed to leaching and contact with liquids. Solidification involves altering the physical properties of the waste, typically resulting in increased compressive strength, decreased permeability, and encapsulation of hazardous constituents (Wilk, 2004).

Stabilization involves chemical reactions aimed at reducing the reactivity, solubility, and leachability of the material (stabilized waste) by converting its constituents into a less soluble, mobile, or toxic form. This can be achieved through appropriate chemical reactions and physical entrapment (microencapsulation) (Ioannidis & Zouboulis, 2005; Mohammad Eisa et al., 2020; Wilk, 2004). Following treatment, the waste can be disposed of as non-hazardous waste since it no longer exhibits hazardous leaching characteristics (Wilk, 2004).

In contrast to other treatment methods, cement-based solidification and stabilization offer numerous advantages. These include relatively low costs, adaptability to various disposal scenarios, ability to meet stringent processing and performance criteria, straightforward and versatile processing, long-term stability, extensive documented usage, compatibility with diverse waste types, well-established materials and technology, ready availability of chemical ingredients, and the non-toxic nature of the chemical reagents (USEPA, 1996), (Malviya & Chaudhary, 2006; Mohammad Eisa et al., 2020; Shi & Spence, 2004).

Given the diverse array of waste constituents and media, a customized mix design should be devised for each specific waste. Most mix designs comprise a combination of the inorganic binding reagents mentioned earlier. Organic binding reagents like asphalt, bitumen, thermoplastic, and urea-formaldehyde have been experimented with as well. However, they are seldom employed on a commercial scale due to their elevated costs compared to inorganic binders (Wilk, 2004).

2.7.1 Solidification and stabilization mechanisms

The selection of binding materials for S/S of wastes must consider several aspects, taking into account the characteristics of the waste: (1) compatibility between the cementitious material and the waste, (2) physical encapsulation of contaminated waste, (3) chemical fixation of contaminants, (4) durability and leachability of the stabilized waste, and (5) cost-effectiveness of the S/S process (Spence & Shi, 2005).

Contaminants are solidified/stabilized by cementitious materials through three primary mechanisms:

Chemical fixation: This involves chemical interactions between the hydration products of the cementitious materials and the wastes, resulting in the immobilization of contaminants.

Physical adsorption: Contaminants adhere to the surface of the hydration products of the cement through physical adsorption.

Physical encapsulation: The contaminated materials are physically enclosed within the hardened pastes, which have low permeability, preventing the release of contaminants.

The effectiveness of the first two mechanisms depends on the characteristics of the hydration products and the contaminants involved. The third mechanism is influenced by both the nature of the hydration products and the density and physical structure of the paste (Spence & Shi, 2005).

Due to its widespread availability and cost-effectiveness, Portland cement stands out as the most utilized binding material. Its selection is primarily based on its capacity to chemically bind free liquids, reduce the permeability of the waste matrix, encase waste particles with an impermeable layer, and chemically stabilize hazardous components, thus decreasing their solubility and mitigating their toxicity. Mix designs typically incorporate supplementary materials or additives alongside Portland cement (Conner, 1997; Wilk, 2004). These supplementary cementitious materials, including granulated or pelletized blast furnace slag, coal fly ash, volcanic ashes, condensed silica fume, rice husk ash, and natural pozzolans, are frequently employed to either reduce costs or enhance mixture performance (Spence & Shi, 2005). For instance, fly ash is commonly added to enhance the pozzolanic effect when combined with hydrating Portland cement. CKD and slag possess minor cementitious properties and are occasionally utilized to lower process costs. Lime and LKD can be employed to regulate pH or reduce water content, utilizing their high heat of hydration. Additionally, limestone, as a source of calcium carbonate, helps maintain an alkaline pH and can be used for pH adjustment and volume increase purposes (Wilk, 2004).

Portland cement is a type of hydraulic cement produced by grinding clinker and calcium sulfate, typically gypsum ($\text{CaSO}_4 \cdot 2\text{H}_2\text{O}$), which is added during final grinding process. Cement clinker primarily consists of tricalcium silicate ($3\text{CaO} \cdot \text{SiO}_2$), dicalcium silicate ($2\text{CaO} \cdot \text{SiO}_2$), tricalcium aluminate ($3\text{CaO} \cdot \text{Al}_2\text{O}_3$), and tetra calcium aluminoferrite ($4\text{CaO} \cdot \text{Al}_2\text{O}_3 \cdot \text{Fe}_2\text{O}_3$) (Spence & Shi, 2005). Generally, the chemical formulas of these components are denoted using the abbreviated

nomenclature based on the oxides of different elements, namely C for CaO, S for SiO₂, A for Al₂O₃, and F for Fe₂O₃ (Taylor, 1997). The traditional abbreviations for each oxide are provided in Table 2.5.

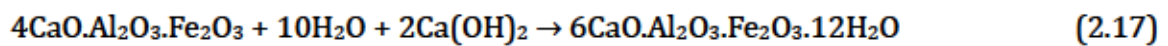
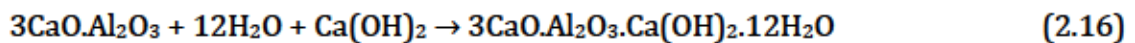
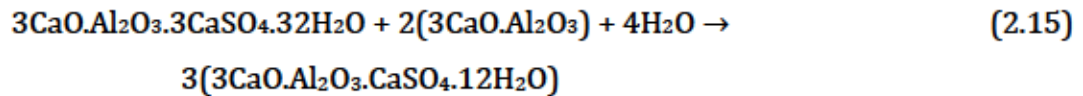
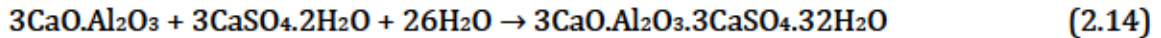
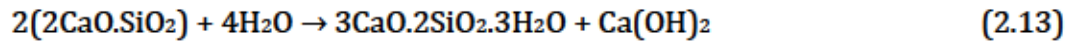
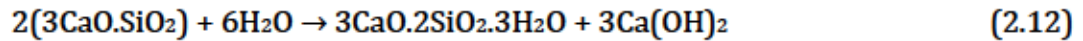
Table 2.5 Chemical formulae and cement nomenclature for major constituents of Portland cement (Taylor, 1997)

Mineral	Chemical formula	Oxide composition	Abbreviation
Tricalcium silicate (alite)	Ca ₃ SiO ₅	3CaO.SiO ₂	C3S
Dicalcium silicate (belite)	Ca ₂ SiO ₄	2CaO.SiO ₂	C2S
Tricalcium aluminate	Ca ₃ Al ₂ O ₄	3CaO.Al ₂ O ₃	C3A
Tetracalcium aluminoferrite	Ca ₄ Al _n Fe _{2-n} O ₇	4CaO.Al _n Fe _{2-n} O ₃	C4AF

Abbreviation notation: C = CaO, S = SiO₂, A = Al₂O₃, F = Fe₂O₃

Various types of Portland cement are manufactured to fulfill specific physical and chemical requirements for different applications, resulting in varying compositions. A typical cement comprises 50-70% C3S, 15-30% C2S, 5-10% C3A, 5-15% C4AF, and 3-8% other additives or minerals (such as calcium and magnesium oxides). The hydration of calcium silicate, aluminate, and aluminoferrite minerals leads to cement hardening or setting. C3S is the crucial phase for strength development in the initial month after mixing, while C2S reacts more slowly, contributing to long-term strength gain. The ratio of C3S to C2S determines the cement's setting rate, with higher C3S content resulting in faster setting. Lower C3A content enhances sulfate resistance, while increased ferrite amounts lead to slower hydration. C4AF forms a continuous phase around other minerals.

In the presence of water, the constituents C3S and C2S in cement undergo hydration to produce calcium-silicate-hydrate (C-S-H) gel and Ca(OH)₂. When calcium sulfate is present, C3A hydrates to yield calcium trisulfoaluminate hydrate (3CaO.Al₂O₃.3CaSO₄.32H₂O - AFt or ettringite) or calcium monosulfoaluminate hydrate (3CaO.Al₂O₃.CaSO₄.12H₂O - AFm or monosulfate). In the absence of calcium sulfate, C3A reacts with water and calcium hydroxide to form tetra calcium aluminate hydrate (3CaO.Al₂O₃.Ca(OH)₂.12H₂O). C4AF reacts with water to generate calcium aluminoferrite hydrates (6CaO.Al₂O₃.Fe₂O₃.12H₂O). These hydration reactions are expressed as follows (Spence & Shi, 2005):



At room temperature, a fully hydrated Portland cement paste forms a heterogeneous multiphase system, typically comprising 50 to 60% C-S-H gel, 20 to 25% $\text{Ca}(\text{OH})_2$, and 15 to 20% ettringite (or AFt) and AFm by volume (Figure 2.8).

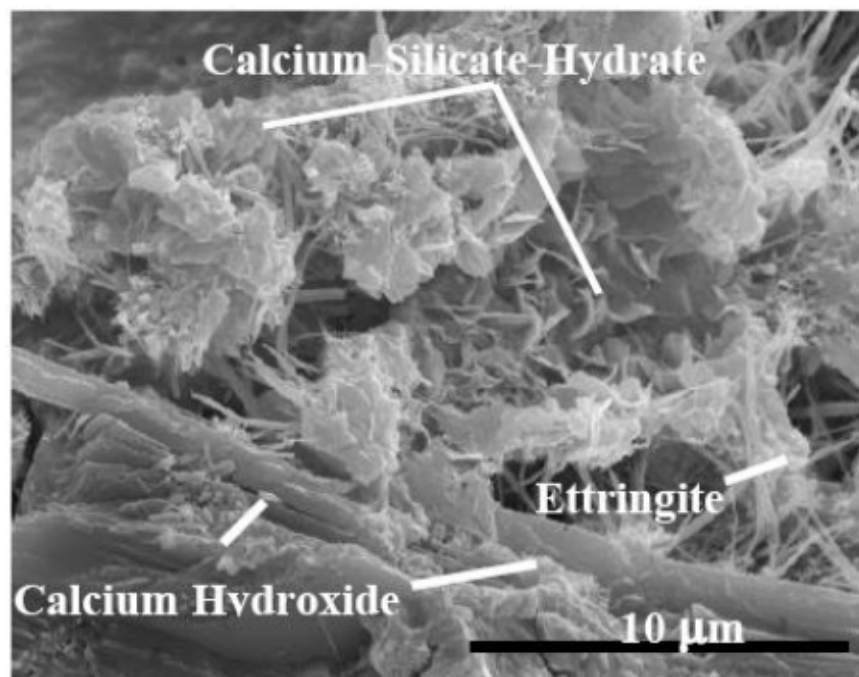


Figure 2.8 A SEM image of hardened Portland cement paste. Figure taken from (Soler, 2007)

These minor hydration products, including $\text{Ca}(\text{OH})_2$, $3\text{CaO}\cdot\text{Al}_2\text{O}_3\cdot 6\text{H}_2\text{O}$, and AFt, develop in small quantities depending on the composition of the cement and the hydration conditions (Spence & Shi, 2005). Despite ongoing research, the detailed structure and mechanics of C-S-H are still

poorly understood. However, it is generally accepted that C-S-H comprises condensed silicate tetrahedra sharing oxygen atoms with a central, calcium hydroxide-like CaO_2 layer (Taylor, 1997). Upon cement hydration, C-S-H progressively forms and precipitates in the capillary pore solution, assembling into a heterogeneous complex gel structure that binds together the solid products. The structure of C-S-H gel exhibits a disordered and heterogeneous mesoscale organization consisting of a few nanometer-sized structural units (Ioannidou et al., 2015).

2.7.2 Arsenic solidification and stabilization

The mobility of arsenic depends on factors such as its valence state, the oxidation-reduction potential of the environment, and the specific arsenic compound in the waste (Turner & Labiosa, 1992). Typically, arsenic mobility is assessed by testing its leachability under acidic conditions. However, in some disposal facilities, arsenic leachability may differ from predictions made by an acidic leach test, particularly when the specific form of arsenic in the waste exhibits increased solubility at higher pH levels, and the waste disposal environment maintains a high pH (USEPA, 2002).

Factors influencing the effectiveness of arsenic solidification and stabilization include (USEPA, 2002):

Valence state: The specific arsenic compound or valence state influences arsenic solubility, thereby affecting the leachability of the treated material.

pH and redox potential: The pH and redox potential of both the waste and the treatment environment can impact arsenic solubility and the leachability of the treated material. These factors may also lead to the formation of more soluble arsenic compounds or encourage the transition to a more soluble valence state.

Presence of organics: The presence of volatile or semi-volatile organic compounds, oil and grease, phenols, or other organic contaminants may diminish the unconfined compressive strength or durability of the solidified/stabilized material. Additionally, these organics can weaken the bonds between the binder and waste particles.

Waste characteristics: The unconfined compressive strength or durability of the solidified/stabilized material may be influenced by the presence of halides, cyanide, sulfate,

calcium, or soluble salts of manganese, tin, zinc, copper, or lead. These substances can also weaken the bonds between the binder and waste particles.

Fine particulates: Fine particulates have the potential to coat the waste particles, weakening the bond between the binder and the waste.

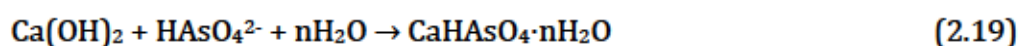
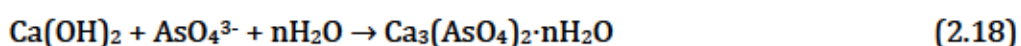
Mixing: Thorough mixing is essential to ensure proper coating of the waste materials with the binder.

Cement-based S/S stands out as a highly effective approach for converting toxic arsenic compounds into less hazardous forms (Vinter et al., 2016). During this process, as cement hydration progresses, an interlocking framework of minerals encapsulates the arsenic found in soils and wastes, subsequently reducing the release of arsenic. This solidified medium exhibits low surface area and permeability, further diminishing the mobility of arsenic within soils and wastes (B.-J. Kim et al., 2016; Mohammad Eisa et al., 2020). Additionally, the utilization of immobilizing agents can enhance the reduction of arsenic mobility through adsorption and co-precipitation mechanisms (Mohammad Eisa et al., 2020).

Research on arsenic solidification and stabilization has been focused on assessing stabilization admixtures and elucidating the chemical principles underlying the stabilization process. Appendix A presents Table A.1, summarizing literature on arsenic management through solidification and stabilization methods. The studies evaluated various S/S agents, including ordinary Portland cement, sulfate-resistant Portland cement (SRPC), quicklime, blast furnace slag (BFS), fly ash, hydrated lime, cement kiln dust, and other binding materials. In most cases, these additives and binders facilitate the oxidation of As (III) to As (V), which can then form insoluble complexes, become immobilized through the formation of strongly adsorbed species, or create insoluble co-precipitates with calcium and/or iron (Randall, 2012). The research highlights that arsenic stabilization and solidification involve both chemical and physical processes. The leaching capacity is greatly influenced by the buffering capacity and pH of the stabilized matrix. Notably, the formation of calcium and ferric arsenites/arsenates and C-S-H gels, along with their precipitation and embedding in the cementitious matrices, emerges as crucial stabilizing mechanisms. Additionally, increasing the Ca:As molar ratios in the cementitious matrices enhances arsenic stabilization, with diffusion identified as the primary mechanism of arsenic leaching from the stabilized samples (Clancey et al., 2015; Dutré & Vandecasteele, 1998; D. G. Liu et al., 2018;

Mohammad Eisa et al., 2020; Moon et al., 2004; Randall, 2012; Singh & Pant, 2006; Tsang et al., 2014; Yoon et al., 2010; H. Zhao et al., 2010).

Previous research (Coussy, Paktunc, et al., 2012; Phenrat et al., 2005; Stronach et al., 1997) has indicated that C-S-H exhibits strong adsorption capabilities for both As (III) and As (V). Furthermore, it has been observed that the SO_4^{2-} ions present in ettringite can undergo partial substitution by AsO_4^{3-} ions (Kumarathasan et al., 1989). Additionally, AsO_4^{3-} ions can undergo conversion into $\text{Ca}_3(\text{AsO}_4)_2 \cdot n\text{H}_2\text{O}$ and $\text{CaHAsO}_4 \cdot n\text{H}_2\text{O}$ through reactions (Equations (2.18) and (2.19)) within the pH range of 11–14 (D. G. Liu et al., 2018; Vandecasteele et al., 2002). These findings suggest that the reduction in arsenic concentration in the leachates may be attributed to these processes.



Arsenic behaves differently from many heavy metal cations during S/S processes due to its inability to form insoluble hydroxides (Büchler et al., 1996a). In solution, arsenic exists predominantly as AsO_3^{3-} for As (III) and AsO_4^{3-} for As (V), with protonated forms of these oxo-anions dependent on pH. While these oxo-anions form various water-soluble salts, numerous insoluble metal arsenates are known. As (III) can readily be oxidized to As (V), even with air alone. Precipitating As (V) with lime yields $\text{Ca}_3(\text{AsO}_4)_2$, which exhibits very low water solubility. However, calcium arsenate is not stable when exposed to atmospheric CO_2 , leading to the formation of CaCO_3 and the release of soluble arsenate. Although there exists a highly insoluble ferric arsenate, $\text{FeAsO}_4 \cdot 2\text{H}_2\text{O}$, its crystalline form, scorodite, exhibits higher solubility under alkaline conditions than under acidic ones. Under alkaline conditions, arsenate precipitation with Fe (III) occurs, yielding "alkaline ferric arsenate," yet the identity and stability of this species remain controversial (Büchler et al., 1996a). These complexities underscore the necessity of testing candidate treatment mixtures with the materials to be treated.

Apart from the conventional method of solidification and stabilization employing cementitious binders, alternative procedures exist to mitigate the mobility of arsenic species and stabilize arsenic without the use of cementitious agents. These methods may involve the addition of ferric iron compounds or the formation of secondary arsenate minerals like scorodite.

➤ **Addition of Ferric iron compounds**

There is a strong interaction between iron and arsenic, leading to the formation of insoluble precipitates, effectively stabilizing arsenic (Lin et al., 2017). Iron oxides, particularly goethite, FeSO_4 , and $\text{Fe}_2(\text{SO}_4)_3$, exhibit significant capability in adsorbing arsenic species, particularly As (V), thereby diminishing the arsenic concentration in natural waters (Davis et al., 2003). Research indicates that ferric sulfate treatment is more efficient in stabilizing available arsenic in tailings compared to ferrous sulfate treatment. Utilizing amorphous Fe precipitates on arsenic-containing mine tailings can effectively stabilize the arsenic content (J. Y. Kim et al., 2003). Various parameters such as Fe/As molar ratio, arsenic contamination level, pH, reaction time, and the presence of competitive ions like sulfate, phosphate, and zinc significantly influence arsenic stabilization. Studies have demonstrated that arsenic can form relatively insoluble ferric iron compounds with solubility products ranging from 10^{-20} to 10^{-24} . The formation of amorphous iron (III) arsenate ($\text{FeAsO}_4 \cdot \text{H}_2\text{O}$) and/or insoluble secondary oxidation minerals like scorodite ($\text{FeAsO}_4 \cdot 2\text{H}_2\text{O}$) can reduce the mobility of arsenic (H. Zhao et al., 2010).

When the pH of mine wastes rises to approximately neutral levels, the precipitation of Fe (oxyhydr)oxides occurs, leading to a decrease in As mobilization. This is attributed to the high As removal capacity of these phases through adsorption or co-precipitation processes. However, if the pH continues to increase, As can become mobilized due to desorption from Fe (oxyhydr)oxides (Álvarez-Ayuso & Murciego, 2021).

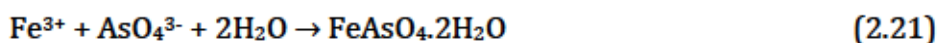
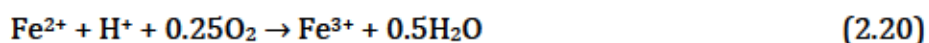
It is understood that under neutral or alkaline conditions, the concentration of Fe (III) in solution diminishes significantly due to its precipitation as Fe (oxyhydr)oxides. In such circumstances, Fe (III) is not present as a sulfide oxidation agent (Lottermoser, 2010). Studies on co-precipitation have demonstrated that at elevated pH levels and relatively low concentrations of As (< 1 mM or Fe/As molar ratios > 5), the removal of As (V) occurs through its strong adsorption onto the surfaces of low-ordered hydrous Fe oxides, commonly known as ferrihydrite. These Fe phases precipitated in-situ exhibit a high capacity for As uptake, up to 0.7 mol of As (V) per mole of Fe (Álvarez-Ayuso & Murciego, 2021).

Recognizing the significant efficacy of ferric salts in eliminating arsenic and the pressing demand for an effective and affordable stabilization method, both FeCl_2 and FeCl_3 have been proposed as stabilizers (Lin et al., 2017). Apart from Fe (oxyhydr)oxides, aluminum-based compounds are also

noted for their significant capacity to trap arsenic. The removal of arsenic by these compounds primarily occurs through adsorption (Álvarez-Ayuso & Murciego, 2021). Following treatment, arsenic bonded to the Fe precipitate may even gain further stability over time (J. Y. Kim et al., 2003).

➤ **Formation of scorodite**

Other measures can also reduce the solubility and mobility of arsenic by promoting the formation of secondary arsenate minerals (Sullivan et al., 2010). The formation of secondary phases on the surfaces of arsenic sulfides can inhibit oxidation reactions, thus hindering the release of As. Furthermore, the stability of these arsenic-bearing secondary minerals in a changing environment can regulate the concentration of As in mine drainage and surface waters (Drahota & Filippi, 2009). Scorodite ($\text{FeAsO}_4 \cdot 2\text{H}_2\text{O}$), or crystalline ferric arsenate, plays a crucial role as an arsenic scavenger, commonly found in such mining environments (Álvarez-Ayuso & Murciego, 2021). It serves as a relatively stable secondary mineral capable of limiting As concentration in pore water within mine tailings. This phase has been previously identified in mine tailings under cold climate conditions in Saskatchewan, Canada (Kocourková-Víšková et al., 2015). Recognizing its pivotal role, treatments for acid-generating mine wastes should aim to preserve the scorodite phase or promote its formation (Álvarez-Ayuso & Murciego, 2021). Typically, it forms through the co-precipitation of ferrous and arsenic ions during air oxidation processes. The primary reaction mechanism involves two steps: oxidation and crystallization precipitation. These reactions can be represented by Equations (2.20) and (2.21) (X. Min et al., 2015):



Ferric arsenate exists in either amorphous or crystalline forms. The rate of oxidation is crucial for achieving crystalline scorodite. Additionally, pH significantly influences scorodite formation in arsenic leaching solutions. Scorodite can be generated at pH levels below 5.0, with high-crystalline scorodite achievable within an initial pH range of 2 to 4. The solubility of crystalline scorodite may be approximately two orders of magnitude lower than that of amorphous ferric arsenates. Amorphous ferric arsenate compounds exhibit high instability, leading to dissolved arsenic levels potentially reaching 20 mg/L.

Various factors, such as pH, the molar ratio of iron to arsenic, and temperature, influence scorodite precipitation. Precise control of pH during scorodite precipitation is crucial. Abrupt pH changes can lead to the formation of poorly crystalline phases and amorphous precipitates. The initial molar ratio of iron to arsenic can impact the rate of arsenic removal and the stability of the precipitate. Studies have shown that achieving a well-crystallized precipitate with As leachability of 0.5 mg/L was possible by increasing the initial molar ratio of Fe (III) to As (V) to 3:1 (X. Min et al., 2015; Singhania et al., 2006). In the upcoming sections, methods for arsenic stabilization and solidification, with a focus on stabilizing arsenic through cemented paste backfill, will be explored.

2.8 Cemented paste backfilling of arsenic-bearing materials

Mine backfilling entails utilizing waste materials like waste rock, deslimed and whole mill tailings, as well as quarried and crushed aggregates, to fill underground mined voids for disposal purposes and/or to serve various engineering functions (Benzaazoua et al., 2002). This practice provides support and a safe working area for mine structures, enabling optimal resource recovery and mitigating surface subsidence risks in underground stopes. Additionally, it offers a disposal site for waste rocks or mill tailings (Ercikdi, Kesimal, et al., 2009). The strength properties of backfill materials can be enhanced by incorporating a small amount of cement or other pozzolanic binders into the waste materials (Benzaazoua et al., 2002), relating the cemented backfill to S/S processes. Generally, there are three types of backfilling methods: hydraulic fill, rock fill, and cemented paste backfill. In recent years, cemented paste backfilling has gained global acceptance, especially in Canada, as a vital component of underground mining operations. The primary advantages of cemented paste backfill include safely depositing hazardous mill tailings (such as sulfide tailings) and other contaminated mine wastes into underground openings to mitigate their environmental impacts and reduce surface disposal and reclamation costs (Ercikdi et al., 2014; Ercikdi, Kesimal, et al., 2009).

Safely placing sulfide-rich wastes underground can substantially reduce significant environmental impacts associated with surface storage under atmospheric conditions, such as the formation of AMD and the release of heavy and toxic metals, as well as soil and groundwater contamination (Yilmaz et al., 2013). The practice of backfilling in underground stopes was initially employed in South African gold mines to provide support and reinforce pillars against geological hazards (Hustrulid & Bullock, 2001). Figure 2.9 illustrates the evolution of mine backfilling technology.

Falconbridge Nickel Mines Ltd. implemented CPB technology at the Hardy Mine in Sudbury, marking the first instance of its use in 1957 (Espley et al., 1970). The Bad Grund Mine in Germany, during the late 1970s, employed fine mill waste aggregate and silty filtered tailings as primary components of CPB (Lerche & Renetzeder, 1984; Tariq & Yanful, 2013). In the mid-1970s, Robinsky introduced thickened tailings as a method for surface disposal of concentrated tailings (Robinsky, 1975). The Hecla Mining Company utilized CPB at the Lucky Friday Mine in the USA. By the 1990s, numerous Canadian and Australian mines had adopted CPB as a viable alternative to rock fill and hydraulic fill methods, positioning them as probable leaders in CPB technology adoption (Qi, 2019; Rankine & Sivakugan, 2007; Tariq & Yanful, 2013). In recent years, CPB has garnered significant attention from academia and industry due to its technical, environmental, and economic advantages.

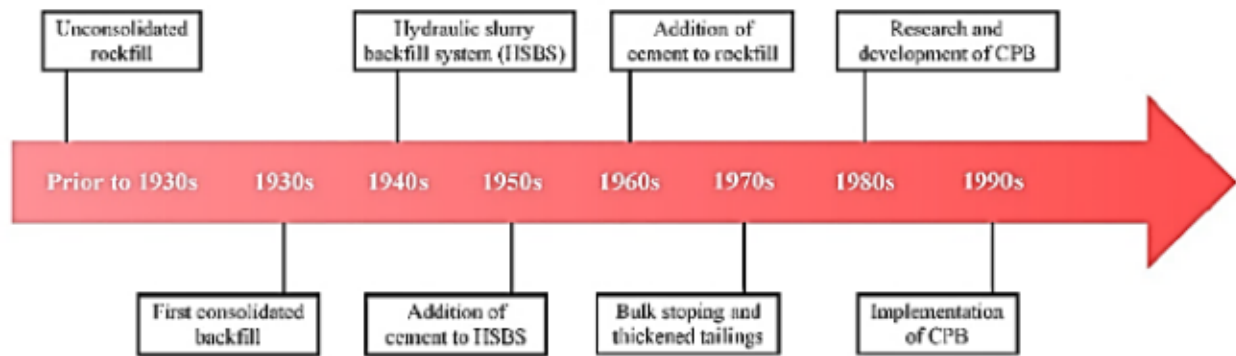


Figure 2.9 History of mine backfilling technology. Figure taken from (Hustrulid & Bullock, 2001)

CPB technology, characterized by a high-density slurry mixture of dewatered tailings, binding agents, and water, is thickened to achieve a non-settling consistency for transportation into mined cavities. CPB offers environmental benefits by diminishing the reactivity potential of sulfides and stabilizing pollutants. Hydraulic binders can undergo reactions during hydration with metals and metalloids, particularly with arsenic, resulting in the formation of stable compounds through precipitation and enhance mechanical strength (Coussy et al., 2011; X. Deng et al., 2017). Figure 2.10 illustrates the various components of cemented paste backfill.

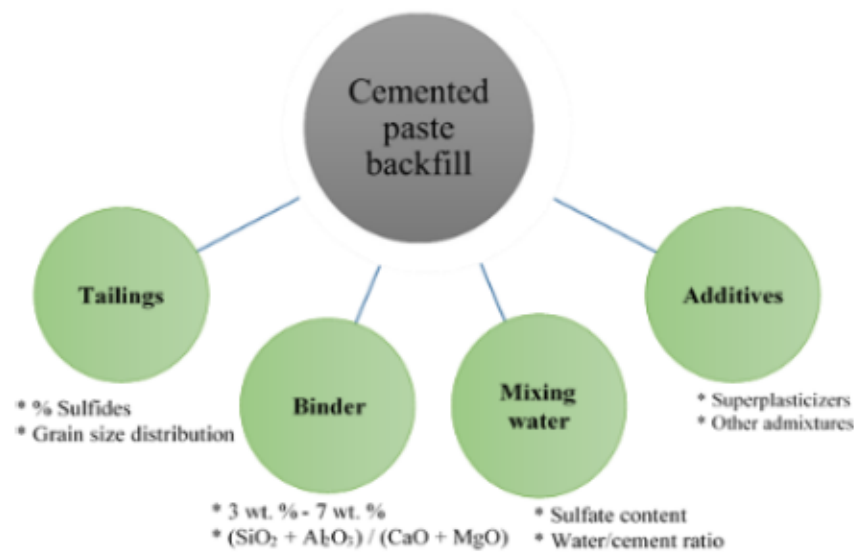


Figure 2.10 Schematic diagram illustrating the different components of paste backfill. Figure taken with modifications from (Benzaazoua et al., 2002)

The non-settling properties and desired rheological behavior of CPB (pumpable, non-Newtonian fluid) can be achieved with a solids content (by total mass) ranging from 70% to 85% and containing adequate fines (with at least 15% particles less than 20 microns) to prevent settlement (Orejarena & Fall, 2010; Rankine & Sivakugan, 2007; Sivakugan et al., 2015). The curing time for CPB is typically longer than that for conventional concrete and mortars. Ultimately, cemented paste backfill will evolve into a material with physical characteristics resembling those of hard soil and soft rock (Belem et al., 2000).

Cemented paste backfill is typically prepared in surface facilities and then transported underground into the stopes using reticulated pipelines. In most modern underground mines, it is customary to transfer and place the CPB within the mined-out stopes in two stages to alleviate pressures on the barricade. The initial stage, known as "plug fill" involves using paste with the highest binder content (7 wt.%). This material is allowed to cure under self-weight consolidation for a few days (usually 2 to 7 days). This delay, considered a conservative approach, enables the CPB to gain strength to protect the backfill barricade during the placement of the final fill (Cao et al., 2018; Ghirian & Fall, 2016; Yilmaz, Belem, Bussi re, et al., 2015). The second stage, termed "residual/mass fill" consists of a lower binder content (typically 3 to 4.5 wt.%) and is left to cure under self-weight for a longer period. The plug fill (with higher cement content) is capable of withstanding additional surcharge loading that could potentially damage the formed cement bonds

(Yilmaz, Belem, Bussi re, et al., 2015). Figure 2.11 depicts a schematic of a typical underground stope filling process.

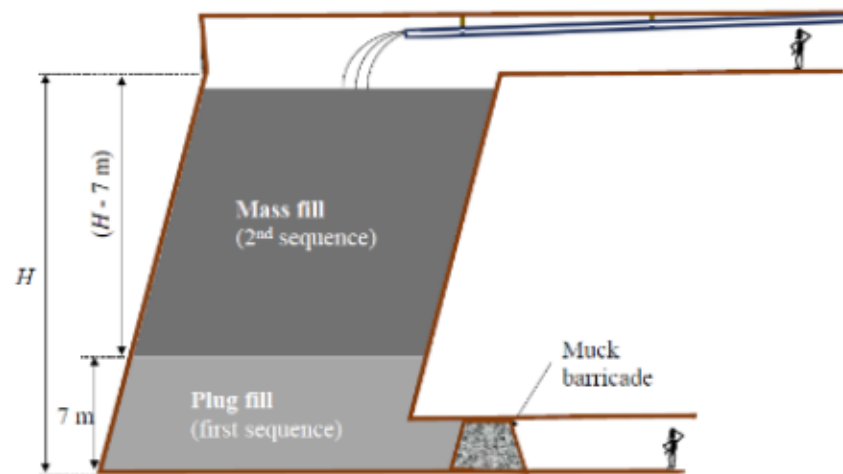


Figure 2.11 A schematic of a typical underground stope filling process. Figure taken from (N. J. F. Koupouli et al., 2016)

One notable characteristic of paste backfill materials is their high water content, typically exceeding the hydration requirements of cementitious materials. The primary reason for this elevated water-to-cement (W/C) ratio, typically ranging between 2.5 and 7, is to ensure the desired consistency and flowability needed for transferring the paste through pipelines via gravity or pumping (Tariq & Yanful, 2013). In contrast, conventional cement concrete and mortars are typically designed with a much lower W/C ratio, usually below 0.5 (Mehta, 1999). Consequently, the matrix of paste backfill can exhibit significant differences in properties compared to conventional concretes and mortars. These disparities may include compressive strength, density, porosity, hydraulic conductivity, durability, and microstructure of hardened samples (Godbout et al., 2007; Ouellet et al., 2007; Tariq & Yanful, 2013).

2.8.1 The quality criteria of CPBs

The quality of CPB samples is influenced by both intrinsic and extrinsic factors (see Figure 2.12). Intrinsic factors encompass all the characteristics of the tailings, cement, and water, as well as their interactions during curing. Extrinsic factors, on the other hand, are induced by variables such as stope dimension or structure, backfill-rock interaction, placement conditions, curing temperature and time, self-weight or time-dependent consolidation, and drainage or bleeding of excess water (S. Yin et al., 2020).

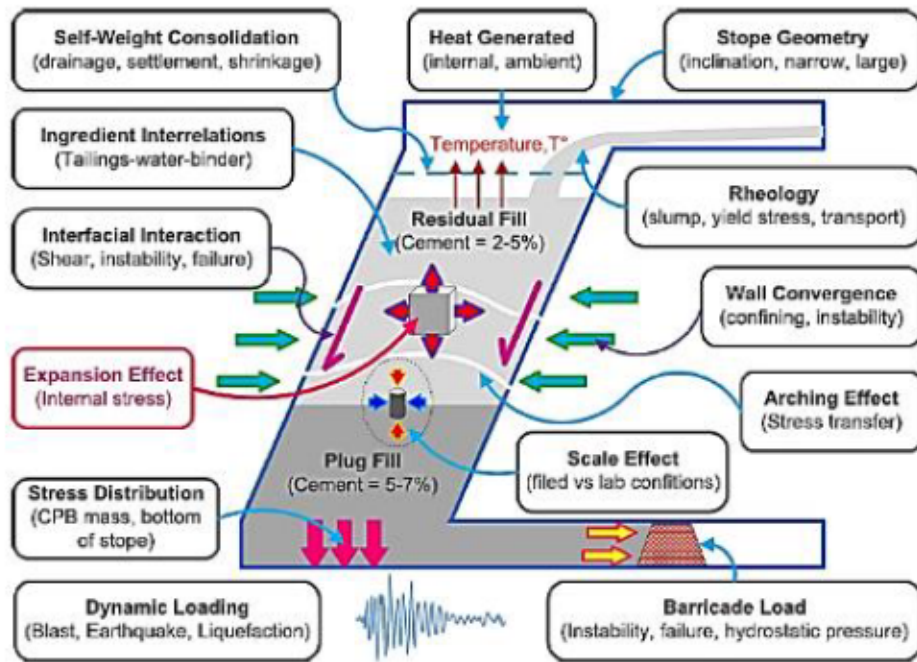


Figure 2.12 Intrinsic and extrinsic factors affect the quality of cement tailings backfill. Figure taken from (S. Yin et al., 2018)

The most crucial design criteria for cemented paste backfill include mechanical strength, workability, environmental performance, hydraulic conductivity, and durability. These parameters are dependent on the physical, chemical, and mineralogical properties of mine tailings and other wastes, mixing waters, additives, binder types, and their proportions (Benzaazoua et al., 2002). Fresh CPB must possess the necessary workability to facilitate efficient pumping/delivery (without clogging or pipeline failure) from the surface paste-fill plant to the underground mined-out stopes. Additionally, the hardened CPB matrix must meet static and dynamic load resistance requirements to ensure a safe underground working environment and serve as a primary construction material (Fall et al., 2009; H. Jiang, Qi, et al., 2019; Simon & Grabinsky, 2013). Each component of cemented paste backfills plays a role in transport, emplacement, and strength acquisition for both short- and long-term durations (B. D. Thompson et al., 2012).

2.8.1.1 The strength of CPBs

Mechanical properties, such as UCS, stress-strain behavior, and shear strength parameters, are important considerations for the safe and efficient design of CPB. These properties must be accurately evaluated to ensure the mechanical stability of CPB, especially when the backfill serves as a support pillar, crucial for ensuring workers safety. UCS is often considered the most common

parameter for determining the stability of CPB structures due to the simplicity and low cost of UCS testing (Q. Chen, Zhang, Fourie, Chen, et al., 2017). Figure 2.13 illustrates the components of CPB that influence its strength.

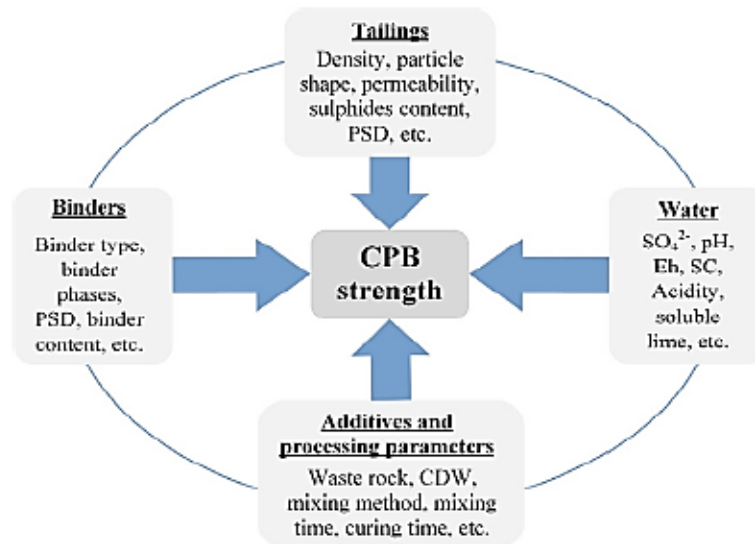


Figure 2.13 Schematic diagram of components of CPB and their associated characteristics that affect CPB strength. Figure taken from (Deb et al., 2017)

The strength of CPB should be adequate to sustain itself, especially in areas where exposed surfaces could lead to ore dilution risks during subsequent mining activities (B. D. Thompson et al., 2012). However, in the context of the Giant Mine, the focus is not on meeting typical strength requirements associated with active mining operations. Instead, the emphasis is on the CPB's ability to maintain its structural integrity under low stress conditions. The acquisition of CPB strength primarily hinges on the development of hydrated and chemically stabilized compounds.

The main distinction between cement stabilization and CPB lies in the strength of the resulting monolith. In CPB, achieving a very high strength monolith is not the primary design objective, and the UCS for CPB is often less than 500 kPa after 28 days of curing (Arcadis, 2017; Fall et al., 2005). Conversely, cement stabilized dust monoliths are engineered to withstand substantial loading and typically have UCS ranging from 4 MPa to greater than 15 MPa (Arcadis, 2017).

Numerous studies have been conducted to investigate the effects of various parameters on the mechanical strength of cemented paste backfill samples. A summary of these studies is provided in Table A.2. These investigations have explored a range of influencing factors, including binder

type and dosage (Benzaazoua et al., 2002; Du et al., 2021; Ercikdi et al., 2014; Ercikdi, Kesimal, et al., 2009; H. Jiang, Qi, et al., 2019; A. Wu et al., 2015; S. Yin et al., 2018; Yue Zhao, Soltani, et al., 2019; Yue Zhao, Taheri, et al., 2019), alternative binders (Cihangir et al., 2018; Ercikdi, Cihangir, et al., 2009; Ercikdi, Kesimal, et al., 2009; Koohestani et al., 2016; Olivier Peyronnard & Benzaazoua, 2011, 2012; Qiu et al., 2019), curing conditions (Belem et al., 2000; Cihangir & Akyol, 2016; Du et al., 2021; Fall & Pokharel, 2010; Hu et al., 2019; H. Jiang, Yi, et al., 2020a; H. Jiang & Fall, 2017a; Kesimal et al., 2005; L. Liu, Yang, et al., 2019; Mbonimpa et al., 2019; Yilmaz, Belem, & Benzaazoua, 2015; S. Yin et al., 2018), tailings properties (Benzaazoua et al., 2002, 2008; Benzaazoua, Fall, et al., 2004; Cihangir et al., 2018; Cihangir & Akyol, 2016; Fall et al., 2005; Kesimal et al., 2005; W. Li & Fall, 2016; Qiu et al., 2020; Su et al., 2019), specific additives such as water reducing agents (Ercikdi et al., 2010; Koohestani et al., 2018; Y. Liu et al., 2020; Mangane et al., 2018; Ouattara et al., 2018; Lei Yang et al., 2018), chemistry of the mixing water (Benzaazoua et al., 2002; H. Jiang & Fall, 2017b, 2017a; A. Wu et al., 2015), and mixing and preparation conditions (Cao et al., 2018; C. Min et al., 2019). In summary, it is evident that the physical, chemical, and mineralogical characteristics of the tailings, along with the chemical properties of the binders and mixing waters, mix design, in-situ stress, and curing conditions, are among the most influential parameters affecting the mechanical strength of cemented paste backfills (Benzaazoua et al., 2002; Benzaazoua, Fall, et al., 2004; Fall et al., 2005). The particle size distribution of tailings and the proportion of fines ($< 20 \mu\text{m}$) can significantly influence the strength of the paste, with coarse and medium tailings being preferable for CPB strength gain. The solid content (the mass of solids to the total mass of the paste) is one of the most influential properties, as higher solid content leads to greater strength gain during curing (X. Deng et al., 2017; Lei Yang et al., 2018). Various binders, including general use (GU) cement (also known as ordinary Portland cement, OPC), ground granulated blast furnace slag (GGBFS), fly ash (types C and F), sulfate-resistant Portland cement, bottom ash (BA), cement kiln dust, and silica fume (SF), as well as different waste and by-product materials serving as supplementary cementitious materials for creating low-cost alternative binders, have been utilized at different dosages. Research findings have demonstrated that the type and dosage of binder significantly impact the strength evolution of cemented paste backfill samples. The pozzolanic contents of the binders affect CPB strength, with higher pozzolanic content contributing to greater long-term stability (Kesimal et al., 2005). Pozzolanic wastes can be employed as binders to replace typical binders and reduce costs (Ercikdi,

Cihangir, et al., 2009). The sulfate content of tailings and mixing waters strongly influence hydration processes and strength gain, with effects dependent on binder type and dosage (Benzaazoua et al., 2002). Increased sulfate concentration in the paste mixture decreases CPB strength and stability, which can be mitigated by higher binder content and longer curing periods. Elevated curing temperatures also contribute to strength gain (Fall & Pokharel, 2010).

The use of water-reducing agents (WRAs) can enhance the mechanical strength of CPB samples and reduce the amount of cement needed for CPB preparation (Y. Liu et al., 2020; Mangane et al., 2018; Ouattara et al., 2018). The degree of improvement relies on the type of WRA materials and the binder (Ercikdi et al., 2010). Moreover, these materials create favorable conditions for the utilization of alternative binders (Y. Liu et al., 2020).

Mix variables should be optimized to achieve the desired strength while minimizing binder usage. The desired strength of paste backfill varies according to its intended purpose. To ensure sufficient ground support, the fill needs to have a minimum UCS of 5 MPa. However, for free-standing fill applications, the UCS typically falls below 1 MPa. A UCS of 100 kPa is frequently used as the threshold for assessing liquefaction potential (Belem & Benzaazoua, 2008). Based on the literature, a UCS ranging from 0.7 to 2 MPa is necessary for cemented backfill in typical underground mining operations (Brackebusch, 1995; Xiong et al., 2022). However, CPB has also been assessed for backfilling applications where load-bearing capacity is not a primary concern (Deschamps et al., 2008; Hamberg et al., 2015a; Yilmaz et al., 2014). In such scenarios, while CPB strength may be less critical (with a minimum UCS of 100 kPa), the objective remains to prevent the release of metal ions and metalloids and minimize AMD production (Hamberg et al., 2015a). For applications with lower strength requirements, proportions of binders in CPB materials can be reduced. Nonetheless, a previous study demonstrated that low binder proportions might not sufficiently suppress AMD generation (Cruz et al., 2001). Therefore, it is essential to investigate the leaching and stability of chemicals in CPB materials, particularly in cases where strength is of lower importance.

Some studies have indicated that there are consistently differences in UCS between field and laboratory CPB samples for a given mix recipe and curing time. The UCS performance of in situ CPB core samples could be at least 50% higher than CPB samples prepared and cured under laboratory conditions (H. Jiang, Yi, et al., 2020a). These discrepancies may arise from various

factors, including differences in mixing and hardening conditions (Lei Yang et al., 2018), the elevated temperatures experienced in CPB-filled stopes (B. D. Thompson et al., 2012), the influence of consolidation within the stope (Yilmaz et al., 2009), and field placement and curing conditions (Fahey et al., 2011).

2.8.1.2 The consistency (workability) of CPBs

Cemented paste backfills can be characterized as high-density slurries. This slurry behaves as a non-Newtonian fluid, requiring an applied force to initiate flow. Due to its high viscosity, backfill paste exhibits plug flow during transportation through a pipe. The outer portions of the slurry shear against the sidewall of the pipe, while the central part travels as a plug (Grice, 1998).

In simple shear, a Newtonian fluid is defined by a linear correlation between the applied shear stress, τ (Pa) and the shear rate, $\dot{\gamma}$ (s^{-1}), expressed as:

$$\tau = \eta\dot{\gamma} \quad (2.22)$$

The constant of proportionality (η) is known as the dynamic viscosity. During recent decades, many materials, particularly those of multi-phase nature, have been produced, deviating from the Newtonian postulate of a linear relationship between applied shear stress (τ) and shear rate ($\dot{\gamma}$). Consequently, the simple shear curve (τ - $\dot{\gamma}$) does not intersect the origin for these materials, leading to their classification as non-Newtonian fluids. In such cases, viscosity, defined as $\tau/\dot{\gamma}$ is not constant and varies as a function of τ or $\dot{\gamma}$. The viscosity of these materials not only depends on flow conditions (such as geometry and shear rate) but also on the kinematic history of the fluid. Based on this definition, three types of behavior are observed: shear-thinning or pseudoplastic behavior, visco-plastic behavior with or without shear-thinning, and shear-thickening or dilatant behavior. Figure 2.14 illustrates the flow curves (rheograms) of these three categories of fluid behavior, alongside the typical flow curve of Newtonian fluids. In the case of shear-thinning fluids, viscosity gradually decreases with increasing shear rate. Visco-plastic fluids are characterized by a threshold stress (referred to as shear yield stress, τ_0), which must be exceeded for the fluid to shear or flow. Below the yield stress, the fluid behaves like an elastic solid, while surpassing τ_0 allows the fluid to exhibit either Newtonian or non-Newtonian behavior. Shear-thickening fluids, on the other hand, lack a yield stress, but their apparent viscosity increases with rising shear rate (Chhabra, 2010).

In the mining industry, the slump test stands out as the most widely used method for measuring the rheological properties and transportation performance of fills in pipelines (Du et al., 2021; H. Jiang, Qi, et al., 2019). A typical slump value for the CPB matrix ranges from 100 to 250 mm (Yilmaz et al., 2012). Various factors, such as solid content, grain size distribution, water quality, temperature, mixing procedures, mineral, and chemical additives, can significantly influence the rheological behavior of the CPB matrix (H. Jiang, Qi, et al., 2019; Lang et al., 2015). The typical solid contents of CPBs, typically ranging between 70 and 85 wt.%, impact the flowability of paste mixtures and the quantity of tailings to be placed underground. Increasing solid content generally enhances the strength of CPB; however, it decreases the consistency (slump) of the mixture. While CPB requires sufficient water content to achieve the desired consistency for transport from the paste plant to underground openings, an increase in the water/cement (W/C) ratio adversely affects the strength and stability of CPB (Ercikdi et al., 2010; Ercikdi, Kesimal, et al., 2009). In such cases, water-reducing admixtures, known as plasticizers and superplasticizers, can be employed to prepare high-strength pastes without escalating the binder dosage. Lignosulphonate, naphthalene sulfonate, and polycarboxylate-based admixtures are renowned for their ability to reduce water content by 5–30% (Ercikdi et al., 2010; Şahmaran et al., 2006). A reduction in the W/C ratio is expected to enhance the microstructure, short- and long-term strength, and stability of CPBs made with sulfide-rich tailings.

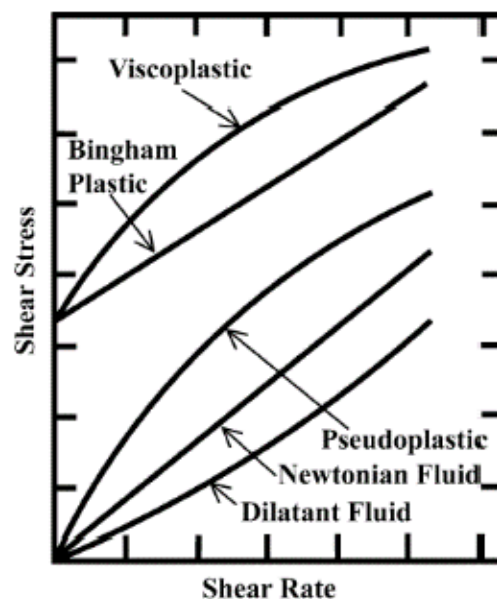


Figure 2.14 Typical flow curves for different types of non-Newtonian fluids. Figure taken from (Chhabra, 2010)

In recent years, several studies have been conducted to assess the impacts of various parameters on the rheological properties of CPBs (Table A.3). These studies have examined the effects of different factors, including: various binders (H. Jiang, Qi, et al., 2019; Kou et al., 2020; Panchal et al., 2018; Qiu et al., 2019; A. Wu et al., 2015), solid contents and its physical properties (X. Deng et al., 2017; H. Jiang, Qi, et al., 2019; Qiu et al., 2020; Lei Yang et al., 2018), curing time and temperature (Haiqiang et al., 2016; Haruna & Fall, 2020; Panchal et al., 2018), mixing water quality (H. Jiang & Fall, 2017a, 2017b; A. Wu et al., 2015), water-reducing admixtures and other superplasticizers (Ercikdi et al., 2010; Haruna & Fall, 2020; Koohestani et al., 2018; Y. Liu et al., 2020; Mangane et al., 2018; Ouattara et al., 2018; Panchal et al., 2018; Simon & Grabinsky, 2013; Lei Yang et al., 2018), mixing time and intensity (C. Min et al., 2019; Liuhua Yang et al., 2019) and time-dependent rheological behavior (H. Cheng et al., 2020; Kou et al., 2020) of CPBs. These studies aim to provide insights into how these parameters influence the rheological characteristics of CPBs, offering valuable information for optimizing their formulation and application in mining operations.

The findings indicate that the incorporation of water reducing agents (WRAs) enhances the consistency and workability of CPB without necessitating additional water (Ercikdi et al., 2010; Koohestani et al., 2018; Y. Liu et al., 2020). Additionally, these materials reduce the yield stress value, with the extent of their impact dependent not only on their type but also on the type and dosage of the binder (Mangane et al., 2018; Ouattara et al., 2018; Simon & Grabinsky, 2013). The type of binder employed also plays a significant role, with samples prepared using alkali-activated slag exhibiting higher workability compared to those prepared using OPC (H. Jiang, Qi, et al., 2019). Mixing intensity significantly affects the rheology of CPB samples, with increased mixing intensity leading to higher fluidity and density and reduced setting time (C. Min et al., 2019; Liuhua Yang et al., 2019). Curing time is another influential factor affecting the viscosity and yield stress of CPB, with both parameters increasing with longer curing times (Haruna & Fall, 2020; Kou et al., 2020; Panchal et al., 2018). However, the effect of curing time is mitigated for samples containing superplasticizers (Haruna & Fall, 2020). Curing at lower temperatures could result in lower yield stress (Haiqiang et al., 2016).

2.8.1.3 The hydraulic conductivity of CPBs

Saturated hydraulic conductivity (k_{sat}) significantly influences both the physical properties (mechanical strength, consolidation, and liquefaction potential) and chemical behavior (sulfide reactivity and contaminant migration) of the paste (Godbout et al., 2007). Hydraulic conductivity is pivotal as it directly influences the groundwater flow rate through the CPB structure in flooded conditions. It significantly impacts the leaching potential and the transport of pollutants through the CPB to groundwater (Fall et al., 2009; Levens et al., 1996). Furthermore, hydraulic conductivity offers pertinent insights into the pore structure of CPB, including characteristics such as coarseness, connectivity, and cracking (Fall et al., 2009; Pokharel & Fall, 2013).

The susceptibility of CPBs to AMD hinges on the reactivity of tailings within the CPB. This reactivity is influenced by the types and quantities of sulfide minerals present in the CPB, as well as the hydraulic properties of the CPB, such as water seepage and oxygen transfer through the CPB matrix. Assessing these properties, particularly the unsaturated hydraulic conductivity, can provide insights into the potential for AMD generation. The inclusion of binders also plays a role in mitigating AMD generation by reducing the hydraulic conductivity of the CPB monolith and neutralizing acids produced.

Several comprehensive studies have investigated the variations in the saturated hydraulic conductivity of CPBs. These studies have explored the effects of various parameters, including binder type and content (Fall et al., 2009; Godbout et al., 2007; Yilmaz et al., 2008; Yilmaz, Belem, Bussière, et al., 2015), curing time and temperature (Fall et al., 2009; Godbout et al., 2007; L. Liu, Zhu, et al., 2019; Pokharel & Fall, 2013; Yilmaz et al., 2008; Yilmaz, Belem, Bussière, et al., 2015), particle size distribution of tailings (Cihangir & Akyol, 2016), sulfate concentrations (Cihangir & Akyol, 2016; W. Li & Fall, 2016; Pokharel & Fall, 2013), water/cement ratio (Fall et al., 2009) and ice/water ratio (L. Liu, Zhu, et al., 2019) on the hydraulic conductivities of CPB samples. A summary of these studies is provided in Table A.4. The findings indicate that increases in binder content, curing time, and curing temperature led to reductions in CPB hydraulic conductivity. This progressive reduction in k_{sat} can be attributed to microstructure evolution and pore refinement during curing, particularly at higher curing temperatures, resulting in changes to the quantity and structure of voids (Godbout et al., 2007). Additionally, the type of binder has a notable effect, with mixed binders containing slag showing greater impacts on k_{sat} reduction

compared to binders made of fly ash (Godbout et al., 2007). CPBs with higher sulfate contents generally exhibit higher permeability (W. Li & Fall, 2016), while decreasing the water/cement ratio leads to reduced k_{sat} (Fall et al., 2009).

2.8.1.4 The leaching behavior of CPBs

Leaching is a physical process wherein a material, whether treated or untreated, is exposed to a liquid solution, and the dissolution rate of its chemical constituents is assessed. This process encompasses several stages, including the initial loss of surface deposits and unfixed components, the penetration of solutions into the substrate pore-space with hydrolysis or dissolution of fixed or complexed components, and the migration of stabilizers to the surface (Randall, 2012). Leaching mobilizes contaminants within the stabilized matrix by dissolving them, a process driven by a combination of chemical and physical mechanisms (Côté et al., 1987; Leist et al., 2003). These mechanisms include the bulk dissolution of mineral phases in the treated waste, the wash-off of surface contaminants, the desorption of contaminants, (or other elements) and changes in chemical parameters such as pH and Eh, both of which significantly affect arsenic and may dissolve previously insoluble phases. In neutral leachants, the leaching rate is primarily governed by the diffusion of solubilized species. Within the solid waste form, the transport of contaminants can occur through convection or diffusion. Since most waste forms have relatively low permeability, diffusion typically dominates. When considering the stabilized solid at the onset of leaching, diffusion is driven by the difference in chemical potential (constituent concentration) between the solid and the fluid leachant. This chemical gradient prompts constituents to migrate from the solid to the leachant (Conner, 1990; Leist et al., 2003). Evidence supporting this diffusion-based leaching mechanism includes the linear relationship observed when plotting the cumulative fraction released against the square root of time (Dutr e & Vandecasteele, 1996; Leist et al., 2003).

Several standardized protocols are available for conducting laboratory leaching studies. Among these, the toxicity characteristic leaching procedure (TCLP) stands out as the most widely used leaching test, recommended by the United States Environmental Protection Agency (USEPA) for assessing the release potential of heavy metals (Lu et al., 2019; Su et al., 2019). This test effectively simulates the process of metal elements permeating groundwater subsequent to the placement of CPB into the slope. In addition to TCLP, leaching tests such as tank and weathering cell experiments can be conducted to evaluate the behavior of arsenic in CPB materials and tailings for

environmental assessment purposes. Due to the complex leaching behavior of arsenic, which cannot be fully captured by a single batch test, other leaching and analytical methods for both untreated and treated samples should be employed. These methods may include pH-based leaching tests and modified sequential extraction procedures (Randall, 2012).

Several studies have investigated the leaching properties of cemented paste backfills, as summarized in Table A.5. These studies examined the leaching behavior of heavy metals such as lead (Pb) (Qiu et al., 2019; Su et al., 2019), cadmium (Cd) (Qiu et al., 2019), and zinc (Zn) (Benzaazoua et al., 2008; Su et al., 2019) in CPB samples prepared from contaminated tailings. Weathering cell tests conducted on CPB prepared using desulfurized tailings showed no acidification after 100 days of leaching (Benzaazoua et al., 2008). The utilization of alkali-activated slag (AAS) as an alternative binder in cemented paste backfill resulted in low leaching concentrations of Pb, while increasing the binder content reduced the leaching concentration of Cd (Qiu et al., 2019). Moreover, the addition of polyaluminium sulfate (PAS) as a stabilizing agent for metal ions in CPB made from lead-zinc tailings effectively controlled the leaching of lead in the CPB (Su et al., 2019).

2.8.1.5 The microstructure of CPB

The microstructure of CPB, including the type, quantity, and distribution of hydration products, along with its micro-morphology, plays a role in determining its properties. Hardened CPB represents a heterogeneous multiphase system, comprising a solid phase with various hydration products, water, and air in the void spaces (L. Liu, Fang, et al., 2020; L. Liu, Xin, et al., 2020). Consequently, it behaves like a multi-phase porous backfill with a distinctive evolving microstructure (S. Chen, Du, Zhang, Zhang, et al., 2020). However, owing to the diverse range of available cemented materials, the relationship between microstructure and macroscopic behavior in filling materials remains incompletely understood. CPB demonstrates a discontinuous, heterogeneous, and anisotropic macrostructure alongside diverse microstructures, all intricately interrelated. Hence, there's a necessity for a comprehensive and efficient study of its microstructure and macroscopic characteristics (L. Liu, Xin, et al., 2020).

The microstructure of hardened paste backfills significantly influences their mechanical properties and durability (Belem et al., 2001). To enhance the quality of CPB, further investigations are required to elucidate the relationship between microstructure and engineering properties. Studies

have indicated that microstructural parameters, such as particle shape, size distribution, arrangement, connecting style, microparticle scale, paste type, pore size, and porosity, play crucial roles in determining the mechanical properties of paste backfill. Therefore, examining the microstructure of CPB can provide valuable insights into understanding its engineering properties (B. Zhang et al., 2018).

In recent decades, numerous scholars have conducted extensive research on the morphology and internal microstructure of cemented paste backfills, employing various technologies including scanning electron microscopy (SEM), X-ray diffractometry (XRD), computed tomography (CT), nuclear magnetic resonance (NMR), and mercury intrusion porosimetry (MIP). A summary of these studies is provided in Table A.6. XRD was utilized to analyze samples, identifying characteristic crystalline substances generated by CPB hydration. SEM tests enabled the intuitive observation of the morphology and structure of CPB hydration products (Du et al., 2021). Furthermore, SEM investigations allowed for the observation of secondary mineral precipitation within CPB samples, contributing to the cohesion of the paste backfill matrix by filling intergranular voids (Benzaazoua et al., 2002). MIP has been widely employed to evaluate total porosity and pore size distribution of various geomaterials, with tests on cemented paste backfills primarily aimed at defining microstructural evolution during hardening and its correlation with mechanical strength (O'Farrell et al., 2001; Ouellet et al., 2007).

In these studies, the effects of various important parameters such as binder type and dosage (Benzaazoua et al., 2002; Cihangir & Akyol, 2016; Du et al., 2021; Ercikdi, Kesimal, et al., 2009; Fall et al., 2009; H. Jiang, Qi, et al., 2019; Yue Zhao, Soltani, et al., 2019), physical and chemical properties of tailings (Cihangir et al., 2018; Cihangir & Akyol, 2016; Fall et al., 2005; Ke et al., 2016; Ouellet et al., 2008; Qiu et al., 2020), curing time (Deschamps et al., 2006; Ercikdi et al., 2013; Ghirian & Fall, 2016; Haiqiang et al., 2016; L. Liu, Zhu, et al., 2019), curing temperature (Du et al., 2021; Fall et al., 2009; Fall & Pokharel, 2010; Haiqiang et al., 2016; Haruna & Fall, 2020; H. Jiang, Yi, et al., 2020b; L. Liu, Yang, et al., 2019; L. Liu, Zhu, et al., 2019; Ouellet et al., 2008; Pokharel & Fall, 2013), different industrial and non-industrial additives (Q. Chen, Zhang, Fourie, & Xin, 2017; X. Chen et al., 2018; Ercikdi, Cihangir, et al., 2009; Hu et al., 2019; H. Jiang, Yi, et al., 2020b; Koohestani et al., 2016; Olivier Peyronnard & Benzaazoua, 2011; Yilmaz et al., 2020), water-reducing admixtures (Ercikdi et al., 2010; Haruna & Fall, 2020; Koohestani et al., 2018; Y. Liu et al., 2020; Mangane et al., 2018), sulfate and salinity (Benzaazoua et al., 1999; Fall

et al., 2009; Fall & Pokharel, 2010; H. Jiang & Fall, 2017a; W. Li & Fall, 2016; Pokharel & Fall, 2013), mixing conditions (C. Min et al., 2019), and specimen size and placement conditions (Yilmaz, Belem, & Benzaazoua, 2015) on the microstructural properties of cemented paste backfills were investigated.

It is widely acknowledged that the strength of porous materials depends on the form, quantity, and distribution of voids (L. Li & Aubertin, 2003; Ouellet et al., 2007). Similar to other engineering materials, the compressive strength of CPB is typically inversely (and non-linearly) related to the total porosity. Generally, an increase in total porosity leads to a decrease in material strength. However, when the voids are filled with precipitated phases, the material strength could increase due to the refinement and segmentation of the porosity and the presence of different precipitated phases (Ouellet et al., 2007).

The mechanical strength of paste backfill mixtures is contingent upon the quality of the cementitious matrix, which is influenced by the chemistry of the tailings, mixing water, and binder. As the paste mixture occurs, the binder is largely dissolved within the mixing water, while the tailings react with the water, releasing sulfates and various metals, thereby decreasing the pH of the resulting solution. The various types of binders used exhibit different chemistries, leading to diverse compositions of the cementitious matrix (Benzaazoua et al., 2002).

The proportion of fine tailings ($< 20 \mu\text{m}$) significantly influences both the overall porosity of the CPB material and its pore size distribution. Using finer tailings material results in increased overall porosity of the CPB. Additionally, the total porosity and void ratio of the paste material are strongly affected by the drainage capacity of the fresh backfill. Drained paste backfill samples exhibit reduced porosity and smaller void ratios compared to undrained samples. This is attributed to water loss through drainage, leading to increased packing density and subsequent reduction in total porosity and void ratio of the backfill material. Drained paste backfill samples demonstrate higher strength than undrained samples. Moreover, paste backfill mixes prepared from coarse tailings tend to gain strength more rapidly than those made from fine tailings (Fall et al., 2005). MIP results on CPB reveal an evolution and refinement of pore size over time due to the presence of hydrates and secondary minerals in the CPB matrix. These minerals precipitate within voids, partially or completely filling them, thereby enhancing compactness (Fall & Benzaazoua, 2005; Ouellet et al., 2007).

2.8.2 Arsenic stabilization in cemented paste backfills

As previously discussed, numerous studies have investigated the behavior of arsenic under classical stabilization/solidification conditions, characterized by a low water/cement (W/C) ratio and high proportions of hydraulic binder. Typically, such conditions are effective in stabilizing arsenic, resulting in lowered leached concentrations as arsenic precipitates into stable phases like calcium arsenite or calcium arsenate (Coussy et al., 2011) except in cases such as the ATRW dust in the Giant Mine (SRK, 2002). However, in the context of CPB characterized by high W/C levels and low proportions of hydraulic binder, hydration conditions may differ from those of classical W/C ratios. This is because high water contents in CPB promote the formation of crystalline precipitates from pore water in addition to direct hydration of the binder reagents. Consequently, the long-term behavior and stability of As-compounds in CPB remain unclear (Coussy et al., 2011).

To date, only a few studies have investigated the potential of CPB for the solidification and stabilization of arsenic, as summarized in Table 2.6. These studies have explored different arsenic-bearing tailings or wastes, along with various binders and additives such as ordinary Portland cement (OPC), fly ash, silico-aluminous fly ash (SAFA), biofuel fly ash, basic oxygen furnace steel slag (BOFSS), flue gas desulfurization gypsum (FGDG), and finely-ground blast furnace slag (FGBFS). The aim of these investigations has been to elucidate the mechanisms involved in the stabilization and leaching of arsenic within CPB matrices.

CPB has been effectively utilized to immobilize arsenic-bearing tailings and spiked arsenic in both natural and synthetic CPB samples. The arsenic minerals and their speciation are outlined in the table. Typically, the proportions of binders used in these studies ranged from 3% to 7%, with the requirement of achieving a strength of less than 1 MPa. Several mechanisms have been proposed to explain the stability of arsenic in these cases, including the formation of calcium arsenates (Coussy et al., 2011; Coussy, Paktunc, et al., 2012; Hamberg et al., 2015a; Hamberg, Alakangas, et al., 2018), entrapment of arsenic in the cementitious matrix through sorption onto calcium-silicate-hydrates (C-S-H) (Bull & Fall, 2020b; Coussy et al., 2011), and the formation of ferric arsenates and ferric-calcium arsenates (Coussy, Paktunc, et al., 2012; Hamberg et al., 2017). Additionally, adsorption of As (V) onto the Fe-precipitates (FEP) and solidification in double salt minerals such as alkaline arsenates (Y. Zhang et al., 2019a) have been identified as contributing mechanisms. The stabilization of arsenic is directly influenced by the type and content of the

binders used. Furthermore, diffusion, dissolution, and precipitation are the primary mechanisms governing arsenic leaching. In CPB materials, the formation of C-S-H is a major contributor to mechanical strength. However, sulfates resulting from sulfide oxidation may react with the C-S-H, leading to the formation of ettringite and gypsum (sulfate attack), which can cause a loss of strength within the CPB (Hamberg, Maurice, et al., 2018).

To the best of the authors' knowledge, limited data exists in the literature regarding the UCS of arsenic-containing samples. Hamberg et al. (Hamberg et al., 2015a) conducted UCS tests on drained CPB samples prepared using arsenopyrite-rich tailings with an arsenic concentration of 1070 ± 30 mg/kg. The strength range for their samples prepared using ordinary Portland cement was between 341 and 426 kPa after 28 days for 3% and 5% cement, respectively. Su et al. (Su et al., 2019) prepared CPB samples using lead-zinc tailings and investigated their strength over 28 days of curing. Their findings indicated that a cement-to-tailings ratio of 1:6 and a slurry concentration of 70% resulted in the highest strength after 28 days. Large mines often generate vast quantities of tailings and other waste materials, and the expense of cement for CPB construction can be considerable. Consequently, numerous studies have investigated alternative binders or methods to reduce cement usage in CPB applications (Benzaazoua, Fall, et al., 2004; Olivier Peyronnard & Benzaazoua, 2012). Zhao (L. Zhao, 2023) utilized flue gas desulfurization gypsum (6%) and limestone (3%) to prepare cemented paste backfill using Cr (VI)-containing tailings. The results showed that the compressive strength of the CPB samples could reach approximately 5.53 MPa with 99.5% immobilization of Cr (VI). Ground granulated blast furnace slag (GGBFS) and biofuel fly ash have been effectively employed to partially substitute cement in CPB, leveraging their pozzolanic and alkaline characteristics (Benzaazoua et al., 2002; Coussy et al., 2011). While alkaline materials like fly ashes and slags are commonly believed to enhance arsenic mobility, some findings suggest that they may actually decrease mobility by facilitating the formation of stable Ca-As complexes (Hamberg et al., 2015a).

Table 2.6 A summary of studies on the incorporation of arsenic-contaminated materials into the cemented paste backfills

Research	Tailings/wastes	Binders	Concepts and results
(Coussy et al., 2011)	Tailings of gold mine ore processing plant (3800 ppm As mainly in arsenopyrite form)	OPC, and mixture of OPC with FA (class C) and BFS	<p><i>Concepts:</i> The behavior of arsenic in CPBs made from arsenopyrite-rich tailings was assessed.</p> <p><i>Results:</i> Tailings contained 3800 mg/kg As, mainly as arsenopyrite. CPB strength increased with curing, reaching up to 3000 kPa for slag-based mixtures after 120 days. Arsenic was less effectively fixed in fly ash-based binders. Tank leaching tests showed cumulative As release of 140 mg/m² for Portland cement CPB, 500 mg/m² for fly ash CPB, and 200 mg/m² for slag CPB after 64 days. As solubility varied with pH, stabilizing at pH 8–10 for Portland cement and below pH 8 for fly ash CPB. Weathering tests indicated cumulative As release of 16 mg/kg (Portland), 40 mg/kg (fly ash), and 26 mg/kg (slag) after 73 days. The release mechanisms of arsenic from the CPB monoliths involved dissolution at the matrix-solution interface. The arsenic compounds varied depending on the binder used: calcium arsenates for OPC, a mix of calcium arsenates and iron-arsenic compounds for OPC-FA, and entrapped arsenopyrite grains within the C–S–H of the cementitious matrix for OPC-BFS samples.</p>
(Coussy, Paktunc, et al., 2012)	Silica powder + synthetic contaminated mine water (As(III) and As(V) in the forms of sodium arsenite and sodium arsenate)	OPC and OPC-SAFA mixture	<p><i>Concepts:</i> The stability of arsenic-bearing compounds formed in the cementitious matrices and the general mechanisms of arsenic release in CPB were investigated.</p> <p><i>Results:</i> The leaching behavior of arsenic depended on the binder used. In the most aggressive leaching tests, arsenic depletion percentages did not exceed 5%. The depletion mechanisms involved both diffusion of arsenic from the pore water and a dissolution/precipitation front in the case of flooded CPB monoliths. The cumulative curves indicate that more As is released during the leaching of fly ash-based samples, with a maximum of 50 mg/m² at the end of the test for fly ash-based samples and 14.8 mg/m² for OPC-based samples.</p>
(Hamberg et al., 2015a)	Arsenic-contaminated sulfide-rich tailings (As-bearing iron (Fe)-precipitates (FEP), 1000 ppm As)	OPC and BFA {3%-7%}	<p><i>Concepts:</i> The management of sulfide-rich tailings from a gold mine was studied by converting them into a monolithic mass using the CPB method, and the arsenic release was assessed.</p> <p><i>Results:</i> The leaching tests (TLT and WCT) showed that the inclusion of As-rich tailings into a cementitious matrix increased leaching of As.</p>

Table 2.6 A summary of studies on the incorporation of arsenic-contaminated materials into the cemented paste backfills (continued)

Research	Tailings/wastes	Binders	Concepts and results
(Hamberg et al., 2015c)	Tailings of a gold mine (As-bearing iron (Fe)-precipitates (FEP), 1000 ppm As)	OPC and BFA	<p><i>Concepts:</i> The leaching behavior of arsenic in both unmodified tailings and CPB samples was studied using TLT.</p> <p><i>Results:</i> Incorporating arsenic-rich tailings into a cementitious matrix increased arsenic leaching. Alkaline conditions in OPC and OPC-BFA during TLT led to a small proportion of arsenic desorbing from arsenic-bearing tailings. The leaching of arsenic in OPC increased more significantly as the pH dropped from 10 to 8, suggesting the formation of calcium arsenates. The addition of binders may positively affect long-term arsenic leaching by enhancing the acid-neutralizing capacity.</p>
(B.-J. Kim et al., 2016)	Arsenic-rich mine tailings (As in the form of arsenopyrite) + natural river sand (as fine aggregate)	OPC	<p><i>Concepts:</i> The engineering properties and leaching behavior of two different controlled low-strength materials (CLSM, mortar, and slurry) made from arsenic-rich mine tailings were assessed.</p> <p><i>Results:</i> Arsenic concentration in the tailings was 225 mg/kg. The slurry-type CLSM mixture spread further, while the mortar-type CLSM mixture was better suited for use as mine backfill with a complex structure. CLSM compressive strength ranged from 0.3 to 8.3 MPa, meeting ACI Committee 229 specifications depending on cement content (10–30% by tailings weight). The leaching fraction of arsenic from CLSM mixtures with 10-30% cement content by weight of the tailings was below 6%, regardless of the mix proportions. Dynamic leaching tests showed cumulative arsenic release stabilizing at 45–55 days.</p>
(Hamberg et al., 2017)	Tailings of a gold mine after cyanidation process (1000 ppm As associated with Fe-(III)oxy-hydroxides)	OPC, BFA (class C) {1-3 wt. %}	<p><i>Concepts:</i> The mobility of arsenic under reduced water saturation levels and during flooding events was assessed.</p> <p><i>Results:</i> Managing cyanidation tailings with CPB containing a low binder fraction led to increased arsenic leaching, regardless of curing conditions. Reducing the water saturation level in CPB mixtures caused the dissolution of cementitious phases. Adding a calcium-rich binder destabilized initially formed arsenic-iron precipitates in unmodified tailings, decreasing the stability of arsenic, particularly in acidic conditions.</p>

Table 2.6 A summary of studies on the incorporation of arsenic-contaminated materials into the cemented paste backfills (continued)

Research	Tailings/wastes	Binders	Concepts and results
(Hamborg, Alakangas, et al., 2018)	Cyanidation tailings (CT) (As in the form of arsenopyrite)	OPC and BFA (class C) {1 - 3 wt.%}	<p><i>Concepts:</i> The geochemical stability of As, Cu, Ni, and Zn in CPB materials under unsaturated conditions was assessed.</p> <p><i>Results:</i> The release of As from OPC and OPC/FA was up to 18 times higher than from CT, with the highest release observed as the pH decreased from 10–11 to 8. A significant portion of arsenic was associated with amorphous iron precipitates. The release of copper, nickel, and zinc in CPB was primarily controlled by water-soluble phases, whereas arsenic release was less pronounced and governed by arsenic (III) species. Arsenic release from CPB was up to 18 times higher than from CT and was most significant as the pH decreased from 10 to 8, due to the dissolution of cementitious arsenic phases or calcium arsenates.</p>
(Y. Zhang et al., 2019a)	High-arsenic-containing tailings of a zinc processing plant (660 µg/L leachable As)	OPC, FGBF S, BOFS S, and FGDG	<p><i>Concepts:</i> The effect of adding various cementitious materials on the properties of CPB samples made from high-arsenic-containing tailings was studied.</p> <p><i>Results:</i> The optimal design of CPB was found to be a specimen with 60% BF slag, 30% SS, and 10% gypsum. The compressive strength reaches 10 MPa at 3 days and 28 MPa at 28 days. Based on FTIR, XPS, and SEM-EDS microscopic results, the mechanism of arsenic stabilization by the cementitious material was presumed to involve primarily the solidification of arsenic into double salt minerals, such as alkaline arsenates, within the system.</p>
(Bull & Fall, 2020a)	Natural tailings of a hard rock gold mine (50000 ppm As ₂ O ₃)	OPC {4.5 wt.%}	<p><i>Concepts:</i> The impact of curing temperature on the arsenic leachability of cemented paste backfills was studied using the ASTM C1308 leaching protocol. This method was employed to determine the leachability of CPB samples subjected to various curing temperatures.</p> <p><i>Results:</i> Curing temperature had a significant impact on the leachability of CPB. As the curing temperature increased from 2°C to 35°C, the performance of CPB in immobilizing arsenic decreased. The cumulative mass of arsenic leached at 2°C is about 4% lower than that of the sample cured at 20°C and approximately 25% lower than the sample cured at 35°C. The pH of the 2°C CPB leachate ranges from 6.4 to 8.3. The 20°C CPB has a pH range of 6.1 to 7.3, while the 35°C CPB exhibits a pH range of 5.6 to 7.1. This temperature-dependent leachability was due to changes in the pore structure of the CPB, the formation and development of hydration products, and the variations in pH within the CPBs during the curing process.</p>

Table 2.6 A summary of studies on the incorporation of arsenic-contaminated materials into the cemented paste backfills (continued)

Research	Tailings/wastes	Binders	Concepts and results
(Bull & Fall, 2020b)	Natural tailings of a hard rock gold mine (50000 ppm As ₂ O ₃)	OPC/Slag {4.5 wt.%}	<p><i>Concepts:</i> The effects of curing temperature (2, 20, and 35°C) on the leachability of arsenic (As (III)) in CPB samples containing blast furnace slag (OPC/Slag-CPB) were studied.</p> <p><i>Results:</i> Arsenic leaching from OPC/Slag-CPB was temperature-dependent. Higher curing temperatures resulted in a decrease in the amount of arsenic released from OPC/Slag-CPB. The immobilization of As(III) was more effective at 35°C (2128 mg leached) than at 2°C (2906 mg leached). Leaching of arsenic from OPC/Slag-CPBs was primarily governed by diffusion, regardless of the curing temperature. The effect of curing temperature on OPC/Slag-CPBs was opposite to that observed for OPC-CPBs.</p>

2.9 Design of Experiments (DOE)

The methodology of delineating and exploring all conceivable conditions in an experiment encompassing multiple factors is termed the design of experiments (Roy, 2010). Designing an experiment involves devising a scheme or framework of the various conditions to be examined. An experiment design should fulfill two primary objectives. Firstly, it should establish the number of trials required. Secondly, it should outline the conditions for each trial. Prior to crafting an experiment, a thorough understanding of the product or process under scrutiny is essential for identifying the factors that are likely to influence the outcome (Roy, 2010). Generally, an experiment may be conducted for one or more of the following purposes (Dean et al., 2017):

- (i) To ascertain the primary factors contributing to variations in a measured response,
- (ii) To identify the conditions that lead to either maximum or minimum responses,
- (iii) To compare the responses attained under various settings of controllable variables,
- (iv) To derive a mathematical model capable of predicting future responses.

When designing an experiment, it's crucial to consider the analysis that will be conducted. The effectiveness of the analysis hinges on the specific experimental design employed to gather the data. Failing to consider these aspects could result in investing substantial time, effort, and resources into collecting data that appear pertinent but offer limited insights into the research questions being addressed (Dean et al., 2017).

Replication, blocking, and randomization are three fundamental techniques in experimental design, each serving distinct purposes:

Replication: Replication involves repeating experimental conditions to enhance the precision of estimated effects and reduce associated variability. By conducting multiple repetitions of the same conditions, researchers can better estimate the true effects of interest and account for any inherent variability in the data.

Blocking: Blocking entails dividing experimental units into groups or blocks based on certain characteristics. The goal is to create blocks where units are relatively similar, allowing treatments applied within each block to be compared under comparable conditions. Blocking helps account for variability due to factors that are not of primary interest, thereby improving the accuracy of treatment effect estimates.

Randomization: Randomization is employed to minimize systematic and personal biases by randomly assigning experimental units to different treatment groups. By randomizing the assignment of treatments, researchers ensure that any observed differences between treatment groups are not influenced by external factors or researcher preferences. Randomization helps control for confounding variables and increases the validity of experimental findings (Dean et al., 2017).

In summary, replication increases precision, blocking accounts for variability, and randomization reduces bias in experimental designs. These techniques work together to improve the reliability and validity of research findings.

2.9.1 Factorial design

In academic literature, the method known as the design of experiments is often termed factorial design. This approach involves structured experimentation enabling the analysis of multiple factors' impacts on a response. By simultaneously altering the levels of all factors during experimentation, rather than sequentially, researchers can examine the interplay among these factors. A full factorial design specifically entails researchers measuring responses across all possible combinations of factor levels (Antony, 2014). For a full factorial design, the number of possible designs, N , is

$$N = L^k \quad (2.23)$$

where L = number of levels for each factor and k = number of factors (Roy, 2010).

A fractional design involves experimenters conducting only a chosen subset or "*fraction*" of the runs present in the full factorial design. These designs are preferable when resources are constrained or when dealing with a large number of factors since they require fewer runs compared to full factorial designs (Antony, 2014). This method offers significant time and cost savings but demands meticulous mathematical handling both during the experiment's design phase and when analyzing the outcomes. Despite being commonly employed and effective, factorial and fractional factorial designs of experiments have some limitations (Roy, 2010):

1. Large numbers of variables can lead to experiments that are costly and time-consuming.
2. Different results may arise from using two different designs for the same experiment.
3. Interpreting experimental results with numerous factors can be challenging due to a lack of straightforward design and analysis guidelines.

2.9.2 Response surface methodology (RSM)

Box and Wilson introduced response surface methodology in 1951 to enhance manufacturing processes within the chemical industry. This approach encompasses a set of contemporary statistical and mathematical techniques valuable for refining, enhancing, and optimizing processes. It holds significant applications in designing, developing, and formulating new products, as well as in refining existing product designs (Myers, Montgomery, & Anderson-cook, 2016). This methodology is applicable for modeling or optimizing any response influenced by the levels of one or more quantitative factors. It also aids in exploring the relative importance of multiple variables within intricate forms of interaction.

RSM finds its most extensive applications in scenarios where multiple input variables have the potential to impact performance measures or quality characteristics of the product or process. These measures or characteristics, known as **responses**, often include attributes, ranks, or sensory perceptions, and are typically measured on a continuous scale. The input variables, also referred to as **independent variables**, are under the control of the scientist conducting the study (Myers, Montgomery, & Anderson-cook, 2016).

In the general scenario, the response is a quantitative continuous variable, such as yield, strength, or cost. The mean response is a smooth but unknown function of the levels of k factors, such as time, temperature, or percentage of materials. These levels are real-valued and accurately controllable. When plotted as a function of the treatment combinations, the mean response forms a surface in $k + 1$ dimensions, which is known as the response surface (Dean et al., 2017).

Most applications of RSM are sequential. Initially, the focus is on determining the most important variables influencing the response, a process known as factor screening or phase zero of the response surface study. Once the significant independent variables are identified, phase one of the study commences, aiming to assess where the collected data lie relative to the ideal response. This outcome could either be near the optimum or remote from it. If the outcome does not align with optimal performance, adjustments to the process variables are necessary to move the process closer to the optimum. Phase two of the study involves developing a model that accurately approximates the response within a relatively small region around the optimum, typically a second-order or occasionally a higher-order polynomial model. Subsequently, the model is analyzed to determine the optimal conditions of the process. The final stage is confirmatory experiments, which are conducted if the optimum is not among the trial runs already completed. This stage aims to confirm that the identified optimum can be achieved by setting the independent variables at the designated values (Myers, Montgomery, & Anderson-cook, 2016). The average result from the confirmation tests should align with the optimum performance, y_{opt} , estimated by the analysis (Roy, 2010).

2.9.2.1 Approximating response functions

Generally, it is assumed that a process involves a response y that depends on the controllable independent variables $\xi_1, \xi_2, \dots, \xi_k$. These variables are sometimes referred to as input variables, process variables, or factors (Myers, Montgomery, & Anderson-cook, 2016). The actual relationship can be expressed as:

$$y = f(\xi_1 + \xi_2 + \dots + \xi_k) + \varepsilon \quad (2.24)$$

In this Equation, the form of the true response function f is unknown and may be highly complex, while ε represents other sources of variability not captured by f . These sources may include measurement errors, inherent variations in the process or system, effects of other unknown variables, and related errors. ε can be regarded as a statistical error, often assumed to follow a

normal distribution with a mean of zero and a variance of σ^2 (Myers, Montgomery, & Anderson-cook, 2016).

The variables $\xi_1, \xi_2, \dots, \xi_k$ in Equation (2.24) are commonly referred to as the natural variables because they are expressed in the natural units of measurement, such as degrees Celsius ($^{\circ}\text{C}$), percent (%), or grams per liter for concentration. Often, it is advantageous to convert the natural variables to coded variables x_1, x_2, \dots, x_k , which are typically dimensionless and standardized to have a mean of zero and the same standard deviation (Myers, Montgomery, & Anderson-cook, 2016). The corresponding response function in terms of the coded variables can be expressed as:

$$\eta = f(x_1 + x_2 + \dots + x_k) \quad (2.25)$$

The true response function (f) needs to be approximated because it is unknown, and the effective use of RSM relies on developing a suitable approximation for f . Typically, a low-order polynomial within a relatively small region of the independent variable space is suitable. In many instances, either a first-order or a second-order model is employed (Myers, Montgomery, & Anderson-cook, 2016). For the scenario involving two independent variables, the first- and second-order models in terms of the coded variables are:

$$\eta = \beta_0 + \beta_1 x_1 + \beta_2 x_2 \quad (2.26)$$

$$\eta = \beta_0 + \beta_1 x_1 + \beta_2 x_2 + \beta_{11} x_1^2 + \beta_{22} x_2^2 + \beta_{12} x_1 x_2 \quad (2.27)$$

The first-order model is typically suitable for approximating the true response surface within a relatively small region of the independent variable space where there is minimal curvature in f . However, since the curvature in the true response surface is often significant, the first-order model may not suffice, necessitating the use of the second-order model. The second-order model is widely favored in response surface methodology for several reasons (Myers, Montgomery, & Anderson-cook, 2016):

1. The second-order model is highly flexible and can represent a wide range of functional forms, making it a reliable approximation for the true response surface.
2. Estimating the coefficient parameters (the β 's) in the second-order model using the method of least squares is straightforward.

3. Extensive practical experience demonstrates the effectiveness of second-order models in solving real response surface problems.

In general, the first- and second-order models can be presented as:

$$\eta = \beta_0 + \beta_1 x_1 + \beta_2 x_2 + \cdots + \beta_k x_k \quad (2.28)$$

$$\eta = \beta_0 + \sum_{j=1}^k \beta_j x_j + \sum_{j=1}^k \beta_{jj} x_j^2 + \sum_{i < j=2}^k \sum_{i=1}^k \beta_{ij} x_i x_j \quad (2.29)$$

The second-order model of Equation (2.29) contains $p = 1 + 2k + k(k - 1)/2$ parameters. Thus, the experimental design must contain at least $1 + 2k + k(k - 1)/2$ distinct design points and at least three levels of each design variable. Here, p represents the number of terms in the second-order model with 1 intercept, k first-order, k pure quadratic, and $k(k - 1)/2$ interaction terms (Myers, Montgomery, & Anderson-cook, 2016).

The geometric nature of the second-order functions is depicted in Figure 2.15. This figure illustrates contours of constant response for a hypothetical scenario with $k = 2$ variables. In Figure 2.15a, the center of the system, or stationary point, represents a maximum response point. In Figure 2.15b, the stationary point represents a minimum response point. In both cases, the response plot exhibits concentric ellipses. In Figure 2.15c, the center is neither a maximum nor a minimum point. This stationary point is termed a saddle point, and the system of contours is termed a (hyperbolic) saddle or minimax system. Detecting the nature of the system and locating the stationary point is a crucial aspect of the second-order analysis. Three-dimensional graphics can aid in determining and comprehending the nature of a response surface (Myers, Montgomery, & Anderson-cook, 2016).

There are two primary types of response surface designs: Central Composite Design (CCD) and Box-Behnken Design (BBD). These two methods will be discussed in the following sections, and their advantages and drawbacks will be evaluated.

2.9.2.2 Central composite design

A Box-Wilson Central Composite Design (CCD), commonly referred to as a "central composite design," stands as one of the most popular second-order designs utilized (Myers, Montgomery, & Anderson-cook, 2016). These designs are advantageous in sequential experiments, often expanding upon factorial experiments by incorporating axial and center points (NIST/SEMATECH, 2012).

The design comprises F factorial points, $2k$ axial points, and n_c center runs. Factorial points offer an optimal design for variance regarding a first-order model or a first-order + two-factor interaction model. Center runs, or star points, contribute information regarding curvature presence. Should curvature be detected, axial points efficiently estimate pure quadratic terms. Flexibility in central composite design usage lies in α selection, the axial distance, and n_c , the number of center-point runs, with both parameters being critical. α choice depends on operability and interest regions, as well as the number of factors involved. Similarly, the number of center-point trials depends on specific design properties. If the distance from the design space center to a factorial point is ± 1 unit for each factor, the distance to a star point is $\pm \alpha$ with $|\alpha| > 1$ (Myers, Montgomery, & Anderson-cook, 2016). Figure 2.12 illustrates the central composite design for two and three-factor designs.

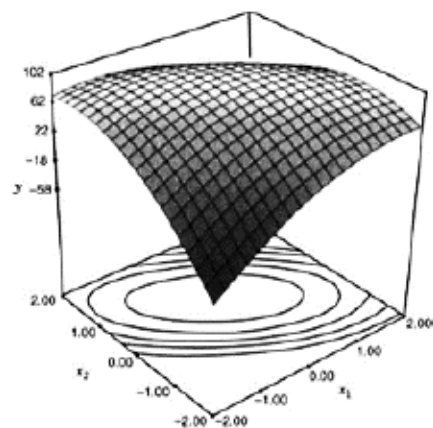
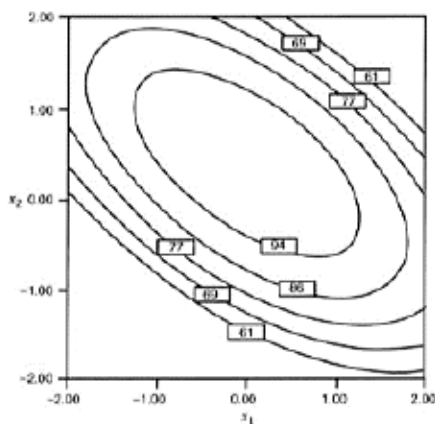
To ensure rotatability, the value of α relies on the number of experimental runs within the factorial portion of the central composite design (NIST/SEMATECH, 2012):

$$\alpha = [\text{Number of factorial runs}]^{\frac{1}{4}} \quad (2.30)$$

If the factorial is a full factorial, then

$$\alpha = [2^k]^{\frac{1}{4}} \quad (2.31)$$

Nonetheless, the factorial portion can also be a fractional factorial design. Table 2.7 illustrates some typical values of α based on the number of factors.



a

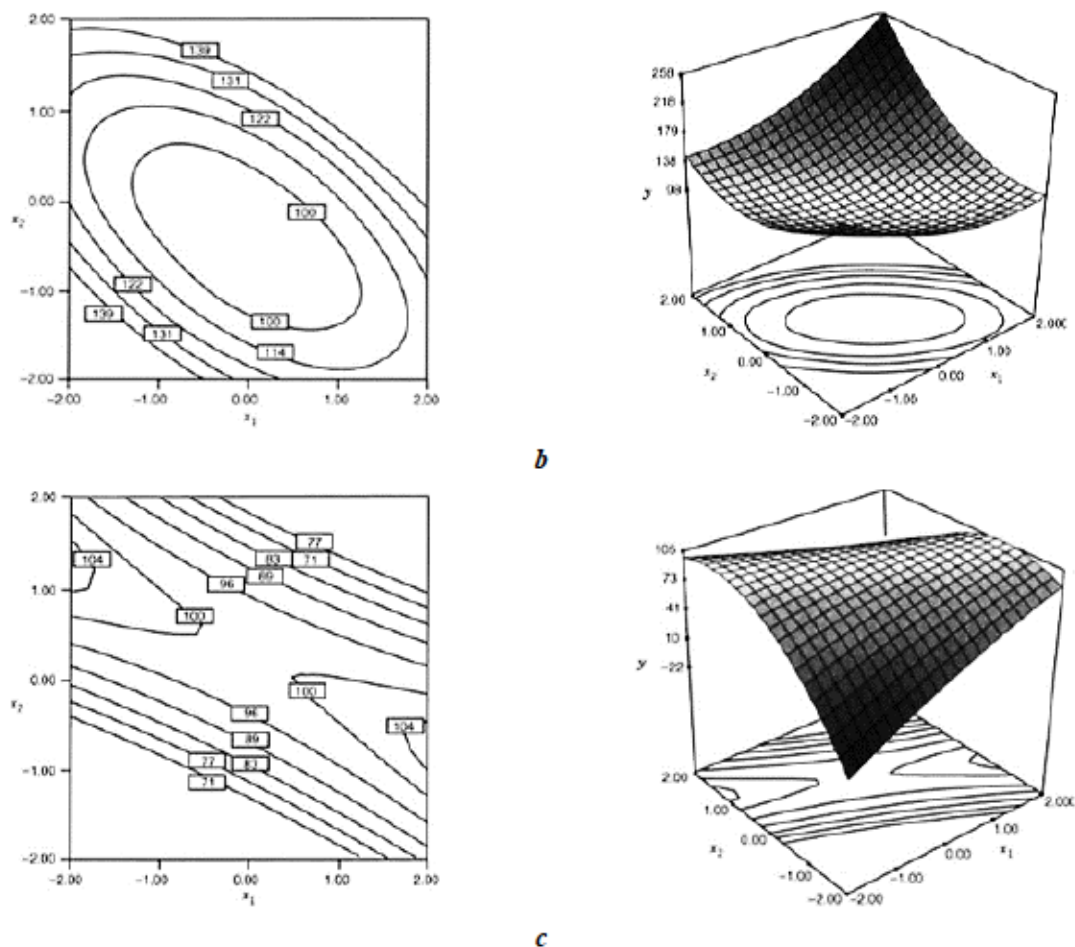


Figure 2.15 Second-order system displaying contour plot and response surface for a) a maximum, b) a minimum, and c) a saddle point. Figure taken from (Myers, Montgomery, & Anderson-cook, 2016)

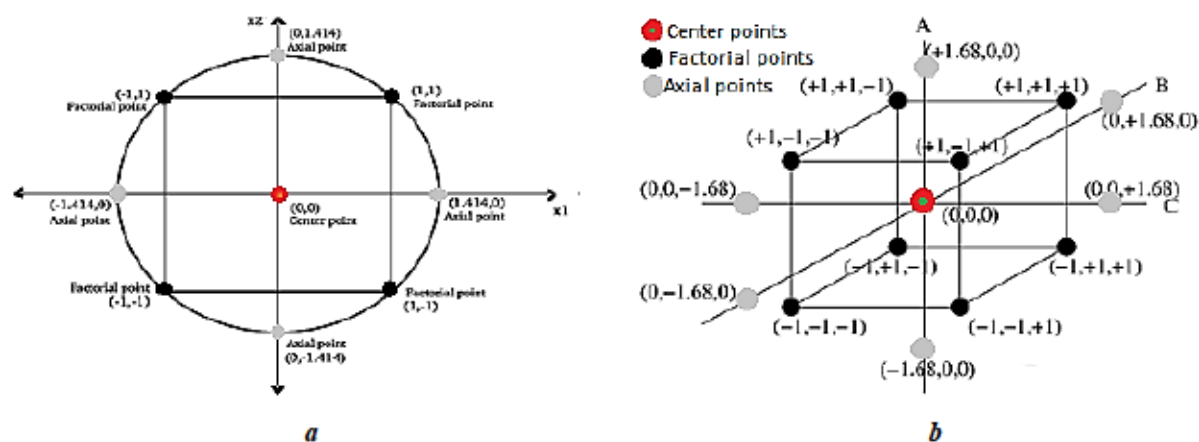


Figure 2.16 Central composite design for a) $k=2$, $a=1.414$; b) $k=3$, $a=1.682$

The central composite design method can reduce the number of experimental runs compared to a factorial design, allowing for the modeling of responses in linear, interaction, full, and pure quadratic manners. However, the expected responses do not vary linearly, and parameters must be carefully selected for the composite factorial design. In this design, each factor's effect is evaluated at five different levels, represented by codified values of $-\alpha$, -1 , 0 , $+1$, and $+\alpha$. Predicting responses becomes less accurate as the distance from the center of the modeled region increases. Therefore, it is advisable to limit the use of models to an area bound by values corresponding to the $-\alpha$ to $+\alpha$ limits (Alqadi et al., 2012).

Table 2.7 Determination of α for rotability

Number of factors (k)	Factorial portion	Scaled value for α relative to ± 1
2	2^2	$2^{2/4} = 1.414$
3	2^3	$2^{3/4} = 1.682$
4	2^4	$2^{4/4} = 2.000$
5	2^5	$2^{5/4} = 2.378$
6	2^6	$2^{6/4} = 2.828$

2.9.2.3 Box-Behnken design (BBD)

Box and Behnken introduced a family of efficient designs for fitting second-order response surfaces, based on balanced incomplete block designs (Myers, Montgomery, & Anderson-cook, 2016). This design category, known as Box-Behnken design, is an independent quadratic design, devoid of an embedded factorial or fractional factorial design. In the BBD, treatment combinations are positioned at the midpoints of edges of the process space and the center (Figure 2.17) (NIST/SEMATECH, 2012). Unlike the CCD, the BBD lacks corner points, ensuring that extreme combinations where all factors are simultaneously high or low never occur. The number of design points in the BBD is comparable to that of the CCD for $k = 3$ and $k = 4$ (no BBD exists for $k = 2$). For $k = 3$, the CCD requires $14 + n_c$ runs, while the BBD requires $12 + n_c$ runs. Similarly, for $k = 4$, both the CCD and BBD entail $24 + n_c$ design points (Myers, Montgomery, & Anderson-cook, 2016). Table 2.8 provides a comparison of the number of runs required for a given number of factors for various Central Composite and Box-Behnken designs.

In numerous scientific investigations necessitating RSM, researchers often prefer to employ three evenly spaced levels. Consequently, the Box-Behnken design emerges as an efficient and vital

alternative to the CCD. Box-Behnken designs are more cost-effective to execute for the same number of factors. They effectively estimate the first- and second-order coefficients; however, they do not incorporate runs from a factorial experiment. Notably, Box-Behnken designs guarantee that all factors are not simultaneously set at their high levels (NIST/SEMATECH, 2012).

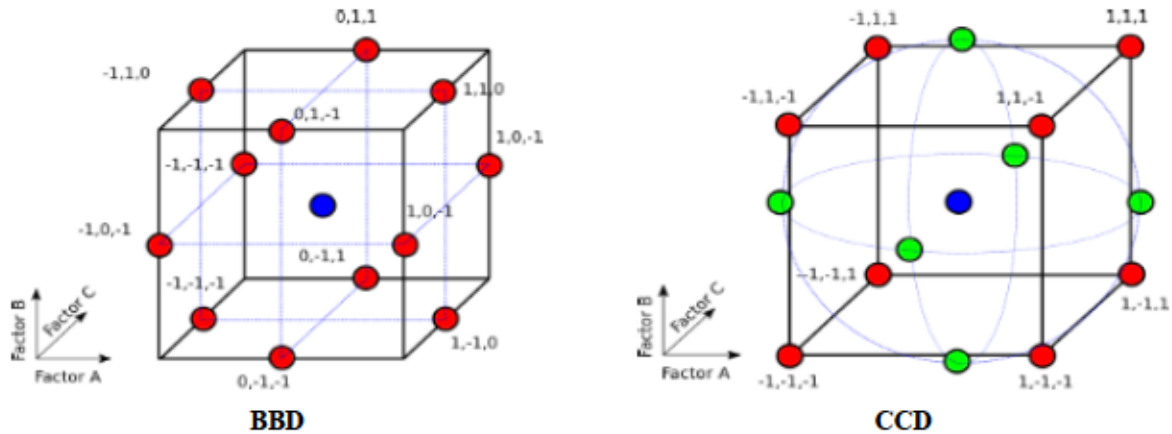


Figure 2.17 Comparison between Box Behnken Design and Central Composite Design with three factors ($k=3$). Figure taken from (NIST/SEMATECH, 2012)

Table 2.8 Number of runs required by Central Composite and Box-Behnken designs

Number of factors	Central Composite Design (CCD)	Box-Behnken Design (BBD)
2	13 ($n_c = 5$)	-
3	20 ($n_c = 6$)	15
4	30 ($n_c = 6$)	29
5	33 (fractional) or 54 (full)	46
6	54 (fractional) or 90 (full)	54

2.9.2.4 ANOVA analysis

Because partial experiments encompass only a selected subset of the full factorial combinations, the analysis of partial experiments must include an assessment of confidence to validate the results. Analysis of Variance (ANOVA), a standard statistical technique, is commonly employed to statistically analyze the effects of factors on responses and to assess the significance of proposed models (Khan et al., 2021; Roy, 2010). ANOVA analysis enables the quantitative determination of the relative influence of factors and interactions between various factors included in the study. This technique does not directly scrutinize the data but instead assesses the variability (variance) of the data, with confidence being gauged from the variance.

In variance analysis, various quantities such as degrees of freedom, sums of squares, and mean square are computed and presented in a standardized tabular format (Roy, 2010). ANOVA effectively assesses the contribution of each factor, their mutual interactions, and their effects on experimental results. The suitability of regression models is evaluated through measures such as lack-of-fit, F-value, and p-value in ANOVA (Khan et al., 2021).

2.9.3 Applicability of the RSM in cemented paste backfills

To ensure that CPB fulfills its roles safely and cost-effectively in underground mining, it is crucial to properly proportion CPB mixtures. Mix proportioning plays a vital role in achieving CPB compositions that meet the desired technical, environmental, and economic design requirements. However, existing guidelines or specifications for CPB mix proportions are lacking. Currently, CPB mix proportioning relies mainly on traditional experimental methods, which entail a significant number of trial mixes to determine the optimal contents of CPB components. An effective mix proportioning method should aim to minimize the number of trial mixes while delivering an economical mixture with the desired properties (Bharatkumar et al., 2001; Fall et al., 2008).

In the absence of engineering approaches for proportioning and optimizing CPB, researchers have turned to mathematical methods such as RSM to analyze and model the performance of cemented paste backfills. These studies aim to develop methodological approaches and mathematical models for CPB mix proportioning, with the goals of minimizing the number of trial mixes, predicting the technical and economic performance of CPBs, analyzing interactions between main ingredients, and developing optimal mixes for specific applications. Table A.7 provides a summary of these studies. Various RSM techniques have been employed to investigate the effects of different parameters on the mechanical (Dai et al., 2019; Fall et al., 2008; G. Feng et al., 2016; Sun et al., 2019; Sun, Wei, et al., 2020), rheological (Dai et al., 2019; Fall et al., 2008; G. Feng et al., 2016; Q. Li et al., 2019; Sun et al., 2019; Sun, Wei, et al., 2020) and microstructural (G. Feng et al., 2016) properties of CPBs. Optimization approaches have been used to develop optimal recipes, prediction models have been proposed, and verification experiments have been conducted to validate the optimization process.

2.10 Research needs

In previous studies, cemented paste backfill technology has effectively stabilized arsenic-bearing materials. However, there is limited experience in stabilizing arsenic trioxide dust using cemented paste backfills. Drawing from existing knowledge on arsenic stabilization mechanisms in cemented paste backfills, it appears feasible to incorporate Giant Mine ATRW dust into cemented paste backfills to stabilize this hazardous waste and reduce its long-term leaching potential. However, the impact of adding arsenic trioxide on mechanical strength and geochemical behaviour may yield a different response as opposed to arsenic sulfide compounds.

CHAPTER 3 EXPERIMENTAL PROCEDURE

3.1 Cemented paste backfilling of ATRW dust

As previously mentioned, since the commencement of gold mining operations in 1947 at the Giant Mine, 237,000 tonnes of ATRW dust have been recovered from the roasting process and stored in old stopes and specially designed chambers in the shallow underground. The aim of the current research is to evaluate the feasibility of incorporating the ATRW dust into cemented paste backfill to stabilize the arsenic. To achieve this, it is necessary to assess the physical, chemical, and mineralogical characteristics of the ATRW dust and tailings from the Giant Mine, as well as the potential binders and other materials. These characteristics can significantly impact the mechanical properties, leachability, hydraulic conductivity, and microstructure of the CPB samples. In this chapter, firstly, preparation, homogenization, and sampling (obtaining a representative sample for testing) of the dusts and tailings samples from the Giant Mine are discussed. Then, the physical, chemical, and mineralogical characterization of the dusts and tailings samples along with potential binders and other materials used are presented. Then, the methodologies for CPB samples preparation including the mix design and formulation, as well as other related procedures are proposed. Finally, the mechanical, leaching, hydraulic conductivity, and microstructural analysis methods for environmental characterization of the stabilized samples to obtain a deeper understanding of the CPB-ATRW behavior are introduced. Figure 3.1 illustrates a summary of the various steps involved in this project.

3.1.1 Preparation, homogenization, and sampling of ATRW dust and tailings

3.1.1.1 ATRW dust samples

The dust samples were dispatched to the UQAT laboratory in nine separate samples from various stopes and chambers. Table 3.1 displays the identification of the received samples and their respective masses after preparation and homogenization. The identification label for each sample includes the name of the stope/chamber and the depth of sampling (in ft), except for samples 7 and 8. Some samples were dry, while others were wet. Figure 3.2 outlines the flowchart of the preparation (deagglomeration) and homogenization of the dust samples.

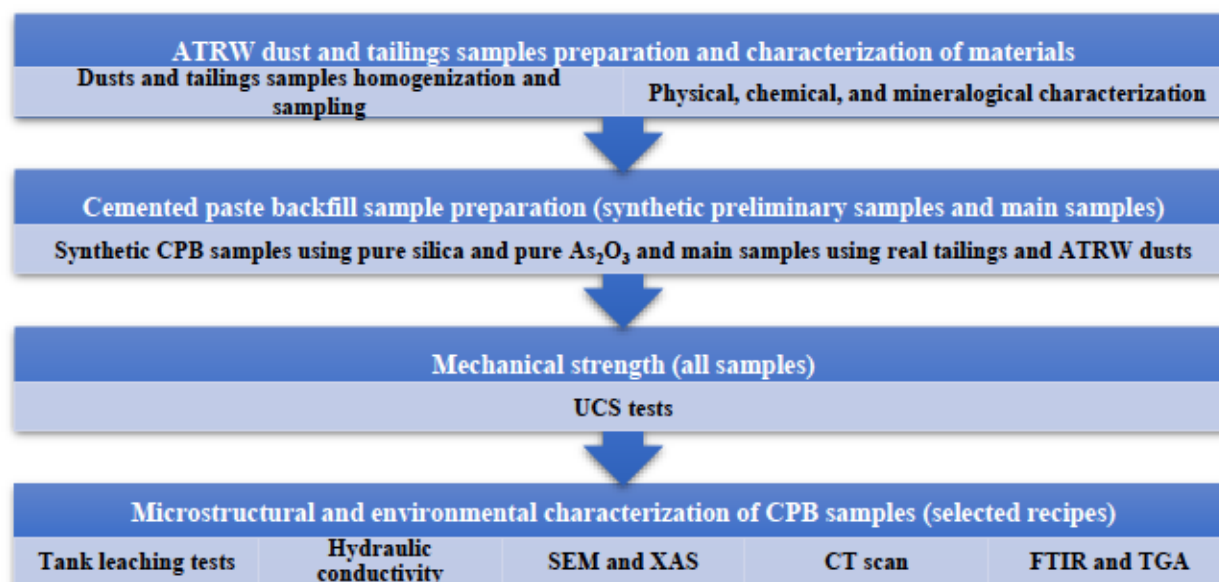


Figure 3.1 A plan of the different steps of the project

Table 3.1 The identification and amounts of the dust samples

#	Sample ID	Available amount (gr)
1	B214-1, 119-143	2994
2	B214-1, 143-179	4005
3	B212-4, 96.5-133	2573
4	B212-4, 133-167	5324
5	B212-4, 217-225	1771
6	B208-1, 106-133	1474
7	B233-P9	2705
8	B235-P13	179
9	C212-2, 140-168	1851
Total		22876

The wet dust samples underwent oven-drying at a temperature of 40° C for approximately 72 hours. Subsequently, all samples were sieved using a mesh size of 420 µm (sieve #40) to remove impurities. For breaking up some of the agglomerated samples, a pestle and mortar were utilized. In cases where certain portions of the samples remained unpassable through the sieve even after using the pestle and mortar, and the grain size was less than 2 mm, a planetary ball mill was employed to pulverize the samples. This apparatus comprises four hollow cylindrical shells rotating about their vertical axes and partially filled with steel balls (Figure 3.3). Rotation of the shells

causes the balls to lift and drop, pulverizing the solid particles between them through impact. Prior to introducing the samples, the inner parts of the cylinders were cleaned by grinding pure silica in the presence of acetone at a speed of 150 rpm for 1 minute. Subsequently, the agglomerated dust particles were added to the cylinders and pulverized at a speed of 150 rpm for 2 minutes.

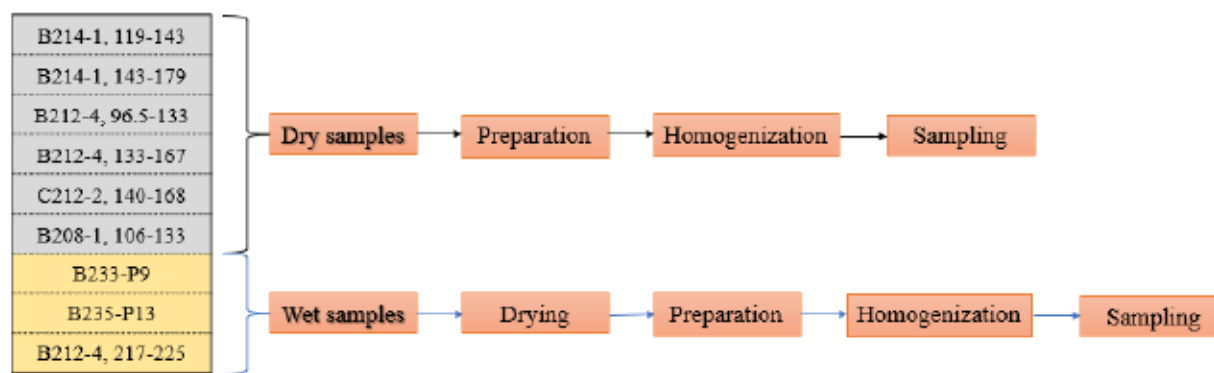


Figure 3.2 Dust samples preparation and homogenization flowchart



Figure 3.3 The planetary ball mill with 4 cylinders

In the case of one dust sample (sample ID: B233-P9), the particle size exceeded 2 mm, prompting the use of the roller mill (Figure 3.4). This apparatus features a pair of grinding rollers mounted on the same axis, rolling in opposite directions. The space between the rollers is adjustable, allowing materials to be poured from the top hopper into the rollers, with the crushed materials collected at the bottom of the equipment. Following the grinding of this sample, as its physical characteristics (such as color and shape of the grains) differed from the other dust samples, it was not mixed with the others to prepare a mixed representative sample. Instead, a separate subsample was prepared

for chemical analysis by ICP. Henceforth, this sample will be referred to as "the odd dust sample" (Figure 3.5).

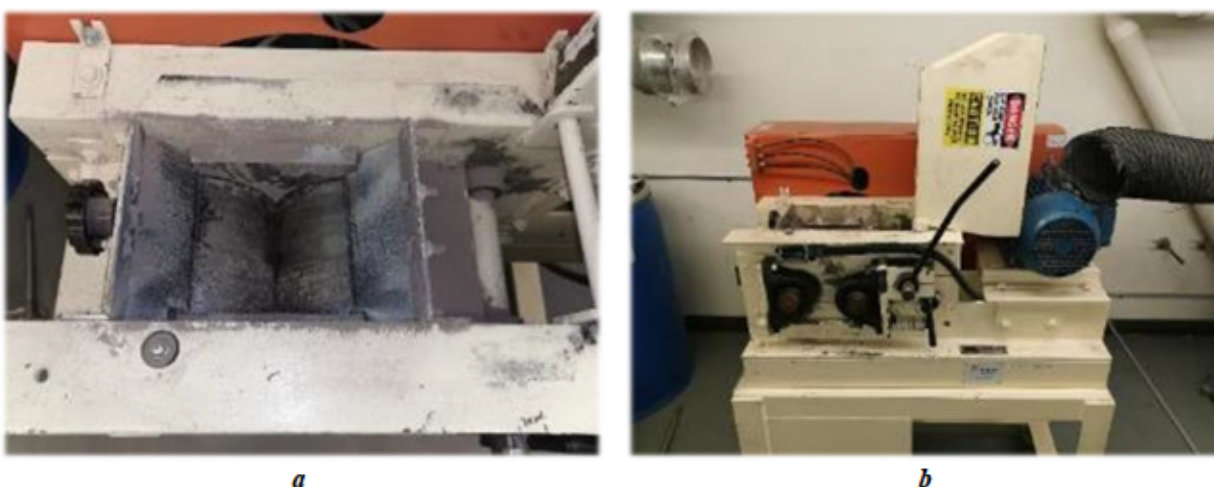


Figure 3.4 Horizontal roller mill, a) top view, b) front view



Figure 3.5 Dust sample B233-P9, a) before, b) after grinding with roller mill

After passing through sieve #40, the ATRW dust samples underwent homogenization and sampling to obtain a 100-gram representative sample. All sieving, homogenization, and sampling procedures were conducted under a ventilation system using a respiratory mask and nitrile gloves, given the toxicity of the ATRW dust. Before commencing the preparation process, the work desk surfaces were cleaned with detergents and paper tissues to prevent sample contamination. This cleaning process was repeated both before and after each stage of material preparation. The materials were then placed on a square plastic membrane for homogenization, and the sample was rolled in four different directions up to 80 times. Subsequently, a row of materials was formed, and using a

spatula, the required amount of materials was sampled from two ends of the row and from the center of the mass to create a representative mixed sample weighing 100 grams. The mixed dust sample was prepared based on the mass ratios of the available dust samples. Figure 3.6 illustrates the various steps involved in homogenization and sampling of the dust samples.



Figure 3.6 Different steps of homogenization, preparation, and sampling of ATRW dusts, a) rolling at different directions, b) the final row of material, c) sampling from the right end, d) sampling from the left end, e) sampling from the center of the mass

The preceding procedure is suitable for samples weighing less than 3 kg. For samples exceeding 3 kg, it is advisable to employ a rotary splitter to reduce the sample size and prevent inaccuracies during homogenization. Rotary sample splitters are highly precise instruments designed for extracting representative samples from dry, granular, or powdered materials. This equipment type helps mitigate the adverse effects of varying grain sizes, specific gravities, average qualities, and particle shapes.

As depicted in Figure 3.7, the apparatus consists of 12 rotating sample bins of identical size, a feed hopper, and a vibratory conveyor fitted with an adjustable frequency controller. Two dust samples weighing more than 3 kg were deposited into the feed hopper and divided randomly into 12 subsamples. Subsequently, one of the subsamples was chosen at random, and the process of homogenization and sampling was carried out on the selected subsample.



Figure 3.7 Rotary sample splitter, a) side view that shows the controller, b) front view

Upon completion of the preparation, homogenization, and sampling procedures, two representative subsamples were prepared (Figure 3.8). One subsample comprised the odd dust sample (B233-P9), intended solely for chemical analysis by ICP. Meanwhile, all characterization tests were conducted on the representative mixed ATRW dust sample, including particle size analysis, specific gravity, specific surface area, chemical analysis by ICP, chemical analysis by XRF, and mineralogical analysis by XRD. The findings of these analyses are detailed in section 4.1.



Figure 3.8 Two representative subsamples for the dust samples, left: a subsample of the odd dust sample, right: a subsample of other eight dust samples

3.1.1.2 Tailings samples

The tailings samples were sourced from the north pond of the Giant Mine site, with a trench dug approximately 2 meters deep to obtain the sample. Predominantly, the tailings exhibited dry to lightly moist conditions, with no visible running water (Figure 3.9).



Figure 3.9 Excavation and sampling of the tailings at the Giant Mine tailings impoundment

Two barrels containing tailings were transported to the laboratory, each barrel being assigned a unique number. Subsamples were extracted from the entire height of the barrels using a hand auger, as shown in Figure 3.10. Due to the slight moisture content and non-uniform humidity distribution

across different sections of the barrels, the subsamples underwent oven-drying at 40 °C for 48 hours before undergoing preparation and homogenization processes.



Figure 3.10 A view of a) two barrels of tailings of the Giant Mine, b) sampling from the whole height of each barrel, c) a view of the hand auger and the collected sample

After drying the tailings samples, their masses were measured. As each sample's mass was below 3 kg, the preparation and homogenization process was conducted directly on the samples under a ventilation system. Initially, the tailings samples were sieved using a mesh size of 841 μm (sieve #20). Subsequently, the samples were spread onto a square plastic membrane, and the homogenization process, involving rolling the sample in four different directions for at least 80 times, was carried out on two samples. Following this, two subsamples weighing 50 grams each were collected from the ends and center of the tailings samples using a spatula. Subsequently, a single tailings sample weighing 100 grams was prepared and sent for characterization tests, including particle size analysis, specific gravity, specific surface area, chemical analysis by ICP, chemical analysis by XRF, and mineralogical analysis by XRD. The results of these tests are detailed in the subsequent chapter. The remaining tailings were thoroughly mixed, placed in previously cleaned buckets, and stored for subsequent experiments. Before preparing the CPB samples, the required mass of tailings underwent oven-drying at 40 °C and was allowed to cool to ambient temperature.

3.1.2 Other materials (binding agents, pure silica and pure As_2O_3)

During this study, five types of binders were utilized. The primary binding agent was general use (GU) Portland cement, chosen for its widespread availability and adaptability. Additionally, mixtures of GU cement with class F fly ash (40/60 and 50/50), GU cement with slag (10/90), GU

cement with lime (50/50), and GU cement with lime kiln dust (LKD, 50/50) were employed. GU cement is favored for CPB preparation due to its versatility and widespread use (H. Jiang, Qi, et al., 2019; Tariq & Yanful, 2013). It consists primarily of tricalcium silicate (C3S), dicalcium silicate (C2S), tricalcium aluminate (C3A), tetracalcium aluminoferrite (C4AF), and gypsum (X. Deng et al., 2017). GU Portland cement supplied by Bomix (Quebec, Canada) was utilized in this study, sourced in two batches. Lafarge (Montreal, Canada) provided the slag and Class F fly ash was supplied by Lehigh Hanson (Calgary, Canada). Lime and lime kiln dust (LKD), as a by-product of the lime industry from Graymont (Bedford, Canada), served as an additional calcium source, primarily manifesting as calcite and portlandite. In the initial phase of this study, synthetic paste mixtures were formulated using pure ground silica to replicate mine tailings, thus mitigating any potential influence of the chemical or mineralogical compositions of the tailings on hydration reactions and minimizing uncertainties. Pure silica has been previously utilized in tailings studies to maintain consistency (Aldhafeeri, 2018; Chang, 2016; N. Koupouli et al., 2017; Sadatalhosseini et al., n.d.). Sulfidic and other reactive minerals and elements in the natural tailings could interact during the cement hydration process and affect the analysis results (Ghirian & Fall, 2016). The choice of Sil-Co-Sil[®] 106 (US Silica, USA) was based on its particle size distribution, which closely resembles that of the Giant Mine tailings. To eliminate impurities from roaster waste dust materials in the synthetic preliminary CPB samples, pure powdered analytical-grade arsenic trioxide (As_2O_3 , purity > 99.5%, Alfa Aesar, USA) was selected as the arsenic source.

3.2 Methods

3.2.1 Physical characteristics

The particle size analysis of all solid materials (except binding agents) was conducted using a laser diffraction particle size analyzer (Malvern Mastersizer 3000) covering a range from 0.005 μm to 900 μm . The specific gravity of all solid samples was determined utilizing the Helium pycnometry method, employing the Ultrapyc 1200e automatic gas pycnometer (Quantachrome Instruments). Additionally, the specific surface area of the ATRW dust, tailings, pure silica and pure As_2O_3 was assessed using the Brunauer–Emmett–Teller (BET) method with liquid nitrogen, facilitated by the Gemini 2375 apparatus from Micromeritics.

3.2.2 Chemical Analyses

The chemical composition of various materials, including tailings, ATRW dust, and binding agents, was determined using X-ray fluorescence spectrometry (S2 Ranger, Bruker AXS). Suppliers provided the chemical composition of pure silica and pure As_2O_3 . Inductively Coupled Plasma Atomic Emission Spectroscopy (ICP-AES) was utilized to quantify the concentrations of elements such as Al, As, Ba, Be, Bi, Ca, Cd, Co, Cr, Cu, Fe, K, Li, Mg, Mn, Mo, Na, Ni, Pb, S, Ti, and Zn. Additionally, Inductively Coupled Plasma Mass Spectrometry (ICP-MS) was employed to measure the concentration of elements like As, Ba, Bi, Cd, Co, Cr, Cu, Mn, Mo, Ni, Pb, Sb, Se, Sn, Sr, Te, Ti, Tl, U, and Zn. The ICP analyses were exclusively conducted on the ATRW dust and tailings from the Giant Mine. Prior to analysis, these samples underwent digestion with HNO_3 , HF, and HCl, employing microwave heating while taking specific precautions to prevent arsenic volatilization. Boric acid (H_3BO_3) was subsequently added after microwave digestion to neutralize any residual HF.

The quality of mixing water can significantly impact the mechanical properties of CPB samples and cement hydration processes. In various studies, different types of mixing waters, such as tap, lake, and process waters, have been employed for CPB preparation using different binding agents. For this study, deionized (DI) water was chosen for preparing the cemented paste backfill samples and other mixtures to mitigate the influence of water's chemical components on CPB behavior. To maintain consistent water quality throughout the study, the required water for sample preparation and analyses was collected in one batch. Additionally, the chemical composition of DI water was analyzed using ICP-MS (Agilent 7800) after acidification with 2% v/v HNO_3 . Throughout the study, the pH and electrical conductivity (EC) of DI water and other mixtures were measured using a multimeter (B30PCI, VWR SympHony).

3.2.3 Mineralogical analysis

The mineralogical analysis of the samples was conducted using x-ray diffraction (XRD) method. First, the samples were ground in Isopropanol using a McCrone mill for 15 minutes. The ground samples were placed on the sample holder utilizing the backloading method. XRD analysis was performed with a Bruker AXS D8 AQ advance instrument equipped with a copper radiation source. The samples underwent scanning over a 2-theta range of $5-70^\circ$ with a step size of 0.02° . The obtained spectra were analyzed using DIFFRAC.EVA software (version 5.2.0.3) to identify phases

and match them with reference databases. Furthermore, the phases were semi-quantified employing TOPAS software (version 4.2) through the Rietveld method.

3.2.4 Cemented paste backfill preparation and curing

CPB, a cement-stabilized material, comprises tailings (and other mine wastes), water, and hydraulic binder(s). The characteristics of each ingredient significantly impact the mechanical, rheological, hydraulic conductivity, durability, leaching properties, and microstructure of CPB samples. Therefore, to determine the most suitable recipe(s), various mixtures must be prepared and tested at different solids (tailings and dusts), binder, and water contents. A 10-quart capacity planetary mixer (Eurodib M10 ETL, China) was utilized for preparing the CPB samples at the IRME-UQAT laboratory in Rouyn-Noranda, Canada. Given the significant presence of arsenic trioxide in the samples, precautionary measures were implemented, including the use of a cartridge mask and other safety protocols, to prevent arsenic inhalation and direct skin contact with the CPB. Initially, a portion of the water was mixed with the binder in the mixer's bowl using a manual spatula. Dry mixing of the tailings (either pure silica or real tailings) and arsenic (ATRW or pure As_2O_3) was conducted before adding them to the mixture. Subsequently, thorough mixing was performed within the bowl using the mixer's beater. The remaining water was gradually introduced into the mixture and mixing continued for up to 5 minutes to achieve a homogeneous paste. In some samples, water was added progressively to achieve the required slump, with the slump measured before molding. The quantity of water added to attain the desired slump was recorded. Following this, the paste was promptly poured into three plastic molds (with a diameter of 2 inches (5.08 cm) and a height of 4 inches (10.16 cm)) in either the drained or undrained condition, with minimal delay after the mixing process due to the paste's rapid initial setting. The casting process involved a single-layer pouring technique. After molding, the paste in the cylinders underwent 25 impacts using a steel rod with a diameter of 9.53 mm (equivalent to 3/8 inches) to eliminate any trapped air bubbles within the paste. A portion of the remaining paste was utilized to determine its final water content, achieved through a three-day drying period in an oven set at 60°C, followed by weighing. The cylindrical samples prepared were sealed and stored in a humid chamber, maintaining approximately 90% humidity and a temperature of 20 °C to simulate typical conditions found in underground mines, for a curing duration of up to 111 days. The environmental conditions were kept constant throughout the curing period to ensure comparability of test results. Figure 3.11 illustrates the process of sample preparation and curing.

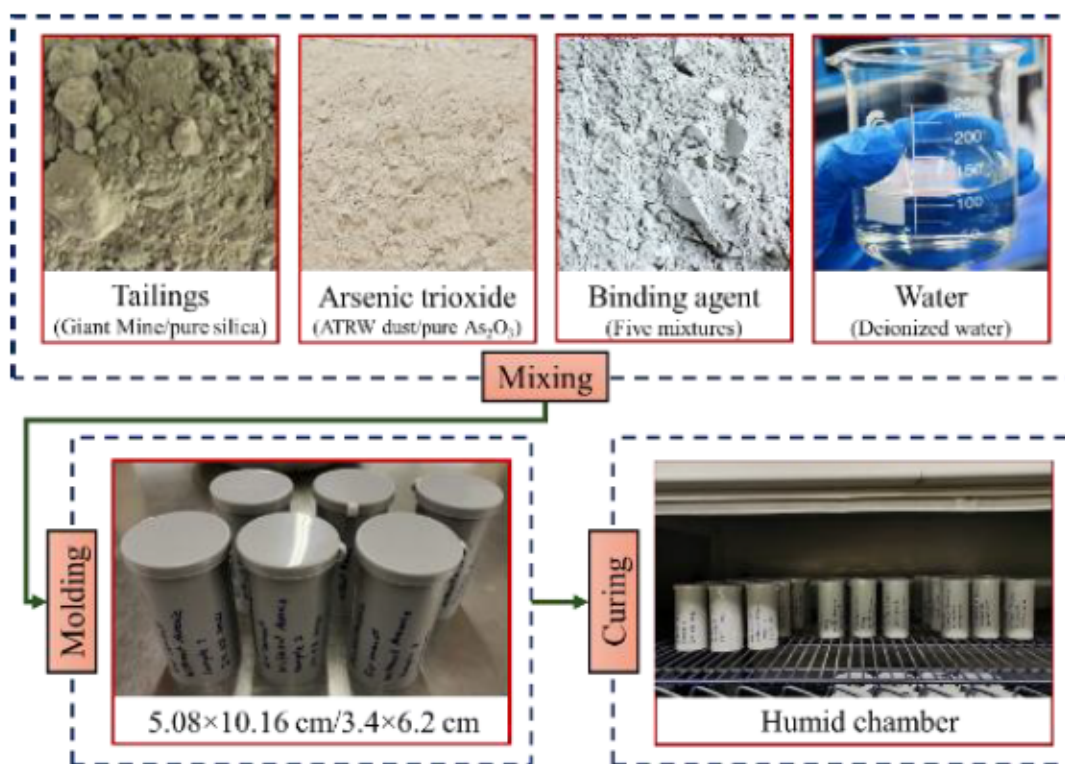


Figure 3.11 Process of the preparation of the preliminary/main CPB samples

In this study, sample preparation and experimentation occurred in two phases: preliminary samples and main samples. The preliminary tests aimed to characterize the arsenic stabilization mechanisms in the cemented paste backfill, compare the effects of synthetic and real mine tailings on arsenic stabilization, and determine the most suitable binder combinations and ATRW dust content in the main samples. Preliminary samples were prepared in two batches (Figure 3.12). The first batch of preliminary samples were prepared using pure silica (Sil-Co-Sil[®] 106) and Giant Mine tailings as tailings, powdered analytical-grade arsenic trioxide as the arsenic source, different binders (GU cement, GU/FA and GU/slag), and DI water, as shown in Table 3.2. Paste mixtures were prepared using pure ground silica to replicate mine tailings and prevent any influence from the chemical or mineralogical compositions of the mine tailings on hydration reactions. Sil-Co-Sil[®] 106 was selected due to its particle size distribution similarity to the Giant Mine tailings. These samples were cured in the undrained condition. To compare the results, some samples were prepared without adding the pure arsenic trioxide.

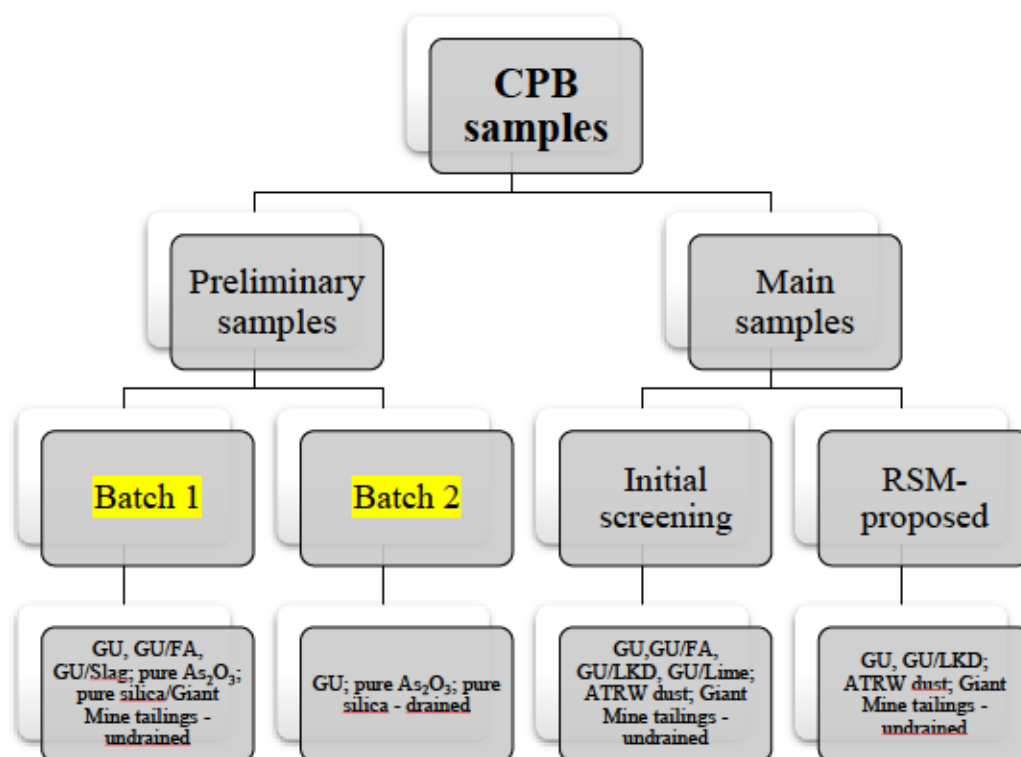


Figure 3.12 The plan of the preliminary and main CPB samples

Table 3.2 The specifications of the first batch of the preliminary CPB samples

#	Binders	GU	FA	Slag	Solids	Binder content	Required slump	Final W/C ratio	Curing condition	Mixing water
1	GU	100%	0	0	Pure As ₂ O ₃ (15%), Sil-Co-Sil/Giant Mine tailings (85%)	10% of solids	180 mm (~7.1 in)	3.60 ^a , 3.13 ^b	28 and 96 days at 20 °C & 90% humidity, undrained	DI water
2	GU/FA	40%	60%	0				3.37 ^a , 2.97 ^b		
3	GU/Slag	10%	0	90%				3.36 ^a , 3.03 ^b		
4	GU	100%	0	0	3.35 ^a , 2.89 ^b					
5	GU/FA	40%	60%	0	3.26 ^a , 2.94 ^b					
6	GU/Slag	10%	0	90%	3.34 ^a , 3.00 ^b					

a: Sil-Co-Sil, b: Tailings

The second batch of preliminary CPB samples aimed to elucidate the mechanisms involved in stabilizing arsenic trioxide within a CPB-like paste and to ascertain the impact of the percentages of pure arsenic trioxide on the strength development and geochemical behavior of the paste. To achieve these objectives, various paste mixtures were prepared using pure silica to simulate the characteristics of tailings and As₂O₃-cement mixtures, followed by specific analyses such as

unconfined compressive strength tests and mineralogical characterization. Table 3.3 outlines the specifications of the second batch of preliminary CPB samples. These samples were formulated with 5% GU cement binder, varying concentrations of arsenic trioxide (referred to as CPB-0%, CPB-5%, CPB-10%, and CPB-15%), and dry pure silica to achieve a final solid content of 74 wt.%. The curing of these samples was conducted under drained conditions.

Table 3.3 The specifications of the second batch of the preliminary CPB samples

Binder	Solids	Binder content	Solid content	Curing condition	Mixing water
GU	Pure As ₂ O ₃ (0 ~ 15%), Sil-Co-Sil® (85 ~ 100%)	5%	74%	7 and 28 days at 20 °C & 90% humidity	DI water

The collection and analysis of drained waters from the samples were initially planned, however, for most CPB samples (excluding CPB-5%), the rapid initial setting of the paste prevented effective water collection. Only a small volume of drained water was obtained from the CPB-5% samples. An alternative experiment was designed to investigate the relationship between cement and arsenic trioxide. GU cement, pure arsenic trioxide, and deionized water, following the same proportions as the second batch of preliminary CPB mixtures outlined in Table 3.3, were added to 2-liter beakers and stirred for 24 hours using magnetic stirrers. Subsequently, the As₂O₃-cement mixtures were transferred to bottles and left for up to 28 days, with intermittent agitation during this period. During the mixing process, samples (2 replicates for each As₂O₃ content) were collected at intervals of 10 minutes, 90 minutes, 3 hours, 5 hours, 24 hours, 7 and 28 days using a 50 ml syringe. These samples were then filtered through a 0.45 µm cellulose syringe filter before pH, EC, and chemical analyses. Finally, the mixtures were extracted from the bottles and dried at 60 °C for three days. The dried As₂O₃-containing mixtures were pulverized using a pestle and mortar and then subjected to solid ICP-MS analysis.

To define the appropriate ATRW dust content as well as the potential binders, the first batch of main CPB samples were prepared at various ATRW dust contents (4%, 6%, 8%, 10%, 12%, and 14% wt.) at solid content of 74% wt. using four different binders (GU cement and a mixture of GU cement with fly ash, GU/FA, lime, GU/LI, and lime kiln dusts, GU/LKD, all in the proportion of 50/50) and Giant Mine tailings. These samples were prepared in the molds with a diameter of 3.4 cm and height of 6.2 cm and cured up to 28 days in the undrained condition. After curing, the UCS

test was done on these samples. Based on the results of the UCS analysis, the ATRW dust content and two potential binders were selected for the preparation of the main samples.

The main samples were prepared using Giant Mine tailings, ATRW dust, two distinct binder combinations (GU and GU/LKD, 50/50), and DI water. CCD-based RSM was employed to determine the optimal recipes. This methodology enables the creation of a polynomial model with the least number of tests necessary, as described in chapter 2 (Behera et al., 2018). Table 3.4 presents the experimental factors, denoted as A (binder content %), B (solid content %), and C (curing time in days), along with their respective ranges, units, and coded values. These values and ranges were determined based on preliminary exploratory experiments. The value of α was established as 1.68 for the three variables in the rotatable design. Table 3.5 provides an overview of the proposed CCD-based RSM method, with the factors being binder content, solid content, and curing time, while the response variable is the UCS. Given the utilization of two distinct binder combinations (GU and GU/LKD), a total of 20 experiments were conducted for each binder type, with three replicates for each formulation. Consequently, 120 undrained CPB samples were prepared and tested

Table 3.4 Independent factors and levels of RSM experiments

Factor	Name	Unit	Low value ($-\alpha = -1.68$)	Min (-1)	Mean (0)	Max (+1)	High value ($+\alpha = +1.68$)
A	Binder content	(%)	3.32	4	5	6	6.68
B	Solid content	(%)	70.64	72	74	76	77.36
C	Curing time	(day)	7	28	59	90	111

The experiments were carried out in a randomized sequence to mitigate the impact of uncontrolled variables on the results. Subsequently, the experimental data was fitted to a quadratic second-order model (Equation (3.1)) using multiple regression analysis.

$$y = \beta_0 + \sum_{i=1}^k \beta_i x_i + \sum_{i=1}^k \beta_{ii} x_{ii}^2 + \sum_{i=1}^k \sum_{i \neq j=1}^k \beta_{ij} x_i x_j + \varepsilon \quad (3.1)$$

Table 3.5 Central composite design in the form of coded and actual values

Run	Point type	Coded values			Actual values		
		A	B	C	A (%)	B (%)	C (day)
1	Axial	$-\alpha$	0	0	3.32	74	59
2	Factorial	-1	-1	-1	4	72	28
3	Factorial	-1	-1	+1	4	72	90
4	Factorial	-1	+1	-1	4	76	28
5	Factorial	-1	+1	+1	4	76	90
6	Axial	0	$-\alpha$	0	5	70.64	59
7	Axial	0	0	$-\alpha$	5	74	7
8	Center	0	0	0	5	74	59
9	Center	0	0	0	5	74	59
10	Center	0	0	0	5	74	59
11	Center	0	0	0	5	74	59
12	Center	0	0	0	5	74	59
13	Center	0	0	0	5	74	59
14	Axial	0	0	$+\alpha$	5	74	111
15	Axial	0	$+\alpha$	0	5	77.36	59
16	Factorial	+1	-1	-1	6	72	28
17	Factorial	+1	-1	+1	6	72	90
18	Factorial	+1	+1	-1	6	76	28
19	Factorial	+1	+1	+1	6	76	90
20	Axial	$+\alpha$	0	0	6.68	74	59

In this Equation, y represents the predicted response value, β_0 denotes the constant term, β_i , β_{ii} , and β_{ij} represent the coefficients for the linear effect, quadratic effect, and interaction effect, respectively. Meanwhile, x_i and x_j denote the dimensionless independent factors, and k represents the number of selected variables [26].

The collected data underwent regression analysis using the Design-Expert® software (Version 13, Stat-Ease Inc., Minneapolis, USA). The statistical significance of the models, as well as each of the independent variables and their interactions, was evaluated through ANOVA within Design-Expert. This software was also utilized to visualize the 3D response surfaces. Factors with a p-value of 0.05 or lower were considered statistically significant and were therefore included in the

predictive regression model. The relationship between the independent variables and the response variables was explored using 3D response surface plots. Additionally, numerical optimization of the independent variables for the cemented pastes was performed to identify the combination of variables that would maximize compressive strength.

Calculations for the required amount of each material were performed based on the following Equations:

$$\text{Solid mass content (\%)} = C_w = \frac{100 \times M_{\text{dry-solid}}}{M_{\text{dry-solid}} + M_{\text{water}}} \quad (3.2)$$

$$\text{Binder content (\%)} = B_w = \frac{100 \times M_{\text{dry-binder}}}{M_{\text{dry-tailings}} + M_{\text{dry-dust}}} \quad (3.3)$$

$$\text{Dust content (\%)} = D_w = \frac{100 \times M_{\text{dry-dust}}}{M_{\text{dry-tailings}} + M_{\text{dry-dust}}} \quad (3.4)$$

$$\text{Tailings content (\%)} = T_w = \frac{100 \times M_{\text{dry-tailings}}}{M_{\text{dry-tailings}} + M_{\text{dry-dust}}} \quad (3.5)$$

Where: M_{water} = Mass of water in the paste and $M_{\text{dry-solid}} = M_{\text{dry-tailings}} + M_{\text{dry-dust}} + M_{\text{dry-binder}}$.

3.2.5 Slump measurement

The slump test is widely recognized as the standard method for measuring the backfills rheological properties (H. Jiang, Qi, et al., 2019; Yilmaz et al., 2012). Slump height, which serves as an empirical indicator of workability, is influenced by material density and yield stress, both of which depend on composition, specific gravity, and particle size (X. Deng et al., 2017). However, due to limited quantity of ATRW dust from the Giant Mine, and the significant volume of paste required for the original Abrams cone slump tests, the mini cone was utilized for slump measurements (the volume of the Abrams cone being approximately eight times that of the mini cone, as depicted in Figure 3.13). Despite not being a standard apparatus for slump measurement, the mini cone has proven effective for this purpose in previous studies (Jia et al., 2016; Roussel et al., 2005; Tan et al., 2017). Slump measurements were conducted following the ASTM C143 standard procedure (ASTM, 2015).

The relationship between slump values measured by the Abrams cone and the mini cone was established as part of the first batch of preliminary tests using ground silica as the tailings, general use Portland cement (10%) as the binder, and DI water. DI water was mixed thoroughly with the binder in a Hobart mixer, followed by the gradual addition of tailings and the remaining DI water. Mixing continued for at least 7 minutes before slump measurement. The slump of the paste was then measured at three water contents using both the Abrams cone and the mini cone. Figure 3.14 illustrates the relationship between these slump values. A conversion factor of 2.52 (the inverse of the slope of the curve) was determined. Considering a slump value of 180 mm in the Abrams cone as the target, the corresponding slump value in the mini cone was determined to be 77 mm. This value was utilized for preparing the first batch of preliminary samples with different binders and measuring the slump of the second batch of preliminary CPB samples with various pure As_2O_3 contents. Other authors have proposed alternative relationships, with Ouattara, Kalonji, and Dikonda suggesting conversion factors of 2.28, 2.20, and 2.29, respectively (Dikonda, 2018; Kalonji, 2016; Ouattara, 2017).

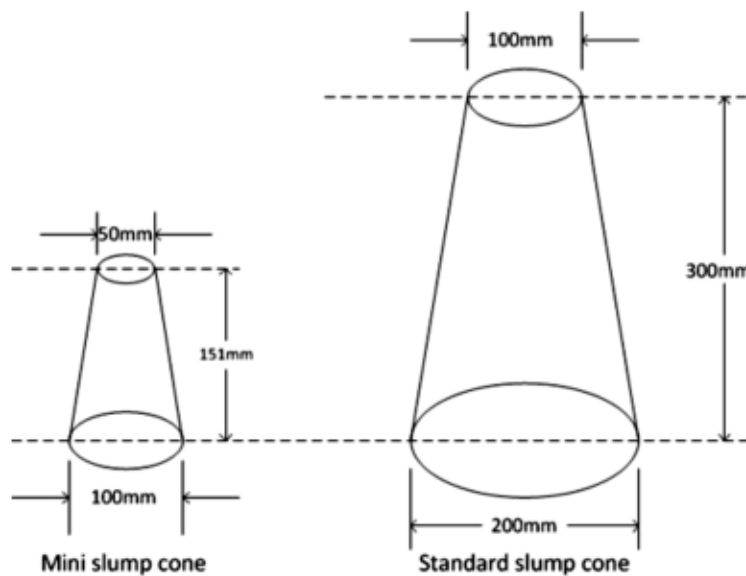


Figure 3.13 A schematic view of the original Abrams cone and the mini cone. Figure taken from (Jia et al., 2016)

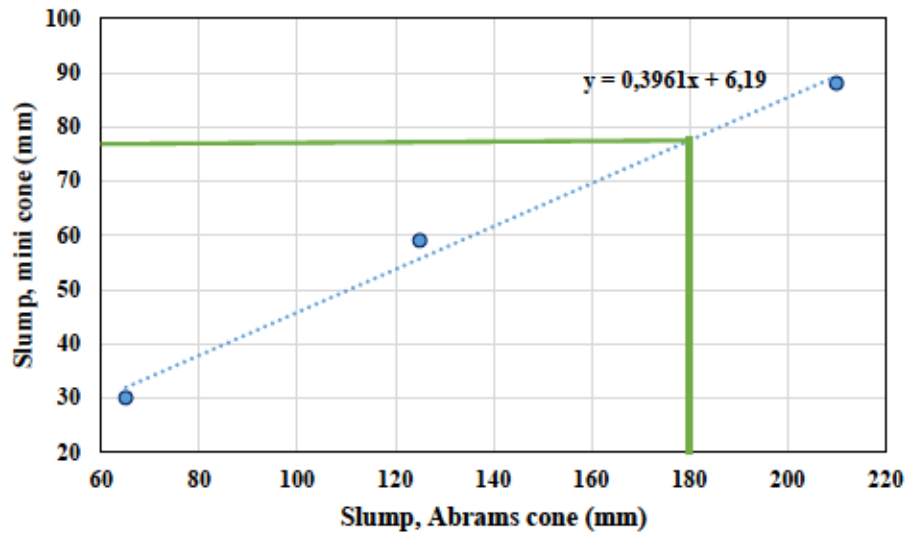


Figure 3.14 The relationship between Abrams cone and mini cone slump measurements

3.2.6 Strength of the CPB samples

The mechanical strength of CPB was assessed to gauge its strength development. This was achieved by conducting UCS tests on three replicate samples for each recipe. Following specific curing durations, CPB samples were removed from molds, and the bases of the cylinders were rectified to ensure their surfaces were parallel to the plates of the mechanical press prior to UCS testing. The UCS tests were conducted using a mechanical press with a normal loading capacity of 10 kN and a displacement rate of 1 mm/min (see Figure 3.15). The UCS parameter represents the maximum stress value attained before failure during the compression test.



Figure 3.15 A view of the UCS test apparatus and data acquisition system

3.2.7 Hydraulic conductivity of the CPB samples

Saturated hydraulic conductivity tests were conducted on main CPB samples exhibiting the highest strength, as determined by UCS analyses. Two recipes were selected, and duplicate samples were prepared, resulting in a total of four samples, each measuring 8 inches in height and 4 inches in diameter. Four more samples were prepared with the same recipe but without ATRW. The samples were cured for a specified duration as per the experimental design, then demolded and positioned within a flexible wall hydraulic conductivity cell equipped with a latex membrane. The samples were saturated over several days, after which hydraulic conductivity measurements were conducted using a flexible wall permeameter in falling head mode, following the ASTM D5084-16 standard. These measurements were repeated at least three times, continuing until the relative difference between consecutive measurements dropped below 10%. After completing the test, each CPB sample was removed from the cell, weighed, and placed in an oven at 60 °C to determine the final water content. Figure 3.16 illustrates the process of saturated hydraulic conductivity testing.



Figure 3.16 The process of preparation and testing of samples in saturated hydraulic conductivity analysis

3.2.8 Monolithic Tank leaching test

A leaching protocol was executed to gauge the extent of arsenic stabilization within the paste backfill matrix and to evaluate the long-term durability of the optimal CPB formulation. The monolithic tank leaching test (TLT), conforming to the Dutch standard EA NEN 7375:2004, was employed. This test method is recognized for yielding representative chemical release data,

particularly for assessing the long-term environmental behavior of CPB. The TLT is suitable for monolithic (low permeability) materials, where the leaching fluid circulates around the material, creating the necessary driving force for sustained leaching.

This leaching protocol was carried out to evaluate the leaching of arsenic and related elements/ions, thus determining the degree of arsenic stabilization within the paste backfill matrix. Cured CPB samples were trimmed to approximately 5.0 cm in height, with 2.5 cm removed from each end of the cylinder. Two samples for each binder with the highest UCS were chosen for the leaching test. Additionally, two samples with lower UCS, featuring different binder and solid contents, were selected for the GU binder to assess the effects of these parameters on leaching analysis results. Duplicate experiments were conducted for each CPB specimen, resulting in a total of 12 samples subjected to leaching. The test involved leaching a monolithic block of CPB with DI water in a closed 2 L HDPE flask reactor, utilizing a sequential total renewal of the leachates. After weighing and measuring the surface area, the cylinders were positioned on plastic supports, ensuring they were 2 cm from the bottom of the HDPE flasks to ensure complete leaching. DI water was then added to achieve a level that ensured a 2 cm water head above the CPB samples. The liquid/solid (L/S) ratio was consistent across all samples, maintained at 10 cm³ of leaching solution per cm² of exposed surface. Throughout the leaching procedure, agitation was achieved using a magnetic stirrer within each flask. Leachate samples were collected and replaced at specific intervals of 6 hours, 1 day, 2.25 days, 4 days, 9 days, 16 days, 36 days, and 64 days (final collection). At each designated time point, 15 mL of leachate was extracted using a plastic syringe and filtered through a membrane filter (0.45 μm). Prior to each solution renewal, the CPB samples were weighed to track changes in mass. The pH and EC of the collected leachates were measured, followed by ion chromatography (IC) and ICP-AES analysis. Each leachate sample was analyzed independently to assess both incremental and total mass leached. After each sampling event, the leaching solution was replenished.

The calculation of the mass transfer of arsenic and other associated components (elements/ions) from CPB samples was conducted utilizing Equation (3.6) in accordance with the EA NEN 7375:2004 standard.:

$$E_i^* = \frac{C_i \times V}{A} \quad (3.6)$$

Where E_i^* (g/m²) stands for the computed mass of the component released during leaching period i , C_i (g/L) represents the concentration of the component during period i , V (L) indicates the volume of the associated leachate, and A denotes the exposed specimen surface area (m²).

Equation (3.7) was employed to calculate the cumulative leaching for each analyzed component at every increment:

$$\varepsilon_n^* = \sum_{i=1}^n E_i^*, \text{ for } i = 1 \text{ to } N \text{ (where } i = n) \quad (3.7)$$

The measured cumulative leaching of a component for period n , encompassing fractions $i = 1$ to n , in grams per square meter of the sample surface area is denoted by ε_n^* . Here, N represents the total number of leachant renewal periods, which is set as 8. Additionally, the cumulative derived leaching is calculated as per Equation (3.8):

$$\varepsilon_n = \frac{E_i^* \times \sqrt{t_i}}{\sqrt{t_i} - \sqrt{t_{i-1}}}, \text{ for } i = 1 \text{ to } N \text{ (where } i = n) \quad (3.8)$$

Where ε_n represents the calculated cumulative leaching for a component for period n , involving fractions $i = 1$ to n , in g/m², t_i is the replenishment time of fraction i in days, and t_{i-1} is the replenishment time of fraction $i - 1$. The cumulative leaching ε_n derived determines solely the cumulative leaching up to and including period i , relying on the measured leaching during period i . Utilizing derived leaching values allows for an assessment of whether leaching is affected by diffusion (EA NEN 7375, 2004). This assessment was conducted by calculating the slopes of the regression lines (r_c) from log-log plots of the cumulative derived leaching versus time for different increments, along with their corresponding standard deviation (Sd_{rc}) and the concentration factor (CF). The descriptions of these parameters and the specified increments are outlined in EA NEN7375 (EA NEN 7375, 2004).

3.2.9 Arsenic trioxide solubility in cement buffering solution

An experiment was designed to verify the contribution of arsenic trioxide and the Giant mine tailings to water geochemistry. The solubility of the reagent grade arsenic trioxide and the constituents of Giant Mine tailings within aqueous solutions made of dissolved cement was evaluated using a series of extra analyses. Four 2-liter beakers were meticulously cleaned and

rinsed with deionized water. 103.3 g GU cement and 759.3 g deionized water ($W/C = 7.35$), following the same proportions as the CPB mixtures outlined in Table 3.3 (for $B_w = 5\%$ and arsenic content = 10%), were added to these beakers and stirred for a few minutes using magnetic stirrers. The pH and EC of the DI water were measured before using in the tests. During the mixing, the pH of the mixture was measured in a continuous manner until the stabilization of the pH value. Once the pH was stabilized, the mixtures were filtered using a vacuum filter system and the filtrates were transferred to new beakers. Then, 413.2 g of reagent-grade As_2O_3 was added to two beakers (each of them 206.6 g) and mixed using magnetic stirrer. Similarly, 206.6 g of Giant Mine tailings was added to the remaining beakers containing the filtrate of the water-cement mixture and mixed using a magnetic stirrer. During the mixing process, samples (2 replicates for each beaker) were collected at intervals of 10 minutes, 30 minutes, 90 minutes, 3 hours, 24 hours, and 48 hours using a 50 ml syringe. These samples were then filtered through a $0.45 \mu m$ cellulose syringe filter before analysis. The pH and EC of the filtrates were measured using a multimeter (B30PCI, VWR SympHony). After pH measurement, the extracted solutions were acidified with 2% (v/v) nitric acid, and their chemical compositions were analyzed using ICP-MS with an Agilent 7800 instrument.

3.3 Parallel extraction tests on synthetic CPB samples, ATRW dust and tailings of the Giant Mine

Parallel extractions were performed to evaluate the geochemical behavior and environmental mobility of different species in the tailings and ATRW dusts of the Giant Mine and CPBs. This approach uses various extractants to selectively dissolve or mobilize specific components, providing insights into the speciation, binding mechanisms, and potential environmental risks of the arsenic. Parallel extraction reveals whether arsenic is adsorbed onto iron oxides, encapsulated in hydration products, or bound in insoluble mineral phases. The extraction steps targeting iron oxides were selected due to the likely relationship between As and iron oxides. This will be evaluated in section 4.6.3 using XAS. The geochemical behavior of CPB samples, ATRW dust, and tailings from the Giant Mine was investigated under various geochemical conditions (extremely acidic, neutral, and extremely alkaline solutions) through parallel extraction analysis using different reagents. The first batch of preliminary CPB samples, prepared with 75.3% solid content, included pure silica tailings, GU cement (10% wt.) as the binder, reagent-grade arsenic trioxide (15% wt.), and DI water ($W/C = 3.60$). These samples were cured for 28 days before

undergoing UCS tests. Subsequently, they were dried and crushed using a pestle and mortar in preparation for extraction analyses. For comparative purposes, ATRW dust and tailings from the Giant Mine were also included in the arsenic extraction analysis. Five different reagents, as detailed in Table 3.6, were employed to target specific phases. One gram of crushed CPB, tailings, and ATRW dust was mixed with predefined volumes of these reagents and digested under various conditions. The pH of the solutions was measured initially in the blank solutions (before adding materials). The mixture containing sodium ascorbate, bicarbonate, and citrate (Na-AscBicCit) was prepared in an oxygen-free glovebox environment. After adding CPB, tailings, and ATRW dust, the tubes were covered using aluminum foil to maintain darkness and subjected to up to 24 hours of agitation in a rotary agitator. Additionally, DI water, NaOH, and HCl samples were prepared at room temperature and agitated in the rotary system for 24 hours for digestion. For samples containing hydroxylamine hydrochloride ($\text{NH}_2\text{OH}\cdot\text{HCl}$), preparation occurred at room temperature with digestion in a temperature-controlled medium, with occasional mixing during digestion.

Table 3.6 The specifications of each extraction analysis

Target phases	Reagent	Sample mass (gr)	Solid/Reagent ratio	Digestion period (h)	Reference
Water-soluble phases	Deionized water	1	1:50	24 (room temp.)	(Ribeta et al., 1995)
Insoluble sulfates	0.3 M NaOH	1	1:30	16 (room temp.)	(G. Yin & Catalan, 2003)
Amorphous oxyhydroxides	0.12 M Na-ascorbate, 0.6 M Na-bicarbonate & 0.17 M Na-citrate (pH = 8)	1	1:20	24 (in dark anaerobic glovebox)	(Amirbahman et al., 1998)
Poorly crystalline phases & carbonates	0.5 M HCl	1	1:10	24 (room temp.)	(Heron et al., 1994)
Amorphous & crystalline oxyhydroxides	2.0 M $\text{NH}_2\text{OH}\cdot\text{HCl}$ in 25% ($\text{v}\cdot\text{v}^{-1}$) acetic acid	1	1:30	24 (at 95 ± 4 °C)	(Ribeta et al., 1995)

Following completion of digestion, leachates were filtered using a 0.45 μm filter. After measuring the pH and acidifying with 2% pure HNO_3 , they were analyzed via ICP-MS.

3.3.1 Characterization of the stabilized arsenic compounds

Arsenic compound characterization in the paste was conducted to understand the microstructural processes influencing arsenic leaching, employing advanced mineralogical techniques including SEM, CT, XAS, FTIR, and TGA techniques, in collaboration with other TERRE-NET co-investigators. SEM coupled with microanalysis in energy-dispersive X-ray spectroscopy (EDS) was utilized to visualize and identify secondary precipitates and stabilized compounds. A key advantage of SEM is its ability to directly visualize the material's microstructure, although quantification of observations can be challenging. However, the limitation lies in the lack of apparent third-dimensional information, necessitating validation of two-dimensional observations for accuracy, particularly when studying connected structures. CT scans were employed to investigate the microstructure and porosity of CPB samples containing ATRW dust. Synchrotron-based X-ray absorption spectroscopy (XAS) was utilized to examine As oxidation states and coordination, aiding in elucidating the mineralogical forms of arsenic. Thermogravimetric analysis (TG/DTG) was conducted to study arsenic stabilization mechanisms within the cemented paste backfills (Bull & Fall, 2020b). Thermogravimetric analysis was also employed to determine the thermal stability of CPB samples and their fraction of volatile components by monitoring weight changes during sample heating at a constant rate. FTIR analysis was utilized to assess the chemical composition and qualitative structural analysis of CPB materials. These characterization tests, except SEM, were performed on various recipes of the main CPB samples based on UCS and TLT results. SEM analysis was conducted on CPB and cement-As₂O₃ mixtures from the second batch of preliminary samples.

3.3.1.1 SEM observations

After conducting UCS tests on the 28-day cured CPB samples and geochemical analyses on the As₂O₃-cement mixtures after 28 days (second batch of preliminary samples), the samples underwent drying and pulverization using a pestle and mortar in preparation for SEM analysis. This analysis focused solely on the As₂O₃-containing samples to visually examine their microstructure and correlate it with the mechanical performance and geochemical characteristics of the mixtures. Samples from each specimen were sprinkled onto aluminum pontils covered with double-sided carbon tape and manually scanned with the SEM, starting from the most As-enriched sample to the least enriched one, to better identify the As-bearing phases. Subsequently, polished

sections were prepared to observe mineral associations, conduct automated mineralogical analysis, and obtain more precise analyses. The samples were cast in a viscosity-controlled epoxy resin to create sections 30 mm in diameter. The surfaces of the sections were polished using alumina and diamond suspensions, followed by coating with a carbon film using a Leica EM ACE600 rotary-table metallizer to facilitate electron drainage to the SEM. The analysis was conducted at the IOS Geosciences laboratory using a Zeiss Sigma 300 VP field effect SEM (FE-SEM) equipped with two Oxford Instruments Ultim-Max 170 mm² energy dispersive spectrometers (EDS-SDD). Electron images were captured in backscattered electron (BSE) mode at an accelerating voltage of 20 kV. Mineralogical analysis was performed using ARTMin-II technology, involving acquisition of chemical maps on the sample to reconstruct the map of mineral phases. Mineral phases were then defined from the X-ray maps using AZtec's AutoPhaseMap clustering algorithm (Oxford Instruments AZtec 5.2 software). These analyses are termed semi-quantitative as they are standardized and utilize factory calibrations of the device.

3.3.1.2 Computerized tomography (CT) scan

X-ray CT scanning was used to examine the microstructure and porosity of the porous material and to explore the relationship between microscopic pore characteristics and strength. In this study, CPB samples containing ATRW and prepared using GU and GU/LKD binders were subjected to CT scanning using a Nikon XT H 225ST Industrial CT scanner (University of Alberta Permafrost Archives Science Laboratory) equipped with an X-ray source featuring a rotating target, and analysis was performed using Nikon's Inspect-X software. Four specific samples were chosen for this analysis, comprising the GU and GU/LKD samples with the highest and lowest UCS values. These samples were prepared and molded in the small cylindrical molds (3.4 cm in diameter and 6.2 cm in length) after performing the UCS tests on all samples and the analysis was done on intact samples after specific curing time. The scan settings were configured as follows: a beam energy of 205 kV, a beam current of 115 μ A, exposure at 8 frames per second, and setting the detector panel to -100 mm. The effective pixel size was established at 22 micrometers, and helical scans were employed for all cases to maximize resolution. Each sample was subjected to a total of approximately 4700 projections, with projections optimized to 3141 per rotation and an averaging of 8 frames per projection. For the reconstruction of the primary scan data, Nikon's CT 3D Pro software was utilized. Additionally, beam-hardening corrections were applied to all scans to minimize artifacts in the images. The reconstructed scans were then converted into .VOL and .VGI

formats and subsequently imported into 3D ORS Dragonfly visualization software. Through three-dimensional reconstruction of CT images, the cores were segmented into three regions, representing pore space, high-density (arsenic-containing) materials, and the remaining sediment matrix. 2D greyscale images along the center of each core in both longitudinal and transverse profiles and 3D images of each core, displaying each segmented region were obtained. The unnecessary regions on each core were cropped to have a smaller sample including the region of interest (ROI) which was obtained as a cylinder with a height of 16 mm and diameter of 8 mm that accurately represented the specimens. Multi-region porosity analysis, with unique measurements for pore volume, mean Feret diameter, and sphericity was done on the ROIs as well. The Feret diameter represents the distance between the two farthest points of a shape measured in a specific direction. In particle size analysis, calculating the Feret diameter is a commonly employed descriptor for assessing particle size distribution (Dražić et al., 2016). Mean Feret diameter is the mean value of the minimum and maximum Feret diameters of each discrete pore's boundary over a sufficient number of orientations. Sphericity (S) is defined as the ratio between the perimeter of a circle with the same area as the projected area of the particle and its real perimeter (C. Jiang et al., 2022). Sphericity quantifies how closely a pore resembles a "sphere" by determining the ratio between the object's volume and surface area, as illustrated in Equation (3.9) (Lorenzoni et al., 2019).

$$S = \frac{\pi^{\frac{1}{3}}(6V)^{\frac{2}{3}}}{A} \quad (3.9)$$

where S is the sphericity of the pore; V is the volume of the pore and A is the superficial area of the pore.

3.3.1.3 XAS analysis

In recent decades, synchrotron-based techniques like X-ray absorption spectroscopy (XAS) have been commonly utilized to understand the chemical and local structural states of a particular element in solids (Komárek et al., 2013; Wogelius & Vaughan, 2012). To supplement the leaching tests, As K-edge XAS spectra were obtained for four selected samples to gain insights into the chemical speciation, bonding, and coordination environments between As and other elements.

A thin layer of dried and powdered sample was spread on polyimide (Kapton) tape and enclosed within another layer of tape before analysis at the BioXAS-Main beamline (07ID-2 M) at the

Canadian Light Source synchrotron (Saskatoon, Canada). The BioXAS-Main beamline contains a Si mirror with a Rh coating, used to focus the beam, and a liquid N₂-cooled pseudo-channel cut double Si (220) crystal monochromator to select the incident energy. All samples were pre-cooled in liquid N₂ before insertion into the liquid N₂-cooled cryostat (Oxford Instruments plc., UK), positioned between the I₁ and I₂ ion chambers. Fluorescence data from each sample were collected using two 32-element Ge detectors (CANBERRA Co., Canada) positioned at 90 degrees to the incident beam and 45 degrees to the sample. Soller slits and a Ge-3 filter were positioned between the sample and the fluorescence detectors to improve the As signal-to-noise ratio by attenuating low energy fluorescent X-rays. Simultaneous L_{III}-edge transmission data from an Au reference foil positioned between ion chambers I₂ and I₃ served for energy calibration and alignment of the As spectra. Each As measurement scanned the range from 200 eV below the theoretical As K-edge (11867 eV) to +885.6 eV ($k = 14 \text{ \AA}^{-1}$), with steps of 5 eV in the pre-edge region (-200 to -30 eV), 0.5 eV in the X-ray absorption near edge structure (XANES) region (-30 to 80 eV), and 0.05 k in the extended X-ray absorption fine structure (EXAFS) region (80 eV to 885.6 eV ($k = 14 \text{ \AA}^{-1}$)). To ensure data quality and the absence of beam-induced sample transformation, two to three replicate scans were collected for each sample.

Data preparation, reduction, and analysis were carried out using the ATHENA modules of the Demeter package (Ravel & Newville, 2005) and the Larch package (Newville, 2013). Scans were imported, corrected for the total flux, and quality checked. Pre- and post-edge normalization, R background determination, and the k -range were selected to optimize the resulting signal with a forward Fourier transform k -range of 3-11 \AA . The critical energy (E_0) of the As K-edge near-edge spectra was determined as the highest point in the main peak of the first derivative and compared to known reference materials containing in the As⁰, As⁺³, and As⁺⁵ oxidation states, which informed subsequent EXAFS modeling.

The amplitude reduction factor ($S\sigma^2$) for the Au reference foil in the non-linear least squares EXAFS fitting process was determined to be 0.868 and then constrained for all samples. Potential paths were chosen based on elemental analysis from sample digestions and the composition of the starting materials.

Preliminary coordination numbers (CN), interatomic distances (r , in \AA), energy shifts (ΔE_0), and Debye-Waller factors (σ^2) were derived from theoretical crystal structures and then refined in

Larch. The fitting process was conducted over an R -range from 1.0 to 5.0 Å. The goodness-of-fit parameters, including the R -factor and χ^2 , were calculated in Larch, where the R -factor indicates the percentage misfit between the model and the data, with smaller values being more desirable. Efforts were made to avoid values above 0.03, indicating a 3% misfit, when possible.

3.3.1.4 Thermogravimetric analysis

Thermogravimetric (TG) analysis was performed on selected CPB specimens using TA Instruments Discovery SDT650 equipment. The analysis covered a temperature range from 25 to 1000 °C, with a heating rate of 10 °C/min under a N₂ atmosphere. Two specific samples were chosen for this analysis based on the results of the UCS and leaching tests. The powdered samples obtained from the UCS test were used for this purpose. TG curves were utilized to calculate the derivative thermogravimetric (DTG) value for each sample. This value was derived by normalizing the weight loss between 25 and 1000 °C to the initial weight of the sample. TG and its first derivative, DTG, offer instantaneous and accurate measurements of weight loss and its rate during analysis (Zheng et al., 2019). Thermogravimetric analysis was utilized to assess the thermal stability of CPB samples containing ATRW and to ascertain their volatile component fraction by monitoring weight changes during sample heating at a constant rate. The results were compared to the standard values obtained from the literature. These measurements help in distinguishing between different materials based on their distinct thermal properties.

3.3.1.5 FTIR analysis

Fourier transform infrared spectroscopy (FTIR) is a method that enables the assessment of the chemical composition and qualitative structural analysis of materials. The FTIR spectrum enables the characterization of various materials by identifying characteristic peaks corresponding to the vibration bands of specific interatomic bonds (Guerrero-Pérez & Patience, 2020). The tests were conducted using the SHIMADZU IRTracer-100 FTIR device (Kyoto, Japan) at the UQAT Biomaterials Laboratory. Upon infrared ray excitation of the material, there was an absorption of energy by the molecules, allowing their vibrations. Subsequently, the machine recorded the intensity of the reflected radiation. Each molecule has a distinct absorption band that serves as a distinguishing feature (Guerrero-Pérez & Patience, 2020). The wavelength range used varied between 4000 cm⁻¹ and 400 cm⁻¹, aligning well with the molecular vibration energy domain. Data processing was performed using the LabSolutionsIR software. This analysis was conducted on the

two samples previously investigated by TG analysis. Comparison with reported data enabled the identification of the characteristic peaks.

surface area was approximately half of that of ATRW and pure As_2O_3 , with the coarsest grains showed the lowest specific surface area.

Table 4.1 Particle size parameters, specific gravity, and specific surface area of ATRW, tailings, pure silica (Sil-Co-Sil[®] 106), and pure As_2O_3

Parameter	Unit	Tailings	ATRW	Pure silica	Pure As_2O_3
$C_u = D_{60}/D_{10}$	(-)	8.46	5.44	24.1	2.4
$C_c = D_{30}^2/(D_{60} \times D_{10})$	(-)	0.80	1.51	2.3	1.0
$U = (D_{90} - D_{10})/D_{50}$	(-)	5.06	2.33	2.90	1.49
Specific gravity (G_s)	(-)	2.77	3.45	2.66	3.74
Specific surface area	m ² /g	3.5899	7.0381	1.090	0.0486

4.1.2 Chemical characterization

Chemical composition of samples is shown in Tables 4.2 and 4.3. As can be seen, more than 57% of the ATRW sample and 41% of the odd dust sample are arsenic. Antimony concentration in the ATRW sample is higher than the odd dust sample (about 1.15 times); whereas, the concentrations of Al, Ca, Fe, Pb, S, and Zn are substantially higher in the odd dust sample (for Fe, Pb, and Zn: about three times; for S: about four times). Due to these significant concentration differences, the odd sample was not mixed with other dust samples, and further experiments were done by using the mixed ATRW sample only. Neutralizing elements, such as Ca and Mg, in the tailings samples are more abundant than sulfur (approximately 0.5%), therefore the tailings can be anticipated as non-acid generating tailings.

Table 4.2 The results of the XRF analysis of the ATRW dusts and tailings samples

Sample	SiO ₂	Al ₂ O ₃	Fe ₂ O ₃	MgO	CaO	Na ₂ O	K ₂ O	TiO ₂	P ₂ O ₅	MnO	Cr ₂ O ₃	V ₂ O ₅	LOI	Sum
	%													
ATRW	4.67	1.91	3.99	8.59	0.66	0.25	0.33	0.15	0.02	0.05	< 0.01	< 0.01	79.4	100.1
Tailings	48.5	9.86	10.9	5.63	8.53	0.44	1.45	0.76	0.08	0.16	0.02	0.03	12.4	98.8

Table 4.4 shows the chemical analysis of pure silica (Sil-Co-Sil[®] 106). The chemical composition of the pure silica showed that SiO₂ accounted for 99.8% wt., followed by negligible impurities of Al₂O₃ (0.16 wt.%) and lesser amounts of other oxides.

Table 4.3 Chemical analysis results of the dusts and tailings samples by ICP-AES and ICP-MS methods

Element (mg/kg)	Al	As	Ba	Ca	Cd	Co	Cr	Cu	Fe	K
Mixed ATRW	10730 ^a	571500 ^a	29 ^a , 40 ^b	5360 ^a	7625 ^a	23 ^a , 38 ^b	34 ^a , 31 ^b	234 ^a , 267 ^b	31720 ^a	2597 ^a
Odd dust	13630 ^a	411300 ^a	32 ^a , 41 ^b	8363 ^a	4041 ^a	63 ^a , 90 ^b	61 ^a , 67 ^b	596 ^a , 692 ^b	94060 ^a	3297 ^a
Tailings	47000 ^a	2747 ^a	86 ^a , 94 ^b	56260 ^a	25 ^a	35 ^a , 46 ^b	113 ^a , 112 ^b	41 ^a , 71 ^b	72520 ^a	10550 ^a
Element (mg/kg)	Mg	Mn	Na	Ni	Pb	S	Sb	Sr	Ti	Zn
Mixed ATRW	3756 ^a	128 ^a , 448 ^b	541 ^a	63 ^a , 88 ^b	1004 ^a , 1095 ^b	2463 ^a	16782 ^b	9 ^b	944 ^a , 918 ^b	529 ^{a, b}
Odd dust	4676 ^a	208 ^a , 435 ^b	853 ^a	144 ^a , 191 ^b	3431 ^a , 3750 ^b	10170 ^a	14526 ^b	11 ^b	1170 ^a , 1191 ^b	1450 ^a , 1460 ^b
Tailings	29780 ^a	1092 ^a , 1317 ^b	3039 ^a	81 ^a , 109 ^b	134 ^a , 158 ^b	5192 ^a	118 ^b	47 ^b	3668 ^a , 3447 ^b	331 ^a , 390 ^b

a: ICP-AES, b: ICP-MS

Table 4.4 Chemical analysis of pure silica (Sil-Co-Sil[®] 106)

Mineralogical phase	SiO ₂	Fe ₂ O ₃	Al ₂ O ₃	TiO ₂	CaO	MgO	Na ₂ O	K ₂ O	LOI
%	99.8	0.012	0.16	0.01	0.02	<0.01	<0.01	0.01	0.1

4.1.3 Mineralogical composition

Mineral composition evaluated by XRD, shown in Table 4.5, indicate that more than 86% of the ATRW sample is arsenolite (As₂O₃). Considering the volatility of arsenic trioxide at elevated temperature, there is conformity between the percent of arsenolite in ATRW and its loss on ignition (LOI) obtained by XRF. The tailings sample mainly includes quartz, chlorite, dolomite, and muscovite.

4.2 Results of preliminary tests

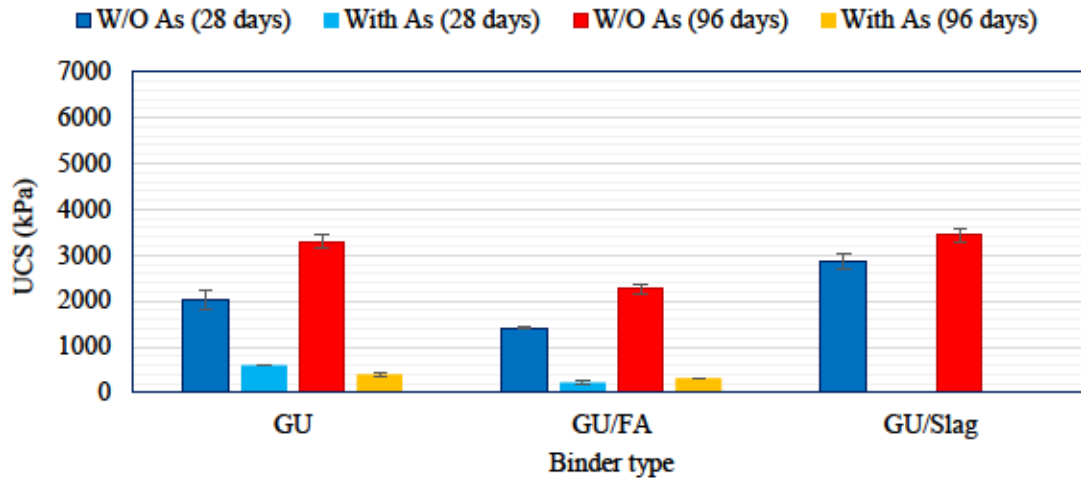
4.2.1 Binder selection

The first batch of preliminary CPB samples was prepared by mixing 15% pure As₂O₃ with 10% of three binders: GU, GU/FA (40/60), and GU/Slag (10/90) into either Sil-Co-Sil[®] or Giant Mine tailings. Figure 4.2 shows that the unconfined compressive strength (UCS) of samples containing pure arsenic trioxide was significantly lower compared to samples without As₂O₃. This difference

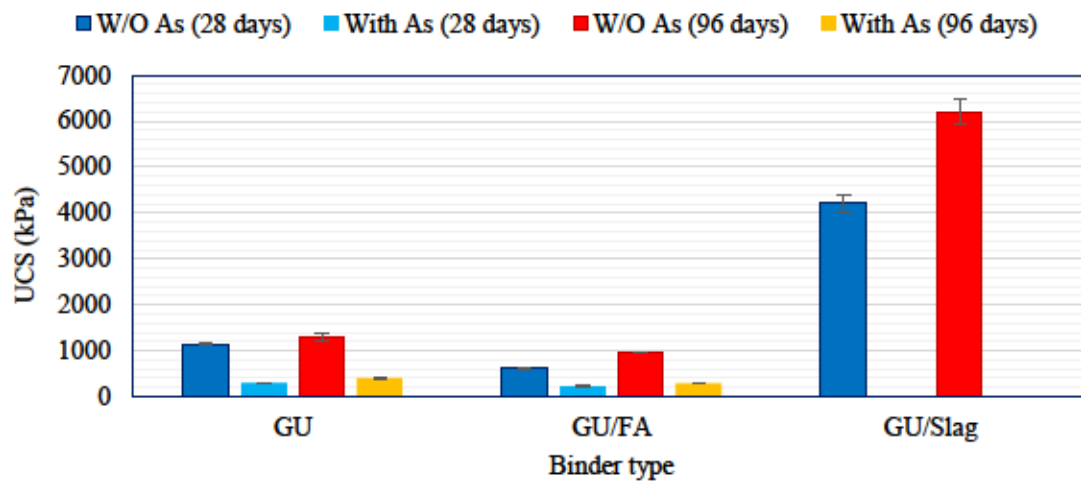
was particularly notable for the GU/Slag binder. While As_2O_3 -free GU/Slag samples exhibited the highest strength (over 6200 kPa and 3400 kPa after 96 days for tailings and Sil-Co-Sil®, respectively), those containing As_2O_3 showed notably weaker strengths, with no setting observed even after 96 days, as depicted in Figure 4.3 where the samples could be easily halved post UCS testing using a cutter. As_2O_3 -containing samples prepared with pure GU binder displayed the highest UCS, followed by GU/FA samples. In most cases, except for As_2O_3 -containing GU/Sil-Co-Sil® samples, increasing curing time from 28 to 96 days resulted in higher UCS for the samples. For intact samples (without As_2O_3), GU and GU/FA samples with pure silica exhibited higher UCS than tailings-containing samples, while GU/Slag samples prepared with tailings demonstrated significantly higher UCS.

Table 4.5 Mineral composition determined by XRD for ATRW and tailings samples

Minerals	ATRW (%)	Tailings (%)
Arsenolite	86.4	-
Quartz	5.0	39.6
Muscovite	1.1	14.8
Chlorite	1.0	19.8
Gypsum	0.7	1.2
Bettertonite ($[Al_6(AsO_4)_3(OH)_9(H_2O)_5] \cdot 11H_2O$)	1.2	-
Pyrrhotite	0.4	-
Dolomite	-	16.4
Albite	-	1.8
Microcline	-	2.5
Augite	-	1.1
Actinolite	-	0.9
Chalcopyrite	-	2
Total	100	100



a



b

Figure 4.2 UCS of the first batch of preliminary CPB samples, prepared with both a) Sil-Co-Sil® and b) Giant Mine tailings, with and without pure arsenic trioxide

Based on the findings, it can be concluded that the addition of arsenic trioxide significantly decreased the strength of CPB samples, with the impact being more pronounced for GU/Slag binder. Consequently, it was decided to exclude the GU/Slag mixture in the subsequent parts of this study.

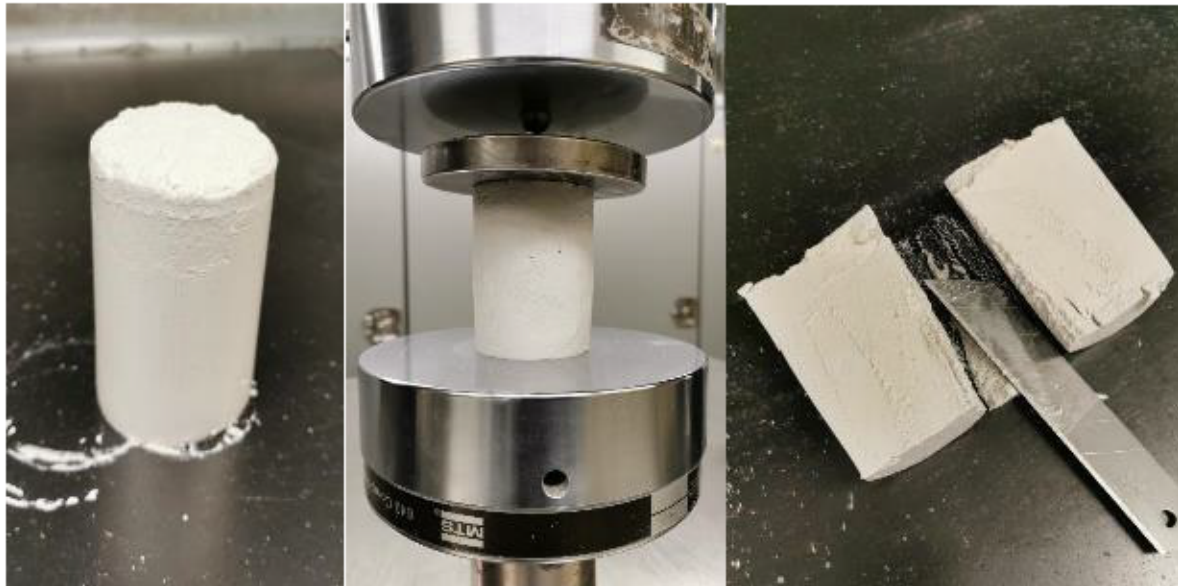


Figure 4.3 CPB sample prepared with GU/Slag binder, Sil-Co-Sil® as tailings, and subjected to a 96-day curing process

4.2.2 Behaviour of simplified CPB: silica as tailings, and pure As_2O_3 as ATRW (Article 1)

The second batch of preliminary CPB samples was prepared using GU as the binder ($B_w = 5\%$), Sil-Co-Sil® to simulate the tailings, and varying percentages of pure arsenic trioxide (0-15%) at a solid content of 74% under drained conditions. Table 4.6 outlines the specifications of these samples.

Table 4.6 Mass of ingredients used for the preparation of the second batch of preliminary CPB samples (Mohammadi, Demers, Benzaazoua, et al., 2023a)

Sample/Parameter	CPB-0%	CPB-5%	CPB-10%	CPB-15%
As_2O_3 content (%) (D_w)	0	5	10	15
Solid percentage (%) (C_w)	74	74	74	74
Cement content (%) (B_w)	5	5	5	5
$M_{dry-tailings}$ (g)	2042.4	1951.5	1859.6	1766.6
$M_{dry-As_2O_3}$ (g)	0.0	102.7	206.6	311.7
$M_{dry-cement}$ (g)	102.1	102.7	103.3	103.9
M_{water} (g)	750.6	754.9	759.3	763.8
Water/binder (W/C)	7.35	7.35	7.35	7.35

These results were presented in an article entitled "The Effects of Arsenic Trioxide Addition on the Mechanical and Geochemical Properties of Cemented Paste Backfill," that was published in Results in Materials journal (Appendix B).

4.2.2.1 Strength acquisition behavior

Table 4.7 displays the slump measured with a mini cone. It appears that the initial inclusion of arsenic trioxide led to a reduction in the slump of the mixtures. However, increasing the arsenic trioxide content from 5% to 15% resulted in higher slump values. Despite all CPB samples being prepared with a consistent water/binder (W/C) ratio, the required water amount in the recipes increased with the rise in As_2O_3 content due to the higher specific gravity of pure arsenic trioxide as opposed to tailings. While the slump test is a valuable index for quality assurance, it's not advisable to rely solely on it to establish design parameters like yield stress, unless supported by additional, more comprehensive testing or when dealing with materials that have been thoroughly studied and confirmed (Fourie & Dunn, 2007).

Table 4.7 Slump results for the CPB samples (Mohammadi, Demers, Benzaazoua, et al., 2023a)

Sample	CPB-0%	CPB-5%	CPB-10%	CPB-15%
Slump _{mini} (mm)	85	78	84	89

Figure 4.4 illustrates the results of UCS tests conducted on drained CPB samples with varying As_2O_3 contents after 7 and 28 days of curing. The increase in mechanical strength was more pronounced for the CPB-0% paste sample. However, the As_2O_3 -containing samples primarily gained their strength within the first 7 days, with a subsequent small, albeit potentially insignificant, increase in strength after 7 days, indicating slow strength development.

The UCS of the CPB-0% sample increased from 428 kPa to 740 kPa, marking a 73% enhancement over the 7 to 28 days of curing period. Meanwhile, the strength acquisition percentages from 7 to 28 days of curing for the As_2O_3 -containing samples were 10%, 22%, and 2.5% for the CPB-5%, CPB-10%, and CPB-15% samples, respectively. The increase in strength can be attributed to various factors that contribute to the enhanced development of CPB strength.

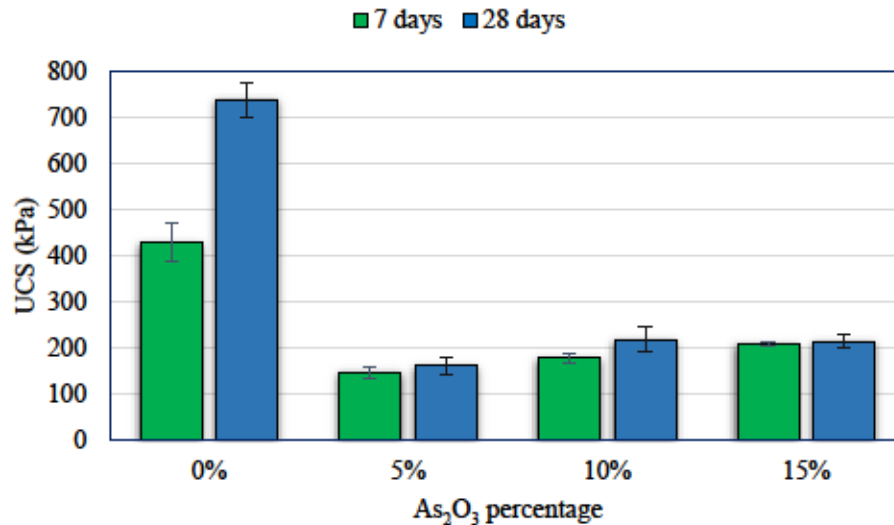


Figure 4.4 UCS tests results on the CPB samples with various As₂O₃ contents after 7 and 28 days of curing (Mohammadi, Demers, Benzaazoua, et al., 2023a)

The results also indicated a notable decrease in the strength of the CPB samples upon adding 5% arsenic trioxide. Prior to conducting the tests, the anticipated outcome was a decline in strength with an increase in As₂O₃ content, as observed in previous studies with high cement content (Arcadis, 2017). In samples with higher percentages of As₂O₃, slight strength increases were noted, with CPB-10% samples ultimately exhibiting the highest strength among the As₂O₃-containing samples after 28 days. The standard deviation (SD) for the triplicate UCS measurements of the pastes ranged from SD = 6.6 kPa to 74 kPa and SD = 26 kPa to 65 kPa for samples cured for 7 and 28 days, respectively. The coefficient of variation (CV) for these samples ranged from CV = 3.2% to 17% and CV = 8.8% to 22%, respectively.

4.2.2.2 Deformation behaviour of CPB

The stress-strain (deformation) curves of the CPB samples obtained from the UCS tests are presented in Figure 4.5 for the samples prepared with various As₂O₃ contents and cured for 7 and 28 days. The axial strain at the break (ϵ_u) represent the material's ductility, with higher values reveal a more ductile/less brittle character (Soltani et al., 2017; Yue Zhao, Soltani, et al., 2019). The stress-strain behavior for all CPB samples exhibited a rise-fall behavior with visually observable peak points. This reveals a strain-softening character accompanied by more ductile sample failure for As₂O₃-containing samples and more brittle sample failure for the CPB-0% samples. With respect to this graph, for most CPB-0% samples, the strain at the failure is less than

2% after 7 and 28 days of curing. The highest strain at the break is mostly related to the CPB-5% samples (with the lowest strength), followed by the CPB-10% and CPB-15% samples for 7-day cured and CPB-15% and CPB-10% for 28-day cured samples, respectively. The order of decrease in the strain at break values was equal to the order of increase in the strength of the samples. In general, the higher the UCS the lower the strain at the failure. It should be noted that, generally, increasing the curing time lowered the strain at the break (lower ductility) for the As_2O_3 -containing samples but it had no significant influence on the deformation behavior of the CPB-0% samples. This behavior is attributed to the combined effect of consolidation and hardening, which results in a CPB sample with less plastic behavior (Ghirian & Fall, 2016).

Figure 4.6 highlights the relationship between the UCS and the modulus of elasticity (E) obtained from the UCS test results. These results are presented for all the CPB samples prepared with and without As_2O_3 and cured for 7 and 28 days. The results showed a relationship between the E and UCS values for most of the samples. The E values after 7 days typically vary between 159 and 272 MPa for the CPB-0% samples and between 18 and 126 MPa for the samples with various contents of As_2O_3 . For the samples cured up to 28 days, these values are between 8 and 146 MPa and between 21 and 82 MPa for the samples without and with As_2O_3 , respectively. Samples with higher compressive strength showed a higher modulus of elasticity (the CPB-0% samples) and arsenic-containing samples with the lower strength revealed lower E values. The most interesting point regarding the E values is the decline in the modulus of elasticity after 7 days. This was more pronounced for the CPB-0% samples, where the E values were mostly higher than 150 MPa after 7 days; however, these values decreased to lower than 150 MPa after 28 days. For the As_2O_3 -containing samples, this reduction was not noticeable.

Based on the general relationship between E , stress (σ), and strain (ϵ), $E = \sigma/\epsilon$, there is a direct linear relationship between E and the inverse of the strain ($1/\epsilon$), as presented in Figure 4.7. As expected, CPB-0% samples showed the highest E and lowest strain value at the break (highest inverse values).

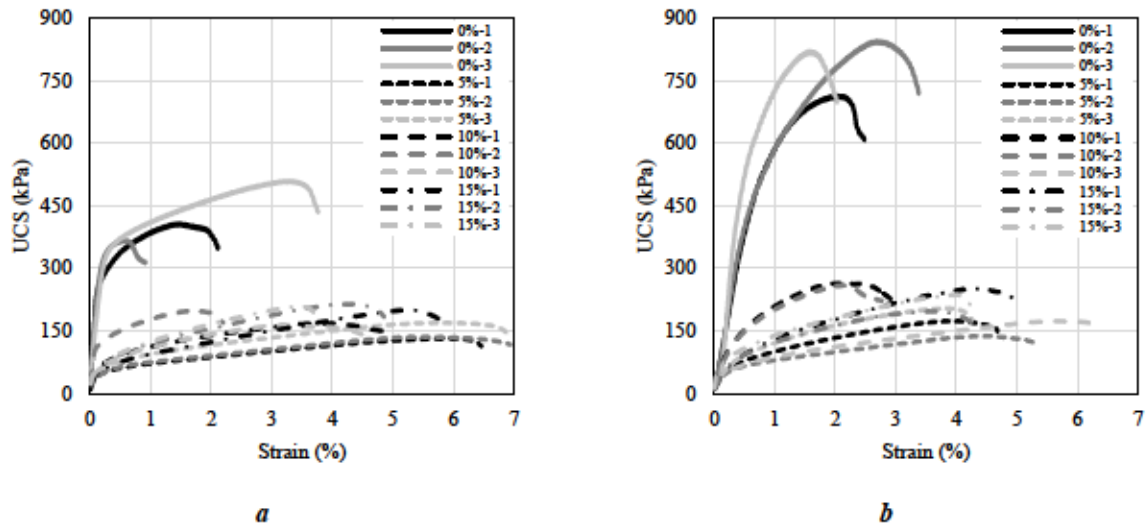


Figure 4.5 Effect of As₂O₃ content on the stress-strain (deformation) behavior of CPB cured for (a) 7 and (b) 28 days (Mohammadi, Demers, Benzaazoua, et al., 2023a)

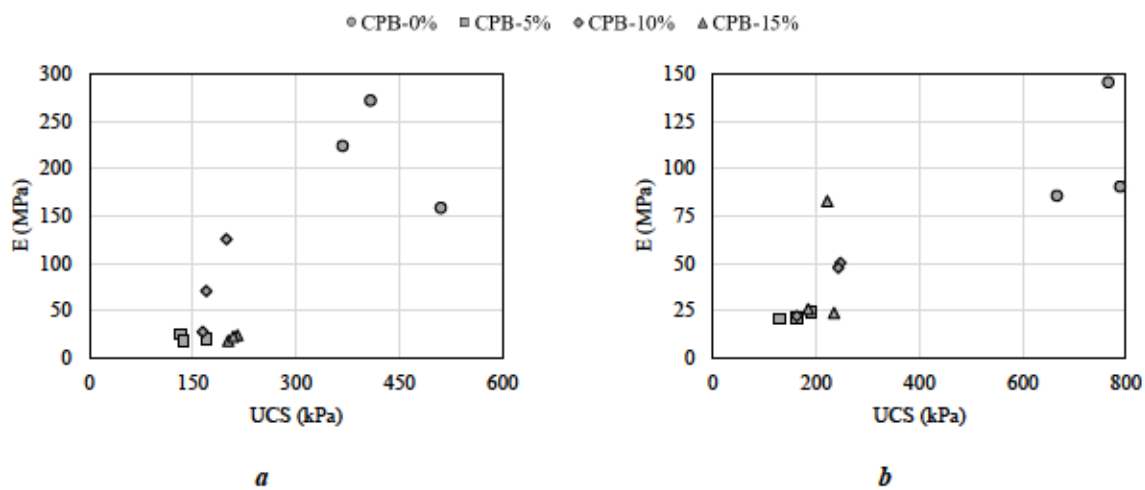


Figure 4.6 Relationship between UCS and modulus of elasticity after (a) 7 days, (b) 28 days (Mohammadi, Demers, Benzaazoua, et al., 2023a)

As mentioned in Chapter 3, it was planned to collect the drained water from the CPB samples after molding and during the curing period. However, a few ml of drained water was collected from the CPB-5% samples after molding since the rate of initial setting of the pastes was very rapid for the other mixtures. The pH of the paste without arsenic was higher than 12 (refer to section 4.2.2.2); however, for the CPB-5% samples, the pH value was 10.45. For optimal cement hydration, pH values above 12 are usually required. The reduction in the pH of the paste could be due to the arsenolite (As₂O₃) dissolution. When arsenic trioxide is dissolved in water, it hydrolyses and dissociates into *o*-arsenous acid, H₃AsO₃ (As III) as follows:

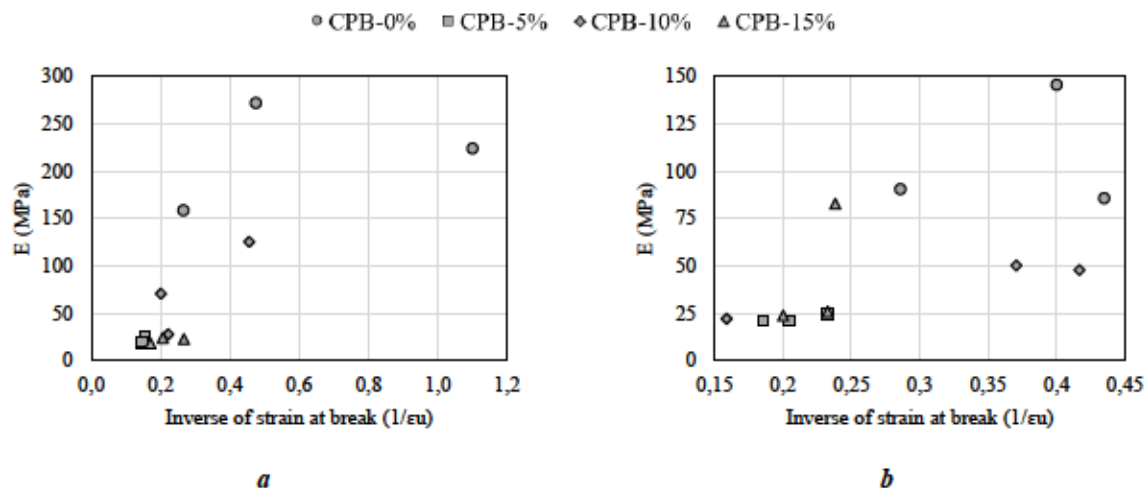
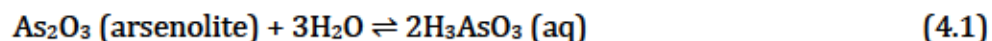
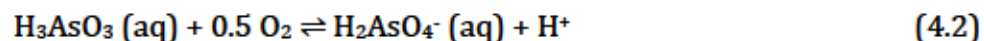


Figure 4.7 Relationship between modulus of elasticity and inverse of strain at break (a) 7 days, (b) 28 days (Mohammadi, Demers, Benzaazoua, et al., 2023a)



and this is followed by the oxidation of As (III) to As (V):



The oxidation of arsenite to arsenate in reaction (4.2) generates H^+ and causes acidity, therefore lowering the pH of the solution (Craw & Bowell, 2014). In an alkaline solution, some anions such as $\text{AsO}(\text{OH})_2^-$, $\text{AsO}_2(\text{OH})^{-2}$, and AsO_3^{-3} might also be present. However, it has been claimed that the *m*-arsenite ion, AsO_2^- , is also present in such solutions (Committee on Medical and Biologic Effects of Environmental et al., 1977). Due to the dissolution of the arsenic trioxide and cement during the preparation of the CPB samples, EC reached 5.51 mS, Ca concentration was 853 mg/L and As concentration was 1671 mg/L in the drained water. The presence of sulfur (748 mg/L) could be due to the presence of calcium sulfate in GU cement. The presence of calcium, sulfur, and arsenic in the CPB pastes could help the formation of amorphous/crystalline secondary minerals and the integration of the arsenic into the structure of the calcium-silicate-hydrate (C-S-H) phases. So, based on these results it can be postulated that the main reason for the drop in strength is the inhibition of hydration due to pH value below 12, and increased strength in the samples with higher arsenic trioxide contents could be due to precipitation of amorphous/crystalline minerals.

4.2.2.3 Cement-As₂O₃ geochemical interactions

To obtain insights into the interactions between binder and arsenic trioxide, the pH, EC, and chemical composition of As₂O₃-cement mixtures were assessed in the absence of pure silica. Figure 4.8 shows the variation of EC and pH of the water in contact with the mixtures for 28 days (672 hours), while Figure 4.9 depicts the variations of the most relevant elements. Dissolution of the GU cement and pure arsenic trioxide influenced the concentration of the various elements during the mixing period, and consequently, affected the pH and electrical conductivity of the solutions. The increase in EC was more pronounced for the solution without arsenic, with a tendency to increase with time, especially during the first 8 hours. This result is correlated to the pH values between 12.19 and 12.86. Conversely, for the As₂O₃-containing solutions, the pH values varied between 9.18 and 10.42 with a decreasing trend during the test period. This drop in pH compared to the arsenic-free solution agrees with the result from the drained water analysis presented in the previous section. Except for the arsenic and antimony in the solutions without arsenic, the dissolution of the elements showed no clear pattern associated with As₂O₃ content. A decrease in Ca concentration after 168 hours (7 days) may indicate the formation of Ca-As precipitates. These calcium-arsenic precipitation reactions can be considered as an important immobilization mechanism of arsenic in CPB. For 0% As₂O₃ mixture, the cement hydration results in the formation of calcium-(aluminate)-silicate-hydrate (C-(A)-S-H) gels; therefore, it decreases the concentration of the dissolved calcium after seven days.

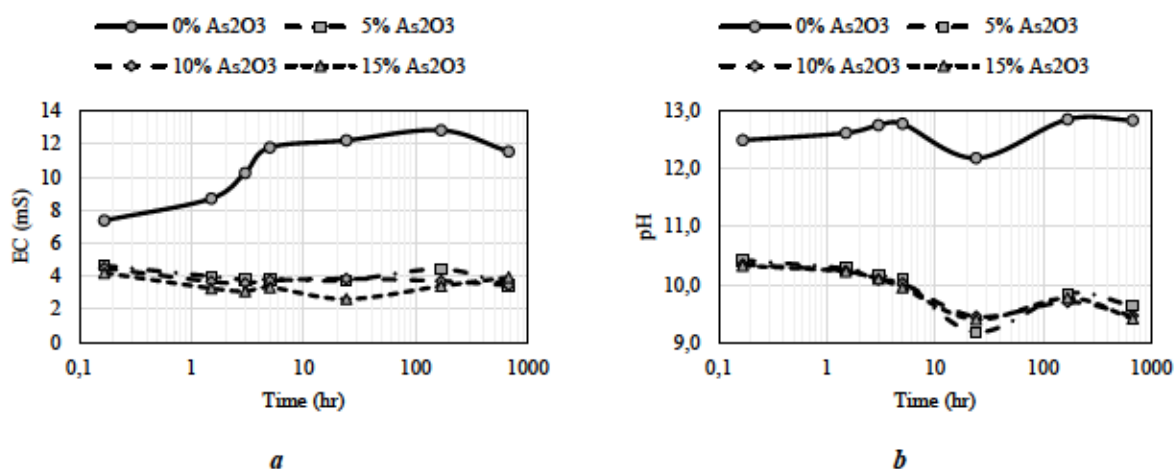


Figure 4.8 Variations of (a) EC and (b) pH of the cement-As₂O₃ mixtures versus time for the mixtures with various As₂O₃ contents (Mohammadi, Demers, Benzaazoua, et al., 2023a)

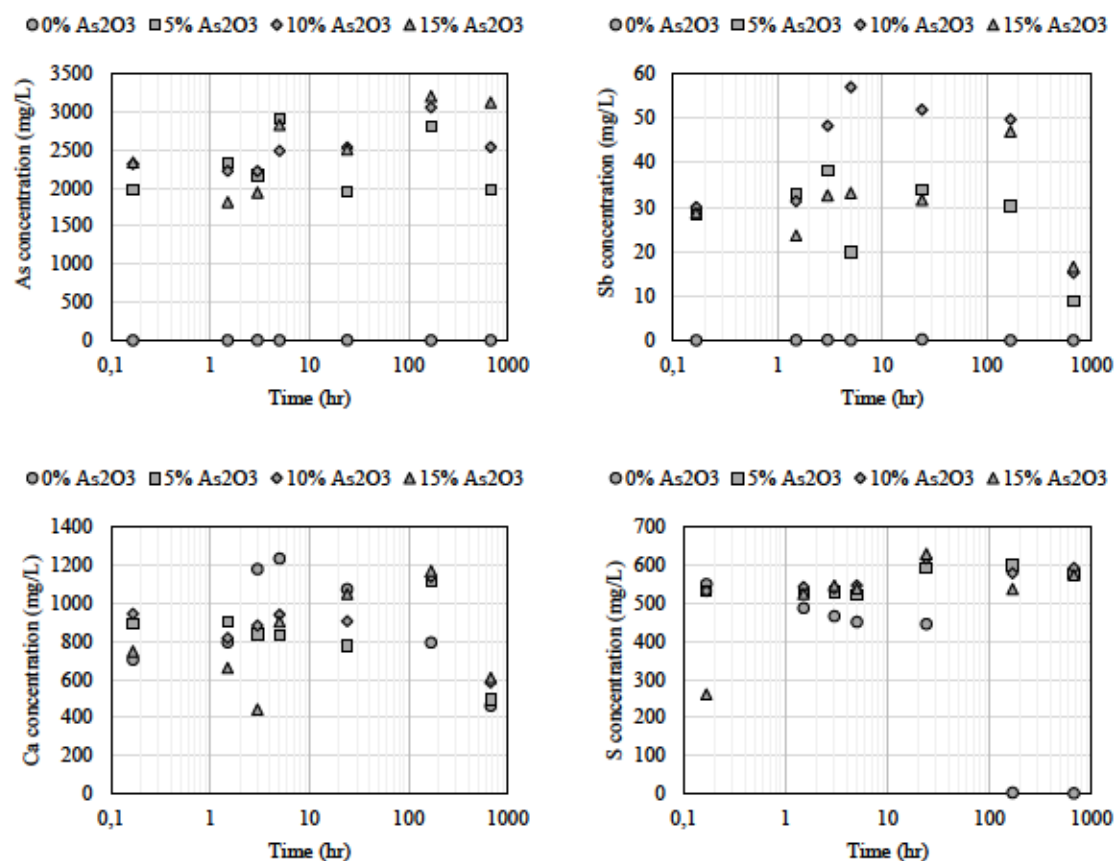


Figure 4.9 Variations of the dissolved elements (As, Sb, Ca, and S) in the cement-As₂O₃ mixtures containing different percentages of arsenic trioxide versus time (Mohammadi, Demers, Benzaazoua, et al., 2023a)

4.2.3 Arsenic trioxide solubility in cement buffering solution

Results in previous sections showed that the addition of arsenic trioxide lowered the solution pH in such a manner that secondary mineral precipitation and arsenic stabilization was affected. Figure 4.10 presents the variations in pH and EC in the pure As₂O₃ and tailings mixtures. The initial pH of the cement buffer mixtures was 12.35 for As₂O₃ and 12.37 for the tailings. However, just 10 minutes after mixing, the pH of the As₂O₃ mixture dropped to 9.67. Although the rate of decline in pH slowed after 3 hours, this reduction trend continued throughout the 48-hour mixing period, reaching a pH of 8.9. The tailings mixture also showed a decreasing trend, but with a much lower rate of reduction. This steady rate of reduction over the 48-hour mixing period resulted in a pH of 10.84. As mentioned in previous section, the dissolution of arsenic trioxide in water forms arsenious acid, which can decrease the pH of the mixture. Additionally, the tailings contain some

acid-neutralizing minerals such as muscovite and dolomite, leading to a much lower reduction in the pH of this mixture.

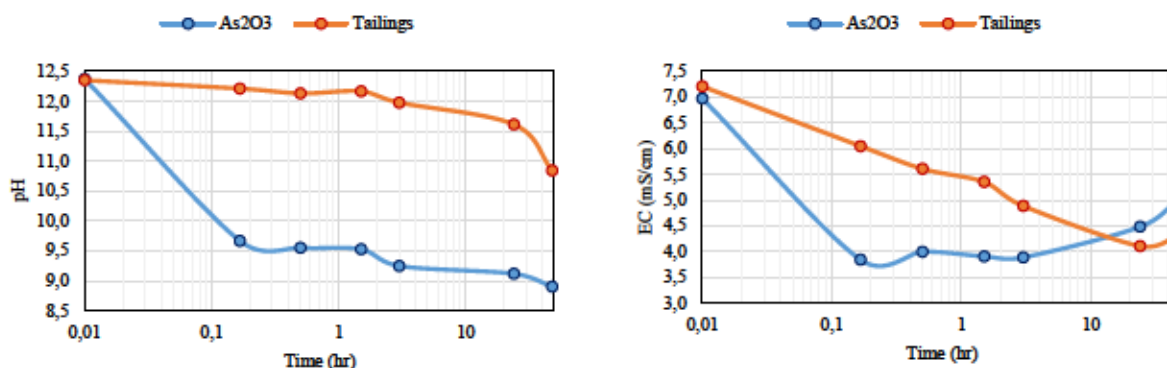


Figure 4.10 Variations of pH and EC of the mixtures with time

The initial EC values for the pure As_2O_3 and tailings mixtures were 6.97 and 7.21 mS/cm, respectively. The EC value in the As_2O_3 mixture showed a significant drop after 10 minutes, followed by some fluctuations before increasing to 5.03 mS/cm after 48 hours. In the tailings mixture, a continuous decreasing trend was observed up to 24 hours, after which it increased slowly, reaching 4.32 mS/cm after 48 hours. It can be concluded that the dissolution of cement constituents (before the addition of tailings and As_2O_3) resulted in a substantial increase in EC. However, the addition of tailings and pure As_2O_3 , along with chemical reactions between the arsenic, the chemical species of the tailings, and the dissolved cement species (calcium, hydroxide, and other metal ions), resulted in the probable formation of new components. This formation decreased the presence of species that readily dissociate in water, consequently lowering the EC of the mixtures. Continuous mixing for up to 48 hours and the reduction in pH could result in the dissolution of some newly-formed substances and other constituents, leading to an increase in the EC of the mixtures.

Figure 4.11 presents the variations of the concentrations of some major elements including arsenic, calcium, sulfur and antimony in both arsenic trioxide and tailings mixtures versus time.

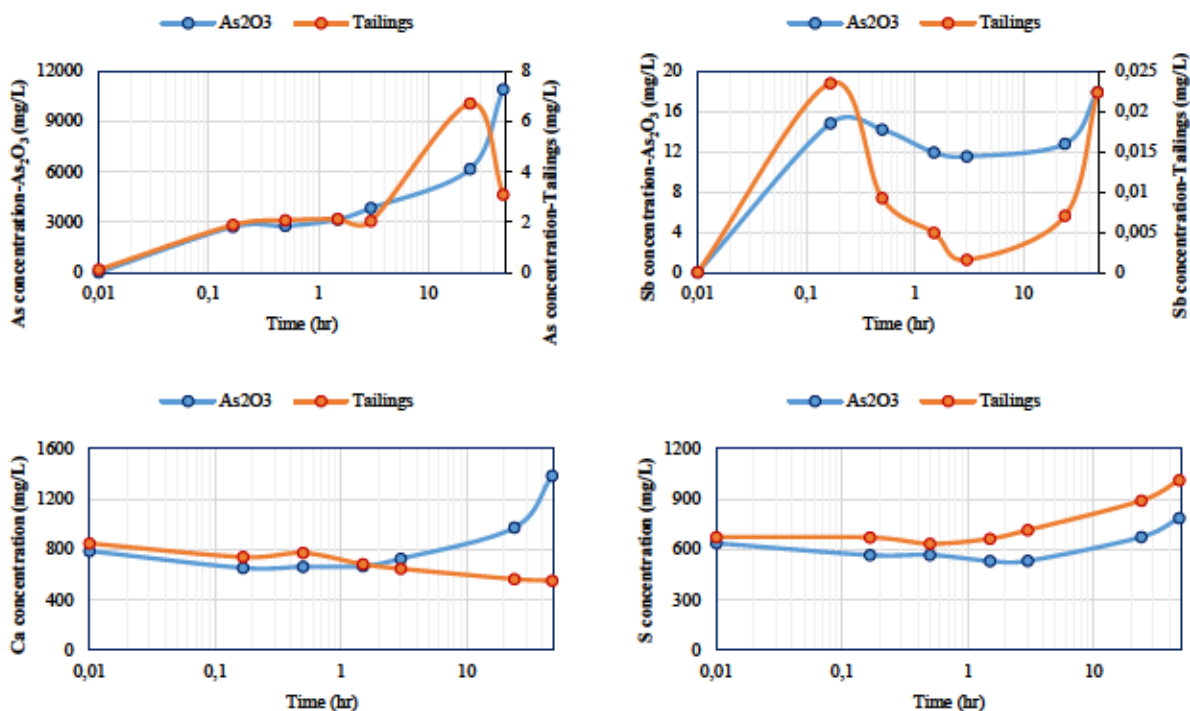


Figure 4.11 Variations of the concentrations of major elements (As, Ca, S, and Sb) in As_2O_3 and tailings mixtures

As shown, a substantial amount of arsenic was dissolved in the cement-buffering solution, with its concentration reaching approximately 10,900 mg/L after 48 hours. As mentioned in Chapter 2, arsenic trioxide is highly soluble in water (theoretical solubility in the range of 10 – 16 g/L). The concentration of arsenic in the solution in contact with the tailings mixture was much lower, as the initial content of arsenic in the tailings was approximately 2700 mg/kg and it may be in another form with lower solubility. In this case, the solubility of arsenic increased for up to 24 hours and then decreased.

The initial concentrations of calcium in the cement-buffering solutions were 787 mg/L for As_2O_3 and 848 mg/L for tailings solutions. Initially, the calcium concentration in the As_2O_3 mixture decreased due to reactions between arsenic and calcium, forming potentially new As-Ca solid products. However, a decline in pH led to the redissolution of calcium and an increase in its content. In the case of the tailings mixture, calcium concentration exhibited a decreasing trend, possibly due to a slight reduction in pH and continuous reactions between tailings species and dissolved calcium. The final amount of dissolved calcium was higher in the arsenic trioxide mixture.

Sulfur showed a similar trend to calcium in the As_2O_3 mixture, initially decreasing followed by an increase after 1.5 hours. In this mixture, sulfur increased due to pH decrease and the dissolution of sulfur-containing cement constituents like calcium sulfate. In contrast, in the tailings mixture, apart from an initial drop in sulfur content, an increasing trend was observed mainly due to the possible dissolution of sulfur from the tailings and a slight drop in mixture pH. The final dissolved sulfur was higher in the tailings mixture due to the initial sulfur content of the tailings.

The dissolution of As_2O_3 in the cement-buffering mixture initially increased the concentration of antimony to approximately 15 mg/L. Subsequently, the antimony content in this solution decreased over three days before increasing again. A similar trend was observed in the tailings mixture; however, the concentration of dissolved antimony was much lower in this mixture. This could be attributed to the fact that the primary source of antimony in these mixtures was from arsenic trioxide, which contains less than 0.5% impurities, including antimony.

4.2.3.1 Microstructure of CPB made with pure As_2O_3

SEM analyses were performed on the dried 28-day cured samples after the UCS tests and the dried As_2O_3 -cement mixtures to better understand the relationships between the strength acquisition process and the microstructure of the cementitious matrices with various arsenic trioxide contents. These investigations were done on the As_2O_3 -containing samples. Automated mineralogical analysis was difficult to achieve due to the complexity of the phases, therefore several phases and species were identified but could not be quantified. Some phases could be specified by their generic names, especially the oxides, such as oxide-As-Al-Ca, oxide-As-Ca-Si, etc. However, for some grains, the chemical analyses could not point to any known mineral species and stoichiometric calculations were inconclusive. These particles were generally mixtures of fine minerals with variable chemical compositions, possibly products of weathering or thermodynamic re-equilibrium or the signal read by the sensor included several very fine grains.

The CPB samples were confirmed to be composed mainly of silicates, with quartz being the main mineral, along with some crystalline arsenic trioxide as the dominant As-bearing phase. Other As-bearing phases were also observed in lesser quantities. Most of the grains were easily observable due to their crystalline system and some grains were perfectly crystallized in bipyramidal (octahedron) shape. Some rounded, uncrystallized grains composed of As-Si-Ca were also found. They seem to be gels formed as precipitates or secondary products. These grains were found in all

CPB samples with varying content of arsenic in the structure of the grains. Semi-quantitative analyses were done on the samples as shown in Figures 4.12 and 4.13. Various silicate and arsenious oxides grains were microanalyzed and revealed that they are mostly composed of As-Si-Ca oxides. In Figure 4.12, spectrums 136 and 138 refer to As-Si-Ca oxides, and spectrum 137 is related to As-Ca-Si oxides. The order of the elements corresponds to their descending occurrence. Traces of antimony were also found in these grains coming from the impurity of reagent grade arsenic trioxide. Spectrums 139 and 140 are related to Si oxides and Ca-Si oxides respectively, with traces of arsenic in their structures. The content of other elements (Mg, Al, S, Cl, and Fe) in the structure of these grains was negligible and mostly less than 1%.

For As_2O_3 -cement samples (Figure 4.13), the microstructure was significantly different due to the absence of quartz. In these samples, the As-Ca-Si-Al oxides were more prominent (no dilution by the quartz), but there were still many intact undissolved As_2O_3 grains. The grains were multiphase, very fine and thin, complex as per their stoichiometry, and randomly shaped. The observed minerals are mainly composed of arsenic oxides with calcium (Ca-arsenite/arsenates). Spot analysis showed various phases, mainly arsenic trioxide, As-Ca oxides and gel phases. Spectrums 35-37, 41, and 44 are arsenic trioxide grains. Spectrums 38 and 43 are As-Ca oxides, and the other spectrums are complex grains enriched in As, Ca, Al, and Si with traces of other elements.

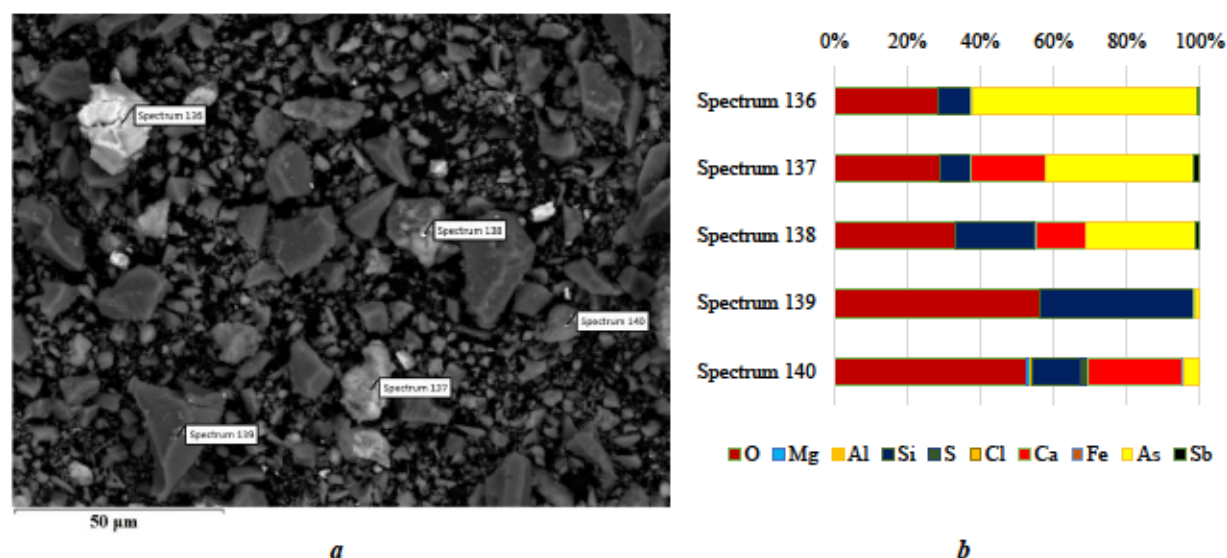


Figure 4.12 BSE image (a) and semi-quantitative EDS analyses (b) of the various silicate and arsenioferous oxides observed in CPB-5% sample (Mohammadi, Demers, Benzaazoua, et al., 2023a)

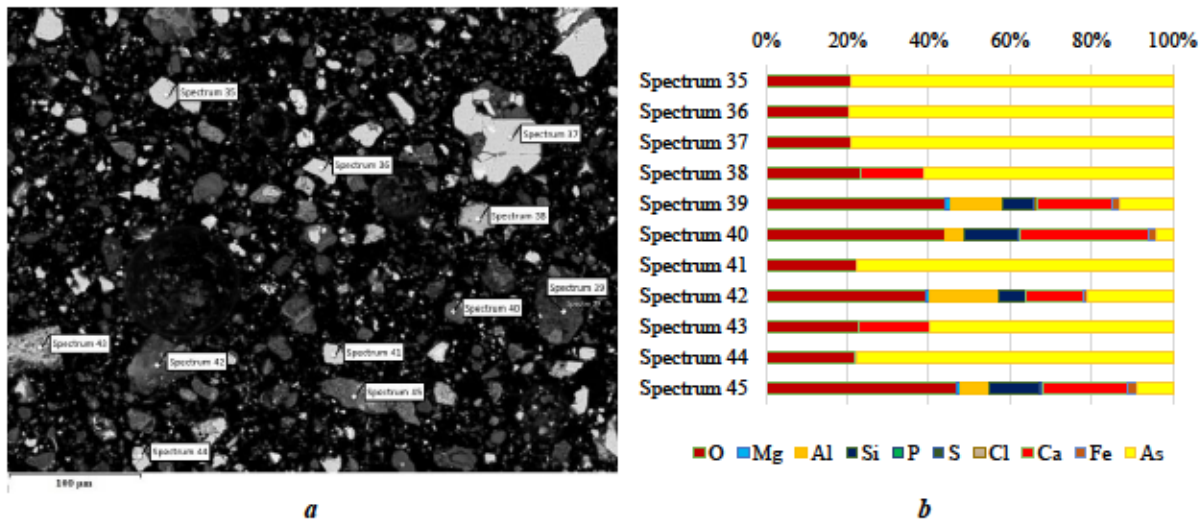


Figure 4.13 BSE image (a) and semi-quantitative EDS analyses (b) of the various silicate and arsenioferous oxides observed in 15% As_2O_3 -cement mixture polished section

4.3 Studies using Giant mine ATRW and tailings

4.3.1 Determination of optimal ATRW content in CPB

Figure 4.14 presents the results of UCS tests for the first batch of main CPB samples (screening batch), prepared using four binding agents to determine the optimal ATRW content for the main samples and the preferred binding agents after 7 and 28 days of curing. Generally, the samples prepared using the GU cement showed the highest strength followed by the GU/LI, GU/LKD, and GU/FA samples. Increasing the curing time did not significantly increase the strength of the samples, except for the samples prepared using GU/LKD binder. Most of the samples gained their strength in the initial days of curing. The strength behavior of the samples was different after 7 and 28 days. After 7 days, the strength of GU samples increased up to 10% of As_2O_3 dust and then decreased; however, after 28 days, a decreasing trend was observed by increasing the As_2O_3 dust content. For the other binding agent, a complex trend was observed. Based on these results, it was decided to prepare the main CPB samples using GU cement and the mixture of GU/LKD, since the improvement in the strength of the GU/LKD samples with time was noticeable. Moreover, 10% was chosen as the fixed ATRW content.

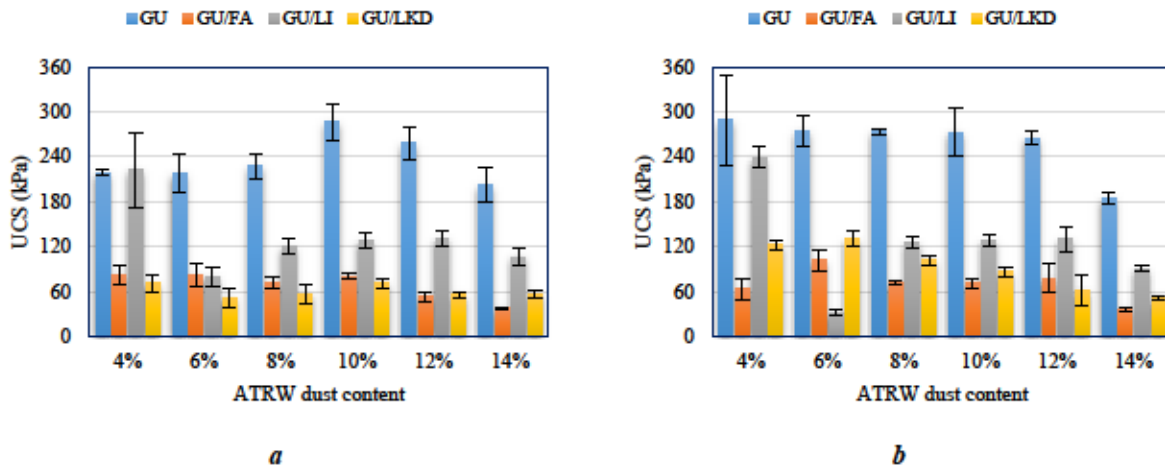


Figure 4.14 The UCS of small CPB samples prepared using various binders after a) 7 days and b) 28 days of curing

4.3.2 Strength development in CPB samples prepared with Giant Mine ATRW and tailings (Article 2)

The second article, titled "Geomechanical aspects of stabilizing arsenic trioxide roaster waste in cemented paste backfill at the Giant Mine, Canada" was published in the Journal of Environmental Management. The complete text of the article is available in Appendix C.

Table 4.8 presents the results of UCS tests conducted on CPB samples prepared with GU cement and GU/LKD binders according to the proposed mix designs (Chapter 3, section 3.2.4), along with the predicted values. The main samples were labeled as '*X-A-B-C*', where '*X*' denotes the type of binder (GU or GU/LKD), '*A*' indicates the binder content in percentage, '*B*' represents the solid content in percentage, and '*C*' denotes the curing time in days. For example, 'GU-4-76-28' represents a sample prepared with 4% GU binder, at a 76% solid content by weight, cured for 28 days before undergoing the UCS test. Examining the UCS results, it is clear that the strength of CPB samples containing ATRW dust prepared with a GU binder was significantly higher than those prepared with the GU/LKD mixture. For both binder types, the maximum strength was observed in samples with 6% binder content and 76% solids content, reaching approximately 491 kPa and 531 kPa for GU, and 214 kPa and 213 kPa for GU/LKD after 28 and 90 days, respectively. Conversely, the lowest strengths were recorded in samples with the lowest binder and solid content.

Table 4.8 Results of the UCS tests on the CPB samples prepared with GU cement and mixture of GU/LKD

Run	Actual factors			Responses (Y) – UCS (kPa)			
				GU		GU/LKD	
	A (%)	B (%)	C (day)	Experimental data	Predicted values	Experimental data	Predicted values
1	3.32	74	59	155	170	27	29
2	4	72	28	154	141	42	37
3	4	72	90	154	140	42	38
4	4	76	28	276	258	92	93
5	4	76	90	249	254	90	90
6	5	70.64	59	154	175	24	33
7	5	74	7	174	199	108	112
8	5	74	59	268	275	76	75
9	5	74	59	282	275	87	75
10	5	74	59	264	275	67	75
11	5	74	59	268	275	48	75
12	5	74	59	276	275	81	75
13	5	74	59	296	275	90	75
14	5	74	111	232	231	109	113
15	5	77.36	59	478	481	178	176
16	6	72	28	260	238	100	95
17	6	72	90	278	279	105	99
18	6	76	28	491	488	214	212
19	6	76	90	531	527	213	212
20	6.68	74	59	472	481	175	181

Various response functions were generated and correlated with the experimental data to derive a regression equation. The quality of the regressions was assessed using sequential sum of squares and lack-of-fit tests. The fit summary and model summary statistics in Tables 4.9 and 4.10 indicate that the quadratic model should be selected for further analysis for both UCS_{GU} and $UCS_{GU/LKD}$ responses under investigation. This selection is justified by the quadratic model's superior fit to the experimental data, demonstrated by its lower standard deviations, higher correlation coefficients, and lower p-values. Additionally, the quadratic model avoids the aliasing issues found in the cubic model, where higher-order terms become confounded with lower-order ones (Watson et al., 2016). Therefore, the experimental results were fitted to a quadratic second-order model equation using multiple regression analysis to establish a relationship between the UCS of the samples and the selected influencing factors. For each response, an analysis was conducted, and the coefficients of the quadratic models for the samples prepared with GU and GU/LKD binders are presented in Table 4.11, both in coded and actual values. The regression coefficients were determined as a function of the sum of a constant (β_0), three linear effects (β_i), three interaction effects (β_{ij}), and

three quadratic effects (β_{ii}). Coded equations were used to evaluate the relative impact of each factor by comparing the factor coefficients. The equation in terms of actual factors was used to make predictions about the response for specific levels of each factor, which must be specified in the original units. However, this equation should not be used to assess the relative impact of each factor. This is because the coefficients are scaled to account for the units of each factor, and the intercept does not correspond to the center of the design space.

Table 4.9 Fit summary results of the UCS (response) for the GU and GU/LKD samples

Source	Sequential p-value	Lack of Fit p-value	Adjusted R ²	Predicted R ²	
UCS _{GU}					
Linear	<0.0001	0.0021	0.8595	0.7864	
2FI	0.1599	0.0028	0.8822	0.8078	
Quadratic	0.0003	0.0855	0.9755	0.9172	Suggested
Cubic	0.5726	0.0223	0.9732	-0.2751	Aliased
UCS _{GU/LKD}					
Linear	<0.0001	0.1382	0.8367	0.7997	
2FI	0.3218	0.1392	0.8449	0.6995	
Quadratic	0.0015	0.9296	0.9539	0.9366	Suggested
Cubic	0.9587	0.4592	0.9300	0.4158	Aliased

Table 4.10 Model summary statistics for the UCS (response) of GU and GU/LKD samples

Source	Std. Dev.	R ²	Adjusted R ²	Predicted R ²	PRESS	
UCS _{GU}						
Linear	44.03	0.8817	0.8595	0.7864	56001.70	
2FI	40.32	0.9194	0.8822	0.8078	50380.49	
Quadratic	18.39	0.9871	0.9755	0.9172	21696.08	Suggested
Cubic	19.22	0.9915	0.9732	-0.2751	3.343E+05	Aliased
UCS _{GU/LKD}						
Linear	22.78	0.8625	0.8367	0.7997	12092.50	
2FI	22.20	0.8939	0.8449	0.6995	18146.86	
Quadratic	12.10	0.9758	0.9539	0.9366	3830.98	Suggested
Cubic	14.91	0.9779	0.9300	0.4158	35271.97	Aliased

Table 4.11 Coefficients for the quadratic model of UCS for GU and GU/LKD samples

Coefficient	Expression	Coded		Actual	
		GU	GU/LKD	GU	GU/LKD
β_0	Constant term	+274.86	+74.73	+28953.97	+15937.12
β_1	Binder content (A)	+92.41	+44.94	-1346.12	-631.69
β_2	Solid content (B)	+91.17	+42.39	-737.70	-409.75
β_3	Curing time (C)	+9.45	+0.20	+1.84	-0.66
β_{11}	Binder content ² (A^2)	+18.04	+10.74	+18.04	+10.74
β_{22}	Solid content ² (B^2)	+18.92	+10.63	+4.73	+2.66
β_{33}	Curing time ² (C^2)	-21.31	+13.50	-0.022	+0.014
β_{12}	Binder content \times Solid content ($A \times B$)	+33.45	+15.35	+16.73	+7.68
β_{13}	Binder content \times Curing time ($A \times C$)	+10.78	+0.68	+0.35	+0.022
β_{23}	Solid content \times Curing time ($B \times C$)	-0.55	-0.93	-0.009	-0.015

Typically, model adequacy checks are conducted to ensure that the fitted model accurately represents the true system and that none of the assumptions of least squares regression are violated. The adequacy of the proposed models, the interactions among independent variables, and the significance of each model term were assessed using analysis of variance (ANOVA). ANOVA was used to evaluate the model's suitability by examining linear, quadratic, and interaction effects, and by calculating the F-value and p-value.

Table 4.12 presents the ANOVA results for both GU and GU/LKD samples. The F-value indicates the model's significance, while the p-value reflects the degree of interaction among each independent variable. Terms are considered significant if their p-values are less than 0.05 (indicating a 95% confidence level) and non-significant if the values exceed 0.1000 (Rahimi & Ebrahimi, 2019; Sahu et al., 2018). The model's F-value, which is 85.04 for GU and 44.73 for GU/LKD, along with p-values less than 0.0001 for both responses, indicates the models' significance. This implies that there is only a 0.01% chance that the "Model F-Value" in Table 4.12 is due to noise. The "lack of fit" concept contrasts with the overall model test, which assesses whether any omitted term is significant. The "Lack of Fit F-value," which is 3.78 for GU and 23.76 for GU/LKD, suggests that the lack of fit is not significant when compared to the pure error. A non-significant lack of fit indicates that the model fits the experimental data well. Furthermore, the results showed a standard deviation of 18.39 for GU (with a mean of 285.56) and 12.10 for

GU/LKD (with a mean of 98.51), which are considered acceptable. The Adeq-Precision value measures the model's predicted value combined with the average prediction error, serving as a measure of the signal-to-noise ratio. A model is considered appropriate and effective for exploring the design space when this ratio exceeds 4. In this study, the Adeq-Precision values for GU and GU/LKD were 29 and 21, respectively. This indicates a sufficient signal level, suggesting that the models are suitable for navigating the design space, conducting analyses, and making predictions regarding the UCS of CPB samples.

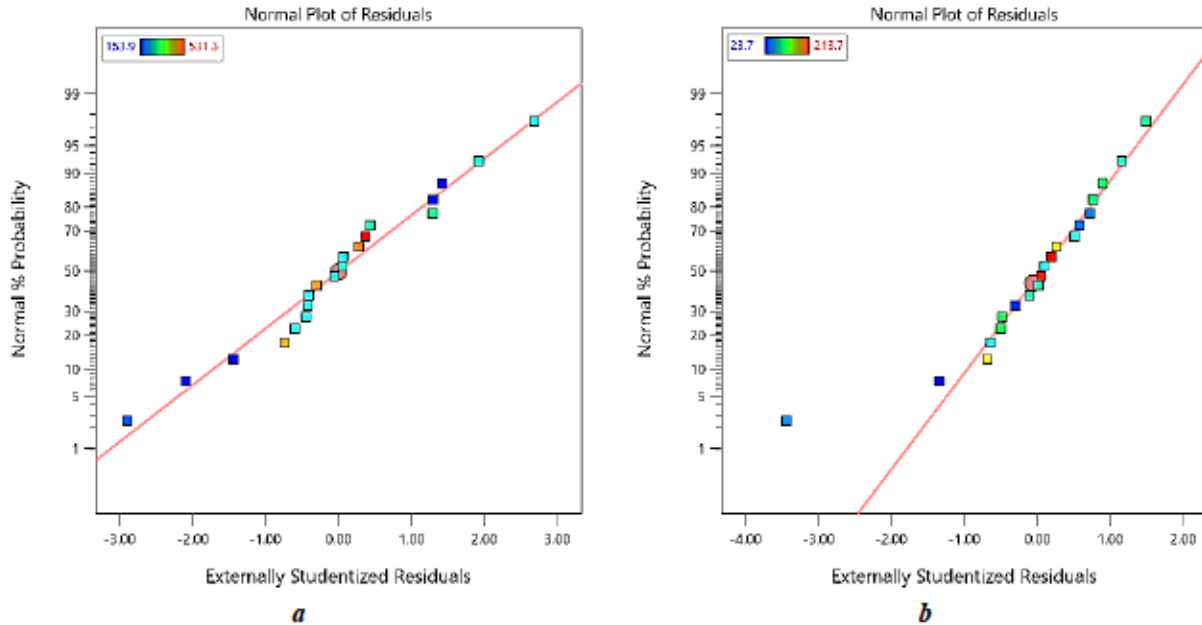
Table 4.12 ANOVA results for ATRW dust containing CPB samples prepared using GU and GU/LKD

Source	Sum of Squares		df		Mean Square		F-value		p-value	
	GU	GU/LKD	GU	GU/LKD	GU	GU/LKD	GU	GU/LKD	GU	GU/LKD
Model	2.59E+05	58917.16	9	9	28755.91	6546.35	85.04	44.73	<0.0001	<0.0001
<i>A</i>	1.17E+05	27558.05	1	1	1.17E+05	27558.05	344.62	188.28	<0.0001	<0.0001
<i>B</i>	1.13E+05	24520.28	1	1	1.13E+05	24520.28	335.44	167.53	<0.0001	<0.0001
<i>C</i>	1216.5	0.55	1	1	1216.50	0.55	3.60	0.004	0.0871	0.9523
<i>A</i> × <i>B</i>	8951.22	1884.98	1	1	8951.22	1884.98	26.47	12.88	0.0004	0.0049
<i>A</i> × <i>C</i>	928.81	3.65	1	1	928.81	3.65	2.75	0.02	0.1284	0.8777
<i>B</i> × <i>C</i>	2.42	6.85	1	1	2.42	6.85	0.007	0.05	0.9343	0.8331
<i>A</i> ²	4674.72	1657.23	1	1	4674.72	1657.23	13.82	11.32	0.0040	0.0072
<i>B</i> ²	5145.1	1624.59	1	1	5145.10	1624.59	15.22	11.10	0.0030	0.0076
<i>C</i> ²	6490.07	2603.96	1	1	6490.07	2603.96	19.19	17.79	0.0014	0.0018
Residual	3381.41	1463.68	10	10	338.14	146.37				
Lack of Fit	2673.63	280.98	5	5	534.73	56.20	3.78	0.2376	0.0855	0.9296
Pure Error	707.78	1182.69	5	5	141.56	236.54				
Cor Total	2.62E+05	60380.84	19	19						

The model's accuracy and variability were also evaluated using the coefficient of determination (R^2). The high R^2 values, close to one (GU: 0.987, GU/LKD: 0.976), along with the adjusted R^2 (GU: 0.976, GU/LKD: 0.954) and predicted R^2 (GU: 0.917, GU/LKD: 0.937) values, indicate a high level of accuracy and an excellent fit, demonstrating a strong alignment of the proposed models with the collected experimental data. This suggests that the quadratic model explains 98.7%

and 97.6% of the total variance, leaving only 1.29% and 2.42% of the variance in GU and GU/LKD samples unexplained. The close match between the predicted R^2 and adjusted R^2 values, with differences of less than 0.2, indicates reasonable agreement.

Figures 4.15a and 4.15b display diagnostic plots, showing the normal probability versus studentized residuals for GU and GU/LKD samples, respectively. Most of the responses exhibit minimal deviation from normality, with the points closely aligning along a nearly straight diagonal line. Figures 4.15c and 4.15d illustrate the externally studentized residuals plotted against the predicted response values, testing the assumption of constant variance. Control limits are provided in the form of two lines (-4.14579 and $+4.14579$) for easier identification of any unusual points, but the points fall well within these limits, with no abnormal points observed. This indicates that the data exhibit a random distribution around the zero line, without any evident clustering. The residuals demonstrate independence from each other, and there is no discernible trend indicating an increase or decrease in variance. Consequently, the assumption of constant variance is accepted, further validating the homoscedasticity and accuracy of the models in predicting the UCS of CPB samples (Rahimi & Ebrahimi, 2019).



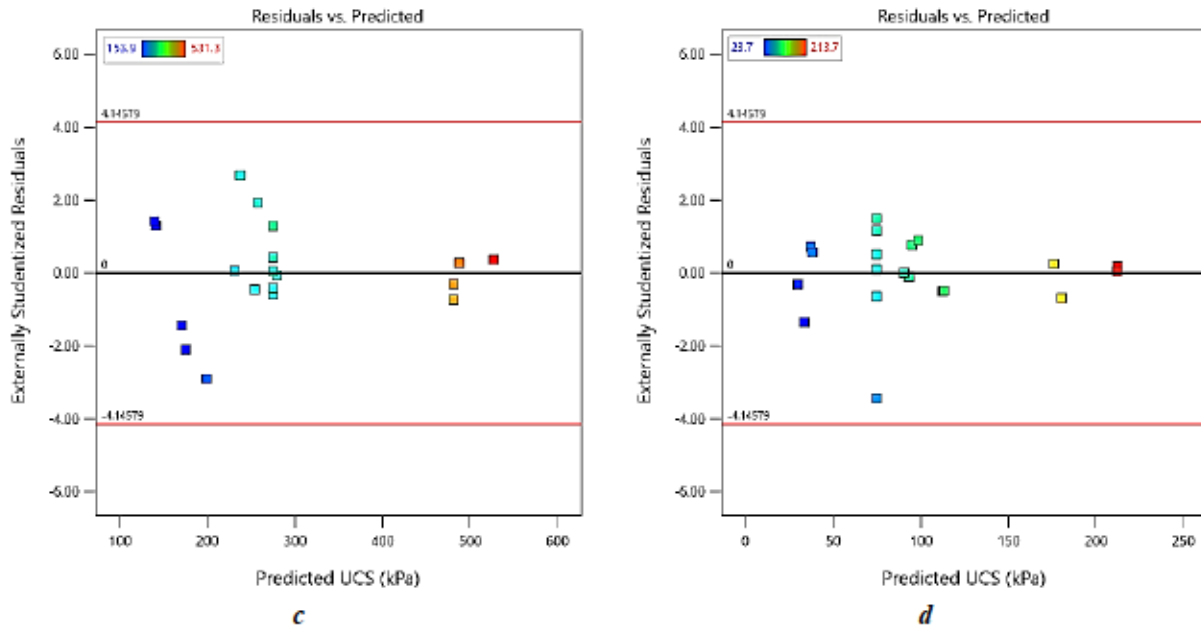


Figure 4.15 Normal plot of residuals for c) GU and d) GU/LKD samples; and predicted vs. externally studentized residuals of e) GU and f) GU/LKD samples in CCD experiments

4.3.2.1 Factors affecting CPB strength

For both GU and GU/LKD samples, the statistical analysis revealed that binder content and solid content (represented as linear terms A and B , respectively), along with the interaction between binder content and solid content ($A \times B$), were significant interaction terms. Additionally, the quadratic terms for binder content (A^2), solid content (B^2), and curing time (C^2) were found to be significant, with p -values below 0.05. In contrast, curing time (C) and the interaction terms involving binder content and solid content with curing time ($B \times C$ and $A \times C$) were not statistically significant. The coded coefficients in Table 4.11 highlight that binder content and solid content had the most significant positive effects on the strength of the CPB samples, with binder content showing a notably stronger impact as reflected by its higher F -value. Surprisingly, curing time did not significantly affect the strength of CPB samples containing ATRW. Among the quadratic terms, the square term of curing time (C^2) had the highest F -value, indicating its substantial influence on CPB sample strength. This effect was negative for GU samples, as indicated by the negative coded coefficient ($\beta_{33} = -21.31$), and positive for GU/LKD samples, as indicated by the positive coded coefficient ($\beta_{33} = +13.50$).

Three-dimensional (3D) surface and two-dimensional (2D) contour graphs were obtained to illustrate the combined impacts of independent variables on the strength of CPB samples and to predict the responses (UCS) for various regions within the experimental domain. These graphical representations are displayed in Figures 4.16 to 4.18 for both GU and GU/LKD samples. In each plot, one factor was held constant, while the influences of the remaining two factors were examined using both two-dimensional and three-dimensional plots. The primary parameters were varied across their entire range, spanning from the lowest level to the highest level, to assess how this variation impacted the strength of CPB samples containing ATRW. Figure 4.16 illustrates the concurrent impacts of binder content and solid content at different curing times on the strength of CPB samples, considering both GU and GU/LKD binders. In Figure 4.17, the simultaneous effects of solid content and curing time on the UCS of both GU and GU/LKD samples are examined, while varying binder content. Figure 4.18 portrays variations in UCS strength at varying solid contents, achieved by simultaneously adjusting binder content and curing time.

4.3.2.1.1 Effect of binder content

Increasing the binder content significantly improved the sample strength. For instance, the UCS of GU-6-76-28 and GU-6-76-90 was 1.78 and 2.13 times higher than that of GU-4-76-28 and GU-4-76-90, respectively. For GU/LKD samples, the ratios (GU/LKD-6-76 to GU/LKD-4-76) were even more pronounced, reaching 2.32 and 2.35 for samples cured for 28 and 90 days, respectively. This indicates that increasing the binder content had a substantial positive impact on the mechanical strength of CPB. This enhancement can be attributed to a higher rate of hydration and an increase in hydration products within the CPB, leading to greater compressive strength. The results demonstrated that the amount of GU-based binder positively influenced strength gain, regardless of the hydration period.

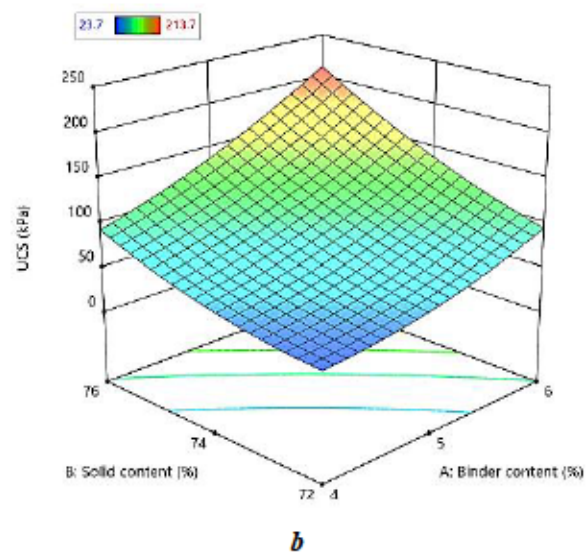
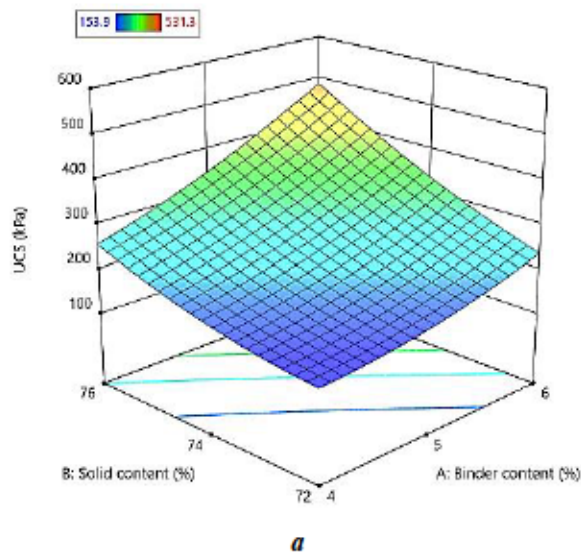
4.3.2.1.2 Effect of solid content

The results depicted in Figures 4.16 to 4.18 also indicate that higher solid content leads to increased strength in CPB for both GU and GU/LKD samples. For instance, in the case of GU samples prepared with 5% binder and cured for 59 days, the strength varied with different solid contents: approximately 154 kPa, 270 kPa (averaging over 6 samples), and 478 kPa for solid contents of 70.64%, 74%, and 77.36%, respectively. For GU/LKD samples, these strength values were 24 kPa, 70 kPa, and 178 kPa, respectively. This clearly demonstrates the positive influence of solid content

on the UCS of CPB samples. Typical solid contents in CPB, from 70 to 85 wt.%, have a notable impact on both the flow characteristics of the paste mixtures and the volume of tailings to be deposited underground. Elevating the solid content generally enhances CPB strength, but it concurrently diminishes the consistency or slump of the mixture. This phenomenon was observed in the current study as well, where the workability of ATRW containing paste became unsatisfactory for solid contents exceeding 76%, making it challenging to place the pastes into molds.

4.3.2.1.3 Effect of curing time

As depicted in Figures 4.16 to 4.18, variations in curing time (ranging from 28 days to 90 days) did not exert a significant influence on the strength of the CPB samples. Curing time was identified as a non-significant factor in the experimental design. According to existing literature, under normal conditions, the mechanical strength of CPB samples typically shows a noticeable increase with longer curing times. Initially, there is rapid strength gain during the first month of curing, followed by a phase where mechanical properties improve marginally (Benzaazoua et al., 2010).



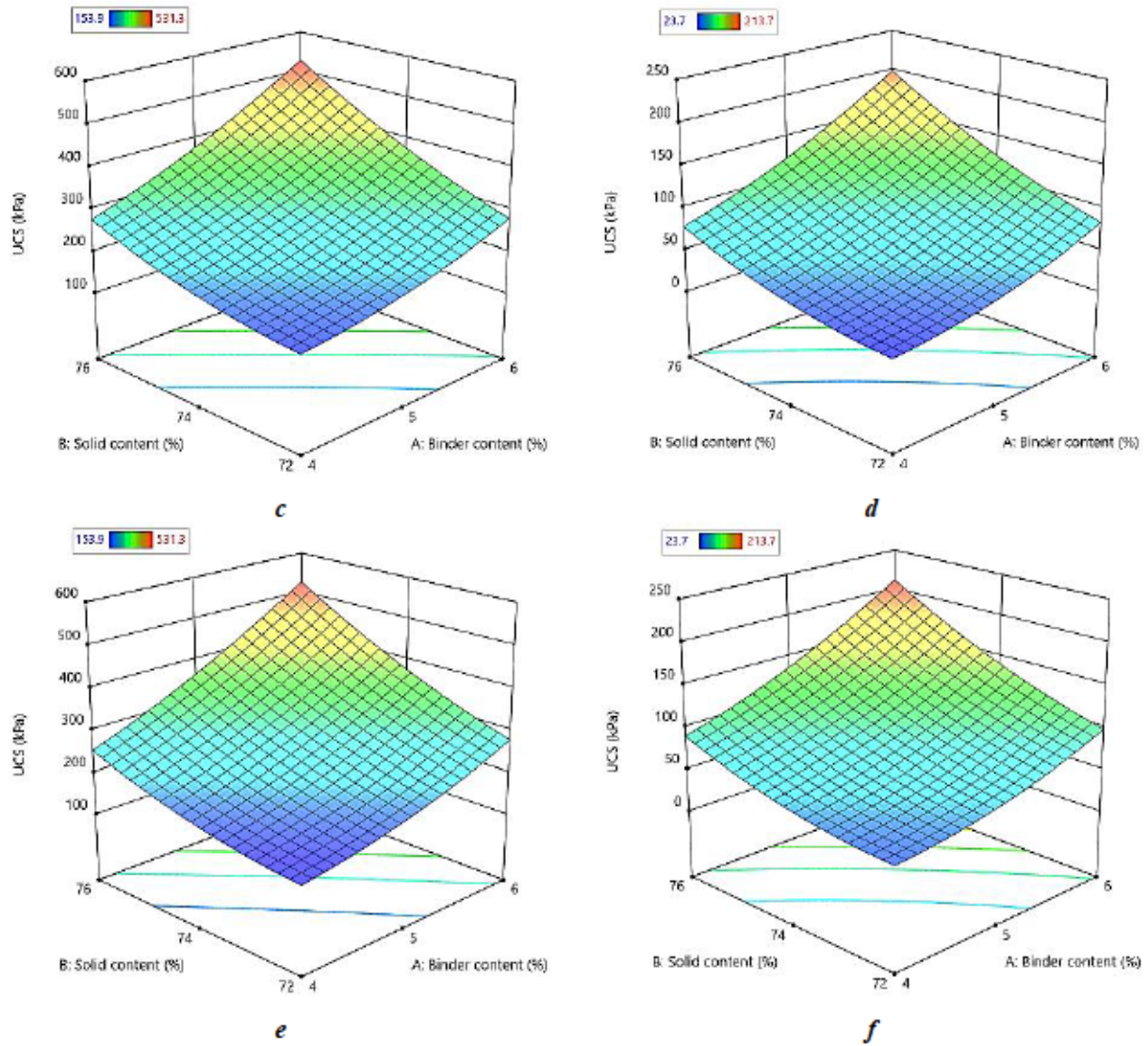


Figure 4.16 Surface plots for the UCS of GU and GU/LKD samples at different curing times: a) GU-28 days, b) GU/LKD-28 days, c) GU-59 days, d) GU/LKD-59 days, e) GU-90 days, and f) GU/LKD-90 days

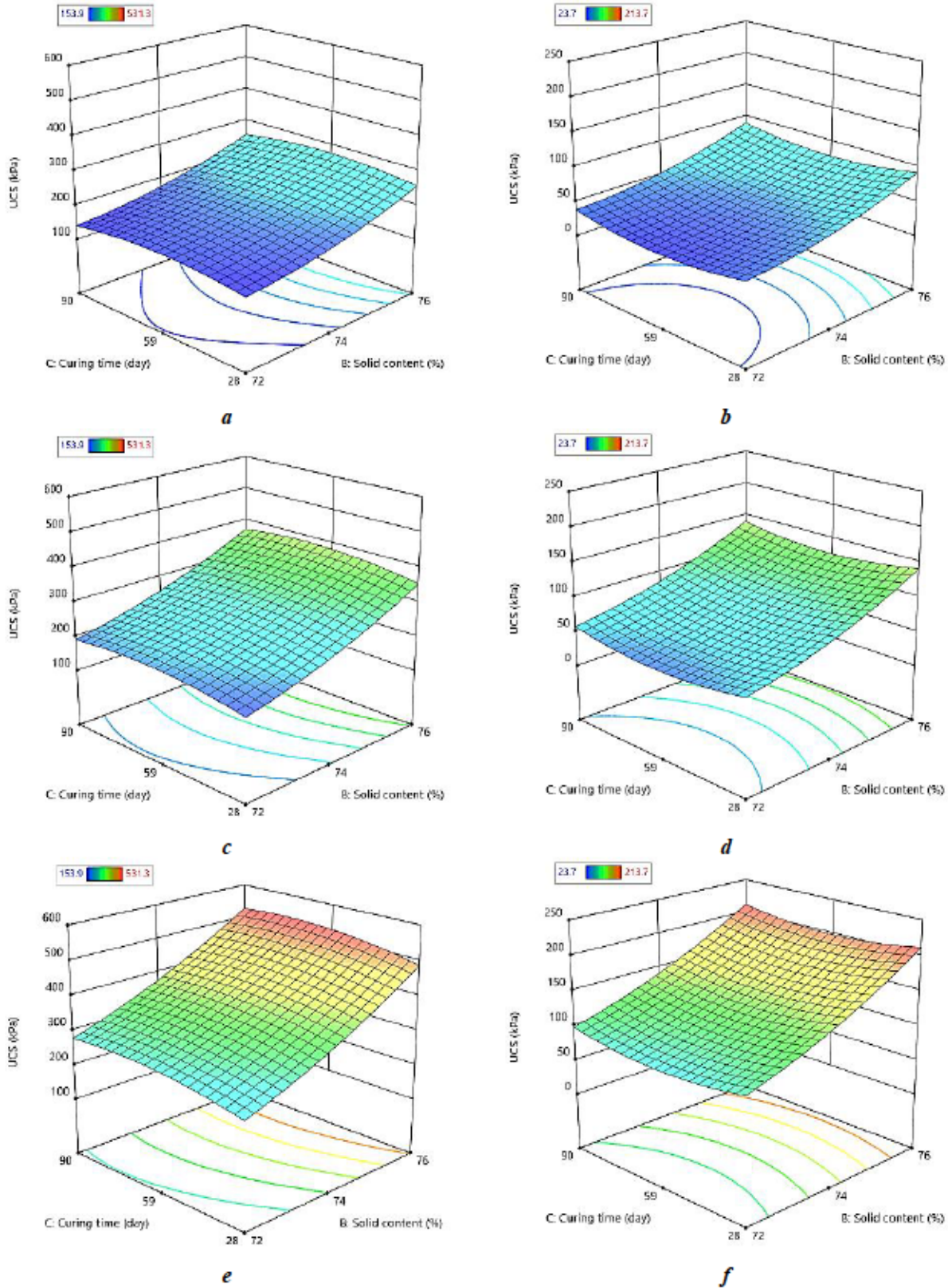


Figure 4.17 Surface plots for the UCS of GU and GU/LKD samples at different binder content: a) GU-4%, b) GU/LKD-4%, c) GU-5%, d) GU/LKD-5%, e) GU-6%, and f) GU/LKD-6%

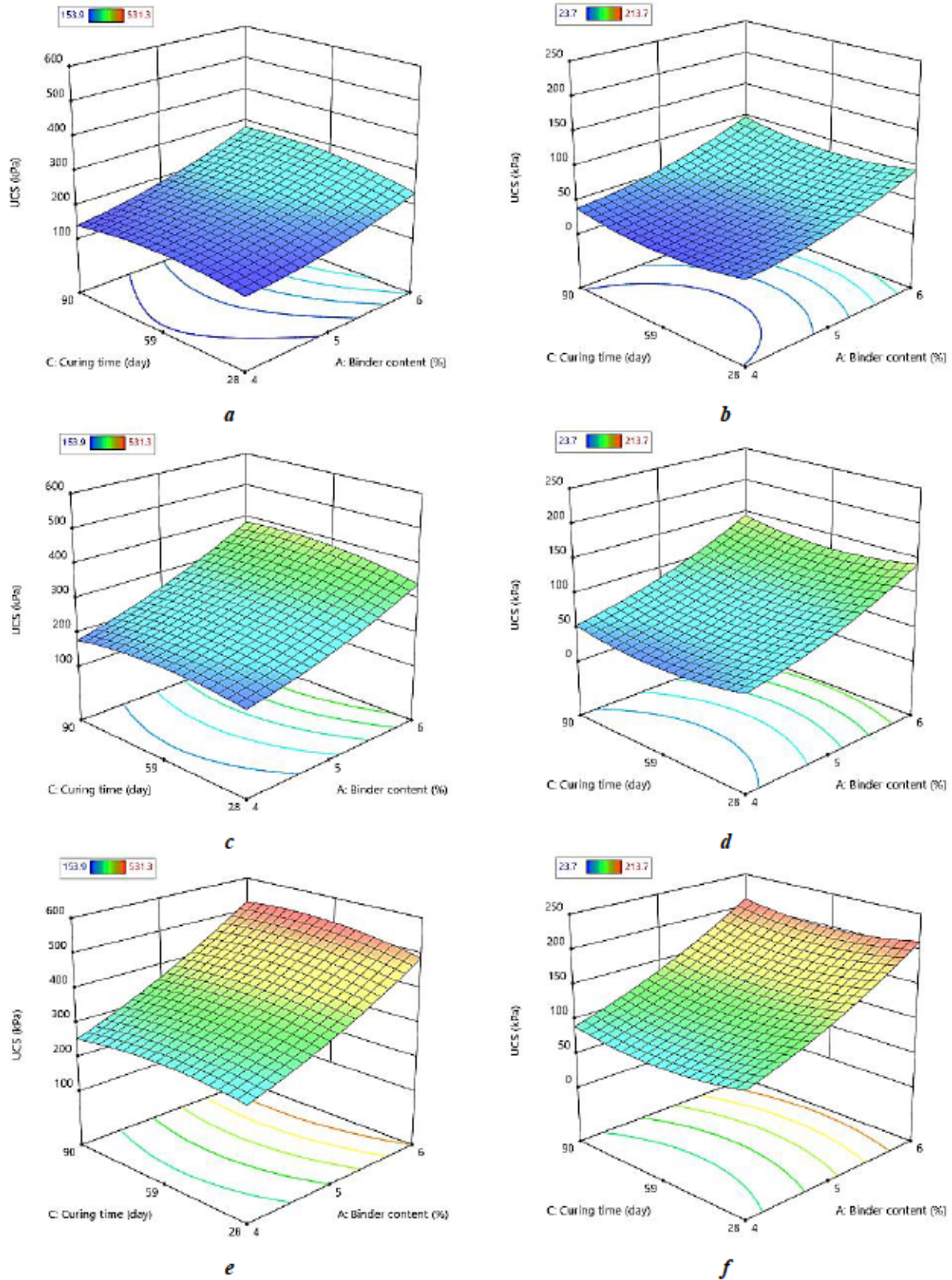


Figure 4.18 Surface plots for the UCS of U and GU/LKD samples at different solid contents: a) GU-72%, b) GU/LKD-72%, c) GU-74%, d) GU/LKD-74%, e) GU-76%, and f) GU/LKD-76%

4.3.2.1.4 Effect of ATRW inclusion in CPB

Several CPB samples consisting of three replicates without ATRW were prepared, varying the binder and solid content, to provide an arsenic-free comparison baseline. Table 4.13 presents the chosen mix designs and the UCS values for these ATRW-free samples. Additionally, this table includes the ratios of UCS for samples with ATRW (UCS_d) to those without ATRW dust (UCS_0).

Table 4.13 The UCS of CPB samples without ATRW prepared using GU and GU/LKD binders

Sample	UCS_0 (kPa)	UCS_d/UCS_0	Sample	UCS_0 (kPa)	UCS_d/UCS_0
GU-4-72-28	274	0.564	GU/LKD-4-72-28	75	0.562
GU-4-76-28	411	0.670	GU/LKD-4-76-28	163	0.567
GU-5-74-59	431	0.640	GU/LKD-5-74-59	153	0.489
GU-6-72-28	371	0.700	GU/LKD-6-72-28	167	0.600
GU-6-76-28	678	0.724	GU/LKD-6-76-28	301	0.710

The incorporation of ATRW resulted in a decrease in strength for both GU and GU/LKD binders. This decrease was more significant in samples with lower binder and solid contents. Increasing the binder and solid contents led to an increase in the UCS_d/UCS_0 ratio. As discussed in sections 4.2.2.1 and 2.8.2, maintaining a stable alkaline environment within CPB is crucial for the formation of hydration products like C-S-H, which drive strength development. Increasing binder and solid content can help counteract strength reduction by enhancing C-S-H formation and raising pH.

4.3.2.2 Model improvement

To improve the models predicting the UCS of GU and GU/LKD samples, only significant terms were incorporated while non-significant ones were excluded. Terms with p-values greater than 0.05 were omitted from the regression equations. As a result, curing time (term C) and its interactions with other factors (terms $A \times C$ and $B \times C$), as well as its square term (C^2), were excluded. The final models describing the relationship between the UCS of CPB samples and binder content (A) and solid content (B) are presented in Table 4.14. Despite the significant nature of the square term of curing time (C^2), it was necessary to remove it from the models to maintain the hierarchy of the adjusted models.

After removing non-significant terms, the values of R^2 , adjusted R^2 , and predicted R^2 were calculated as 0.9542, 0.9378, and 0.9322, respectively, for the revised GU model. Meanwhile, for

the adjusted GU/LKD model, these metrics were 0.9325, 0.9083, and 0.8603, respectively, encompassing R^2 , adjusted R^2 , and predicted R^2 . This indicates a slight decrease in R^2 and adjusted R^2 values for both models, with a notable reduction in predicted R^2 for the adjusted GU/LKD model. However, it's noteworthy that predicted R^2 , a critical measure, increased for the revised GU model. Despite these fluctuations in R^2 values, the revised models remained highly statistically significant for both GU and GU/LKD samples.

Table 4.14 Coefficients for the modified quadratic model of UCS for GU and GU/LKD samples

Coefficient	Expression	Coded		Actual	
		GU	GU/LKD	GU	GU/LKD
β_0	Constant term	+257.51	+85.72	+31861.89	+14125.25
β_1	Binder content (A)	+92.41	+44.94	-1346.38	-617.26
β_2	Solid content (B)	+91.17	+42.39	-815.03	-361.97
β_{11}	Binder content ² (A^2)	+20.11	+9.43	+20.11	+9.43
β_{22}	Solid content ² (B^2)	+21.00	+9.32	+5.25	+2.33
β_{12}	Binder content \times Solid content ($A \times B$)	+33.45	+15.35	+16.73	+7.68

4.3.2.3 Optimization and confirmation

After analyzing the independent variables, a multi-objective simultaneous nonlinear optimization approach was employed to enhance the UCS of CPB samples for each binder. The optimization aimed to identify the most favorable combination of independent variables that yield the highest UCS values. It is important to note that varying levels of weight and significance can be assigned to the optimization objectives. However, in this study, all target factors and responses were equally weighted and considered significant. Using a numerical optimization algorithm within the DX13 software, the optimal UCS values were predicted based on the regression models. All factors were constrained within the initial study range, while maximizing UCS to achieve the highest desirability. From the solutions provided by the DX13 software, the first solution with the highest desirability was selected for each binder. An experiment with a desirability value close to unity is considered optimal based on the obtained results. The maximum strength for GU samples (531 kPa) was attained with a binder content of 6%, a solid content of 76%, and a curing time of approximately 64 days, resulting in a desirability value of 1.000. For GU/LKD binder, the optimal conditions yielding the highest UCS (212 kPa) included a binder content of 6%, a solid content of

76%, and a 28-day curing time, resulting in a desirability value of 0.993. Detailed results are presented in Figure 4.19.

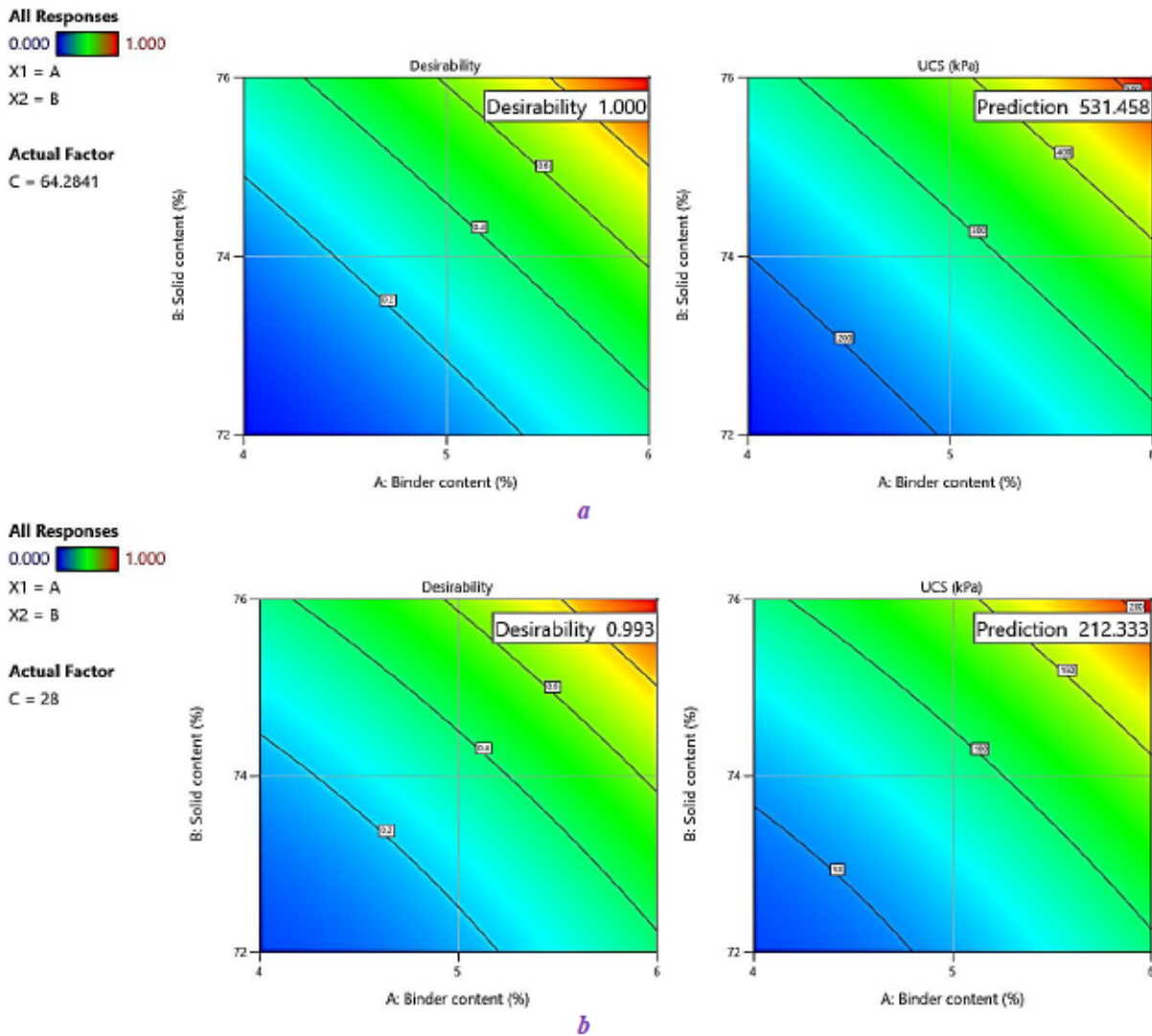


Figure 4.19 The optimization (prediction and desirability) of a) GU and b) GU/LKD samples for the scenario of all parameters in their initial ranges

From an economic standpoint, achieving optimal operational conditions may also involve minimizing binder content during the optimization process. Binder costs represent the most significant expense in any paste backfilling operation (up to 80%) (Benzaazoua et al., 2010), prompting mining companies to reduce these costs by minimizing binder quantities in CPB mixtures. Therefore, any economical optimization of CPB should prioritize efficient binder utilization. Subsequently, the optimization procedure was rerun with the objective of minimizing binder content, along with two other factors (solid content and curing time) within their initial

ranges. For the GU binder, optimal conditions were identified with a binder content of 4.44%, a solid content of 76%, and a curing time of 61.04 days, resulting in a desirability value of 0.586 and UCS equal to 320 kPa. Similarly, for the GU/LKD binder, the optimum conditions were determined to be a binder content of 4.17%, a solid content of 76%, and a curing time of 28 days, resulting in a desirability value of 0.606 and UCS of 100 kPa. The desirability and prediction graph for each binder are depicted in Figure 4.20.

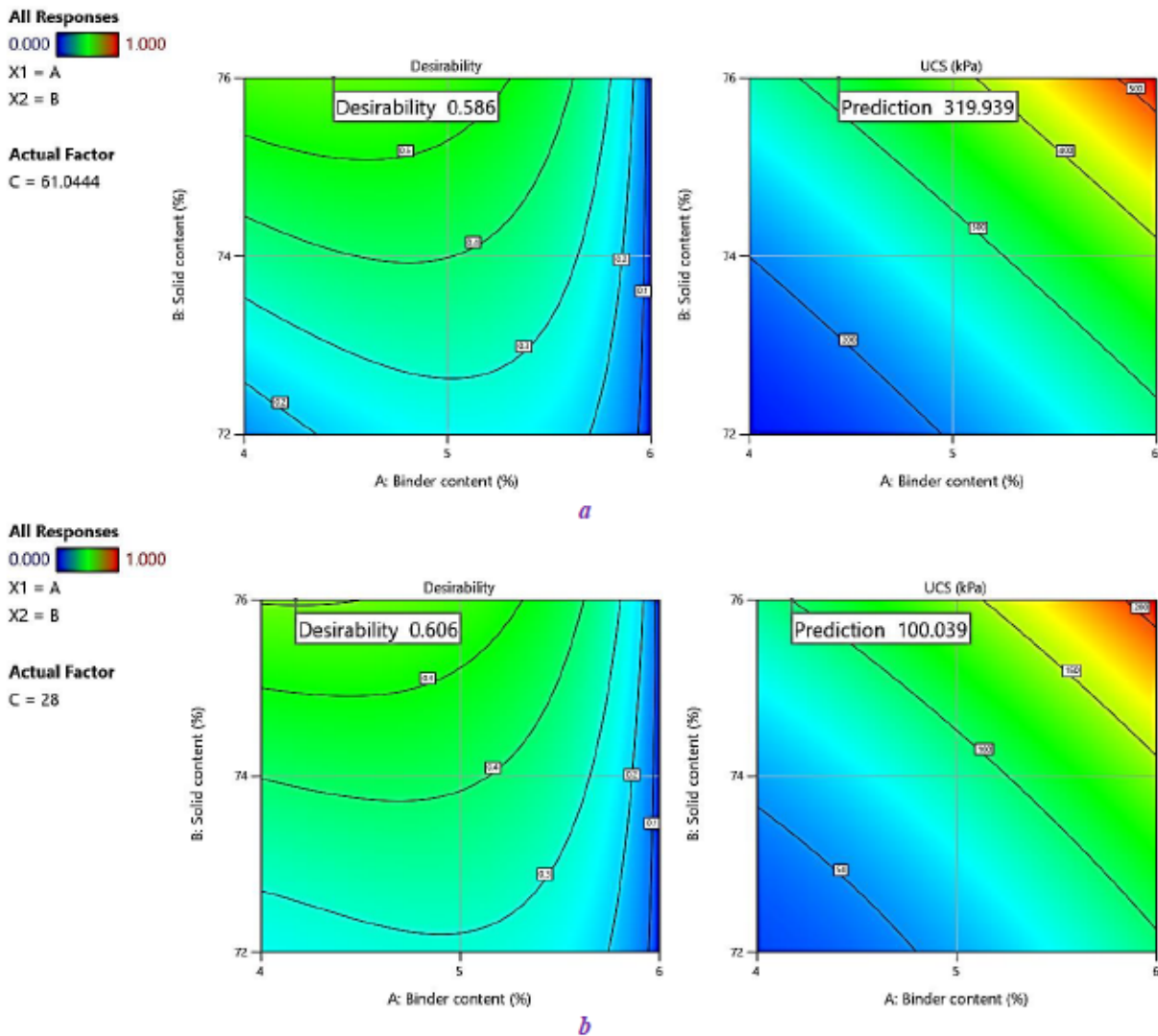


Figure 4.20 The optimization (prediction and desirability) of a) GU and b) GU/LKD samples for the scenario of minimized binder content

To evaluate the reliability and precision of the optimization of the RSM model based on the central composite design, duplicate experiments were conducted under the selected optimized conditions. A new batch of specimens was prepared in triplicate using the optimal mix ratios for both GU and

GU/LKD binders. It was observed that the actual UCS and predicted UCS exhibited a relative error of 4.16% for GU, whereas the error was 2.35% for GU/LKD in the initial scenario where all parameters were within their initial ranges. In the second scenario, which involved minimizing binder content, the relative error was found to be 2.17% for GU and 3.15% for GU/LKD. Consequently, it was affirmed that the second-order polynomial regression equation accurately predicts the strength of CPB samples containing ATRW dust.

4.4 Pore structure of CPBs

4.4.1 Saturated hydraulic conductivity

Once the conditions for optimal strength acquisition were known, the microstructure of the CPB samples was investigated due to its significant role in contaminant transport. Two mix designs that demonstrated the highest strength (GU-6-76-28 and GU-6.68-74-59) with and without ATRW were selected for microstructure evaluation via saturated hydraulic conductivity and computed tomography. k_{sat} results are presented in Table 4.15.

Table 4.15 Saturated hydraulic conductivity of CPB samples

Sample	k_{sat} (cm/s)	
	Without ATRW	With ATRW
GU-6-76-28-1	4.70E-06	3.12E-06
GU-6-76-8-2	4.25E-06	3.20E-06
GU-6.68-74-59-1	1.54E-06	3.33E-06
GU-6.68-74-59-2	1.71E-06	3.74E-06

There is no notable distinction in the saturated hydraulic conductivity between CPB samples with and without ATRW, as the discrepancies fall within the precision limit of the tests, which is half an order of magnitude (Godbout et al., 2007). Saturated hydraulic conductivity can provide insights into changes in microstructure resulting from mineral precipitation and binder hydration during curing. These alterations can modify the quantity and arrangement of voids within CPB, potentially decreasing the hydraulic conductivity of CPB mixtures. The inclusion of Portland cement can lead to the formation of C-S-H gels within the pores early in the curing process. These newly formed gels can restrict water movement within the pores, thereby reducing the k_{sat} of CPB samples (Benzaazoua, Fall, et al., 2004; Godbout et al., 2007). The slight difference in k_{sat} between GU-6-76-28 and GU-6.68-74-59 is insignificant, likely due to their similar microstructure despite a small

difference (less than 1%) in binder content. Furthermore, the addition of ATRW did not significantly impact the hydraulic conductivity of the CPB samples.

4.4.2 CT scanning

Due to the inability of hydraulic conductivity measurements to distinguish microstructural variations among different CPB samples, CT scanning was employed to directly observe the microstructure. The goal was to analyze potential porosity and assess how differences in CPB strength could impact the microstructure of CPB samples containing ATRW. Four samples were chosen for CT scanning: GU-6-76-28 and GU/LKD-6-76-28, which exhibited the highest UCS values, and GU-4-72-28 and GU/LKD-5-70.64-59, which showed the lowest UCS values. Each core was segmented into three regions representing the pore space, high-density (arsenic-containing) materials, and the remaining sediment matrix. From this segmentation, 2D greyscale images were obtained along the center of each core in both longitudinal and transverse profiles (Figure 4.21). These figures clearly distinguish the gray matrix, black pores, and white high-density regions, along with indicating the locations of the region of interest (ROI) in the center of each core.

Figure 4.21 illustrates higher quantities of high-density materials (depicted in white) in samples with higher UCS values (GU-6-76-28 and GU/LKD-6-76-28). These dense materials likely originate from both the initial unreacted ATRW and the formation of arsenic-containing compounds during the hardening process of CPB samples. It is important to note that all samples initially contained the same percentage of ATRW dust ($D_w = 10\%$ wt.), indicating that the formation of secondary materials was notably higher in samples exhibiting greater strength. Essentially, the presence of these materials seems to be the primary factor contributing to the enhanced strength observed in these samples. Another significant observation from these 2D images relates to the quantity and size distribution of pores within the samples. Throughout the stages of preparation, hydration, and hardening, various types of pores form within CPB samples, including intercalated pores filled with C-S-H gels, capillary pores resulting from water evaporation, and bubble pores formed by residual air during slurry mixing (K. Cheng et al., 2021; Pichler et al., 2008, 2009). The sizes of these pores can change due to the filling effect of hydration products, which significantly impacts the mechanical properties and flow characteristics of CPB (Huan et al., 2021; Huang et al., 2021; H. Jiang, Fall, et al., 2020). Interestingly, in the current

samples, both the size and quantity of pores appear to be higher in CPB samples with the highest strength. The matrices of GU-4-72-28 and GU/LKD-5-70.64-59 samples were denser compared to those of GU-6-76-28 and GU/LKD-6-76-28, showing a less prominent internal pore structure. However, most previous studies have established an inverse correlation between porosity (volume of voids to the total volume) and strength (K. Cheng et al., 2021; H. Deng et al., 2021; Grabinsky et al., 2022). Typically, higher porosity corresponds to lower strength in CPB samples. Unfortunately, generating histograms for full core cylinders to obtain porosity and other parameters was not feasible due to the computational intensity required for calculating scalar values for each pore, which exceeded the capabilities of the available computer.

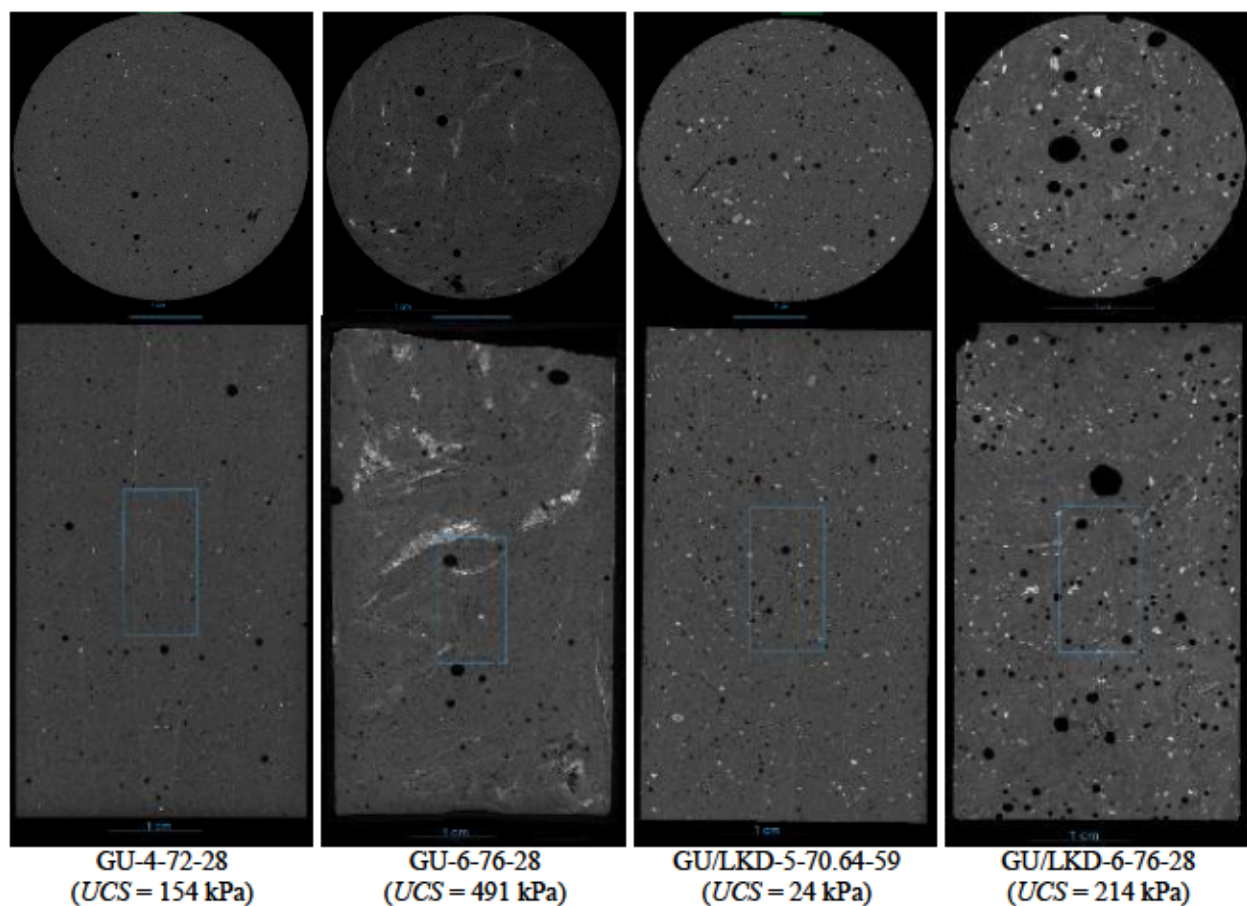
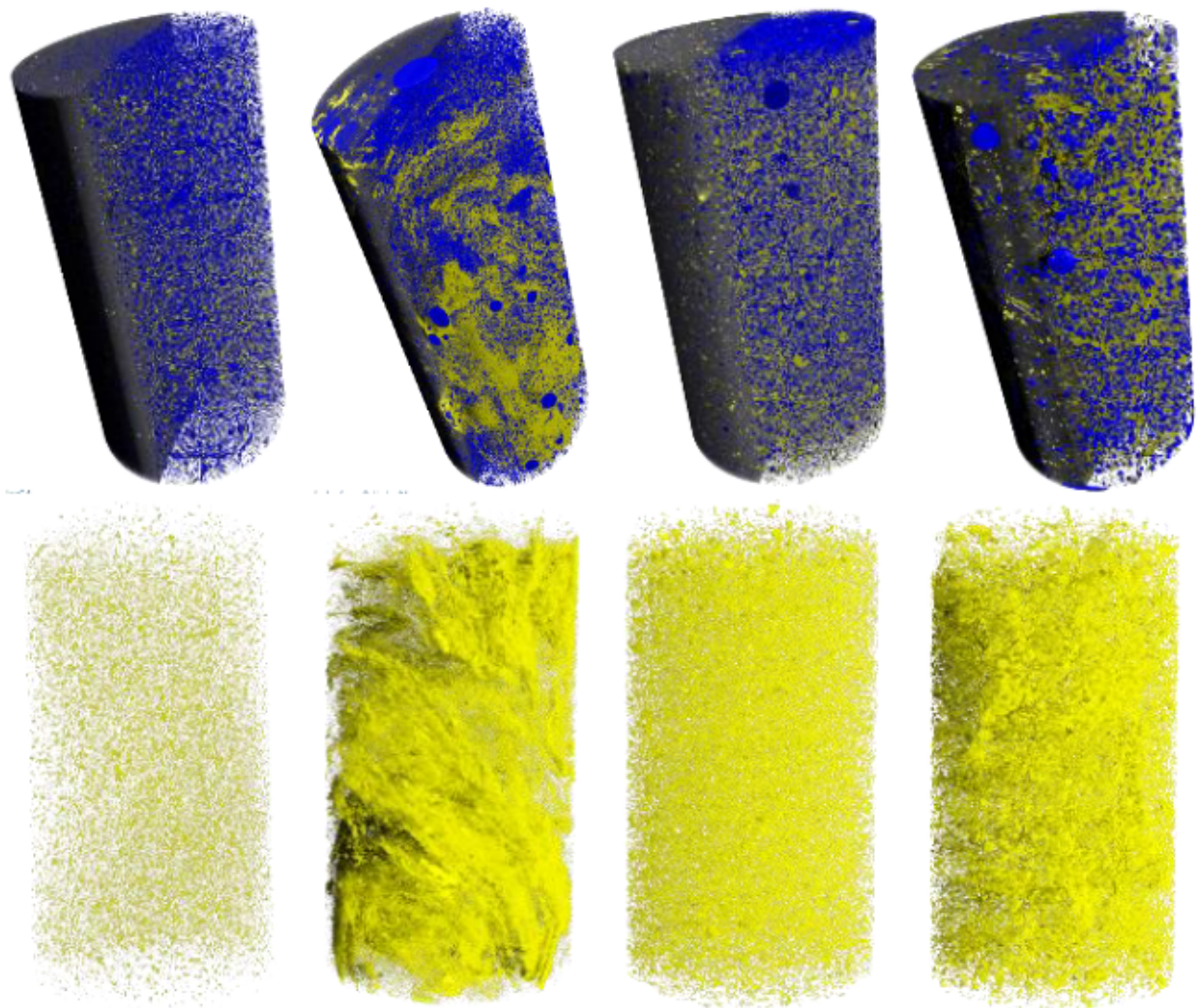


Figure 4.21 2D greyscale images along the center of each core in both longitudinal and transverse profiles containing the segmented regions (black: pores, white: high-density materials, and gray: CPB matrix) and the location of ROIs

The 2D tomographic images obtained do not provide a visual representation of the evolution of pores and high-density materials within the CPB sample structure (Fang et al., 2023). Instead, they offer distribution information concerning minerals and pores within a specific cross-section of the CPB. Therefore, the 2D CT data obtained from the specimens were converted into 3D images to enable visual examination of the internal structure of the CPB samples. Furthermore, since the scanned images were grayscale, pseudo-color enhancement of the resulting two-dimensional slices was performed to facilitate differentiation of substances in the images. This process involved converting each grayscale level of the original image using linear or nonlinear mapping functions to generate color images of the 2D slices and 3D images (Z. Li et al., 2023). Figure 4.22 presents the 3D visual representations of the CPB samples, including separate depictions of the segmented pore structure and high-density materials.



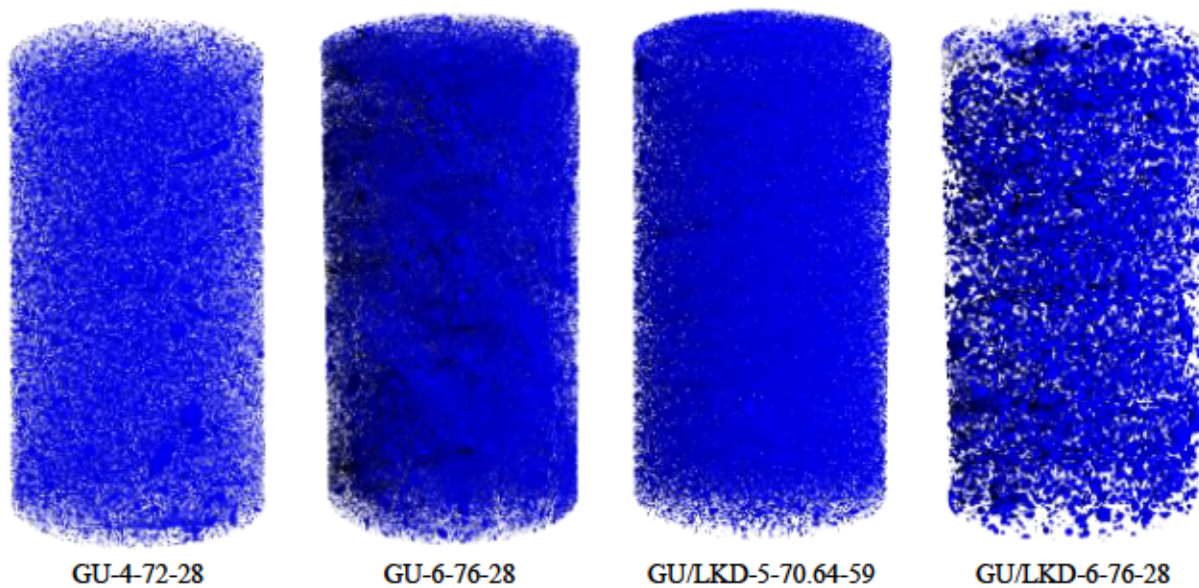
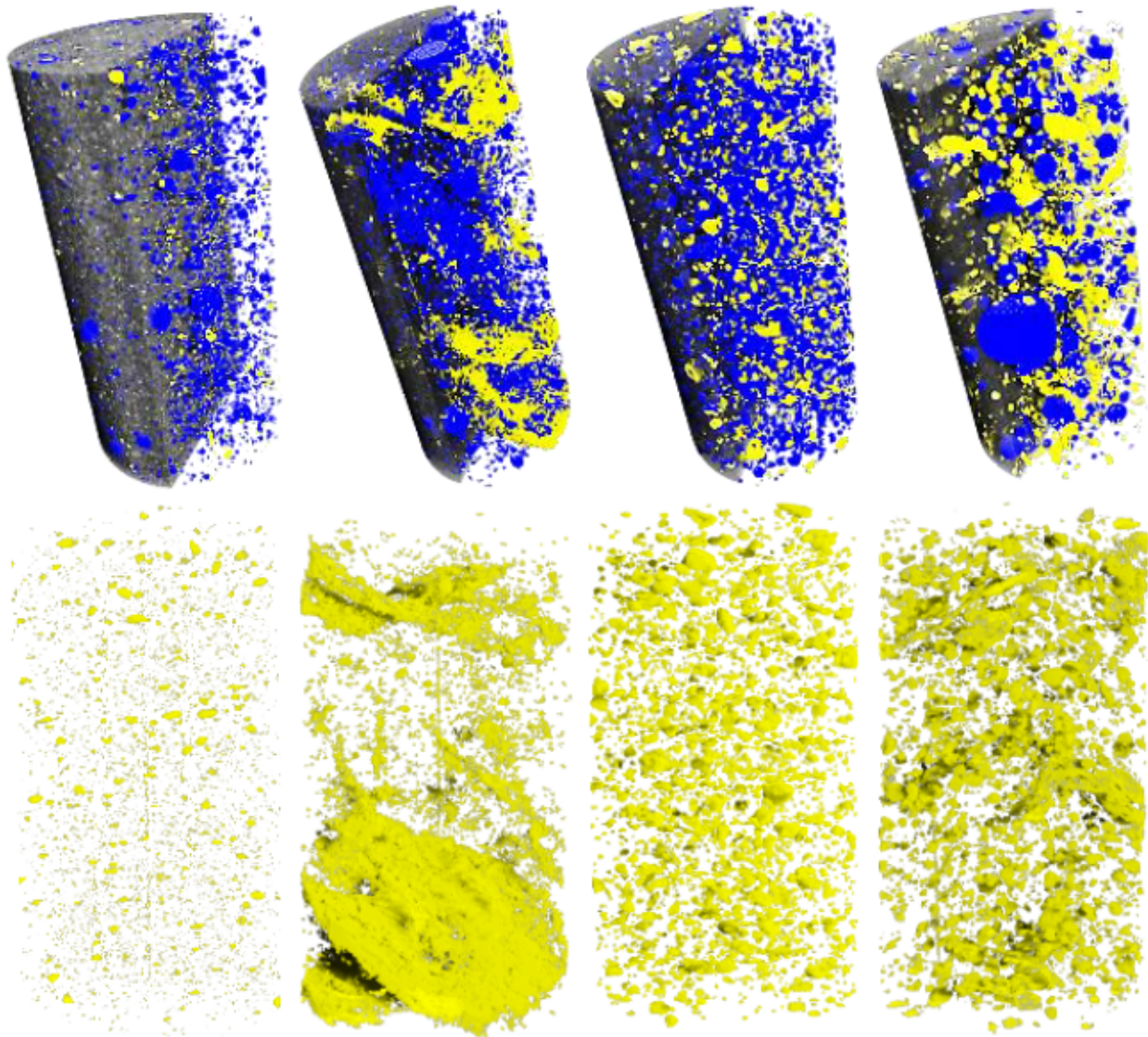


Figure 4.22 3D model of each core cut in half lengthwise, displaying each segmented region (blue: pores, yellow: high-density materials, and gray: CPB matrix)

These 3D visualizations provide a more distinct portrayal of how high-density materials and pores are distributed within the structure of CPB samples. Since the samples underwent natural consolidation rather than full compaction, it is evident that pores are dispersed throughout the samples and clearly visible as blue areas. However, the distribution of pores varies significantly, ranging in size from macroscale to microscale and exhibiting diverse shapes. Samples with the highest UCS display interconnected pores, whereas those with lower strength tend to have pores distributed separately. Moreover, there is a noticeable difference in the distribution of high-density materials among samples with varying strengths. Specifically, in the GU-6-76-28 sample with the highest UCS, there is a notably higher concentration of high-density materials compared to the other samples. In contrast, in the remaining three samples, most high-density materials are randomly dispersed as individual particles, whereas in GU-6-76-28, these materials form a continuous structure. Therefore, it can be inferred that the formation and random distribution of these arsenic-containing high-density materials during the hydration and curing process of CPB samples were the primary factors contributing to the observed strength gain in the GU-6-76-28 sample.

Using larger dimensions can encompass more variability, providing a broader representation of the entire core, but it may also lead to decreased spatial resolution (Reedy & Reedy, 2022). Hence, the Dragonfly software was utilized to reconstruct the 3D image of ROIs (with a height of 16 mm and

diameter of 8 mm), as illustrated in Figure 4.23. This figure presents the 3D depiction of each ROI along with clear representations of the pore and high-density material structures in three dimensions.



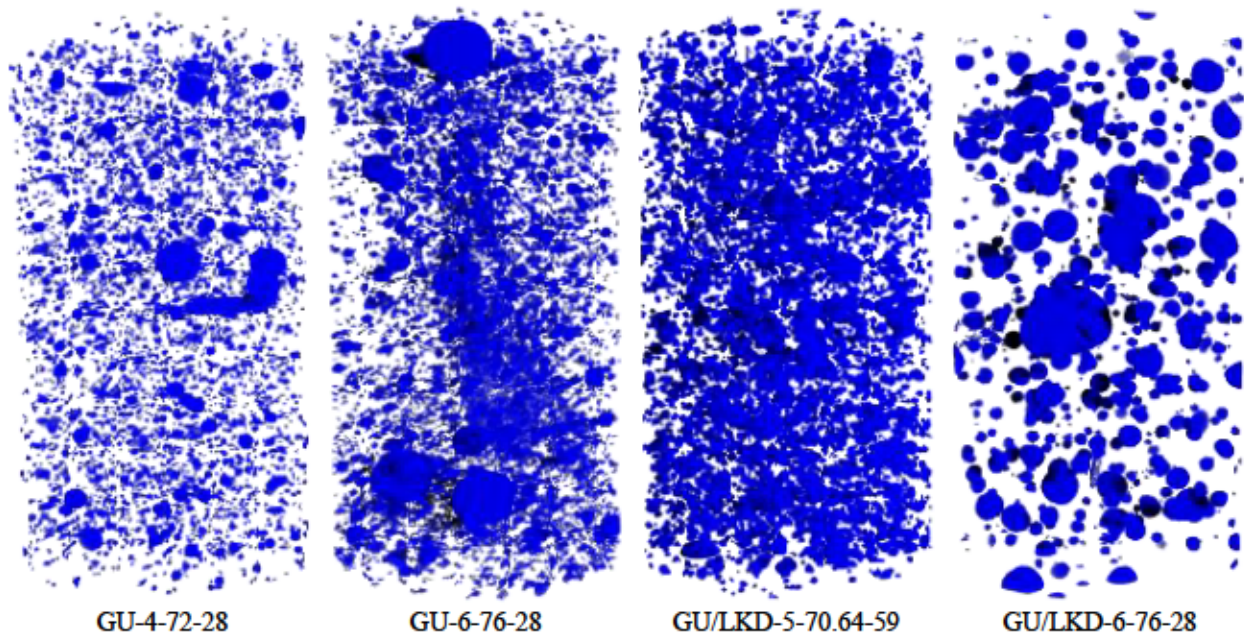


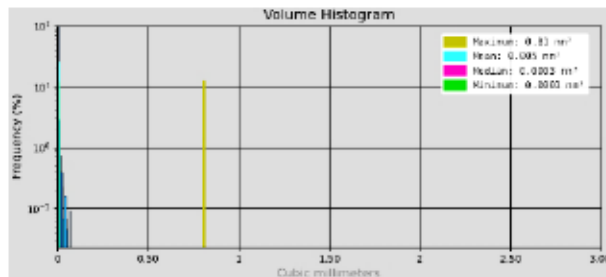
Figure 4.23 3D model of each ROI cut in half lengthwise, displaying each segmented region individually (gray: sediment matrix, yellow: high-density materials, blue: pores)

The pore structure within the ROIs of the investigated CPBs was characterized using several metrics such as pore volume, mean Feret diameter, and sphericity. Table 4.16 displays the key statistical parameters including minimum, median, mean, and maximum values for these metrics. Additionally, Figures 4.24 to 4.26 depict histograms that offer detailed insights into the distribution of pore volume, mean Feret diameter, and sphericity, respectively.

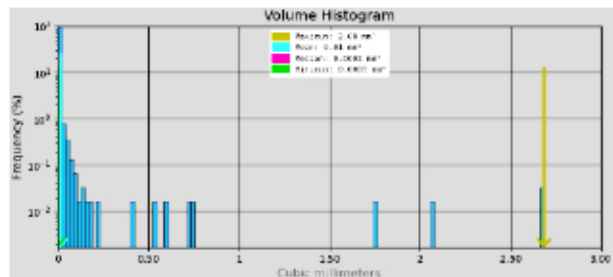
In all samples, both the median and minimum pore volumes were identical, indicating that half of the pores had the minimum volume. Samples GU-4-72-28 and GU/LKD-5-70.64-59, which exhibited the lowest strength, demonstrated significantly smaller maximum pore volumes compared to the samples with the highest strength. These observations were visually confirmed by examining the 3D ROIs of the samples as well as their longitudinal and transverse sections. Regarding the statistical analysis of the mean Feret diameter of the pores, it was observed that CPB samples with lower strength exhibited smaller pores, as indicated by lower mean values of this metric. These findings align with the pore volume analysis of these samples. The quantification of pore shape properties in CPB samples involved calculating the sphericity of the pores using Equation 3.9. Interestingly, although samples with lower strength had smaller pore structures, their pores tended to have higher sphericity. In contrast, sample GU-6-76-28, which had the highest UCS, exhibited the lowest sphericity with a mean value of 0.72.

Table 4.16 The statistical parameters related to the main scalars of the pores in ROI of the CPB samples

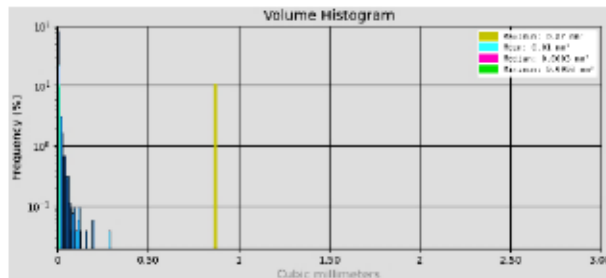
Scalar	Statistical parameter	GU-4-72-28 (UCS = 154 kPa)	GU-6-76-28 (UCS = 491 kPa)	GU/LKD-5-70.64-59 (UCS = 24 kPa)	GU/LKD-6-76-28 (UCS = 214 kPa)
Pore volume (mm ³)	Minimum	0.0003	0.001	0.0003	0.00001
	Median	0.0003	0.001	0.0003	0.00001
	Mean	0.005	0.02	0.01	0.07
	Maximum	0.81	2.68	0.87	8.38
Mean Feret diameter (mm)	Minimum	0.09	0.14	0.10	0.03
	Median	0.15	0.23	0.19	0.30
	Mean	0.18	0.28	0.23	0.34
	Maximum	1.57	6.08	3.97	2.79
Sphericity	Minimum	0.22	0.11	0.30	0.28
	Median	0.89	0.74	0.88	0.81
	Mean	0.85	0.72	0.86	0.81
	Maximum	1.03	0.98	1.00	1.02



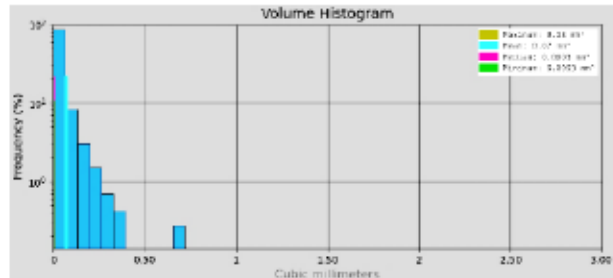
GU-4-72-28



GU-6-76-28



GU/LKD-5-70.64-59



GU/LKD-6-76-28

Figure 4.24 Pore volume histograms of the ROIs of CPB samples

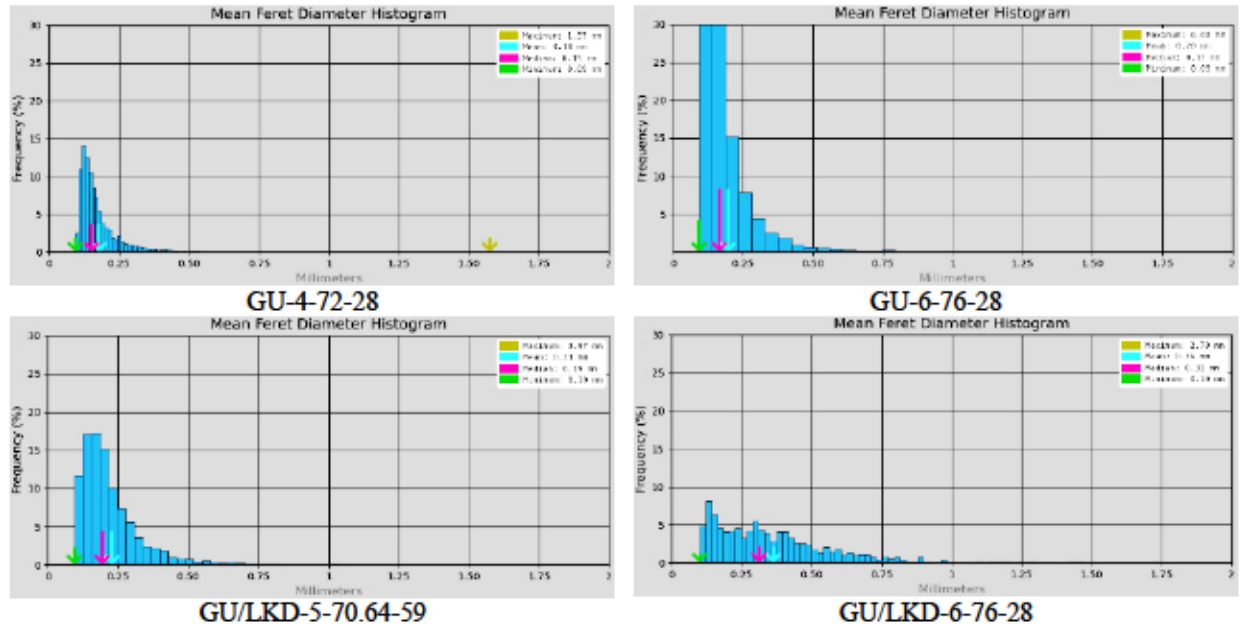


Figure 4.25 Mean Feret diameter histograms of the ROIs of CPB samples

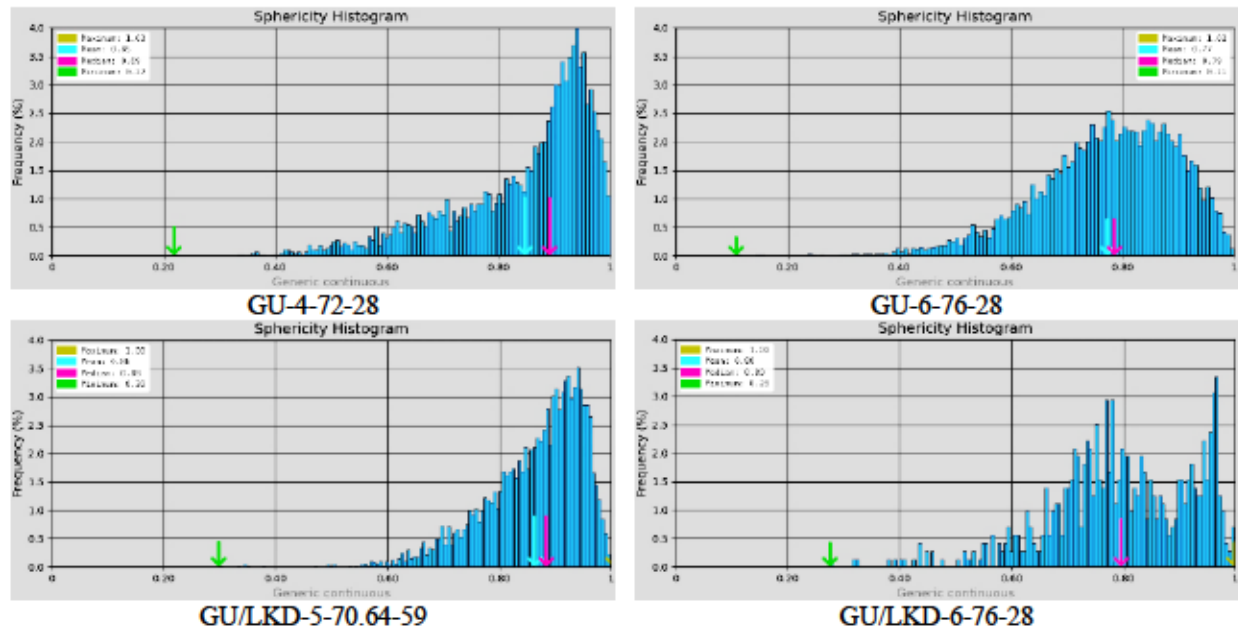


Figure 4.26 Sphericity histograms of the ROIs of CPB samples

In this study, pores were classified based on their volume: pores with volume $<0.001 \text{ mm}^3$ were categorized as small pores, those with $0.001 \text{ mm}^3 \leq \text{volume} < 0.1 \text{ mm}^3$ as medium pores, and pores with $0.1 \text{ mm}^3 \leq \text{volume} < 10 \text{ mm}^3$ as large pores. Figure 4.27 illustrates the curves depicting the distribution of different pore volumes in the ROIs of the four CPB samples, each exhibiting distinct patterns in pore number distribution. The majority of observed pores in three samples—GU-6-76-

28 (99.34%), GU/LKD-5-70.64-59 (67.57%), and GU/LKD-6-76-28 (61.72%)—were categorized as medium pores. In contrast, more than 63% of pores in sample GU-4-72-28 fell into the small pore category, with less than 1% categorized as large pores, except for GU/LKD-6-76-28 (9.47%). The total number of pores observed in the central ROIs of these samples were as follows: GU-4-72-28 (4430 pores), GU-6-76-28 (2434 pores), GU/LKD-5-70.64-59 (5223 pores), and GU/LKD-6-76-28 (781 pores). To classify pores according to their shape, individual pores with varying sphericity were identified from the histograms. Pores generally transition from spherical to irregular shapes. As a pore deviates from a perfect sphere (sphericity value of 1), its irregularity increases, approaching a value closer to 0 (J. Li et al., 2023). Three main types of pores were distinguished: spherical or quasi-spherical pores with a sphericity between 0.8 and 1, semi-spherical pores with a sphericity of 0.5–0.8, and non-spherical pores with a sphericity less than 0.5. Figure 4.27 illustrates the distribution of pores categorized by their sphericities. With the exception of some relatively large pores observed in sample GU-6-76-28, the sphericity of pores ranged from 0.2 to 1 across all CPB samples.

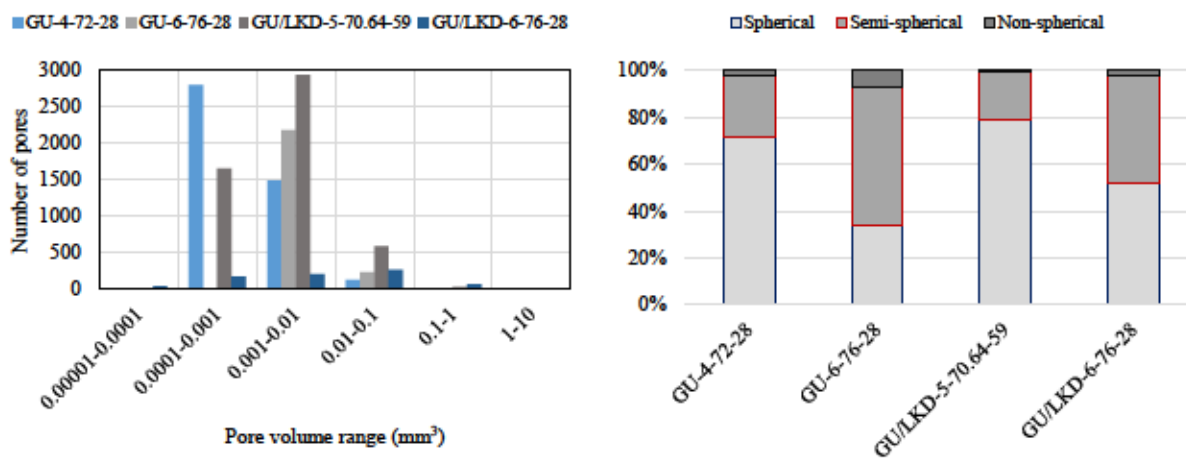


Figure 4.27 The number of different volumes of pores (left) and the distribution of the sphericity of the pores (right)

Figure 4.28 depicts the correlation between pore volume and sphericity within the central ROIs of CPB samples. In the case of GU samples, as pore volume increases, there is a trend of decreasing sphericity, indicating a shift towards more irregularly shaped pores. Moreover, the data reveals an increase in the dispersion of sphericity values with increasing pore volume. For the GU/LKD-5-70.64-59 sample, there is also a decrease in pore sphericity as pore volume increases, although the changes in sphericity distribution are relatively minor with increasing pore volume. In the

GU/LKD-6-76-28 sample, the smallest and largest pores exhibit the highest sphericities, while mid-range pores (with volumes between 0.001 and 0.1 mm³) display lower sphericities.

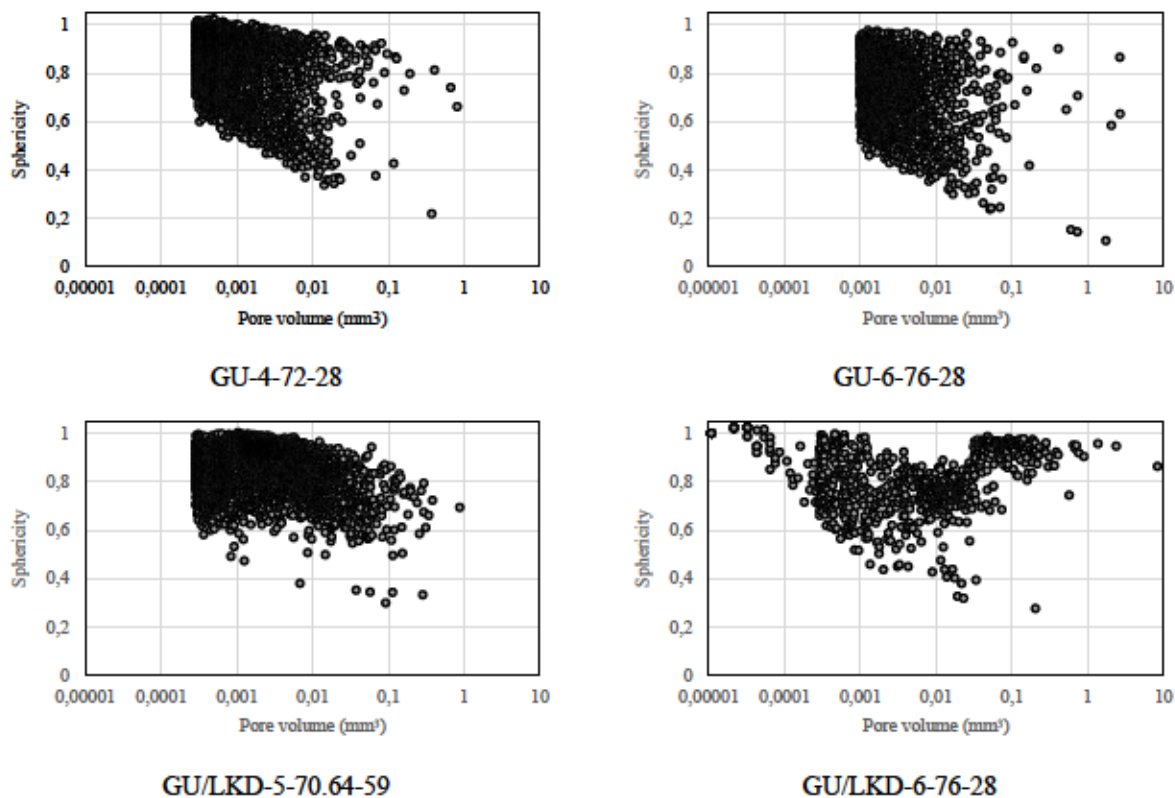


Figure 4.28 Relationship between sphericity and pore volume

4.5 Leaching analysis (Article 3)

The third article entitled “Study on the Leaching Behavior of Cemented Paste Backfill Containing Arsenic Trioxide Roaster Waste (ATRW)” was published in the Discover Civil Engineering journal (Advances in Sustainable Mining Waste Management collection) and is available in Appendix D.

While the hydration process of cement contributes to mechanical strength development, the geochemical behaviour of CPB must be evaluated to prevent potential groundwater contamination. The leaching behaviors of arsenic and other elements within the CPB matrix were assessed through tank leaching tests. Six recipes were chosen, with duplicates for each recipe, resulting in 12 cylinders leached under identical conditions (e.g., GU-4-76-28-1, GU-4-76-28-2, GU-5-74-59-1, GU-5-74-59-2, GU-6-76-28-1, GU-6-76-28-2, GU-6.68-74-59-1, GU-6.68-74-59-2 as GU representatives, and GU/LKD-6-76-28-1, GU/LKD-6-76-28-2, GU/LKD-6.68-74-59-1, and

GU/LKD-6.68-74-59-2 as GU/LKD representatives). However, some samples disintegrated during leaching, halting the process for those specific samples. Among the GU samples, only two recipes (GU-6-76-28 and GU-6.68-74-59) maintained their structural integrity throughout the leaching process. Other GU samples disintegrated after 24 hours (GU-5-74-59) and 54 hours (GU-4-76-28), leading to an early termination of the leaching test. Similarly, among the GU/LKD samples, GU/LKD-6.68-74-59 disintegrated after 24 hours, while GU/LKD-6-76-28 lasted up to 16 days before the leaching was stopped (Figure 4.29).

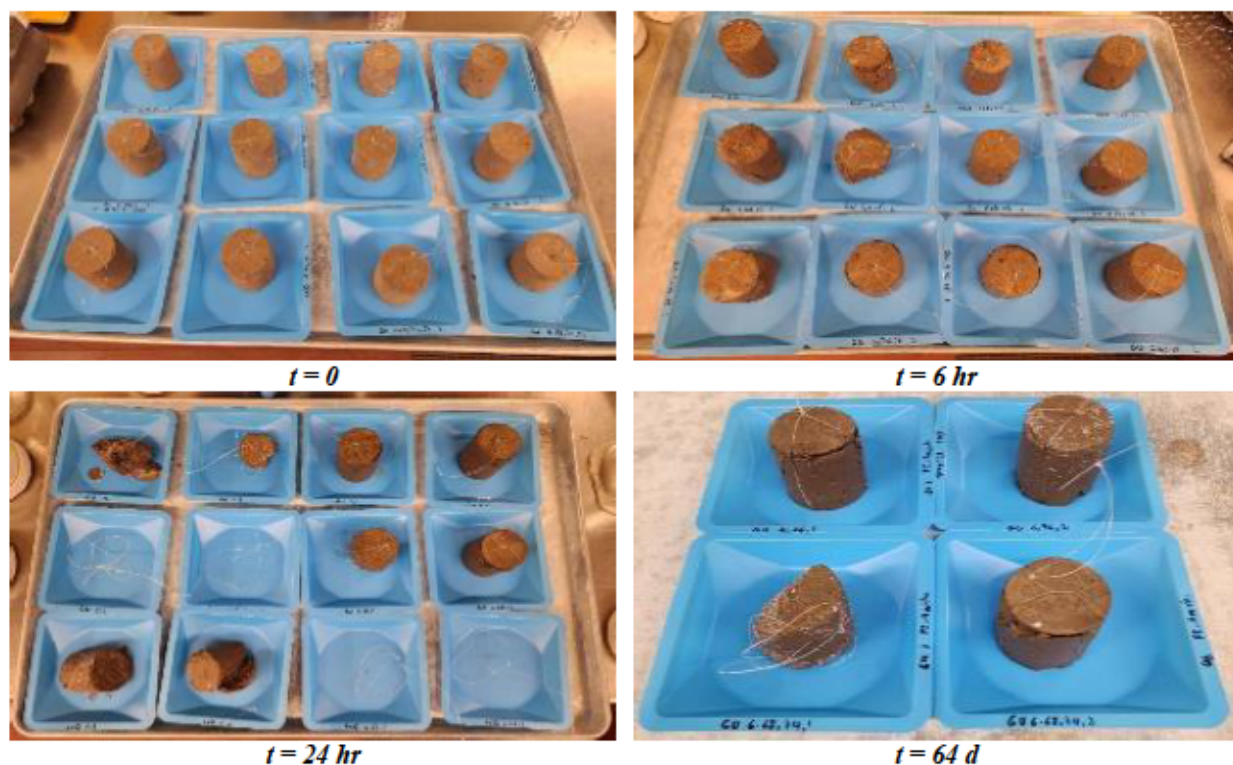


Figure 4.29 A view of the samples (with a diameter of 5.2 cm and a length of about 5 cm) after various time intervals (start of the analysis and after 6 hr, 24 hr, and 64 days)

Table 4.17 summarizes the total calculated mass (E_i^*) of arsenic, calcium, and sulfate leached, expressed as the emission of mass per unit of external surface area during each leachate renewal cycle. With the exception of the GU-6-76-28 samples, there were minimal deviations in the release of elements/ions across duplicate samples. For the four main samples, the highest arsenic release during a leachate renewal cycle was 61.3 g/m² (GU-6-76-28-1 after 16 days), 63.1 g/m² (GU-6-76-28-2 after 36 days), 45.8 g/m² (GU-6.68-74-59-1 after 24 hours), and 47.6 g/m² (GU-6.68-74-59-2 after 36 days). For calcium, the maximum masses leached during a leachate renewal cycle were observed after 36 days for all four samples: 24.8 g/m² for GU-6-76-28-1, 26.0 g/m² for GU-6-76-

28-2, 21.1 g/m² for GU-6.68-74-59-1, and 23.2 g/m² for GU-6.68-74-59-2. In the case of sulfate, the highest leached masses were 20.4 g/m² (GU-6-76-28-1 after 54 hours), 15.9 g/m² (GU-6-76-28-2 after 9 days), 22.1 g/m² (GU-6.68-74-59-1 after 24 hours), and 17.6 g/m² (GU-6.68-74-59-2 after 9 days).

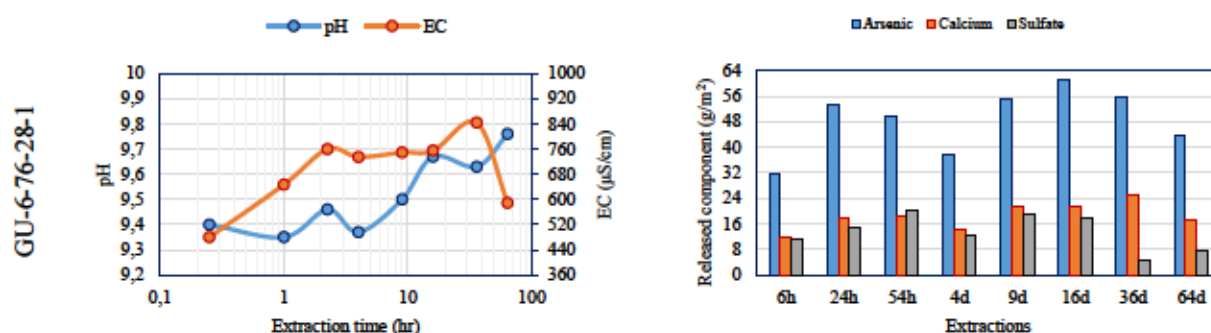
Table 4.17 Calculated leached mass of each component (E^*) during each leaching period

Sample	Element/ion (g/m ²)	6h	24h	54h	4d	9d	16d	36d	64d	
GU-4-76-28-1	Arsenic	89.3	185.6	114.1						
GU-4-76-28-2		45.1	181.3	62.5						
GU-5-74-59-1		90.1	192.7							
GU-5-74-59-2		61.5	169.6							
GU-6-76-28-1		31.4	53.2	49.6	37.6	55.0	61.3	55.5	44.0	
GU-6-76-28-2		23.9	43.3	51.0	24.3	45.1	47.8	63.1	44.6	
GU-6.68-74-59-1		24.1	45.8	44.5	25.9	37.6	36.5	41.5	35.9	
GU-6.68-74-59-2		23.2	38.4	36.0	21.2	41.7	39.6	47.6	38.3	
GU/LKD-6-76-28-1		39.9	117.3	85.4	29.5	62.2	60.2			
GU/LKD-6-76-28-2		67.3	78.1	100.2	22.5	45.5	43.8			
GU/LKD-6.68-74-59-1		103.0	172.0							
GU/LKD-6.68-74-59-2		51.5	122.9							
GU-4-76-28-1		Calcium	24.4	46.1	31.3					
GU-4-76-28-2			12.8	44.6	18.9					
GU-5-74-59-1	27.7		54.4							
GU-5-74-59-2	19.3		50.2							
GU-6-76-28-1	11.8		17.6	18.3	14.0	21.6	21.7	24.8	17.1	
GU-6-76-28-2	9.4		14.3	20.1	9.1	17.7	17.5	26.0	20.3	
GU-6.68-74-59-1	10.3		20.8	20.6	12.0	17.8	15.9	21.1	15.6	
GU-6.68-74-59-2	10.8		16.4	18.3	9.4	19.2	17.8	23.2	18.7	
GU/LKD-6-76-28-1	12.2		33.1	27.4	10.1	19.9	19.4			
GU/LKD-6-76-28-2	21.4		21.3	32.2	7.7	14.9	14.0			
GU/LKD-6.68-74-59-1	32.6		49.7							
GU/LKD-6.68-74-59-2	15.2		33.6							

Table 4.17 Calculated leached mass of each component (E^*_i) during each leaching period (continued)

Sample	Element/ion (g/m^2)	6h	24h	54h	4d	9d	16d	36d	64d
GU-4-76-28-1	Sulfate	24.2	50.7	27.2					
GU-4-76-28-2		11.8	52.8	13.8					
GU-5-74-59-1		19.2	63.6						
GU-5-74-59-2		29.5	57.2						
GU-6-76-28-1		11.3	15.1	20.4	12.3	18.9	17.6	4.6	7.8
GU-6-76-28-2		8.2	12.3	15.6	6.8	15.9	12.9	4.4	15.2
GU-6.68-74-59-1		9.7	22.1	19.6	6.9	15.0	10.6	4.6	8.7
GU-6.68-74-59-2		10.1	15.7	17.1	6.8	17.6	14.3	4.6	12.5
GU/LKD-6-76-28-1		11.6	33.2	22.8	6.4	15.8	13.0		
GU/LKD-6-76-28-2		19.3	22.3	29.0	5.4	11.1	7.8		
GU/LKD-6.68-74-59-1		33.3	59.9						
GU/LKD-6.68-74-59-2		16.1	42.4						

The influence of pH and electrical conductivity (EC) on the hydration process and leaching of components in CPB samples is well recognized (Fan et al., 2010). Figure 4.30 presents the release of arsenic, calcium, and sulfate, as well as the evolution of pH and EC for the four samples that endured the entire leaching process at various intervals. Although the measured pH may not precisely match the porewater pH due to concentration gradients, it serves as an approximate representation of the pore solution pH (Bull, 2019).



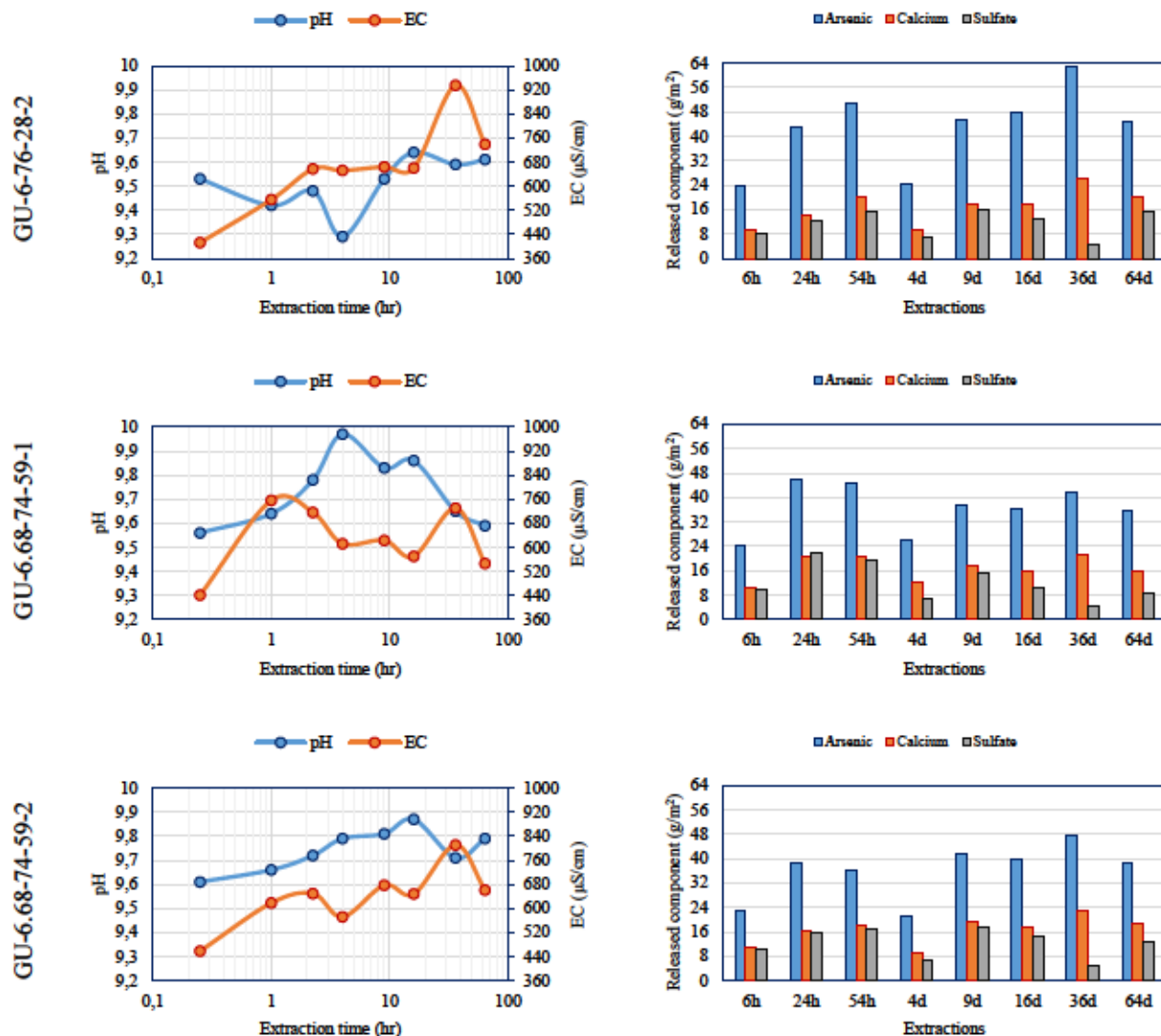


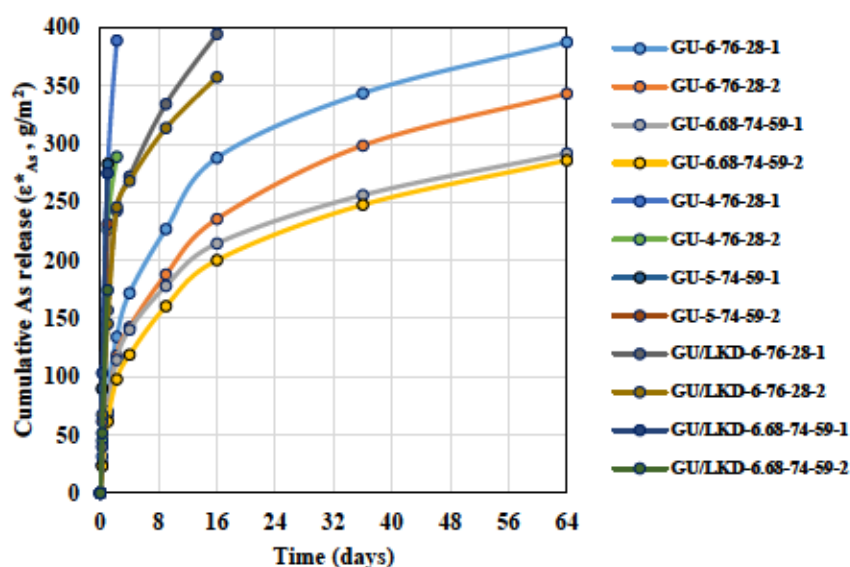
Figure 4.30 Variations in released mass of arsenic, calcium, and sulfate in relation to pH and EC during each TLT extraction

As shown in Figure 4.30, all CPB samples had pH values between 9.2 and 10. GU-6-76-28 exhibited lower pH values compared to GU-6.68-74-59, which have a slightly higher binder content. The largest observed difference occurred after four days, with a pH variation of more than 0.5 units between these two sets of samples. The pH of the DI water used for the leaching process was 5.8. In all samples, the ongoing dissolution of cementitious phases (Hamberg, Maurice, et al., 2018) and the continuous generation of OH^- during the cement hydration process (Su et al., 2019) led to an increase in the pH of the TLT leachates. No specific trends were observed for the pH values. For GU-6.68-74-59, the release of As, Ca, and SO_4^{2-} varied with each extraction and did

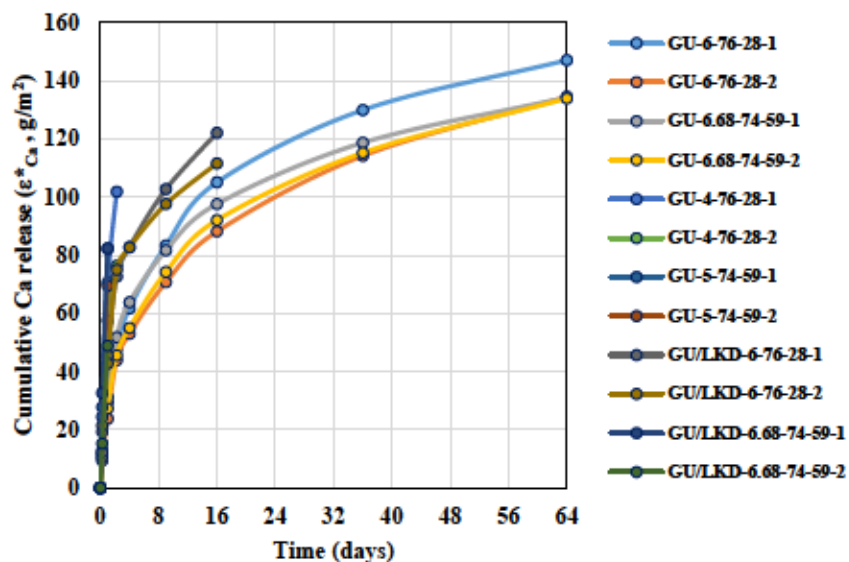
not align with the pH behavior. Conversely, for GU-6-76-28, the changes in As, Ca, and SO_4^{2-} levels appear to be pH-dependent, indicating increased solubility of these components at higher pH values. These findings should be interpreted with caution given the minor discrepancies observed in pH measurements

The electrical conductivity (EC) of leachates ranged from 412 to 935 $\mu\text{S}/\text{cm}$ for GU-6-76-28 and from 441 to 811 $\mu\text{S}/\text{cm}$ for GU-6.68-74-59 throughout the leaching periods. All four samples showed a consistent pattern in EC variations. Except for GU-6.68-74-59-1, EC of all leachates increased during the first three cycles (6-54 hours), followed by a slight drop at the fourth interval (after 4 days). EC values then peaked at 36 days before gradually decreasing. Overall, all samples exhibited low EC values, which is corroborated by the amount of leached Na^+ , K^+ , and Mg^{+2} . Apart from Ca^{+2} and SO_4^{-2} , the concentrations of other released ions were negligible and are not included in this discussion.

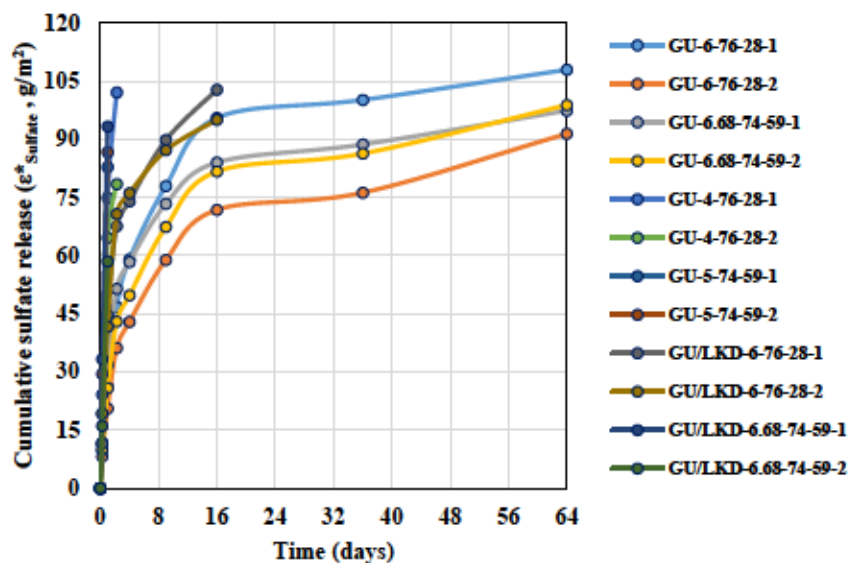
Figure 4.31 shows the cumulative released content (ϵ^*) of arsenic, calcium, and sulfate for all 12 samples during the tank leaching test. For samples that disintegrated during the process, the cumulative leached content was calculated up to the point of disintegration. The leached contents of other elements/ions were significantly lower and are not displayed.



a



b



c

Figure 4.31 Cumulative released contents of components during TLT; a) arsenic, b) calcium, and c) sulfate

The cumulative release of arsenic was more pronounced in GU-6-76-28 compared to GU-6.68-74-59. However, the rate of release, as indicated by the graph's slope, was lower for arsenic in these four samples than in others, even though the other samples did not remain intact throughout the process. The arsenic release trends from GU-6-76-28 and GU-6.68-74-59 suggest that a plateau was not reached, indicating that arsenic release might continue beyond the 64-day leaching period. Cumulative calcium release was notably higher in GU-6-76-28-1 compared to others, while GU-

6-76-28-2 and GU-6.68-74-59 showed similar cumulative calcium releases. The rate of calcium release for these four samples was comparable to GU/LKD-6-76-28; however, the other samples exhibited a higher release rate, despite not maintaining their integrity until the end. The cumulative calcium release from GU-6-76-28 and GU-6.68-74-59 did not reach a plateau, suggesting that calcium release could persist beyond the 64-day period. For sulfate release, there was a notable difference between duplicates of GU-6-76-28, with SO_4^{2-} release from GU-6.68-74-59 being higher than GU-6-76-28-2 and lower than GU-6-76-28-1. All four samples displayed a similar trend, and despite a minor sulfate release between the 6th and 7th cycles, which indicated equilibrium conditions, an increase in sulfate release was observed in the final leachate renewal cycle.

Figure 4.32 illustrates the depletion curves for two key elements (As and Ca) across the four main samples. For GU-6-76-28-1, 40.8% of the total arsenic was leached, while GU-6-76-28-2 showed 35.4% leaching (leaving 64.6% of the total arsenic in the sample). In comparison, GU-6.68-74-59-1 and GU-6.68-74-59-2 samples had leached 32.8% and 31.6% of the total arsenic, respectively, which is lower than the amounts for GU-6-76-28 samples. This indicates that arsenic was less bound in GU-6-76-28 samples than in GU-6.68-74-59 samples. Although GU-6-76-28 samples demonstrated greater UCS strength, the higher binder content in GU-6.68-74-59 samples had a more significant effect on arsenic stabilization than the higher solid content in GU-6-76-28 samples. Furthermore, since arsenic was not fully depleted during the TLT test, it suggests that this contaminant might continue to be released over a longer period under natural conditions. Regarding calcium depletion, the values across all samples were quite similar. GU-6-76-28-1 exhibited the highest calcium depletion at 17.3% after 64 days of leaching, followed by GU-6.68-74-59-1 (16.9%), GU-6.68-74-59-2 (16.6%), and GU-6-76-28-2 (15.6%). Calcium release typically results from the dissolution of cementitious calcium-bearing minerals like portlandite, calcium aluminates, or calcium-silicate-hydrates (C-S-H) in alkaline conditions (Coussy et al., 2011; Glass & Buenfeld, 1999; O Peyronnard et al., 2009). However, the low pH observed in the current CPBs suggests that portlandite was not present in significant quantity. Therefore, the dissolution primarily affected C-S-H. Additionally, the notable carbonate content (16.4 % wt. dolomite) in Giant Mine tailings may also dissolve during leaching. Thus, the release of calcium is likely due to the dissolution of both carbonates from the tailings and cementitious minerals.

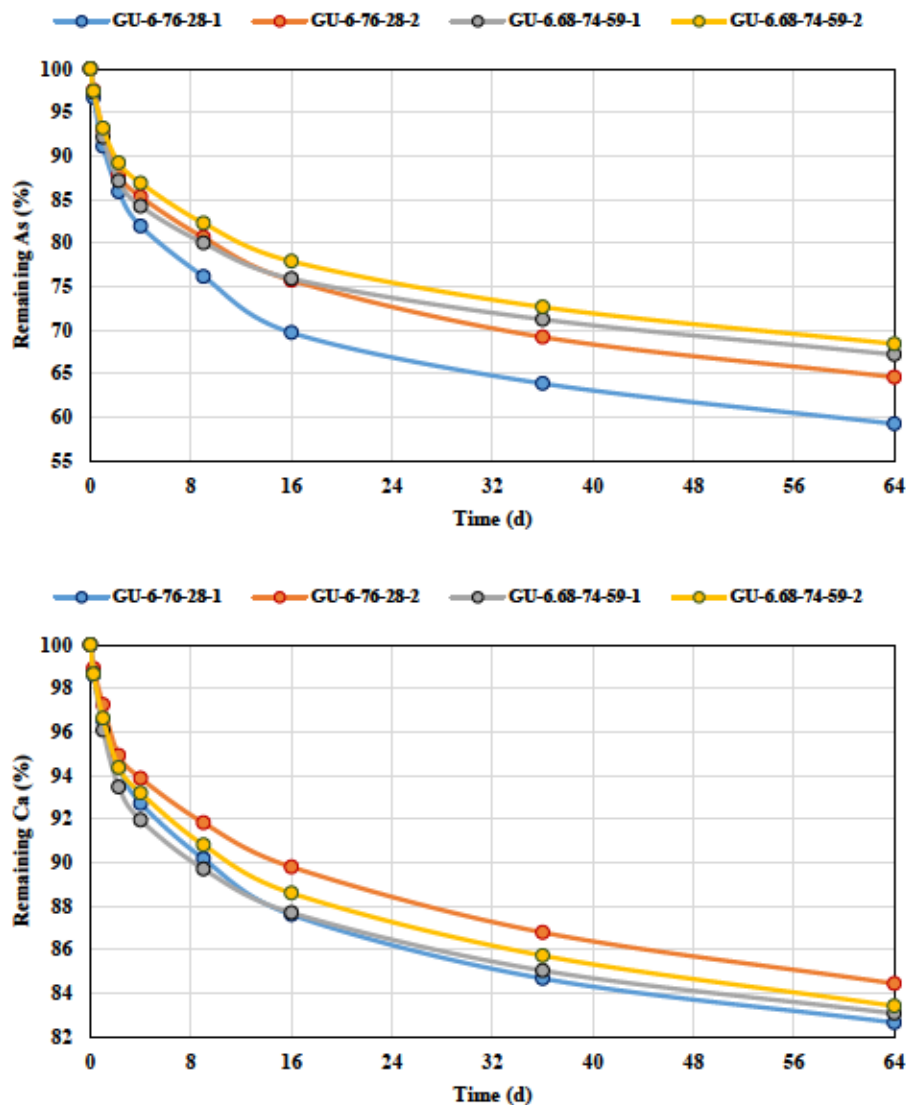


Figure 4.32 Depletion curves of As and Ca from the leached samples

Table 4.18 summarizes the calculations performed according to EA NEN 7375 (EA NEN 7375, 2004). For accurate determination of the leaching mechanism and quantification of each component, it is essential that the material matrix does not dissolve (EA NEN 7375, 2004). The cumulative leaching (ϵ_n) graphs of arsenic, calcium, and sulfate were used to assess the leaching mechanisms of these components from CPB samples.

Table 4.18 The calculated values encompass the slopes of the regression lines (r_c), their corresponding standard deviations (Sd_{rc}), concentration factors (CF), and the leaching mechanisms for As, Ca, and SO_4^{2-} in the four main samples, based on EA NEN 7375 (EA NEN 7375, 2004)

Sample	Increment	Arsenic				Calcium				Sulfate			
		CF	r_c	Sd_{rc}	Mechanism	CF	r_c	Sd_{rc}	Mechanism	CF	r_c	Sd_{rc}	Mechanism
GU-6-76-28-1	Increment 2-7	19265.72	0.153	0.067	Surface wash-off	1787.93	0.214	0.051	Surface wash-off	148.07	-0.138	0.221	Surface wash-off
	Increment 5-8	19978.53	-0.041	0.151	Depletion	1937.75	-0.002	0.104	Depletion	122.09	-0.553	0.446	Depletion
	Increment 4-7	19180.72	0.087	0.153	Depletion	1825.77	0.154	0.093	Depletion	133.44	-0.516	0.422	Depletion
	Increment 3-6	18836.20	0.234	0.097	Depletion	1717.62	0.226	0.066	Depletion	172.88	0.085	0.105	Depletion
	Increment 2-5	18084.55	0.188	0.062	Depletion	1623.92	0.262	0.078	Depletion	166.63	0.244	0.170	Depletion
	Increment 1-4	15904.81	0.588	0.129	Diffusion	1402.36	0.589	0.102	Diffusion	147.62	0.594	0.140	Diffusion
GU-6-76-28-2	Increment 2-7	16956.29	0.202	0.076	Surface wash-off	1586.19	0.241	0.085	Surface wash-off	113.31	-0.091	0.196	Surface wash-off
	Increment 5-8	18579.91	0.119	0.102	Depletion	1850.69	0.204	0.059	Depletion	121.16	-0.141	0.564	Depletion
	Increment 4-7	16699.39	0.322	0.091	Depletion	1596.15	0.356	0.064	Diffusion	100.10	-0.295	0.433	Depletion
	Increment 3-6	15581.78	0.156	0.202	Depletion	1462.95	0.132	0.209	Depletion	128.10	0.146	0.220	Depletion
	Increment 2-5	15166.67	0.140	0.180	Depletion	1391.46	0.205	0.217	Depletion	126.62	0.221	0.218	Depletion
	Increment 1-4	13202.28	0.583	0.222	Diffusion	1203.29	0.578	0.215	Diffusion	107.28	0.518	0.223	Diffusion
GU-6.68-74-59-1	Increment 2-7	14311.96	0.078	0.052	Surface wash-off	1640.41	0.095	0.046	Surface wash-off	131.50	-0.252	0.149	Surface wash-off
	Increment 5-8	14028.78	0.077	0.084	Depletion	1600.41	0.066	0.049	Depletion	97.52	-0.312	0.387	Depletion
	Increment 4-7	13107.80	0.107	0.082	Depletion	1519.59	0.135	0.040	Depletion	93.03	-0.299	0.355	Depletion
	Increment 3-6	13383.25	0.053	0.121	Depletion	1510.14	0.031	0.104	Depletion	130.29	-0.052	0.251	Depletion
	Increment 2-5	14244.76	0.061	0.113	Depletion	1620.33	0.080	0.115	Depletion	159.02	-0.077	0.231	Depletion
	Increment 1-4	12996.50	0.576	0.194	Diffusion	1449.68	0.606	0.199	Diffusion	145.84	0.467	0.327	Diffusion
GU-6.68-74-59-2	Increment 2-7	13854.40	0.189	0.054	Surface wash-off	1580.87	0.205	0.066	Surface wash-off	126.94	-0.126	0.198	Surface wash-off
	Increment 5-8	15472.20	0.070	0.070	Depletion	1792.70	0.107	0.053	Depletion	122.61	-0.279	0.515	Depletion
	Increment 4-7	13887.77	0.248	0.113	Depletion	1582.50	0.285	0.101	Depletion	108.25	-0.276	0.466	Depletion
	Increment 3-6	12820.95	0.236	0.134	Depletion	1472.35	0.190	0.170	Depletion	139.56	0.167	0.257	Depletion
	Increment 2-5	12713.42	0.180	0.112	Depletion	1439.68	0.198	0.160	Depletion	143.10	0.149	0.238	Depletion
	Increment 1-4	11003.00	0.513	0.178	Diffusion	1248.35	0.517	0.188	Diffusion	124.34	0.443	0.250	Diffusion

Slopes (r_c) below 0.35 indicate either surface wash-off or depletion: surface wash-off refers to elements that are released from the surface of the CPB, while depletion involves the gradual removal of a component from the solid material by the leachant. A slope between 0.35 and 0.65 suggests that the release is controlled by diffusion due to concentration gradients. Slopes exceeding 0.65 indicate dissolution. The eluate fractions analyzed in periods 1 to 8 were divided into intervals long enough to determine the leaching mechanism. According to the standard (EA NEN 7375, 2004), increments 2-7 (the first increment) are considered as a “total increment” for the entire leaching test, while the first increment for a component is regarded as the “leaching mechanism determining increment” for that component. For all samples, surface wash-off was identified as the primary mechanism for arsenic, calcium, and sulfate leaching. Additionally, if the increment analysis shows that at least two of the increments 2-5, 3-6, 4-7, and/or 5-8 have r_c values below 0.35 and CF values above 1.5, depletion of the component may have occurred. These criteria were confirmed for all samples. As a summary, considering the relationship between the strength of CPB samples and the leaching of arsenic from these samples, it can be stated that strength and leaching are interconnected and influenced by key factors such as microstructural development, porosity reduction, and chemical stabilization. Higher strength in CPB samples indicates a well-developed microstructure with densely packed hydration products (e.g., calcium silicate hydrate (C-S-H), and, to a lesser extent, ettringite and portlandite). These phases encapsulate arsenic-bearing particles more effectively, reducing pathways for water ingress and arsenic leaching.

Strong CPB samples are more likely to chemically immobilize arsenic through adsorption or precipitation reactions, forming arsenic-bearing compounds. These compounds are less soluble and more resistant to leaching. In contrast, lower-strength CPB samples, with insufficient hydration or poor binder distribution, can lead to incomplete arsenic stabilization, increasing arsenic solubility and leachability. High-strength CPB samples are better able to maintain their integrity during the leaching process and are more likely to withstand environmental stresses (e.g., wet-dry and freeze-thaw cycles), thereby reducing arsenic leaching over the long term.

4.6 Characterisation of bonds within CPB

4.6.1 Thermogravimetric analysis

Two main samples, identified as GU-6-76-28 and GU-6.68-74-59, were selected for thermogravimetric analysis on parts that had not been subjected to leaching tests. The DTG and

TG curves shown in Figure 4.33 reveal four distinct temperature ranges characterized by significant weight loss and observable phase changes. The initial peak is observed between about 90 and 140 °C, followed by a second peak ranging from 500 to 650 °C. The final two prominent peaks are detected between 660 and 770 °C. Comparable findings have been documented in the literature, where researchers have examined the thermal characteristics of cemented paste backfills and tailings. Water loss from the interlayer and the dehydroxylation of C-S-H and ettringite typically happen over a wide temperature range, from approximately 50 to 600 °C (Yingliang Zhao, Qiu, et al., 2022).

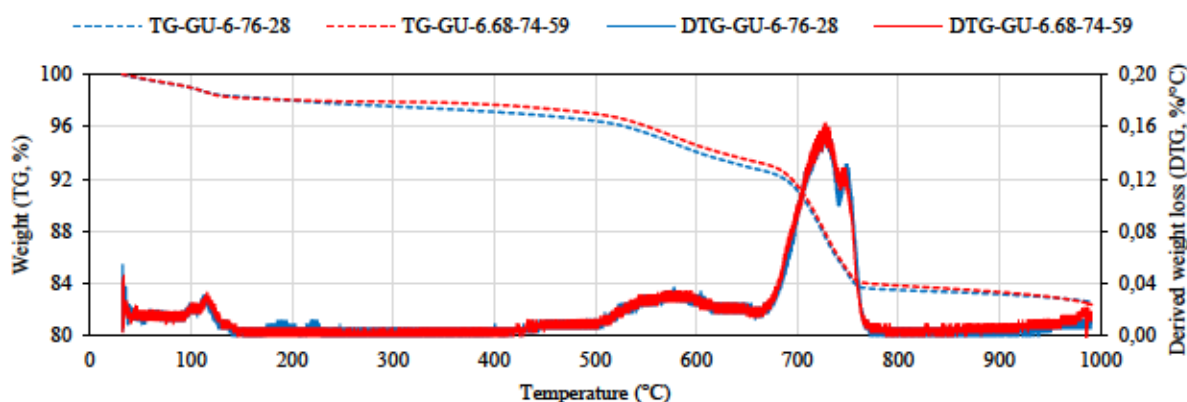


Figure 4.33 TG and DTG curves of two main CPB samples

The first peak, occurring between approximately 90 and 140 °C, along with the associated weight loss, is primarily due to the evaporation of free water and the dehydration of C-(A)-S-H gels, as well as possibly other hydrates such as ettringite and monosulfate (Q. Chen et al., 2022; Yingliang Zhao, Gu, et al., 2022; Yingliang Zhao, Qiu, et al., 2022). These hydrates were important in affecting the strength of CPB (H. Jiang, Fall, et al., 2019). This conclusion is based on previous findings by the authors, which showed that these samples contained small amounts of ettringite and gypsum. The next peak, observed between 500 and 650 °C, is likely associated with the dehydroxylation and decomposition of portlandite (Q. Chen et al., 2022; H. Jiang, Fall, et al., 2019). Other compounds may also decompose between 400 and 600 °C. For example, calcium hydroxide present in ettringite may also decompose, contributing to weight loss in this temperature range. Due to the presence of multiple hydrated phases, their overlapping weight loss can complicate interpretation. In contrast to CPBs studied earlier that did not contain arsenic trioxide, the paste samples with As_2O_3 had significantly lower pH values than 12, which is not optimal for portlandite

formation in cementitious mixtures. As a result, the amount of portlandite and ettringite in these samples, and therefore the related weight loss peak, is relatively minor.

The third peak, and possibly the fourth peak occurring between 660 and 770 °C, is likely attributed to the carbonization of calcite and the decomposition of carbonate phases, such as calcite, along with other carbonate-based secondary minerals that release CO₂ (Q. Chen et al., 2022; H. Jiang & Fall, 2017a; Yingliang Zhao, Qiu, et al., 2022). These peaks show the greatest intensity compared to others in these samples. Previous research has indicated that the first peak (C-S-H) and the second peak (CH) exhibit higher intensities in samples with greater strength, which is related to longer curing times and higher binder contents. It is important to note that both C-S-H phases and portlandite play a role in the strength of CPB samples. The lower intensities of these peaks suggest that these phases were either not extensively formed or were consumed during the hydration process. Additionally, in the current samples, there is no notable difference in the intensity of the second peak (CH decomposition), but the intensities of the third and fourth peaks are slightly higher in GU-6.68-74-59. This suggests that increasing the binder content did not lead to the formation of more portlandite, likely due to the presence of arsenic trioxide and the associated lower pH conditions. UCS test results (section 4.3.2) also show that the GU-6.68-74-59 sample (UCS = 472 kPa) had slightly lower strength compared to the GU-6-76-28 sample (UCS = 491 kPa). The additional binding agent in GU-6.68-74-59 may have contributed to the formation of a higher quantity of secondary minerals, potentially carbonate-based, which decomposed between 660 and 770 °C. These secondary minerals may have bound the arsenic, leading to reduced arsenic release during the leaching period.

4.6.2 FTIR analysis

Figure 4.34 presents the infrared spectra of GU-6-76-28 and GU-6.68-74-59. While the spectra for both samples exhibit nearly identical peaks, slight variations in normalized absorbance are noted, as shown in Table 4.19.

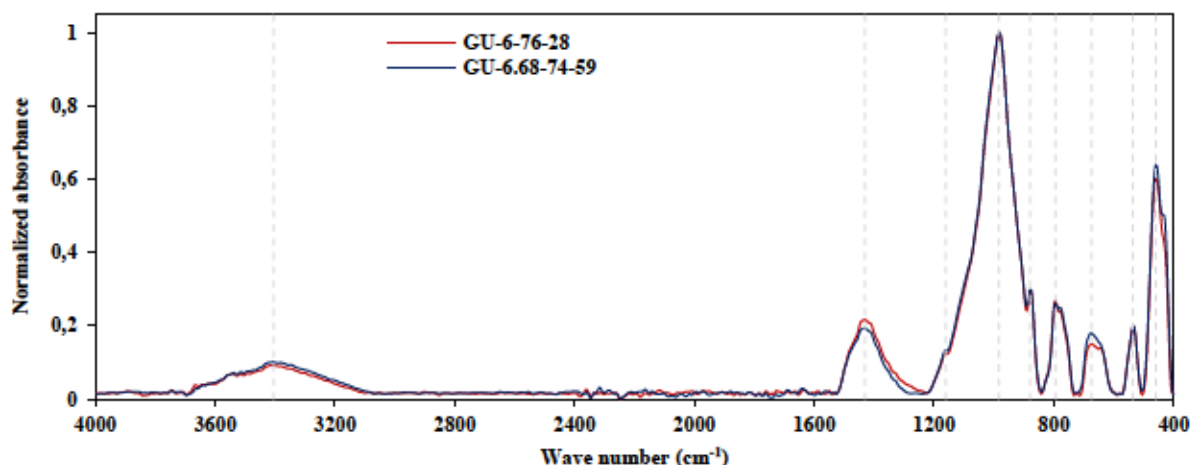


Figure 4.34 FTIR spectra of two CPB samples (dashed lines indicate positions of the observed peaks)

Table 4.19 The observed peaks and their corresponding normalized absorbances

Peak (cm ⁻¹)	459	536	675	795	880	984	1161	1431	3400
Normalized absorbance (GU-6-76-28)	0.601	0.199	0.150	0.269	0.295	1.000	0.123	0.217	0.092
Normalized absorbance (GU-6.68-74-59)	0.639	0.198	0.179	0.262	0.298	1.000	0.133	0.193	0.101

The two CPB samples displayed two main spectral peaks at approximately 459 cm⁻¹ and 984 cm⁻¹. The peak at 459 cm⁻¹ is associated with the in-plane bending vibrations of Si–O and Al–O bonds (C. Wang et al., 2023), while the peak at 984 cm⁻¹ corresponds to the asymmetric stretching vibrations of Si–O(Al) bonds (Y. Feng et al., 2023; F. Zhang et al., 2022). Additionally, a peak at 795 cm⁻¹ is attributed to the asymmetric stretching vibrations of Si–O(Al) in C-S-H gels (Y. Feng et al., 2023). Structural bands observed at 1161 cm⁻¹ and 1431 cm⁻¹ are linked to the asymmetric stretching vibrations of S–O in SO₄²⁻ and the symmetrical vibrations of O–C–O in CO₃²⁻, due to the carbonization of the sample in air (S. Chen, Du, Zhang, Yin, et al., 2020; F. Zhang et al., 2022), respectively. The broad band around 3400 cm⁻¹ is related to the asymmetric stretching vibrations of absorbed OH⁻ groups, indicative of weakly chemically bound water molecules, which may be surface adsorbed or trapped (Álvarez-Ayuso et al., 2008; Yingliang Zhao, Qiu, et al., 2022). In addition to these bands, two extra peaks were observed at approximately 536 cm⁻¹ and 880 cm⁻¹, which likely arise from the out-of-plane bending vibrations of Si–O–Si and CO₃²⁻, respectively (Y. Feng et al., 2023). Lastly, the peak at 675 cm⁻¹ is associated with the stretching vibration of SiO₂.

(Sun, Li, et al., 2020). The lack of a band around 1600 cm^{-1} indicates the unlikely presence of portlandite (O-H vibrations) in these samples (Yingliang Zhao, Wu, et al., 2022). Furthermore, vibrations related to the As-O bond in arsenate molecules are found in the ranges of $900\text{--}750\text{ cm}^{-1}$ and $500\text{--}400\text{ cm}^{-1}$ (Gomez et al., 2010). However, these interactions are relatively weak compared to other complexes and only slightly affect the intensities of the FTIR bands (Perez Mora et al., 2019). The differences between the two samples were minimal, with similar normalized absorbances and only minor variations. The most noticeable differences were observed in the bands at 459 cm^{-1} , 675 cm^{-1} , and 1431 cm^{-1} . Specifically, GU-6.68-74-59 showed higher normalized absorbance at the first two bands, but lower normalized absorbance at the last band.

4.6.3 XAS analysis

Four samples with different binder and solid contents—GU-4-76-28, GU-6-76-28, GU-6.68-74-59, and GU/LKD-6-76-28—were chosen for XAS analysis. The XANES absorption spectra for these samples, including CPB samples and reference compounds, are shown in the left panel of Figure 4.35. The white line, which represents the peak of intense absorption near the edge, was consistently located at 11870 eV for all samples, indicating that arsenic is mainly in the +3 oxidation state. However, a minor peak at 11874 eV suggests a small presence of As^{5+} . To refine the analysis, 3–4 reference materials were used in the linear combination fitting (LCF), with some being adjusted or excluded based on the Hamilton test (Downward et al., 2006). The LCF results showed that GU-6-76-28 and GU-6.68-74-59, as well as GU/LKD-6-76-28 and GU-4-76-28, displayed similarities. While the spectra could generally be fitted using the same reference spectra, the proportions differed. Additionally, differences between E-space and $\chi(k)$ space LCF within each sample suggested variations in local and extended structures.

The local structure of arsenic in GU-6-76-28 and GU-6.68-74-59 was best approximated by about 90% schneiderhohnite [$\text{Fe}^{2+}\text{Fe}^{3+}_3\text{As}^{3+}_5\text{O}_{13}$], while GU/LKD-6-76-28 and GU-4-76-28 were best represented by approximately 80% schneiderhohnite. The remaining portion in all samples was best described by arsenolite [$\text{As}^{3+}_2\text{O}_3$]. Although these references provided a good fit, this method alone may not conclusively identify all components. Both arsenolite and schneiderhohnite contain arsenite, and the white line energy further indicates that most of the arsenic in the samples is in the +3 oxidation state. The presence of schneiderhohnite suggests that As-Fe bonding might be significant in the local structure.

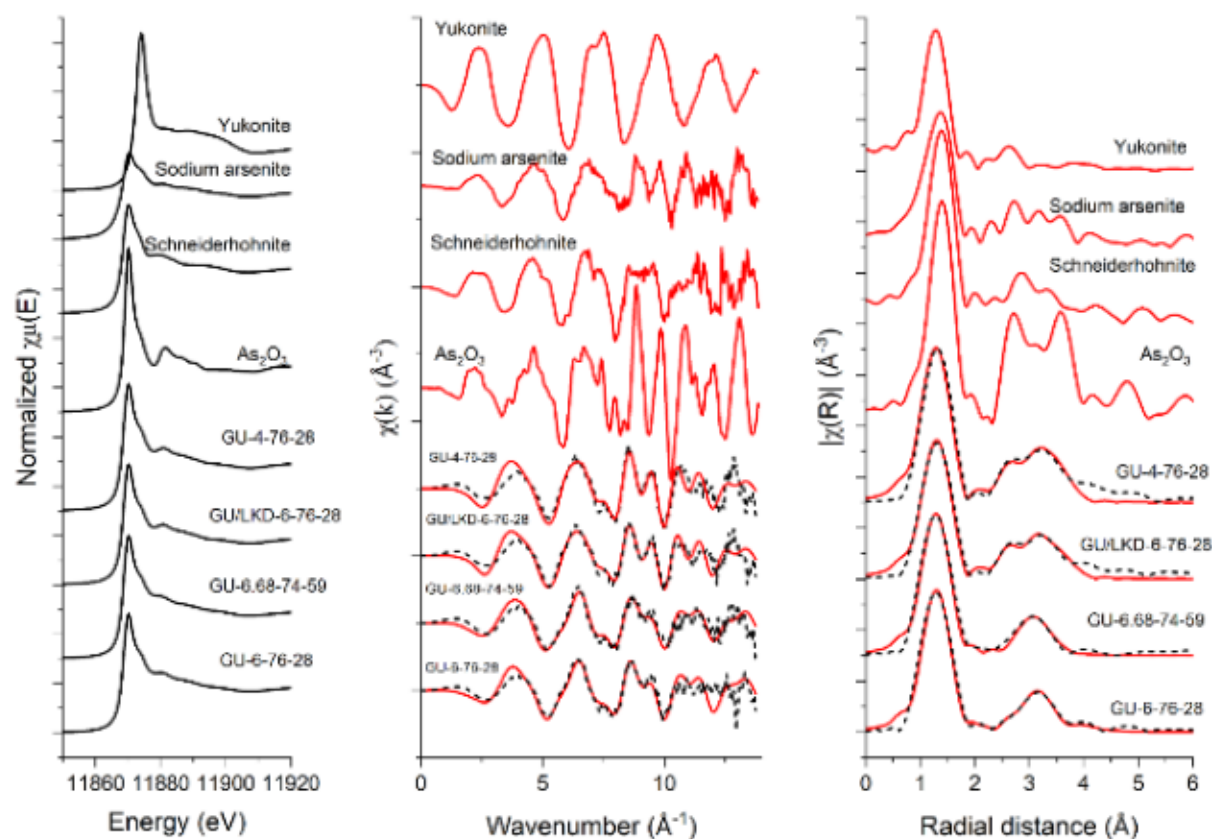


Figure 4.35 (a) Normalized As K-edge XANES spectra for four CPB samples and reference compounds; (b) Measured (solid red lines) and modelled (black dashed lines) $\chi(k)$ EXAFS spectra (c) Measured (solid red lines) and modelled (black dashed lines) magnitudes of Fourier transformed EXAFS spectra

In contrast, $\chi(k)$ space focuses on the EXAFS region, which provides information about the atomic neighbors surrounding the central arsenic atom. The LCF analysis revealed that approximately 12–15 weight percent of yukonite $[\text{Ca}_3\text{Fe}^{3+}(\text{AsO}_4)_2(\text{OH})_3 \cdot 5\text{H}_2\text{O}]$ was present in all samples. For GU-6-76-28 and GU-6.68-74-59, around 20% and 45% of arsenolite and schneiderhohnite were required, respectively, while GU-4-76-28 and GU/LKD-6-76-28 each needed about 40% arsenolite and schneiderhohnite. The presence of yukonite in the $\chi(k)$ LCF suggests that As-Ca bonding may also be significant. It is important to note that the reference materials used were select minerals and commercial compounds and do not cover all possible substances in the cement field. Therefore, additional EXAFS modeling was performed to provide a more accurate and detailed understanding of atomic interactions.

In the EXAFS region, all samples showed a first shell oxygen peak at approximately 1.78 Å, indicating that arsenic is coordinated with about 3–4 oxygen atoms. GU-6-76-28 and GU-6.68-74-

59 exhibited an As-As bond at around 3.55 Å, but GU-6-76-28 also required two additional As-Fe paths at distances of 3.37 Å and 4.65 Å for a precise fit. This suggests that in GU-6-76-28, arsenic remained bound to iron, implying that the ATRW remained largely intact without dissociating, and arsenic was not associated with other elements like calcium. ATRW is known to contain significant amounts of As-Fe compounds, with over 30 g/kg of iron. In contrast, arsenic in GU-6.68-74-59 may have leached out of the ATRW but remained isolated as an As-O based compound. This indicates a partial breakdown of the ATRW without any atomic integration into the paste mixtures. Although these two samples showed the highest UCS, no chemical bonds between arsenic and calcium were detected, suggesting that the hydration products responsible for the strength increase do not contain As-Ca compounds. Additionally, these products may not stabilize arsenic or reduce its leaching, despite achieving reasonable strength. For GU/LKD-6-76-28 and GU-4-76-28, which have lower strength, the modeling revealed As-Fe bonding at approximately 3.34 Å, As-Ca bonding at around 3.66 Å, and As-As bonding at 3.87 Å. This suggests that some As-Ca bonding may have occurred in these CPB samples. Although the original ATRW contains significant calcium (5.36 g/kg), no As-Ca bonds were observed in the initial ATRW, implying that any new As-Ca bonding observed might be a result of the hydration process. In other words, the formation of As-Ca bonds does not appear to have contributed to the strength gains or changes in porosity due to the hydration products.

4.7 Parallel extraction tests on synthetic CPB samples, ATRW dust and tailings of the Giant Mine

Parallel extractions were performed to evaluate the geochemical behavior and environmental mobility of different species in the tailings and ATRW dusts of the Giant Mine and CPBs. Table 4.20 presents variations in pH among the mixtures, including both blank and extracted solutions. Referring to this table, it can be noted that the dissolution of ATRW in all reagents except HCl resulted in a reduction in pH. This effect was most pronounced in DI water, followed by NaOH. In neutral and alkaline solutions (DI, NaOH, and Na-AscBicCit), the presence of binder in the CPB samples helped maintain higher pH levels compared to the other samples.

Figure 4.36 depicts the concentration of extracted arsenic for each extraction reagent. Samples containing ATRW showed the highest arsenic concentrations, followed by CPB samples. The amount of arsenic extracted from tailings was significantly lower than from other samples, possibly

due to the tailings' lower initial arsenic content. The results indicated that ATRW leached significantly more arsenic than CPB for all reagents, demonstrating the partial positive effect of cement on arsenic stabilization. The highest arsenic extraction (for both CPB and ATRW) was observed in $\text{NH}_2\text{OH.HCl}$ under highly acidic conditions, followed by NaOH (for ATRW) and Na-AscBicCit (for CPB). The lowest arsenic extraction was observed in HCl and NaOH solutions for ATRW and CPB samples, respectively.

Table 4.20 The pH of the solutions before and after extraction using different reagents

Sample	DI water	NaOH	Na-AscBicCit	HCl	$\text{NH}_2\text{OH.HCl}$
Blank solution	4.9	13.3	8.16	0.29	0.81
CPB	9.65	13.13	8.43	0.37	-0.52
ATRW	5.98	12.04	7.86	0.43	-0.53
Tailings	7.61	13.3	8.21	0.9	-0.45

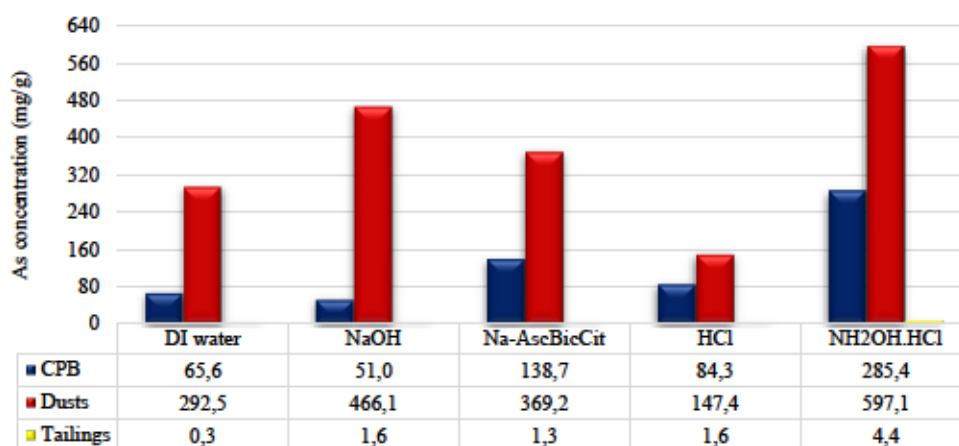


Figure 4.36 Arsenic leached during the parallel extraction experiment using various reagents

Table 4.21 displays the concentrations of each arsenic species (As^{+3} and As^{+5}) in the extracted solutions calculated from geochemical modeling with Visual Minteq 3.1. Arsenic was predominantly present as As^{+5} species, especially in the extracted arsenic from DI water, HCl , and NaOH reagents. Chemical analyses indicate that arsenic in the extracted waters existed in various compounds, including aluminum, calcium, and ferro-arsenates, as well as dissolved secondary minerals such as arsenolite, claudetite, and realgar, although in relatively small concentrations. Table 4.22 lists arsenic-containing minerals along with their saturation indices. A negative saturation index indicates undersaturation conditions, while a positive index indicates

oversaturation. Except for $\text{Ca}_3(\text{AsO}_4)_2 \cdot 4\text{H}_2\text{O}$ in DI and Na-AscBicCit solutions, the other minerals were found to be undersaturated. Geochemical modeling suggests that incorporating arsenic trioxide into cemented paste backfill reduces arsenic mobility. This is achieved by creating an alkaline environment through the addition of binding agents, as evidenced by the NaOH solution exhibiting the highest pH value and the lowest arsenic extraction from the CPB sample. The decrease in arsenic concentration following the DI extraction step is attributed to insoluble iron oxide phases, which may have adsorbed some arsenic during the CPB mixing and hydration process. As the leaching steps became more aggressive, these oxides became more soluble and released the adsorbed arsenic.

Table 4.21 Concentration of each arsenic species (As^{3+} and As^{5+}) in the extracted leachates using various reagents

Species/Reagent		DI	HCl	Na-AscBicCit	NaOH	$\text{NH}_2\text{OH.HCl}$
As (III) (mol/L)	H_3AsO_3	3.23E-19	1.81E-09	2.55E-04	1.82E-30	1.00E-02
	H_2AsO_3^-	1.20E-18	4.42E-18	7.39E-05	2.48E-26	3.21E-12
	HAsO_3^{2-}	7.67E-23	2.06E-31	3.11E-10	6.81E-27	8.15E-27
	Sum As (III)	1.52E-18	1.81E-09	3.28E-04	3.16E-26	1.00E-02
As (V) (mol/L)	H_3AsO_4	7.58E-13	1.11E-01	7.76E-10	6.13E-22	1.17E-01
	H_2AsO_4^-	2.09E-05	2.01E-03	1.67E-03	6.17E-11	2.77E-04
	HAsO_4^{2-}	1.72E-02	1.21E-09	9.04E-02	2.19E-04	9.04E-12
	AsO_4^{3-}	3.24E-04	2.07E-20	1.19E-04	2.25E-02	4.74E-24
	Sum As (V)	1.75E-02	1.13E-01	9.22E-02	2.27E-02	1.17E-01

Table 4.22 Various arsenic-containing minerals in the extracted solutions and their saturation indices based on geochemical modeling

Arsenic-containing mineral	Saturation index ($= \log IAP - \log K_s$)				
	DI	HCl	Na-AscBicCit	NaOH	$\text{NH}_2\text{OH.HCl}$
$\text{AlAsO}_4 \cdot 2\text{H}_2\text{O}$ (s)	-9.318	-8.327	-2.552	-19.4	-9.91
Arsenolite (As_2O_3)	-35.589	-15.97	-5.552	-58	-2.156
As_2O_5 (s)	-31.72	-9.274	-25.458	-49.8	-8.899
$\text{Ca}_3(\text{AsO}_4)_2 \cdot 4\text{H}_2\text{O}$ (s)	2.756	-27.566	2.001	-1.85	-31.556
Claudetite (As_2O_3)	-35.629	-16.01	-5.592	-58	-2.196
$\text{FeAsO}_4 \cdot 2\text{H}_2\text{O}$ (s)	-3.941	-4.355	-2.49	-17.7	-8.273

CHAPTER 5 DISCUSSIONS

In Chapter 4, the main results used to fulfill the research objectives were presented. In this chapter, the implications of the entire project's results for the stabilization of ATRW dust will be discussed, revisiting the initial hypothesis.

The primary objective of this study was to investigate the potential of incorporating ATRW into cemented paste backfill to stabilize water-soluble arsenic and prevent its release into the environment. The main hypothesis suggested that adding ATRW dust to CPB could securely stabilize the dust, ensuring mechanical stability for the stopes and minimizing arsenic leaching into nearby waters. While some studies explored the stabilization of arsenic compounds within CPB, the specific stabilization mechanisms of ATRW dust had not been previously investigated. Additionally, existing research on immobilizing ATRW dust from the Giant Mine had not thoroughly examined the application of CPB. Therefore, the specific objectives of this study were to:

- Identify the most effective binders and optimize their proportions for the long-term stabilization of ATRW dust.
- Optimize the content of dust and tailings within the CPB samples.
- Elucidate the arsenic speciation and stabilization mechanisms occurring during the cement hardening and curing processes, and their impacts on leaching properties.

In addition to these objectives, preliminary studies were conducted to assess the interaction mechanisms of pure arsenic trioxide in cement mixtures in the absence of impurities, aiming to reduce the number of influencing parameters on the mechanical and geochemical behavior of arsenic trioxide. Below, a comprehensive discussion of the results is presented, focusing on their implications, underlying mechanisms, and relevance to the broader context of the study.

- Performance of binding agents

Among the five binding agents used in this study, pure (100%) GU cement demonstrated the best performance in providing the necessary strength for the CPB samples.

Impact of ATRW on Cement Reactions: The addition of ATRW to cement mixtures altered geochemical conditions by lowering the pH, which is critical for the dissolution and hydration of cement constituents. A high pH environment (above 12) is crucial for the dissolution of cement

constituents, which then react to form hydration products such as C-S-H gels, portlandite, and ettringite. Maintaining this high pH environment helps stabilize the primary hydration products (especially C-S-H), which is the main strength-giving phase in hardened CPB. Additionally, a high pH environment promotes the formation of denser and more refined microstructures, enhancing long-term strength and resistance to aggressive environments (e.g., sulfate attack, salinity).

Limitations of lower pH: Lower pH environment reduces the dissolution rate of binders and the formation and stabilization of hydration products, particularly portlandite, which precipitates at high pH and maintains the alkaline medium over time. Some binders, like slag, are less reactive than cement and require a high pH environment to hydrate effectively.

- Utilization of Supplementary Cementitious Materials (SCMs)

Other binding agents, such as FA and LKD, were partially used as supplementary cementitious materials (SCM) to replace GU cement, aiming to reuse byproduct materials, reduce process costs, and lower CO₂ emissions. These materials, along with lime, were also intended to provide and maintain alkaline conditions in the ATRW-containing CPB. However, these materials proved ineffective in maintaining the required conditions for ATRW-containing CPB.

- Strength and Deformation Behavior

Strength performance: Samples containing ATRW showed relatively favorable strength compared to ATRW-free samples, depending on the mine site's specific requirements. At Giant Mine, minimal strength (100 kPa) was required due to the inactive operation, yet arsenic leaching was a critical limitation.

Ductility and cracking: The addition of ATRW to CPB altered its deformation behavior from brittle to ductile. This more ductile behavior, along with higher strain at break, led to the formation of additional cracks and voids in the samples, which reduced the overall strength of the CPB.

- Cement Hydration and Pore Refinement

Cement hydration involves a chemical reaction between cement and water, producing hydration products such as calcium silicate hydrate (C-S-H), portlandite (Ca(OH)₂), and calcium sulfoaluminate hydrates (ettringite/monosulfate) (Soto-Pérez et al., 2015). However, in ATRW-containing CPBs, slight cement hydration occurred, but not as much as expected, and this could explain the low strength in the As-enriched CPB. Very low amount of ettringite and portlandite were observed within these samples because of the low amount of sulfur in the samples and low pH of the mixtures. For the As₂O₃-cement mixtures, the observations show some interactions

between As_2O_3 and cement, but many As_2O_3 grains remained intact. The main species identified were C-S-H gels, As-Ca-Si-Al oxides or As-Ca-Al-Si oxides.

In CPBs containing ATRW, additional materials such as secondary arsenic-containing minerals and C-S-H gels may form. These arise from the dissolution of cement particles and their reaction with arsenic trioxide in the presence of water, resulting in the formation of arsenic-containing hydration products. However, these newly formed materials may not completely occupy the pore spaces, especially when the paste sets rapidly due to the use of GU as the binder in the presence of ATRW dust. In such cases, the hydration process of cement slows down or stops abruptly. As a result, larger pores cannot be further filled by hydration products, leading to stabilization of the pore structure within the CPB (Huan et al., 2021).

- Impact of Drainage

Although CPB must contain adequate water to achieve the desired consistency for transport from the paste plant to the underground openings, an increase in the water to cement ratio has an adverse effect on CPB strength and stability (Ercikdi et al., 2010; Ercikdi, Kesimal, et al., 2009). In this study, it seems that the drainage could not help strength improvement, mainly because of the rapid reaction of the GU cement and significantly low drainage from the pastes. As mentioned in Chapter 4, the sample with drained water (CPB-5%), showed the lowest UCS.

- Arsenic Leaching

Mechanisms: The key determinant for adopting cemented paste backfill technology for ATRW management was the potential leaching of arsenic from the stabilized form. Despite acceptable strength data for samples made with 100% GU cement, the critical factor was the concentration of arsenic leaching. The leaching of arsenic from CPBs containing ATRW was significant and deemed unacceptable. The leaching mechanism was found to be due to surface wash-off and the depletion of arsenic from CPB samples.

Despite the low sulfur contents in the tailings and ATRW (0.52% and 0.25%, respectively) and the minimum possibility of sulfuric acid generation, the dissolution of arsenic trioxide and the formation of weak arsenious acid were the main reactions responsible for the leachate pH drop to below 10 during CPB formation and curing (Mohammadi, Demers, Benzaazoua, et al., 2023a). Additionally, the initially low pH of the leachates indicates a limited presence of portlandite, suggesting that the primary dissolved phases are likely C-S-H (Coussy et al., 2011).

The reduced leaching rates of As, Ca, and SO_4^{2-} in high UCS samples can be attributed to the formation of reaction gels, which led to a denser matrix with increased compressive strength. This mechanical strength contributed to the immobilization of these elements; samples with greater strength were better able to maintain their integrity during leaching, thereby limiting the release of As, Ca, and SO_4^{2-} .

Mitigation strategies: Although arsenic leaching did not reach a plateau and might continue beyond the 64-day period, the decrease in leached arsenic after 36 days (as shown in Figure 4.29) across all CPB samples suggests that the rate of arsenic release slowed due to reduced availability at the CPB matrix-leaching solution interface. This implies that the available arsenic, calcium, and other components on the exposed surfaces were already transferred into the solution. To effectively reduce arsenic release, it would be beneficial to minimize the exposed surfaces by creating a dense paste with minimal porosity and cracks. Increasing binder content could be a viable strategy, as observed in this study where the addition of less than 1% (0.68%) of binder decreased arsenic release by up to 9% (as shown in Figure 4.31). Alternative methods to reduce arsenic release include lowering arsenic solubility by oxidizing As(III) to As(V), converting arsenic trioxide to arsenic sulfide (which is 10,000 times less soluble), transforming ATRW into stable glass (vitrification), or converting ATRW into iron-arsenic solids ((GMOB), 2023). These transformed materials could be incorporated into CPB to further reduce environmental exposure.

- **Microstructure and Density**

Considering the visual differences observed among the samples, a distinct contrast is evident in the distribution of high-density materials within the ROIs, similar to the full CPB core. Particularly notable is the GU-6-76-28 sample, which exhibits the highest UCS; here, there is a significantly higher concentration of high-density materials compared to the other samples. Conversely, in samples with lower strength, high-density materials are predominantly dispersed randomly as individual particles. In contrast, in high-strength samples, specifically GU-6-76-28, these materials are arranged in a continuous pattern. Therefore, it can be inferred that the formation and random dispersion of these high-density materials containing arsenic during the hydration and curing processes likely contribute significantly to the enhanced strength observed in these CPB samples. However, the distinct pore characteristics of these samples, characterized by larger and more irregular pores, resulted in increased arsenic release during leaching process (section 4.5).

- **Key Implications for ATRW Management**

In summary, the results of this study suggest that incorporating ATRW dust into CPB appeared to be a feasible management option initially. This is supported by the acceptable mechanical strength observed in ATRW-containing CPB samples. However, leaching and microstructural analyses indicate that the interaction between arsenic and other CPB components (especially calcium) does not lead to strong stabilization of arsenic or a significant reduction in its leaching behavior. Nevertheless, the positive combined effects of binder and solid percentages in CPB samples contributed to maintaining sample integrity and reducing arsenic leaching rates.

CHAPTER 6 CONCLUSIONS AND RECOMMENDATIONS

6.1 Conclusions

The main objective of this study was to evaluate the feasibility of stabilizing ATRW dust within the cemented paste backfill. This study enhanced the understanding of the effects of arsenic trioxide (both pure and from roaster waste) on the geomechanical, geochemical, and microstructural behavior of cemented paste backfills. This was achieved by evaluating potential binding agents and their optimal content, the applicable ATRW dust content, the leaching behavior of ATRW-containing CPB samples, and the effects of ATRW on the microstructure of CPB samples. At first, initial characterization analyses and preliminary tests were conducted, after which CPB samples were prepared with various amounts of pure As_2O_3 , GU cement, and pure silica to study the strength and stability of CPB samples containing pure As_2O_3 . Additionally, As_2O_3 -cement mixtures were prepared to investigate the geochemical behavior of these mixtures and evaluate potential reactions, particularly arsenic release, with other elements in cementitious matrices. Microstructural characterization was performed using SEM analysis to observe the microstructure of As_2O_3 -containing CPB and cementitious mixtures. The results were presented in the first article (Section 4.2.2 and Appendix B).

Based on the results of this part of the study, the following conclusions were drawn:

- The addition of pure arsenic trioxide significantly decreased the UCS of the CPB samples, primarily due to the drop in pH and likely due to hardening inhibition during the early curing stage. The pH of the arsenic-containing pastes dropped below 10.5, which delayed and inhibited the hydration of the cement in the CPB structure. However, some increases in the strength of CPB samples with higher As_2O_3 content were observed, possibly due to microstructure refinement from the formation of secondary minerals and C-S-H gels.
- The As_2O_3 -containing CPB samples primarily gained their strength in the initial days of curing, with only a slight increase in strength observed after 7 days. These samples exhibited more ductile failure modes, whereas the mechanical behavior of the samples without arsenic trioxide was more brittle.
- The chemical analysis of As_2O_3 -cement mixtures demonstrated that the dissolution of arsenic in cementitious matrices and the formation of arsenious acid cause a reduction in pH.

- SEM observations identified oxide phases containing various percentages of Si, Al, Ca, and As. A small proportion of mineral phases containing As, Ca, and Si were observed as potentially stabilized species.

The second phase of the study involved the preparation and testing of CPB with real mine tailings and ATRW. The effect of pH reduction observed in the first phase was evaluated, and measures were considered to potentially mitigate it. The main objective was to assess the behavior of CPB incorporating ATRW into Giant Mine tailings for arsenic physical and chemical stabilization. Preliminary CPB samples were prepared using four binding agents and various ATRW contents to identify the most effective binders and optimal ATRW content.

The CPB samples were prepared by incorporating 10% wt. of ATRW into Giant Mine tailings as the solid matrix, using GU cement and a mixture of GU and LKD as binders. To better understand the effects of binder content, solid content, and curing time as independent variables, two response functions (for GU and GU/LKD binders) were formulated as second-order polynomials, and the impacts of each parameter were assessed using ANOVA. Optimal conditions were identified, and saturated hydraulic conductivity and computed tomography tests were conducted on selected samples to relate the microstructure of the CPB samples to their strength.

The findings of this investigation are presented in Article 2 (Section 4.3.2 and Appendix C), with the following conclusions derived:

- CPB samples prepared with GU cement exhibited significantly greater strength compared to those prepared using a 50/50 mixture of GU and LKD.
- A three-factor central composite design was employed to model the UCS of CPB containing ATRW. Binder content and solid content exhibited the highest significance, while the effect of curing time was deemed non-significant. Optimal mix designs (6% binder, 76% solids at various curing times) were determined using the modeled relationship and validated by comparing predicted and measured UCS values.
- CPB samples with higher binder content and greater solid content displayed increased strength, with binder content exerting a more pronounced influence. The addition of 10% wt. ATRW reduced the UCS of CPB samples by more than 30%, particularly in samples with lower binder and solid contents.

- Microstructure differences were not observable through saturated hydraulic conductivity experiments. There were no significant differences in the saturated hydraulic conductivity of CPB samples with the highest UCS when comparing GU samples with and without ATRW. However, CT scan observations indicated that the formation of high-density arsenic-containing materials was significantly greater in samples with the highest UCS, especially those prepared using GU binder. Additionally, these samples exhibited greater pore volumes. Samples with the highest UCS exhibited a significant reduction in the presence of spherical and semi-spherical pores.

Overall, the study demonstrated that incorporating ATRW into cemented paste backfill CPB is a viable option for physically stabilizing ATRW at the Giant Mine site. The CPB samples tested in the laboratory exhibited sufficient strength to meet the site's minimal requirements. However, for a comprehensive solution, further investigation into the chemical stabilization of arsenic was necessary to fully address the inclusion of ATRW in CPB.

Therefore, in the next and final phase of this study, the stability of arsenic-bearing compounds formed within CPB cementitious matrices and the mechanisms of arsenic release from CPB samples were investigated. Based on UCS test results conducted in previous phases of the study, specific samples were chosen for monolithic tank leaching tests to evaluate the behavior and stability of arsenic in CPBs under dynamic conditions. Additionally, the microstructure of selected CPBs was analyzed using TGA, FTIR, XAS to explore the relationship between microstructure and leachability. The findings from this phase of the study were presented in the third article (Sections 4.4 to 4.6 and Appendix D), and the conclusions drawn from this investigation are as follows:

- The TLT selected samples included both high-strength and mid-strength samples. However, only the high-strength samples (GU-6-76-28 and GU-6.68-74-59) successfully endured the entire leaching process, while the mid-strength samples disintegrated before the process was complete.
- The pH of the leachates collected during TLT was below 10, indicating that the dissolution of ATRW lowered the paste's pH. For GU-6-76-28 samples, changes in the levels of arsenic, calcium, and sulfate (SO_4^{2-}) appeared to be pH-dependent. However, for GU-6.68-74-59 samples, these changes did not correspond with pH variations. The electrical

conductivity (EC) of all leachates was very low due to the negligible concentrations of ions other than calcium.

- The leaching of arsenic, calcium, and sulfate did not stabilize and could continue beyond the 64-day leaching period. Additionally, the primary leaching mechanism for arsenic in the CPB samples was identified as surface wash-off, with some contribution from depletion.
- Thermogravimetric analysis indicated that the formation of C-S-H gels and portlandite was minimal in ATRW-containing CPBs. The primary weight loss observed was mainly due to the carbonization of calcite and the decomposition of carbonate phases.
- XAS analysis showed that the high-strength samples exhibited consistent behavior, with no chemical bonding observed between arsenic and other elements, particularly calcium. This suggests that the hydration process and subsequent strength gain in these samples did not result in arsenic stabilization through the formation of As-Ca compounds. In contrast, some As-Ca bonding was observed in the lower-strength samples, but it did not lead to strength gain or arsenic stabilization.
- Incorporating ATRW as a partial replacement for tailings in CPBs may provide adequate strength and meet on-site requirements. However, the leaching of arsenic from CPBs containing ATRW could be significant and considered unacceptable.

6.2 Recommendations for future works

Based on the findings outlined in this thesis, suggestions for further studies focusing on integrating ATRW dust into CPB can be proposed:

Given the northern location of Giant Mine, concerns arise regarding discontinuous permafrost and ongoing ground freezing, which can impact the strength of CPBs. These conditions often lead to freeze-thaw cycles known to diminish the strength of cementitious materials. Researchers at the University of Alberta will investigate the freeze-thaw durability of CPBs by subjecting samples to freeze-thaw cycles and prolonged curing under various temperatures (-10°C, 5°C, and room temperature). The primary goals are to evaluate the effects of these conditions on CPB strength, chemical stability, hydration, and fracture patterns, and to assess particle dispersion and porosity changes using Micro CT scans.

As discussed in section 4.6, modifying ATRW before incorporation into CPBs to decrease its exposure to leaching solutions represents the most effective strategy for reducing arsenic leachability from CPB samples. Hence, investigating the feasibility of modifying ATRW to transform it into a less soluble and less toxic material before its incorporation into CPB is suggested. Additives to rapidly neutralise arsenious acid could also be investigated.

In this study, CPB preparation utilized DI water, yet the impact of chemical constituents presents in real water sources, such as processed or fresh water, merits consideration. Water impurities can disrupt the hydration process of cement, potentially delaying or preventing the formation of strong cementitious bonds. Impurities can also impact the rheological properties, geochemical behavior, and microstructure of CPBs.

Another critical aspect to address is the use of only 10% ATRW in CPB sample preparation. Exploring the feasibility of increasing this percentage to decrease backfill volume and utilize more ATRW is an important aspect for further investigation.

Under conditions of high binder and solid contents, which are optimal, there is a significant decrease in sample fluidity and workability, with the paste beginning to set rapidly - a concern that could potentially be mitigated with specific additives like plasticizers. The applicability of these supplementary materials could be studied.

The use of alkali-activated slags (AAS) as binding agents for stabilizing ATRW dust was not explored in this project. However, these binders have the capability to partially or completely replace GU cement, encapsulating contaminants and reducing leachability while enhancing durability.

REFERENCES

- (GMOB), G. M. O. B. (2021). *Giant Mine Oversight Board Research Program Summary Report*.
1.
- (GMOB), G. M. O. B. (2023). *Research program report* (Issue November).
- Abdul-Hussain, N., & Fall, M. (2011). Unsaturated hydraulic properties of cemented tailings backfill that contains sodium silicate. *Engineering Geology*, 123(4), 288–301. <https://doi.org/10.1016/j.enggeo.2011.07.011>
- Ait-khouia, Y., Benzaazoua, M., Elghali, A., Chopard, A., & Demers, I. (2022). Feasibility of reprocessing gold tailings: Integrated management approach for the control of contaminated neutral mine drainage. *Minerals Engineering*, 187(May). <https://doi.org/10.1016/j.mineng.2022.107821>
- Aldhafeeri, Z. (2018). *Reactivity of Cemented Paste Backfill*.
- Alqadi, A. N. S., Mustapha, K. N. Bin, Naganathan, S., & Al-Kadi, Q. N. S. (2012). Uses of central composite design and surface response to evaluate the influence of constituent materials on fresh and hardened properties of self-compacting concrete. *KSCE Journal of Civil Engineering*, 16(3), 407–416. <https://doi.org/10.1007/s12205-012-1308-z>
- Álvarez-Ayuso, E., & Murciego, A. (2021). Stabilization methods for the treatment of weathered arsenopyrite mine wastes: Arsenic immobilization under selective leaching conditions. *Journal of Cleaner Production*, 283. <https://doi.org/10.1016/j.jclepro.2020.125265>
- Álvarez-Ayuso, E., Querol, X., Plana, F., Alastuey, A., Moreno, N., Izquierdo, M., Font, O., Moreno, T., Diez, S., Vázquez, E., & Barra, M. (2008). Environmental, physical and structural characterisation of geopolymer matrixes synthesised from coal (co-)combustion fly ashes. *Journal of Hazardous Materials*, 154(1–3), 175–183. <https://doi.org/10.1016/j.jhazmat.2007.10.008>
- Amirbahman, A., Schönenberger, R., Johnson, C. A., & Sigg, L. (1998). Aqueous- and solid-phase biogeochemistry of a calcareous aquifer system downgradient from a municipal solid waste landfill (Winterthur, Switzerland). *Environmental Science and Technology*, 32(13), 1933–1940. <https://doi.org/10.1021/es970810j>

- Antony, J. (2014). 6 - Full Factorial Designs. In J. Antony (Ed.), *Design of Experiments for Engineers and Scientists (Second Edition)* (Second Edi, pp. 63–85). Elsevier. <https://doi.org/https://doi.org/10.1016/B978-0-08-099417-8.00006-7>
- Arcadis. (2017). *Giant Mine State of Knowledge Review: Arsenic Dust Management Strategies* (Issue August).
- ASTM. (2015). ASTM C143/C143M-12 Standard Test Method for Slump of Hydraulic-Cement Concrete. *Annual Book of ASTM Standards*, 1–4. https://doi.org/10.1520/C0143_C0143M-12
- ASTM. (2016). ASTM D5084-16a Standard Test Methods for Measurement of Hydraulic Conductivity of Saturated Porous Materials Using a Flexible Wall Permeameter. *Annual Book of ASTM Standards*.
- ASTM. (2021). ASTM C39/C39M-21 Standard Test Method for Compressive Strength of Cylindrical Concrete Specimens. *Annual Book of ASTM Standards*, 04.02, 1–8. https://doi.org/10.1520/C0039_C0039M-21
- Barger, G. S., Bayles, J., Blair, B., Brown, D., Chen, H., Conway, T., & Hawkins, P. (2001). Ettringite Formation and the Performance of Concrete. In *Portland Cement Association* (Issue 2166).
- Baur, I., & Johnson, C. A. (2003). The solubility of selenate-Aft ($3\text{CaO}\cdot\text{Al}_2\text{O}_3\cdot 3\text{CaSeO}_4\cdot 37.5\text{H}_2\text{O}$) and selenate-AFm ($3\text{CaO}\cdot\text{Al}_2\text{O}_3\cdot\text{CaSeO}_4\cdot x\text{H}_2\text{O}$). *Cement and Concrete Research*, 33(11), 1741–1748. [https://doi.org/https://doi.org/10.1016/S0008-8846\(03\)00151-0](https://doi.org/https://doi.org/10.1016/S0008-8846(03)00151-0)
- Behera, S. K., Meena, H., Chakraborty, S., & Meikap, B. C. (2018). Application of response surface methodology (RSM) for optimization of leaching parameters for ash reduction from low-grade coal. *International Journal of Mining Science and Technology*, 28(4), 621–629. <https://doi.org/https://doi.org/10.1016/j.ijmst.2018.04.014>
- Belem, T., & Benzaazoua, M. (2008). Design and application of underground mine paste backfill technology. *Geotechnical and Geological Engineering*, 26(2), 147–174. <https://doi.org/10.1007/s10706-007-9154-3>
- Belem, T., Benzaazoua, M., & Bussi re, B. (2000). Mechanical behaviour of cemented paste backfill. *Proceedings of 53rd Canadian Geotechnical Conference*, 1(February 2016), 373–

380. [http://web2.uqat.ca/gnm1002/Cours#8_mecanique des remblais \(geotech\)/PaperConfCanadianGeotech2000.pdf](http://web2.uqat.ca/gnm1002/Cours#8_mecanique_des_remblais_(geotech)/PaperConfCanadianGeotech2000.pdf)
- Belem, T., Bussi re, B., & Benzaazoua, M. (2001). The effect of microstructural evolution on the physical properties of paste Backfill. *Proceedings Tailings and Mine Waste 01*.
- Belem, T., Peyronnard, O., & Benzaazoua, M. (2010). *A model of formulation of blended binders for use in cemented mine backfills*. 433–447. https://doi.org/10.36487/acg_rep/1008_36_belem
- Benzaazoua, M., Belem, T., & Bussi re, B. (2002). Chemical factors that influence the performance of mine sulphidic paste backfill. *Cement and Concrete Research*, 32(7), 1133–1144. [https://doi.org/10.1016/S0008-8846\(02\)00752-4](https://doi.org/10.1016/S0008-8846(02)00752-4)
- Benzaazoua, M., Bussi re, B., Demers, I., Aubertin, M., Fried,  .E., & Blier, A. (2008). Integrated mine tailings management by combining environmental desulphurization and cemented paste backfill: Application to mine Doyon, Quebec, Canada. *Minerals Engineering*, 21(4), 330–340. <https://doi.org/10.1016/j.mineng.2007.11.012>
- Benzaazoua, M., Fall, M., & Belem, T. (2004). A contribution to understanding the hardening process of cemented pastefill. *Minerals Engineering*, 17(2), 141–152. <https://doi.org/10.1016/j.mineng.2003.10.022>
- Benzaazoua, M., Marion, P., Picquet, I., & Bussi re, B. (2004). The use of pastefill as a solidification and stabilization process for the control of acid mine drainage. *Minerals Engineering*, 17(2), 233–243. <https://doi.org/10.1016/j.mineng.2003.10.027>
- Benzaazoua, M., Peyronnard, O., Belem, T., Stephant, A., & Dublet, G. (2010). Key issues related to behaviour of binders in cemented paste backfilling. *Proceedings of the Thirteenth International Seminar on Paste and Thickened Tailings*, 345–363. https://doi.org/10.36487/acg_rep/1063_30_benazzaoua
- Benzaazoua, M., Quellet, J., Servant, S., Newman, P., & Verburg, R. (1999). Cementitious backfill with high sulfur content physical, chemical, and mineralogical characterization. *Cement and Concrete Research*, 29(5), 719–725. [https://doi.org/10.1016/S0008-8846\(99\)00023-X](https://doi.org/10.1016/S0008-8846(99)00023-X)
- Bharatkumar, B. H., Narayanan, R., Raghuprasad, B. K., & Ramachandramurthy, D. S. (2001). Mix proportioning of high performance concrete. *Cement and Concrete Composites*, 23(1),

71–80. [https://doi.org/10.1016/S0958-9465\(00\)00071-8](https://doi.org/10.1016/S0958-9465(00)00071-8)

- Blanchard, P. E. R., Van Loon, L. L., Reid, J. W., Cutler, J. N., Rowson, J., Hughes, K. A., Brown, C. B., Mahoney, J. J., Xu, L., Bohan, M., & Demopoulos, G. P. (2017). Investigating arsenic speciation in the JEB Tailings Management Facility at McClean Lake, Saskatchewan using X-ray absorption spectroscopy. *Chemical Geology*, 466(August 2016), 617–626. <https://doi.org/10.1016/j.chemgeo.2017.07.014>
- Brackebusch, F. W. (1995). Basics of paste backfill systems. *International Journal of Rock Mechanics and Mining Sciences and Geomechanics Abstracts*, 32(3), 122A.
- Bromstad, M. J., Wrye, L. A., & Jamieson, H. E. (2017a). The characterization, mobility, and persistence of roaster-derived arsenic in soils at Giant Mine, NWT. *Applied Geochemistry*, 82, 102–118. <https://doi.org/10.1016/j.apgeochem.2017.04.004>
- Bromstad, M. J., Wrye, L. A., & Jamieson, H. E. (2017b). The characterization, mobility, and persistence of roaster-derived arsenic in soils at Giant Mine, NWT. *Applied Geochemistry*, 82, 102–118. <https://doi.org/https://doi.org/10.1016/j.apgeochem.2017.04.004>
- Büchler, P., Hanna, R. A., Akhter, H., Cartledge, F. K., & Tittlebaum, M. E. (1996a). Solidification/stabilization of arsenic: Effects of arsenic speciation. *Journal of Environmental Science and Health - Part A Toxic/Hazardous Substances and Environmental Engineering*, 31(4), 747–754. <https://doi.org/10.1080/10934529609376385>
- Büchler, P., Hanna, R. A., Akhter, H., Cartledge, F. K., & Tittlebaum, M. E. (1996b). Solidification/stabilization of arsenic: Effects of arsenic speciation. *Journal of Environmental Science and Health . Part A: Environmental Science and Engineering and Toxicology*, 31(4), 747–754. <https://doi.org/10.1080/10934529609376385>
- Bull, A. J. (2019). Temperature dependence of the reactivity of cemented paste backfill [University of Ottawa]. In *Faculty of Engineering, University of Ottawa*. <https://doi.org/10.1016/j.apgeochem.2016.06.005>
- Bull, A. J., & Fall, M. (2020a). Curing temperature dependency of the release of arsenic from cemented paste backfill made with Portland cement. *Journal of Environmental Management*, 269(March), 110772. <https://doi.org/10.1016/j.jenvman.2020.110772>
- Bull, A. J., & Fall, M. (2020b). Thermally induced changes in metalloid leachability of cemented

- paste backfill that contains blast furnace slag. *Minerals Engineering*, 156(April), 106520. <https://doi.org/10.1016/j.mineng.2020.106520>
- Camacho, J., Wee, H.-Y., Kramer, T. A., & Autenrieth, R. (2009a). Arsenic stabilization on water treatment residuals by calcium addition. *Journal of Hazardous Materials*, 165(1), 599–603. <https://doi.org/https://doi.org/10.1016/j.jhazmat.2008.10.038>
- Camacho, J., Wee, H. Y., Kramer, T. A., & Autenrieth, R. (2009b). Arsenic stabilization on water treatment residuals by calcium addition. *Journal of Hazardous Materials*, 165(1–3), 599–603. <https://doi.org/10.1016/j.jhazmat.2008.10.038>
- Cao, S., Song, W., & Yilmaz, E. (2018). Influence of structural factors on uniaxial compressive strength of cemented tailings backfill. *Construction and Building Materials*, 174, 190–201. <https://doi.org/10.1016/j.conbuildmat.2018.04.126>
- Cesbron, F. (2001). Minéralogie des composés oxydés de l'arsenic et leur stabilité dans le milieu supergène. *Les Techniques de l'industrie Minérale*, 11, 41–50.
- Chai, L., Yang, J., Zhang, N., Wu, P.-J., Li, Q., Wang, Q., Liu, H., & Yi, H. (2017). Structure and spectroscopic study of aqueous Fe(III)-As(V) complexes using UV-Vis, XAS and DFT-TDDFT. *Chemosphere*, 182, 595–604. <https://doi.org/https://doi.org/10.1016/j.chemosphere.2017.05.018>
- Chang, S. (2016). *Strength and Deformation Behaviour of Cemented Paste Backfill in Sub-Zero Environment*.
- Chen, Q., Tao, Y., Zhang, Q., & Qi, C. (2022). The rheological, mechanical and heavy metal leaching properties of cemented paste backfill under the influence of anionic polyacrylamide. *Chemosphere*, 286(P1), 131630. <https://doi.org/10.1016/j.chemosphere.2021.131630>
- Chen, Q., Zhang, Q., Fourie, A., & Xin, C. (2017). Utilization of phosphogypsum and phosphate tailings for cemented paste backfill. *Journal of Environmental Management*, 201, 19–27. <https://doi.org/10.1016/j.jenvman.2017.06.027>
- Chen, Q., Zhang, Q. li, Fourie, A., Chen, X., & Qi, C. (2017). Experimental investigation on the strength characteristics of cement paste backfill in a similar stope model and its mechanism. *Construction and Building Materials*, 154, 34–43. <https://doi.org/10.1016/j.conbuildmat.2017.07.142>

- Chen, S., Du, Z., Zhang, Z., Yin, D., Feng, F., & Ma, J. (2020). Effects of red mud additions on gangue-cemented paste backfill properties. *Powder Technology*, 367, 833–840. <https://doi.org/https://doi.org/10.1016/j.powtec.2020.03.055>
- Chen, S., Du, Z., Zhang, Z., Zhang, H., Xia, Z., & Feng, F. (2020). Effects of chloride on the early mechanical properties and microstructure of gangue-cemented paste backfill. *Construction and Building Materials*, 235, 117504. <https://doi.org/10.1016/j.conbuildmat.2019.117504>
- Chen, X., Shi, X., Zhou, J., Chen, Q., Li, E., & Du, X. (2018). Compressive behavior and microstructural properties of tailings polypropylene fibre-reinforced cemented paste backfill. *Construction and Building Materials*, 190, 211–221. <https://doi.org/10.1016/j.conbuildmat.2018.09.092>
- Chen, X., Shi, X., Zhou, J., Du, X., Chen, Q., & Qiu, X. (2019). Effect of overflow tailings properties on cemented paste backfill. *Journal of Environmental Management*, 235, 133–144. <https://doi.org/https://doi.org/10.1016/j.jenvman.2019.01.040>
- Cheng, H., Wu, S., Li, H., & Zhang, X. (2020). Influence of time and temperature on rheology and flow performance of cemented paste backfill. *Construction and Building Materials*, 231, 117117. <https://doi.org/10.1016/j.conbuildmat.2019.117117>
- Cheng, H., Wu, S., Zhang, X., & Li, J. (2019). A Novel Prediction Model of Strength of Paste Backfill Prepared from Waste-Unclassified Tailings. *Advances in Materials Science and Engineering*, 2019(MI). <https://doi.org/10.1155/2019/3574190>
- Cheng, K., Tu, B., Liu, L., Zhang, B., & Qiu, H. (2021). Damage Strengthening Constitutive Model of Cemented Paste Backfill. *Advances in Civil Engineering*, 2021. <https://doi.org/10.1155/2021/5593983>
- Chhabra, R. P. (2010). Non-Newtonian fluids: An introduction. In *Rheology of Complex Fluids* (pp. 3–34). https://doi.org/10.1007/978-1-4419-6494-6_1
- Choi, W. H., Lee, S. R., & Park, J. Y. (2009). Cement based solidification/stabilization of arsenic-contaminated mine tailings. *Waste Management*, 29(5), 1766–1771. <https://doi.org/10.1016/j.wasman.2008.11.008>
- Cihangir, F., & Akyol, Y. (2016). Mechanical, hydrological and microstructural assessment of the durability of cemented paste backfill containing alkali-activated slag. *International Journal*

- of Mining, Reclamation and Environment*, 32(2), 123–143.
<https://doi.org/10.1080/17480930.2016.1242183>
- Cihangir, F., Ercikdi, B., Kesimal, A., Ocak, S., & Akyol, Y. (2018). Effect of sodium-silicate activated slag at different silicate modulus on the strength and microstructural properties of full and coarse sulphidic tailings paste backfill. *Construction and Building Materials*, 185, 555–566. <https://doi.org/10.1016/j.conbuildmat.2018.07.105>
- Clancey, T. M., Snyder, K. V., Reddy, R., Lanzirotti, A., Amrose, S. E., Raskin, L., & Hayes, K. F. (2015). Evaluating the cement stabilization of arsenic-bearing iron wastes from drinking water treatment. *Journal of Hazardous Materials*, 300, 522–529. <https://doi.org/10.1016/j.jhazmat.2015.07.051>
- Clark, I. D., & Raven, K. G. (2004). Sources and circulation of water and arsenic in the Giant Mine, Yellowknife, NWT, Canada. *Isotopes in Environmental and Health Studies*, 40(2), 115–128. <https://doi.org/10.1080/10256010410001671014>
- Committee on Medical and Biologic Effects of Environmental, Pollutants, SCIENCES, D. O. M., SCIENCES, A. O. L., & COUNCIL, N. R. (1977). *ARSENIC, Medical and Biologic Effects of Environmental Pollutants*. <https://www.nap.edu/catalog/20333/carbon-monoxide>
- Conner, J. R. (1990). Chemical fixation and solidification of hazardous wastes. In *Van Nostrand Reinhold* (Vol. 30, Issue 1). http://news.qq.com/a/20120613/%0A000024_1.htm
- Conner, J. R. (1997). *Guide to Improving the Effectiveness of Cement-based Stabilization/Solidification*.
- Côté, P. L., Constable, T. W., & Moreira, A. (1987). An evaluation of cement-based waste forms using the results of approximately two years of dynamic leaching. *Nuclear and Chemical Waste Management*, 7(2), 129–139. [https://doi.org/https://doi.org/10.1016/0191-815X\(87\)90007-6](https://doi.org/https://doi.org/10.1016/0191-815X(87)90007-6)
- Coussy, S., Benzaazoua, M., Blanc, D., Moszkowicz, P., & Bussière, B. (2011). Arsenic stability in arsenopyrite-rich cemented paste backfills: A leaching test-based assessment. *Journal of Hazardous Materials*, 185(2–3), 1467–1476. <https://doi.org/10.1016/j.jhazmat.2010.10.070>
- Coussy, S., Benzaazoua, M., Blanc, D., Moszkowicz, P., & Bussière, B. (2012). Assessment of arsenic immobilization in synthetically prepared cemented paste backfill specimens. *Journal*

- of Environmental Management*, 93(1), 10–21. <https://doi.org/10.1016/j.jenvman.2011.08.015>
- Coussy, S., Paktunc, D., Rose, J., & Benzaazoua, M. (2012). Arsenic speciation in cemented paste backfills and synthetic calcium-silicate-hydrates. *Minerals Engineering*, 39, 51–61. <https://doi.org/10.1016/j.mineng.2012.05.016>
- Craw, D., & Bowell, R. J. (2014). The characterization of arsenic in mine waste. *Reviews in Mineralogy and Geochemistry*, 79(1), 473–505. <https://doi.org/10.2138/rmg.2014.79.10>
- Cruz, R., Bertrand, V., Monroy, M., & González, I. (2001). Effect of sulfide impurities on the reactivity of pyrite and pyritic concentrates: a multi-tool approach. *Applied Geochemistry*, 16(7), 803–819. [https://doi.org/https://doi.org/10.1016/S0883-2927\(00\)00054-8](https://doi.org/https://doi.org/10.1016/S0883-2927(00)00054-8)
- Cui, L., & Fall, M. (2016). Mechanical and thermal properties of cemented tailings materials at early ages: Influence of initial temperature, curing stress and drainage conditions. *Construction and Building Materials*, 125, 553–563. <https://doi.org/10.1016/j.conbuildmat.2016.08.080>
- Dai, C., Wu, A., Qi, Y., & Chen, Z. (2019). The Optimization of Mix Proportions for Cement Paste Backfill Materials via Box–Behnken Experimental Method. *Journal of The Institution of Engineers (India): Series D*, 100(2), 307–316. <https://doi.org/10.1007/s40033-019-00180-7>
- Davis, A. M., Holland, H. D., & Turekian, K. K. (2003). *Treatise on Geochemistry*. In Elsevier Ltd. (Vol. 1).
- Dean, A., Voss, D., & Draguljić, D. (2017). *Design and analysis of experiments* (2nd editio). Springer. <http://link.springer.com/10.1007/978-3-319-52250-0>
- Deb, D., Sreenivas, T., Dey, G. K., & Panchal, S. (2017). Paste Backfill Technology: Essential Characteristics and Assessment of its Application for Mill Rejects of Uranium Ores. *Transactions of the Indian Institute of Metals*, 70(2), 487–495. <https://doi.org/10.1007/s12666-016-0999-0>
- Dell'Orso, M., Mangialardi, T., Paolini, A. E., & Piga, L. (2012). Evaluation of the leachability of heavy metals from cement-based materials. *Journal of Hazardous Materials*, 227, 1–8.
- Demers, I., Bussière, B., Benzaazoua, M., Mbonimpa, M., & Blier, A. (2008). Column test investigation on the performance of monolayer covers made of desulphurized tailings to

- prevent acid mine drainage. *Minerals Engineering*, 21(4), 317–329. <https://doi.org/https://doi.org/10.1016/j.mineng.2007.11.006>
- Deng, H., Liu, Y., Zhang, W., Yu, S., & Tian, G. (2021). Study on the strength evolution characteristics of cemented tailings backfill from the perspective of porosity. *Minerals*, 11(1), 1–14. <https://doi.org/10.3390/min11010082>
- Deng, X., Zhang, J., Klein, B., Zhou, N., & de Wit, B. (2017). Experimental characterization of the influence of solid components on the rheological and mechanical properties of cemented paste backfill. *International Journal of Mineral Processing*, 168, 116–125. <https://doi.org/10.1016/j.minpro.2017.09.019>
- Dermatas, D., Moon, D. H., Menounou, N., Meng, X., & Hires, R. (2004). An evaluation of arsenic release from monolithic solids using a modified semi-dynamic leaching test. *Journal of Hazardous Materials*, 116(1–2), 25–38. <https://doi.org/10.1016/j.jhazmat.2004.04.023>
- Deschamps, T., Benzaazoua, M., Bussière, B., Aubertin, M., & Belem, T. (2008). Microstructural and geochemical evolution of paste tailings in surface disposal conditions. *Minerals Engineering*, 21(4), 341–353. <https://doi.org/https://doi.org/10.1016/j.mineng.2007.12.002>
- Deschamps, T., Benzaazoua, M., Bussière, B., Belem, T., & Aubertin, M. (2006). A Laboratory Study of the Hydro-Geochemical Behaviour of Paste Tailings Disposal. *Proceedings of the Ninth International Seminar on Paste and Thickened Tailings*, 255–265. https://doi.org/10.36487/acg_repo/663_22
- Dikonda, R. kabanga. (2018). *Influence de l'énergie spécifique de malaxage sur les propriétés rhéologiques et mécaniques des remblais en pâte cimentés*. <https://doi.org/10.2307/j.ctv18pghjp.2>
- Downward, L., Booth, C. H., Lukens, W. W., & Bridges, F. (2006). A variation of the F-test for determining statistical relevance of particular parameters in EXAFS fits. *AIP Conference Proceedings*, 882(2), 129–131. <https://doi.org/10.1063/1.2644450>
- Drahota, P., & Filippi, M. (2009). Secondary arsenic minerals in the environment: A review. *Environment International*, 35(8), 1243–1255. <https://doi.org/10.1016/j.envint.2009.07.004>
- Dražić, S., Sladoje, N., & Lindblad, J. (2016). Estimation of Feret's diameter from pixel coverage representation of a shape. *Pattern Recognition Letters*, 80, 37–45.

<https://doi.org/10.1016/j.patrec.2016.04.021>

- Du, Z., Chen, S., Wang, S., Liu, R., Yao, D., & Mitri, H. S. (2021). Influence of Binder Types and Temperatures on the Mechanical Properties and Microstructure of Cemented Paste Backfill. *Advances in Civil Engineering*, 2021, 1–10. <https://doi.org/10.1155/2021/6652176>
- Dutr e, V., & Vandecasteele, C. (1996). An evaluation of the solidification/stabilisation of industrial arsenic containing waste using extraction and semi-dynamic leach tests. *Waste Management*, 16(7), 625–631. [https://doi.org/10.1016/S0956-053X\(97\)00003-2](https://doi.org/10.1016/S0956-053X(97)00003-2)
- Dutr e, V., & Vandecasteele, C. (1998). Immobilization mechanism of arsenic in waste solidified using cement and lime. *Environmental Science and Technology*, 32(18), 2782–2787. <https://doi.org/10.1021/es971090j>
- EA NEN 7375. (2004). *Leaching characteristics of moulded or monolithic building and waste materials. Determination of leaching of inorganic components with the diffusion test. The tank test.*
- Ercikdi, B., Baki, H., & Izki, M. (2013). Effect of desliming of sulphide-rich mill tailings on the long-term strength of cemented paste backfill. *Journal of Environmental Management*, 115, 5–13. <https://doi.org/10.1016/j.jenvman.2012.11.014>
- Ercikdi, B., Cihangir, F., Kesimal, A., Deveci, H., & Alp, I. (2009). Utilization of industrial waste products as pozzolanic material in cemented paste backfill of high sulphide mill tailings. *Journal of Hazardous Materials*, 168(2–3), 848–856. <https://doi.org/10.1016/j.jhazmat.2009.02.100>
- Ercikdi, B., Cihangir, F., Kesimal, A., Deveci, H., & Alp, I. (2010). Utilization of water-reducing admixtures in cemented paste backfill of sulphide-rich mill tailings. *Journal of Hazardous Materials*, 179(1–3), 940–946. <https://doi.org/10.1016/j.jhazmat.2010.03.096>
- Ercikdi, B., Kesimal, A., Cihangir, F., Deveci, H., & Alp, I. (2009). Cemented paste backfill of sulphide-rich tailings: Importance of binder type and dosage. *Cement and Concrete Composites*, 31(4), 268–274. <https://doi.org/10.1016/j.cemconcomp.2009.01.008>
- Ercikdi, B., Yilmaz, T., & K ulekci, G. (2014). Strength and ultrasonic properties of cemented paste backfill. *Ultrasonics*, 54(1), 195–204. <https://doi.org/10.1016/j.ultras.2013.04.013>

- Espley, G. H., Beattie, H. F., & Pasiaka, A. R. (1970). Cemented hydraulic backfill within the Falconbridge Group of Companies. *CIM Trans.*, *73*, 218–226.
- Fahey, M., Helinski, M., & Fourie, A. (2011). Development of Specimen Curing Procedures that Account for the Influence of Effective Stress During Curing on the Strength of Cemented Mine Backfill. *Geotechnical and Geological Engineering*, *29*(5), 709–723. <https://doi.org/10.1007/s10706-011-9412-2>
- Fall, M., Adrien, D., Célestin, J. C., Pokharel, M., & Touré, M. (2009). Saturated hydraulic conductivity of cemented paste backfill. *Minerals Engineering*, *22*(15), 1307–1317. <https://doi.org/https://doi.org/10.1016/j.mineng.2009.08.002>
- Fall, M., Belem, T., Samb, S., & Benzaazoua, M. (2007). Experimental characterization of the stress–strain behaviour of cemented paste backfill in compression. *Journal of Materials Science*, *42*(11), 3914–3922. <https://doi.org/10.1007/s10853-006-0403-2>
- Fall, M., & Benzaazoua, M. (2005). Modeling the effect of sulphate on strength development of paste backfill and binder mixture optimization. *Cement and Concrete Research*, *35*(2), 301–314. <https://doi.org/https://doi.org/10.1016/j.cemconres.2004.05.020>
- Fall, M., Benzaazoua, M., & Ouellet, S. (2005). Experimental characterization of the influence of tailings fineness and density on the quality of cemented paste backfill. *Minerals Engineering*, *18*(1), 41–44. <https://doi.org/10.1016/j.mineng.2004.05.012>
- Fall, M., Benzaazoua, M., & Saa, E. G. (2008). Mix proportioning of underground cemented tailings backfill. *Tunnelling and Underground Space Technology*, *23*(1), 80–90.
- Fall, M., Célestin, J. C., Pokharel, M., & Touré, M. (2010). A contribution to understanding the effects of curing temperature on the mechanical properties of mine cemented tailings backfill. *Engineering Geology*, *114*(3), 397–413. <https://doi.org/https://doi.org/10.1016/j.enggeo.2010.05.016>
- Fall, M., & Pokharel, M. (2010). Coupled effects of sulphate and temperature on the strength development of cemented tailings backfills: Portland cement-paste backfill. *Cement and Concrete Composites*, *32*(10), 819–828. <https://doi.org/10.1016/j.cemconcomp.2010.08.002>
- Fan, Y. F., Hu, Z. Q., Zhang, Y. Z., & Liu, J. L. (2010). Deterioration of compressive property of concrete under simulated acid rain environment. *Construction and Building Materials*, *24*(10),

1975–1983.

- Fang, K., Zhang, J., Tang, H., Hu, X., Yuan, H., Wang, X., An, P., & Ding, B. (2023). A quick and low-cost smartphone photogrammetry method for obtaining 3D particle size and shape. *Engineering Geology*, 322, 107170. <https://doi.org/https://doi.org/10.1016/j.enggeo.2023.107170>
- Feng, G., Li, Z., Guo, Y., Wang, J., Li, D., Qi, T., Liu, G., Song, K., & Kang, L. (2016). Mix ratio optimization of cemented coal gangue backfill (CGB) based on response surface method. *Journal of Residuals Science and Technology*, 13(3), 175–184. <https://doi.org/10.12783/issn.1544-8053/13/3/1>
- Feng, Y., Qi, W., Zhao, Q., Huang, Y., Ren, Q., Qi, W., & Kong, F. (2023). Synthesis and characterization of cemented paste backfill: Reuse of multiple solid wastes. *Journal of Cleaner Production*, 383(July 2022), 135376. <https://doi.org/10.1016/j.jclepro.2022.135376>
- Foster, A. L., Brown, G. E., Tingle, T. N., & Parks, G. A. (1998). Quantitative arsenic speciation in mine tailings using X-ray absorption spectroscopy. *American Mineralogist*, 83(5–6), 553–568. <https://doi.org/10.2138/am-1998-5-616>
- Fourie, A., & Dunn, F. (2007). Limitations to the Use of the Modified Slump Test for Yield Stress Determination. In R. Jewell & A. Fourie (Eds.), *Paste 2007: Proceedings of the Tenth International Seminar on Paste and Thickened Tailings*. Australian Centre for Geomechanics.
- Fuessle, R. W., & Taylor, M. A. (2004). Stabilization of arsenite wastes with prior oxidation. *Journal of Environmental Engineering*, 130(9), 1063–1066. [https://doi.org/10.1061/\(ASCE\)0733-9372\(2004\)130:9\(1063\)](https://doi.org/10.1061/(ASCE)0733-9372(2004)130:9(1063))
- Gencil, O., Nodehi, M., Bozkurt, A., Sari, A., & Ozbakkaloglu, T. (2023). The use of computerized tomography (CT) and image processing for evaluation of the properties of foam concrete produced with different content of foaming agent and aggregate. *Construction and Building Materials*, 399(July 2022). <https://doi.org/10.1016/j.conbuildmat.2023.132433>
- Genty, T., Bussière, B., Potvin, R., Benzaazoua, M., & Zagury, G. J. (2012). Dissolution of calcitic marble and dolomitic rock in high iron concentrated acid mine drainage: Application to anoxic limestone drains. *Environmental Earth Sciences*, 66(8), 2387–2401. <https://doi.org/10.1007/s12665-011-1464-3>

- Ghirian, A., & Fall, M. (2016). Strength evolution and deformation behaviour of cemented paste backfill at early ages: Effect of curing stress, filling strategy and drainage. *International Journal of Mining Science and Technology*, 26(5), 809–817. <https://doi.org/10.1016/j.ijmst.2016.05.039>
- Glass, G. K., & Buenfeld, N. R. (1999). Differential acid neutralisation analysis. *Cement and Concrete Research*, 29(10), 1681–1684. [https://doi.org/https://doi.org/10.1016/S0008-8846\(99\)00127-1](https://doi.org/10.1016/S0008-8846(99)00127-1)
- Godbout, J., Bussière, B., Aubertin, M., & Belem, T. (2007). Evolution of cemented past backfill saturated hydraulic conductivity at early curing time. *Proceedings of the OttawaGeo2007*, 2230–2230. <http://www.polymtl.ca/enviro-geremi/pdf/articles/CGS2007095.pdf>
- Gomez, M. A., Assaoudi, H., Becze, L., Cutler, J. N., & Demopoulos, G. P. (2010). Vibrational spectroscopy study of hydrothermally produced scorodite (FeAsO₄·2H₂O), ferric arsenate sub-hydrate (FAsH; FeAsO₄·0.75H₂O) and basic ferric arsenate sulfate (BFAS; Fe[(AsO₄)_{1-x}(SO₄)_x(OH)_x]·wH₂O). *Journal of Raman Spectroscopy*, 41(2), 212–221. <https://doi.org/https://doi.org/10.1002/jrs.2419>
- Government of Northwest Territories. (2019). *Responding to climate change in the NWT*.
- Grabinsky, M., Jafari, M., & Pan, A. (2022). Cemented Paste Backfill (CPB) Material Properties for Undercut Analysis. *Mining*, 2(1), 103–122. <https://doi.org/10.3390/mining2010007>
- Grice, T. (1998). Underground Mining with Backfill. *The 2nd Annual Summit-Mine Tailings Disposal System*, 1–14.
- Guerrero-Pérez, M. O., & Patience, G. S. (2020). Experimental methods in chemical engineering: Fourier transform infrared spectroscopy—FTIR. *The Canadian Journal of Chemical Engineering*, 98(1), 25–33. <https://doi.org/https://doi.org/10.1002/cjce.23664>
- Guo, B., Liu, B., Yang, J., & Zhang, S. (2017). The mechanisms of heavy metal immobilization by cementitious material treatments and thermal treatments: A review. *Journal of Environmental Management*, 193, 410–422. <https://doi.org/https://doi.org/10.1016/j.jenvman.2017.02.026>
- Haiqiang, J., Fall, M., & Cui, L. (2016). Yield stress of cemented paste backfill in sub-zero environments: Experimental results. *Minerals Engineering*, 92, 141–150. <https://doi.org/10.1016/j.mineng.2016.03.014>

- Hakkou, R., Benzaazoua, M., & Bussière, B. (2008). Acid Mine Drainage at the Abandoned Kettara Mine (Morocco): 2. Mine Waste Geochemical Behavior. *Mine Water and the Environment*, 27(3), 160–170. <https://doi.org/10.1007/s10230-008-0035-7>
- Hakkou, R., Benzaazoua, M., & Bussière, B. (2009). Laboratory Evaluation of the Use of Alkaline Phosphate Wastes for the Control of Acidic Mine Drainage. *Mine Water and the Environment*, 28(3), 206–218. <https://doi.org/10.1007/s10230-009-0081-9>
- Hamberg, R., Alakangas, L., & Maurice, C. (2018). *Cementation of cyanidation tailings – Effects on the release of As, Cu, Ni and Zn*. November.
- Hamberg, R., Maurice, C., & Alakangas, L. (2015a). The use of low binder proportions in cemented paste backfill - Effects on As-leaching. *Minerals Engineering*, 78, 74–82. <https://doi.org/10.1016/j.mineng.2015.04.017>
- Hamberg, R., Maurice, C., & Alakangas, L. (2015b). Use of cemented paste backfill based on arsenic – rich tailings from cyanidation. *10th International Conference on Acid Rock Drainage and IMWA Annual Conference*.
- Hamberg, R., Maurice, C., & Alakangas, L. (2015c). *Use of cemented paste backfill in arsenic-rich tailings*. 17, 15400.
- Hamberg, R., Maurice, C., & Alakangas, L. (2017). Lowering the water saturation level in cemented paste backfill mixtures – Effect on the release of arsenic. *Minerals Engineering*, 112(May), 84–91. <https://doi.org/10.1016/j.mineng.2017.05.005>
- Hamberg, R., Maurice, C., & Alakangas, L. (2018). The formation of unsaturated zones within cemented paste backfill mixtures—effects on the release of copper, nickel, and zinc. *Environmental Science and Pollution Research*, 25(21), 20809–20822. <https://doi.org/10.1007/s11356-018-2222-9>
- Haruna, S., & Fall, M. (2020). Time- and temperature-dependent rheological properties of cemented paste backfill that contains superplasticizer. *Powder Technology*, 360, 731–740. <https://doi.org/10.1016/j.powtec.2019.09.025>
- Heron, G., Crouzet, C., Bourg, A. C. M., & Christensen, T. H. (1994). Speciation of Fe(II) and Fe(III) in Contaminated Aquifer Sediments Using Chemical Extraction Techniques.

Environmental Science and Technology, 28(9), 1698–1705.
<https://doi.org/10.1021/es00058a023>

- Hetzner, H., Schmid, C., Tremmel, S., Durst, K., & Wartzack, S. (2014). Empirical-statistical study on the relationship between deposition parameters, process variables, deposition rate and mechanical properties of a-C:H: W coatings. *Coatings*, 4(4), 772–795.
<https://doi.org/10.3390/coatings4040772>
- Hu, J., Zhao, F., Ren, Q., Kuang, Y., Zhou, T., & Luo, Z. (2019). Microscopic characterization and strength characteristics of cemented backfill under different humidity curing conditions. *Royal Society Open Science*, 6(12). <https://doi.org/10.1098/rsos.191227>
- Huan, C., Zhu, C., Liu, L., Wang, M., Zhao, Y., Zhang, B., & Zhang, X. (2021). Pore Structure Characteristics and Its Effect on Mechanical Performance of Cemented Paste Backfill. *Frontiers in Materials*, 8(July), 1–10. <https://doi.org/10.3389/fmats.2021.700917>
- Huang, Z., Yilmaz, E., & Cao, S. (2021). Analysis of Strength and Microstructural Characteristics of Mine Backfills Containing Fly Ash and Desulfurized Gypsum. *Minerals*, 11(4). <https://doi.org/10.3390/min11040409>
- Hustrulid, W. A., & Bullock, R. L. (2001). *Underground Mining Methods: Engineering Fundamentals and International Case Studies*.
- Ioannidis, T. A., & Zouboulis, A. I. (2005). Solidification/Stabilization of Hazardous Solid Wastes. In J. H. Lehr & J. Keeley (Eds.), *Water Encyclopedia*.
- Ioannidou, K., Masoero, E., Levitz, P., Pellenq, R. J.-M., & Gado, E. Del. (2015). Hydration Kinetics and Gel Morphology of C-S-H. *10th ASCE International Conference on Mechanics and Physics of Creep, Shrinkage, and Durability of Concrete and Concrete Structures*.
- Jia, Q., Yang, Q., Guo, L., Knutsson, S., Xue, P., Liu, G., & Jiang, L. (2016). Effects of fine content, binder type and porosity on mechanical properties of cemented paste backfill with co-deposition of tailings sand and smelter slag. *Electronic Journal of Geotechnical Engineering*, 21(22), 7017–7032.
- Jiang, C., Ding, X., Pang, L., Deng, L., & Shi, Z. (2022). An Image-Based Gradation Calculation Method considering Crushed Stone Morphology. *Geofluids*, 2022, 0–30.
<https://doi.org/10.1155/2022/7291223>

- Jiang, H., & Fall, M. (2017a). Yield stress and strength of saline cemented tailings in sub-zero environments: Portland cement paste backfill. *International Journal of Mineral Processing*, *160*, 68–75. <https://doi.org/10.1016/j.minpro.2017.01.010>
- Jiang, H., & Fall, M. (2017b). Yield stress and strength of saline cemented tailings materials in sub-zero environments: slag-paste backfill. *Journal of Sustainable Cement-Based Materials*, *6*(5), 314–331. <https://doi.org/10.1080/21650373.2017.1280428>
- Jiang, H., Fall, M., Li, Y., & Han, J. (2019). An experimental study on compressive behaviour of cemented rockfill. *Construction and Building Materials*, *213*, 10–19. <https://doi.org/https://doi.org/10.1016/j.conbuildmat.2019.04.061>
- Jiang, H., Fall, M., Yilmaz, E., Li, Y., & Yang, L. (2020). Effect of mineral admixtures on flow properties of fresh cemented paste backfill: Assessment of time dependency and thixotropy. *Powder Technology*, *372*, 258–266. <https://doi.org/https://doi.org/10.1016/j.powtec.2020.06.009>
- Jiang, H., Qi, Z., Yilmaz, E., Han, J., Qiu, J., & Dong, C. (2019). Effectiveness of alkali-activated slag as alternative binder on workability and early age compressive strength of cemented paste backfills. *Construction and Building Materials*, *218*, 689–700. <https://doi.org/10.1016/j.conbuildmat.2019.05.162>
- Jiang, H., Yi, H., Yilmaz, E., Liu, S., & Qiu, J. (2020a). Ultrasonic evaluation of strength properties of cemented paste backfill: Effects of mineral admixture and curing temperature. *Ultrasonics*, *100*(December 2018), 105983. <https://doi.org/10.1016/j.ultras.2019.105983>
- Jiang, H., Yi, H., Yilmaz, E., Liu, S., & Qiu, J. (2020b). Ultrasonic evaluation of strength properties of cemented paste backfill: Effects of mineral admixture and curing temperature. *Ultrasonics*, *100*(August 2019), 105983. <https://doi.org/10.1016/j.ultras.2019.105983>
- Jiang, H., Zheng, J., Fu, Y., Wang, Z., Yilmaz, E., & Cui, L. (2024). Slag-based stabilization/solidification of hazardous arsenic-bearing tailings as cemented paste backfill: Strength and arsenic immobilization assessment. *Case Studies in Construction Materials*, *20*(November 2023), e03002. <https://doi.org/10.1016/j.cscm.2024.e03002>
- Jiao, H., Wu, A., Wang, H., Yang, S., Li, R., & Xiao, Y. (2011). The Influence of Cemented Paste Backfill on Groundwater Quality. *Procedia Earth and Planetary Science*, *2*, 183–188.

<https://doi.org/https://doi.org/10.1016/j.proeps.2011.09.030>

- Joussemet, R., Yvon, J., & Marion, P. (2001). Inertage de l'arsenic en milieu minier. *Les Techniques de l'industrie Minérale*, 11, 102–110.
- Kalonji, K. (2016). *Étude des propriétés rhéologiques et du transport du remblai cimenté en pâte en conditions nordiques*.
- Ke, X., Zhou, X., Wang, X., Wang, T., Hou, H., & Zhou, M. (2016). Effect of tailings fineness on the pore structure development of cemented paste backfill. *Construction and Building Materials*, 126, 345–350. <https://doi.org/10.1016/j.conbuildmat.2016.09.052>
- Keeling, A., & Sandlos, J. (2017). *Indigenous Knowledge and Environmental Remediation in Extractive Development*. 1–12.
- Kerr, D. E. (2006). *Surficial geology and exploration geochemistry, Yellowknife area*. <https://www.scopus.com/record/display.uri?eid=2-s2.0-85019204376&origin=inward#>
- Kesimal, A., Ercikdi, B., & Yilmaz, E. (2003). The effect of desliming by sedimentation on paste backfill performance. *Minerals Engineering*, 16(10), 1009–1011. [https://doi.org/10.1016/S0892-6875\(03\)00267-X](https://doi.org/10.1016/S0892-6875(03)00267-X)
- Kesimal, A., Yilmaz, E., Ercikdi, B., Alp, I., & Devenci, H. (2005). Effect of properties of tailings and binder on the short-and long-term strength and stability of cemented paste backfill. *Materials Letters*, 59(28), 3703–3709. <https://doi.org/10.1016/j.matlet.2005.06.042>
- Khan, M. I., Sutanto, M. H., Napiah, M. Bin, Khan, K., & Rafiq, W. (2021). Design optimization and statistical modeling of cementitious grout containing irradiated plastic waste and silica fume using response surface methodology. *Construction and Building Materials*, 271, 121504. <https://doi.org/https://doi.org/10.1016/j.conbuildmat.2020.121504>
- Kim, B.-J., Jang, J.-G., Park, C.-Y., Han, O.-H., & Kim, H.-K. (2016). Recycling of arsenic-rich mine tailings in controlled low-strength materials. *Journal of Cleaner Production*, 118, 151–161. <https://doi.org/10.1016/j.jclepro.2016.01.047>
- Kim, J. Y., Davis, A. P., & Kim, K. W. (2003). Stabilization of available arsenic in highly contaminated mine tailings using iron. *Environmental Science and Technology*, 37(1), 189–195. <https://doi.org/10.1021/es020799+>

- Klein, K., & Simon, D. (2006). Effect of specimen composition on the strength development in cemented paste backfill. *Canadian Geotechnical Journal*, 43(3), 310–324. <https://doi.org/10.1139/t06-005>
- Kocourková-Višková, E., Loun, J., Sracek, O., Houzar, S., & Filip, J. (2015). Secondary arsenic minerals and arsenic mobility in a historical waste rock pile at Kaňk near Kutná Hora, Czech Republic. *Mineralogy and Petrology*, 109(1), 17–33. <https://doi.org/10.1007/s00710-014-0356-0>
- Komárek, M., Vaněk, A., & Ettler, V. (2013). Chemical stabilization of metals and arsenic in contaminated soils using oxides - A review. *Environmental Pollution*, 172, 9–22. <https://doi.org/10.1016/j.envpol.2012.07.045>
- Koohestani, B., Khodadadi Darban, A., & Mokhtari, P. (2018). A comparison between the influence of superplasticizer and organosilanes on different properties of cemented paste backfill. *Construction and Building Materials*, 173, 180–188. <https://doi.org/10.1016/j.conbuildmat.2018.03.265>
- Koohestani, B., Koubaa, A., Belem, T., Bussière, B., & Bouzahzah, H. (2016). Experimental investigation of mechanical and microstructural properties of cemented paste backfill containing maple-wood filler. *Construction and Building Materials*, 121, 222–228. <https://doi.org/10.1016/j.conbuildmat.2016.05.118>
- Kou, Y., Jiang, H., Ren, L., Yilmaz, E., & Li, Y. (2020). Rheological Properties of Cemented Paste Backfill with Alkali-Activated Slag. *Minerals*, 10(3), 288. <https://doi.org/10.3390/min10030288>
- Koupouli, N., Belem, T., & Rivard, P. (2017). *Shear strength between cemented paste backfill and natural rock surface replicas*. 2005, 375–385. https://doi.org/10.36487/acg_rep/1710_29_koupouli
- Koupouli, N. J. F., Belem, T., Rivard, P., & Effenguet, H. (2016). Direct shear tests on cemented paste backfill–rock wall and cemented paste backfill–backfill interfaces. *Journal of Rock Mechanics and Geotechnical Engineering*, 8(4), 472–479. <https://doi.org/10.1016/j.jrmge.2016.02.001>
- Kumarathasan, P., McCarthy, G. J., Hassett, D. J., & Pflughoeft-Hassett, D. F. (1989). Oxyanion

- Substituted Ettringites: Synthesis and Characterization; and their Potential Role In Immobilization of As, B, Cr, Se and V. *MRS Proceedings*, 178, 83. <https://doi.org/10.1557/PROC-178-83>
- Kundu, S., & Gupta, A. K. (2008). Immobilization and leaching characteristics of arsenic from cement and/or lime solidified/stabilized spent adsorbent containing arsenic. *Journal of Hazardous Materials*, 153(1–2), 434–443. <https://doi.org/10.1016/j.jhazmat.2007.08.073>
- Landriault, D. (1995a). Paste backfill mix design for Canadian underground hard rock mining. *Proceedings of the 12th Annual CIM Mine Operators Conference*, 1–10.
- Landriault, D. (1995b). Paste backfill mix design for Canadian underground hard rock mining. *97th Annual General Meeting of CIM. Rock Mechanics and Strata Control Session. Halifax, Nova Scotia*, 238–239.
- Lang, L., Song, K. Il, Lao, D., & Kwon, T. H. (2015). Rheological properties of cemented tailing backfill and the construction of a prediction model. *Materials*, 8(5), 2076–2092. <https://doi.org/10.3390/ma8052076>
- Leist, M., Casey, R. J., & Caridi, D. (2003). The fixation and leaching of cement stabilized arsenic. *Waste Management*, 23(4), 353–359. [https://doi.org/10.1016/S0956-053X\(02\)00116-2](https://doi.org/10.1016/S0956-053X(02)00116-2)
- Lerche, R., & Renetzeder, H. (1984). Development of ‘pumped fill’ at Grund mine, Preussag AG Metall. *Proceedings of the 9th International Conference on the Hydraulic Transport of Solids in Pipes, Rome, Italy*, 24.
- Lessard, F., Bussière, B., Côté, J., Benzaazoua, M., Boulanger-Martel, V., & Marcoux, L. (2018). Integrated environmental management of pyrrhotite tailings at Raglan Mine: Part 2 desulphurized tailings as cover material. *Journal of Cleaner Production*, 186, 883–893. <https://doi.org/https://doi.org/10.1016/j.jclepro.2018.03.132>
- Levens, R. L., Marcy, A. D., & Boldt, C. M. K. (1996). *Environmental Impacts of Cemented Mine Waste Backfill*.
- Li, C., Sun, H., Yi, Z., & Li, L. (2010). Innovative methodology for comprehensive utilization of iron ore tailings: Part 2: The residues after iron recovery from iron ore tailings to prepare cementitious material. *Journal of Hazardous Materials*, 174(1), 78–83. <https://doi.org/https://doi.org/10.1016/j.jhazmat.2009.09.019>

- Li, J., Cao, S., & Song, W. (2023). Distribution development of pore/crack expansion and particle structure of cemented solid-waste composites based on CT and 3D reconstruction techniques. *Construction and Building Materials*, 376(November 2022), 130966. <https://doi.org/10.1016/j.conbuildmat.2023.130966>
- Li, J. S., Beiyuan, J., Tsang, D. C. W., Wang, L., Poon, C. S., Li, X. D., & Fendorf, S. (2017). Arsenic-containing soil from geogenic source in Hong Kong: Leaching characteristics and stabilization/solidification. *Chemosphere*, 182, 31–39. <https://doi.org/10.1016/j.chemosphere.2017.05.019>
- Li, J. S., Wang, L., Tsang, D. C. W., Beiyuan, J., & Poon, C. S. (2017). Dynamic leaching behavior of geogenic As in soils after cement-based stabilization/solidification. *Environmental Science and Pollution Research*, 24(36), 27822–27832. <https://doi.org/10.1007/s11356-017-0266-x>
- Li, L., & Aubertin, M. (2003). A general relationship between porosity and uniaxial strength of engineering materials. *Canadian Journal of Civil Engineering*, 30(4), 644–658. <https://doi.org/10.1139/l03-012>
- Li, Q., Feng, G., Guo, Y., Qi, T., Du, X., Wang, Z., & Li, H. (2019). The dosage of superplasticizer in cemented coal waste backfill material based on response surface methodology. *Advances in Materials Science and Engineering*, 2019. <https://doi.org/10.1155/2019/5328523>
- Li, W., & Fall, M. (2016). Sulphate effect on the early age strength and self-desiccation of cemented paste backfill. *Construction and Building Materials*, 106, 296–304. <https://doi.org/10.1016/j.conbuildmat.2015.12.124>
- Li, Y., Min, X., Ke, Y., Fei, J., Liu, D., & Tang, C. (2019). Immobilization potential and immobilization mechanism of arsenic in cemented paste backfill. *Minerals Engineering*, 138(April), 101–107. <https://doi.org/10.1016/j.mineng.2019.04.041>
- Li, Z., Sun, W., Gao, T., Zhao, J., Lu, K., & Cheng, H. (2023). Experimental study on evolution of pore structure of inclined layered cemented tailings backfill based on X-ray CT. *Construction and Building Materials*, 366(253), 130242. <https://doi.org/10.1016/j.conbuildmat.2022.130242>
- Lin, Y., Wu, B., Ning, P., Qu, G., Li, J., Wang, X., & Xie, R. (2017). Stabilization of arsenic in waste slag using FeCl₂ or FeCl₃ stabilizer. *RSC Advances*, 7(87), 54956–54963.

<https://doi.org/10.1039/c7ra10169d>

- Liu, D. G., Min, X., Ke, Y., Chai, L., Liang, Y. Jie, Li, Y. C., Yao, L. W., & Wang, Z. B. (2018). Co-treatment of flotation waste, neutralization sludge, and arsenic-containing gypsum sludge from copper smelting: solidification/stabilization of arsenic and heavy metals with minimal cement clinker. *Environmental Science and Pollution Research*, 25(8), 7600–7607. <https://doi.org/10.1007/s11356-017-1084-x>
- Liu, L., Fang, Z., Wang, M., Qi, C., Zhao, Y., & Huan, C. (2020). Experimental and numerical study on rheological properties of ice-containing cement paste backfill slurry. *Powder Technology*, 370, 206–214. <https://doi.org/10.1016/j.powtec.2020.05.024>
- Liu, L., Xin, J., Qi, C., Jia, H., & Song, K. I. I. L. (2020). Experimental investigation of mechanical, hydration, microstructure and electrical properties of cemented paste backfill. *Construction and Building Materials*, 263, 120137. <https://doi.org/10.1016/j.conbuildmat.2020.120137>
- Liu, L., Yang, P., Qi, C., Zhang, B., Guo, L., & Song, K. I. I. L. (2019). An experimental study on the early-age hydration kinetics of cemented paste backfill. *Construction and Building Materials*, 212, 283–294. <https://doi.org/10.1016/j.conbuildmat.2019.03.322>
- Liu, L., Zhu, C., Qi, C., Wang, M., Huan, C., Zhang, B., & Song, K. I. I. L. (2019). Effects of curing time and ice-to-water ratio on performance of cemented paste backfill containing ice slag. *Construction and Building Materials*, 228, 116639. <https://doi.org/10.1016/j.conbuildmat.2019.08.020>
- Liu, Y., Li, H., Wang, K., Wu, H., & Cui, B. (2020). Effects of accelerator–water reducer admixture on performance of cemented paste backfill. *Construction and Building Materials*, 242, 118187. <https://doi.org/10.1016/j.conbuildmat.2020.118187>
- Lorenzoni, R., Paciornik, S., & Silva, F. A. (2019). Characterization by microcomputed tomography of class G oil well cement paste exposed to elevated temperatures. *Journal of Petroleum Science and Engineering*, 175(September 2018), 896–904. <https://doi.org/10.1016/j.petrol.2019.01.022>
- Lottermoser, B. G. (2010). Mine Wastes, Characterization, Treatment and Environmental Impacts. In *Waste*. Springer. <https://doi.org/10.1016/b978-0-12-381475-3.10005-1>
- Lu, C.-C., Hsu, M. H., & Lin, Y.-P. (2019). Evaluation of heavy metal leachability of incinerating

- recycled aggregate and solidification/stabilization products for construction reuse using TCLP, multi-final pH and EDTA-mediated TCLP leaching tests. *Journal of Hazardous Materials*, 368, 336–344. <https://doi.org/10.1016/j.jhazmat.2019.01.066>
- Lum, J. E., Schoepfer, V. A., Jamieson, H. E., McBeth, J. M., Radková, A. B., Walls, M. P., & Lindsay, M. B. J. (2023). Arsenic and antimony geochemistry of historical roaster waste from the Giant Mine, Yellowknife, Canada. *Journal of Hazardous Materials*, 458(July), 0–1. <https://doi.org/10.1016/j.jhazmat.2023.132037>
- Ma, D., Zhang, J., Duan, H., Huang, Y., Li, M., Sun, Q., & Zhou, N. (2021). Reutilization of gangue wastes in underground backfilling mining: Overburden aquifer protection. *Chemosphere*, 264, 128400. <https://doi.org/10.1016/j.chemosphere.2020.128400>
- Malviya, R., & Chaudhary, R. (2006). Factors affecting hazardous waste solidification/stabilization: a review. *Journal of Hazardous Materials*, 137(1), 267–276. <https://doi.org/10.1016/j.jhazmat.2006.01.065>
- Mangane, M. B. C., Argane, R., Trauchessec, R., Lecomte, A., & Benzaazoua, M. (2018). Influence of superplasticizers on mechanical properties and workability of cemented paste backfill. *Minerals Engineering*, 116(October), 3–14. <https://doi.org/10.1016/j.mineng.2017.11.006>
- Mbonimpa, M., Kwizera, P., & Belem, T. (2019). Mine backfilling in the permafrost, part II: Effect of declining curing temperature on the short-term unconfined compressive strength of cemented paste backfills. *Minerals*, 9(3). <https://doi.org/10.3390/min9030172>
- Mehta, P. K. (1999). *Concrete Technology for Sustainable Developmente an Overview of Essential Principles, Concrete Technology for Sustainable Development in the Twenty-First Century. Cement Manufacturers' Association.*
- MEND. (2006). *Paste Backfill Geochemistry – Environmental Effects of Leaching and Weathering* (Issue April). <http://mend-nedem.org/wp-content/uploads/2013/01/10.2.pdf>
- Min, C., Li, X., He, S., Zhou, S., Zhou, Y., Yang, S., & Shi, Y. (2019). Effect of mixing time on the properties of phosphogypsum-based cemented backfill. *Construction and Building Materials*, 210, 564–573. <https://doi.org/10.1016/j.conbuildmat.2019.03.187>
- Min, X., Liao, Y. P., Chai, L., Yang, Z. H., Xiong, S., Liu, L., & Li, Q. Z. (2015). Removal and

- stabilization of arsenic from anode slime by forming crystal scorodite. *Transactions of Nonferrous Metals Society of China (English Edition)*, 25(4), 1298–1306. [https://doi.org/10.1016/S1003-6326\(15\)63728-1](https://doi.org/10.1016/S1003-6326(15)63728-1)
- Mohammad Eisa, H., Vaezi, I., & Mahboubi Ardakani, A. (2020). Evaluation of solidification/stabilization in arsenic-contaminated soils using lime dust and cement kiln dust. *Bulletin of Engineering Geology and the Environment*, 79(4), 1683–1692. <https://doi.org/10.1007/s10064-019-01698-6>
- Mohammadi, A., Demers, I., Beier, N. A., & Benzaazoua, M. (2023). Study of the effects of arsenic trioxide roaster waste dusts on the mechanical behaviour of cemented paste backfills. In G. W. Wilson, N. A. Beier, D. C. Segó, A. B. Fourie, & D. Reid (Eds.), *Paste 2023: Proceedings of the 25th International Conference on Paste, Thickened and Filtered Tailings* (pp. 71–81). University of Alberta, Edmonton, and Australian Centre for Geomechanics, Perth. https://doi.org/10.36487/ACG_repo/2355_05
- Mohammadi, A., Demers, I., Benzaazoua, M., & Beier, N. (2023a). The effects of arsenic trioxide addition on the mechanical and geochemical properties of the cemented paste backfill. *Results in Materials*, 19(August), 100440. <https://doi.org/10.1016/j.rinma.2023.100440>
- Mohammadi, A., Demers, I., Benzaazoua, M., & Beier, N. A. (2023b). Arsenic speciation in cemented paste backfill using parallel extraction. *Sustainable Mining 2023: Proceedings of the 8th International Congress on Environment and Social Responsibility in Mining*, 180–182.
- Mollah, M. Y. A., Kesmez, M., & Cocke, D. L. (2004). An X-ray diffraction (XRD) and Fourier transform infrared spectroscopic (FT-IR) investigation of the long-term effect on the solidification/ stabilization (S/S) of arsenic(V) in Portland cement type-V. *Science of the Total Environment*, 325(1–3), 255–262. <https://doi.org/10.1016/j.scitotenv.2003.09.012>
- Montgomery, D. C. (2017). *Design and analysis of experiments*. John Wiley & sons.
- Moon, D. H., & Dermatas, D. (2007). Arsenic and lead release from fly ash stabilized/solidified soils under modified semi-dynamic leaching conditions. *Journal of Hazardous Materials*, 141(2), 388–394. <https://doi.org/https://doi.org/10.1016/j.jhazmat.2006.05.085>
- Moon, D. H., Dermatas, D., & Grubb, D. G. (2010). Release of arsenic (As) and lead (Pb) from

- quicklime-sulfate stabilized/solidified soils under diffusion-controlled conditions. *Environmental Monitoring and Assessment*, 169(1–4), 259–265. <https://doi.org/10.1007/s10661-009-1167-3>
- Moon, D. H., Dermatas, D., & Menounou, N. (2004). Arsenic immobilization by calcium-arsenic precipitates in lime treated soils. *Science of the Total Environment*, 330(1–3), 171–185. <https://doi.org/10.1016/j.scitotenv.2004.03.016>
- Myers, R. H., Montgomery, D. C., & Anderson-cook, C. M. (2016). *Response Surface Methodology; Process and product optimization using designed experiments* (Fourth Edi).
- Myers, R. H., Montgomery, D. C., & Anderson-Cook, C. M. (2016). *Response Surface Methodology: Process and Product Optimization Using Designed Experiments* (4th Editio). Wiley.
- Newville, M. (2013). Larch: An analysis package for XAFS and related spectroscopies. *Journal of Physics: Conference Series*, 430(1). <https://doi.org/10.1088/1742-6596/430/1/012007>
- NIST/SEMATECH. (2012). *e-Handbook of Statistical Methods*. <https://doi.org/https://doi.org/10.18434/M32189>
- Northwest Consulting Limited. (2003). *An examination of arsenic contamination in the roaster and gas handling complex*.
- O'Day, P. A. (2006). Chemistry and mineralogy of arsenic. *Elements*, 2(2), 77–83. <https://doi.org/10.2113/gselements.2.2.77>
- O'Farrell, M., Wild, S., & Sabir, B. B. (2001). Pore size distribution and compressive strength of waste clay brick mortar. *Cement and Concrete Composites*, 23(1), 81–91. [https://doi.org/https://doi.org/10.1016/S0958-9465\(00\)00070-6](https://doi.org/https://doi.org/10.1016/S0958-9465(00)00070-6)
- Orejarena, L., & Fall, M. (2008). Mechanical response of a mine composite material to extreme heat. *Bulletin of Engineering Geology and the Environment*, 67(3), 387–396. <https://doi.org/10.1007/s10064-008-0148-z>
- Orejarena, L., & Fall, M. (2010). The use of artificial neural networks to predict the effect of sulphate attack on the strength of cemented paste backfill. *Bulletin of Engineering Geology and the Environment*, 69(4), 659–670. <https://doi.org/10.1007/s10064-010-0326-7>

- Ouattara, D. (2017). *Étude expérimentale des propriétés rhéologiques et mécaniques des remblais miniers en pâte cimentés incorporant des superplastifiants*. UNIVERSITÉ DU QUÉBEC EN ABITIBI TÉMISCAMINGUE.
- Ouattara, D., Belem, T., Mbonimpa, M., & Yahia, A. (2018). Effect of superplasticizers on the consistency and unconfined compressive strength of cemented paste backfills. *Construction and Building Materials*, *181*, 59–72. <https://doi.org/10.1016/j.conbuildmat.2018.05.288>
- Ouellet, S., Bussière, B., Aubertin, M., & Benzaazoua, M. (2007). Microstructural evolution of cemented paste backfill: Mercury intrusion porosimetry test results. *Cement and Concrete Research*, *37*(12), 1654–1665. <https://doi.org/https://doi.org/10.1016/j.cemconres.2007.08.016>
- Ouellet, S., Bussière, B., Aubertin, M., & Benzaazoua, M. (2008). Characterization of cemented paste backfill pore structure using SEM and IA analysis. *Bulletin of Engineering Geology and the Environment*, *67*(2), 139–152. <https://doi.org/10.1007/s10064-007-0117-y>
- Palfy, P., Vircikova, E., & Molnar, L. (1999). Processing of arsenic waste by precipitation and solidification. *Waste Management*, *19*(1), 55–59. [https://doi.org/10.1016/S0956-053X\(99\)00014-8](https://doi.org/10.1016/S0956-053X(99)00014-8)
- Panchal, S., Deb, D., & Sreenivas, T. (2018). Variability in rheology of cemented paste backfill with hydration age, binder and superplasticizer dosages. *Advanced Powder Technology*, *29*(9), 2211–2220. <https://doi.org/10.1016/j.apt.2018.06.005>
- Perez Mora, B., Bellú, S., Mangiameli, M. F., Frascaroli, M. I., & González, J. C. (2019). Response surface methodology and optimization of arsenic continuous sorption process from contaminated water using chitosan. *Journal of Water Process Engineering*, *32*(July), 100913. <https://doi.org/10.1016/j.jwpe.2019.100913>
- Peyronnard, O., Benzaazoua, M., Blanc, D., & Moszkowicz, P. (2009). Study of mineralogy and leaching behavior of stabilized/solidified sludge using differential acid neutralization analysis: Part I: Experimental study. *Cement and Concrete Research*, *39*(7), 600–609. <https://doi.org/https://doi.org/10.1016/j.cemconres.2009.03.016>
- Peyronnard, Olivier, & Benzaazoua, M. (2011). Estimation of the cementitious properties of various industrial by-products for applications requiring low mechanical strength. *Resources*,

- Conservation and Recycling*, 56(1), 22–33. <https://doi.org/10.1016/j.resconrec.2011.08.008>
- Peyronnard, Olivier, & Benzaazoua, M. (2012). Alternative by-product based binders for cemented mine backfill: Recipes optimisation using Taguchi method. *Minerals Engineering*, 29, 28–38. <https://doi.org/10.1016/j.mineng.2011.12.010>
- Phenrat, T., Marhaba, T. F., & Rachakornkij, M. (2005). A SEM and X-ray study for investigation of solidified/stabilized arsenic-iron hydroxide sludge. *Journal of Hazardous Materials*, 118(1–3), 185–195. <https://doi.org/10.1016/j.jhazmat.2004.10.019>
- Phenrat, T., Marhaba, T. F., & Rachakornkij, M. (2008). Leaching Behaviors of Arsenic from Arsenic-Iron Hydroxide Sludge during TCLP. *Journal of Environmental Engineering*, 134(8), 671–682.
- Pichler, B., Hellmich, C., & Eberhardsteiner, J. (2009). Spherical and acicular representation of hydrates in a micromechanical model for cement paste: prediction of early-age elasticity and strength. *Acta Mechanica*, 203(3), 137–162. <https://doi.org/10.1007/s00707-008-0007-9>
- Pichler, B., Scheiner, S., & Hellmich, C. (2008). From micron-sized needle-shaped hydrates to meter-sized shotcrete tunnel shells: micromechanical upscaling of stiffness and strength of hydrating shotcrete. *Acta Geotechnica*, 3(4), 273–294. <https://doi.org/10.1007/s11440-008-0074-z>
- Pokharel, M., & Fall, M. (2013). Combined influence of sulphate and temperature on the saturated hydraulic conductivity of hardened cemented paste backfill. *Cement and Concrete Composites*, 38, 21–28. <https://doi.org/10.1016/j.cemconcomp.2013.03.015>
- Pokrovski, G., Gout, R., Schott, J., Zotov, A., & Harrichoury, J.-C. (1996). Thermodynamic properties and stoichiometry of As (III) hydroxide complexes at hydrothermal conditions. *Geochimica et Cosmochimica Acta*, 60(5), 737–749. [https://doi.org/https://doi.org/10.1016/0016-7037\(95\)00427-0](https://doi.org/https://doi.org/10.1016/0016-7037(95)00427-0)
- Qi, C. (2019). *Machine-Learning Aided Design for Cemented Paste Backfill* (Issue October). The University of Western Australia.
- Qiao, X. C., Poon, C. S., & Cheeseman, C. R. (2006). Transfer mechanisms of contaminants in cement-based stabilized/solidified wastes. *Journal of Hazardous Materials*, 129(1–3), 290–296. <https://doi.org/10.1016/j.jhazmat.2005.09.029>

- Qiu, J., Guo, Z., Yang, L., Jiang, H., & Zhao, Y. (2020). Effect of tailings fineness on flow, strength, ultrasonic and microstructure characteristics of cemented paste backfill. *Construction and Building Materials*, 263, 120645. <https://doi.org/10.1016/j.conbuildmat.2020.120645>
- Qiu, J., Zhao, Y., Long, H., Guo, Z., Xing, J., & Sun, X. (2019). Low-Carbon Binder for Cemented Paste Backfill: Flowability, Strength and Leaching Characteristics. *Minerals*, 9(11). <https://doi.org/10.3390/min9110707>
- Rahimi, B., & Ebrahimi, A. (2019). Photocatalytic process for total arsenic removal using an innovative BiVO₄/TiO₂/LED system from aqueous solution: Optimization by response surface methodology (RSM). *Journal of the Taiwan Institute of Chemical Engineers*, 101, 64–79. <https://doi.org/10.1016/j.jtice.2019.04.036>
- Randall, P. M. (2012). Arsenic encapsulation using Portland cement with ferrous sulfate/lime and Terra-Bond™ technologies - Microcharacterization and leaching studies. *Science of the Total Environment*, 420, 300–312. <https://doi.org/10.1016/j.scitotenv.2011.12.066>
- Rankine, R. M., & Sivakugan, N. (2007). Geotechnical properties of cemented paste backfill from Cannington Mine, Australia. *Geotechnical and Geological Engineering*, 25(4), 383–393. <https://doi.org/10.1007/s10706-006-9104-5>
- Ravel, B., & Newville, M. (2005). ATHENA, ARTEMIS, HEPHAESTUS: data analysis for X-ray absorption spectroscopy using IFEFFIT. *Journal of Synchrotron Radiation*, 12(4), 537–541. <https://doi.org/10.1107/S0909049505012719>
- Reedy, C. L., & Reedy, C. L. (2022). High-resolution micro-CT with 3D image analysis for porosity characterization of historic bricks. *Heritage Science*, 10(1), 1–22. <https://doi.org/10.1186/s40494-022-00723-4>
- Reimann, C., Matschullat, J., Birke, M., & Salminen, R. (2009). Arsenic distribution in the environment: The effects of scale. *Applied Geochemistry*, 24(7), 1147–1167. <https://doi.org/https://doi.org/10.1016/j.apgeochem.2009.03.013>
- Rey, N. J., Demers, I., Bussière, B., & Mbonimpa, M. (2020). Laboratory study of low-sulfide tailings covers with elevated water table to prevent acid mine drainage. *Canadian Geotechnical Journal*, 57(12), 1998–2009. <https://doi.org/10.1139/cgj-2018-0875>

- Ribeta, I., Ptacek, C. J., Blowes, D. W., & Jambor, J. L. (1995). The potential for metal release by reductive dissolution of weathered mine tailings. *Journal of Contaminant Hydrology*, 17(3), 239–273. [https://doi.org/10.1016/0169-7722\(94\)00010-F](https://doi.org/10.1016/0169-7722(94)00010-F)
- Robinsky, E. (1975). Thickened discharge - A new approach to tailings disposal. *CIM Bulletin*, 68, 47–53.
- Roussel, N., Stefani, C., & Leroy, R. (2005). From mini-cone test to Abrams cone test: Measurement of cement-based materials yield stress using slump tests. *Cement and Concrete Research*, 35(5), 817–822. <https://doi.org/10.1016/j.cemconres.2004.07.032>
- Roy, R. K. (2010). A primer on the Taguchi method. In *SpringerReference*. https://doi.org/10.1007/springerreference_7290
- Sadatalhosseini, R., Benzaazoua, M., & Tikou, B. (n.d.). *Development of an Artificial Neural Networks (Anns) Model for Estimating Cemented Paste Backfill Performance*. May 2014.
- Şahmaran, M., Christianto, H. A., & Yaman, İ. Ö. (2006). The effect of chemical admixtures and mineral additives on the properties of self-compacting mortars. *Cement and Concrete Composites*, 28(5), 432–440. <https://doi.org/https://doi.org/10.1016/j.cemconcomp.2005.12.003>
- Sahu, U. K., Mahapatra, S. S., & Patel, R. K. (2018). Application of Box–Behnken Design in response surface methodology for adsorptive removal of arsenic from aqueous solution using CeO₂/Fe₂O₃/graphene nanocomposite. *Materials Chemistry and Physics*, 207, 233–242. <https://doi.org/10.1016/j.matchemphys.2017.11.042>
- Saikia, R., Goswami, R., Bordoloi, N., Senapati, K. K., Pant, K. K., Kumar, M., & Kataki, R. (2017). Removal of arsenic and fluoride from aqueous solution by biomass based activated biochar: Optimization through response surface methodology. *Journal of Environmental Chemical Engineering*, 5(6), 5528–5539. <https://doi.org/10.1016/j.jece.2017.10.027>
- Schafer, W. (2016). Geochemical Evaluation of Cemented Paste Tailings in a Flooded Underground Mine. *Mining Meets Water - Conflicts and Solutions*, 714–724.
- Seipel, K. S., Sheumaker, D. L., & Kirk, L. B. (2017). Kinetic Tests of Non-Amended and Cemented Paste. *IMWA - Mine Water and Circular Economy*, June, 1–7.

- Shi, C., & Spence, R. D. (2004). Designing of Cement-Based Formula for Solidification/Stabilization of Hazardous, Radioactive, and Mixed Wastes. *Critical Reviews in Environmental Science and Technology*, 34(4), 391–417. <https://doi.org/10.1080/10643380490443281>
- Shin, H. S., Kim, K. Y., & Pande, G. N. (2013). Porosity and pore-size distribution of geomaterials from X-ray CT scans. *Springer Series in Geomechanics and Geoengineering*, 3, 177–186. https://doi.org/10.1007/978-3-642-32492-5_21
- Silke, R. (2009). The Operational History of Mines in the Northwest Territories, Canada. *Northwest Territories Geoscience Office*, 1–513. www.nwtgeoscience.ca
- Silke, R. (2013). *Giant Mine Milling and Roasting Process, Yellowknife, NWT A Historical Summary* (Issue July).
- Simon, D., & Grabinsky, M. W. (2013). Apparent yield stress measurement in cemented paste backfill. *International Journal of Mining, Reclamation and Environment*, 27(4), 231–256. <https://doi.org/10.1080/17480930.2012.680754>
- Singh, T. S., & Pant, K. K. (2006). Solidification/stabilization of arsenic containing solid wastes using portland cement, fly ash and polymeric materials. *Journal of Hazardous Materials*, 131(1–3), 29–36. <https://doi.org/10.1016/j.jhazmat.2005.06.046>
- Singhania, S., Wang, Q., Filippou, D., & Demopoulos, G. P. (2006). Acidity, valency and third-ion effects on the precipitation of scorodite from mixed sulfate solutions under atmospheric-pressure conditions. *Metallurgical and Materials Transactions B*, 37(2), 189–197. <https://doi.org/10.1007/BF02693148>
- Sivakugan, N., Veenstra, R., & Naguleswaran, N. (2015). Underground Mine Backfilling in Australia Using Paste Fills and Hydraulic Fills. *International Journal of Geosynthetics and Ground Engineering*, 1(2), 1–7. <https://doi.org/10.1007/s40891-015-0020-8>
- Soler, J. M. (2007). *Thermodynamic Description of the Solubility of C-S-H Gels in Hydrated Portland Cement* (Issue Working Report 2007-88).
- Soltani, A., Taheri, A., Khatibi, M., & Estabragh, A. R. (2017). Swelling Potential of a Stabilized Expansive Soil: A Comparative Experimental Study. *Geotechnical and Geological Engineering*, 35(4), 1717–1744. <https://doi.org/10.1007/s10706-017-0204-1>

- Soto-Pérez, L., López, V., & Hwang, S. S. (2015). Response Surface Methodology to optimize the cement paste mix design: Time-dependent contribution of fly ash and nano-iron oxide as admixtures. *Materials and Design*, *86*, 22–29. <https://doi.org/10.1016/j.matdes.2015.07.049>
- Spence, R. D., & Shi, C. (2005). *Stabilization and Solidification of Hazardous, Radioactive, and Mixed Wastes*. CRC Press.
- SRK. (2002). *Indian and Northern Affairs Canada Final Report Arsenic Trioxide Management Alternatives* (Issue December).
- SRK. (2007). *Giant Mine Remediation Plan* (Issue July).
- Stronach, S. A., Walker, N. L., Macphee, D. E., & Glasser, F. P. (1997). ORIGINAL CONTRIBUTION REACTIONS BETWEEN CEMENT AND As (III) OXIDE : THE SYSTEM CaO-SiO₂-As₂O₃-H₂O AT 25 ° C. *Science*, *17*(1), 9–13.
- Su, Z., Chen, Q., Zhang, Q., & Zhang, D. (2019). Recycling lead–zinc tailings for cemented paste backfill and stabilisation of excessive metal. *Minerals*, *9*(11). <https://doi.org/10.3390/min9110710>
- Sullivan, C., Tyrer, M., Cheeseman, C. R., & Graham, N. J. D. (2010). Disposal of water treatment wastes containing arsenic - A review. *Science of the Total Environment*, *408*(8), 1770–1778. <https://doi.org/10.1016/j.scitotenv.2010.01.010>
- Sun, Q., Li, T., & Liang, B. (2020). Preparation of a new type of cemented paste backfill with an Alkali-Activated fume and slag composite binder. *Materials*, *13*(2). <https://doi.org/10.3390/ma13020372>
- Sun, Q., Tian, S., Sun, Q., Li, B., Cai, C., Xia, Y., Wei, X., & Mu, Q. (2019). Preparation and microstructure of fly ash geopolymer paste backfill material. *Journal of Cleaner Production*, *225*, 376–390. <https://doi.org/10.1016/j.jclepro.2019.03.310>
- Sun, Q., Wei, X., Li, T., & Zhang, L. (2020). Strengthening behavior of cemented paste backfill using Alkali-activated slag binders and bottom ash based on the response surface method. *Materials*, *13*(4). <https://doi.org/10.3390/ma13040855>
- Taha, Y., Benarchid, Y., & Benzaazoua, M. (2021). Environmental behavior of waste rocks based concrete: Leaching performance assessment. *Resources Policy*, *74*, 101419.

<https://doi.org/https://doi.org/10.1016/j.resourpol.2019.101419>

- Taha, Yassine, Benzaazoua, M., Edahbi, M., Mansori, M., & Hakkou, R. (2018). Leaching and geochemical behavior of fired bricks containing coal wastes. *Journal of Environmental Management*, 209, 227–235. <https://doi.org/https://doi.org/10.1016/j.jenvman.2017.12.060>
- Tan, Z., Bernal, S. A., & Provis, J. L. (2017). Reproducible mini-slump test procedure for measuring the yield stress of cementitious pastes. *Materials and Structures/Materiaux et Constructions*, 50(6), 1–12. <https://doi.org/10.1617/s11527-017-1103-x>
- Tariq, A., & Yanful, E. K. (2013). A review of binders used in cemented paste tailings for underground and surface disposal practices. *Journal of Environmental Management*, 131, 138–149. <https://doi.org/10.1016/j.jenvman.2013.09.039>
- Taylor, H. F. W. (1997). *Cement chemistry* (2nd editio). Thomas Telford Publishing. <https://doi.org/10.1680/cc.25929>
- Thomas, K. G. (1988). Metallurgical treatment of refractory gold ores. *Intermountain Mining and Processing Operators Symposium*.
- Thomas, K. G., & Cole, A. P. (2016). Roasting Developments – Especially Oxygenated Roasting. In *Gold Ore Processing* (pp. 373–392). Ken Thomas & Murray Pearson. <https://doi.org/10.1016/b978-0-444-63658-4.00023-2>
- Thompson, B. D., Bawden, W. F., & Grabinsky, M. W. (2012). In situ measurements of cemented paste backfill at the Cayeli mine. *Canadian Geotechnical Journal*, 49(7), 755–772. <https://doi.org/10.1139/T2012-040>
- Thompson, N., Spencer, P., & Green, P. (2002). *Management of arsenic trioxide bearing dust at Giant Mine, Yellowknife, northwest territories*.
- Tommaseo, C. E., & Kersten, M. (2002). Aqueous Solubility Diagrams for Cementitious Waste Stabilization Systems. 3. Mechanism of Zinc Immobilization by Calcium Silicate Hydrate. *Environmental Science & Technology*, 36(13), 2919–2925. <https://doi.org/10.1021/es0102484>
- Tsang, D. C. W., Yip, A. C. K., Olds, W. E., & Weber, P. A. (2014). Arsenic and copper stabilisation in a contaminated soil by coal fly ash and green waste compost. *Environmental*

Science and Pollution Research, 21(17), 10194–10204. <https://doi.org/10.1007/s11356-014-3032-3>

Turner, R., & Labiosa, J. (1992). *Arsenic and Mercury - Workshop on Removal, Recovery, Treatment and Disposal*.

USEPA. (1994). Extraction and beneficiation of ores and minerals, Vol. 2: Gold, Technical resource document. In *U.S. Environmental Protection Agency* (Issue November).

USEPA. (1996). Stabilization/solidification processes for mixed waste. In *Epa 402-R-96-014* (Issue 2). <https://www.epa.gov/sites/production/files/2015-05/documents/402-r-96-014.pdf>

USEPA. (2002). Arsenic treatment technologies for solid, waste, and water. *USEPA Report EPA-542-R-02-004*.

Van Hees, E. H. P., Shelton, K. L., McMenemy, T. A., Ross, L. M., Cousens, B. L., Falck, H., Robb, M. E., & Canam, T. W. (1999). Metasedimentary influence on metavolcanic-rock-hosted greenstone gold deposits: Geochemistry of the Giant mine, Yellowknife, Northwest Territories, Canada. *Geology*, 27(1), 71–74. [https://doi.org/10.1130/0091-7613\(1999\)027<0071:MIOMRH>2.3.CO;2](https://doi.org/10.1130/0091-7613(1999)027<0071:MIOMRH>2.3.CO;2)

Vandecasteele, C., Dutré, V., Geysen, D., & Wauters, G. (2002). Solidification/stabilisation of arsenic bearing fly ash from the metallurgical industry. Immobilisation mechanism of arsenic. *Waste Management*, 22(2), 143–146. [https://doi.org/10.1016/S0956-053X\(01\)00062-9](https://doi.org/10.1016/S0956-053X(01)00062-9)

Vespa, M., Dähn, R., & Wieland, E. (2014). Competition behaviour of metal uptake in cementitious systems: An XRD and EXAFS investigation of Nd- and Zn-loaded 11Å tobermorite. *Physics and Chemistry of the Earth, Parts A/B/C*, 70–71, 32–38. <https://doi.org/https://doi.org/10.1016/j.pce.2014.01.001>

Vinter, S., Montanes, M. T., Bednarik, V., & Hrivnova, P. (2016). Stabilization/solidification of hot dip galvanizing ash using different binders. *Journal of Hazardous Materials*, 320, 105–113. <https://doi.org/10.1016/j.jhazmat.2016.08.023>

Wang, C., Qi, Y., Jing, J., Ma, J., Zhou, Y., Ping, H., Zheng, Y., Zhai, Y., & Liu, F. (2023). Properties and microstructure of total tailings cemented paste backfill material containing mining and metallurgical solid waste. *Frontiers in Earth Science*, 11(April), 1–13. <https://doi.org/10.3389/feart.2023.1181952>

- Wang, Y., Wang, S., Song, Y., Zhang, P., Ma, X., Lin, J., Lv, H., Zhang, D., Yao, S., & Jia, Y. (2022). A novel method for in situ stabilization of calcium arsenic residues via yukonite formation. *Science of the Total Environment*, 819. <https://doi.org/10.1016/j.scitotenv.2022.153090>
- Watson, M. A., Tubić, A., Agbaba, J., Nikić, J., Maletić, S., Molnar Jazić, J., & Dalmacija, B. (2016). Response surface methodology investigation into the interactions between arsenic and humic acid in water during the coagulation process. *Journal of Hazardous Materials*, 312, 150–158. <https://doi.org/10.1016/j.jhazmat.2016.03.002>
- Wilk, C. M. (2004). Solidification/stabilization treatment and examples of use at port facilities. *Port Development in the Changing World, PORTS 2004, Proceedings of the Conference*, 907–916. [https://doi.org/10.1061/40727\(2004\)92](https://doi.org/10.1061/40727(2004)92)
- Williams, A. G. B., Scheckel, K. G., Tolaymat, T., & Impellitteri, C. A. (2006). Mineralogy and characterization of arsenic, iron, and lead in a mine waste-derived fertilizer. *Environmental Science and Technology*, 40(16), 4874–4879. <https://doi.org/10.1021/es060853c>
- Wogelius, R. A., & Vaughan, D. J. (2012). Analytical, experimental and computational methods in environmental mineralogy. In D. J. Vaughan & R. A. Wogelius (Eds.), *Environmental Mineralogy II* (Vol. 13, p. 0). Mineralogical Society of Great Britain and Ireland. <https://doi.org/10.1180/EMU-notes.13.2>
- Wrye, L. A. (2008). *Distinguishing between natural and anthropogenic sources of arsenic in soils from the Giant mine, Northwest Territories and the North Brookfield mine, Nova Scotia*. <http://qspace.library.queensu.ca/handle/1974/1547>
- Wu, A., Wang, Y., Wang, H., Yin, S., & Miao, X. (2015). Coupled effects of cement type and water quality on the properties of cemented paste backfill. *International Journal of Mineral Processing*, 143, 65–71. <https://doi.org/10.1016/j.minpro.2015.09.004>
- Wu, D. (2020). Mine Waste Management in China: Recent Development. In *Springer Nature Singapore*. <https://doi.org/10.1007/978-981-32-9216-1>
- Wu, D., Hou, Y., Deng, T., Chen, Y., & Zhao, X. (2017). Thermal, hydraulic and mechanical performances of cemented coal gangue-fly ash backfill. *International Journal of Mineral Processing*, 162, 12–18. <https://doi.org/10.1016/j.minpro.2017.03.001>

- Wu, J., Feng, M., Chen, Z., Mao, X., Han, G., & Wang, Y. (2018). Particle size distribution effects on the strength characteristic of cemented paste backfill. *Minerals*, 8(8). <https://doi.org/10.3390/min8080322>
- Wu, J., Feng, M., Han, G., Ni, X., & Chen, Z. (2019). Experimental investigation on mechanical properties of cemented paste backfill under different gradations of aggregate particles and types and contents of cementing materials. *Advances in Materials Science and Engineering*, 2019. <https://doi.org/10.1155/2019/9456861>
- Xiong, S., Liu, Z., Min, C., Shi, Y., Zhang, S., & Liu, W. (2022). Compressive Strength Prediction of Cemented Backfill Containing Phosphate Tailings Using Extreme Gradient Boosting Optimized by Whale Optimization Algorithm. *Materials (Basel, Switzerland)*, 16(1). <https://doi.org/10.3390/ma16010308>
- Yang, Lei, Yilmaz, E., Li, J., Liu, H., & Jiang, H. (2018). Effect of superplasticizer type and dosage on fluidity and strength behavior of cemented tailings backfill with different solid contents. *Construction and Building Materials*, 187, 290–298. <https://doi.org/10.1016/j.conbuildmat.2018.07.155>
- Yang, Liuhua, Wang, H., Li, H., & Zhou, X. (2019). Effect of high mixing intensity on rheological properties of cemented paste backfill. *Minerals*, 9(4). <https://doi.org/10.3390/min9040240>
- Yilmaz, E., Belem, T., & Benzaazoua, M. (2012). One-dimensional consolidation parameters of cemented paste backfills. *Gospodarka Surowcami Mineralnymi*, 28, 29–45.
- Yilmaz, E., Belem, T., & Benzaazoua, M. (2015). Specimen size effect on strength behavior of cemented paste backfills subjected to different placement conditions. *Engineering Geology*, 185, 52–62. <https://doi.org/10.1016/j.enggeo.2014.11.015>
- Yilmaz, E., Belem, T., Bussière, B., Mbonimpa, M., & Benzaazoua, M. (2015). Curing time effect on consolidation behaviour of cemented paste backfill containing different cement types and contents. *Construction and Building Materials*, 75, 99–111. <https://doi.org/10.1016/j.conbuildmat.2014.11.008>
- Yilmaz, E., Belem, T., Bussière, B., & Mostafa Benzaazoua. (2008). Consolidation characteristics of early age cemented paste backfill. *GeoEdmonton'08, July 2015*, 797–804.
- Yilmaz, E., Benzaazoua, M., Belem, T., & Bussière, B. (2009). Effect of curing under pressure on

- compressive strength development of cemented paste backfill. *Minerals Engineering*, 22(9), 772–785. <https://doi.org/https://doi.org/10.1016/j.mineng.2009.02.002>
- Yilmaz, E., Benzaazoua, M., Bussière, B., & Pouliot, S. (2014). Influence of disposal configurations on hydrogeological behaviour of sulphidic paste tailings: A field experimental study. *International Journal of Mineral Processing*, 131, 12–25. <https://doi.org/https://doi.org/10.1016/j.minpro.2014.08.004>
- Yilmaz, E., Kesimal, A., & Ercikdi, B. (2013). Evaluation of acid producing sulphidic mine tailings as a paste backfill. *TURKISH JOURNAL OF EARTH SCIENCES*, 17, 11–20.
- Yin, G., & Catalan, L. J. J. (2003). Use of Alkaline Extraction to Quantify Sulfate Concentration in Oxidized Mine Tailings. *Journal of Environmental Quality*, 32(6), 2410–2413. <https://doi.org/10.2134/jeq2003.2410>
- Yin, S., Shao, Y., Wu, A., Wang, Y., & Chen, X. (2018). Expansion and strength properties of cemented backfill using sulphidic mill tailings. *Construction and Building Materials*, 165, 138–148. <https://doi.org/10.1016/j.conbuildmat.2018.01.005>
- Yin, S., Shao, Y., Wu, A., Wang, Z., & Yang, L. (2020). Assessment of expansion and strength properties of sulfidic cemented paste backfill cored from deep underground stopes. *Construction and Building Materials*, 230, 116983. <https://doi.org/10.1016/j.conbuildmat.2019.116983>
- Yilmaz, T., Ercikdi, B., & Cihangir, F. (2020). Evaluation of the neutralization performances of the industrial waste products (IWPs) in sulphide-rich environment of cemented paste backfill. *Journal of Environmental Management*, 258(November 2019), 110037. <https://doi.org/10.1016/j.jenvman.2019.110037>
- Yilmaz, T., Ercikdi, B., & Deveci, H. (2021). Evaluation of geochemical behaviour of flooded cemented paste backfill of sulphide-rich tailings by dynamic-tank leaching test. *International Journal of Mining, Reclamation and Environment*, 35(5), 336–355. <https://doi.org/10.1080/17480930.2020.1829778>
- Yoon, I. H., Moon, D. H., Kim, K. W., Lee, K. Y., Lee, J. H., & Kim, M. G. (2010). Mechanism for the stabilization/solidification of arsenic-contaminated soils with Portland cement and cement kiln dust. *Journal of Environmental Management*, 91(11), 2322–2328.

<https://doi.org/10.1016/j.jenvman.2010.06.018>

Zhang, B., Xin, J., Liu, L., Guo, L., & Song, K. II. (2018). An Experimental Study on the Microstructures of Cemented Paste Backfill during Its Developing Process. *Advances in Civil Engineering*, 2018. <https://doi.org/10.1155/2018/9783046>

Zhang, F., Li, Y., Zhang, J., Gui, X., Zhu, X., & Zhao, C. (2022). Effects of slag-based cementitious material on the mechanical behavior and heavy metal immobilization of mine tailings based cemented paste backfill. *Heliyon*, 8(9), e10695. <https://doi.org/10.1016/j.heliyon.2022.e10695>

Zhang, Y., Gao, W., Ni, W., Zhang, S., Li, Y., Wang, K., Huang, X., Fu, P., & Hu, W. (2020). Influence of calcium hydroxide addition on arsenic leaching and solidification/stabilisation behaviour of metallurgical-slag-based green mining fill. *Journal of Hazardous Materials*, 390, 122161. <https://doi.org/https://doi.org/10.1016/j.jhazmat.2020.122161>

Zhang, Y., Zhang, S., Ni, W., Yan, Q., Gao, W., & Li, Y. (2019a). Immobilisation of high-arsenic-containing tailings by using metallurgical slag-cementing materials. *Chemosphere*, 223, 117–123. <https://doi.org/10.1016/j.chemosphere.2019.02.030>

Zhang, Y., Zhang, S., Ni, W., Yan, Q., Gao, W., & Li, Y. (2019b). Immobilisation of high-arsenic-containing tailings by using metallurgical slag-cementing materials. *Chemosphere*, 223, 117–123. <https://doi.org/https://doi.org/10.1016/j.chemosphere.2019.02.030>

Zhao, H., Zhang, H., Tang, M., & Li, F. (2010). In situ chemical stabilization of arsenic contaminated soils using ferrous sulfate. *2010 4th International Conference on Bioinformatics and Biomedical Engineering, ICBBE 2010*, 1–5. <https://doi.org/10.1109/ICBBE.2010.5517439>

Zhao, L. (2023). Immobilization of Cr (VI)- containing tailings by using slag - cementing materials for cemented paste backfill: influence of sulfate and limestone addition. *Environmental Science and Pollution Research*, Vi. <https://doi.org/10.1007/s11356-023-28605-7>

Zhao, Yingliang, Gu, X., Qiu, J., Zhang, S., Guo, Z., & Sun, X. (2022). Recycling of arsenic-containing biohydrometallurgy waste to produce a binder for cemented paste backfill: Influence of additives. *Journal of Cleaner Production*, 363(May), 132515.

<https://doi.org/10.1016/j.jclepro.2022.132515>

Zhao, Yingliang, Qiu, J., Xing, J., & Sun, X. (2020). Chemical activation of binary slag cement with low carbon footprint. *Journal of Cleaner Production*, 267, 121455. <https://doi.org/https://doi.org/10.1016/j.jclepro.2020.121455>

Zhao, Yingliang, Qiu, J., Zhang, S., Guo, Z., Ma, Z., Sun, X., & Xing, J. (2020). Effect of sodium sulfate on the hydration and mechanical properties of lime-slag based eco-friendly binders. *Construction and Building Materials*, 250, 118603. <https://doi.org/https://doi.org/10.1016/j.conbuildmat.2020.118603>

Zhao, Yingliang, Qiu, J., Zhang, S., Guo, Z., Wu, P., Sun, X., & Gu, X. (2022). Recycling of arsenic-containing biohydrometallurgy waste to produce a binder for cemented paste backfill: Mix proportion optimization. *Powder Technology*, 398, 117155. <https://doi.org/10.1016/j.powtec.2022.117155>

Zhao, Yingliang, Wu, P., Qiu, J., Guo, Z., Tian, Y., Sun, X., & Gu, X. (2022). Recycling hazardous steel slag after thermal treatment to produce a binder for cemented paste backfill. *Powder Technology*, 395, 652–662. <https://doi.org/10.1016/j.powtec.2021.10.008>

Zhao, Yue, Soltani, A., Taheri, A., Karakus, M., & Deng, A. (2019). Application of slag–cement and fly ash for strength development in cemented paste backfills. *Minerals*, 9(1). <https://doi.org/10.3390/min9010022>

Zhao, Yue, Taheri, A., Soltani, A., Karakus, M., & Deng, A. (2019). Strength development and strain localization behavior of cemented paste backfills using Portland cement and fly ash. *Materials*, 12(20), 1–21. <https://doi.org/10.3390/ma12203282>

Zheng, J., Sun, X., Guo, L., Zhang, S., & Chen, J. (2019). Strength and hydration products of cemented paste backfill from sulphide-rich tailings using reactive MgO-activated slag as a binder. *Construction and Building Materials*, 203, 111–119. <https://doi.org/10.1016/j.conbuildmat.2019.01.047>

Zhu, Z., Xu, W., Chen, H., Wang, Y., Gou, X., Liu, L., & Gu, Y. (2021). Diffusivity of cement paste via a continuum-based microstructure and hydration model: Influence of cement grain shape. *Cement and Concrete Composites*, 118(December 2020), 103920. <https://doi.org/10.1016/j.cemconcomp.2020.103920>

APPENDIX A COMPLEMENTARY LITERATURE REVIEWS

Table A.1 A summary of the studies on the solidification and stabilization of arsenic-contaminated materials by different binders

Research	Waste(s)	Binder(s)	Results
(Dutré & Vandecasteele, 1996)	An industrial waste material with 32 wt.% As_2O_3	Cement, lime, and BFS	Raising the calcium content in the S/S sample decreased the leachability of arsenic. Lime was more effective than cement in achieving this, whereas the addition of slag had a negative impact.
(Dutré & Vandecasteele, 1998)	A waste fly ash from a Cu refining process with As between 23 to 47 wt.%	BFS, quick lime, and cement	The optimal solidification mixture lowered the arsenic concentration in the extraction test leachate from 5 g/L to 5 mg/L. This substantial reduction was due to the formation of $CaHAsO_3$ in the leachate when $Ca(OH)_2$ was present. However, according to the speciation program MINTEQA2, the formation of $CaHAsO_3$ alone cannot bring the arsenic concentration below 55 mg/L.
(Palfy et al., 1999)	Arsenic sludge of a reaction tower	Calcium oxide and ferric sulfate	The key factor for effective arsenic fixation is the incorporation of calcium and ferric arsenates/arsenites into the cement matrix. This method decreased the original arsenic solubility from 6,430 mg/L in untreated waste to 0.823 mg/L in the final solidified sample.
(J. Y. Kim et al., 2003)	Arsenic-contaminated mine tailings	Amorphous iron precipitates	Adsorption/coprecipitation tests performed with mixed As (III) and Fe (III) solutions significantly improved arsenic sequestration by interacting with amorphous iron compounds as the pH increased.
(Leist et al., 2003)	As_2O_3 , As_2O_5 , Na_3AsO_3 , Na_3AsO_4	OPC, hydrated lime, ferrous sulfate	Samples with the highest Ca:As mole ratios proved to be the most effective. Ettringite was found in the formulations that included cement and ferrous sulfate.
(Dermatas et al., 2004)	Arsenic-contaminated soils	Quicklime and FA	The leaching mechanism for all treated soils was primarily governed by diffusion, with the S/S treatment reducing the effective diffusion coefficients (D_e). Arsenic stabilization was mainly achieved through precipitation.
(Fuessle & Taylor, 2004)	As (III)-laden solid wastes	Hydrogen peroxide (as oxidizer), OPC, FA, and ferrous sulfate	The effectiveness of air oxidation was limited and influenced by the water content. Hydrogen peroxide oxidation proved effective but was hindered by interactions with calcium hydroxide. After oxidation, the arsenate waste produced was successfully stabilized with ferric sulfate.

Table A.1 A summary of the studies on the solidification and stabilization of arsenic-contaminated materials by different binders (continued)

Research	Waste(s)	Binder(s)	Results
(Mollah et al., 2004)	As (V)-bearing wastes	SRPC (type V)	The presence of AsO_4^{3-} hinders the early hydration of cement by forming highly insoluble $\text{Ca}_3(\text{AsO}_4)_2$ on the surface of hydrating cement particles. Despite this, Portland cement can be considered a potential matrix for immobilizing As(V)-bearing wastes.
(Moon et al., 2004)	Arsenic-contaminated slurries	Kaolinite and hydrated lime	Immobilization was primarily governed by precipitation. The efficiency of immobilizing both As (III) and As (V) in the slurries appeared to improve with increasing Ca:As molar ratios.
(Qiao et al., 2006)	Synthetic heavy metal (copper and zinc) sludge	Fine FA and rejected FA	A new radial leach test (RLT) was utilized to study the movement of heavy metals. During leaching, contaminants migrate from the inner core of the S/S waste to the surface, accumulating near the edge. The degree of this accumulation depends on the type of contaminant and the $\text{Ca}(\text{OH})_2$ content.
(Singh & Pant, 2006)	Arsenic contaminated active alumina	OPC, FA, calcium hydroxide (CH)	The reduced leaching of arsenic was due to the formation of calcite and the precipitation of calcium arsenite.
(Kundu & Gupta, 2008)	As (III) and As (V) adsorption processes sludge	OPC and $\text{Ca}(\text{OH})_2$	The low arsenic leaching from the solidified/stabilized samples was mainly because calcite formed, precipitated, and converted into insoluble forms like calcium arsenite, calcium hydrogen arsenate hydrates, and calcium hydrogen arsenates.
(Phenrat et al., 2008)	Arsenic-Iron hydroxide sludge	Ferric chloride	Adsorption, along with other mechanisms like precipitation, co-precipitation, and occlusion, is considered a major factor in arsenic immobilization. The desorption and resorption of arsenic onto the leached sludge are the primary processes influencing arsenic leachability under TCLP conditions.
(Camacho et al., 2009b)	Iron based treatment residuals	Quicklime (CaO) and OPC	The addition of lime as a stabilizing agent decreased arsenic leaching from field treatment residuals. The S/S method using lime and OPC was effective in immobilizing arsenic in water treatment residuals.

Table A.1 A summary of the studies on the solidification and stabilization of arsenic-contaminated materials by different binders (continued)

Research	Waste(s)	Binder(s)	Results
(Choi et al., 2009)	Three abandoned mine tailings contaminated with arsenic and lead	OPC	Incorporating more than 5% cement content met the UCS requirements. The most effective reduction in arsenic leachability and achievement of conservative levels were observed with a 7.5% cement addition. The primary mechanisms for arsenic immobilization in cement-based S/S were the precipitation of $\text{Ca}_3(\text{AsO}_4)_2$ and sorption onto cement hydrates.
(Moon et al., 2010)	Two soil samples contaminated with As and Pb	Quicklime and sulfate	The addition of quicklime-sulfate treatment significantly reduced the release of arsenic and lead compared to untreated samples. This treatment was more effective than using quicklime alone. The release of As and Pb was governed by diffusion processes.
(Yoon et al., 2010)	Arsenic contaminated soils	OPC and CKD	Arsenic concentrations in the leachate treated with OPC and CKD were significantly reduced at pH levels above 3. Important phases identified in the PC- and CKD-treated slurries included calcium arsenite (Ca-As-O) and sodium calcium arsenate hydrate ($\text{NaCaAsO}_4 \cdot 7.5\text{H}_2\text{O}$), which played crucial roles in immobilizing As(III) and As(V), respectively.
(H. Zhao et al., 2010)	Sodium arsenite contaminated soil	Ferrous sulfate	At different arsenic contamination levels, arsenic stabilization efficiency exceeds 90% when the Fe:As molar ratio reaches 6. Within the soil pH range of 8.10 to 8.57, ferrous sulfate performed best, with pH 8.23 being identified as the most effective value.
(Randall, 2012)	Chromated copper arsenate (CCA)-treated wood materials; scorodite-rich mine tailings, and a soil/smelter dust mixture	OPC with ferrous sulfate and lime (PFL) and Terra-Bond™ technologies	Both S/S techniques reduced the amount of arsenic released in leaching tests. The PFL treatment process did not alter the oxidation state of arsenic. Sequential extraction results showed that sodium hydroxide was effective in extracting arsenic from the mine tailings.
(Tsang et al., 2014)	Arsenic and copper contaminated field soil	Coal FA and/or green waste compost; limestone, bentonite, and lignite	Arsenic leaching was reduced through high-affinity adsorption, co-precipitation, and the pozzolanic reaction enabled by coal fly ash. The combined use of coal fly ash and carbonaceous materials was effective in reducing copper leachability. Green waste compost proved more effective than lignite for this purpose.

Table A.1 A summary of the studies on the solidification and stabilization of arsenic-contaminated materials by different binders (continued)

Research	Waste(s)	Binder(s)	Results
(Clancey et al., 2015)	Arsenic-bearing iron oxide wastes	OPC	Cement stabilization reduced arsenic leaching at high pH levels but led to increased leaching at pH values below 4.2 compared to non-stabilized wastes.
(B.-J. Kim et al., 2016)	Arsenic-rich mine tailings	OPC	The leaching fraction of arsenic from the mixtures remained under 6%, regardless of the mix proportions and sample grinding.
(J. S. Li, Beiyuan, et al., 2017)	Different arsenic containing soils	OPC	The immobilization of arsenic in soils treated with S/S primarily depended on physical encapsulation within the interlocking structure of hydration products.
(J. S. Li, Wang, et al., 2017)	Different arsenic containing soils	OPC, FA (class F), FBA, GGBFS	Mineral admixtures with higher calcium content and greater pozzolanic activity were more effective at reducing leached arsenic concentrations. The long-term leaching of naturally occurring arsenic from the monolithic samples was regulated by diffusion processes.
(D. G. Liu et al., 2018)	Flotation waste of copper slag (FWCS), neutralization sludge (NS), and arsenic-containing gypsum sludge (GS)	Cement clinker	The primary hydration products of the matrix were portlandite and calcium silicate hydrate, essential for the S/S of arsenic and heavy metals. The concentrations of heavy metals in the leachate were well below the limits set by the China standard leaching test, suggesting that the stabilized samples could potentially be used as bricks in construction.
(Mohammad Eisa et al., 2020)	Arsenic-contaminated soils	CKD and lime dust	Lime dust had a minor impact on the strength of the samples but significantly affected arsenic sorption. In contrast, CKD had a substantial effect on both the strength of the samples and the immobilization of arsenic.

Table A.2 A Summary of the studies on the mechanical strength of the cemented paste backfills

Research	Tailings	Binders and additives	Mixing waters	Concepts and results
(Benzaazoua et al., 1999)	Abitibian pyrite-rich tailings	Mixture of FA and OPC (40/60) {4.5%}	Mine process water	<p>Concepts: Some strength tests were done on the laboratory prepared CPB samples and in situ cores sampled from a stope.</p> <p>Results: Chemical alterations can significantly impact the long-term strength of backfill. These alterations extend beyond surface oxidation effects and can affect the entire mass of the backfill material.</p>
(Belem et al., 2000)	Two Canadian mill tailings from polymetallic mines with differing sulfide contents	Mixture of OPC with SRPC, FA, and slag {3% - 6%}	Mine process water	<p>Concepts: The mechanical behavior of cemented paste backfill with the mid-term (up to 91 days) and long term (more than 91 days) curing times were assessed.</p> <p>Results: The mid-term mechanical strength consistently improved with higher binder proportions, regardless of curing time, tailings type, or binder type. The hydration of binders was closely linked to particle size distribution and the mineralogy, particularly sulfur content, of the tailings. Long-term cohesion and friction angle of the backfill were influenced by the type of binder and its hydration characteristics. The long-term cohesion specifically depended on the sulfur content of the tailings.</p>

Table A.2 A Summary of the studies on the mechanical strength of the cemented paste backfills (continued)

Research	Tailings	Binders and additives	Mixing waters	Concepts and results
(Benzaazoua et al., 2002)	Mine tailings from four Canadian hard-rock mines	OPC, SRPC, FAs and slags {3% - 6%}	Lake water, municipal water, mine process waters	<p>Concepts: The study evaluated the impact of various chemical factors from mill tailings, binders, and mixing waters on the strength development of paste backfill. Six types of binders and six types of mixing water were utilized to create different paste backfill mixtures.</p> <p>Results: The sulfate content of the mixing water significantly influences the hydration processes, which vary depending on the type of binder and curing time. The interaction between binder chemistry and mixing water chemistry plays a crucial role in the formation of primary and secondary hydrates during the strengthening of paste backfill.</p>
(Benzaazoua, Fall, et al., 2004)	Sulfidic tailings from five Canadian hard rock mines	OPC, SRPC, HSFPC, FA and slag {4.5% and 6%}	Different mixing waters	<p>Concepts: The study focused on investigating the key parameters that influence the performance and hardening process of paste backfill.</p> <p>Results: The mechanical resistance of paste backfill at both short- and long-term curing times is primarily influenced by the physical and chemical properties of the tailings, the type and quantity of binders used, and the chemistry of the water, particularly the content of soluble sulfates. These factors play critical roles in determining the overall performance and durability of the backfill material.</p>
(Fall et al., 2005)	Tailings from a gold and a polymetallic mine	OPC in combination with type V PC and BFS	Tap water	<p>Concepts: The study assessed how the size and density of tailings particles affect the mechanical strength of CPB samples.</p> <p>Results: The amount of fines (<20 μm) in tailings significantly impacts the strength development of CPB. Coarse and medium-sized tailings are more conducive to enhancing CPB strength. The UCS increases with decreasing grain fineness, up to around 35–55% for the undrained paste backfill samples.</p>

Table A.2 A Summary of the studies on the mechanical strength of the cemented paste backfills (continued)

Research	Tailings	Binders and additives	Mixing waters	Concepts and results
(Kesimal et al., 2005)	Two different sulfidic tailings (T1 and T2)	Two PCC {4 - 7 wt.%}	Tap water	<p>Concepts: The study investigated how the physical, chemical, and mineralogical attributes of tailings and binders influence the short- and long-term (up to 360 days) strength of CPB samples.</p> <p>Results: In the initial 28 days, only the paste backfill samples made from 7 wt.% of tailings T1 showed UCS values of ≥ 0.7 MPa. This was linked to the enhanced water retention capability of tailings T2, likely due to its higher silicate content. The amount of additives in binders significantly influences both short-term strength and long-term durability in CPB. Higher pozzolanic content correlates with improved long-term stability of CPB.</p>
(Benzaazoua et al., 2008)	Doyon mine tailings and concentrates after desulfurization	OPC and slag (30/70) {5%}	?	<p>Concepts: The study evaluated how environmental desulfurization affects the mechanical strength of CPB samples prepared using tailings and concentrates from Doyons mine.</p> <p>Results: Environmental desulfurization has the potential to generate non-acidic, low-sulfide tailings and a sulfide concentrate. The sulfide concentrate could then be utilized to create a cemented paste backfill with sufficient strength.</p>
(Ercikdi, Kesimal, et al., 2009)	Sulfide rich mill tailings from a copper-zinc flotation plant	OPC, PCC, and SRPC {5%-7%}	Tap water	<p>Concepts: The study examined how the type and amount of binder affect the mechanical properties of CPB.</p> <p>Results: The binders appeared to be not particularly suitable for CPB of sulfide-rich tailings at low binder dosages (e.g., 5 wt.%). The long-term mechanical performance of CPB was sustained when sulfate-resistant cements were used alone (SRPC) or when blended with OPC. Reducing the w/c ratio also alleviates the loss of strength of CPB samples of PCC.</p>

Table A.2 A Summary of the studies on the mechanical strength of the cemented paste backfills (continued)

Research	Tailings	Binders and additives	Mixing waters	Concepts and results
(Ercikdi, Cihangir, et al., 2009)	Sulfide rich mill tailings of a backfill plant	OPC + WG, FA, GBFS and SF as additives	Tap water	<p>Concepts: The potential use of industrial waste products such as waste glass (WG), fly ash (FA), granulated blast furnace slag (GBFS), and silica fume (SF) as pozzolanic additives for partially replacing OPC in CPB was investigated.</p> <p>Results: A general trend of strength loss in CPB samples was observed in the long term, occurring after the initial 56-day curing period when OPC was used in the binder phase. However, incorporating pozzolanic wastes such as FA, GBFS, and SF into the binder phase appeared to mitigate these long-term strength losses. Although the initial strength development of CPB samples tended to slow down with increased dosages of these pozzolanic wastes in the binder phase, their inclusion helped reduce long-term strength degradation.</p>
(Ercikdi et al., 2010)	sulphide rich mine tailings from a copper-zinc underground mine	OPC and PCC, Three different WRAs	Tailings water and tap water	<p>Concepts: The impact of three different water-reducing admixtures (WRAs) on the mechanical properties of CPB samples was evaluated.</p> <p>Results: The addition of WRAs seemed to enhance the consistency and strength development of CPB. The effectiveness of a WRA largely depended on the type of WRA and the binder used. OPC-based CPB samples achieved the desired mechanical performance (i.e., ≥ 0.7 MPa UCS over ≥ 28 days) only when WRAs were present.</p>

Table A.2 A Summary of the studies on the mechanical strength of the cemented paste backfills (continued)

Research	Tailings	Binders and additives	Mixing waters	Concepts and results
(Fall & Pokharel, 2010)	Ground silica	OPC {4.5 wt.%}	Distilled water	<p>Concepts: The combined effects of curing temperature (0 - 50°C, up to 150 days) and sulfate concentration (0 - 25,000 ppm) on the strength development of hardened CPB samples were evaluated.</p> <p>Results: The interactions between sulfate, temperature, and cement hydration can influence mechanical strength either positively or negatively. The extent of these effects depends on the initial sulfate content and the curing temperature. Higher curing temperatures ($\geq 35^\circ\text{C}$) and initial sulfate contents ($\geq 15,000$ ppm) result in a greater absorption of sulfate ions by the C-S-H.</p>
(Olivier Peyronnard & Benzaazoua, 2011)	Pure silica	OPC, GGBFS, FA (C and F) {4.5%} + 8 by-products (fluorogypsum, CKD, wood BA, wood FA, deinking sludge FA, CAISiFrit, copper slag, WG)	Ferrous sulfate solution	<p>Concepts: The suitability of eight different by-products as supplementary cementitious materials for creating low-cost alternative binders was assessed.</p> <p>Results: The tested pozzolanic by-products are reactive enough to form alternative binders that achieve the required mechanical strength. These by-products exhibit cementitious properties similar to those of coal fly ash. Their reuse for applications requiring low mechanical strength, such as cemented paste backfill or stabilization/solidification purposes, was approved. The economic viability of reusing these by-products depends on their treatment and shipping costs, as well as potential savings in storage costs.</p>

Table A.2 A Summary of the studies on the mechanical strength of the cemented paste backfills (continued)

Research	Tailings	Binders and additives	Mixing waters	Concepts and results
(Olivier Peyronnard & Benzaazoua, 2012)	Pure silica and mill tailings	OPC and GGBFS + Wood BA, copper slag, WG and type F coal FA, as pozzolanic by-products; CKD and Anh as activating by-products	Tap water	<p>Concepts: Four pozzolanic by-products (waste glass, copper slag, wood bottom ash, and coal fly ash) and two hydration-activating by-products (CKD and anhydrite) were combined with OPC and GGBFS to develop low-cost binders for use in CPB. The binder formulations were optimized using the Taguchi method.</p> <p>Results: Due to their high reactivity, GGBS enables the development of high mechanical strength, and its content in binders can be adjusted to meet the strength requirements for mine exploitation. By-products contribute to strength gain, and higher quantities accelerate strength development. When mixed with Portland cement, anhydrite serves as a calcium source for pozzolanic reactions, with its sulfate content promoting the formation of sulfated minerals that enhance strength in CPB. CKD is an effective alkaline activator but should be used in small amounts (5%).</p>
(Ercikdi et al., 2013)	Two different sulfide-rich mill tailings of a copper-zinc plant	PCC {4.5-8.5 % wt.}	Tap water	<p>Concept: The impact of desliming two different sulfide tailings on the short- and long-term mechanical performance of CPB was assessed.</p> <p>Results: The strength and stability of CPB improved with higher binder dosages. Desliming the tailings significantly enhanced both the short- and long-term UCS of CPB samples.</p>

Table A.2 A Summary of the studies on the mechanical strength of the cemented paste backfills (continued)

Research	Tailings	Binders and additives	Mixing waters	Concepts and results
(Ercikdi et al., 2014)	Two different mill tailings samples from a copper plant	BFS cement {5 - 7 wt%}	Tap water	<p>Concepts: The UCS and UPV properties of CPB made from two different mill tailings were evaluated at various binder dosages and curing periods.</p> <p>Results: The strength and UPV properties of CPB samples improved with higher binder dosages and lower w/c ratios. Smaller (5×10 cm) CPB samples consistently exhibited higher UCS values (1.0–1.69 times greater) compared to larger (10×20 cm) samples across all curing times. A linear correlation was observed between UCS and UPV values for a given binder dosage and w/c ratio. The UPV test, being cost-effective, quick, and practical, can reliably assess UCS and the quality of CPB samples.</p>
(A. Wu et al., 2015)	Tailings from a lead/zinc mine and slag (as a coarse aggregate)	Three types of OPC {8.89%}	Tailings pore water and distilled water	<p>Concepts: The impact of various cement types and mixing water qualities on CPB properties was evaluated.</p> <p>Results: The type of cement used had a significant impact on the UCS of the paste. In contrast, water quality had only a minor effect on the UCS, as paste strength is primarily governed by cement hydration.</p>
(Yilmaz, Belem, & Benzaazoua, 2015)	Tailings from the paste backfill plant	OPC and BFS {3, 4.5, and 7%}	Tap water	<p>Concepts: The effects of specimen size and curing conditions (capped/uncapped, drained/undrained) on the strength properties of CPB samples were evaluated using UCS tests.</p> <p>Results: The diameter of the specimen significantly impacts the overall mechanical strength, given a constant height-to-diameter ratio. The optimal specimen size for both the rate of strength development and ultimate strength was determined to be 5×10 cm. Placement and curing conditions also notably influence sample strength. Drained paste backfills consistently exhibit higher strengths than undrained ones due to the removal of excess water within the CPB.</p>

Table A.2 A Summary of the studies on the mechanical strength of the cemented paste backfills (continued)

Research	Tailings	Binders and additives	Mixing waters	Concepts and results
(Cihangir & Akyol, 2016)	sulfide-rich full tailings (FT) and delimed tailings (DT)	OPC and AAS	Tap water	<p>Concepts: The mechanical strength of CPB samples made from sulfide-rich full tailings (FT) and delimed tailings (DT) was examined over a curing period of 360 days.</p> <p>Results: Desliming tailings enhanced strength development by 1.5–2.3 times, with improvements increasing over time, and extended the durability of OPC samples in the long term. However, a decrease of 11.4% in strength was observed after 224 days in OPC/DT samples. The poor performance of OPC in aggressive environments is likely due to its high C3A and C3S contents.</p>
(Cui & Fall, 2016)	Artificial tailings (ground silica)	OPC	Tap water	<p>Concepts: An experimental setup was created to allow for the curing of CPB samples under varying stresses, filling rates, initial temperatures, and drainage conditions. This setup was used to investigate how these parameters affect the mechanical properties of the CPB samples.</p> <p>Results: The initial temperature of CPB has a significant impact on its mechanical and thermal properties at early ages. Higher initial temperatures lead to increased UCS, elastic modulus, and cohesion, while decreasing thermal conductivity. Additionally, under drained conditions, CPB exhibits higher UCS, elastic modulus, and cohesion, and lower thermal conductivity. This is because drained water significantly alters the degree of saturation and suction in CPB, thereby increasing the effective stress.</p>
(Ghirian & Fall, 2016)	artificial silica tailings	OPC {4.5 wt.%}	Tap water	<p>Concepts: A pressure cell apparatus has been developed to examine the early-age evolution of strength and deformation behavior in cemented paste backfill.</p> <p>Results: Curing time and curing stress enhance the mechanical properties and deformation behavior of CPB samples at early ages.</p>

Table A.2 A Summary of the studies on the mechanical strength of the cemented paste backfills (continued)

Research	Tailings	Binders and additives	Mixing waters	Concepts and results
(Koohestani et al., 2016)	Tailings from an ore processing plant	GU and GGBFS (20/80) {2, 4.5, and 7 wt.%} + maple wood sawdust	Tap water	<p>Concepts: The impact of adding maple-wood sawdust on the mechanical and microstructural properties of CPB was investigated.</p> <p>Results: Adding 12.5% maple-wood sawdust (by dry mass of binder) enhances the strength development of CPB specimens at later hydration ages (91 curing days). However, at a higher maple-wood sawdust content of 14.5%, the UCS improvement is reduced.</p>
(W. Li & Fall, 2016)	Artificial silica tailings	OPC	Distilled water (with specified amount of sulfate)	<p>Concepts: The effects of sulfate on the early-age strength (up to 28 days) and self-desiccation of CPB samples were evaluated.</p> <p>Results: Sulfate negatively impacts the early-age strength of CPB, with the effect becoming more pronounced as sulfate concentration increases. The absorption of sulfate by C-S-H contributes to the reduction in early strength, potentially leading to the formation of a weaker C-S-H gel.</p>
(Q. Chen, Zhang, Fourie, Chen, et al., 2017)	Iron tailings	A specific cement and furnace slag	Tap water	<p>Concepts: A series of experiments were conducted using a large-scale similar stope model (SSM) to simulate the consolidation of CPB within a stope. Following this, UCS tests were performed on specimens cored from various positions within the CPB sample.</p> <p>Results: The strength exhibits a wave-like variation along the horizontal flow direction of the paste. In the vertical direction, strength decreases gradually from the bottom to the top of the SSM, with sharp changes observed at certain top sections of the SSM.</p>

Table A.2 A Summary of the studies on the mechanical strength of the cemented paste backfills (continued)

Research	Tailings	Binders and additives	Mixing waters	Concepts and results
(Q. Chen, Zhang, Fourie, & Xin, 2017)	Phosphogypsum (PG) and phosphate tailings (PTS)	OPC, slag and CaO	?	<p>Concepts: The feasibility of using phosphogypsum (PG) and phosphate tailings (PTS) for CPB production was analyzed.</p> <p>Results: PTS and PG are not ideal backfill materials due to their low strength and the substantial amounts of gases they release, such as CO₂ and SO₂. While slags can significantly enhance backfill strength, they also produce various gases, including H₂S. Cement serves as a suitable binder and can also act as an effective activator, potentially binding PG and PTS to create a stronger backfill.</p>
(X. Deng et al., 2017)	Waste rock (sandstone and sandy shale) as coarse aggregate and FA as fines	OPC, FA and lime slag (as a FA activator)	Tap water	<p>Concepts: The effects of solids content and composition on the mechanical characteristics of CPB were investigated.</p> <p>Results: The mechanical strength of CPB improves significantly with increased solid content. Additionally, higher OPC content leads to much better mechanical performance of the CPB.</p>
(H. Jiang & Fall, 2017a)	Non-reactive silica tailings (ST)	OPC {4.5 wt.%}	distilled water with various NaCl concentrations	<p>Concepts: The study examined how the strength and deformation characteristics of CPB change over time at various saline concentrations in a sub-zero environment (-6 °C).</p> <p>Results: Higher salinity leads to a notable reduction in UCS because increased salinity correlates with more unfrozen water in the CPB, which weakens its strength. The transition from strain-softening in CPB samples with no salinity to strain-hardening in samples with high NaCl concentrations is attributed to the rise in unfrozen water content as salinity increases.</p>

Table A.2 A Summary of the studies on the mechanical strength of the cemented paste backfills (continued)

Research	Tailings	Binders and additives	Mixing waters	Concepts and results
(H. Jiang & Fall, 2017b)	artificial silica tailings (ST)	A mixture of OPC and slag (50/50) {4.5 wt.%}	distilled water with various NaCl contents	<p>Concepts: The effect of different sodium chloride (NaCl) concentrations (0, 5, 35, and 100 g/L) on the development of strength in CPB samples under sub-zero conditions was examined.</p> <p>Results: The UCS of the CPB samples declined with increasing NaCl concentration, primarily due to the higher amount of unfrozen water. Comparing the mechanical performance, CPB samples with no salinity showed that substituting OPC with Slag enhanced strength regardless of curing time. However, CPB samples made with OPC demonstrated a more rapid increase in strength after 28 days of curing.</p>
(D. Wu et al., 2017)	Coal gangue	OPC and FA	Tap water	<p>Concepts: A testing apparatus was developed to examine the mechanical performance, specifically lateral expansion, of cemented coal gangue-fly ash backfill (CGFB) columns under pressure in both drained and laterally constrained conditions.</p> <p>Results: A higher OPC/FA ratio leads to greater temperature rise in CGFB due to increased cement hydration reactions that release more heat. Raising the OPC/FA ratio and curing temperature can speed up cement chemical reactions, resulting in quicker and greater strength development in CGFB. Additionally, a higher OPC/FA ratio and curing temperature are linked to reduced porosity in CGFB.</p>
(Cao et al., 2018)	Dried mine tailings	OPC	Tap water	<p>Concepts: The impact of structural factors—including filling time (FT, 1-4 stages), filling interval time (FIT, 12-48 hours), and filling surface angle (FSA, 0-60°)—on the UCS of CPB samples was experimentally studied.</p> <p>Results: The UCS of the CPB samples decreased as the FT increased. As the FIT was extended, the UCS values of the CPB samples gradually declined. The UCS exhibited a U-shaped pattern with FSA, initially decreasing and then increasing as the FSA increased.</p>

Table A.2 A Summary of the studies on the mechanical strength of the cemented paste backfills (continued)

Research	Tailings	Binders and additives	Mixing waters	Concepts and results
(X. Chen et al., 2018)	Tailings of a lead-zinc mine	OPC + Monofilament polypropylene (PP) fibers	Tap water	<p>Concepts: The effect of polypropylene (PP) fiber on the compressive properties of the CPB sample was investigated.</p> <p>Results: While fiber parameters may not be as critical as cement content and solid mass concentration for CPB strength, they still play a significant role in enhancing UCS. The impact of PP fiber on the backfill's strength is more pronounced at early (3 days) and later (28 days) curing stages compared to the medium stage (7 days).</p>
(Cihangir et al., 2018)	Full tailings (FT) and coarse (deslimed) tailings (CT)	SSAS at different silicate modulus (Ms), OPC {7%}, sodium hydroxide (SH) for Ms adjustment, Na ₂ O as an activator	?	<p>Concepts: The short- and long-term strength development of full (FT) and coarse sulphidic tailings (CT) cemented paste backfill (CPB) produced from SSAS at various Ms levels was examined.</p> <p>Results: Strengths achieved with SSAS at various Ms levels were 1.5 to 3.5 times greater in the long term compared to those with OPCs. SSAS also provided 3.0 to 7.6 times the strength of FT and CT at 360 days when Ms was between 1.0 and 1.5, surpassing the required threshold strength for the long term.</p>
(Koohestani et al., 2018)	A sulfidic and a non-sulfidic tailings	GU cement + Three types of WRAs	Tap water	<p>Concepts: The effect of water repellency, induced by non-polar organosilanes (vinyl and methyl) and polycarboxylate superplasticizer, on the strength development of CPB made from sulfidic and non-sulfidic tailings was investigated.</p> <p>Results: The inclusion of vinyl silane in CPB resulted in higher UCS values and reduced the water needed for a given slump height. However, adding vinyl and methyl organosilanes was less beneficial for CPBs made from sulfidic tailings, as it led to reduced early strength development.</p>

Table A.2 A Summary of the studies on the mechanical strength of the cemented paste backfills (continued)

Research	Tailings	Binders and additives	Mixing waters	Concepts and results
(Mangane et al., 2018)	Tailings from a polymetallic mine	GU (OPC) and mixture of GU/Slag (20/80) + various superplasticizers	Deionised water	<p>Concepts: The effect of different dosages of superplasticizer on the strength of CPB samples was examined.</p> <p>Results: The addition of superplasticizers to CPB improved its mechanical strength. Among them, the polycarboxylate-based superplasticizer was particularly effective, increasing mechanical strength by 100% to 250% at 28 days.</p>
(Ouattara et al., 2018)	Polymetallic ore tailings and gold ore tailings	GGBFS and OPC {3.5 - 6%} + different superplasticizers	Deionized water	<p>Concepts: The impact of various high-range water reducers (HRWRs) on the UCS of CPB samples was studied.</p> <p>Results: The UCS of CPB incorporating HRWR improved as the binder content increased from 3.5% to 6%. PC-type HRWR produced similar UCS values across different HRWR types. Using HRWR in CPB formulations could potentially reduce the binder content by approximately 1%.</p>
(J. Wu et al., 2018)	Natural tailings	PCC	?	<p>Concepts: Ultrasonic testing, uniaxial and triaxial compression experiments, and acoustic emission (AE) monitoring were conducted on CPB.</p> <p>Results: The strength parameter model for CPB, considering the combined effects of confining pressure and particle size distribution, is linked to the material's cohesiveness and internal friction properties, with each parameter having specific physical significance. Increased confining pressure enhances the peak strength and compressibility of CPB and significantly boosts its ductility.</p>

Table A.2 A Summary of the studies on the mechanical strength of the cemented paste backfills (continued)

Research	Tailings	Binders and additives	Mixing waters	Concepts and results
(Lei Yang et al., 2018)	Dried tailings of a mineral processing plant	OPC + three superplasticizers	Tap water	<p>Concepts: The combined effects of solid content, superplasticizer type, and dosage on the strength properties of CPB were evaluated.</p> <p>Results: Increasing the superplasticizer dosage resulted in higher UCS for CPB samples, particularly those with longer curing times. Additionally, a higher solid content also contributed to greater UCS, especially at 28 days of curing.</p>
(S. Yin et al., 2018)	Sulfidic tailings from an underground copper mine	OPC	Tap water	<p>Concepts: The impact of curing time, sulfur content, cement dosage, and solids concentration on the free expansion ratio (FER) of CPB specimens was evaluated.</p> <p>Results: Expansion is a crucial factor affecting the strength and stability of swelling CPB. Samples with high binder content (less than 16%) may still experience structural deformation in a standard curing environment. OPC alone is not effective for maintaining long-term mechanical strength in sulfidic backfill; it results in both strength loss and continued expansion. The expansion ratio of CPB specimens increases with higher solids concentration.</p>
(H. Cheng et al., 2019)	Unclassified dried tailings from a nickel mine	OPC	Tap water	<p>Concepts: An orthogonal design was employed in the experiments to investigate the effects of various factors on the strength development of CPB samples.</p> <p>Results: Based on the experimental results and existing strength prediction models, a new strength prediction model for waste rock unclassified tailings paste was proposed. The relationship between strength and the water-cement ratio followed a negative exponential trend. Additionally, UCS and cement-tailings ratio exhibited an exponential relationship. The strength increase with the tailings-waste ratio was nonlinear, and the relationship between strength and curing time was logarithmic.</p>

Table A.2 A Summary of the studies on the mechanical strength of the cemented paste backfills (continued)

Research	Tailings	Binders and additives	Mixing waters	Concepts and results
(Hu et al., 2019)	mineral processing discharge products from the concentrator	OPC and stone powder	Tap water	<p>Concepts: The impact of various humidity conditions during curing on the mechanical strength of CPB samples was investigated.</p> <p>Results: As curing humidity increased, both the pore size and the proportion of small pores grew. Under consistent humidity conditions, the UCS of the specimens decreased with a higher amount of stone powder. The UCS was found to be linearly and inversely proportional to the size of the small pores. Both hydration products and stone powder influenced pore size, thereby affecting the compactness of the CPB. Using stone powder instead of cement effectively reduced filling costs.</p>
(H. Jiang, Qi, et al., 2019)	Processing tailings of a gold flotation plant	OPC and AAS + A combination NaOH and Na ₂ SiO ₃) solutions as the alkaline activator	Tap water	<p>Concepts: The effects of solid content, binder dosage, activator-to-binder (Al/Bi) ratio, sodium silicate-to-sodium hydroxide (SS/SH) ratio and curing temperature on the fresh and hardened properties of AAS-CPB were experimentally investigated.</p> <p>Results: For a given backfill recipe and curing time, the AAS-CPB matrix shows significantly better UCS performance (2.2 to 3.3 times higher) compared to the OPC CPB matrix. UCS improves with higher solid content, and increased binder dosage also enhances the strength of the AAS-CPB matrix.</p>
(L. Liu, Zhu, et al., 2019)	Tailings of a copper mine	OPC	Tap water + ice slag	<p>Concepts: The performance of ICED CPB under the combined effects of curing time and ice/water ratio (IWR) was investigated experimentally.</p> <p>Results: UCS decreased with increasing curing time due to the continuous cement hydration over time. Regarding the IWR, UCS initially increased but then decreased as the IWR increased.</p>

Table A.2 A Summary of the studies on the mechanical strength of the cemented paste backfills (continued)

Research	Tailings	Binders and additives	Mixing waters	Concepts and results
(Mbonimpa et al., 2019)	Tailings obtained by grinding core samples	HEPC (type III) and mixture of GGBFS/GU (80/20) {3 and 5 wt. %}	Deionised water with salt concentration of 5 g/L	<p>Concepts: The effect of decreasing curing temperature (above freezing) on the evolution of UCS in CPB was studied.</p> <p>Results: For CPB mixtures cured in the humidity chamber, HEPC achieved higher UCS compared to GGBFS-GU binder. Across both binder types, UCS was consistently higher for CPB cured in the humidity chamber than for those cured under decreasing temperatures in a temperature-controlled chamber, regardless of curing time. At a given curing temperature, UCS progressively increased from the permafrost wall towards the center of the CPB matrix.</p>
(C. Min et al., 2019)	A solid waste phosphogypsum (PG)	Yellow phosphorous slag, FA, and cement clinker in 4:1:1 ratio + 16–20% lime	?	<p>Concepts: The impact of mixing time on the cemented backfill process was investigated.</p> <p>Results: The mechanical strength of the hardened backfill was influenced by the mixing time, with samples mixed for 60 minutes achieving the highest UCS. Additionally, it appears that porosity, rather than the hydration products, is the primary factor affecting the UCS of the backfill.</p>
(Qiu et al., 2019)	Mine tailings from an iron mine	BFS, OPC, and gypsum + NaOH solution as the alkaline activator	Tap water	<p>Concepts: BFS served as the primary raw material for producing alkali-activated slag (AAS) in CPB preparation, and the strength properties of the CPB samples were analyzed to develop a predictive model for their compressive strength.</p> <p>Results: A predictive model for the compressive strength of CPB samples was developed using multivariate analysis. The fitting equations had correlation coefficients (R^2) greater than 0.9, demonstrating high predictive accuracy.</p>

Table A.2 A Summary of the studies on the mechanical strength of the cemented paste backfills (continued)

Research	Tailings	Binders and additives	Mixing waters	Concepts and results
(Su et al., 2019)	Tailings of a lead-zinc mine	OPC + Polyaluminium chloride (PAC) and polyaluminium sulfate (PAS)	?	<p>Concepts: The mechanical properties of CPB samples produced from lead-zinc tailings (LZT) were examined.</p> <p>Results: The UCS test results indicated that CPB made from LZT could serve as a viable alternative for large-scale utilization of lead-zinc tailings.</p>
(J. Wu et al., 2019)	Waste rock	Clay, gypsum and PCC	Distilled water	<p>Concepts: The impact of aggregate particle Talbot indices, as well as the types and amounts of cementing materials, on the mechanical properties of CPB was analyzed.</p> <p>Results: The mechanical parameters of CPB specimens made with cement were notably higher compared to those cemented with clay or gypsum. Additionally, the UCS of CPB specimens increased with a higher content of cementing material.</p>
(Yue Zhao, Taheri, et al., 2019)	Tailings of a copper-gold underground mine	OPC {1 - 5%} + Class C FA {0 - 3%}	Processed mine water	<p>Concepts: The combined effects of OPC (as the binder) and FA (as the additive) on enhancing the mechanical performance of a CPB system for a copper-gold underground mine were evaluated.</p> <p>Results: Higher OPC content and/or longer curing periods resulted in greater strength, stiffness, and toughness. The addition of FA to OPC further enhanced strength and stiffness by promoting secondary pozzolanic reactions. The analysis of axial and lateral strains revealed that strain localization begins in the pre-peak phase, approximately at 80% of the UCS.</p>

Table A.2 A Summary of the studies on the mechanical strength of the cemented paste backfills (continued)

Research	Tailings	Binders and additives	Mixing waters	Concepts and results
(Yue Zhao, Soltani, et al., 2019)	Tailings of a copper-gold underground mine	Slag-blended cement {1.5-3%} + Class C FA {0 - 2.5%}	Processed mine water	<p>Concepts: The effectiveness of a newly developed slag-blended cement (MC) combined with fly ash (FA) in enhancing the mechanical performance of CPB samples as a sustainable solution was evaluated.</p> <p>Results: Higher MC content and/or longer curing periods resulted in increased strength, toughness, and stiffness. The addition of FA to MC enhanced the bond between tailings aggregates, leading to better mechanical performance compared to similar MC inclusions without FA. For any given FA content, increasing the MC content further improved the mechanical properties.</p>
(H. Jiang, Yi, et al., 2020b)	Artificial silica tailings	OPC in combination with FA and BFS	Tap water	<p>Concepts: The impact of mineral admixtures and curing temperature on the UCS and UPV behavior of laboratory-prepared CPB samples was investigated.</p> <p>Results: The addition of FA can either increase or decrease the UCS and UPV behavior of CPB samples, depending on the level of admixture replacement. Both UPV and UCS decreased with higher BFS replacement levels due to its low pozzolanic reactivity. Curing temperature significantly affects UCS and UPV behavior, with the impact varying based on the curing time.</p>
(Y. Liu et al., 2020)	Coal gangue	Cement and FA + Na ₂ SO ₄ with two superplasticizers	Tap water	<p>Concepts: The impact of an accelerator-water reducer admixture on the UCS performance of CPB was studied experimentally.</p> <p>Results: The addition of the accelerator-water reducer admixture enhanced the UCS of the CPB, reduced cement usage by 2%, and improved the utilization rates of fly ash and coal gangue.</p>
(Qiu et al., 2020)	Artificial silica tailings	OPC	Tap water	<p>Concepts: The impact of tailings fineness on the UCS of CPB was evaluated.</p> <p>Results: The UCS of hardened CPB initially decreased with increasing tailings fineness up to 54.42%, and then increased slightly.</p>

Table A.3 A summary of the studies on the rheological properties of the cemented paste backfills

Research	Tailings	Binders and additives	Mixing waters	Concepts and results
(Ercikdi et al., 2010)	Sulphide rich mine tailings from a copper-zinc underground mine	OPC and PCC + Three different WRAs	Tailings water and tap water	<p>Concepts: The impact of three different water-reducing admixtures (WRAs) on the rheological properties of CPB samples was assessed.</p> <p>Results: The consistency of CPB mixtures improved with higher dosages of WRAs. The effectiveness of WRAs seemed to vary with the binder type, being more effective for OPC compared to PCC.</p>
(Simon & Grabinsky, 2013)	Typical mine tailings	OPC and FA (70/30) + two superplasticizers (PCA and NSF)	Deionised water	<p>Concepts: The impact of specimen composition on the rheological properties of CPB was studied.</p> <p>Results: The presence of the binder blend increased the apparent yield stress initially, likely due to denser particle packing. Both admixtures reduced the apparent yield stress of the mixtures, but the extent of reduction varied depending on the type and concentration of the admixture.</p>
(A. Wu et al., 2015)	Tailings from a lead/zinc mine and slag (as a coarse aggregate)	Three types of OPC {8.89%}	Tailings pore water and distilled water	<p>Concepts: The impact of various cement types and mixing water qualities on CPB properties was assessed.</p> <p>Results: The influence of cement type and water quality on CPB slump was minimal, as the slump is primarily determined by aggregate size and water content.</p>
(Haiqiang et al., 2016)	Artificial silica tailings (ST), gold tailings (GT), and zinc tailings (ZT)	OPC in combination with FA and slag (50/50)	Tap and distilled waters with different amounts of NaCl	<p>Concepts: The combined effects of time and sub-zero temperatures on the yield stress of CPB were investigated.</p> <p>Results: The yield stress of CPB samples exposed to sub-zero temperatures was found to be much lower compared to samples kept at room temperature. Higher water-cement ratios and sodium chloride concentrations, as well as lower sub-zero curing temperatures, resulted in reduced yield stress.</p>
(X. Deng et al., 2017)	Waste rock (sandstone and sandy shale) as coarse aggregate and FA as fines	OPC, FA and lime slag (as FA activator)	Tap water	<p>Concepts: The impact of solids content and composition on the rheological characteristics of CPB was studied.</p> <p>Results: Workability of CPB decreased with reduced water content and also declined as the proportion of lime slag increased.</p>

Table A.3 A summary of the studies on the rheological properties of the cemented paste backfills (continued)

Research	Tailings	Binders and additives	Mixing waters	Concepts and results
(H. Jiang & Fall, 2017a)	Non-reactive silica tailings (ST)	OPC {4.5 wt.%}	Distilled water with various NaCl contents	<p>Concepts: The time-dependent changes in yield stress of CPB with varying saline concentrations in a sub-zero environment ($-6\text{ }^{\circ}\text{C}$) were investigated.</p> <p>Results: The addition of NaCl significantly enhanced the flowability of CPB in a sub-zero environment. Yield stress decreased with increasing salinity, primarily due to the adsorption of chloride ions onto the surfaces of cement particles and hydration products (e.g., C-S-H), which increased the zeta potential of these particles and products.</p>
(H. Jiang & Fall, 2017b)	Artificial silica tailings (ST)	A mixture of OPC and slag (50/50) {4.5 wt.%}	Distilled water with various NaCl contents	<p>Concepts: The impact of different sodium chloride (NaCl) concentrations (0, 5, 35, and 100 g/L) on the yield stress of CPB samples in sub-zero environments was investigated.</p> <p>Results: The addition of NaCl reduces the yield stress of fresh Slag-CPB, enhancing its flowability. Increased salinity in the pore fluid leads to a reduction in yield stress.</p>
(X. Chen et al., 2018)	Tailings of a lead-zinc mine	OPC + Monofilament polypropylene (PP) fibres	Tap water	<p>Concepts: The effect of polypropylene (PP) fiber on the slump values of CPB samples was studied.</p> <p>Results: The slump values for both unreinforced and fiber-reinforced backfill were nearly identical, indicating that the addition of fiber did not affect the backfill's fluidity.</p>
(Koohestani et al., 2018)	A sulfidic and a non-sulfidic tailing	GU cement + Three types of WRAs	Tap water	<p>Concepts: The impact of non-polar organosilanes (vinyl and methyl) and polycarboxylate superplasticizer on the flow behavior of cemented paste backfill (CPB) made from both sulfidic and non-sulfidic tailings was examined.</p> <p>Results: Adding vinyl silane to the CPB decreased the amount of water needed to achieve a specific slump height. A strong correlation coefficient (0.98–0.99) was observed between the amount of admixtures used and the reduction in water requirement.</p>

Table A.3 A summary of the studies on the rheological properties of the cemented paste backfills (continued)

Research	Tailings	Binders and additives	Mixing waters	Concepts and results
(Mangane et al., 2018)	Tailings from a polymetallic mine	GU (OPC) and mixture of GU/Slag (20/80) + three superplasticizers	Deionised water	<p>Concepts: The effect of different superplasticizer dosages on the workability of the CPB samples was investigated.</p> <p>Results: Incorporating superplasticizers into CPB reduced water demand by 6–10% and enhanced both slump and workability. The effectiveness of the superplasticizers varied depending on the type used, with the polycarboxylate-based superplasticizer proving to be the most effective at reducing water demand in this study.</p>
(Ouattara et al., 2018)	Polymetallic ore tailings and gold ore tailings	GGBFS and OPC {3.5 - 6%} + different types of superplasticizers	Deionised water	<p>Concepts: The impact of various high-range water reducers (HRWR) on the consistency of CPB samples was explored.</p> <p>Results: Higher dosages of HRWR enhanced the consistency of CPB, irrespective of the solids and binder contents. Additionally, increasing the binder content from 3.5% to 6% led to better slump in CPB with HRWR. Among the different HRWR types, PC-type HRWR yielded a higher slump compared to PNS- and PMS-type HRWR. Using HRWR in CPB formulations could potentially allow for a reduction in binder content by approximately 1%.</p>
(Panchal et al., 2018)	Tailings from dolostone hosted uranium ore processing mill	OPC + Polycarboxylate (PC) based superplasticizer	Tap water	<p>Concepts: A method for assessing yield stress, plastic viscosity, and thixotropic behavior of the CPB mixture based on hydration age, binder content, and superplasticizer dosages was described.</p> <p>Results: Yield stress, thixotropy, and plastic viscosity change linearly with hydration age for a given binder and PC dosages. The mini-slump test confirms the logarithmic increase in yield stress with hydration age. Multivariate linear regression modeling reveals strong correlations between rheological parameters and input variables, indicating that the rheology of CPB is more responsive to PC dosage than to hydration age.</p>

Table A.3 A summary of the studies on the rheological properties of the cemented paste backfills (continued)

Research	Tailings	Binders and additives	Mixing waters	Concepts and results
(Lei Yang et al., 2018)	Dried tailings from the discharge of a mineral processing plant	OPC + Naphthalene sulfonic acid-formaldehyde (S1), ether- and ester-based polycarboxylate (S2 & S3) superplasticizers	Tap water	<p>Concepts: The combined impact of solid content and the type and dosage of superplasticizer on the fluidity properties of CPB was evaluated.</p> <p>Results: The impact of superplasticizer on the fluidity of fresh CPB samples was analyzed with respect to solid content, superplasticizer type, and dosage. Superplasticizer S1 had a more significant effect on fluidity compared to S2 and S3. Additionally, as the solid content increased, CPB samples with higher superplasticizer dosages exhibited reduced fluidity.</p>
(H. Jiang, Qi, et al., 2019)	Processing tailings of a gold flotation plant	OPC and AAS + A combination NaOH and Na ₂ SiO ₃ solutions as the alkaline activator	Tap water	<p>Concepts: The experimental investigation focused on the effects of solid content, binder dosage, activator-to-binder (Al/Bi) ratio, sodium silicate-to-sodium hydroxide (SS/SH) ratio and curing temperature on the fresh and hardened properties of AAS-CPB mass.</p> <p>Results: For a specific backfill recipe and curing time, the AAS-CPB matrix demonstrates significantly better workability compared to the OPC-CPB matrix. Workability diminishes as solid content increases. A higher binder dosage enhances the workability of the AAS-CPB matrix. Additionally, an increased Al/Bi ratio improves the workability of fresh AAS-CPB by creating greater interparticle distance.</p>
(C. Min et al., 2019)	A solid waste phosphogypsum (PG)	Yellow phosphorous slag, FA, and cement clinker in 4:1:1 ratio + 16–20% lime	?	<p>Concepts: The impact of mixing time on the cemented backfill process was examined.</p> <p>Results: Mixing time affected the characteristics of the slurry, with properly mixed backfill slurry showing improved fluidity, higher density, and shorter setting time.</p>
(Qiu et al., 2019)	Mine tailings from an iron mine	BFS, OPC, and gypsum + NaOH solution as alkaline activator	Tap water	<p>Concepts: BFS served as the main raw material for alkali-activated slag (AAS) in CPB preparation. The flow spread and yield stress of the CPB samples were investigated.</p> <p>Results: Increasing the solid content raised the yield stress of the CPB slurry, which subsequently reduced its flowability. Conversely, a higher binder dosage decreased the yield stress and improved the flowability of the slurry.</p>

Table A.3 A summary of the studies on the rheological properties of the cemented paste backfills (continued)

Research	Tailings	Binders and additives	Mixing waters	Concepts and results
(Lihua Yang et al., 2019)	Full process tailings of a copper mine	OPC	Deionised water	<p>Concepts: The relationship between mixing intensity and the rheological behavior of the CPB was examined.</p> <p>Results: The rheological behavior of CPB samples was significantly influenced by their shear history. Changing the preparation mixing speed altered the chemical and physical properties of the CPB. Two mixing speed thresholds were identified (360 and 600 s^{-1}); within this range, the paste generally exhibited lower viscosity and optimal fluidity.</p>
(H. Cheng et al., 2020)	Unclassified tailings from a nickel mine	OPC	Tap water	<p>Concepts: A calculation model for resistance was developed using COMSOL Multiphysics software to analyze the impact of time and temperature on paste rheology.</p> <p>Results: As shear time increases, yield stress decreases exponentially, while plastic viscosity decreases linearly. Yield stress also decreases with rising temperature, following a negative exponential function. A calculation model for paste resistance, accounting for both time and temperature effects, has been established.</p>
(Kou et al., 2020)	Tailings from a gold mine	OPC and slag with different Blaine fineness	?	<p>Concepts: The time-dependent rheological behavior of CPB with alkali-activated slag (AAS) was investigated.</p> <p>Results: Both yield stress and plastic viscosity of AAS-CPB samples increased gradually with curing time, binder content (up to 8%), and slag specific surface. AAS-CPBs exhibited greater sensitivity to changes in curing temperature compared to OPC-CPBs, particularly regarding the rate of increase in yield stress and plastic viscosity.</p>
(Y. Liu et al., 2020)	Coal gangue	Cement and FA + Na_2SO_4 with polycarboxylate (PCS) and naphthalene-based (NS) superplasticizer	Tap water	<p>Concepts: The impact of various accelerator-water reducer admixtures on the workability of CPB was studied experimentally.</p> <p>Results: Mixing 0.5% Na_2SO_4 with 0.2% PCS or 0.5% NS produced CPB with the best transportation properties for use in coal mines. However, an excessive amount of Na_2SO_4 resulted in a slump flow that was too low, causing the CPB to lose its fluidity.</p>

Table A.3 A summary of the studies on the rheological properties of the cemented paste backfills (continued)

Research	Tailings	Binders and additives	Mixing waters	Concepts and results
(Haruna & Fall, 2020)	An artificial silica tailings (ST), and two natural tailings	OPC + Master Glenium 7500 (as the superplasticizer)	Tap water	<p>Concepts: The impact of a superplasticizer on the rheological properties, particularly yield stress and viscosity, of CPB prepared and cured at different temperatures was investigated.</p> <p>Results: Both viscosity and yield stress of CPB increase with curing time, regardless of whether a superplasticizer is used, although the increase is slower in CPB containing a superplasticizer. Adding a superplasticizer significantly reduces the yield stress and viscosity of CPB for both artificial and natural tailings. CPB samples made from natural tailings show higher yield stress and viscosity compared to those made from artificial tailings, due to differences in mineralogical composition and pore water chemistry.</p>
(Qiu et al., 2020)	Artificial silica tailings with different fineness	OPC	Tap water	<p>Concepts: The impact of tailings fineness on the fluidity of CPB was assessed.</p> <p>Results: A higher void ratio (i.e., lower packing density) required more water to fill the voids, which reduced the water film thickness and consequently decreased the fluidity of fresh CPB.</p>

Table A.4 A summary of the studies on the hydraulic conductivity of the cemented paste backfills

Research	Tailings	Binders and additives	Mixing waters	Concepts and results
(Godbout et al., 2007)	Tailings from a volcanogenic sulfide mine	Mixtures of OPC/slag (20%/80%, CPSG) and OPC/FA (70%/30%, CPFA) {1 - 4.5%}	Process water	<p>Concepts: The saturated hydraulic conductivity of the CPB samples was assessed during the early curing periods.</p> <p>Results: The addition of binder decreased the saturated hydraulic conductivity (k_{sat}) of the tailings by up to 1.5 orders of magnitude over 28 days. The proportion of binder directly influenced the reduction in k_{sat}, with a higher binder proportion leading to a greater decrease. CPSG binder had a more significant effect on reducing k_{sat} compared to CPFA binder. A straightforward predictive equation was proposed to estimate the evolution of k_{sat} in the studied CPBs.</p>
(Yilmaz et al., 2008)	Sulfide-rich mill tailings	OPC and GGBFS mixture (20%/80%) {0 - 7 wt%}	Recycled process and tap waters	<p>Concepts: The impact of binder content on one-dimensional (1-D) consolidation and hydraulic properties of CPB samples at various curing ages was evaluated.</p> <p>Results: The calculated k_{sat}, determined using Taylor's method from consolidation test data, and the degree of saturation (S_r) decreased with increased curing time. These calculated values were consistent with the measured values reported in the literature.</p>
(Fall et al., 2009)	Natural tailings (NT, hard magmatic rocks) and ground silica (SI)	OPC and mixture of OPC and BFS (50/50)	Tap water (with specified amount of sulfate)	<p>Concepts: The hydraulic conductivity of CPBs was assessed, and a model was developed to predict its evolution over time.</p> <p>Results: The hydraulic conductivity of CPB decreased with a lower water-to-cement (W/C) ratio and increased with a decrease in binder content. It was found to be time-dependent, decreasing as curing time increased and also reducing with higher curing temperatures. A straightforward function was proposed to predict the evolution of hydraulic conductivity in CPBs.</p>

Table A.4 A summary of the studies on the hydraulic conductivity of the cemented paste backfills (continued)

Research	Tailings	Binders and additives	Mixing waters	Concepts and results
(Pokharel & Fall, 2013)	Artificial silica tailings	OPC {4.5 wt. %}	Distilled water (with specified amount of sulfate)	<p>Concepts: The combined effects of temperature and sulfate on the permeability of hardened CPB were investigated.</p> <p>Results: Except for highly sulfated samples cured at 50°C, the hydraulic conductivity of CPBs decreased with increasing curing temperatures. This reduction is attributed to the refinement of the pore structure caused by the increased precipitation of hydration products at higher temperatures. Cold curing temperatures (2°C) resulted in the highest hydraulic conductivity for the CPBs, regardless of initial sulfate content. At higher curing temperatures (35°C and 50°C), sulfate-containing CPBs exhibited the lowest hydraulic conductivity due to the refinement of their pore structure and the restriction on the formation of expansive minerals within the pores of highly sulfated CPBs.</p>
(Yilmaz, Belem, Bussi�re, et al., 2015)	Tailings from a polymetallic mine	OPC, BFS, FA type C {1, 3, 4.5, and 7%}	Tap water	<p>Concepts: The effect of curing time, binder type, and binder content on the saturated hydraulic conductivity of CPB samples was investigated using a laboratory apparatus known as CUAPS (Curing Under Applied Pressure System).</p> <p>Results: The measured k_{sat} for uncemented tailings averaged a constant value of 7.7×10^{-6} cm/s. With the addition of 4.5 wt.% binder, k_{sat} decreased rapidly over the first three days of curing, from 6.6×10^{-6} to 5.1×10^{-7} cm/s, reflecting a one-order-of-magnitude reduction. After seven days of curing, k_{sat} further decreased to 3.1×10^{-7} cm/s, indicating a nearly 100% reduction.</p>
(Cihangir & Akyol, 2016)	Sulfide-rich full (FT) and delimed (DT) tailings	OPC and AAS	Tap water	<p>Concepts: The saturated hydraulic conductivity test was conducted using the falling-head method on CPB samples prepared from sulfide-rich full tailings (FT) and delimed tailings (DT).</p> <p>Results: Permeability tests revealed that the particle size distribution (PSD) of tailings and the microstructure of CPB significantly influence fluid transport through the CPB material. Consequently, pH and sulfate levels were monitored and reduced when delimed tailings (DT) and alkali-activated slag (AAS) were used.</p>

Table A.4 A summary of the studies on the hydraulic conductivity of the cemented paste backfills (continued)

Research	Tailings	Binders and additives	Mixing waters	Concepts and results
(W. Li & Fall, 2016)	Artificial silica tailings	OPC	Distilled water (with specified amount of sulfate)	<p>Concepts: Saturated hydraulic conductivity tests were conducted on CPB samples with varying sulfate concentrations to evaluate the impact of sulfate on the pore structure of CPB at early ages.</p> <p>Results: CPB samples with sulfate (excluding those with a sulfate content of 5000 ppm) exhibited higher permeability compared to sulfate-free CPB, indicating a coarser pore structure with more interconnected pores. For the sample with a sulfate content of 5000 ppm, sulfate could either refine or coarsen the pore structure of the CPB.</p>
(L. Liu, Zhu, et al., 2019)	Tailings of a copper mine	OPC	Tap water + ice slag	<p>Concepts: The performance of ICED_CPB under the combined effects of curing time and ice/water ratio (IWR) was investigated experimentally.</p> <p>Results: Hydraulic conductivity increased with curing time. k_{sat} decreased up to an ice/water ratio (IWR) of 1.2, after which it increased as the IWR was raised from 1.2 to 1.6.</p>

Table A.5 A summary of the studies on the leaching behavior of the cemented paste backfills

Research	Tailings	Binders and additives	Mixing waters	Concepts and results
(Benzaazoua et al., 2008)	Mine tailings and concentrates after desulfurization	OPC and slag (30/70) {5%}	?	<p>Concepts: The combined effects of environmental desulfurization and cemented paste backfill on the leaching of tailings from Doyons mine were evaluated using humidity cell tests.</p> <p>Results: Environmental desulfurization can generate non-acid generating, low-sulfide tailings and a sulfide concentrate. The sulfide concentrate can be utilized to produce a cemented paste backfill with enhanced environmental performance.</p>
(Qiu et al., 2019)	An iron mine tailings	BFS, OPC, and gypsum + NaOH solution as the alkaline activator	Tap water	<p>Concepts: BFS served as the primary raw material for AAS in CPB preparation. The leaching of lead (Pb) and cadmium (Cd) from the CPB samples was evaluated using the TCLP method.</p> <p>Results: The leaching concentration of lead (Pb) was below the threshold when using AAS as an alternative binder for CPB. Additionally, the leaching concentration of cadmium (Cd) decreased as binder content increased.</p>
(Su et al., 2019)	Tailings of a lead-zinc mine	OPC + Polyaluminium chloride (PAC) and polyaluminium sulfate (PAS)	?	<p>Concepts: The environmental properties of CPB samples made from lead-zinc tailings (LZT) were investigated.</p> <p>Results: The addition of 2 mg/L PAS effectively controlled lead leaching in the CPB. All monitored metals met the Chinese standards for groundwater quality in the dynamic leaching test.</p>

Table A.6 A summary of the studies on the microstructure of the cemented paste backfills

Research	Tailings	Binders and additives	Mixing waters	Concepts and results
(Benzaazoua et al., 1999)	Abitibian pyrite-rich tailings	Mixture of FA and OPC (40/60) {4.5%}	Mine process water	<p>Concepts: The study examined how the mechanical strength of the fill is influenced by chemical and mineralogical changes (weathering) over time.</p> <p>Results: Core sample analysis revealed a network of fine fractures along with oxidation traces, indicative of chemical weathering. Additionally, chemical and mineralogical analysis identified that sulfides in the tailings led to the dissolution of calcic phases in the cement hydrates and facilitated the development of swelling phases.</p>
(Benzaazoua et al., 2002)	Mine tailings from four Canadian hard-rock mines	OPC, SRPC, FAs and slags {3% - 6%}	Lake water, municipal water, mine process waters	<p>Concepts: SEM micrography was used to investigate the relationships between the development of compressive strength and the texture of paste backfill samples.</p> <p>Results: The chemistry of the binder, along with the chemistry of the mixing water, influenced the development of primary and secondary hydrates during the strengthening of paste backfill. Sulfates hindered the formation of hydrates with slag-based binders, whereas Portland-cement-based binders more readily formed gypsum, which contributed to the increase in paste backfill strength.</p>
(Fall et al., 2005)	Tailings from a gold and a polymetallic mine	Mixture of OPC with type V PC and BFS	Tap water	<p>Concepts: The impact of tailings particle size and density on the microstructure of CPB samples was assessed.</p> <p>Results: The proportion of fine tailings (<20 μm) had a significant effect on both the overall porosity and the pore size distribution of the CPB material. As the fineness of the tailings increased, the overall porosity of the CPB also increased.</p>
(Deschamps et al., 2006)	Tailings from a gold mine	Mixture of OPC (30%) and slag (70%) {2%}	Tap water	<p>Concepts: The hydrogeological and geochemical properties of CPB samples were examined after an extended curing period.</p> <p>Results: The volumetric water content profiles of the samples varied with the age of the paste. Water geochemistry indicated binder loss after 20 months of curing. Additionally, sulfate distribution within the paste suggested that sulfide oxidation had taken place.</p>

Table A.6 A summary of the studies on the microstructure of the cemented paste backfills (continued)

Research	Tailings	Binders and additives	Mixing waters	Concepts and results
(Ouellet et al., 2008)	Ground silica	OPC, OPC/GGBFS and OPC/FA {5%}	Deionised and two sulfate-rich mine waters	<p>Concepts: The quantitative analysis of pore structure evolution in CPB samples was characterized by total porosity (n), pore size distribution (PSD), and tortuosity (T), using SEM–IA.</p> <p>Results: The total porosity values obtained through SEM–IA were comparable to those from mercury intrusion porosimetry (MIP) for short curing periods. The tortuosity factor (T^2) values, assessed using the skeletonization method, were consistent with expectations for materials with similar porosities. Samples made with a combination of OPC and GGBFS demonstrated more effective pore refinement over the curing period.</p>
(Ercikdi, Kesimal, et al., 2009)	Sulfide rich mill tailings from a copper–zinc flotation plant	OPC, PCC, and SRPC {5%–7%}	Tap water	<p>Concepts: The effect of binder type and dosage on the microstructure of CPB was examined.</p> <p>Results: SEM studies offered additional insights into the microstructure of CPB, confirming the harmful formation of gypsum as an expansive phase. XRD analysis showed the presence of gypsum and portlandite only in the CPB sample prepared with OPC as the sole binder.</p>
(Ercikdi, Cihangir, et al., 2009)	Sulfide rich mill tailings of a backfill plant	OPC, WG, FA, GBFS and SF	Tap water	<p>Concepts: The potential use of industrial waste products—such as waste glass (WG), fly ash (FA), granulated blast furnace slag (GBFS), and silica fume (SF)—as pozzolanic additives for partially replacing OPC, and their effects on the microstructure of CPB, were investigated.</p> <p>Results: The inclusion of pozzolanic materials in the binder phase was anticipated to improve the microstructure of CPB, resulting in denser packing with reduced porosity and permeability. Additionally, it was expected to lessen the oxidation of pyrite in the CPB by reducing moisture and air ingress.</p>
(Fall et al., 2009)	Natural tailings (NT) and ground silica (SI)	OPC and mixture of OPC and BFS (50/50)	Tap water (with specified sulfate)	<p>Concepts: The microstructure of CPB samples, including pore structure and binder hydration products, was assessed.</p> <p>Results: Elevated curing temperatures enabled CPB samples to produce a substantial amount of hydration products. These products filled the voids, decreasing porosity and resulting in lower hydraulic conductivity at higher curing temperatures.</p>

Table A.6 A summary of the studies on the microstructure of the cemented paste backfills (continued)

Research	Tailings	Binders and additives	Mixing waters	Concepts and results
(Ercikdi et al., 2010)	Sulphide rich mine tailings from a copper-zinc mine	OPC and PCC, Three different WRAs	Tailings water and tap water	<p>Concepts: The impact of three different water-reducing admixtures (WRAs) on the mineralogical properties of CPB samples after curing was investigated using SEM and XRD analysis.</p> <p>Results: SEM and EDX analysis of CPB samples revealed the presence of sulfate phases, such as secondary gypsum and ferrous sulfate, in samples containing WRAs. However, XRD studies did not identify ettringite or gypsum in these CPB samples.</p>
(Fall & Pokharel, 2010)	Ground silica	OPC {4.5 wt.%}	Distilled water	<p>Concepts: The combined impact of curing temperature (ranging from 0 to 50 °C, over a period of up to 150 days) and sulfate concentration (ranging from 0 to 25,000 ppm) on the mineralogical composition of hardened CPB samples was evaluated.</p> <p>Results: The combined effect of temperature and sulfate significantly influences the mineralogical composition of CPB. The results strongly suggest that sulfate absorption by C–S–H could lead to the formation of lower-quality C–S–H.</p>
(Olivier Peyronnard & Benzaazoua, 2011)	Pure silica	OPC, GGBS, FAs {4.5%} + 8 by-products	Ferrous sulfate solution	<p>Concepts: The feasibility of using eight different by-products as supplementary cementitious materials for developing low-cost alternative binders was evaluated.</p> <p>Results: The tested pozzolanic by-products and coal fly ash exhibited similar cementitious properties. These favorable performances were attributed to the by-products' suitable chemical and mineralogical compositions, as well as their physical characteristics.</p>
(Ercikdi et al., 2013)	Two different sulfide-rich mill tailings	PCC {4.5–8.5 wt.%}	Tap water	<p>Concepts: The impact of desliming two different sulfide tailings on the short- and long-term microstructure and porosity of CPB was assessed.</p> <p>Results: The fines content in the tailings significantly influenced the drainage capacity of CPB mixtures at a given consistency. Desliming decreased the water retention capacity of the tailings and enhanced the microstructure of CPB samples, resulting in a less porous and denser matrix.</p>

Table A.6 A summary of the studies on the microstructure of the cemented paste backfills (continued)

Research	Tailings	Binders and additives	Mixing waters	Concepts and results
(Pokharel & Fall, 2013)	Artificial silica tailings	OPC {4.5 wt. %}	Distilled water (with specified sulfate)	<p>Concepts: The combined effects of temperature and sulfate on the microstructure of CPB were investigated.</p> <p>Results: At cold-curing temperatures (2 °C), high permeability was attributed to the coarsening of the CPB pore structure due to the low temperature's inhibition of cement hydration and high sulfate content ($\geq 15,000$ ppm). Increasing sulfate content, which promoted the precipitation of larger amounts of ettringite and gypsum, led to higher expansive pressure from these minerals, adversely affecting permeability.</p>
(Yilmaz, Belem, & Benzaazoua, 2015)	Tailings from the paste backfill plant of a mine	OPC and BFS {3, 4.5, and 7%}	Tap water	<p>Concept: The impact of specimen size and placement conditions on the microstructure of CPB samples was examined.</p> <p>Results: Drained CPB samples exhibited lower porosity due to water loss from drainage, which caused the backfill to settle and reduced the CPB void ratio. In contrast, undrained samples had higher porosity compared to CUAPS-consolidated backfills, as the hydration and precipitation processes were less extensive in the consolidated samples.</p>
(Cihangir & Akyol, 2016)	sulfide-rich full tailings (FT) and delimed tailings (DT)	OPC and AAS	Tap water	<p>Concepts: The microstructure of CPB samples made from sulfide-rich full tailings (FT) and delimed tailings (DT) was analyzed using SEM-EDS and MIP tests.</p> <p>Results: Utilizing DT and AAS resulted in CPBs with a reduced total volume of porosity by decreasing the number of macropores and increasing the number of mesopores, which refined the microstructure.</p>
(Ghirian & Fall, 2016)	artificial silica tailings	OPC {4.5 wt.%}	Tap water	<p>Concepts: A pressure cell apparatus was designed to study the early-age development of the microstructure in CPB.</p> <p>Results: Extended curing times led to the formation of additional cement hydrates, which refined the pore structure. Curing stress also induced particle rearrangement in the undrained samples, resulting in higher packing density and reduced porosity.</p>

Table A.6 A summary of the studies on the microstructure of the cemented paste backfills (continued)

Research	Tailings	Binders and additives	Mixing waters	Concepts and results
(Haiqiang et al., 2016)	Artificial silica tailings (ST), gold tailings (GT), and zinc tailings (ZT)	OPC mixed with FA and Slag (50/50)	Tap and distilled water with various NaCl contents	<p>Concepts: The interaction between time and sub-zero temperatures on the microstructure of CPB was investigated.</p> <p>Results: Experimental results show that higher temperatures lead to increased formation of hydration products such as calcium hydroxide (CH) and C–S–H, while lower temperatures inhibit cement hydration and reduce the amount of these products. This suggests that curing conditions significantly impact the development of hydration products in CPB. It is crucial to consider how various temperature regimes and curing environments might affect the long-term performance and stability of CPB materials. Exploring different temperature conditions and their effects on hydration could provide a more comprehensive understanding of optimizing CPB properties.</p>
(Ke et al., 2016)	Two types of tailings from copper plants	PCC	Tap water	<p>Concepts: The impact of particle-size distribution on the development of pore structure in CPB samples was examined.</p> <p>Results: The total porosity of CPB samples showed a slight increase with the rise in tailings fineness, ranging from 4.18 to 27.55 wt.%. Tailings fineness influenced the proportions of different pore sizes, with larger pores (>10 μm) generally decreasing and smaller pores (<10 μm) increasing as tailings fineness increased. The filling effect of finer tailings played a crucial role in this process.</p>
(Koohestani et al., 2016)	Tailings from an ore processing plant	GU and GGBFS (20/80) {2, 4.5, and 7 wt.%} + maple wood sawdust	Tap water	<p>Concepts: The effect of adding maple-wood sawdust on the microstructural properties of CPB was studied.</p> <p>Results: MIP and SEM analysis showed that adding 12.5% wood filler made the CPB material less porous and more compact by enhancing the mineral content from cement hydration. The beneficial effect of maple-wood sawdust on CPB was linked to higher binder content ($\geq 5\%$) and extended curing times (≥ 56 days).</p>

Table A.6 A summary of the studies on the microstructure of the cemented paste backfills (continued)

Research	Tailings	Binders and additives	Mixing waters	Concepts and results
(W. Li & Fall, 2016)	Artificial silica tailings	OPC	Distilled water (with specified amount of sulfate)	<p>Concepts: The impact of sulfate on the early-age strength and self-desiccation of CPB samples, up to 28 days, was evaluated.</p> <p>Results: Sulfate inhibited and delayed the cement hydration process in the early stages, leading to the production of more ettringite and less calcium hydroxide. Suction monitoring indicated that sulfate adversely affected the self-desiccation of CPB during early ages, with the extent of this effect increasing as sulfate concentration rises.</p>
(Q. Chen, Zhang, Fourie, Chen, et al., 2017)	Iron tailings	A specific cement and furnace slag	Tap water	<p>Concepts: A series of experiments using a large-scale similar stope model (SSM) were designed to simulate the consolidation of CPB in a stope. Subsequent SEM analysis was performed on cored samples from various positions within the CPB sample.</p> <p>Results: SEM analysis revealed that specimens with higher strength exhibited a more compact structure and denser hydration products, including Aft, C-S-H, and Ca(OH)₂.</p>
(Q. Chen, Zhang, Fourie, & Xin, 2017)	Phosphogypsum (PG) and phosphate tailings (PTS)	OPC, slag and CaO	?	<p>Concepts: The feasibility of using phosphogypsum (PG), phosphate tailings (PTS), and CaO for CPB production was evaluated through scanning electron microscopy (SEM) tests.</p> <p>Results: After adding CaO, the acid in the PG primarily reacted with the strong alkali, preventing the utilization of valuable components in the material. Additionally, slag was found to be an unsuitable binder for CPB preparation.</p>
(H. Jiang & Fall, 2017a)	Non-reactive silica tailings (ST)	OPC {4.5 wt.%}	distilled water with various NaCl concentrations	<p>Concepts: The microstructure of CPB under various saline concentrations in a sub-zero environment (-6 °C) was examined.</p> <p>Results: The microstructural analysis revealed that binder hydration products were influenced by salinity. Evidence suggests that the absorption of Na⁺ ions by C-S-H led to a reduction in the strength of CPB samples with varying NaCl concentrations.</p>

Table A.6 A summary of the studies on the microstructure of the cemented paste backfills (continued)

Research	Tailings	Binders and additives	Mixing waters	Concepts and results
(X. Chen et al., 2018)	Tailings of a lead-zinc mine	OPC + Monofilament polypropylene (PP) fibres	Tap water	<p>Concepts: Macrostructural failure analysis and microstructural tests using SEM were employed to investigate crack development and structural changes in CPB reinforced with PP fibers.</p> <p>Results: The role of PP fibers in CPB was examined from both macro and micro perspectives. When an adequate amount of fiber is used, it forms a thick fiber sheet within the CPB specimens, which helps prevent significant damage to the CPB. Additionally, PP fibers do not impair the workability of the backfill.</p>
(Cihangir et al., 2018)	Full tailings (FT) and coarse (deslimed) tailings (CT)	SSAS at different silicate modulus (M_s), OPC {7%}, NaOH for M_s adjustmen, Na_2O as an activator	?	<p>Concepts: The microstructural development of full (FT) and coarse sulfide tailings (CT) cemented paste backfill produced from SSAS at different moisture contents (M_s) was investigated.</p> <p>Results: Increasing the M_s of SSAS and using coarse tailings (CT) significantly reduced porosity and refined the pore structure, resulting in a more compact microstructure of CPB. This improvement was attributed to a more condensed and polymerized C-S-H gel structure. For the microchemical structure of C-S-H, the highest Ca/Si ratios were observed at $M_s = 1.25-1.50$ for FT-CPBs and at $M_s = 1.25-2.0$ for CT-CPBs after 360 days.</p>
(Koohestani et al., 2018)	A sulfidic and a non-sulfidic tailings	GU cement + Three types of WRAs	Tap water	<p>Concepts: The impact of non-polar organosilanes (vinyl and methyl) and polycarboxylate superplasticizers on the microstructural properties of CPB, made from both sulfidic and non-sulfidic tailings, was investigated.</p> <p>Results: The differential thermogravimetric (DTG), mercury intrusion porosimetry (MIP), and scanning electron microscopy (SEM) results indicated that vinyl silane was more effective in densifying the CPB matrix. This was attributed to improved hydration and the formation of additional C-S-H gel, particularly in non-sulfidic CPBs.</p>

Table A.6 A summary of the studies on the microstructure of the cemented paste backfills (continued)

Research	Tailings	Binders and additives	Mixing waters	Concepts and results
(Mangane et al., 2018)	Tailings from a polymetallic mine	GU (OPC) and mixture of GU/Slag (20/80) + three superplasticizers	Deionised water	<p>Concepts: The effect of different superplasticizer dosages on the strength of CPB samples was investigated.</p> <p>Results: The addition of superplasticizers delayed cement hydration, depending on their type. Specifically, the inclusion of polycarboxylate superplasticizers improved CPB durability by refining the pore structure and reducing porosity from 41.3% to 35.6%.</p>
(Hu et al., 2019)	Mineral processing discharge from the concentrator	OPC and stone powder	Tap water	<p>Concepts: The impact of varying humidity conditions during curing on the microstructure of CPB samples was examined.</p> <p>Results: As the amount of stone powder in the specimens increased, their internal structure became denser, and porosity decreased. Conversely, with higher curing humidity, the pore size and proportion of smaller pores increased.</p>
(H. Jiang, Qi, et al., 2019)	Processing tailings of a gold flotation plant	OPC and AAS + A combination of NaOH and Na ₂ SiO ₃ solutions as the alkaline activator	Tap water	<p>Concepts: The impact of various parameters on the microstructural properties of AAS-CPB was experimentally investigated.</p> <p>Results: The SEM-EDS results showed that the hydration products of the AAS binder were predominantly composed of sodium and calcium aluminosilicate hydrates (C-A-S-H and N-A-S-H), whereas OPC yielded calcium hydroxide (CH) and C-S-H gels. The AAS binder exhibited a higher Ca/Si molar ratio (0.89) compared to OPC (1.34).</p>
(L. Liu, Zhu, et al., 2019)	Tailings of a copper mine	OPC	Tap water + ice slag	<p>Concepts: The microstructural performance of ICED_CPB under the combined effects of curing time and ice/water ratio (IWR) was investigated experimentally.</p> <p>Results: Increasing the ice/water ratio (IWR) reduced moisture diffusion from the ICED_CPB system to the environment by decreasing the free water content (water in the fluid state). The fusion of ice absorbed significant heat, lowering the internal temperature during cement hydration. This temperature reduction slowed self-desiccation and slightly increased water content.</p>

Table A.6 A summary of the studies on the microstructure of the cemented paste backfills (continued)

Research	Tailings	Binders and additives	Mixing waters	Concepts and results
(L. Liu, Yang, et al., 2019)	Tailings from a copper mine	OPC	Tap water	<p>Concepts: The early-age hydration kinetics of CPB samples were studied experimentally.</p> <p>Results: High temperatures accelerated the dissolution of cement phases. Increasing the tailings-to-cement ratio reduced the early-age normalized heat flow and accumulated heat because of the lower cement content.</p>
(C. Min et al., 2019)	A solid waste phosphogypsum (PG)	Yellow phosphorous slag, FA, and cement clinker in 4:1:1 ratio + 16–20% lime	?	<p>Concepts: The impact of mixing time on the cemented backfill process was investigated.</p> <p>Results: Backfill samples with optimized mixing time displayed the lowest porosity, whereas insufficient mixing and overmixing resulted in higher porosity.</p>
(Yue Zhao, Soltani, et al., 2019)	Tailings of a copper-gold underground mine	Slag-blended cement {1.5-3%} + Class C FA {0 - 2.5%}	Processed mine water	<p>Concepts: The combined effectiveness of a newly developed slag-blended cement (MC) and fly ash (FA) in enhancing the microstructure of CPB samples was investigated as a sustainable solution.</p> <p>Results: The inclusion of fly ash (FA) significantly enhanced the bonding and connection interfaces between tailings aggregates, leading to a marked reduction in both the number and size of inter- and intra-assembly pore spaces. When slag-blended cement (MC) was used as the primary binder, the additional silicate and aluminates units in the slag particles reacted gradually with $\text{Ca}(\text{OH})_2$ and water, forming additional cementation products through secondary pozzolanic reactions. This further contributed to densifying the matrix.</p>
(H. Jiang, Yi, et al., 2020b)	Artificial silica tailings	OPC in combination with FA and BFS	Tap water	<p>Concepts: The impact of mineral admixtures and curing temperature on the microstructural properties of laboratory-prepared CPB samples was investigated.</p> <p>Results: TG/DTG analyses of OPC-FA pastes with varying blend ratios revealed that the binder hydration products, especially C-S-H and portlandite, decreased with increasing FA content. Replacing 20% of OPC with FA significantly reduced the porosity, coarseness of the pore structure, and proportion of macropores within CPB samples.</p>

Table A.6 A summary of the studies on the microstructure of the cemented paste backfills (continued)

Research	Tailings	Binders and additives	Mixing waters	Concepts and results
(Y. Liu et al., 2020)	Coal gangue	Cement and FA + Na ₂ SO ₄ with two superplasticizers	Tap water	<p>Concepts: The impact of an accelerator-water reducer admixture on the microstructure of CPB was studied experimentally.</p> <p>Results: An accelerator-water reducer admixture could speed up the hydration reactions of tricalcium silicate and dicalcium silicate, and enhance the activity of fly ash in the later stages, leading to increased formation of hydration products such as Aft and C-S-H.</p>
(Haruna & Fall, 2020)	An artificial silica tailings (ST) and two natural tailings	OPC + Master Glenium 7500 (as the superplasticizer)	Tap water	<p>Concepts: The impact of a superplasticizer on the microstructure of CPB prepared and cured at different temperatures was investigated.</p> <p>Results: More hydration products were produced in the CPB without the superplasticizer, whereas fewer solid products were formed during hydration in the presence of the superplasticizer.</p>
(Qiu et al., 2020)	Artificial silica tailings with different fineness	OPC	Tap water	<p>Concepts: The impact of tailings fineness on the microstructural properties of CPB was examined.</p> <p>Results: The packing density of solid particles decreased as tailings became finer, while the void ratio increased. Over time, the total porosity decreased due to the refinement of pore structures caused by the increased production of hydration products.</p>

Table A.6 A summary of the studies on the microstructure of the cemented paste backfills (continued)

Research	Tailings	Binders and additives	Mixing waters	Concepts and results
(Yılmaz et al., 2020)	Sulphide rich floatation plant tailings	OPC + C-FA, BFS, calcitic (CL) and dolomitic (DL) limestone	Tap water	<p>Concepts: The effectiveness of calcium oxide (CaO)-rich industrial waste products (IWPs) in neutralizing the sulfide-rich environment of CPB was assessed.</p> <p>Results: The production of acid and sulfate in all cemented paste backfills (CPBs) rose with extended curing time. Using industrial waste products (IWPs) with neutralization capabilities as a partial replacement for sulfide-rich tailings in CPB mixtures reduced the acid and sulfate generation. The oxidation of pyrite intensified with curing time. The hydroxide ions (OH⁻) released from alkaline minerals such as calcite and dolomite in IWPs neutralized the acidic by-products in the CPB. Free calcium ions from IWPs and sulfate ions from sulfide minerals formed secondary gypsum within the CPB, which helped mitigate acid and sulfate attacks.</p>
(Du et al., 2021)	Coal gangue	RM, PC, SC + FA	?	<p>Concepts: The combined effects of binder type and temperature on the microstructural evolution of CPB were investigated.</p> <p>Results: The microstructures of the three types of binder varied. Higher temperatures accelerated the dissolution of the clinker phase, thereby speeding up the binder's hydration process. This resulted in an increase in hydration products, such as AFt and C-S-H gel, with temperature. However, AFt could disrupt the flocculent structure of the C-S-H gel, reducing its overall integrity.</p>

Table A.7 A summary of the studies on the application of response surface methodology in the cemented paste backfills

Research	Tailings	Binders and additives	Mixing waters	Concepts and results
(Fall et al., 2008)	Tailings samples from two polymetallic mines	OPC/BFS	Tap water	<p>Concepts: A mix proportioning design method for CPB was established to minimize the number of trial mixes and provide optimal mix proportions by combining Response Surface Methodology (RSM) with the desirability approach.</p> <p>Results: Increasing the amount of cement led to higher strength. For any given binder proportion or tailing grain size, a lower water-to-cement (W/C) ratio resulted in greater CPB compressive strength. The highest compressive strength was achieved when tailings contained 40–45% fine particles (<20 μm). Higher binder proportions increased CPB slump by widening the average distance between tailings particles, thereby reducing friction, collisions, and blocking. Conversely, slump decreased as tailings density increased, and tailings fineness also influenced the CPB slump.</p>
(G. Feng et al., 2016)	Coal gangue samples	OPC and FA + Highly effective poly carboxylic acid water reducer	Tap water	<p>Concepts: Central composite design (CCD) experiments were conducted to investigate the effects of cement content, fine gangue rate, and water reducer content on the compressive strength, workability, and microstructure of cemented coal gangue backfill (CGB).</p> <p>Results: Increasing the cement content led to greater strength in the cemented coal gangue backfill (CGB). The water reducer helped disperse the cement particles and facilitated the release of free water trapped in cement flocs. This increased water availability promoted hydration and pozzolanic reactions, enhancing the strength of CGB. As cement content increased, the yield stress initially decreased and then increased. The long side chains of the polycarboxylic acid water reducer tightened the connections between particles and aggregates, promoting the formation of a dense and compact C-S-H gel structure.</p>

Table A.7 A summary of the studies on the application of response surface methodology in the cemented paste backfills (continued)

Research	Tailings	Binders and additives	Mixing waters	Concepts and results
(Dai et al., 2019)	Tailings of a copper mine + waste rock	OPC + powdered polycarboxylic acid pumping agent	?	<p>Concepts: A Box–Behnken design experimental program was conducted to test the optimal mix proportions using unclassified tailings.</p> <p>Results: The UCS was positively correlated with rock content and mass concentration. The optimal mix proportions for CPB using unclassified tailings were found to be 76.75% mass concentration, a 3.35 tailing-to-rock ratio, 0.1 cement/(tailing + rock), and 1.24% pumping agent addition. The slump initially decreased and then increased with the rising pumping agent content. It also decreased with increasing mass concentration and cement content. The relationships between CPB slump and these influential factors can be quantitatively described using equations derived from regression analysis.</p>
(Q. Li et al., 2019)	Coal gangue	FA (Class F) and OPC, A naphthalene sulphate-based SP	Fresh water	<p>Concepts: The effects of FA content, fine gangue ratio, and mass concentration on superplasticizer (SP) dosage and slump were analyzed using a central composite design.</p> <p>Results: The solid mass concentration, FA content, and fine gangue ratio affected the SP dosage in varying degrees, from high to low. The interaction between the fine gangue ratio and mass concentration had the most significant impact on the SP dosage.</p>
(Sun et al., 2019)	Coal gangue	OPC, FA, slag, sodium silicate + NaOH and triethanolamine	Tap water	<p>Concepts: A new mixing technique was proposed to analyze the effects of solid mass concentration, fine gangue ratio, and FA content on the strength and consistency of the paste backfill material using RSM.</p> <p>Results: The optimal mixture was achieved, and microanalysis revealed that the early formation of calcium silicate gel encapsulated and bonded the coarse and fine aggregates, contributing to the strength. In the later stage, amorphous hydrated calcium aluminate gel coated ettringite and calcium carbonate, creating a flocculated structure between the FA particles that gradually evolved into a condensation-crystallization structure. As the solid mass concentration increased, the slump of the paste backfill materials decreased. This reduction in slump was due to decreased water consumption and porosity as the solid mass concentration increased.</p>

APPENDIX B ARTICLE 1: THE EFFECTS OF ARSENIC TRIOXIDE ADDITION ON THE MECHANICAL AND GEOCHEMICAL PROPERTIES OF THE CEMENTED PASTE BACKFILL

This article was published in the journal of Results in Materials (volume 19) under number 100440.

This article was submitted on 12 June 2023, accepted on 16 August 2023, and published online on 18 August 2023. This appendix reproduces the full text.

Amirhossein Mohammadi¹, Isabelle Demers^{1,2}, Mostafa Benzaazoua¹, Nicholas Beier³

1. UQAT-Polytechnique Research Institute on Mines and the Environment, Rouyn-Noranda, QC, Canada

2. Canada Research Chair on Integration of the Environment in the Mine Life Cycle, Rouyn-Noranda, QC, Canada

3. Department of Civil and Environmental Engineering, University of Alberta, Edmonton, AB, Canada

CRedit authorship contribution statement

Amirhossein Mohammadi: Conceptualization, Methodology, Investigation, Writing – original draft, Visualization. **Isabelle Demers:** Conceptualization, Methodology, Validation, Formal analysis, Writing – original draft, Writing – review & editing, Supervision, Funding acquisition. **Mostafa Benzaazoua:** Conceptualization, Methodology, Writing – review & editing, Validation. **Nicholas Beier:** Conceptualization, Methodology, Writing – review & editing, Validation.

Keywords

Cemented paste backfill, Arsenic trioxide, Solidification/stabilization, Unconfined compressive strength (UCS), geochemical behavior

¹ Corresponding author; amirhossein.mohammadi@uqat.ca

Abstract

Cemented paste backfill (CPB) technology, a densified mixture of mine tailings, binding material, and water, thickens to form a non-settling paste that is transported to fill mined cavities. CPB could provide environmental advantages by preventing the release of contaminants through hydraulic binder stabilization/solidification. Up to now, only few studies have been carried out to examine the feasibility of arsenic (As) fixation within cemented paste backfills. The main objective of the current study is to assess the impacts of incorporating pure arsenic trioxide on the geomechanical and geochemical properties of cemented paste backfill. CPB samples were prepared using pure ground silica (Sil-Co-Sil[®]) mimicking mine tailings, general use (GU) cement, deionized water, and reagent-grade pure As₂O₃ at different arsenic contents (0, 5, 10, and 15%). The samples were cured for up to 28 days and unconfined compressive strength (UCS) tests were conducted after 7 and 28 days of curing. Moreover, to evaluate the geochemical behavior of the pastes, mixtures of GU cement, pure As₂O₃ (0 to 15%), and deionized water with the same proportions as the CPB samples were prepared and mixed for up to 28 days. Then, pH, EC and chemical composition of the mixtures were evaluated. Results showed that the addition of pure arsenic trioxide (as a partial substitution for pure silica) leads to a substantial decrease in the mechanical strength of the CPB samples. However, this adverse effect was more substantial for the arsenic content of 5 wt.%. The strength of the As₂O₃-containing samples did not improve significantly after 7 days of curing and arsenic addition lowered the pH of the solutions. Microstructural analysis using SEM proved the formation of some C-S-H gels that contained arsenic in their structures as well as some complex mixture of oxides for the case of the As₂O₃-cement mixtures.

B.1 Introduction

Arsenic (As) as the 53rd most abundant element, constitutes about 1.5 ppm of the Earth's crust. Arsenic can be found naturally in the environment through weathering and volcanism in the form of many diverse minerals, usually in combination with sulfur and metals and as a pure elemental crystal (Mohammad Eisa et al., 2020). Primary sources of arsenic in the environment are mineral weathering and dissolution, geothermal activity, and industrial activities like mining and smelting of metal ores (Moon et al., 2004). Mining activities are one of the most important sources of arsenic contamination. The Giant Mine (Northwest Territories, Canada) is an abandoned gold mine that operated from 1948 until 1999. Most of the gold from this mine occurred as extremely fine-grained

particles that are “refractory,” i.e., mainly encased and confined within the crystal structure of arsenopyrite (FeAsS) and to a lesser degree arsenian pyrite (FeS_2) (SRK, 2002). The roasting process used to liberate the gold produced SO_2 emissions and As-rich vapors that precipitated as arsenic trioxide (As_2O_3)-rich dust from the oxidation of As (-I) to As (III) in dust precipitators (Bromstad et al., 2017a). The As_2O_3 -rich dust was stored in underground stopes and chambers. The arsenic trioxide dust is approximately 60% arsenic, hazardous to both people and the environment. Arsenic trioxide can dissolve in water, and it is more soluble than other natural arsenic compounds (Bull & Fall, 2020a; Committee on Medical and Biologic Effects of Environmental et al., 1977). After mine closure, various potential treatment options were reviewed aiming in the stabilization of the arsenic wastes, and more than 50 technologies were assessed to determine the most promising option. Finally, the “Frozen Block” method was selected as the most appropriate management approach available in that time. However, since arsenic is not stabilized chemically or removed from the area, it is inherently soluble, and it may be released if left unmaintained or if the frozen block thaws (Arcadis, 2017).

Different technologies are employed to clean up arsenic-bearing wastes or arsenic-contaminated soils and sediments. Cleanup methods may include site isolation, physical separation, bioremediation, phytoremediation, washing, heating, electrokinetics, permeable reactive barriers, solidification and stabilization (S/S), or in rare cases, in-situ vitrification. However, the most cost-effective solution for land remediation could be solidification and stabilization (S/S) technologies that physically and chemically change arsenic through encapsulation into a less mobile and less toxic species (Randall, 2012). Arsenic does not form an insoluble hydroxide, and hence the mechanism of the solidification and stabilization of many heavy metal cations does not work for As (Büchler et al., 1996b). With an extensively documented history, arsenic solidification and stabilization research has focused on evaluating stabilization admixtures and understanding underlying chemical principles. Solidification and hardening of the cement-containing pastes occur due to the formation of hydration products, such as calcium-silicate-hydrates (C-S-H), portlandite (calcium hydroxide), and ettringite (calcium alumina hydrates, AFt). During the hydration of the cementitious materials, at both microscale and macroscale, the material properties change, ensuring the solidification (i.e., skeletal development) and hardening of the paste (Klein & Simon, 2006). Researchers have assessed the S/S process to immobilize arsenic using diverse S/S agents such as general use Portland cement (GU) (Clancey et al., 2015; B.-J. Kim et al., 2016; J. S. Li, Beiyan,

et al., 2017; J. S. Li, Wang, et al., 2017; Yoon et al., 2010), sulfate-resistant Portland cement (SRPS) (Mollah et al., 2004), quicklime (Camacho et al., 2009b; Dermatas et al., 2004; Dutré & Vandecasteele, 1998; Moon et al., 2010), blast furnace slag (BFS) (Dutré & Vandecasteele, 1996, 1998; J. S. Li, Wang, et al., 2017), fly ash (FA) (Dermatas et al., 2004; Fuessle & Taylor, 2004; Qiao et al., 2006; Singh & Pant, 2006; Tsang et al., 2014), hydrated lime (Leist et al., 2003; Moon et al., 2004), cement kiln dust (CKD) (Mohammad Eisa et al., 2020; Yoon et al., 2010), and other binding agents (J. Y. Kim et al., 2003; D. G. Liu et al., 2018; Phenrat et al., 2008; H. Zhao et al., 2010). In most cases, additives and binders act to oxidize As (III) to As (V), which can either form insoluble complexes or become immobilized due to the formation of strongly adsorbed species; or form insoluble co-precipitates with calcium and/or iron (Randall, 2012). These studies have shown that arsenic stabilization and solidification are a combination of both chemical and physical processes. The leaching capacity is highly dependent on the buffering capacity and pH of the stabilized matrix. The formation of calcium and ferric arsenites/arsenates and calcium-silicate-hydrate (C-S-H) gels and their precipitation and embedding in the cementitious matrices were found to be the most important stabilizing mechanisms.

Solidification and stabilization methodologies usually use a substantial amount of cement or other binding agents to properly stabilize the hazardous materials, and the cost of these binders could act as a determinative parameter. In the mining industry, a similar technology has been developed and widely used to manage hazardous and non-hazardous mine wastes. Cemented paste backfills (CPB) technology is an interesting tailings management approach for underground mines. CPB can be considered as a high-density, non-segregating, and low-plasticity mixture of mine tailings, binder (3-7 wt%), and a high proportion of water, which typically contains 70%–85% solids by total mass and enough fines to avoid particle settlement (i.e., no bleed water) and particle segregation during pumping and transportation through pipelines (Klein & Simon, 2006; Landriault, 1995a). The most significant advantages of CPB comprise providing ground support and safely placing the hazardous mill tailings (e.g., sulfide tailings) into underground openings to mitigate their environmental impacts and reduce their surface disposal and reclamation costs (Ercikdi et al., 2014; Ercikdi, Kesimal, et al., 2009). CPB is a mixture like concrete and GU is the most commonly used binder, used either alone or in combination with other binders. Mixture proportions are tailored to achieve the required rheological and hardened strength characteristics. Some factors including binder content, moisture content, mineralogical composition and particle-size distribution of the tailings,

curing time, pore fluid chemistry, and the presence of mineral and (or) chemical additives influence the properties of CPB (Benzaazoua et al., 2002; Klein & Simon, 2006; Landriault, 1995b).

Although there are some differences between the cemented paste backfill and S/S technologies (e.g., higher cement content and elevated strength of the solidified/stabilized samples, and higher water content of the CPB samples), the CPB could be considered as one of the solidification and stabilization technologies. CPB technology has also been considered as an alternative resource disposal technology for arsenic-containing waste. Currently, physical encapsulation and chemical reactions can be considered as the immobilization mechanisms of heavy metals in CPBs (Guo et al., 2017; Y. Li et al., 2019). Generally, physical encapsulation mechanisms are commonly found in cementitious material immobilization techniques. The chemical immobilization mechanism of some heavy metal ions such as Pb^{2+} , Zn^{2+} , CrO_4^{2-} , and SeO_4^{2-} in cementitious matrices has also been investigated (Baur & Johnson, 2003; Y. Li et al., 2019; Tommaseo & Kersten, 2002). These metal ions can be placed at various potential positions in the structure of calcium-silicate-hydrate (C-S-H) or replace SO_4^{2-} ions in ettringite (Y. Li et al., 2019; Vespa et al., 2014). Moreover, these metal ions can also form some low-dissolved hydroxide precipitates at high pH levels. However, the above immobilization mechanisms of heavy metals are not qualified for arsenic due to the lack of effective chemical immobilization (Kundu & Gupta, 2008). Although some studies have been done to investigate the possibility of arsenic stabilization within cemented paste backfill, the mechanisms of arsenic immobilization in CPB are still unclear. Some researchers stated that Ca-As precipitates are the main forms of arsenic in CPB (Benzaazoua, Fall, et al., 2004; Coussy, Benzaazoua, et al., 2012; Moon et al., 2004). Basically, a few researchers have investigated the other immobilization mechanisms for arsenic in cementitious materials at various hydration times (Chai et al., 2017; Y. Li et al., 2019). Moreover, the available studies about the effects of arsenic on the strength of the cemented paste backfill materials are extremely limited. To enhance the inclusion of arsenic-containing wastes in CPB, it is needed to understand the mechanism of arsenic immobilization and stabilization in the structure of the CPB.

In this context, this study aims to highlight the mechanisms of arsenic trioxide stabilization in a CPB-like paste (which have never been studied before) and to define the effects of the presence of pure arsenic trioxide on the strength acquisition and geochemical behavior of the paste prepared using pure silica to mimic the tailings. To reach this goal, different mixtures of paste samples, as well as As_2O_3 -cement mixtures, were prepared and some specific analyses such as unconfined

compressive strength tests and mineralogical characterization were done. The results of this study could help to verify the possibility of the incorporation of the Giant Mine arsenic trioxide roaster waste dust within the cemented paste backfill and to investigate the solidification/stabilization of arsenic.

B.2 Materials and Methods

B.2.1 Materials

The main materials for the preparation of the cemented paste backfills that have been used in the current study consist of a binding agent, synthetic tailings, pure chemical reagent arsenic trioxide, and mixing water. The physical, chemical, and mineralogical characteristics of these ingredients can substantially affect the strength and stability of the CPBs (Belem et al., 2000; Ercikdi, Cihangir, et al., 2009; Kesimal et al., 2005). In this study, paste mixtures were prepared using pure ground silica to mimic mine tailings and avoid any impact of chemical or mineralogical compositions of mine tailings on the hydration reactions, and minimize uncertainties. Pure silica was also used in the previous studies as the tailings (Aldhafeeri, 2018; Chang, 2016; N. Koupouli et al., 2017; Sadatalhosseini et al., n.d.). Sulfidic and other reactive minerals and elements in the natural tailings could interact during the cement hydration process and affect the analysis results (Ghirian & Fall, 2016). Sil-Co-Sil® 106 (US Silica, USA) was chosen because its particle size distribution is similar to the particle size distribution of the Giant Mine tailings. Ordinary Portland cement (OPC), also called general use (GU) cement, is the most widely used binding agent for the preparation of CPB due to its availability and versatility (H. Jiang, Qi, et al., 2019; Tariq & Yanful, 2013). The main components of GU cement include tricalcium silicate (C3S), dicalcium silicate (C2S), tricalcium aluminate (C3A), tetracalcium aluminoferrite (C4AF), and gypsum (X. Deng et al., 2017). GU Portland cement supplied by Bomix (Quebec, Canada) was used as the binding agent for the preparation of the cemented paste backfill.

In order to omit the effects of roaster waste dust materials' impurity on the results, pure powdered analytical-grade arsenic trioxide (As_2O_3 , purity > 99.5%, Alfa Aesar, USA) was used as the arsenic source. The quality of mixing water could also affect the mechanical properties of CPB samples and cement hydration mechanisms. In the literature, various mixing waters such as tap, lake, and process waters are used for the preparation of CPB produced with different binding agents (Fall et al., 2010; H. Jiang, Qi, et al., 2019). During this study, deionized (DI) water was used for the

preparation of the cemented paste backfill samples and the other mixtures in order to eliminate the effects of the chemical components of water on the CPB behavior. The required water for the preparation of the samples and performing the analysis was collected at once to keep the quality of water persistent throughout this study.

B.2.2 Methods

B.2.2.1 Solid and liquid characterizations

Before sample preparation, the physical and chemical characteristics of the materials were investigated. The specific gravity (G_s) of pure silica, GU cement, and pure arsenic trioxide was measured using an automatic gas pycnometer (Ultracyc 1200e, Quantachrome Instruments). The particle size distribution (PSD) of Sil-Co-Sil[®] and pure arsenic trioxide was analyzed by a laser diffraction particle size analyzer (Malvern Mastersizer 3000). The specific surface of Sil-Co-Sil[®] and pure arsenic trioxide was analyzed by Brunauer-Emmett-Teller (BET) method using liquid nitrogen (Gemini 2375, Micromeritics). The chemical composition of the GU cement was obtained by X-ray fluorescence spectrometry (S2 Ranger, Bruker AXS). The chemical composition of the pure silica was provided by the supplier (US Silica). Inductively Coupled Plasma Mass Spectrometry (ICP-MS, Agilent 7800) was used for the analysis of the chemical composition of the DI. The pH and electrical conductivity (EC) of this water were also measured using a multimeter (B30PCI, VWR SympHony) followed by acidification by a 2% (v/v) nitric acid and Inductively Coupled Plasma Mass Spectrometry (ICP-MS) analysis using an Agilent 7800.

B.2.2.2 Preparation and curing of the cemented paste backfills

The mix designs (recipes) of the cemented paste backfill samples (the amount of required water, pure silica, binder, and arsenic trioxide) were prepared considering the specific gravity of the Sil-Co-Sil[®], GU cement, arsenic trioxide, as well as the solids, arsenic trioxide, and binder contents of the mixtures. The calculations of the required amount of each ingredient were done using a spreadsheet software based on the following equations:

$$\text{Solid content (\%)} = C_w = \frac{100 \times M_{\text{dry-solid}}}{M_{\text{dry-solid}} + M_{\text{water}}} \quad (\text{B.1})$$

$$\text{Cement content (\%)} = B_w = \frac{100 \times M_{\text{dry-cement}}}{M_{\text{dry-tailings}} + M_{\text{dry-As}_2\text{O}_3}} \quad (\text{B.2})$$

$$\text{As}_2\text{O}_3 \text{ content (\%)} = D_w = \frac{100 \times M_{\text{dry-As}_2\text{O}_3}}{M_{\text{dry-tailings}} + M_{\text{dry-As}_2\text{O}_3}} \quad (\text{B.3})$$

where M_{water} = Mass of water in the paste, $M_{\text{dry-tailings}}$ = dry mass of tailings, $M_{\text{dry-cement}}$ = dry mass of cement, $M_{\text{dry-As}_2\text{O}_3}$ = dry mass of arsenic trioxide, and $M_{\text{dry-solid}} = M_{\text{dry-tailings}} + M_{\text{dry-As}_2\text{O}_3} + M_{\text{dry-cement}}$.

Table B.1 shows the calculated mass of each ingredient of the CPB samples which were prepared with 5% of binder, zero to 15% percent of arsenic trioxide (hereafter referred to as CPB-0%, CPB-5%, CPB-10%, and CPB-15%) and dry silica to achieve a final solid content of 74 wt.%. The selection of the arsenic trioxide percentages was done considering the available arsenic trioxide (pure and dusts of the Giant Mine) and a previous study on the stabilization of Giant Mine arsenic trioxide dust using Portland cement (SRK, 2002). These calculations were based on the preparation of 6 cylindrical samples (for each As_2O_3 content) with the dimension of 2×4 inches (diameter × height, 50.8×101.6 cm) considering 20% additional materials to consider the possible losses during the preparation and molding.

For the preparation of the cemented paste backfills, a Hobart mixer with a capacity of 5 quarts was used. All the preparations were done in the laboratory. Since the samples had appreciable levels of arsenic trioxide, a cartridge mask and other safety measures were necessary to minimize the risk of arsenic inhalation and to avoid paste contact with the skin. To maximize binder integration within the mix, a part of the water was mixed with the binder in the bowl of the mixer using a hand spatula. Then, the pure silica tailings and the arsenic trioxide were added to the mixture, and they were mixed thoroughly within the bowl using the beater of the mixer. The remaining water was added progressively to the mixture and the mixing was continued for up to 5 minutes to achieve a homogenous paste. Meanwhile, the mini cone and a steel plate were rinsed using deionized water and the slump measurement was done. After measuring the slump, the paste was remixed for one minute, and then, it was poured into the three plastic molds. To allow the drainage and collection of the excess water from the CPB samples, 13 holes with 2 mm diameter were perforated at the bottom of each mold before molding the paste. Then, a layer of geotextile was put on the bottom to prevent the loss of the fine grains after pouring. It's worth mentioning that, in practice, drainage

is not allowed in all backfilled mine stopes, especially in the case of a high rate of filling and unfractured rock mass surrounding the paste backfill (Ercikdi et al., 2013). The paste was poured into the molds in a single layer with minimum delay after mixing, because of the rapid initial setting of the samples. After molding, to expel the air bubbles from the pastes, the cylinders were hammered 25 times by inserting a steel rod with a diameter of 9.53 mm (3/8 in). Then the sides of the molds were hammered until no air bubble was observed on the top of the paste. The prepared cylindrical samples were labeled, sealed, and stored in a humidity chamber (approximately 90% humidity and 20 °C temperature; conditions typical of underground mine storage) for 7 and 28 days to cure before testing. The conditions remained unchanged over the curing period to ensure the comparability of tests and limit the number of influencing factors. The specimens were removed from the molds after the above-mentioned curing days, and unconfined compressive strength (UCS) tests were done on the samples. Figure B.1 shows the process of the preparation, mixing, curing, and testing of the CPB samples.

Table B.1 The calculated mass of CPB ingredients used for the preparation of the pastes

Sample	CPB-0%	CPB-5%	CPB-10%	CPB-15%
As_2O_3 content (%) (D_w)	0	5	10	15
Solid percentage (%) (C_w)	74	74	74	74
Cement content (%) (B_w)	5	5	5	5
$M_{dry-tailings}$ (g)	2042.4	1951.5	1859.6	1766.6
$M_{dry-As_2O_3}$ (g)	0.0	102.7	206.6	311.7
$M_{dry-cement}$ (g)	102.1	102.7	103.3	103.9
M_{water} (g)	750.6	754.9	759.3	763.8
Water to cement ratio (W/C)	7.35	7.35	7.35	7.35



Figure B.1 Process of preparation, mixing, curing, and testing of the cemented paste backfill samples

B.2.2.3 Slump measurement

Workability and rheological properties are among the major parameters for the assessment of the performance of CPB mixtures. In the mining industry, the slump test is the most universally accepted method of measuring the backfill's rheological properties (H. Jiang, Qi, et al., 2019; Yilmaz et al., 2012). The slump height, an empirical measure of workability, is dependent on both the material density and yield stress, which in turn are dependent on composition, specific gravity, and the size of the particles (X. Deng et al., 2017). In this study, the workability of fresh CPB mixtures was evaluated by measuring the slump using a mini cone instead of the Abrams cone because of the limited volume of the materials. The mini cone, which already shows its effectiveness for that measurement (Jia et al., 2016; Roussel et al., 2005; Tan et al., 2017), has the following dimensions: height, 150 mm; top diameter, 50 mm; and bottom diameter, 100 mm. These measurements were carried out by ASTM C143 (Standard test method for slump of hydraulic-cement concrete) (ASTM, 2015) standard procedure. After mixing the paste for 5 minutes, it was poured into the mini cone in three layers, each layer was hammered 25 times using a steel rod with a diameter of 9.53 mm (3/8 in). Then, the cone was lifted vertically in three seconds. The final slump, i.e., the height between the top of an initial state of the paste (molded into the cone) and its final state (after removing the cone), was measured. Before the preparation of the samples, to convert the measurement to the standard values, some paste samples were prepared at various water contents, their slumps were measured using both Abrams and mini cone and a conversion factor equal to 2.52 was established between the slump values for these cones ($\text{Slump}_{\text{Abrams}} = 2.52 \times \text{Slump}_{\text{mini}}$). Other authors have also proposed some other relationships. Ouattara, Kalonji, and

Dikonda have proposed a conversion factor of 2.28, 2.20, and 2.29, respectively (Dikonda, 2018; Kalonji, 2016; Ouattara, 2017).

B.2.2.4 Preparation of the cement-As₂O₃ mixtures

To study the geochemical evolution of the pastes during curing (early and latest stages), collecting and analyzing the drained waters from the samples were planned during the curing period. However, it was impossible for most of the CPB samples (except the CPB-5%) because of the rapid initial setting of the paste; only a few ml of drained water was collected from the CPB-5% samples. Therefore, it was decided to investigate the chemical behavior of the paste mixtures by removing the synthetic tailings (Sil-Co-Sil[®]) from the fresh mixtures. Since the synthetic tailings are mostly comprised of inert pure silica, this change in the paste mixtures does not affect their geochemical compositions and provides a dilute mixture that would be much easier to analyse after filtration. Four beakers with a volume of 2 liters were thoroughly cleaned and rinsed with deionized water. GU cement, pure arsenic trioxide, and deionized water with the same amount of the CPB mixtures (Table B.1) were poured into these beakers and mixed for 24 hours using magnetic stirrers. After 24 hours, the As₂O₃-cement mixtures were transferred to the bottles and kept for up to 28 days with some occasional agitations during this period. The pH and EC of the DI water were measured before mixing. During the mixing, samples (2 replicates for each As₂O₃ content) were collected after 10 min, 90 min, 3 hr, 5 hr, and 24 hr using a 50 ml syringe and then filtered with a 0.45 µm cellulose syringe filter prior to analysis. The pH and EC of the filtrates were measured using a multimeter (B30PCI, VWR SympHony). Following the pH measurement, the extracted solutions were acidified with a 2% (v/v) nitric acid, and their chemical compositions were analyzed by Inductively Coupled Plasma Mass Spectrometry (ICP-MS) using an Agilent 7800. Some samples were also collected after 7 and 28 days, filtered, and after pH and EC measurements, they were sent for the ICP analysis. Finally, the mixtures were extracted from the bottles and dried at 60°C for three days. The dried As₂O₃-containing mixtures were pulverized using a pestle and mortar and sent for the solid ICP-MS analysis after acid digestion with a mixture of HNO₃ and HCl acids.

B.2.2.5 Unconfined compressive strength (UCS) tests

UCS can be considered as the most general parameter used to determine the physical stability and strength acquisition of the CPB structure due to its simplicity and low cost (Q. Chen, Zhang, Fourie, Chen, et al., 2017) and it can be considered as a routine quality control program at the mine.

Generally, the UCS for rock, concrete, and CPB structures is obtained from cylindrical samples with a height-to-diameter ratio of 2:1 (USEPA, 1996). The strength evolution in the pastes was assessed by performing UCS determinations on three replicated specimens for each mix design (based on Table B.1). UCS tests were carried out based on the ASTM C39 (Standard test method for compressive strength of cylindrical concrete specimens) (ASTM, 2021) standard by a computer-controlled mechanical press with a normal loading capacity of 50 kN and a 1 mm/min displacement rate and the stress-strain data were recorded for each sample. The samples were taken out of molds after 7 and 28 days of curing. The bases of the cylinders were first rectified and smoothed to get their surfaces flat and parallel to the plates of the mechanical press before the UCS tests. The mass and the dimensions of the samples were measured before testing. The UCS parameter corresponds to the maximum stress value before failure during the compression test. All the measurements were carried out in triplicate and the average values were taken as the final compressive strengths. The values of modulus of elasticity and strain at the break were also obtained from the results. After the UCS tests, a subsample of each specimen was collected, weighed, and put in the oven (60° C) to assess the water content of the samples after curing. After drying for three days, the samples were kept for some complementary tests (i.e., scanning electron microscopy and ICP analyses).

B.2.2.6 SEM observations (microstructural analysis)

After performing the UCS tests on the 28-day cured CPB samples and geochemical analyses on the As_2O_3 -cement mixtures after 28 days, the samples were dried and pulverized using a pestle and mortar and prepared for the scanning electron microscope (SEM) analysis. This analysis was done only on the As_2O_3 -containing samples to provide a visual insight into the microstructure of these samples and to correlate the microstructure and mineralogy of these samples to the mechanical performance and geochemical characteristics of the mixtures. The study was carried out by IOS Geosciences laboratory using a Zeiss Sigma 300 VP field effect SEM (FE-SEM) equipped with two Oxford Instruments Ultim-Max 170 mm² energy dispersive spectrometers (EDS-SDD). The EDS-equipped SEM analysis helps to perform the chemical characterization and identification of cementitious phases (Ercikdi, Kesimal, et al., 2009). The electron images were recorded in backscattered electron (BSE) mode at an accelerating voltage of 20 kV. Oxford Instruments AZtec 5.2 software was used for the acquisition of the microanalyses, the automation of the acquisitions of X-ray maps, the deconvolution of the energy spectra, and the processing of the data, according

to previously calibrated parameters. The analyses are called semi-quantitative because they are 100% standardized and use the factory calibrations of the device. A portion of the material from each sample was sprinkled onto aluminum pontils covered with double-sided carbon tape. The samples were manually scanned with SEM, from the most As-enriched sample to the least enriched one, in order to better identify the As-bearing phases. Following the initial observations, some polished sections were prepared in order to observe the mineral associations, carry out an automated mineralogical analysis, and obtain more precise analyses. The samples were cast in a viscosity-controlled epoxy resin to make a section 30 mm in diameter. The surface of the sections was polished using an alumina suspension, then using a diamond suspension (0.2 μm). The polished surfaces were coated with a carbon film 8.0 ± 0.3 nm thick using a Leica EM ACE600 rotary-table metallizer to allow electron drainage to the SEM. Mineralogical analysis was performed using ARTMin-II technology. This technology consists of acquiring chemical maps on the sample to reconstruct the map of the mineral phases. The mineral phases are then defined from the X-ray maps by AZtec's AutoPhaseMap clustering algorithm.

B.3 Results and discussions

Results of the initial characterization of the materials, slump of the pastes, and the mechanical strength tests (UCS) are shown first, to give some information on the characteristics and the effects of arsenic trioxide addition on the mechanical properties of the pastes. Then, the results of the geochemical analysis are presented to understand the behavior of As and some other related elements for each CPB mixture, followed by the results of the microstructural observations to provide some insights into the composition of the occurring phases that formed within the structure of the CPB and As_2O_3 -cement samples.

B.3.1 Initial characterization

The specific gravity of the materials used for the preparation of the cemented paste backfill was 2.66, 3.17, and 3.45 for the pure silica, GU cement, and arsenic trioxide, respectively. These values were used for the calculation of the required materials to obtain the CPB formulation with the previously-defined mix designs: $B_w = 5\%$, $C_w = 74\%$, and $D_w = 0$ to 15% with the same water to cement (W/C) ratio for all of the samples. Figure 2 depicts the cumulative PSD of the Sil-Co-Sil[®] and the pure arsenic trioxide as well as the cumulative PSD of four mine tailings in Quebec, Canada (Demers et al., 2008; Lessard et al., 2018; Rey et al., 2020) to compare the PSD of pure silica with

typical mine tailings. Table B.2 presents some widely used indicators associated with PSD and specific surface (S_s). Based on Figure B.2, about 40% of Sil-Co-Sil[®] and 10% of arsenic trioxide are finer than 20 μm . Particle size distribution of the pure silica tailings and the proportion of the fines (< 20 μm) can substantially affect the strength of the paste, and coarse and medium tailings are preferable for the strength gain of the CPB (Benzaazoua, Marion, et al., 2004; Kesimal et al., 2003). The proportion of fine fraction of the tailings (< 20 μm) also strongly affects both the pore size distribution and the overall porosity of the CPB material. The finer the tailings material used, the greater the overall porosity of the CPB becomes. In these CPB samples, zero to 15% of the pure silica tailings (Sil-Co-Sil[®]) were substituted by the arsenic trioxide which is coarser and more uniform than the Sil-Co-Sil[®]. Most of the arsenic trioxide grains are in the range of 10 to 100 μm .

The chemical composition of the pure silica showed that SiO_2 accounted for 99.8 wt.%, followed by negligible impurities of Al_2O_3 (0.16 wt.%) and lesser amounts of other oxides. Table B. 3 summarizes the chemical composition of the GU cement based on the elemental components and Table B. 4 shows the chemical composition of the DI water. The initial pH and EC of the DI water used as the mixing water was equal to 8.63 and 0.0009 mS, respectively. The pH was unexpectedly high due to a malfunction of the DI water generator; however, it was decided to maintain the mixtures with high-pH water as it may represent alkaline process water from mineral processing. This could be due to the presence of some ions such as bicarbonate and carbonate which were not measured in this study.

B.3.2 Slump and UCS results

Table B.5 presents the results of the slump to evaluate the rheology of the mixtures, using the conversion factor developed in this study. It seems that the addition of the arsenic trioxide resulted in a decrease in the slump of the mixtures; however, increasing the amount of arsenic trioxide from 5% to 15% has led to an increase in the slump values. Although all the CPB samples were prepared at a constant water-to-cement (W/C) ratio, the water amount required in the recipes increased with the As_2O_3 content increase, since arsenic trioxide dust has higher specific gravity. The slump test is a highly valuable index test and should be employed for quality assurance purposes. However, using it solely to establish design parameters like yield stress is not advisable unless supported by additional, more comprehensive testwork or when dealing with materials already thoroughly studied and confirmed (Fourie & Dunn, 2007). This test was conducted on a small sample using a

mini cone in a controlled laboratory environment. It may not fully represent the behavior of CPB in actual field conditions since the obtained values should be converted to standard values (Abrams cone), and other factors like pumping, segregation, and settling may influence the workability of the paste. The results can also vary depending on the experience and judgment of the operator, introducing inconsistencies in the measured values.

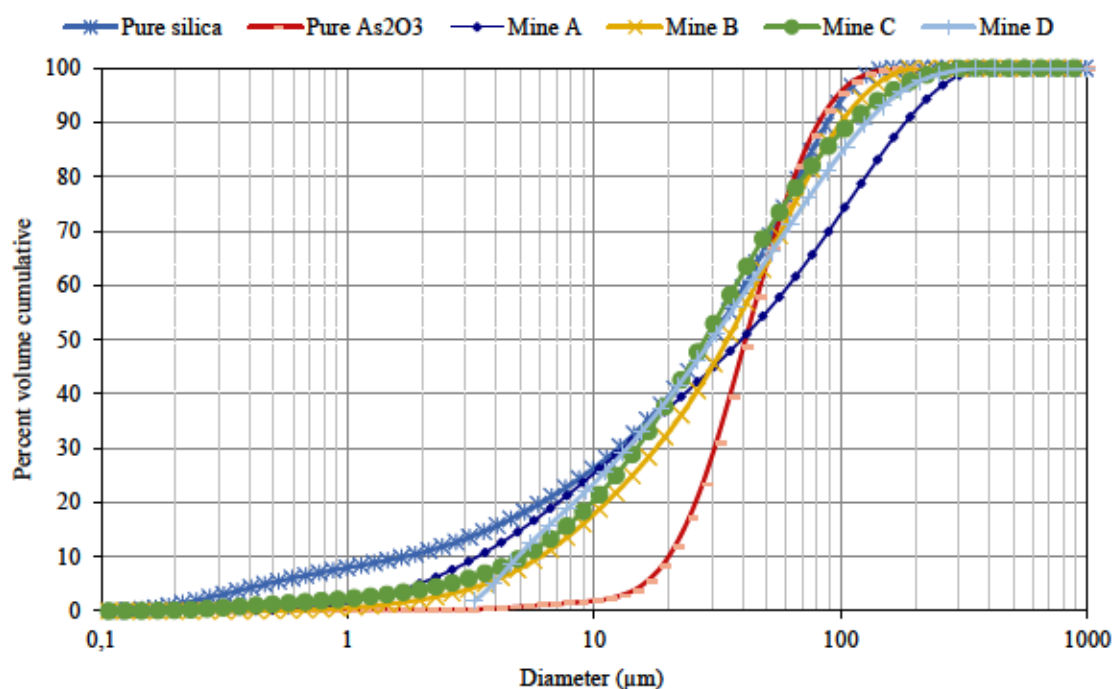


Figure B.2 Grain size distribution of pure silica and pure arsenic trioxide

Table B.2 Parameters related to the grain size distribution and the specific surface of the material used for CPB preparation

Parameter	Unit	Value	
		As ₂ O ₃	Sil-Co-Sil®
D ₁₀	(μm)	22.6	1.7
D ₃₀	(μm)	34.8	12.5
D ₆₀	(μm)	53.6	40.7
$C_u = D_{60}/D_{10}$	(-)	2.4	24.1
$C_c = D_{30}^2/(D_{60} \times D_{10})$	(-)	1.00	2.3
Specific surface (S_v)	m ² /kg	48.6	1090.1

Table B.3 Chemical composition of the general use (GU) cement

GU cement	O	Cl	Ca	K	Sr	Al	S	Mg	Zn	Fe	Mn	Ti	P	Si	Sum
	%														
	51.51	0.02	34.25	0.80	0.19	2.12	1.50	1.20	0.02	1.73	0.03	0.07	0.08	6.46	99.97

Table B.4 Chemical composition of the deionized water

pH	EC	Al	Sb	As	Ca	Fe	Mg	K	Na	S
	(mS)	(mg/L)								
8.63	0.0009	<0.005	<0.0001	<0.0005	0.41	<0.01	0.07	60.54	0.3	0.29

Table B.5 Results of the slump of the CPB samples

Sample	CPB-0%	CPB-5%	CPB-10%	CPB-15%
Slump _{mini} (mm)	85	78	84	89
Slump _{Abrams} (mm)	214	197	212	224

Figure B.3 depicts the results of UCS tests on the drained CPB samples with various As_2O_3 contents after 7 and 28 days of curing. The mechanical strength increase was more pronounced for the CPB-0% paste sample; however, the As_2O_3 -containing samples gained their strength mostly in the first 7 days and there was a small, but maybe not significant, increase in the strength after 7 days displaying slow strength acquisition. The UCS of the CPB-0% paste improved from 428 kPa to 740 kPa (72.7% increase) during 7 to 28 days of curing. The percentages of improvement in strength acquisition from 7 to 28 days of curing for the As_2O_3 -containing samples were 10.1%, 22.4%, and 2.5%, for the CPB-5%, CPB-10%, and CPB-15% samples, respectively. This strength augmentation could be attributed to the effect of several factors that contribute to more CPB strength development. A longer curing time results in the precipitation of higher amounts of cement hydration products (Ghirian & Fall, 2016), higher water consumption (stronger self-desiccation) and gradual evaporation (L. Liu, Xin, et al., 2020). This results in the development and strengthening of the cohesion between pure silica and As_2O_3 particles that helps to provide a stronger cemented matrix. Furthermore, an increase in cement hydration products causes the refinement of the pore structure (lower porosity and pore tortuosity (L. Liu, Xin, et al., 2020)), which in turn improves the strength. The higher strength augmentation in the CPB-0% sample also could be due to the more fineness and lower amount of available water.

Results also showed a significant drop in the strength of the CPB samples by adding 5% of arsenic trioxide. Before the implementation of the tests, the expected results were a decrease in the strength with an increase in the As_2O_3 content, as observed in previous studies with high cement content (Arcadis, 2017). However, in the samples with higher As_2O_3 percentages, some increases were observed in the strength of the samples and finally, CPB-10% samples showed the highest strength among the As_2O_3 -containing samples after 28 days. The standard deviation (SD) for the triplicate UCS of the pastes was found in the range of SD = 6.6 kPa and 73.6 kPa and SD = 26 kPa and 65.1 kPa, for the samples cured for 7 and 28 days, respectively. The coefficient of variation (CV) for these samples was in the range of CV = 3.2% and 17.2% and CV = 8.8% and 21.9%, respectively. To the best of the authors' knowledge, there is limited data available in the literature regarding the UCS of the arsenic-containing samples. Hamberg et al. (Hamberg et al., 2015a) had completed UCS tests on drained CPB samples prepared using the arsenopyrite-rich tailings with an arsenic concentration of 1070 ± 30 mg/kg and the range of the strength for their samples prepared using ordinary Portland cement was between 341 and 426 kPa after 28 days for 3% and 5% of cement, respectively. Su et al. (Su et al., 2019) prepared some CPB samples using lead-zinc tailings and studied the strength of these samples for up to 28 days of curing. The findings showed that the cement-to-tailings ratio of 1:6 and a slurry concentration of 70% resulted in the maximum strength after 28 days. Zhao (L. Zhao, 2023) used flue gas desulfurization gypsum (6%) and limestone (3%) to prepare cemented paste backfill using Cr(VI)-containing tailings. Result showed that the compressive strength of the CPB samples could reach about 5.53 MPa with 99.5% of Cr(VI) immobilization.

In the literature, it has been mentioned that the drainage could also contribute to the strength gain in drained CPB samples through mechanisms including the curing under higher effective stress through the dissipation of excess pore water pressure which results in the formation of stronger bonding between the tailings and cement hydrates; and a reduced W/C ratio due to gravity drainage that could be associated with higher mechanical strength (reduced porosity easy to be filled) (Ghirian & Fall, 2016). Moreover, the drainage results in consolidation, pore refinement, and porosity reduction which could help to strength augmentation. In this study, it seems that the drainage could not help strength improvement, mainly because of the rapid reaction of the GU cement and significantly low drained water from the pastes. As mentioned before, the sample with some drained water (CPB-5%), showed the lowest UCS.

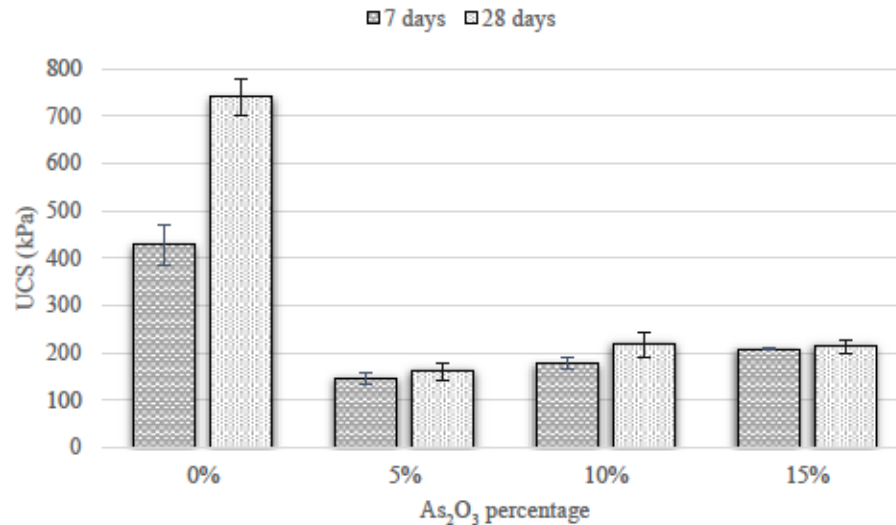


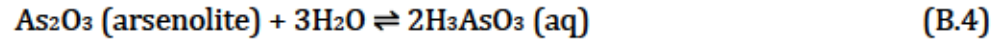
Figure B.3 Results of the UCS tests on the cemented paste backfill samples with various As₂O₃ contents after 7 and 28 days of curing

The stress-strain (deformation) curves of the CPB samples obtained from the UCS tests are presented in Figure B.4 for the samples prepared with various As₂O₃ contents and cured for 7 and 28 days. The axial strain at the break (ϵ_u) represent the material's ductility, with higher values reveal a more ductile/less brittle character (Soltani et al., 2017; Yue Zhao, Soltani, et al., 2019). The stress-strain behavior for all CPB samples exhibited a rise-fall behavior with visually observable peak points. This reveals a strain-softening character accompanied by more ductile sample failure for As₂O₃-containing samples and more brittle sample failure for the CPB-0% samples. With respect to this graph, for most CPB-0% samples, the strain at the failure is less than 2% after 7 and 28 days of curing. The highest strain at the break is mostly related to the CPB-5% samples (with the lowest strength), followed by the CPB-10% and CPB-15% samples for 7-day cured and CPB-15% and CPB-10% for 28-day cured samples, respectively. The order of decrease in the strain at break values was equal to the order of increase in the strength of the samples. In general, the higher the UCS the lower the strain at the failure. It should be noted that, generally, increasing the curing time lowered the strain at the break (lower ductility) for the As₂O₃-containing samples but it had no significant influence on the deformation behavior of the CPB-0% samples. This behavior is attributed to the combined effect of consolidation and hardening, which results in the CPB sample with less plastic behavior (Ghirian & Fall, 2016).

Figure B.5 highlights the relationship between the UCS and the modulus of elasticity (E) obtained from the UCS test results. These results are presented for all the CPB samples prepared with and without As_2O_3 and cured for 7 and 28 days. The results showed a relationship between the E and UCS values for most of the samples. The E values after 7 days typically vary between 159 and 272 MPa for the CPB-0% samples and between 18 and 126 MPa for the samples with various contents of As_2O_3 . For the samples cured up to 28 days, these values are between 8 and 146 MPa and between 21 and 82 MPa for the samples without and with As_2O_3 , respectively. Samples with the higher compressive strength showed a higher modulus of elasticity (the CPB-0% samples) and arsenic-containing samples with the lower strength revealed lower E values. The most interesting point regarding the E values is the decline in the modulus of elasticity after 7 days. This was more pronounced for the CPB-0% samples, where the E values were mostly higher than 150 MPa after 7 days; however, these values decreased to lower than 150 MPa after 28 days. For the As_2O_3 -containing samples, this reduction was not noticeable.

The modulus of elasticity and strain values at the break were obtained from the stress-strain curves to evaluate how curing time and As_2O_3 content affect the deformation behavior of CPB. Based on the general relationship between the modulus of elasticity, E , stress, σ , and strain, ϵ ($E = \sigma/\epsilon$), it is evident that there is a direct linear relationship between the E value and the inverse of the strain ($1/\epsilon$). Therefore, the relationship between the modulus of elasticity (E) and the inverse of the strain at the break ($1/\epsilon_u$) is presented in Figure B.6 for the samples with various As_2O_3 contents and cured for 7 and 28 days. As expected, the CPB-0% samples mostly showed the highest modulus of elasticity and lowest strain value at the break (highest inverse values).

As mentioned before, it was planned to collect the drained water from the CPB samples after molding and during the curing period. However, just for the CPB-5% samples, a few ml of drained water was collected after molding since the rate of initial setting of the pastes was very high for the other paste samples. Table B.6 lists the chemical analysis of the collected water as well as the EC and pH values. The pH of the paste without arsenic was higher than 12 (refer to section 3-3); however, for the CPB-5% samples, the pH value was lower than 10.5. For optimal cement hydration, higher pH values are usually required. The reduction in the pH of the paste could be due to the arsenolite (As_2O_3) dissolution. When arsenic trioxide is dissolved in water, it hydrolyses and dissociates into *o*-arsenous acid, H_3AsO_3 (As III) as follows:



and this is followed by the oxidation of As III to As V:

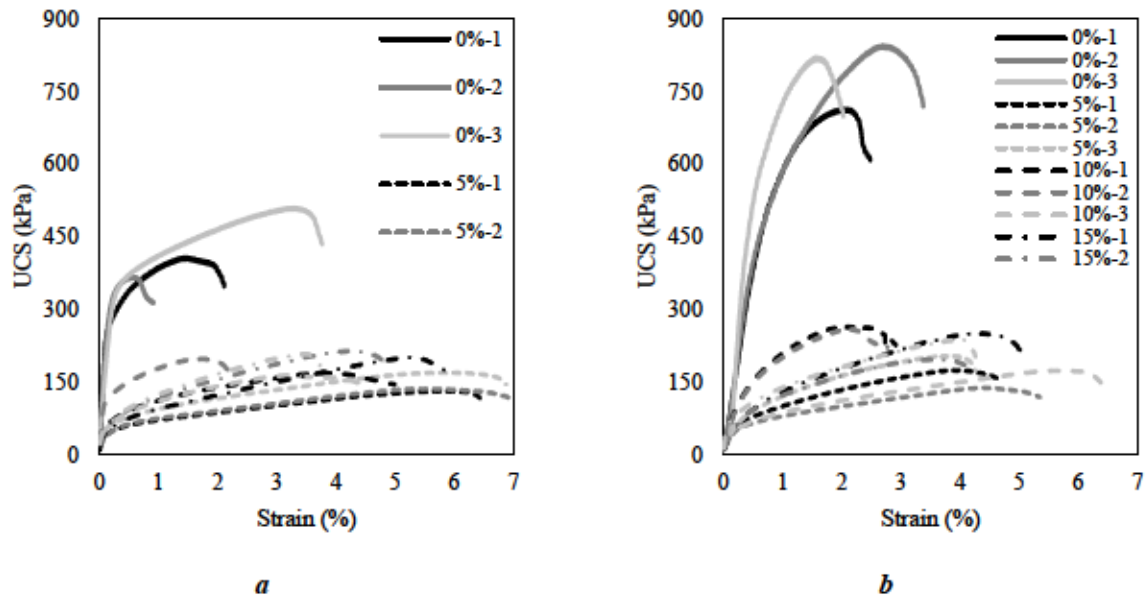
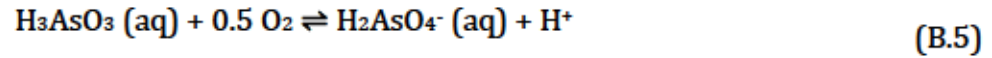


Figure B.4 The effect of As_2O_3 content on the stress-strain (deformation) behavior of CPB cured for (a) 7 and (b) 28 days

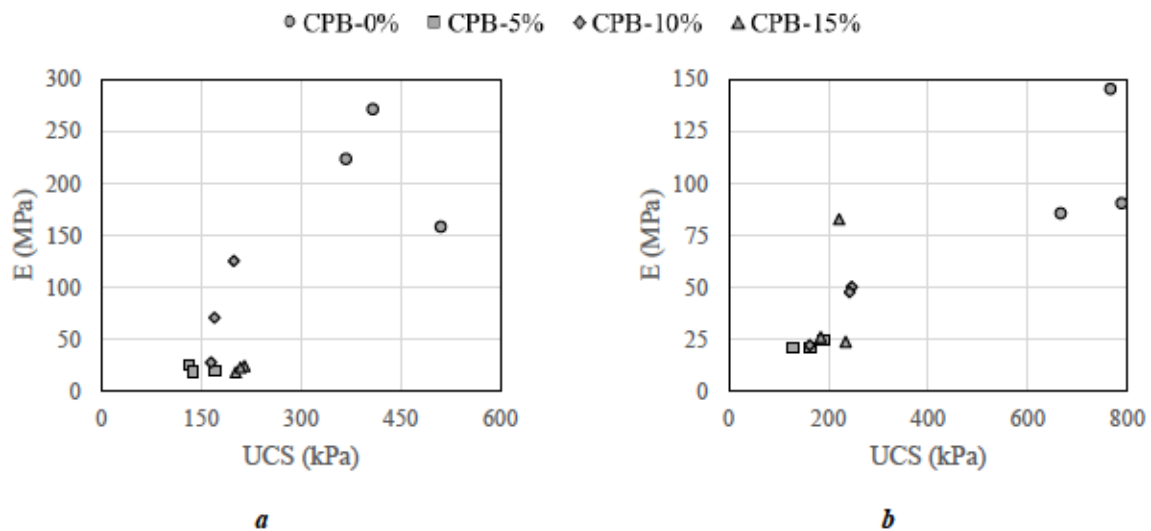


Figure B.5 Relationship between UCS and modulus of elasticity after (a) 7 days, (b) 28 days

The oxidation of arsenite to arsenate in reaction (2) generates H^+ and causes acidity, therefore lowering the pH of the solution (Craw & Bowell, 2014). In an alkaline solution, some anions such as $AsO(OH)_2^-$, $AsO_2(OH)^{-2}$, and AsO_3^{-3} might also be present. However, it has been claimed that the *m*-arsenite ion, AsO_2^- , is also present in such solutions (Committee on Medical and Biologic Effects of Environmental et al., 1977). Due to the dissolution of the arsenic trioxide and cement during the preparation of the CPB samples, the electrical conductivity (EC) and the concentration of the elements increased in the collected drained water. The concentration of the dissolved arsenic is notable in this water and the presence of sulfur could be due to the presence of the calcium sulfate in the structure of the GU cement which is added to control early hydration reactions to prevent flash setting, improve strength development, and reduce drying shrinkage (Barger et al., 2001). The presence of calcium, sulfur, and arsenic in the CPB pastes could help the formation of some amorphous/crystalline secondary minerals and the integration of the arsenic into the structure of the calcium-silicate-hydrate (C-S-H) phases. So, based on these results it can be considered that the main reason for a significant drop in the UCS would be the inhibition of the hydration due to the drop in pH value, and increased strength in the samples with higher arsenic trioxide contents could be due to precipitation of some amorphous/crystalline minerals. The latter hypothesis will be assessed in the next section.

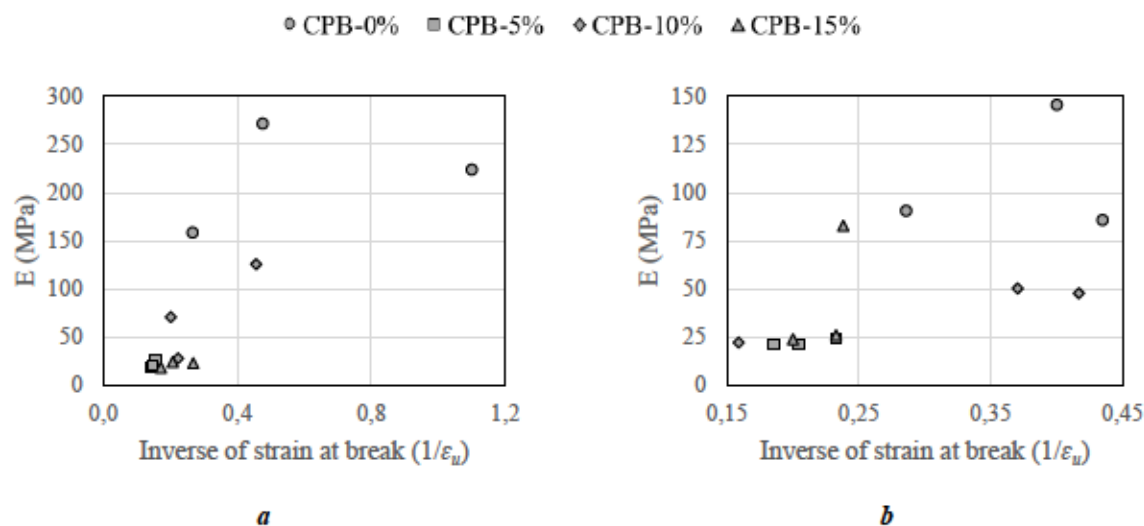


Figure B.6 Relationship between modulus of elasticity and inverse of strain at break (a) 7 days, (b) 28 days

B.3.3 Cement- As_2O_3 mixtures

To obtain insights into the interactions between binder and arsenic trioxide, the As_2O_3 -cement mixtures were assessed in the absence of pure silica. Figure B.7 shows the variation of the EC and pH of the water in contact with the mixtures for 28 days (672 hours). Figure B.8 depicts the variations of the most relevant elements versus time for the contact water with various As_2O_3 contents in the solid mixtures. Dissolution of the GU cement and pure arsenic trioxide influenced the concentration of the various elements during the mixing period, and consequently, affected the pH and electrical conductivity of the solutions. The increase in EC was more pronounced for the solution without arsenic, with a tendency to increase with time, especially during the first seven days (up to 168 hours). This result is correlated to the pH values between 12.19 and 12.86 measured for the solution without As_2O_3 with a tendency to increase with time. Conversely, for the As_2O_3 -containing solutions, the pH values varied between 9.18 and 10.42 with a decreasing trend during the test period. This drop in pH compared to the arsenic-free solution agrees with the result from the drained water analysis presented in Table B.6. Except for the arsenic and antimony in the solutions without arsenic, the dissolution of the elements has shown the same pattern in most of the cases, i.e., an increasing trend. The variations of antimony in these solutions could be attributed to the impurity of the arsenic trioxide. A decrease in Ca concentration after 168 hours (7 days) may indicate the formation of Ca-As precipitates. These calcium-arsenic precipitation reactions can be considered as an important immobilization mechanism of arsenic in CPB. For 0% As_2O_3 mixture, the cement hydration results in the formation of calcium-(aluminate)-silicate-hydrate (C-(A)-S-H) gels; therefore, it decreases the concentration of the dissolved calcium after seven days.

Table B.6 Chemical composition of the drained water

Parameter /Element	CPB-5%
EC (mS)	5.51
pH	10.45
Sb (mg/L)	2.4
As (mg/L)	1670.9
Ca (mg/L)	853.0
K (mg/L)	777.3
Na (mg/L)	230.0
S (mg/L)	748.1

In this study, the synthetic CPB samples were prepared using pure silica (quartz) to simplify the analysis; however, it's worth mentioning that for the real CPBs (i.e., CPB made of real tailings instead of pure silica), physical, chemical, and mineralogical composition of the tailings could also exert influence on the hydration processes, mechanical behavior of CPB, and the geochemical behavior of arsenic (Coussy et al., 2011; Coussy, Benzaazoua, et al., 2012; Coussy, Paktunc, et al., 2012).

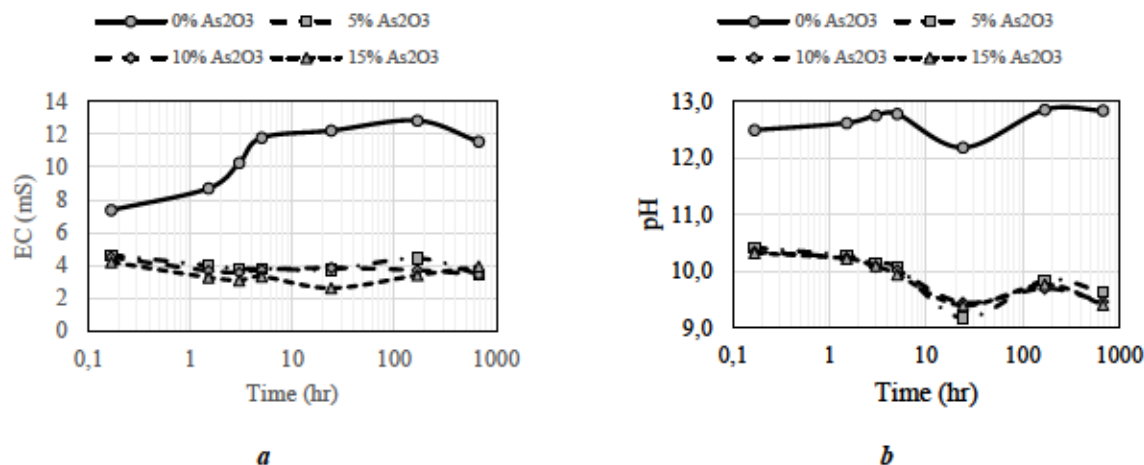


Figure B.7 Variations of (a) EC and (b) pH of the cement-As₂O₃ mixtures versus time for the mixtures with various As₂O₃ contents

B.3.4 SEM results

SEM analyses were performed on the dried 28-day cured samples after the UCS tests and the dried As₂O₃-cement mixtures to better understand some of the relationships between the compressive strength acquisition process and the texture of each paste backfill sample as well as the microstructure of the cementitious matrices with various arsenic trioxide contents. These investigations were done just on the As₂O₃-containing samples and some of the observations are presented here. The effects of microstructure on the strength and stability of CPB has been emphasized in many studies (Benzaazoua et al., 2002; Ercikdi, Kesimal, et al., 2009; Ouellet et al., 2007). The automated mineralogical analysis was difficult to achieve due to the complexity of the phases, therefore several phases and species were identified but could not be quantified. Some phases could be specified by their generic names, especially the oxides such as oxide-As-Al-Ca, oxide-As-Ca-Si, etc. However, for some grains, the chemical analyzes could not point to any known mineral species and stoichiometric calculations were inconclusive. These particles were

generally mixtures of fine minerals with variable chemical compositions, possibly products of weathering or thermodynamic re-equilibrium.

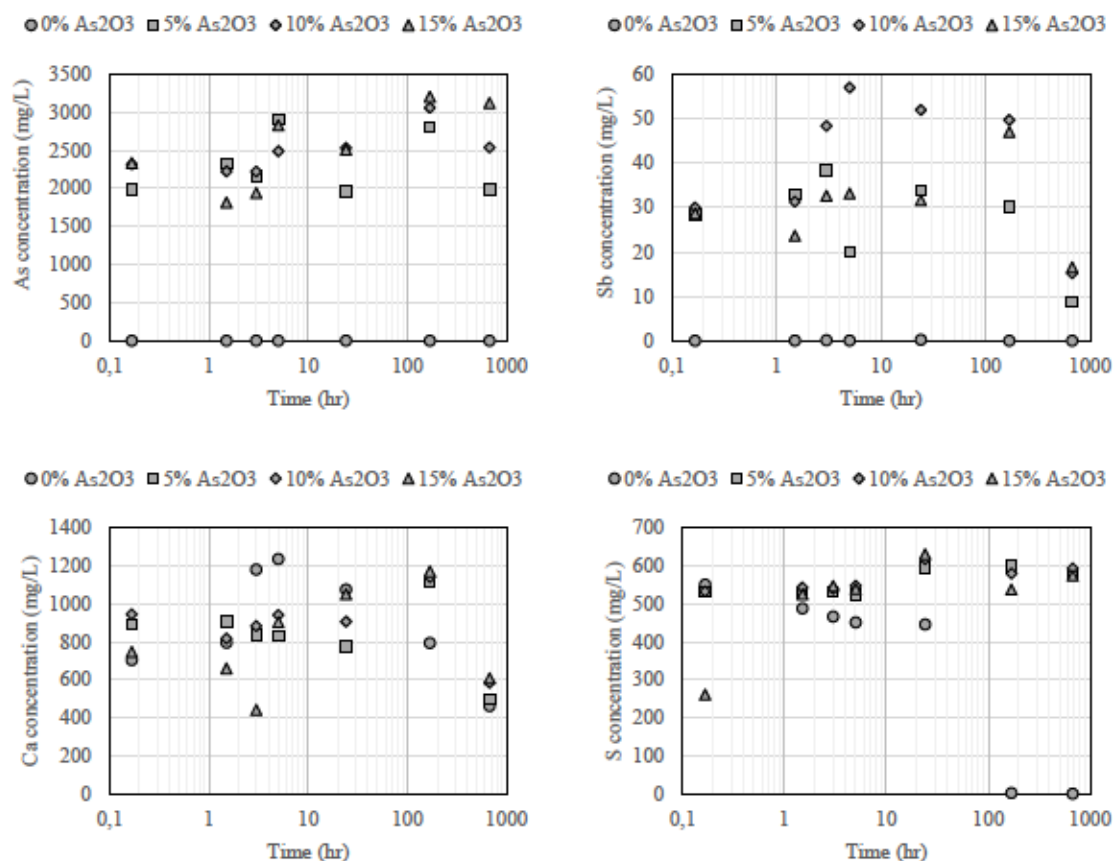


Figure B.8 Variations of the dissolved elements (As, Sb, Ca, and S) in the cement-As₂O₃ mixtures containing different percentages of arsenic trioxide versus time

The CPB samples were confirmed to be composed mainly by silicates, with quartz being the main mineral, along with some crystalline arsenic trioxide as the dominant As-bearing phase and some other As-bearing phases were also observed in lesser quantities. Most of the grains were easily observable due to their crystalline system and some grains were perfectly crystallized in bipyramidal (octahedron) shape. Some rounded, uncrystallized grains composed of As-Si-Ca were also found. They seem to be gels formed as precipitates or secondary products. These conditions were the same for all the CPB samples and the difference between the samples was just the content of arsenic in the structure of the grains. Semi-quantitative analyses were done on the samples as shown in Figure 10. In these analyses, various silicate and arsenious oxides are microanalyzed at various points of the grains which indicated that they are mostly composed of oxides of As-Si-Ca.

In Figure B.9, spectrums 136 and 138 refer to the As-Si-Ca oxides, and spectrum 137 is related to the As-Ca-Si oxides. The order of the elements is based on their descending occurrence. Some small amounts of antimony were also quantified in these grains coming from the impurity of the arsenic trioxide. Spectrums 139 and 140 are related to the Si oxides and Ca-Si oxides respectively, with some small amounts of arsenic in their structures. The content of other elements (Mg, Al, S, Cl, and Fe) in the structure of these grains was negligible and mostly less than 1%.

For As_2O_3 -cement samples (Figure B.10), the structure was significantly different due to the absence of quartz. In these samples, the As-Ca-Si-Al oxides were more prominent (no dilution by the quartz), but there were still many intact undissolved As_2O_3 grains. The grains were multiphase, very fine and thin, complex as per their stoichiometry, and randomly shaped. The observed minerals are mainly comprised of arsenic oxides with calcium (Ca-arsenite/arsenates). Figure B.10 shows the complexities of the grains with the coexistence of various phases. Spot analysis showed various phases, mainly the arsenic trioxide, as well as the As-Ca oxides and various gel phases. In this graph, the spectrums 35-37, 41, and 44 are the arsenic trioxide grains. Spectrums 38 and 43 are the oxide-As-Ca and the other spectrums are related to the complex grains enriched in As, Ca, Al, and Si with some minor amounts of other elements.

Slight cement hydration occurred, but not as much as expected, and this could explain the low strength in the As-enriched CPB. No ettringite and portlandite were observed within these samples because of the low amount of sulfur in the samples and lowered pH of the mixtures. For the As_2O_3 -cement mixtures, the observations show some interactions between As_2O_3 and cement, but many As_2O_3 grains remain intact. The main identified species were the C-S-H gels, some mixed species, and oxide-As. The gel phases comprised variable percentages of arsenic trioxide and the identified mixed species were oxide-As-Ca-Si-Al or oxide-As-Ca-Al-Si.

B.4 Conclusions

This study provided a better understanding of the effects of the presence of arsenic trioxide on the geomechanical and geochemical behavior of the cemented paste backfills. CPB samples were prepared using various amounts of pure As_2O_3 , GU cement, and pure silica in order to study the strength and stability of the As_2O_3 -containing CPB samples. Moreover, As_2O_3 -cement mixtures were also prepared to investigate the geochemical behavior of the mixtures and evaluate the possible reactions, in particular the As release, with other elements in cementitious matrices.

Microstructural characterization was also carried out using SEM analysis to observe of the microstructure of the As_2O_3 -containing CPB and cementitious mixtures.

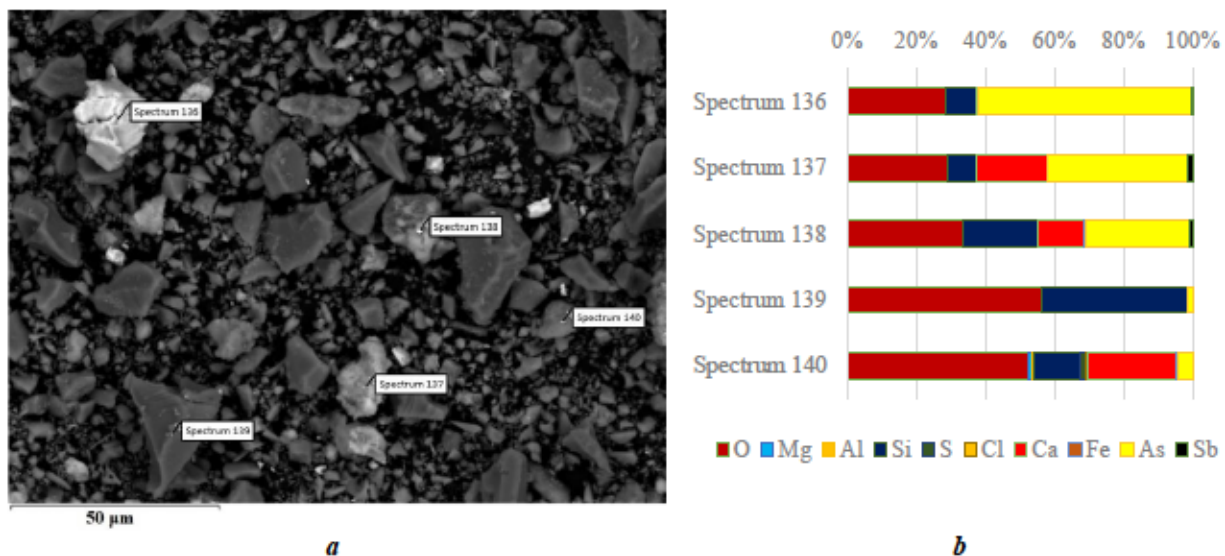


Figure B.9 The BSE image (a) and semi-quantitative EDS analyzes (b) of the various silicate and arsenioferous oxides observed in CPB-5% sample

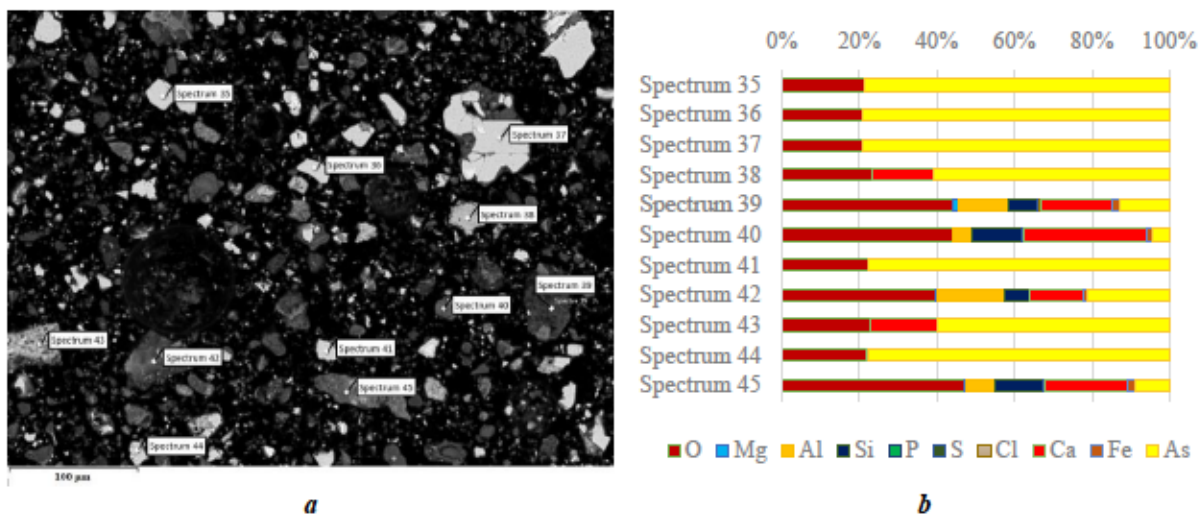


Figure B.10 The BSE image (a) and semi-quantitative EDS analyzes (b) of the various silicate and arsenioferous oxides observed in 15% As_2O_3 -cement mixture polished section

Based on the results of this study, the following conclusions can be drawn:

- The addition of arsenic trioxide led to a substantial decrease in the UCS of the CPB samples mainly due to the drop in the pH value and most probably to hardening inhibition during the early stage of curing. The pH of the arsenic-containing pastes was decreased to lower than 10.5 which retarded and inhibited the hydration of the cement in the CPB structure. Some increases in the

strength of CPB samples were observed in the samples with higher As_2O_3 content which could be the result of the pore refinement due to the formation of secondary minerals and C-S-H gels.

- The As_2O_3 -containing CPB samples mostly gained their strength in the initial days of curing since there is only a slight increase in the strength of the samples after 7 days. These samples showed more ductile failure modes whereas the mechanical behavior of the samples without arsenic trioxide was more brittle.

- The results of chemical analysis of As_2O_3 -cement mixtures proved that the dissolution of arsenic in cementitious matrices and formation of the arsenious acid cause a pH reduction.

- The SEM observations helped to identify oxide phases with various percentages of Si, Al, Ca, and As. A small proportion of mineral phases containing As, Ca, Si were observed as potentially stabilized species.

- As_2O_3 stabilization in cemented paste backfill is a potential option for geochemical risk prevention from arsenic waste material with further optimization.

- Upcoming work includes CPB preparation and testing with real mine tailings and arsenic trioxide roaster waste. The effect of pH reduction observed in the present study will be closely monitored, and potentially mitigated.

Declaration of competing interest

The authors declare that they have no known competing financial interests or personal relationships that could have appeared to influence the work reported in this paper.

Acknowledgments

The authors would like to acknowledge the “Giant Mine Oversight Board (GMOB)” and “Unité de Recherche et de Service en Technologie Minérale (URSTM)” for their financial and technical support. The authors also thank Jonathan Tremblay and “IOS Services Géoscientifiques inc” for performing and analyzing the SEM experiments.

APPENDIX C ARTICLE 2: GEOMECHANICAL ASPECTS OF STABILIZING ARSENIC TRIOXIDE ROASTER WASTE IN CEMENTED PASTE BACKFILL AT THE GIANT MINE, CANADA

This article was published in the journal of Environmental Management (volume 370) under number 123022. This article was submitted on 13 June 2024, accepted on 20 October 2024, and published online on 22 October 2024. This appendix reproduces the full text.

Amirhossein Mohammadi¹, Isabelle Demers¹, Nicholas Beier²

1. Research Institute on Mines and the Environment, Université du Québec en Abitibi-Témiscamingue (UQAT)
Rouyn-Noranda, QC, Canada

2. Department of Civil and Environmental Engineering, University of Alberta, Edmonton, AB, Canada

Highlights

- A three-factor CCD was utilized to model the UCS of CPB that included arsenic trioxide roaster waste.
- Binder and solid contents had the most significant impact whereas curing time was non-significant.
- More high-density arsenic materials formed in samples with the highest UCS.

CRediT author statement

Amirhossein Mohammadi: Conceptualization, Methodology, Investigation, Writing – Original Draft, Visualization; **Isabelle Demers:** Conceptualization, Methodology, Validation, Formal Analysis, Writing – Review and Editing, Supervision, Funding Acquisition; **Nicholas Beier:** Conceptualization, Methodology, Writing – Review and Editing, Validation, funding acquisition.

¹ Corresponding author; amirhossein.mohammadi@uqat.ca

Keywords

Arsenic trioxide roaster waste, cemented paste backfill, response surface methodology, unconfined compressive strength, hydraulic conductivity, computed tomography

Abstract

Giant Mine, an abandoned gold mine near Yellowknife in the Northwest Territories of Canada, generated significant arsenic trioxide roaster waste (ATRW) during its operations, posing a substantial environmental hazard. This study explored the feasibility of stabilizing ATRW by incorporating it into cemented paste backfill (CPB). Using response surface methodology (RSM), CPB samples with varying mixing ratios were analyzed to identify key parameters influencing strength. Unconfined compressive strength (UCS) tests assessed physical stability, while saturated hydraulic conductivity and computed tomography (CT) analyses examined the microstructure of the CPB. The results revealed that CPB samples prepared with general use (GU) cement exhibited significantly higher strength than those with a GU and lime kiln dust (LKD) mixture. Binder and solid contents were identified as the most critical factors influencing UCS, with binder content having a more pronounced influence. Curing time was found to be non-significant. Higher binder and solid contents correlated with higher UCS values in the CPB samples. The addition of 10% wt. ATRW reduced the UCS by over 30%, particularly in samples with lower binder and solid contents. Although microstructure differences were not evident in saturated hydraulic conductivity tests, CT scans showed increased formation of high-density arsenic-containing materials in samples with the highest UCS, especially those using GU binder. These findings suggest that optimizing binder and solid contents is crucial for enhancing CPB strength and effectively stabilizing ATRW.

C.1 Introduction

The mining and mineral processing industry generates a significant volume of processed materials, resulting in the production of numerous waste products. Managing solid waste and wastewater at modern mining sites is particularly challenging due to the presence of hazardous substances including heavy metals, metalloids, radioactive materials, acids, process chemicals, and arsenic-rich roasting wastes. Proper handling of these materials necessitates monitoring, treatment, and secure disposal (Lottermoser, 2010). Tailings and roaster waste from refractory gold mining

operations often contain elevated concentrations of arsenic and heavy metals, posing substantial risks to both humans and ecosystems in the vicinity of the mine.

The former Giant Mine is located on Great Slave Lake, approximately five kilometers north of Yellowknife, in the Northwest Territories, Canada. The Giant Mine is an abandoned gold mine that was active from 1948 until 2004; between 1999 and 2004, gold ore was transported elsewhere for processing. During operation, more than 17 million tonnes of tailings were produced and stored in tailings ponds (Silke, 2009, 2013). The ore at the Giant Mine had a complex mineral composition, with most of the gold primarily enclosed and embedded within the crystal structure of arsenopyrite (FeAsS) and, to a lesser extent, arsenian pyrite (FeS₂). To make the gold accessible to cyanide-leaching solutions, it was necessary to undergo an oxidation process that transformed the dense sulfide grains into porous structures (Northwest Consulting Limited, 2003). The roasting procedure at the Giant Mine resulted in the release of SO₂ emissions and the generation of As-rich vapors originating from arsenopyrite concentrates. These vapors subsequently condensed into dust rich in arsenic trioxide (As₂O₃) due to the oxidation of As (-I) to As (III) (Bromstad et al., 2017a):



The arsenic trioxide roaster waste (ATRW) was collected, transported, and deposited underground into ten purpose-built chambers and five mined-out stopes. In total, approximately 237,000 tonnes of ATRW were stored underground, and an additional 20,000 tonnes were released into the atmosphere (Silke, 2009). The ATRW, which consists of approximately 60% arsenic, is soluble in water, presenting a threat to both human health and the environment if it were to reach Great Slave Lake or Baker Creek, which runs through the mine site (SRK, 2002). The long-term management of ATRW dust at the Giant Mine is challenging due to its substantial quantity, its dusty nature, and its present storage conditions within subsurface chambers and stopes. The current approach implemented at the Giant Mine involves freezing the ground around the ATRW chambers and stopes. While initially viewed as a temporary measure for up to 100 years, the existing toxic state of the ATRW necessitates a more enduring solution (Arcadis, 2017; SRK, 2002).

In recent years, cemented paste backfill (CPB) has garnered global recognition, particularly in Canada where it plays a crucial role in underground mining operations, including at the Giant Mine (Ercikdi et al., 2014; Ercikdi, Kesimal, et al., 2009). CPB is a widely adopted method for managing tailings and waste that aims to reduce tailings discharge, provide support to the roofs of

underground stopes, and address associated geotechnical and environmental challenges (Fall et al., 2007; Ma et al., 2021; F. Zhang et al., 2022). CPB is a heterogeneous, multiphase substance comprised of dewatered mine tailings and various solid mine waste components, accounting for 70–85% of the total mass. Binders make up approximately 3–7% of the total solids mass, and it is mixed with either fresh or processed water (F. Zhang et al., 2022). CPB exhibits a non-settling quality and can be easily transported and deposited into underground openings at a desired consistency, resulting in minimal waste production.

CPB has the potential to offer environmental benefits by diminishing the reactivity of sulfides and stabilizing pollutants. Sulfide minerals in mine tailings can produce acid mine drainage (AMD) when they come into contact with air and water, leading to significant environmental pollution. By filling mine voids with CPB, the sulfides are shielded from oxygen, lowering the potential for AMD development. During the hydration process, hydraulic binders react with metals and metalloids, including arsenic (As), leading to the formation of stable compounds through precipitation (Coussy et al., 2011).

The primary design criteria for CPB structures include mechanical strength, workability, environmental performance, hydraulic conductivity, and durability. These factors depend on the physical, chemical, and mineralogical characteristics of the mine tailings and waste materials, as well as the characteristics of the mixing waters and additives, the types of binders, and their respective proportions (Benzaazoua et al., 2002; B. D. Thompson et al., 2012). Among these criteria, unconfined compressive strength (UCS) stands out as the most commonly used parameter for assessing the stability of CPB structures, mainly due to its simplicity and cost-effectiveness (Q. Chen, Zhang, Fourie, Chen, et al., 2017). The key factors influencing CPB strength include the type of cement, cement content, water-to-cement (w/c) ratio, aggregate gradation, curing temperature and humidity, curing duration, and bonding between cement and aggregate (L. Liu, Xin, et al., 2020).

Numerous studies have already been undertaken to understand how arsenic behaves under conditions of conventional stabilization/solidification, characterized by a low w/c ratio and high proportions of hydraulic binder (Choi et al., 2009; Fuessle & Taylor, 2004; J. Y. Kim et al., 2003; Qiao et al., 2006). The conditions for stabilizing arsenic in such matrices are generally effective, resulting in reduced levels of arsenic leaching. This occurs because arsenic tends to precipitate as

stable phases such as calcium arsenite or calcium arsenate (Coussy et al., 2011). However, CPB conditions are characterized by elevated w/c ratios and a reduced proportion of hydraulic binder; as such, the hydration process might differ because higher w/c ratios facilitate the creation of crystalline precipitates from the pore water, alongside the direct hydration of the binder components. Consequently, the long-term behavior and stability of arsenic compounds in CPB remains uncertain due to uncertainties about the process of arsenic immobilization and its impacts on the mechanical strength and other characteristics of CPB (Coussy et al., 2011). Nevertheless, in previous research, CPB technology has been effectively employed for stabilizing arsenic-bearing materials (Bull & Fall, 2020a; Coussy et al., 2011; Coussy, Benzaazoua, et al., 2012; H. Jiang et al., 2024; Y. Li et al., 2019; Su et al., 2019; Y. Wang et al., 2022; Yoon et al., 2010). The findings of these studies revealed that the introduction of arsenic, up to a concentration of 3%, led to an increase in the compressive strength of CPB, primarily due to the formation of novel arsenic-containing compounds. However, when the arsenic content reached 5%, there was a significant decrease in the compressive strength of CPB: this was attributed to an excessive production of arsenic-containing compounds. Most researchers concur that calcium-arsenic (Ca-As) precipitates constitute the primary form of arsenic in CPB (Coussy, Benzaazoua, et al., 2012; Mohammadi, Demers, Benzaazoua, et al., 2023a; Moon et al., 2004; Moon & Dermatas, 2007) and physical encapsulation contributes to the immobilization of arsenic (Y. Li et al., 2019). Generally, arsenic reacts with calcium in alkaline pore water to form anions such as HAsO_4^{2-} and AsO_4^{3-} , leading to the precipitation of calcium arsenate or calcium arsenite (Camacho et al., 2009a). Consequently, only a limited number of researchers have explored the possibility of alternative mechanisms such as the formation of As-ettringite for immobilizing arsenic in cement-based materials, as well as the immobilization mechanisms of arsenic at various stages of hydration (Chai et al., 2017; Y. Li et al., 2019). Despite these investigations, prior experience stabilizing arsenic trioxide-bearing mine waste using CPB is quite limited.

Given the existing understanding of the mechanisms for stabilizing arsenic in a cemented paste, it appears plausible to consider incorporating the Giant Mine ATRW into CPB; this could serve to stabilize this hazardous waste material and limit its potential for long-term As leaching. However, several critical questions remain unanswered. For example, what are the key factors affecting the stabilization of ATRW in CPB? How do the mechanical and immobilization properties evolve over

curing time? What impact do different binders have on the stabilization of ATRW in CPB? Currently, no research has addressed these significant issues.

The primary objective of this study was to evaluate the possibility of incorporating ATRW into CPB for long-term physical and chemical stabilization of arsenic. Prior to this, the effects of pure arsenic trioxide on the mechanical and geochemical behavior of CPB prepared with pure silica were investigated (Mohammadi, Demers, Benzaazoua, et al., 2023a). This previous study revealed that the addition of pure arsenic trioxide decreased the CPB strength and hindered the hydration of cementitious materials due to a pH reduction in the mixture. In the current study, it was hypothesized that real mine tailings with some neutralization capacity would counterbalance the pH decrease observed previously. CPB samples containing ATRW were prepared with different mixing proportions to discern the most influential parameters impacting strength. UCS was utilized to assess the physical stability of the CPB structure and was investigated with response surface methodology (RSM) (Q. Chen, Zhang, Fourie, Chen, et al., 2017). Saturated hydraulic conductivity and computed tomography (CT) analyses were performed to provide a better assessment of CPB microstructure. By focusing on how arsenic behaves in CPB under varying conditions to better understand long-term performance and stability, this study provides a novel and practical solution for effective management of ATRW from the Giant Mine and offers valuable guidance for the large-scale application of ATRW in CPB, presenting a sustainable and cost-effective approach to waste stabilization. Overall, the results from this study have advanced waste management practices and contributed to environmental protection by introducing a new application of CPB technology and optimizing its use for mitigating environmental contamination.

C.2 Materials and methods

C.2.1 Materials

CPB was prepared using two binding agents, mine tailings, ATRW, and deionized (DI) water. The tailings were collected from the northern pond of the Giant Mine site by excavating a trench to a depth of 2 m. Samples were mixed in the laboratory and oven-dried at 40°C for 48 hours to account for humidity variations within different parts of the tailings; this was followed by preparation, homogenization, and characterization.

GU Portland cement, provided by Bomix (Quebec, Canada), served as the primary binding agent, while a 50/50 blend of GU cement and lime kiln dust (LKD; supplied by Graymont in Bedford,

Quebec, Canada) was used as an additional binding agent. Eight distinct samples of ATRW from the Giant Mine were collected from diverse stopes and chambers; a blended representative sample was produced for characterization and incorporation into the CPB recipes. Throughout this study, DI water was utilized for preparing CPB samples, thus eliminating the impact of the water chemistry on CPB behavior.

C.2.2 Methods

Figure C.1 depicts the sequential steps that were followed to examine the impact of various factors on the strength of CPB incorporating ATRW.

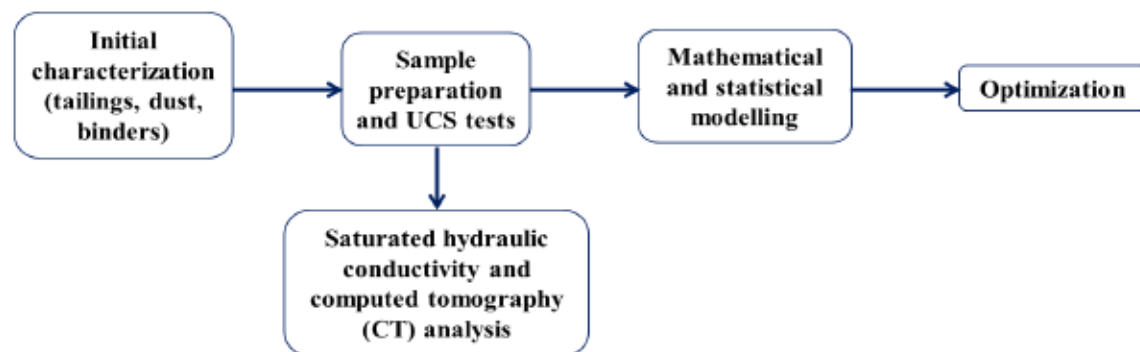


Figure C.1 Flow diagram of the project steps

C.2.2.1 Initial characterizations

An Ultrapyc 1200e automatic gas pycnometer (Quantachrome Instruments) was employed to determine the specific gravity (G_s) of the tailings, ATRW, GU cement, and LKD. Additionally, the particle size distribution (PSD) of the tailings and ATRW was assessed using a laser diffraction particle size analyzer (Malvern Mastersizer 3000). The specific surface area of the tailings and ATRW was evaluated with the Brunauer-Emmett-Teller (BET) method using liquid nitrogen (Gemini 2375, Micromeritics).

C.2.2.2 Preparation and curing of the cemented paste backfills

The formulations (recipes) for the CPB samples were developed considering the specific gravity of the tailings, binders, and ATRW, along with the solid (tailings + ATRW) content (C_w), binder content (B_w), and ATRW content (D_w) in the mixtures. The quantity needed for each component was calculated as the ratio of the dry mass of binder and ATRW dust to the mass of tailings and ATRW dust, respectively. These calculations were established based on the volume of three

cylindrical specimens (for each recipe measuring 2×4 inches (diameter \times height, equivalent to 50.8×101.6 mm), while considering an additional 20% of material to accommodate potential losses during the preparation and molding phases.

A 10-quart capacity planetary mixer (Eurodib M10 ETL, China) was employed to prepare the CPB samples at the IRME-UQAT laboratory (Rouyn-Noranda, Canada). Given the notable presence of arsenic trioxide in the samples, safety precautions such as the use of a cartridge mask and gloves were taken to prevent arsenic inhalation and direct skin contact. A portion of the water was blended with the binder in the mixer bowl using a manual spatula. The tailings and ATRW were dry mixed before being added to the bowl, then the contents were thoroughly mixed with the beater. The remaining water was gradually added while mixing continued for up to 5 minutes to achieve a uniform paste. The paste was then promptly poured into three plastic molds without draining, using a single layer pouring approach, ensuring minimal delay due to the rapid initial setting of the paste. The paste in the cylinders was then subjected to 25 impacts using a steel rod with a 9.53 mm diameter (equivalent to 3/8 inches) to eliminate any trapped air bubbles. A portion of the remaining paste was used to assess the final water content (three-day drying period at 60°C , followed by weighing). The samples were denoted as ' X - A - B - C ', with X representing the type of binder (GU or GU/LKD), A indicating the binder content as a percentage, B representing the solid content as a percentage, and C representing the curing time in days. For instance, 'GU-5-74-59' denotes a sample prepared using 5% GU binder, at a 74% wt. solid content, and 59 days curing duration before undergoing the UCS test. Based on the results of some preliminary tests, the CPB samples were prepared by maintaining a fixed percentage of ATRW ($D_w = 10\%$ wt.). The prepared cylindrical samples were sealed and stored within a humidity chamber (maintaining roughly 90% humidity and 20°C , simulating typical conditions of underground mines) for a curing duration of up to 111 days. The environmental conditions remained unchanged throughout the curing period, ensuring test comparability.

C.2.2.3 Experimental design and mathematical modeling

To identify the optimal experimental conditions, a thorough examination was conducted to determine how the binder content, solid content, curing time, and their interactions influenced the UCS of CPB samples containing ATRW. Analyzing each factor individually would have been time-consuming and would not have detected interactions between these factors. Hence, RSM was

employed to establish a relationship between the dependent and independent (influencing) variables. RSM uses mathematical and statistical techniques to optimize processes based on experimental data (Behera et al., 2018). The Box-Wilson central composite design (CCD), a common RSM method, was used to assess the mathematical relationships between independent and dependent variables (Soto-Pérez et al., 2015). The modeling and optimization process involves three key steps: conducting statistically designed experiments, obtaining the mathematical model and its coefficients, and subsequently predicting and validating the response of the model (Montgomery, 2017).

The CCD method involves a full-factorial second-level experimental design with a center point (coded as 0) and axial points positioned at distances of $-\alpha$ and $+\alpha$ from the center. The low and high levels for the factors are denoted as -1 and $+1$, respectively; this results in a total of five levels for each factor. The number of experiments required for the CCD technique can be determined using Equation C.2. In this equation, N represents the number of trials, k signifies the number of factors, and n_c represents the number of center points.

$$N = 2^k + 2k + n_c \quad (\text{C.2})$$

The number of center points varies according to the chosen design scheme, while the specific value of α depends on both the selected design and the number of factors. The axial points are instrumental in determining curvature in the computations: their number equals twice the number of factors (Figure C.F1).

Based on the experimental data, regression analysis was used to illustrate the relationships between independent variables and the UCS. The CCD included eight factorial points, six axial (star) points, and six replicates at the center points (Myers, Montgomery, & Anderson-Cook, 2016; Saikia et al., 2017). Table C.1 lists the experimental factors (A : binder content (%), B : solid content (%), and C : curing time (days)) with their ranges, units, and coded values. These values and ranges were chosen based on preliminary exploratory experiments (Mohammadi, Demers, Benzaazoua, et al., 2023a). The value of α was set to 1.68 for the three variables in the rotatable design. Table C.2 outlines the CCD-based RSM method, with binder content, solid content, and curing time as factors and UCS as the response variable. Two binder combinations (GU and GU/LKD) were tested in 20 experiments, each resulting in a minimum of 120 CPB samples to explore interactions among the independent variables and determine the optimal conditions for maximum strength.

CPB samples were formulated and prepared with varying binder content, solid content, and curing duration according to the experimental design, while keeping the ATRW content constant. The experiments were conducted in a randomized sequence to minimize the influence of uncontrolled variables. The experimental data were fitted to a quadratic second-order model (Equation C.3) using multiple regression analysis.

Table C.1 Independent factors and levels of RSM experiments

Factor	Name	Unit	Low value ($-\alpha = -1.68$)	Min (-1)	Mean (0)	Max (+1)	High value ($+\alpha = +1.68$)
A	Binder content	(%)	3.32	4	5	6	6.68
B	Solid content	(%)	70.64	72	74	76	77.36
C	Curing time	(day)	7	28	59	90	111

$$y = \beta_0 + \sum_{i=1}^k \beta_i x_i + \sum_{i=1}^k \beta_{ii} x_{ii}^2 + \sum_{i=1}^k \sum_{i \neq j=1}^k \beta_{ij} x_i x_j + \varepsilon \quad (\text{C.3})$$

In this equation, y represents the predicted response value (UCS), β_0 stands for the constant term, β_i , β_{ii} , and β_{ij} represent the coefficients for the linear effect, quadratic effect, and interaction effect, respectively, x_i and x_j denote the dimensionless independent factors, and k represents the number of selected variables (Myers, Montgomery, & Anderson-Cook, 2016).

The data were analyzed with Design-Expert[®] software (Version 13 (DX13), Stat-Ease Inc., Minneapolis, USA) to assess the statistical significance through analysis of variance (ANOVA) and to visualize the 3D response surfaces. Factors with a p-value of 0.05 or lower were deemed statistically significant and included in the regression model. The relationship between the independent variables and the UCS was examined using 3D response surface plots. Numerical optimization was also performed to determine the optimal combination of variables for maximizing compressive strength.

Table C.2 Central composite design in the form of coded and actual values

Run	Point type	Coded values			Actual values		
		A	B	C	A (%)	B (%)	C (day)
1	Axial	$-\alpha$	0	0	3.32	74	59
2	Factorial	-1	-1	-1	4	72	28
3	Factorial	-1	-1	+1	4	72	90
4	Factorial	-1	+1	-1	4	76	28
5	Factorial	-1	+1	+1	4	76	90
6	Axial	0	$-\alpha$	0	5	70.64	59
7	Axial	0	0	$-\alpha$	5	74	7
8	Center	0	0	0	5	74	59
9	Center	0	0	0	5	74	59
10	Center	0	0	0	5	74	59
11	Center	0	0	0	5	74	59
12	Center	0	0	0	5	74	59
13	Center	0	0	0	5	74	59
14	Axial	0	0	$+\alpha$	5	74	111
15	Axial	0	$+\alpha$	0	5	77.36	59
16	Factorial	+1	-1	-1	6	72	28
17	Factorial	+1	-1	+1	6	72	90
18	Factorial	+1	+1	-1	6	76	28
19	Factorial	+1	+1	+1	6	76	90
20	Axial	$+\alpha$	0	0	6.68	74	59

C.2.2.4 Unconfined compressive strength

The strength of the pastes was evaluated by conducting UCS tests on three distinct specimens for each recipe (as outlined in Table C.2). Following the curing period, which spanned 7, 28, 59, 90, and 111 days, the samples were taken out of their molds; the bases of the cylindrical specimens were rectified and smoothed, ensuring their surfaces were even and parallel to the plates of the mechanical press. Then, the mass and dimensions of the samples were measured. UCS tests were carried out following the ASTM C39 (ASTM, 2021) standard, employing a computer-controlled mechanical press with a normal loading capacity of 50 kN and a displacement rate of 1 mm/min

(strain-controlled loading). The UCS corresponds to the highest stress point achieved before failure during the compression test. The average value obtained from triplicate sample measurements was taken as the UCS for the given recipe.

C.2.2.5 Saturated hydraulic conductivity

Saturated hydraulic conductivity tests, following the ASTM D5084-16 (ASTM, 2016) standard, were carried out on two intact CPB samples with the highest strength, as determined by UCS analysis. Two different recipes were chosen, and duplicate samples were prepared, resulting in a total of eight samples (each measuring 8 inches in height and 4 inches in diameter), with half containing ATRW and the other half without (only tailings as solid matrix). After curing, each CPB sample was demolded and placed within a flexible wall hydraulic conductivity cell using a latex membrane. The sample was saturated over several days, after which hydraulic conductivity measurements were conducted. These measurements were repeated at least three times, continuing until the relative difference between consecutive measurements fell below 10%. Upon completion of the test, the CPB sample was removed from the cell, weighed, and oven-dried at 60°C to determine the final water content.

C.2.2.6 Computerized tomography (CT) scan

Numerous researchers have found that the microstructural properties of backfills are closely linked to strength (H. Deng et al., 2021), with porosity and pore size distribution being parameters affecting CPB mechanical properties (K. Cheng et al., 2021). Research methods for examining the microstructure of porous materials include nuclear magnetic resonance (NMR), computerized tomography (CT) scanning, scanning electron microscopy (SEM), and mercury intrusion porosimetry (MIP) (K. Cheng et al., 2021; H. Deng et al., 2021).

In this study, CT scanning was used to investigate the microstructure of CPB samples containing ATRW and formulated with both GU and GU/LKD binders. A CT scanner consists of three main parts: an X-ray source for generating X-rays, a detector to measure their penetration through the scanned object, and a manipulator to position and rotate the object in a full 360° rotation (Shin et al., 2013). In this imaging technique, hundreds or even thousands of X-ray projection images are captured at various rotation angles around a specimen. X-rays passing through the sample are absorbed, resulting in varying degrees of radiation attenuation depending on the densities within the object. A computer algorithm reconstructs a 3D volume, generating maps of X-ray attenuation

based on material composition/density, with each pixel assigned an intensity value corresponding to the component/phase it represents (Reedy & Reedy, 2022). This X-ray imaging technique non-destructively produces high-resolution images of an object (Gencel et al., 2023), facilitating quantitative exploration of the relationship between microstructure and mechanical properties (Huan et al., 2021).

Four specific samples were selected for analysis, comprising GU and GU/LKD samples with the highest and lowest UCS values. These samples were prepared and molded in small cylindrical molds (30 mm in diameter and 63 mm in length) after UCS testing, and analysis was conducted on intact samples after specific curing times using a Nikon XT H 225ST industrial CT scanner equipped with an X-ray source featuring a rotating target. Nikon's Inspect-X software was employed for analysis. Scan settings were configured with a beam energy of 205 kV, a beam current of 115 μ A, exposure at 8 frames per second, and the detector panel set to -100 mm. The effective pixel size was set at 22 micrometers and helical scans were employed for all cases to maximize resolution. Each sample underwent approximately 4,700 projections, with optimizations to 3,141 projections per rotation and an average of 8 frames per projection. Nikon's CT 3D Pro software was used for primary scan data reconstruction, with beam-hardening corrections applied to minimize artifacts in the images. The reconstructed scans were converted into .VOL and .VGI formats and imported into 3D ORS Dragonfly visualization software. Through 3D reconstruction of CT images, a segmentation model was created: the cores were segmented into three regions representing pore space, high-density (arsenic-containing) materials, and the remaining sediment matrix. 2D grayscale images along the center of each core in both longitudinal and transverse profiles and 3D images of each core, displaying each segmented region, were obtained.

C.3 Results and discussion

This section provides the findings from the initial characterization of the materials, the mechanical strength of the CPB samples, as well as the hydraulic conductivity and CT scan analysis.

C.3.1 Initial characterization

The specific gravity (G_s) of the materials used in the preparation of the CPB was 2.77 for tailings, 3.45 for ATRW, 3.05 for GU cement, and 2.79 for LKD. Figure C.F2 illustrates the cumulative PSD of both the tailings and ATRW, while Table S1 presents various commonly used indicators related to PSD. In these CPB samples, ten percent of the tailings were replaced with ATRW, which

possesses a finer and more uniform PSD compared to the tailings. Indeed, 94% of the ATRW particles and 53% of the tailings particles had diameters less than 20 μm , with most ATRW grains falling within the range of 1 to 20 μm . Additionally, Table C.T1 shows that the specific surface area (S_s) of the tailings was approximately half that of the ATRW. The gradation of the tailings plays a crucial role in CPB performance: an ideal gradation should feature a balanced representation of all particle sizes, with the recommended uniformity coefficient (C_u) falling in the range of 4–6 and curvature coefficient (C_c) in the range of 1–3 (X. Chen et al., 2019; F. Zhang et al., 2022). However, in this study, the tailings exhibited C_u and C_c values of 8.46 and 0.8, respectively, indicating that they were not well graded. The predominant minerals in the tailings were quartz (39.6%), chlorite (19.8%), dolomite (16.4%), and muscovite (14.8%). ATRW was composed of 86.4% arsenolite (As_2O_3).

C.3.2 UCS of the CPB samples

Table C.3 displays the results of UCS tests conducted on the CPB samples, along with the predicted values. It is evident that the strength of the CPB samples containing ATRW prepared using the GU binder was significantly higher than those prepared with the GU/LKD mixture. For both types of binders, the highest strength was observed in samples with 6% binder and 76% solids, reaching approximately 491 kPa and 531 kPa for GU and 214 kPa and 213 kPa for GU/LKD after 28 and 90 days, respectively. On the other hand, the lowest strengths were recorded in samples with the lowest binder and solid contents.

Various response functions were generated and correlated with the experimental data to derive a regression equation. The quality of the regressions was assessed based on sequential sum of squares and lack-of-fit tests. The quadratic model was selected for the responses under investigation (UCS of GU and GU/LKD samples) due to the best fit to the experimental data, as evidenced by the lower standard deviations, higher correlation coefficients, and lower p-values (Tables C.T2 and C.T3). Additionally, the quadratic model avoids the aliasing issues that arise in the cubic model, where higher-order terms become confounded with lower-order ones (Watson et al., 2016). Hence, the experimental results were fitted to a quadratic second-order model equation using multiple regression analysis to establish a relationship between the UCS and the selected influencing factors. For each response, an analysis was conducted: the coefficients of the quadratic models for the samples prepared with GU and GU/LKD binders are presented in Table C.T4 in both coded and

actual values. The quadratic models in the case of actual values are presented in Equations C.4 and C.5:

$$UCS_{GU} = 28953.97 - 1346.12A - 737.70B + 1.84C + 18.04A^2 + 4.73B^2 - 0.02C^2 + 16.73A \times B + 0.35A \times C - 0.009B \times C \quad (C.4)$$

$$UCS_{GU/LKD} = 15937.12 - 631.69A - 409.75B - 0.66C + 10.74A^2 + 2.66B^2 + 0.014C^2 + 7.68A \times B + 0.02A \times C - 0.015B \times C \quad (C.5)$$

Table C.3 Results of the UCS tests on the CPB samples prepared with GU cement and mixture of GU/LKD

Run	Actual factors			Responses (Y) – UCS (kPa)			
				GU		GU/LKD	
	A (%)	B (%)	C (day)	Experimental data	Predicted values	Experimental data	Predicted values
1	3.32	74	59	155	170	27	29
2	4	72	28	154	141	42	37
3	4	72	90	154	140	42	38
4	4	76	28	276	258	92	93
5	4	76	90	249	254	90	90
6	5	70.64	59	154	175	24	33
7	5	74	7	174	199	108	112
8	5	74	59	268	275	76	75
9	5	74	59	282	275	87	75
10	5	74	59	264	275	67	75
11	5	74	59	268	275	48	75
12	5	74	59	276	275	81	75
13	5	74	59	296	275	90	75
14	5	74	111	232	231	109	113
15	5	77.36	59	478	481	178	176
16	6	72	28	260	238	100	95
17	6	72	90	278	279	105	99
18	6	76	28	491	488	214	212
19	6	76	90	531	527	213	212
20	6.68	74	59	472	481	175	181

The regression coefficients were determined as a function of the sum of a constant (β_0), three linear effects (β_i), three interaction effects (β_{ij}), and three quadratic effects (β_{ii}). Coded equations were employed to assess the relative impact of each factor by comparing the coefficients of the factors. The equation in terms of actual factors was employed for making predictions regarding the response for specific levels of each factor. It is important to note that these levels must be specified in the original units for each factor. However, it is not advisable to use this equation for assessing

the relative impact of each factor, because the coefficients are scaled to account for the units of each factor, and the intercept does not align with the center of the design space.

Typically, model adequacy checks are performed to examine the fitted model, ensuring that it accurately approximates the true system and confirming that none of the assumptions of least squares regression are violated. ANOVA was employed to determine the suitability of the model by examining linear, quadratic, and interaction effects, and by obtaining the F-value and p-value. The F-value represents the significance of the model, while the p-value denotes the degree of interaction among each independent variable. Terms are considered significant if their p-values are less than 0.05 (with a 95% confidence level) and non-significant if the values exceed 0.10. Table 4 displays the ANOVA results for both the GU and GU/LKD samples. The F-values, which were 85.04 for GU and 44.73 for GU/LKD, along with p-values less than 0.0001 for both responses, indicate the significance of the model. The concept of "Lack of fit" stands in contrast to the overall model test, which assesses whether any omitted term is significant. The "Lack of Fit F-value," which was 3.78 for GU and 23.76 for GU/LKD, suggests that the lack of fit was not significant when compared to the pure error. Furthermore, the results exhibited a standard deviation of 18.39 for GU (with a mean of 285.56) and 12.10 for GU/LKD (with a mean of 98.51), which were considered acceptable. The Adeq-Precision value signifies the model's predicted value when combined with the average prediction error, serving as a measure of the signal-to-noise ratio. Adeq-Precision values for GU and GU/LKD were determined to be 29 and 21, respectively; values exceeding 4 indicate a sufficient signal level, implying that the models are appropriate for navigating the design space, performing analyses, and making predictions about the UCS of CPB samples.

The accuracy and variability of the model were also evaluated using the coefficient of determination (R^2). The R^2 values, which were high and nearly equal to 100% (GU: 98.71%, GU/LKD: 97.58%), along with the adjusted R^2 (GU: 97.55%, GU/LKD: 95.39%) and predicted R^2 (GU: 91.72%, GU/LKD: 93.66%) values, signify a high level of accuracy and excellent fit, demonstrating the strong alignment of the proposed models with the collected experimental data. The predicted R^2 values for both models closely matched the adjusted R^2 , with differences of less than 20%, indicating reasonable agreement. Figures C.F3a and C.F3b display the diagnostic plots, illustrating the normal probability versus studentized residuals for GU and GU/LKD samples, respectively. As is evident from these graphs, most of the responses exhibited a minimal deviation

from normality, with the points closely aligning along a nearly straight line along the diagonal in both cases. Figures C.F3c and C.F3d depict the values of externally studentized residuals plotted against the predicted response values, serving as a test for the assumption of constant variance. In this diagram, control limits are provided in the form of two lines (-4.14579 and +4.14579) for easier identification of any unusual points; however, the points fell well within these limits and no abnormal points were observed. This indicates that the data exhibit a random distribution around the zero line, without any evident clustering (Rahimi & Ebrahimi, 2019).

Table C.4 ANOVA results for ATRW dust containing CPB samples prepared using GU and GU/LKD

Source	Sum of Squares		df		Mean Square		F-value		p-value	
	GU	GU/LKD	GU	GU/LKD	GU	GU/LKD	GU	GU/LKD	GU	GU/LKD
Model	2.588E+05	58917.16	9	9	28755.91	6546.35	85.04	44.73	<0.0001	<0.0001
A-Binder content	1.165E+05	27558.05	1	1	1.165E+05	27558.05	344.62	188.28	<0.0001	<0.0001
B-Solid content	1.134E+05	24520.28	1	1	1.134E+05	24520.28	335.44	167.53	<0.0001	<0.0001
C-Curing time	1216.5	0.5517	1	1	1216.50	0.5517	3.60	0.0038	0.0871	0.9523
A × B	8951.22	1884.98	1	1	8951.22	1884.98	26.47	12.88	0.0004	0.0049
A × C	928.81	3.65	1	1	928.81	3.65	2.75	0.0249	0.1284	0.8777
B × C	2.42	6.85	1	1	2.42	6.85	0.0072	0.0468	0.9343	0.8331
A ²	4674.72	1657.23	1	1	4674.72	1657.23	13.82	11.32	0.0040	0.0072
B ²	5145.1	1624.59	1	1	5145.10	1624.59	15.22	11.10	0.0030	0.0076
C ²	6490.07	2603.96	1	1	6490.07	2603.96	19.19	17.79	0.0014	0.0018
Residual	3381.41	1463.68	10	10	338.14	146.37				
Lack of Fit	2673.63	280.98	5	5	534.73	56.20	3.78	0.2376	0.0855	0.9296
Pure Error	707.78	1182.69	5	5	141.56	236.54				
Cor Total	2.622E+05	60380.84	19	19						

C.3.2.1 The effect of various factors on strength of the samples

For both the GU and GU/LKD samples, the statistical analysis revealed that binder content and solid content (represented as linear terms A and B , respectively), along with the interaction between binder content and solid content ($A \times B$), were identified as significant interaction terms. Additionally, the square terms for binder content (A^2), solid content (B^2), and curing time (C^2) were

found to be significant, as their p-values were below 0.05. In contrast, curing time (C) and the interaction terms involving binder content and solid content with curing time ($B \times C$ and $A \times C$ terms) were not deemed statistically significant. The coded coefficients in Table S4 highlight that binder content and solid content exerted the most significant positive effects on the strength of the CPB samples. Furthermore, the significance of the binder content was notably stronger, as reflected in its higher F-value. Surprisingly, the impact of curing time on the strength of CPB samples containing ATRW was not deemed significant. Among the quadratic terms, in both cases, the square term of curing time (C^2) stood out with the highest F-value, signifying its substantial influence on the CPB sample strength. This effect was negative for GU samples, as indicated by the negative coded coefficient ($\beta_{33} = -21.31$), and positive for GU/LKD samples, as indicated by the positive coded coefficient ($\beta_{33} = +13.50$).

3D surface and 2D contour graphs were obtained to investigate the combined impacts of independent variables on the strength of CPB samples and to predict the responses (UCS) for various regions within the experimental domain. These graphical representations are displayed in Figures C.2 and C.3 as well as Figure C.F4 for both GU and GU/LKD samples. Improved visualizations of the contour plots are also presented in Figures C.F5–C.F7 in the supplementary materials. In each plot, one factor was held constant while the influences of the remaining two factors were examined using both 2D and 3D plots. The primary parameters were varied across their entire range, spanning from the lowest level to the highest level, to assess how this variation impacted the strength of CPB samples containing ATRW. Figure C.F4 illustrates the concurrent impacts of binder content and solid content at different curing times on the strength of CPB samples, considering both GU and GU/LKD binders. In Figure C.2, the simultaneous effects of solid content and curing time on the UCS of both GU and GU/LKD samples are examined, while varying binder content. Figure C.3 portrays variations in UCS strength at varying solid contents, achieved by simultaneously adjusting binder content and curing time. Further discussion on the influence of each factor on the UCS of CPB samples containing ATRW dust is provided in the subsequent sections.

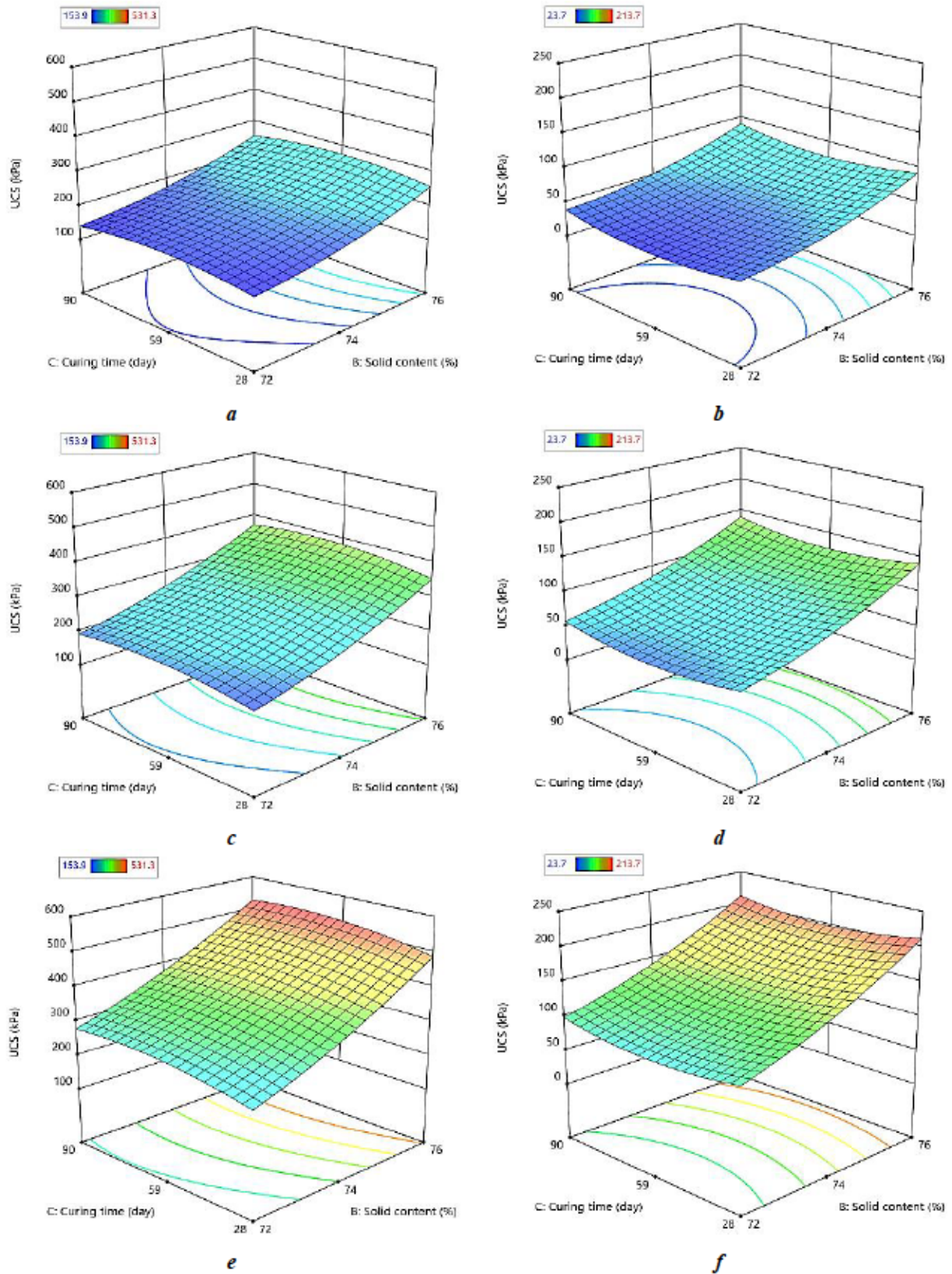


Figure C.2. Surface plots for the UCS of GU and GU/LKD samples at different binder content: a) GU-4%, b) GU/LKD-4%, c) GU-5%, d) GU/LKD-5%, e) GU-6%, and f) GU/LKD-6%

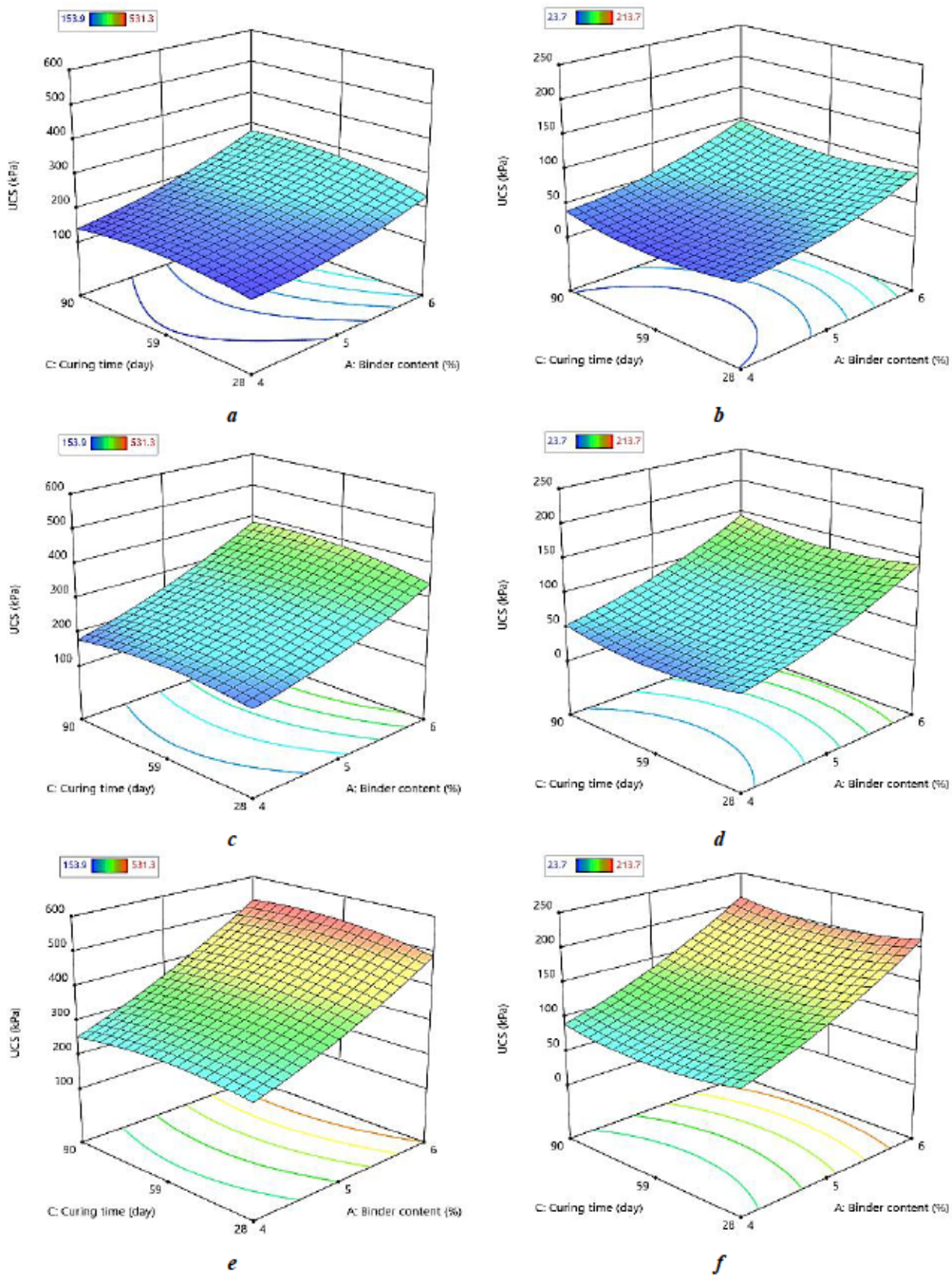


Figure C.3. Surface plots for the UCS of GU and GU/LKD samples at different solid content: a) GU-72%, b) GU/LKD-72%, c) GU-74%, d) GU/LKD-74%, e) GU-76%, and f) GU/LKD-76%

C.3.2.1.1 The effects of binder content

Increasing binder content significantly improved CPB strength. For instance, the UCS of GU-6-76-28 and GU-6-76-90 was 1.78 and 2.13 times higher than that of GU-4-76-28 and GU-4-76-90, respectively. In GU/LKD samples, the effect was even more pronounced, with ratios (GU/LKD-6-76 to GU/LKD-4-76) reaching 2.32 and 2.35 for samples cured for 28 and 90 days, respectively. This indicates that increasing the cementitious material (binder) content had a substantial positive impact on the mechanical strength of the CPB. This improvement can be attributed to an accelerated hydration process and an increase in hydration products within the CPB, which promotes compressive strength development. The results demonstrated that the quantity of GU-based cementitious material positively influenced the strength gain, regardless of the hydration period. Cement hydration involves a chemical reaction between cement and water, resulting in the formation of hydration products such as calcium silicate hydrate (C-S-H), portlandite ($\text{Ca}(\text{OH})_2$), and calcium sulfoaluminate hydrates (ettringite/monosulfate) (Soto-Pérez et al., 2015). The hardening of paste backfill takes place in two primary phases: the initial phase, marked by dissolution-hydration, primarily driven by the dissolution process; and the subsequent phase, characterized by precipitation and the direct hydration of binding agents (Benzaazoua et al., 2010). The rate and extent of cement hydration depend mainly on the type of cementitious materials used, the inclusion of additives, and the mixture proportions. C-S-H gels represent the primary hydration products of cement and significantly contribute to the early strength development of CPB (Soto-Pérez et al., 2015). Additionally, the long-term stability of C-S-H is a fundamental requirement for the sustained mechanical strength and stability of CPB (L. Liu, Xin, et al., 2020). Beyond improving cohesion and strength, the binder may also contribute to the neutralization of potential acidity and provide fixation and stabilization properties for mobile contaminants like zinc, nickel, and arsenic (Benzaazoua et al., 2010; Benzaazoua, Marion, et al., 2004).

C.3.2.1.2 The effects of solid content

The results depicted in Figures C.2, C.3, and C.F4 indicate that a higher solid content increased the strength of the CPB for both GU and GU/LKD samples. For instance, in the GU samples with 5% binder cured for 59 days, the strength varied with different solid contents: approximately 154 kPa, 270 kPa (average of 6 samples), and 478 kPa for solid contents of 70.64%, 74%, and 77.36%, respectively. For the GU/LKD samples, these strength values were 24 kPa, 70 kPa, and 178 kPa, respectively. This clearly demonstrates the positive influence of solid content on the UCS of CPB

samples. Typical solid contents in CPB, ranging from 70 to 85 wt.%, have a notable impact on both the flow characteristics of the paste mixtures and the volume of tailings to be deposited underground. While increasing the solid content generally enhances CPB strength, it concurrently reduces the consistency or slump of the mixture. This phenomenon was observed in the current study as well, where the workability of ATRW-containing paste became unsatisfactory at solid contents above 76%, making it challenging to place the pastes into molds. Although CPB requires adequate water to achieve the desired consistency for transport from the paste plant to the underground openings, an increase in the w/c ratio has an adverse effect on CPB strength and stability (Ercikdi et al., 2010; Ercikdi, Kesimal, et al., 2009). Consequently, providing a balance between workability and the strength of CPB samples is imperative.

C.3.2.1.3 The effects of curing period

As depicted in Figures C.2, 3C., and C.F4, changes in curing time (ranging from 28 to 90 days) did not significantly influence the strength of the CPB samples. Curing time was also identified as a nonsignificant factor in the experimental design. According to the literature, the mechanical strength of CPB samples typically demonstrates a noticeable increase with extended curing time under normal conditions. This behavior is generally marked by a rapid strength gain in the first month of curing, followed by a phase where mechanical properties exhibit only marginal improvements (Benzaazoua et al., 2010). The curing process promotes the hydration reaction and the formation of various hydration products, including C-S-H, ettringite, and portlandite. The generation of hydration products leads to increased microstructure density and reduced overall porosity (Ait-khouia et al., 2022). Consequently, this results in an enhancement of mechanical strength and the immobilization of hazardous materials within the CPB structure. This behavior is influenced by numerous factors pertaining to the three constituents (tailings, water, and binder), as well as the conditions under which the CPB is placed (e.g., drainage, consolidation, temperature, etc.) (Benzaazoua et al., 2010). However, when ATRW is present, it appears that the hydration process primarily occurs within the initial hours or days of curing. Prolonging the curing time did not appear to significantly impact the UCS of the CPB samples in this context. These findings are consistent with those reported by (Mohammadi, Demers, Benzaazoua, et al., 2023a), who observed that the strength of CPB samples containing pure As_2O_3 did not exhibit significant improvement after seven days of curing. The setting of the binder is heavily influenced by the speed of the binder reaction: a faster reaction results in the formation of more reaction gels in a shorter period,

contributing to a rapid setting process (Yingliang Zhao, Qiu, Zhang, et al., 2020). However, excessively fast setting of the binder can hinder the growth and diffusion of reaction gels, subsequently leading to the formation of weak hydration products and a reduction in UCS values (Yingliang Zhao, Qiu, Xing, et al., 2020). This rapid initial setting of the paste was observed during the sample preparation process in this study, particularly for the GU mixtures.

C.3.2.1.4 The effects of ATRW inclusion in CPB

While the primary objective of this study was to assess the impacts of various parameters on the UCS of CPB samples containing ATRW, it was also important to compare them with samples without ATRW. Therefore, some CPB samples (consisting of three replicates) were prepared without ATRW, varying the binder and solid content. Table C.T5 displays the selected recipes the measured UCS, and the ratios of UCS for samples with ATRW (UCS_d) to those without ATRW (UCS_0).

The inclusion of ATRW led to a decrease in strength for both GU and GU/LKD binders. This reduction was more pronounced in samples with lower binder and solid contents: increasing the binder and solid contents improved the UCS_d/UCS_0 ratio. Previous studies (Mohammadi, Demers, Beier, et al., 2023; Mohammadi, Demers, Benzaazoua, et al., 2023a) found that adding arsenic trioxide to the paste mixture results in a pH reduction to below 11, attributed to the dissolution of arsenic trioxide and the formation of arsenious acid (H_2AsO_3). However, for the stable formation of hydration products like C-S-H, a continuous alkaline environment is essential; this is typically provided by the pore solution within the CPB (L. Liu, Xin, et al., 2020). Inadequate provision of the alkaline environment by the pore solution can negatively affect the strength development of CPB (C. Li et al., 2010). Calcium hydroxide (portlandite) is a major component in cementitious materials but is highly susceptible to pH decreases, as it buffers the pH at 12.5. On the other hand, C-S-H gels, which play a crucial role in material cohesion, exhibit greater stability even when subjected to pH levels near 9 (Benzaazoua et al., 2010). Ettringite also contributes to the hardening and strength development of CPB samples; however, the stability of ettringite relies heavily on the availability of Ca^{2+} and SO_4^{2-} ions. Inadequate amounts of these ions can cause ettringite to transform into monosulfate, which does not effectively contribute to strength gain (Yingliang Zhao, Qiu, et al., 2022). The tailings used in this study contained less than 0.5% sulfur, resulting in an insufficient supply of sulfate for ettringite formation. Consequently, for samples containing

ATRW, the formation and presence of C-S-H gels became the primary hydration products that facilitated strength development. Increasing binder and solid contents could compensate for the reduction in UCS since a higher binder content promotes the generation of C-S-H and provides mixtures with higher pH values.

C.3.3 Model improvement

The models for predicting the UCS of GU and GU/LKD samples can be enhanced by exclusively incorporating significant terms and eliminating non-significant ones. Based on the preceding discussions and the results in Table C.4, all terms with non-significant p-values (p-value > 0.05) were excluded from the regression equations. Consequently, the curing time (term C) and its interactions with other factors (terms $A \times C$ and $B \times C$), along with its square term (C^2), were omitted. The final models for describing the relationship between the UCS of CPB samples and the binder content (A) and solid content (B) are presented in Table C.T6. Although the square term of curing time (C^2) was significant, it had to be removed to maintain the hierarchy of the modified models. The modified quadratic models for GU and GU/LKD samples in the form of actual values are shown in Equations C.6 and C.7:

$$UCS_{GU}^* = 31861.89 - 1346.38A - 815.03B + 20.11A^2 + 5.25B^2 + 16.73A \times B \quad (C.6)$$

$$UCS_{GU/LKD}^* = 14125.25 - 617.26A - 361.97B + 9.43A^2 + 2.33B^2 + 7.68A \times B \quad (C.7)$$

The values of R^2 , adjusted R^2 , and predicted R^2 were determined to be 0.9542, 0.9378, and 0.9322, respectively, for the modified GU model. Meanwhile, for the modified GU/LKD model, these values were 0.9325, 0.9083, and 0.8603, respectively. This indicates that there was a slight decrease in the values of R^2 and adjusted R^2 for both models, as well as for predicted R^2 in the modified GU/LKD model. Despite these variations in the various R^2 values, the proposed modified models remained highly significant for both GU and GU/LKD samples.

C.3.4 Optimization and confirmation

Following the analysis of independent variables, a multi-objective simultaneous nonlinear optimization approach was applied to optimize the UCS of CPB samples for each binder. The optimization objectives identified the most favorable combination of independent variables that yielded the highest UCS values. The optimization objectives can be assigned varying levels of

weight and significance; however, in the present study, all target factors and responses were considered equally weighted and significant. Using a numerical optimization algorithm within the DX13 software, the optimal values for UCS were predicted based on the regression models. All factors were constrained within the initial study range, while the UCS was set to its maximum value to attain the highest desirability. Based on the solutions provided by the DX13 software, the first solution with the highest desirability was chosen for each binder. An experiment with a desirability value close to unity is regarded as the optimal condition based on the obtained results. The maximum strength for GU samples (531 kPa) was achieved with a binder content of 6%, a solid content of 76%, and a curing time of approximately 64 days, resulting in a desirability value of 1.000. In the case of the GU/LKD binder, the optimal condition (yielding the highest UCS equal to 212 kPa) consisted of a 6% binder content, a 76% solid content, and a 28-day curing time, resulting in a desirability value of 0.993. The obtained results are shown in Figure C.F8.

From an economic perspective, achieving optimal operational conditions can also involve minimizing the binder content during the optimization process. Binder cost constitutes the most significant expense in any paste backfilling operation (up to 80%, (Grice, 1998)), and mining companies aim to reduce these costs by minimizing the binder quantity in CPB mixtures. Hence, any economical optimization of CPB should aim for efficient binder utilization. The optimization procedure was subsequently rerun with the objective of minimizing binder content, while keeping solid content and curing time within their initial ranges; the findings are depicted in Figure C.F9. In the case of the GU binder, the optimal conditions were identified with a binder content of 4.44%, a solid content of 76%, and a curing time of 61 days, yielding a desirability value of 0.586. As for the GU/LKD binder, the optimum conditions were determined to be a binder content of 4.17%, a solid content of 76%, and a curing time of 28 days, resulting in a desirability value of 0.606.

To assess the reliability and precision of the optimization of the RSM model based on the central composite design, duplicate experiments were conducted under the selected optimized conditions. Specimens were prepared in triplicate using the optimal mix ratios for both GU and GU/LKD. It was observed that the actual UCS and predicted UCS exhibited a relative error of 1.97% for GU, while the error was 1.35% for GU/LKD. Consequently, it was confirmed that the second-order polynomial regression equation was capable of accurately predicting the strength of CPB samples containing ATRW.

C.3.5 Saturated hydraulic conductivity of CPB

Two recipes demonstrating the highest strength (GU-6-76-28 and GU-6.68-74-59) were chosen for saturated hydraulic conductivity tests. CPB samples were prepared with and without ATRW; Table C.5 provides the results.

There was no significant difference between the saturated hydraulic conductivity of the CPB samples with and without ATRW because the differences fell within the precision limit of the tests, which was half an order of magnitude (Godbout et al., 2007). The saturated hydraulic conductivity can provide hints on the changes in microstructure resulting from mineral precipitation and binder hydration during curing. These changes can alter the quantity and structure of voids within the CPB, which may reduce the hydraulic conductivity of CPB mixtures. The inclusion of Portland cement can result in the formation of C-S-H gels within the pores during the initial stages of curing. These newly-formed gels can impede water movement within the pores, consequently reducing the k_{sat} of CPB samples (Benzaazoua, Fall, et al., 2004; Godbout et al., 2007). The difference between k_{sat} of GU-6-76-28 and GU-6.68-74-59 was not significant since there was a small difference (less than 1%) between the binder content of these samples, and it seems that these two samples had a similar microstructure.

Table C.5 Saturated hydraulic conductivity of CPB samples

Sample	k_{sat} (cm/s)	
	Without ATRW	With ATRW
GU-6-76-28-1	4.70E-06	3.12E-06
GU-6-76-8-2	4.25E-06	3.20E-06
GU-6.68-74-59-1	1.54E-06	3.33E-06
GU-6.68-74-59-2	1.71E-06	3.74E-06

C.3.6 Computed tomography (CT) scan results

Since hydraulic conductivity measurements were unable to identify variations in microstructure in the different CPB samples, CT scanning was conducted for a more direct observation of the microstructure. Four samples were selected for CT observation: GU-6-76-28 and GU/LKD-6-76-28, which demonstrated the highest UCS values, and GU-4-72-28 and GU/LKD-5-70.64-59, which exhibited the lowest UCS values. To facilitate differentiation of substances in the grayscale images, pseudo-color enhancement of the resulting 2D slices was performed. This entailed converting each

grayscale level of the original image using linear or nonlinear mapping functions to generate color images of the 2D slices and 3D images (Z. Li et al., 2023). In these images, the red matrix, blue pores, and yellow high-density regions are clearly distinguished.

Figure C.4 shows a greater proportion of high-density materials (depicted by yellow areas) in samples exhibiting higher UCS values (GU-6-76-28 and GU/LKD-6-76-28). These dense materials could be attributed to both the initial unreacted ATRW and the formation of arsenic-containing compounds during the hardening process. It is noteworthy that all samples contained the same initial percentage of ATRW dust ($D_w = 10\%$ wt.), indicating that the formation of secondary materials was significantly higher in samples with greater strength. In essence, the formation of these materials appears to be the primary factor contributing to the higher strength observed in these samples.

Another notable observation in these 2D images pertains to the quantity and size distribution of pores within the samples. Throughout the preparation, hydration, and hardening stages, various types of pores are formed in CPB, including intercalated pores of C-S-H gel, capillary pores resulting from water evaporation, and bubble pores formed by residual air during slurry mixing (K. Cheng et al., 2021; Pichler et al., 2008, 2009). The size of these pores may change due to the filling effect of hydration products, which significantly influences the mechanical properties and flow characteristics of CPBs (Huan et al., 2021; Huang et al., 2021; H. Jiang, Fall, et al., 2020). Surprisingly, in the current samples, both the size and quantity of pores appear to be higher in CPBs with the highest strength. The matrices of the GU-4-72-28 and GU/LKD-5-70.64-59 samples were denser compared to those of the GU-6-76-28 and GU/LKD-6-76-28 samples, with a less pronounced internal pore structure. However, most previous studies have established an inverse relationship between porosity (volume of voids to the total volume) and strength (K. Cheng et al., 2021; H. Deng et al., 2021; Grabinsky et al., 2022): higher porosity typically corresponds to lower strength in CPB samples. Unfortunately, generating histograms for the full core cylinders to obtain porosity and other parameters was not feasible due to the computational intensity required for generating scalar values for every pore.

The 2D tomographic images obtained lack the ability to visually depict the evolution of pores and high-density materials within the structure of CPB samples (Fang et al., 2023); they only provide distribution information regarding minerals and pores within a specific section of the CPB. As

such, the 2D CT data scanned from the specimens were converted into 3D images to enable visual examination of the internal structure of the CPB samples. Figure C.5 displays the 3D visual representations of the CPB samples, including separate depictions of the segmented pore structure and high-density materials.

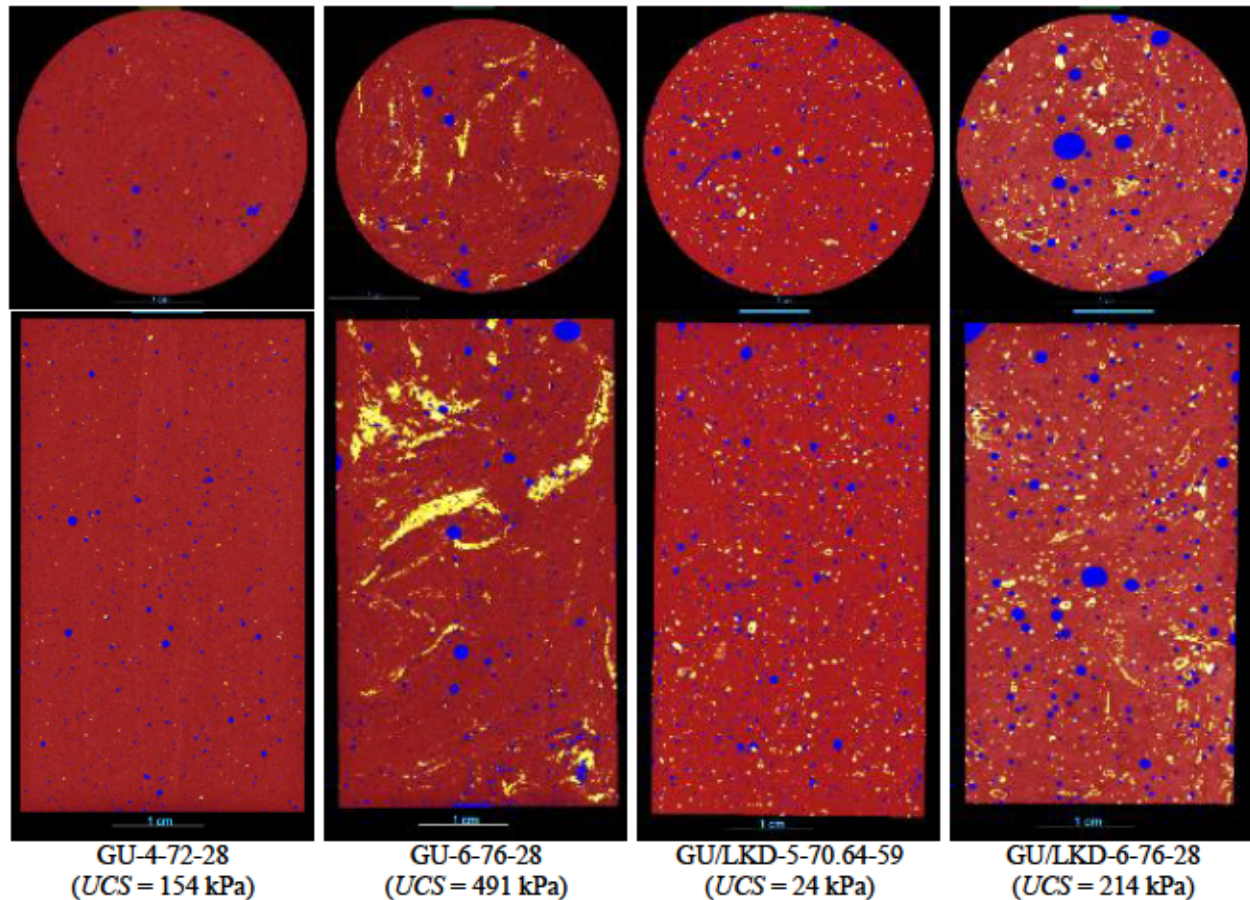


Figure C.5 2D greyscale images along the center of each core in both longitudinal and transverse profiles containing the segmented regions (blue: pores, yellow: high-density materials, and red: CPB matrix)

These 3D images offer a clearer representation of the distribution of high-density materials and pores within the structure of the CPB samples. Given that the samples underwent natural consolidation rather than full compaction, it is apparent that pores were scattered throughout the samples, distinctly visible as blue areas in the images. However, the distribution of pores was intricate, ranging in size from macroscale to microscale with various shapes. In samples with the highest UCS, interconnected pores were noticeable, whereas in those with the lowest strength, it appeared that the pores were primarily distributed as separate entities. Furthermore, a notable disparity was observed in the distribution of high-density materials within the structures of samples

with the highest strength. Specifically, in the GU-6-76-28 sample with the highest UCS, the concentration of high-density materials appeared significantly greater than in other samples. In the three other samples, most of the high-density materials were randomly dispersed as individual particles, whereas in the GU-6-76-28 sample, these materials were arranged in a continuous manner. Consequently, it can be inferred that the formation and random distribution of these arsenic-containing high-density materials during the hydration and curing process of CPB samples were the primary factors contributing to the higher strength gain observed in the GU-6-76-28 sample.

The microstructure of CPB comprises hydration products, anhydrous cement particles, and capillary pores. The volume fraction of each phase gradually changes over time as hydration progresses (Zhu et al., 2021). Typically, as cement hydration advances, cement particles dissolve and react with water to produce hydration products. The outward expansion of hydration products connects the components to form a solid framework, gradually filling the pore space. The formation, destruction, and expansion of initial pores significantly impact strength, stiffness, damage failure, and other fundamental mechanical parameters (K. Cheng et al., 2021). In the case of ATRW-containing CPB, the formed materials may include secondary arsenic-containing minerals and C-S-H gels, which result from the dissolution of cement particles and their reactions with arsenic trioxide in the presence of water to form arsenic-containing hydration products. However, the formation of these materials may not entirely fill the pore spaces, primarily due to the rapid setting of the paste prepared using GU as the binding agent in the presence of ATRW dust. In such instances, the cement hydration process slows down rapidly, and even halts. Consequently, the larger pores cannot be further filled by hydration products, and the change in pore structure within CPB becomes stabilized (Huan et al., 2021).

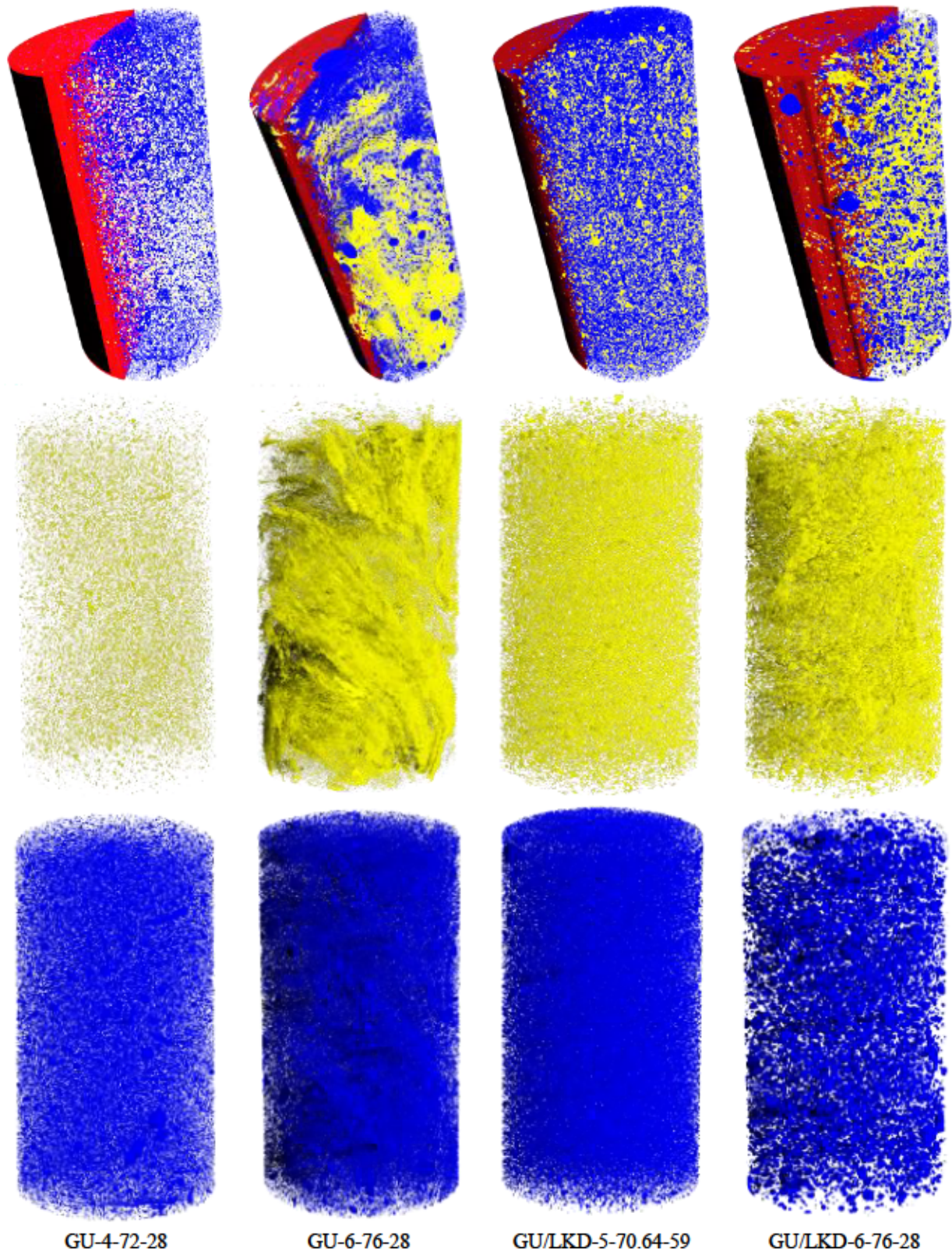


Figure C.6 3D model of each core cut in half lengthwise, displaying each segmented region (blue: pores, yellow: high-density materials, and red: CPB matrix)

C.3.7 Comments on the findings

The primary objective of this study was to explore the potential of incorporating ATRW into CPB to stabilize water-soluble arsenic and prevent its release into the environment. The findings of this research indicate a relatively favorable strength in samples containing ATRW compared to those without, depending on the strength requirements at the given mine site. As Giant Mine is inactive, strength requirements are based on minimal structural capacity: no self-supported faces will eventually be exposed. The results from this study, along with prior research conducted by the authors (Mohammadi, Demers, Beier, et al., 2023; Mohammadi, Demers, Benzaazoua, et al., 2023a), support the feasibility of employing CPB technology for ATRW management, especially considering the optimal conditions achieved in this study. However, it should be noted that with high binder and solid contents, which are optimal conditions, the fluidity and workability of the samples decreased substantially, and the paste started to set rapidly—a concern that can be addressed with specific additives. Moreover, in this study, DI water was used for CPB preparation; the effects of the chemical constituents of actual water resources such as processed or fresh water should be considered.

An additional crucial consideration is the use of only 10% ATRW in CPB sample preparation. The possibility of increasing this percentage to reduce backfill volume and utilize more ATRW is a significant aspect to explore. Nevertheless, the key determinant for adopting this technology for ATRW management is the potential leaching of arsenic from the stabilized form. Despite acceptable strength data for samples made with 100% GU cement, the decisive factor is the concentration of arsenic leaching, a facet that is also being addressed in this project (though the results are not presented in this paper).

C.4 Conclusions

The main objective of this study was to evaluate the effectiveness of incorporating ATRW dust from the Giant Mine into CPB to achieve physical and chemical stabilization of arsenic. CPB samples containing ATRW were prepared by incorporating 10% wt. of ATRW into Giant Mine tailings as the solid matrix and using GU cement and a mixture of GU and LKD as the binder to determine the most influential parameters affecting strength. UCS was utilized to assess the physical stability of the CPB structure, which was investigated using response surface methodology. To gain a deeper understanding of the relationships between these independent

variables, two response functions were formulated as second-order polynomials, and the impacts of each parameter were assessed using ANOVA. Additionally, saturated hydraulic conductivity and CT analyses were conducted to relate the microstructure of the CPB samples to their strength. The key findings and their broader implications are as follows:

- The CPB samples prepared with GU cement exhibited significantly higher strength as compared to those prepared using a GU and LKD (50/50) mixture. This suggests that the choice of binder has an influence on the strength acquisition mechanisms, and the most GU is desirable in the specific mixture tested.
- Using a three-factor central composite design, the study modeled the UCS of CPB containing ATRW. The analysis revealed that binder content and solid content were the most influential factors, while curing time had minimal impact. Optimal recipes were determined (6% GU and 76% solids) using the modeled relation and validated by comparing predicted and measured UCS values.
- CPB samples with higher binder content and greater solid content displayed increased strength, with the binder content exerting a more pronounced influence. Incorporating 10% wt. ATRW into the tailings led to a more than 30% reduction in the UCS, particularly in mixtures with lower binder and solid contents. This finding highlights the need for careful consideration of ATRW content in CPB formulations to maintain structural integrity.
- Saturated hydraulic conductivity tests showed no significant differences in permeability between CPB samples with and without ATRW. However, CT scan results revealed that high-density arsenic-containing materials were more prevalent in high-strength CPB samples, especially those prepared with GU binder. Additionally, these samples exhibited visually higher porosity compared to others. This indicates that ATRW incorporation affects the microstructure of CPB, which may impact long-term performance.
- The study showed that the incorporation of ATRW into CPB is a viable option to physically stabilize ATRW at the Giant Mine. The laboratory-tested CPB samples met the site's minimal strength requirements, suggesting that this approach could be effectively used in field applications. However, further investigation into the chemical stabilization of arsenic is necessary to fully realize the benefits of ATRW in CPB solutions. Overall, this study underscores the potential of using ATRW in CPB for environmental management and highlights the importance of optimizing binder and solid content to enhance the stability and effectiveness of the stabilization process.

Declaration of competing interest

The authors declare that they do not have any identifiable financial conflicts of interest or personal associations that might have appeared to exert an influence on the research presented in this paper.

Acknowledgements

The authors express their gratitude to the "Giant Mine Oversight Board (GMOB)," NSERC (Alliance Grant), and the "Unité de Recherche et de Service en Technologie Minérale (URSTM)" for their financial and technical support. Special thanks are extended to the University of Alberta Permafrost Archives Science Laboratory for their assistance with CT scanning and image processing. Additionally, the authors would like to acknowledge Oumou Bah for her valuable assistance in sample preparation and testing.

C.5 Supplementary material for “stabilization of arsenic trioxide roaster waste in cemented paste backfill: geomechanical aspects”

Table C.T1 Particle size analysis, specific gravity, and specific surface area of representative ATRW and tailings samples (Mohammadi, Demers, Beier, et al., 2023)

Parameter	Unit	Tailings	ATRW
$C_u = D_{60}/D_{10}$	(-)	8.46	5.44
$C_c = D_{30}^2/(D_{60}*D_{10})$	(-)	0.80	1.51
$U = (D_{90}-D_{10})/D_{50}$	(-)	5.06	2.33
Specific gravity (G_s)	(-)	2.77	3.45
Specific surface area (S_p)	(m^2/g)	3.59	7.04

Table C.T2 Fit summary results of the UCS (response) for the GU and GU/LKD samples

Source	Sequential p-value	Lack of Fit p-value	Adjusted R^2	Predicted R^2	
UCS-GU					
Linear	<0.0001	0.0021	0.8595	0.7864	
2FI	0.1599	0.0028	0.8822	0.8078	
Quadratic	0.0003	0.0855	0.9755	0.9172	Suggested
Cubic	0.5726	0.0223	0.9732	-0.2751	Aliased
UCS-GU/LKD					
Linear	<0.0001	0.1382	0.8367	0.7997	
2FI	0.3218	0.1392	0.8449	0.6995	
Quadratic	0.0015	0.9296	0.9539	0.9366	Suggested
Cubic	0.9587	0.4592	0.9300	0.4158	Aliased

Table C.T3 Model summary statistics for the UCS (response) of GU and GU/LKD samples

Source	Std. Dev.	R ²	Adjusted R ²	Predicted R ²	PRESS	
UCS-GU						
Linear	44.03	0.8817	0.8595	0.7864	56001.70	
2FI	40.32	0.9194	0.8822	0.8078	50380.49	
Quadratic	18.39	0.9871	0.9755	0.9172	21696.08	Suggested
Cubic	19.22	0.9915	0.9732	-0.2751	3.343E+05	Aliased
UCS-GU/LKD						
Linear	22.78	0.8625	0.8367	0.7997	12092.50	
2FI	22.20	0.8939	0.8449	0.6995	18146.86	
Quadratic	12.10	0.9758	0.9539	0.9366	3830.98	Suggested
Cubic	14.91	0.9779	0.9300	0.4158	35271.97	Aliased

Table C.T4 Coefficients for the quadratic model of UCS for GU and GU/LKD samples

Coefficient	Expression	Coded		Actual	
		GU	GU/LKD	GU	GU/LKD
β_0		+274.86	+74.73	+28953.97311	+15937.11522
β_1	Binder content (<i>A</i>)	+92.41	+44.94	-1346.12433	-631.69382
β_2	Solid content (<i>B</i>)	+91.17	+42.39	-737.69753	-409.74588
β_3	Curing time (<i>C</i>)	+9.45	+0.2012	+1.83956	-0.655521
β_{11}	Binder content ² (<i>A</i> ²)	+18.04	+10.74	+18.03809	+10.73999
β_{22}	Solid content ² (<i>B</i> ²)	+18.92	+10.63	+4.73096	+2.65842
β_{33}	Curing time ² (<i>C</i> ²)	-21.31	+13.50	-0.022171	+0.014044
β_{12}	Binder content × Solid content (<i>A</i> × <i>B</i>)	+33.45	+15.35	+16.72500	+7.67500
β_{13}	Binder content × Curing time (<i>A</i> × <i>C</i>)	+10.78	+0.6750	+0.347581	+0.021774
β_{23}	Solid content × Curing time (<i>B</i> × <i>C</i>)	-0.5500	-0.9250	-0.008871	-0.014919

Table C.T5 The UCS of CPB samples without ATRW prepared using GU and GU/LKD binders

Sample	UCS ₀ (kPa)	UCS_d/UCS_0	Sample	UCS ₀ (kPa)	UCS_d/UCS_0
GU-4-72-28	274	0.564	GU/LKD-4-72-28	75	0.562
GU-4-76-28	411	0.670	GU/LKD-4-76-28	163	0.567
GU-5-74-59	431	0.640	GU/LKD-5-74-59	153	0.489
GU-6-72-28	371	0.700	GU/LKD-6-72-28	167	0.600
GU-6-76-28	678	0.724	GU/LKD-6-76-28	301	0.710

Table C.T6 Coefficients for the modified quadratic model of UCS for GU and GU/LKD samples

Coefficient	Expression	Coded		Actual	
		GU	GU/LKD	GU	GU/LKD
β_0		+257.51	+85.72	+31861.89207	+14125.25005
β_1	Binder content (<i>A</i>)	+92.41	+44.94	-1346.37686	-617.25945
β_2	Solid content (<i>B</i>)	+91.17	+42.39	-815.03213	-361.97228
β_{11}	Binder content ² (<i>A</i> ²)	+20.11	+9.43	+20.11407	+9.42502
β_{22}	Solid content ² (<i>B</i> ²)	+21.00	+9.32	+5.24996	+2.32968
β_{12}	Binder content × Solid content (<i>A</i> × <i>B</i>)	+33.45	+15.35	+16.72500	+7.67500

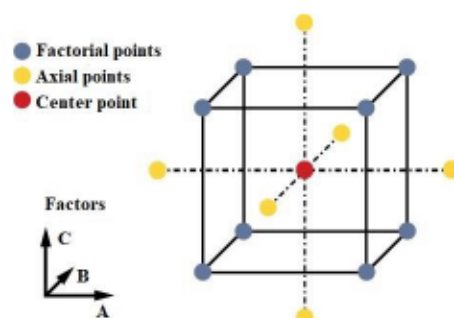


Figure C.F1 Schematic of a central composite design with three factors (Hetzner et al., 2014)

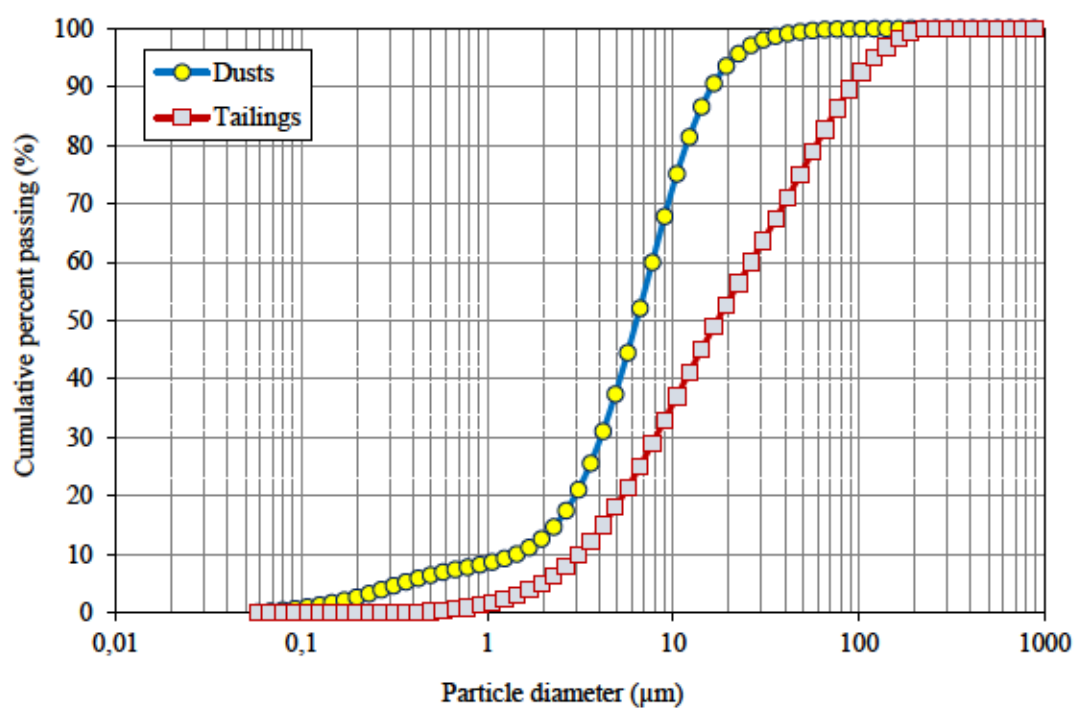


Figure C.F2 Particle size distribution of representative ATRW (dust) and tailings samples (Mohammadi, Demers, Beier, et al., 2023)

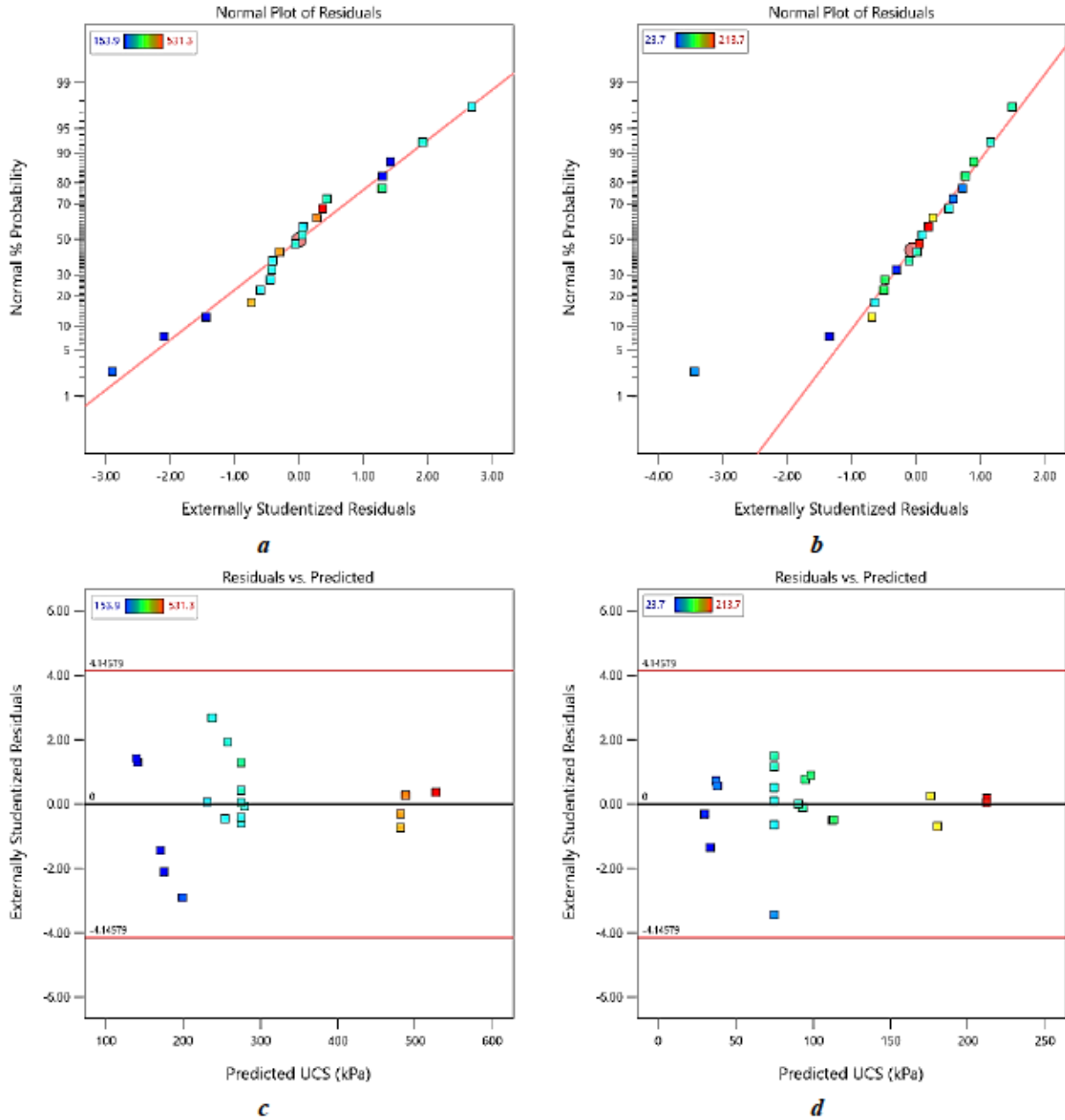


Figure C.F3 Normal plot of residuals for a) GU and b) GU/LKD samples; and predicted vs. externally studentized residuals of c) GU and d) GU/LKD samples in CCD experiments

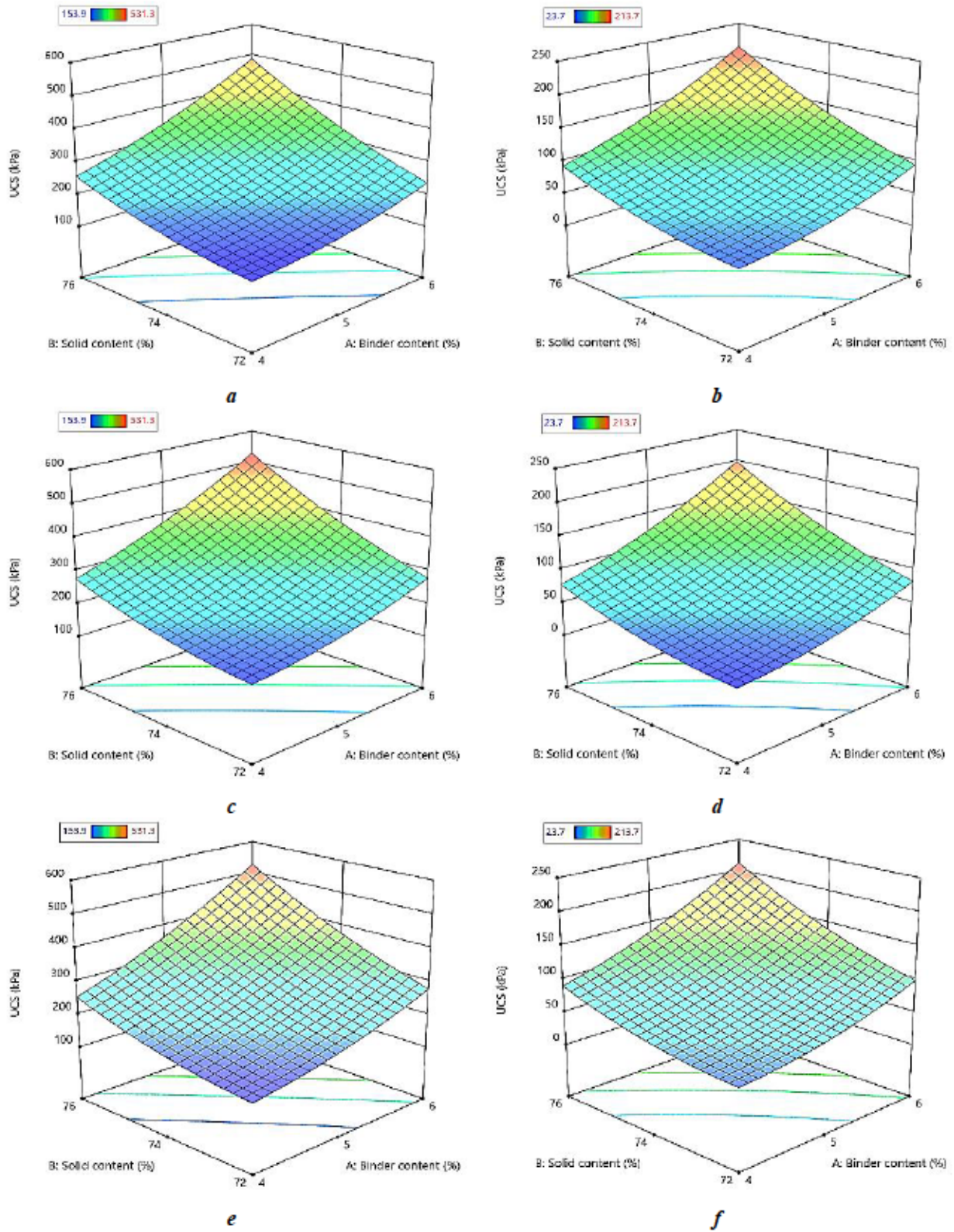
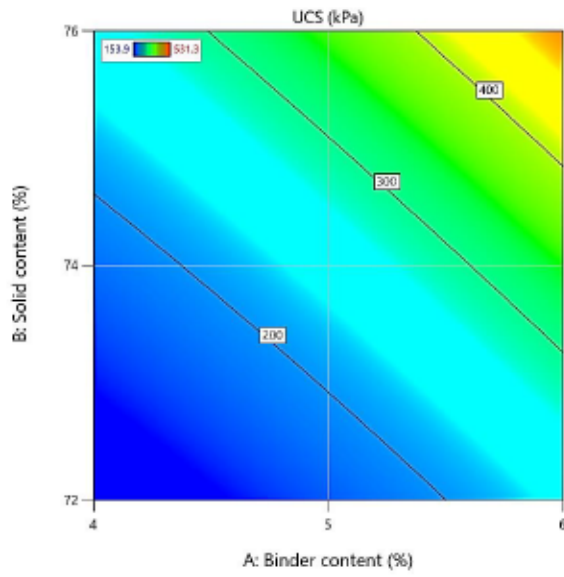
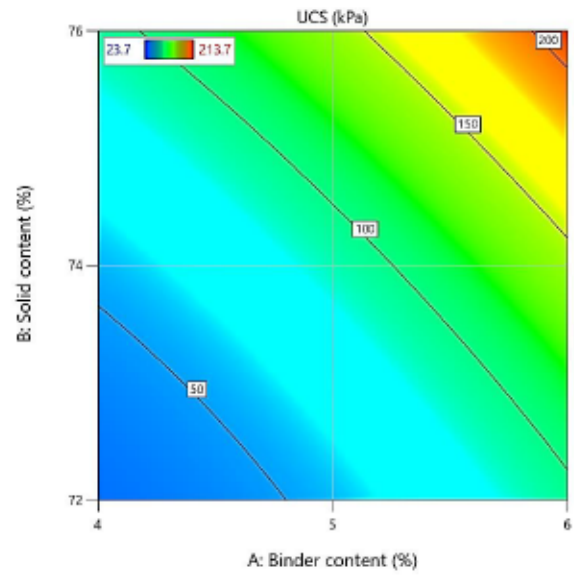
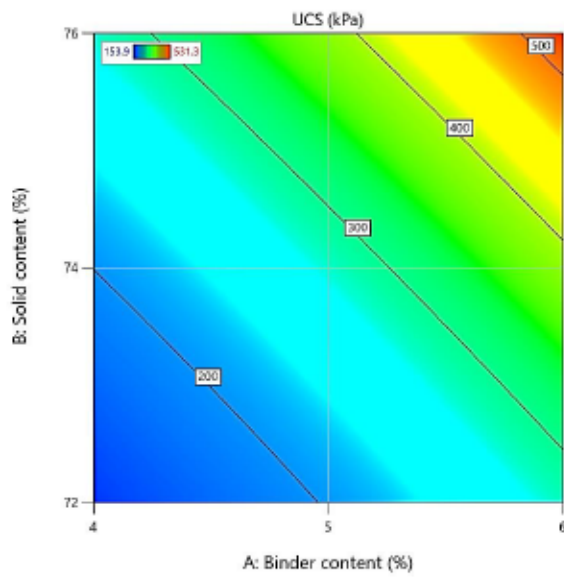
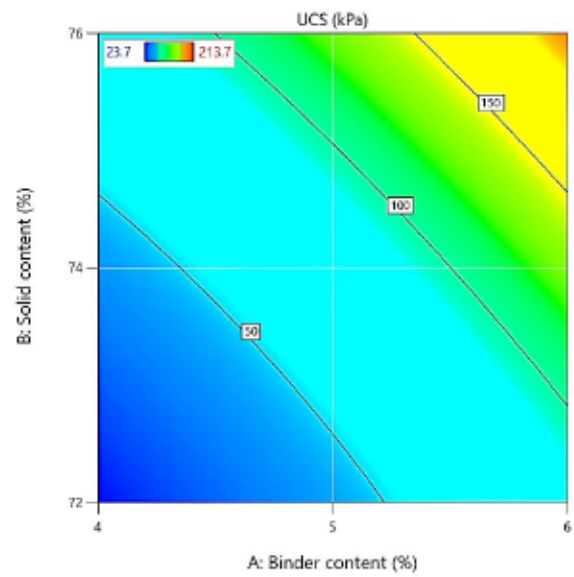


Figure C.F4 Surface plots for the UCS of GU and GU/LKD samples at different curing times: a) GU-28 days, b) GU/LKD-28 days, c) GU-59 days, d) GU/LKD-59 days, e) GU-90 days, and f) GU/LKD-90 days

***a******b******c******d***

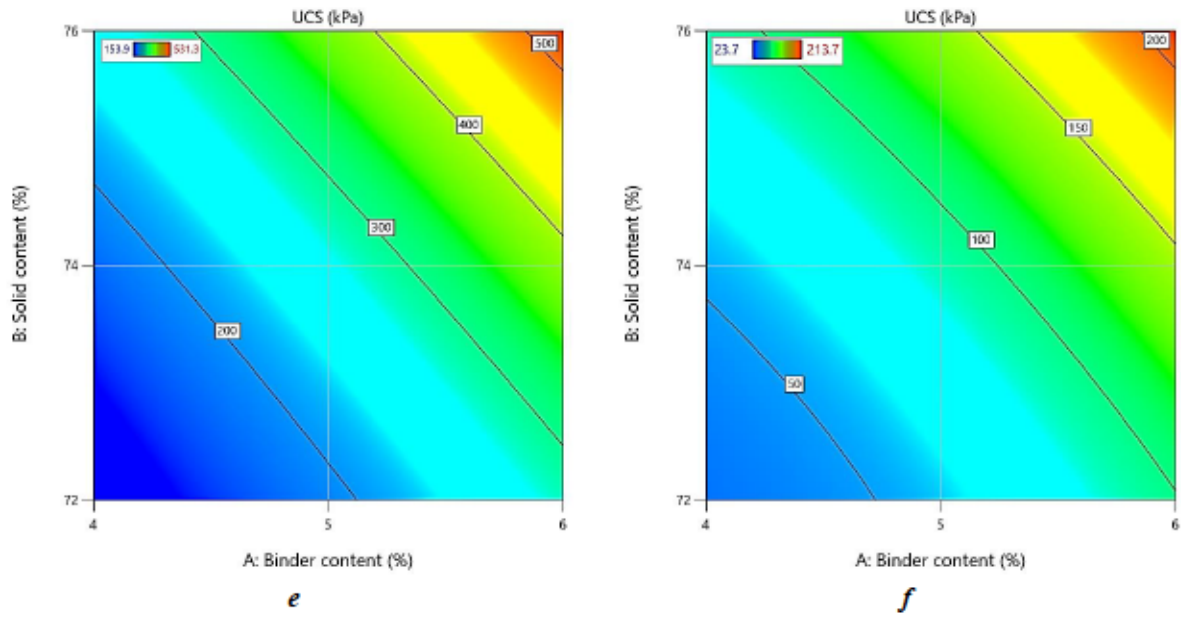
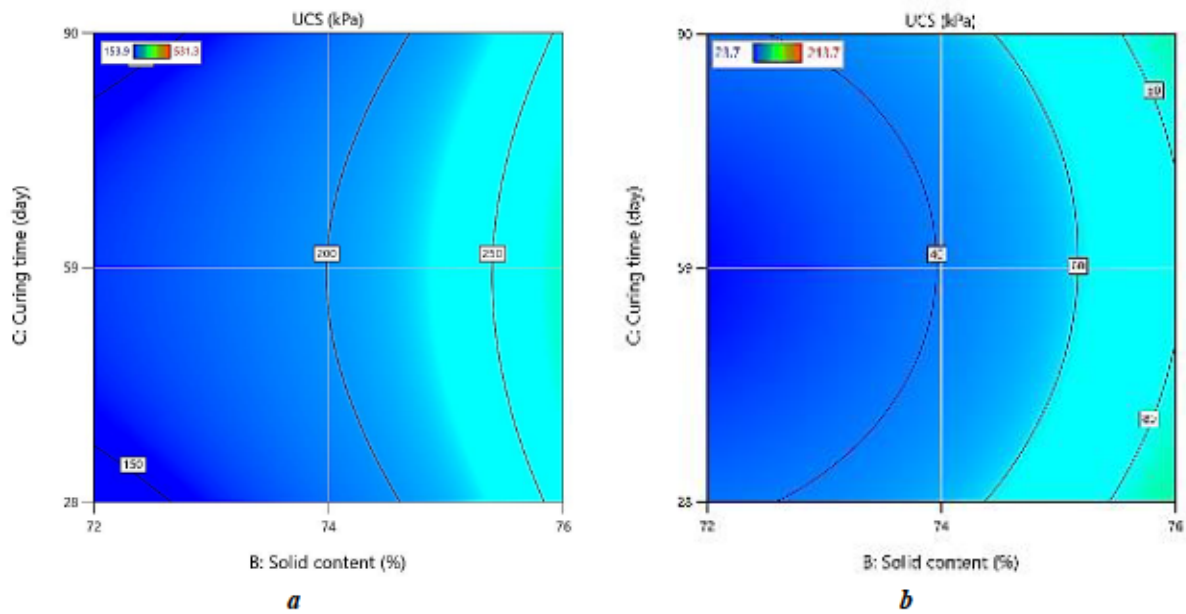


Figure C.F5. Contour plots for the UCS of GU and GU/LKD samples at different curing times: a) GU-28 days, b) GU/LKD-28 days, c) GU-59 days, d) GU/LKD-59 days, e) GU-90 days, and f) GU/LKD-90 days



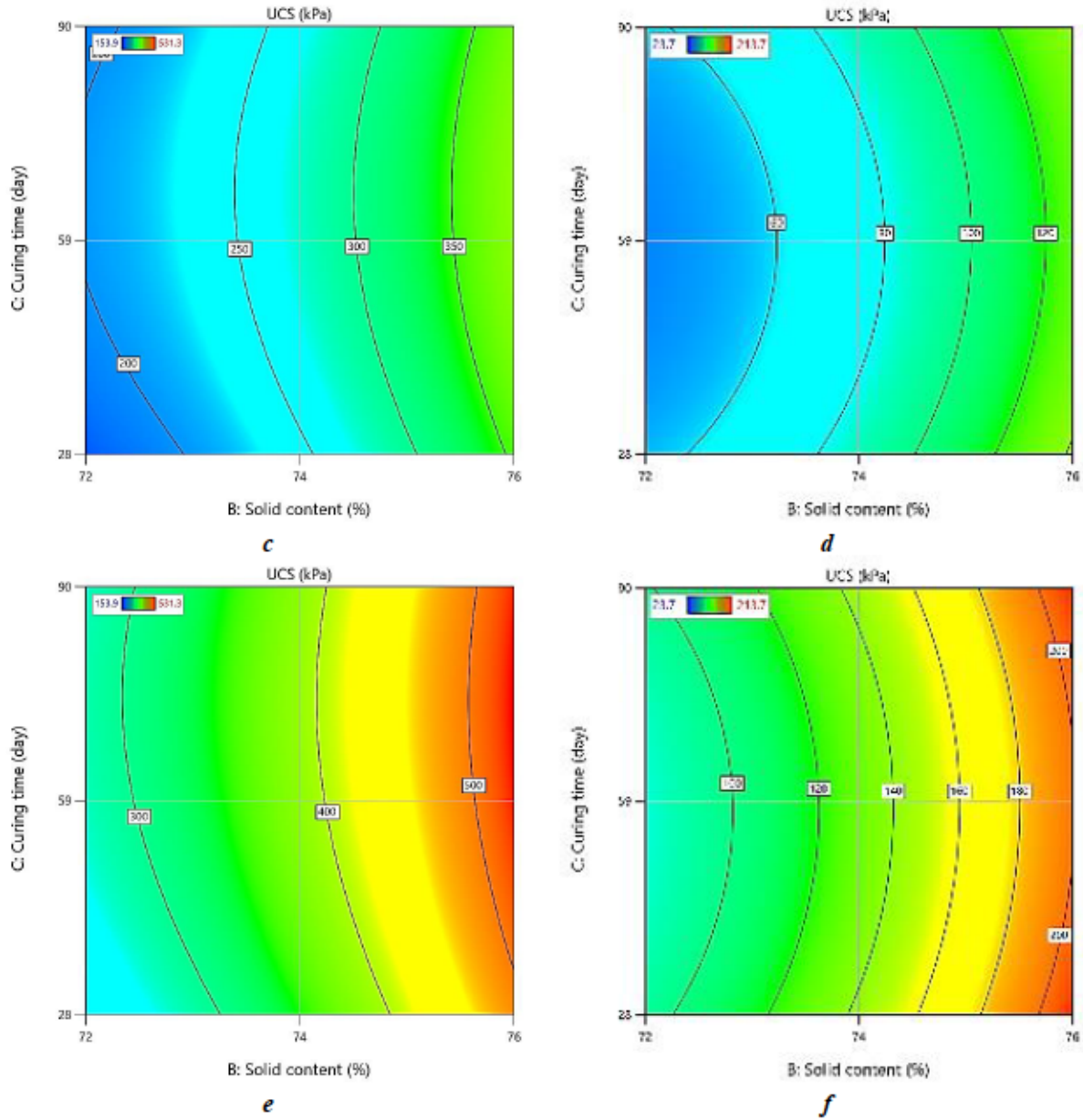
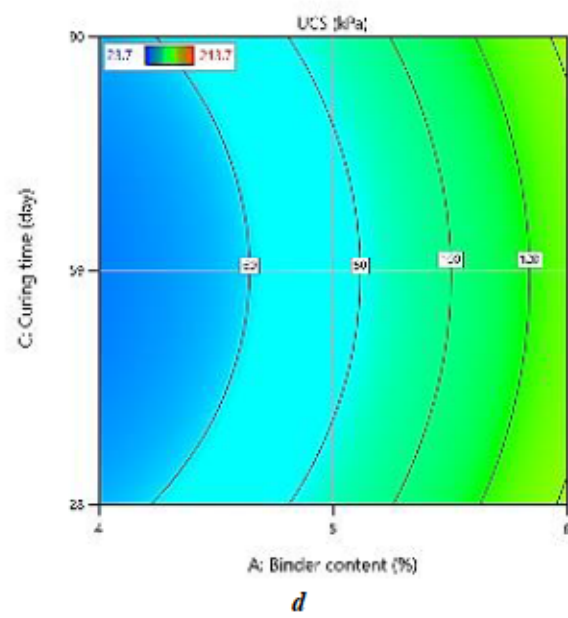
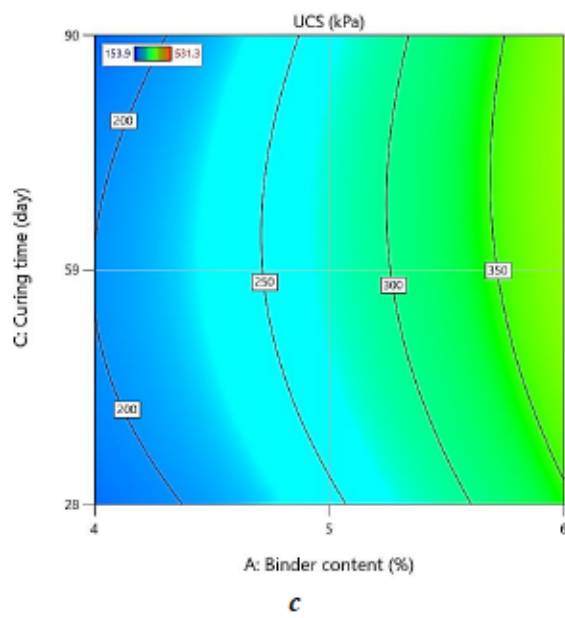
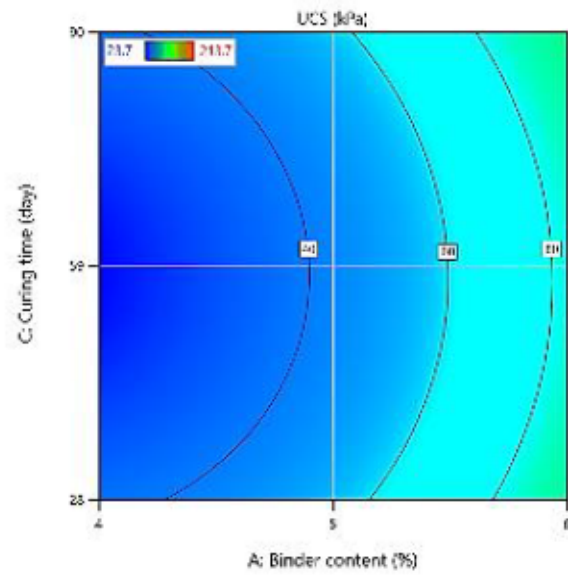
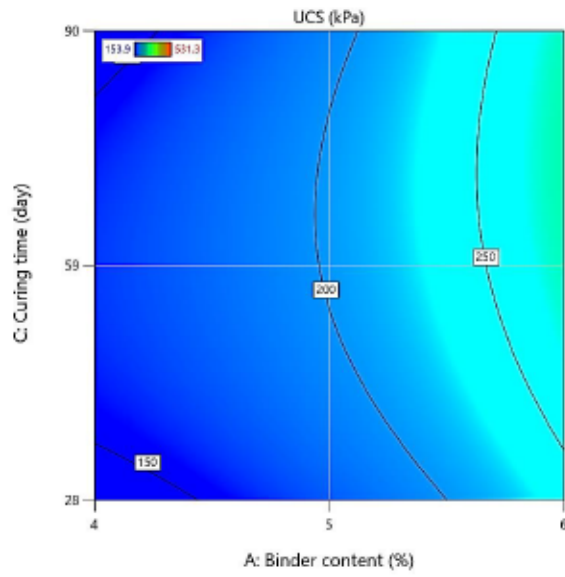


Figure C.F6 Contour plots for the UCS of GU and GU/LKD samples at different binder content: a) GU-4%, b) GU/LKD-4%, c) GU-5%, d) GU/LKD-5%, e) GU-6%, and f) GU/LKD-6%



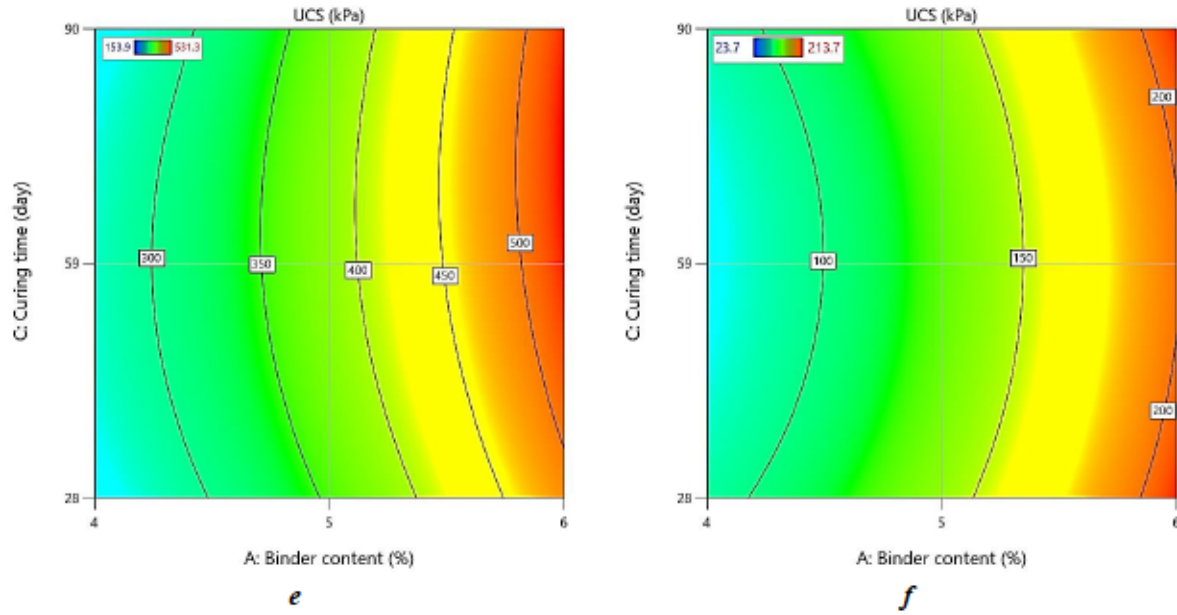


Figure C.F7 Contour plots for the UCS of GU and GU/LKD samples at different solid content: a) GU-72%, b) GU/LKD-72%, c) GU-74%, d) GU/LKD-74%, e) GU-76%, and f) GU/LKD-76%

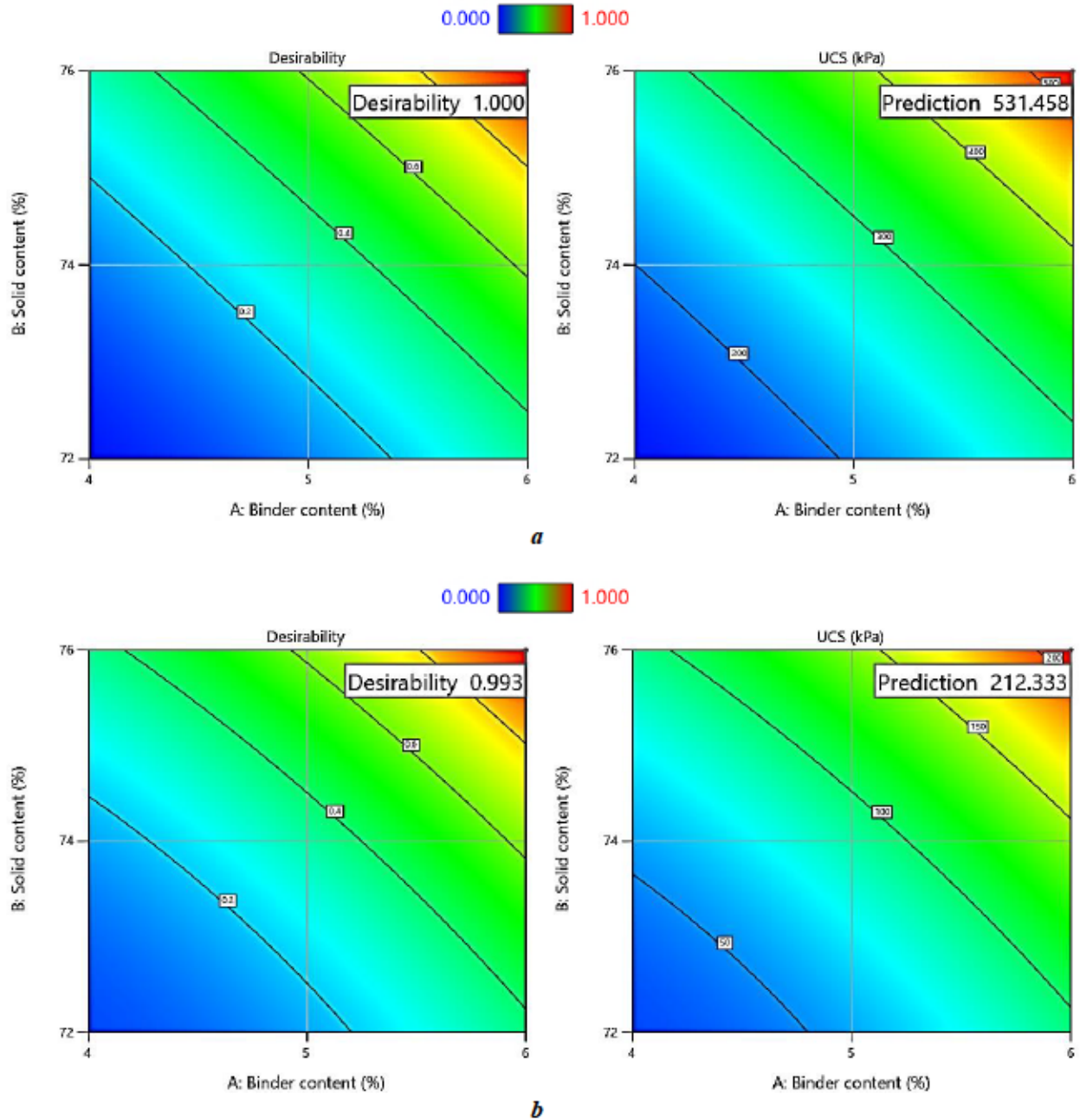


Figure C.F8 The optimization (prediction and desirability) of a) GU and b) GU/LKD samples for the scenario of all parameters in their initial ranges

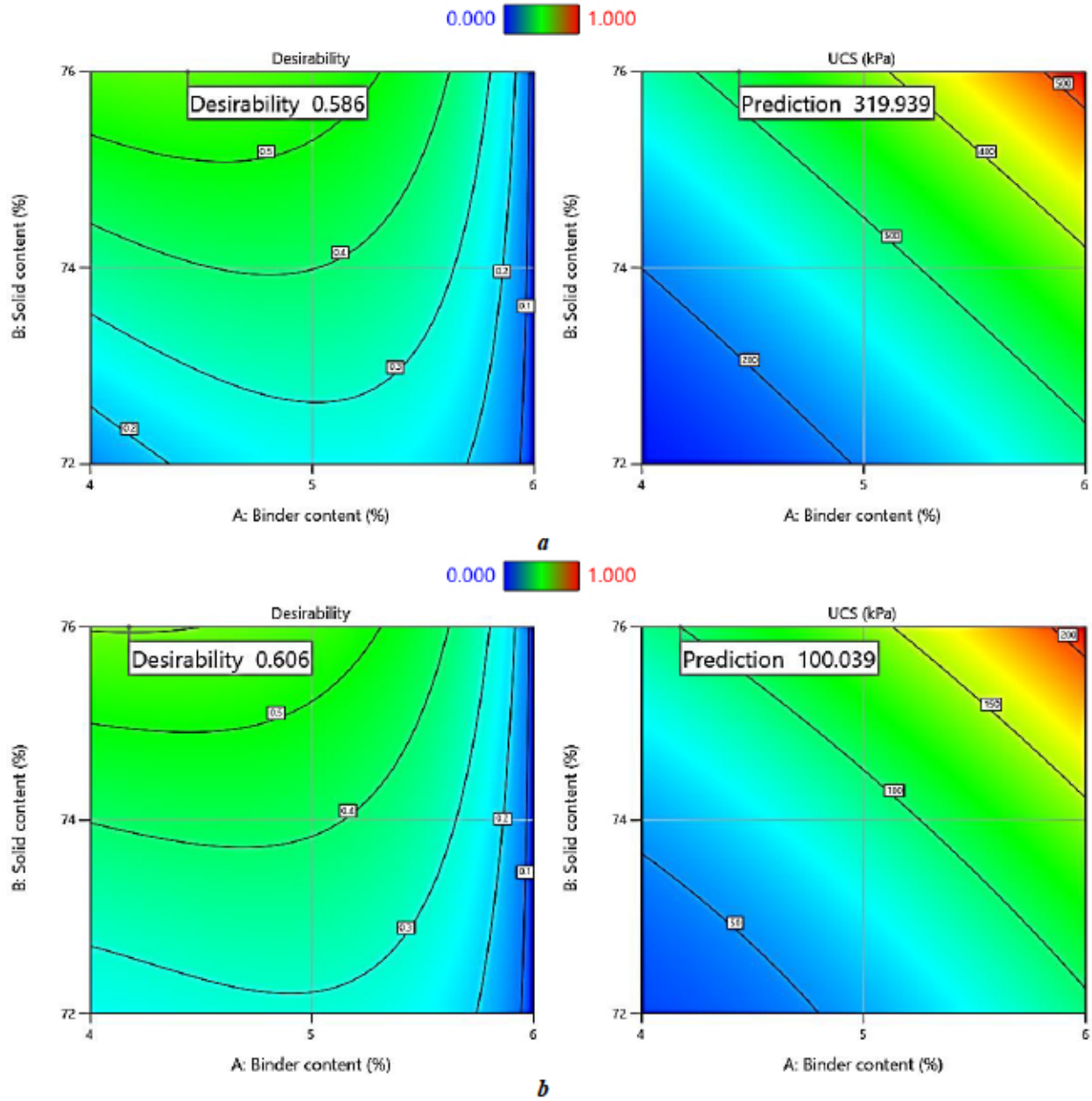


Figure C.F9 The optimization (prediction and desirability) of a) GU and b) GU/LKD samples for the scenario of minimized binder content

APPENDIX D ARTICLE 3: STUDY ON THE LEACHING BEHAVIOR OF CEMENTED PASTE BACKFILL CONTAINING ARSENIC TRIOXIDE ROASTER WASTE (ATRW)

This article was published in Discover Civil Engineering journal (volume 1, Advances in Sustainable Mining Waste Management topical collection). This article was submitted on 26 July 2024, accepted on 18 November 2024, and published online on 2 December 2024. This appendix reproduces the full text.

Amirhossein Mohammadi^{1*}, Valerie A Schoepfer², Isabelle Demers¹, Nicholas A Beier³

¹ Research Institute on Mines and the Environment, Université du Québec en Abitibi-Témiscamingue, Rouyn-Noranda, QC, Canada, J9X 5E4

² Department of Geological Sciences, University of Saskatchewan, Saskatoon, SK, Canada, S7N 5E2

³ Department of Civil and Environmental Engineering, University of Alberta, Edmonton, AB, Canada, T6G 1H9

Highlights

- ATRW dissolution lowered the paste's pH and blocked some hydration products.
- Arsenic leaching in CPB was mainly due to surface wash-off and depletion.
- Arsenic leaching from ATRW-containing CPBs could be significant and unacceptable.
- CPB hydration and strength gain did not stabilize arsenic via As-Ca minerals.

CRedit author statement

Amirhossein Mohammadi: Conceptualization, Data Curation, Investigation, Methodology, Visualization, Writing – Original Draft; **Valerie A Schoepfer:** Conceptualization, Investigation, Methodology, Validation, Writing – Original Draft, Writing – Review and Editing; **Isabelle**

* Corresponding author; amirhossein.mohammadi@uqat.ca

Demers: Conceptualization, Formal Analysis, Funding Acquisition, Methodology, Project Administration, Supervision, Validation, Writing – Review and Editing; **Nicholas Beier:** Conceptualization, Funding Acquisition, Methodology, Validation, Writing – Review and Editing.

Keywords: Arsenic trioxide roaster waste (ATRW), cemented paste backfill (CPB), leaching, arsenic stabilization, microstructure

Abstract

After decades of mining at Giant Mine in Yellowknife, Northwest Territories, a significant amount of arsenic trioxide roaster waste (ATRW), containing around 60% arsenic, was stored underground, posing serious health hazards. This study explored solidification and stabilization of ATRW through its incorporation into cemented paste backfill (CPB). It evaluated the stability of arsenic-bearing compounds and the mechanisms of arsenic trioxide stabilization within CPB. Based on the results of unconfined compressive strength (UCS) tests on CPB samples, certain samples were selected for monolithic tank leaching tests (TLT) and a range of microstructural analyses, including thermogravimetry, X-ray absorption spectroscopy, Fourier-transform infrared spectroscopy, and computed tomography. These tests aimed to examine the leaching behavior of arsenic and the microstructure of the selected CPB samples, and to investigate the relationship between their strength, leaching behavior, and pore characteristics. Findings indicated significant arsenic release from CPB surfaces, even in high-strength samples, with calcium-silicate-hydrate (C-S-H) gels as the main hydration product, though in low quantities. No chemical bonding between arsenic and calcium was detected, and high-strength samples had higher pore volumes and lower pore sphericities. The study concluded that ATRW incorporation into CPB requires modifications to reduce arsenic solubility and minimize exposed leachable surfaces.

Environmental implication

The disposal of arsenic trioxide roaster waste from gold mining operations presents significant environmental challenges. The stability and leachability of As_2O_3 in cemented paste backfill are critical concerns due to the compound's high toxicity and solubility in water. This study investigates the stability and leachability of arsenic-bearing compounds within CPB matrices, focusing on arsenic trioxide stabilization mechanisms. Leaching tests were conducted to evaluate arsenic behavior in CPB under dynamic conditions. Additionally, the microstructure and hydration

products of CPB were analyzed to understand the relationship between microstructure and leachability.

D.1 Introduction

The Giant Mine, situated 5 km north of Yellowknife in the Northwest Territories, is an abandoned underground gold mine that operated for more than fifty-five years, spanning from 1948 to 2004. Gold in the ore was linked to arsenic-bearing minerals (SRK, 2002) and processing generated approximately 237,000 tonnes of arsenic trioxide roaster waste (ATRW) as a by-product, which were stored underground in stopes and chambers. Additionally, over 17 million tonnes of tailings were stored in tailings storage ponds. Arsenic trioxide is known to be the most toxic, bioaccessible, and soluble solid form of arsenic (Lum et al., 2023). ATRW as a fine-grained pyrometallurgical byproduct primarily consists of arsenolite. Arsenolite is water-soluble over a broad pH range, dissolving to form H_3AsO_3 or other complexes depending on the pH. Exposure to oxygen further promotes its dissolution and oxidation to arsenate, resulting in a solution that is less toxic but still hazardous. Arsenic that escapes the underground storage is captured by a water collection system within the mine. The collected water is treated to remove arsenic before being discharged into the environment (SRK, 2002). The high abundance of As^{+3} in the ATRW and its mobility are critical factors to consider for long-term environmental remediation (Foster et al., 1998; Pokrovski et al., 1996). These factors are crucial for the physical and chemical stabilization of ATRW and their weathering products, as well as for planning and implementing future remediation strategies (Lum et al., 2023). Prior research on the treatability of arsenic compounds through cement stabilization indicated that effectively stabilizing highly arsenic-containing wastes through cement stabilization and solidification is indeed feasible (Choi et al., 2009; Clancey et al., 2015; Fuessle & Taylor, 2004; B.-J. Kim et al., 2016; Kundu & Gupta, 2008; Moon et al., 2004; Phenrat et al., 2008; Singh & Pant, 2006).

Cemented paste backfill (CPB) technology has emerged as a prominent management solution for underground mining. CPB is a carefully engineered blend consisting of dewatered tailings from the mineral processing operation, hydraulic binders (comprising 3–7% of the total solids weight), and either fresh or process water. This high-density slurry, comprising between 70–85% solids by weight, forms a non-Newtonian fluid that is pumped and/or transported by gravity into stopes (Bull, 2019). Hydraulic binders such as Portland cements, lime, pulverized fly ash, and blast

furnace slag serve as binding agents in CPB. The compressive strength of CPB, a critical quality metric, is affected by the physico-chemical properties and mineralogy of tailings, along with the chemical composition of the mixing water and the types of binders employed (Belem et al., 2010). Furthermore, CPB offers significant environmental advantages for tailings management by enhancing the neutralization potential and reducing the porosity of tailings through cement addition, mitigating sulfide oxidation and acid mine drainage (AMD) generation in the long term, especially under flooding conditions after mine closure, and stabilizing heavy and toxic metal pollutants such as copper, lead, arsenic, zinc, etc. (Coussy et al., 2011; MEND, 2006; Yılmaz et al., 2021). Enhancing CPB performance hinges on identifying an appropriate cementitious material that not only enhances strength but also ensures the immobilization of metal(loid)s within the hardened CPB (F. Zhang et al., 2022). Furthermore, in certain cases, such as the Giant Mine, the primary concern is not the strength of the CPB but rather the chemical stabilization and release of metal(loid)s within the CPB structure. Indeed, the hydraulic binders employed in CPB undergo reactions with metals and metalloids to produce more stable compounds (Coussy, Benzaazoua, et al., 2012); however, the stability and long-term behavior of arsenic in CPB remain uncertain, primarily due to the unique hydration mechanisms in CPB, e.g. high water-to-cement ratio and aggressive mixing water (Benzaazoua, Fall, et al., 2004; Coussy, Benzaazoua, et al., 2012) and prior studies have been conducted to address these uncertainties.

Recent studies on the fixation of metal(loid)s, specifically arsenic, within CPBs are relatively scarce (Benzaazoua, Marion, et al., 2004; Coussy et al., 2011; Coussy, Benzaazoua, et al., 2012; Y. Zhang et al., 2019b). These investigations have effectively utilized CPB to immobilize arsenopyrite, scorodite, and artificially introduced As in both natural and synthetic CPB. The proportions of binders utilized in these studies varied from 1% to 7%. The immobilization of arsenic in CPB materials has been attributed to the formation of stable arsenic precipitates, notably calcium arsenates, as well as the entrapment of arsenic in the cementitious matrix through sorption onto calcium-silicate-hydrates (C-S-H) or substitution within the crystal lattice of secondary cementitious minerals (Coussy et al., 2011; Hamberg et al., 2015c). For instance, Coussy et al. (Coussy et al., 2011) investigated the stability of arsenic in CPB samples rich in arsenopyrite by using 5% wt. of three different mixtures of binding agents and conducting various leaching tests. The findings indicated that fly ash-based CPB samples exhibited higher arsenic release compared to those based on slag and Portland cement. Neutralizing minerals of tailings (such as carbonates)

in the CPB influenced arsenic leaching by reducing the oxidation of arsenic-bearing sulfides. The nature of arsenic compounds varied with the binder: Portland cement resulted in calcium arsenates, while fly ash led to a mix of calcium arsenates and iron-arsenic compounds. For slag-based samples, arsenopyrite grains were trapped within the C-S-H gel structure without forming new compounds. Hamberg et al. (Hamberg et al., 2015c) studied the leaching behavior of arsenic in CPB containing a low percentage (1-3% wt.) of biofuel fly ash and ordinary cement, as well as tailings with arsenopyrite-loellingite inclusions. They also examined the effect of $\text{Fe}_2(\text{SO}_4)_3$ treatment, which forms stable arsenic-bearing iron precipitates (FEPs), under leaching tests. The results showed that incorporating arsenic-rich tailings into the cementitious matrix increased arsenic leaching due to the rise in pH and the transformation of desorbed arsenic from FEPs into less acid-tolerant species such as calcium arsenates and cementitious arsenic phases.

While binding arsenic-containing compounds in CPB can mitigate the risk of contamination, there remains a possibility of groundwater contamination if these compounds can leach from the cement matrix. Therefore, it is crucial to assess the arsenic behavior and leachability from CPBs containing stabilized arsenic. Additionally, careful consideration must be given when selecting a leaching test for a CPB sample. A key consideration is that CPB is monolithic in the field; therefore, any leaching test that necessitates particle size reduction is considered invalid (Bull, 2019). To tackle this issue, several studies have utilized the dynamic tank leaching test (TLT) on monolithic CPB samples under laboratory conditions, aiming to determine the leaching characteristics of CPB (Coussy et al., 2011; Hamberg et al., 2015a, 2015c, 2017; Hamberg, Maurice, et al., 2018; Jiao et al., 2011; Seipel et al., 2017; Y. Zhang et al., 2019b, 2020). While there have been studies investigating the stabilization mechanisms and leachability of arsenic compounds within CPB, the stabilization mechanisms of arsenic trioxide have not been explored previously. Furthermore, since the ATRW from the Giant Mine contains not only arsenic trioxide but also other constituents and impurities, such as antimony, these additional elements may affect the solubility, stabilization performance, and leachability of arsenic (Lum et al., 2023). The effects of these impurities on the speciation of arsenic during stabilization and leaching must be considered. This study aims to examine the stability of As-bearing compounds formed within CPB matrices and comprehend the mechanisms of arsenic trioxide stabilization in CPB. The leaching test results presented in this paper enabled the assessment of As behavior in CPB under dynamic conditions (mass transfer-based leaching tests). Additionally, the microstructure and hydration products of CPB underwent

analysis to comprehend the relationship between microstructure and leachability. The main hypothesis of this research suggests that adding ATRW to cemented paste backfill is a potential solution for long-term stabilization of arsenic trioxide. The outcomes of this study will contribute to a deeper understanding of the environmental behavior of CPBs containing arsenic trioxide.

D.2 Materials and methods

D.2.1 Materials

In this study, the preparation of CPB involved using two binding agents, mine tailings, ATRW, and deionized (DI) water. The tailings were sourced from the northern pond of the Giant Mine site and then transported to the laboratory. To address humidity variations within the tailings, they underwent thorough mixing and homogenization, followed by oven-drying at a temperature of 40 °C for 48 hours before further preparation and characterization. General use (GU) Portland cement, the primary binding agent, was provided by Bomix (Quebec, Canada). An additional binding agent was prepared by combining GU cement with lime kiln dust (LKD) from Graymont in Bedford, Quebec, Canada, in a 50/50 mass ratio. GU cement primarily consists of tricalcium silicate (C3S), dicalcium silicate (C2S), tricalcium aluminate (C3A), calcium ferroaluminates (C4AF), and gypsum (Spence & Shi, 2005). LKD, a by-product of the lime industry, serves as an additional source of calcium and appears as calcite and portlandite. Eight distinct samples of ATRW from various stopes and chambers at the Giant Mine were received, and a blended representative sample was prepared for characterization and incorporation into the CPB recipes. Throughout the study, DI water was utilized for preparing cemented paste backfill samples and conducting leaching experiments, thereby eliminating the influence of the chemical constituents of water on the results.

D.2.2 Methods

D.2.2.1 Initial characterizations

The physical, chemical, and mineralogical characteristics of the materials underwent investigation. The specific gravity (G_s) of tailings, ATRW, GU cement, and LKD was measured using an automatic gas pycnometer (Ultracyc 1200e, Quantachrome Instruments). The particle size distribution (PSD) of tailings and ATRW was analyzed by a laser diffraction particle size analyzer (Malvern Mastersizer 3000). The specific surface area of tailings and ATRW was determined by the Brunauer-Emmett-Teller (BET) method using liquid nitrogen (Gemini 2375, Micromeritics).

The chemical composition (oxides) of GU cement, LKD, as well as tailings and ATRW, was obtained through X-ray fluorescence (XRF) spectrometry (S2 Ranger, Bruker AXS). Inductively Coupled Plasma Atomic Emission Spectroscopy (ICP-AES) and Inductively Coupled Plasma Mass Spectrometry (ICP-MS) were utilized to measure the elemental concentration. The samples underwent digestion with HNO₃, HF, and HCl through microwave heating, with specific care taken to avoid arsenic volatilization. Boric acid (H₃BO₃) was added post-microwave digestion to neutralize the residual HF. ICP-MS (Agilent 7800) was also utilized to analyze the chemical composition of liquid samples after acidification with 2% v/v HNO₃. The pH and electrical conductivity (EC) were measured using a multimeter (B30PCI, VWR SympHony). Mineralogical analysis of the tailings and ATRW samples was evaluated by X-Ray Diffractometry (XRD) method using a Bruker AXS D8 AQ advance with a copper radiation source on samples ground in Isopropanol with a McCrone mill for 15 minutes. The samples were placed on the sample holder using the backloading method. Samples were scanned over a 2-theta range of 5–70° with a 0.02° step size. The spectra were analyzed through DIFFRAC.EVA software (version 5.2.0.3) to identify phases and match them with reference databases, and the phases were semi-quantified using TOPAS software (version 4.2) through the Rietveld method.

D.2.2.2 CPB preparation and UCS tests

The formulation and preparation of CPB samples, along with the results of UCS tests, are detailed in (Mohammadi, Demers, Beier, et al., 2023). Based on the UCS test results, certain CPB samples were chosen for leaching and microstructural analyses. Table D.1 provides an overview of the performed analyses, the selected samples, and the reasons for their selection. The samples were labeled as '*X-A-B-C*', where *X* represents the type of binder (GU or GU/LKD), *A* indicates the binder content in percentage, *B* represents the solid content in percentage, and *C* represents the curing time in days. For example, 'GU-4-76-28' denotes a sample prepared with 4% GU binder, at a 76% wt. solid content, and a 28-day curing duration before undergoing the UCS test. The CPB samples were prepared by maintaining a fixed percentage of ATRW (10% wt.).

Table D.1 The selected samples for the leaching and microstructural analyses in this study

Analysis	Selected samples	Reasons
Tank leaching test	GU-4-76-28, GU-5-74-59, GU-6-76-28, GU-6.68-74-59, GU/LKD-6-76-28, GU/LKD-6.68-74-59	Two samples for each binder with the highest UCS and two GU samples with mid-range UCS
XAS	GU-4-76-28, GU-6-76-28, GU-6.68-74-59, GU/LKD-6-76-28	Samples with the highest UCS for both binders
TG & FTIR	GU-6-76-28, GU-6.68-74-59	GU samples with the highest UCS
CT scan	GU-4-72-28, GU-6-76-28, GU/LKD-5-70.64-59, GU/LKD-6-76-28,	Samples with the highest and the lowest UCS for both binders

D.2.2.3 Leaching analysis

The monolithic tank leaching test (TLT, Dutch standard EA NEN 7375 (EA NEN 7375, 2004)) was employed to grasp the sequential leaching behavior and leaching mechanism of monolithic cement-based materials within a diffusion-controlled environment (Schafer, 2016; Yılmaz et al., 2021). The protocol was devised to determine the leaching of inorganic components from molded and monolithic materials under aerobic conditions. A TLT is suitable for monolithic materials with low permeability, where the leaching fluid circulates around the material, generating the driving force to sustain leaching (Hamberg et al., 2017). This leaching protocol was implemented to evaluate the leaching of arsenic and other related elements/ions and to ascertain the degree of arsenic stabilization within the paste backfill matrix. Cured CPB samples were trimmed to approximately 5.0 cm in height by removing 2.5 cm from each end of the cylinder. As mentioned in Table 1, two samples for each binder with the highest UCS (GU-6-76-28, GU-6.68-74-59, GU/LKD-6-76-28, and GU/LKD-6.68-74-59) were chosen for the leaching test. In the case of the GU binder, two additional samples with lower UCS and different binder and solid contents (GU-4-76-28 and GU-5-74-59) were also selected to assess the effects of binder and solid content, as well as the strength level, on the leaching analysis results. Duplicate experiments were conducted for each CPB specimen, resulting in a total of 12 samples being subjected to leaching. After weighing and measuring the surface area, the cylinders were positioned on plastic supports in closed HDPE flask reactors, ensuring they were 2 cm from the bottom of the flasks to guarantee the complete leaching of the cylinders. DI water was then added to achieve a level that ensured a 2 cm water head above the CPB samples and stirred with a magnetic stirrer. The liquid/solid (L/S)

ratio was consistent across all samples, maintained at 10 cm³ of leaching solution per cm² of exposed surface. Leachates were collected and renewed at intervals of 6 hours, 1 day, 2.25 days (54 hours), 4 days, 9 days, 16 days, 36 days, and 64 days (final collection). At each scheduled interval, 15 mL of leachate was extracted using a plastic syringe and filtered with a membrane filter (0.45 μm). Prior to each renewal of the solution, the CPB samples were weighed, and changes in masses were recorded. The pH and EC of the collected leachates were measured, followed by ion chromatography (IC) and ICP-AES analysis.

The mass transfer (E^*_i) and cumulative leaching (ϵ^*_n) of As and other related components (elements/ions) from CPB samples were calculated based on the EA NEN 7375 (EA NEN 7375, 2004) standard. Cumulative derived leaching is also calculated according to Equation D.1:

$$\epsilon_n = \frac{E^*_i \times \sqrt{t_i}}{\sqrt{t_i} - \sqrt{t_{i-1}}}, \text{ for } i = 1 \text{ to } N \text{ (where } i = n) \quad (\text{D.1})$$

Where ϵ_n represents the calculated cumulative leaching for a component for period n , involving fractions $i = 1$ to n , in g/m², E^*_i (g/m²) represents the calculated mass of the component released during a leaching period i , t_i is the replenishment time of fraction i in days, t_{i-1} is the replenishment time of fraction $i - 1$, and N denotes the total number of leachant renewal periods ($N = 8$). The derived cumulative leaching ϵ_n determines only the cumulative leaching up to and including period i based on the measured leaching in period i . Derived leaching values can be used to evaluate whether leaching is affected by diffusion (EA NEN 7375, 2004). This was achieved by computing the slopes of the regression lines (r_c) of log–log plots of the cumulative derived leaching vs. time for various increments, their associated standard deviation (Sd_{r_c}), and the concentration factor (CF). The definitions of these parameters and the considered increments are presented in (EA NEN 7375, 2004) and section D.3.3 of this paper.

D.2.2.4 Thermogravimetric analysis

Thermogravimetric analysis was utilized to assess the thermal stability of CPB samples containing ATRW and to ascertain their volatile component fraction by monitoring weight changes during sample heating at a constant rate. These measurements help distinguish between different materials based on their distinct thermal properties. Thermogravimetric (TG) analysis was performed on selected powdered CPB specimens using TA Instruments Discovery SDT650 equipment. The analysis covered a temperature range from 25 to 1000 °C, with a heating rate of 10 °C/min under

a N₂ atmosphere. Based on Table 1, two GU samples with the highest UCS (GU-6-76-28 and GU-6.68-74-59) were chosen for this analysis. TG curves were utilized to calculate the derivative thermogravimetric (DTG) value for each sample. This value was derived by normalizing the weight loss between 25 and 1000 °C to the initial weight of the sample. Results were compared to databases of known values.

D.2.2.5 FTIR analysis

Fourier transform infrared spectroscopy (FTIR) enables the characterization of various materials by identifying characteristic peaks corresponding to the vibration bands of specific interatomic bonds (Guerrero-Pérez & Patience, 2020). The tests were conducted using the SHIMADZU IRTracer-100 FTIR device (Kyoto, Japan) at the UQAT Biomaterials Laboratory. This analysis was conducted on the two samples previously investigated by TG analysis. Upon infrared ray excitation of the material, there was an absorption of energy by the molecules, causing their vibrations. Subsequently, the machine recorded the intensity of the reflected radiation. Each molecule has a distinct absorption band that serves as a distinguishing feature (Guerrero-Pérez & Patience, 2020). The wavelength range used varied between 4000 cm⁻¹ and 400 cm⁻¹, aligning well with the molecular vibration energy domain. Data processing was performed using the LabSolutionsIR software.

D.2.2.6 XAS analysis

In recent decades, synchrotron-based techniques like X-ray absorption spectroscopy (XAS) have been commonly utilized to understand the chemical and local structural states of a particular element in solids (Komárek et al., 2013; Wogelius & Vaughan, 2012). To supplement the leaching tests, As K-edge XAS spectra were obtained for four selected samples (Table D.1) to gain insights into the chemical speciation, bonding, and coordination environments between As and other elements.

A thin layer of dried and powdered sample, equivalent to < 20 µg, was spread on polyimide (Kapton) tape with excess brushed off and enclosed within another layer of tape before analysis at the BioXAS-Main beamline (07ID-2 M) at the Canadian Light Source synchrotron (Saskatoon, Canada). The BioXAS-Main beamline contains a Si mirror with a Rh coating, used to focus the beam, and a liquid N₂-cooled pseudo-channel cut double Si (220) crystal monochromator to select the incident energy. All samples were pre-cooled in liquid N₂ before insertion into the liquid N₂-

cooled cryostat (Oxford Instruments plc., UK), positioned between the I₁ and I₂ ion chambers. Fluorescence data from each sample were collected using two 32-element Ge detectors (CANBERRA Co., Canada) positioned at 90 degrees to the incident beam and 45 degrees to the sample. Soller slits and a Ge-3 filter were positioned between the sample and the fluorescence detectors to improve the As signal-to-noise ratio by attenuating low energy fluorescent X-rays. Simultaneous L_{III}-edge transmission data from an Au reference foil positioned between ion chambers I₂ and I₃ served for energy calibration and alignment of the As spectra. Each As measurement scanned the range from 200 eV below the theoretical As K-edge (11867 eV) to +885.6 eV ($k = 14 \text{ \AA}^{-1}$), with steps of 5 eV in the pre-edge region (-200 to -30 eV), 0.5 eV in the X-ray absorption near edge structure (XANES) region (-30 to 80 eV), and 0.05 k in the extended X-ray absorption fine structure (EXAFS) region (80 eV to 885.6 eV ($k = 14 \text{ \AA}^{-1}$)). To ensure data quality and the absence of beam-induced sample transformation, two to three replicate scans were collected for each sample.

Data preparation, reduction, and analysis were carried out using the ATHENA modules of the Demeter package (Ravel & Newville, 2005) and the Larch package (Newville, 2013). Scans were imported, corrected for the total flux, and quality checked. Pre- and post-edge normalization, *R* background determination, and the *k*-range were selected to optimize the resulting signal with a forward Fourier transform *k*-range of 3-11 \AA . The critical energy (E_0) of the As K-edge near-edge spectra was determined as the highest point in the main peak of the first derivative and compared to known reference materials containing in the As⁰, As⁺³, and As⁺⁵ oxidation states, which informed subsequent EXAFS modeling.

The amplitude reduction factor (S_0^2) for the Au reference foil in the non-linear least squares EXAFS fitting process was determined to be 0.868 and then constrained for all samples. Potential paths were chosen based on elemental analysis from sample digestions and the composition of the starting materials.

Preliminary coordination numbers (*CM*), interatomic distances (*r*, in \AA), energy shifts (ΔE_0), and Debye-Waller factors (σ^2) were initially derived from theoretical crystal structures and then refined in Larch. The fitting process was conducted over an *R*-range from 1.0 to 5.0 \AA . The goodness-of-fit parameters, including the *R*-factor and χ^2 , were calculated in Larch, where the *R*-factor indicates the percentage misfit between the model and the data, with smaller values being

more desirable. Efforts were made to avoid values above 0.03, indicating a 3% misfit, when possible.

D.2.2.7 CT scan analysis

This X-ray imaging method generates high-resolution images of an object non-destructively by capturing images from various angles around an axis (Gencel et al., 2023) to explore and determine the relationship between the microstructure and mechanical properties quantitatively. Four specific samples were chosen for this analysis, comprising the GU and GU/LKD samples with the highest UCS (GU-6-76-28 and GU/LKD-6-76-28) and lowest UCS (GU-4-72-28 and GU/LKD-5-70.64-59). These samples were prepared and molded in the small cylindrical molds (30 mm in diameter and 63 mm in length) after performing the UCS tests on all samples and the analysis was done on intact samples after specific curing time. In this study, samples were subjected to CT scanning using a Nikon XT H 225ST Industrial CT scanner equipped with an X-ray source featuring a rotating target, and analysis was performed using Nikon's Inspect-X software. The scan settings were configured as follows: a beam energy of 205 kV, a beam current of 115 μ A, exposure at 8 frames per second, and setting the detector panel to -100 mm. The effective pixel size was established at 22 micrometers, and helical scans were employed for all cases to maximize resolution. Each sample was subjected to a total of approximately 4700 projections, with projections optimized to 3141 per rotation and an averaging of 8 frames per projection. For the reconstruction of the primary scan data, Nikon's CT 3D Pro software was utilized. Additionally, beam-hardening corrections were applied to all scans to minimize artifacts in the images. The reconstructed scans were then converted into .VOL and .VGI formats and subsequently imported into 3D ORS Dragonfly visualization software. Through three-dimensional reconstruction of CT images, the cores were segmented into three regions, representing pore space, high-density (arsenic-containing) materials, and the remaining solid matrix. 2D greyscale images along the center of each core in both longitudinal and transverse profiles and 3D images of each core, displaying each segmented region were obtained. The unnecessary regions on each core were cropped to have a smaller sample including the region of interest (ROI) which was obtained as a cylinder with a height of 16 mm and diameter of 8 mm that accurately represented the specimens. Multi-region porosity analysis, with unique measurements for pore volume, mean Feret diameter, and sphericity was done on the ROIs. The Feret diameter represents the distance between the two farthest points of a shape measured in a specific direction. In particle size analysis, calculating the

Feret diameter is a commonly employed descriptor for assessing particle size distribution (Dražić et al., 2016). Mean Feret diameter is the mean value of the minimum and maximum Feret diameters of each discrete pore's boundary over a sufficient number of orientations. Sphericity (S) is defined as the ratio between the perimeter of a circle with the same area as the projected area of the particle and its real perimeter (C. Jiang et al., 2022). Sphericity quantifies how closely a pore resembles a "sphere" by determining the ratio between the object's volume and surface area, as illustrated in Equation D.2 (Lorenzoni et al., 2019).

$$S = \frac{\pi^{\frac{1}{3}}(6V)^{\frac{2}{3}}}{A} \quad (\text{D.2})$$

where S is the sphericity of the pore; V is the volume of the pore and A is the superficial area of the pore.

D.3 Results and discussion

The initial part of this section presents the characterization results of CPB components. Subsequently, the TLT results are discussed, followed by the presentation of microstructural analyses. These analyses aim to provide insights into the leaching behavior and microstructure of CPB samples containing ATRW.

D.3.1 Initial characteristics

The specific gravity values for the materials employed in the preparation of cemented paste backfill were 2.77, 3.45, 3.05, and 2.79 for tailings, ATRW, GU cement, and LKD, respectively. The detailed information on the particle size distribution of tailings and ATRW, along with relevant parameters and specific surface area results, are presented in (Mohammadi, Demers, Beier, et al., 2023). The chemical composition of GU cement and LKD, as determined by XRF, is presented in Table D.2 in terms of oxides. Table D.3 provides the selected results of the ICP-AES, ICP-MS, and XRF tests conducted on the ATRW and tailings samples. It is evident from this table that arsenic constitutes more than 57% of the mixed ATRW sample, with other predominant metals including iron, antimony, aluminum, and cadmium. The tailings, on the other hand, are predominantly composed of iron, calcium, aluminum, and magnesium, with the concentration of arsenic being significantly lower than in the ATRW.

Table D.2 Selected results from the XRF analysis (Mohammadi, Demers, Beier, et al., 2023)

Sample	SiO ₂	Al ₂ O ₃	Fe ₂ O ₃	MgO	CaO	Na ₂ O	K ₂ O	P ₂ O ₅	SO ₃	LOI
	%									
GU cement	17.2	4.84	3.26	2.30	64.3	0.30	1.80	0.32	5.15	<0.01
LKD	7.94	4.70	1.39	0.90	75.8	0.20	1.88	0.16	6.16	<0.01

Table D.3 Selected chemical analysis results of the ATRW and tailings samples by ICP-AES, ICP-MS and XRF methods

Element	Al	As	Ca	Cd	Co	Cr	Cu	Fe	K	Mg	Mn
	mg/kg										
ATRW	10730	571500	5360	7625	23	34	234	31720	2597	3756	448
Tailings	47000	2747	56260	25	35	113	41	72520	10550	29780	1317
Element	Na	Ni	Pb	S	Sb	Ti	Zn	SiO ₂	Na ₂ O	P ₂ O ₅	LOI
	mg/kg							%			
ATRW	541	63	1004	2463	16782	944	529	4.67	0.25	0.02	79.4
Tailings	3039	81	134	5192	118	3668	331	48.5	0.44	0.08	12.4

The XRD analysis results for the tailings and ATRW, outlined in Table D.4, indicate that the minerals in the tailings are predominantly composed of quartz (39.6%), chlorite (19.8%), dolomite (16.4%), and muscovite (14.8%), with minor phases of microcline (2.5%), chalcopyrite (2.0%), albite (1.8%), and trace amounts of other minerals. The presence of neutralizing elements like Ca and Mg (in the form of dolomite) in the tailings is considerably higher than the sulfur content (about 0.5%), classifying the tailings as potentially non-acid generating. Over 86% of the mixed ATRW sample consist of arsenolite (As₂O₃) mineral, followed by quartz (5%) and trace amounts of other minerals. The arsenic trioxide in the ATRW was generated during the roasting process, resulting in a mineralogical composition slightly different from naturally occurring arsenic trioxides.

D.3.3 Leaching analysis

While the hydration process of cement does contribute to a degree of mechanical strength, the leaching of metals and metalloids present in CPB poses a potential risk of groundwater contamination. In order to investigate the leaching behavior of arsenic and other heavy metals, six CPB samples were selected for tank leaching tests and duplicates were conducted for each CPB

recipe, resulting in a total of 12 cylinders leached under identical conditions (e.g., GU-4-76-28-1, GU-4-76-28-2, GU-5-74-59-1, GU-5-74-59-2, GU-6-76-28-1, GU-6-76-28-2, GU-6.68-74-59-1, GU-6.68-74-59-2 as GU samples, and GU/LKD-6-76-28-1, GU/LKD-6-76-28-2, GU/LKD-6.68-74-59-1, and GU/LKD-6.68-74-59-2 as GU/LKD samples). However, during leaching, some samples were unable to endure the entire process and disintegrated, resulting in the termination of leaching for these specific samples. Among GU samples, only two series (GU-6-76-28 and GU-6.68-74-59) retained their structural integrity throughout the leaching process. Other GU samples disintegrated after 24 hours (GU-5-74-59) and 54 hours (GU-4-76-28), necessitating an early end to the leaching test. Similarly, for GU/LKD samples, GU/LKD-6.68-74-59 disintegrated after 24 hours, while GU/LKD-6-76-28 endured leaching for up to 16 days before discontinuation (Figure D.1).

Table D.4 Types and amounts of different minerals in the tailings and ATRW

Minerals	ATRW (%)	Tailings (%)
Arsenolite	86.4	-
Quartz	5.0	39.6
Muscovite	1.1	14.8
Chlorite	1.0	19.8
Gypsum	0.7	1.2
Bettertonite ($[Al_6(AsO_4)_3(OH)_9(H_2O)_5] \cdot 11H_2O$)	1.2	-
Pyrrhotite	0.4	-
Dolomite	-	16.4
Albite	-	1.8
Microcline	-	2.5
Augite	-	1.1
Actinolite	-	0.9
Chalcopyrite	-	2
Total	100	100

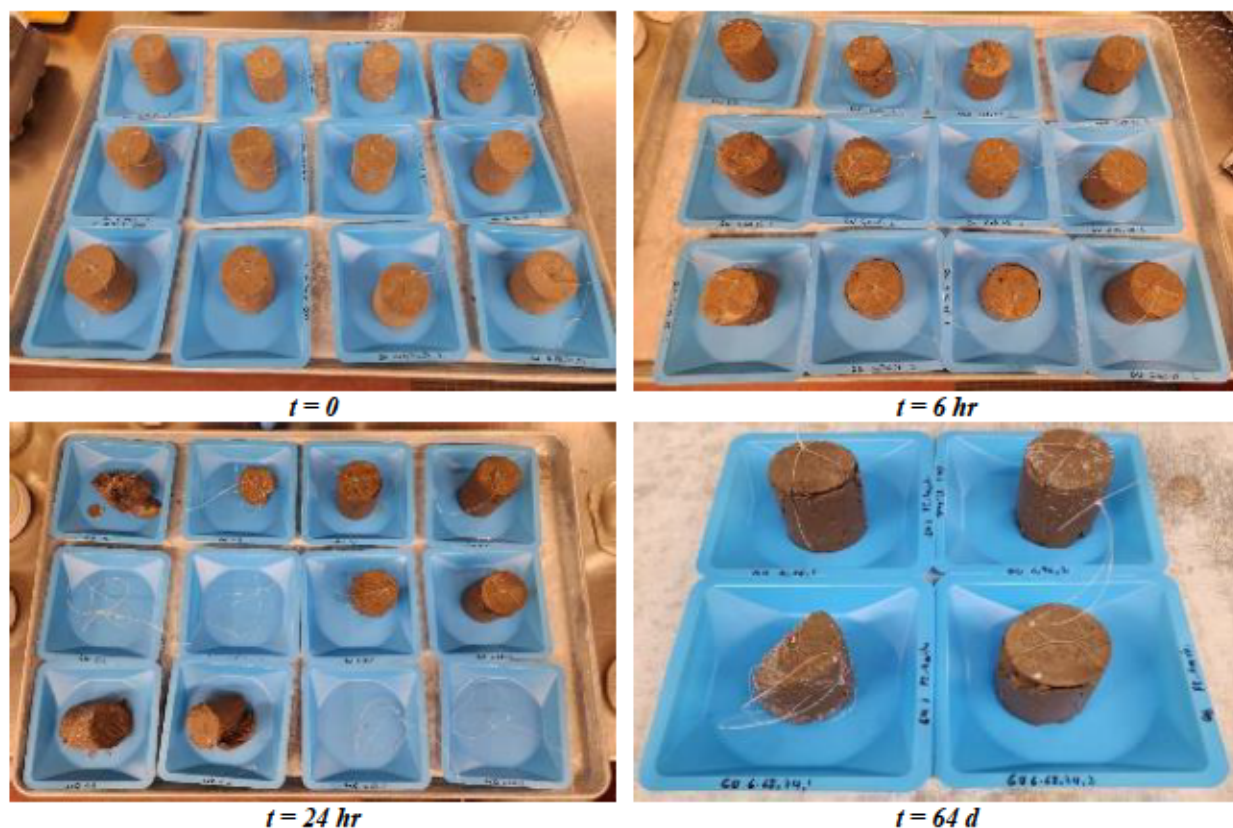


Figure D.1 A view of the samples (with a diameter of 5.2 cm and a length of about 5 cm) after various time intervals (start of the analysis and after 6 hr, 24 hr, and 64 days)

Table D.T.1 in the supplementary materials provides a summary of the total calculated mass (E^*) of arsenic, calcium, and sulfate leached, expressed as the emission of mass per unit of external surface area during each leachate renewal cycle. In this table, the highest leached mass of each component during the leaching process is bolded. Except for the GU-6-76-28 samples, minimal deviations were observed in the release of elements/ions across duplicated samples. For the four main samples, the highest release of arsenic during a leachate renewal cycle were 61.3 g/m^2 (for GU-6-76-28-1 sample after 16 days), 63.1 g/m^2 (for GU-6-76-28-2 sample after 36 days), 45.8 g/m^2 (for GU-6.68-74-59-1 sample after 24 hours), and 47.6 g/m^2 (for GU-6.68-74-59-2 sample after 36 days). For calcium, the maximum concentrations leached during a leachate renewal cycle were observed after 36 days for all four samples (24.8 g/m^2 for GU-6-76-28-1, 26.0 g/m^2 for GU-6-76-28-2, 21.1 g/m^2 for GU-6.68-74-59-1, and 23.2 g/m^2 for GU-6.68-74-59-2). In the case of sulfate, the highest leached concentrations were 20.4 g/m^2 (for GU-6-76-28-1 sample after 54 hours), 15.9 g/m^2 (for GU-6-76-28-2 sample after 9 days), 22.1 g/m^2 (for GU-6.68-74-59-1 sample after 24 hours), and 17.6 g/m^2 (for GU-6.68-74-59-2 sample after 9 days).

The influence of pH and EC on the hydration process and leaching of components in CPB samples is widely acknowledged (Fan et al., 2010). The release of arsenic, calcium, and sulfate and the evolution of the pH and EC for the four samples that endured the entire leaching process sample at various time intervals are presented in Figure D.2. It is noteworthy that while the measured pH may not precisely correspond to the porewater pH due to concentration gradients, it serves as an approximate representation of the pore solution pH (Bull, 2019). As illustrated in Figure D.2, all CPB samples displayed pH values within the range of 9.2 to 10, with GU-6-76-28 samples exhibiting lower pH values compared to GU-6.68-74-59 samples, which have a slightly higher binder content. The maximum observed difference occurred after four days, with a pH variation of more than 0.5 units between these two sets of samples. The pH of the DI water used for the leaching process was 5.8. In all samples, the ongoing dissolution of cementitious phases (Hamberg, Maurice, et al., 2018) and the continuous generation of OH^- during the cement hydration process (Su et al., 2019) led to an increase in the pH of the TLT leachates. No specific trends were observed for the pH values. For GU-6.68-74-59 samples, the release of As, Ca, and SO_4^{2-} varied with each extraction and did not align with the pH behavior. Conversely, for GU-6-76-28 samples, the changes in As, Ca, and SO_4^{2-} levels appear to be pH-dependent, indicating increased solubility of these components at higher pH values. These findings should be interpreted with caution given the minor discrepancies observed in pH measurements (Coussy et al., 2011). Despite the low sulfur contents in the tailings and ATRW (0.52% and 0.25% for tailings and ATRW, respectively), the dissolution of arsenic trioxide and the formation of weak arsenious acid seem to have led to a decrease in leachate pH, resulting in values lower than 10 during CPB formation and curing (Mohammadi, Demers, Benzaazoua, et al., 2023a). Moreover, the initially low pH of the leachates implies a limited presence of portlandite, suggesting that the primarily dissolved phases are likely C-S-H (Coussy et al., 2011). In contrast to the current study, previous research documented relatively higher leachate pH levels and reduced acid formation (with pH values ranging from 10.4 to 11.9) from TLT tests conducted over leaching periods of up to 64 days on CPBs containing low sulfide tailings (Coussy et al., 2011; Y Taha et al., 2021). The pH level plays a critical role in influencing the mobility of metals within the cement matrix (Dell'Orso et al., 2012). The trend observed suggests that metals tend to be highly mobile at low pH levels. As the pH approaches neutral to slightly alkaline, the mobility of metals decreases, and with a pH that is very alkaline, mobility tends to increase (Bull, 2019).

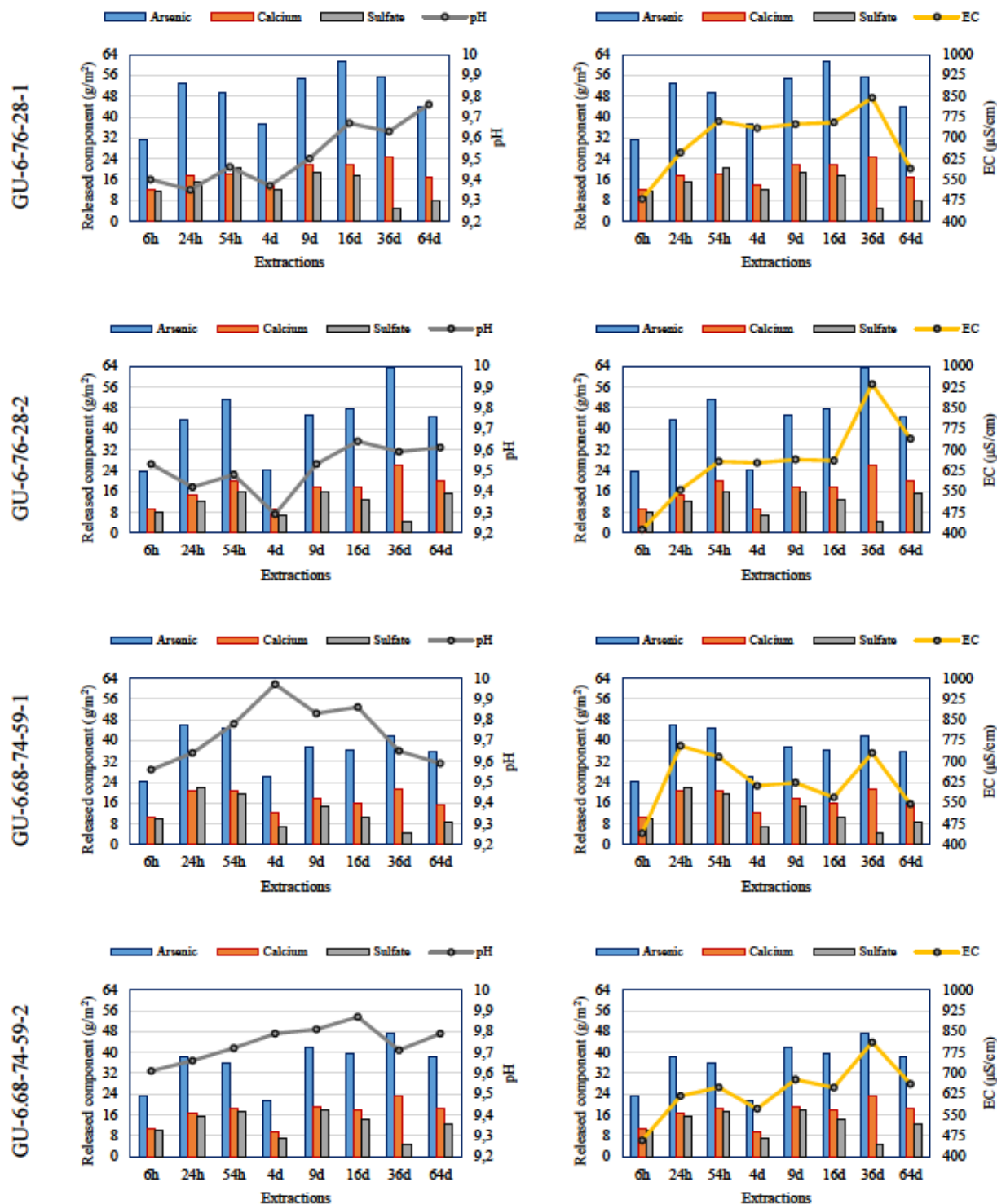


Figure D.2 Variations in released arsenic, calcium, and sulfate concentrations in relation to pH and EC during each TLT extraction

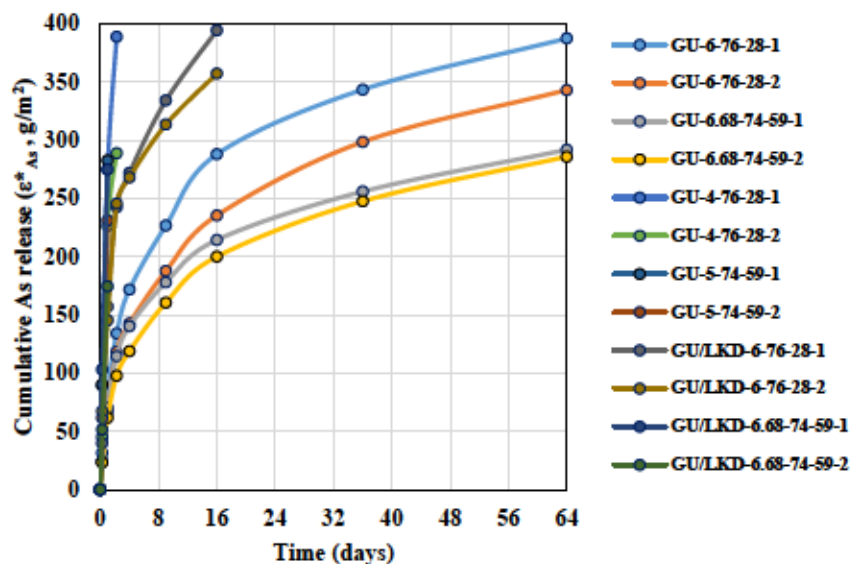
The EC of leachates ranged from 412 to 935 $\mu\text{S}/\text{cm}$ for GU-6-76-28 samples and from 441 to 811 $\mu\text{S}/\text{cm}$ for GU-6.68-74-59 samples across all leaching periods. The variations in EC for all four

samples exhibited a consistent pattern. Except for GU-6.68-74-59-1 sample, EC of all leachates appeared to increase during the initial three cycles (6-54 hours), followed by a slight drop in the fourth interval (after 4 days). Subsequently, EC values peaked at 36 days and then gradually decreased. Overall, all samples displayed low EC values, a fact supported by the concentrations of leached Na^+ , K^+ , and Mg^{+2} . With the exception of Ca^{+2} and SO_4^{-2} , the released concentrations of other ions were negligible and are therefore not presented in this article. The decline in EC can be attributed to the reduction in the release of water-soluble ions, associated with the increase in pH, as these ions are anticipated to have a notable impact on conductivity changes (Y Taha et al., 2021; Yassine Taha et al., 2018; Yilmaz et al., 2021), and also observed in previous studies (Hakkou et al., 2008, 2009; Y Taha et al., 2021). The low values may also result from the precipitation of some metal ions combined with OH^- , and the adsorption or stabilization of a large number of ions by C-S-H gel produced during cement hydration (Su et al., 2019).

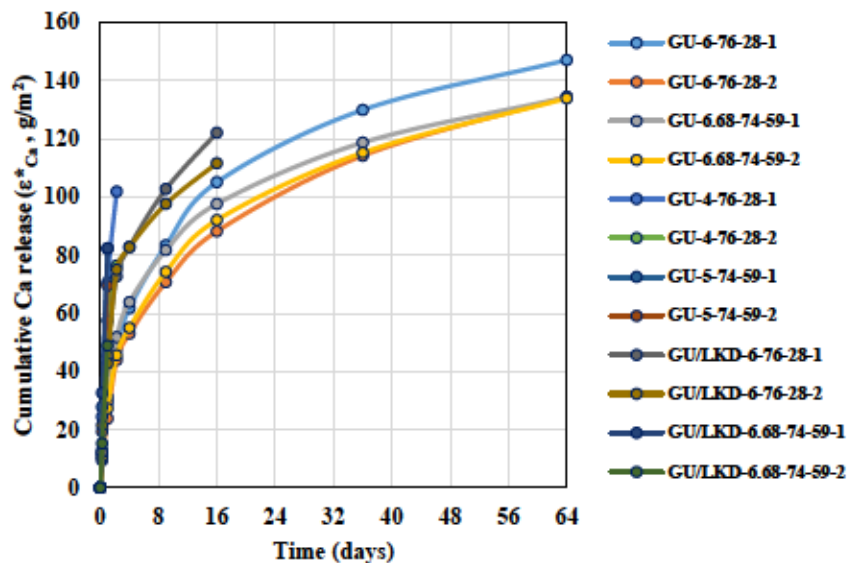
Figure D.3 illustrates the cumulative released content (ϵ^*) of arsenic, calcium, and sulfate during the tank leaching test for all 12 leached samples. For samples that disintegrated during the process, the cumulative leached content was calculated up to the time interval when the samples stopped being in the form of monolithic specimens. Additionally, the leached contents of other elements/ions were significantly lower and are not shown.

The cumulative release of arsenic was more notable in GU-6-76-28 samples compared to GU-6.68-74-59 samples. However, the rate of release, indicated by the slope of the graph, for arsenic in these four samples was lower than in other samples, even though the other samples did not maintain their integrity until the end of the process. The trend in the progression of As-release from GU-6-76-28 and GU-6.68-74-59 samples indicates that a plateau was not reached. Therefore, the release of As could continue beyond the 64-day leaching period. The cumulative release of calcium was more pronounced in GU-6-76-28-1 samples than in other samples, whereas GU-6-76-28-2 and GU-6.68-74-59 samples exhibited the same cumulative released calcium. The rate of calcium release from these four samples fell within the range of GU/LKD-6-76-28 samples; however, the rest of the samples displayed a higher release rate, even though they could not maintain their integrity until the end of the process. The cumulative calcium release from GU-6-76-28 and GU-6.68-74-59 samples did not reach a plateau. Therefore, calcium release could continue beyond the 64-day period. Sulfate release in the duplicates of GU-6-76-28 exhibited a significant difference, with the SO_4^{-2} release from GU-6.68-74-59 samples being higher than GU-

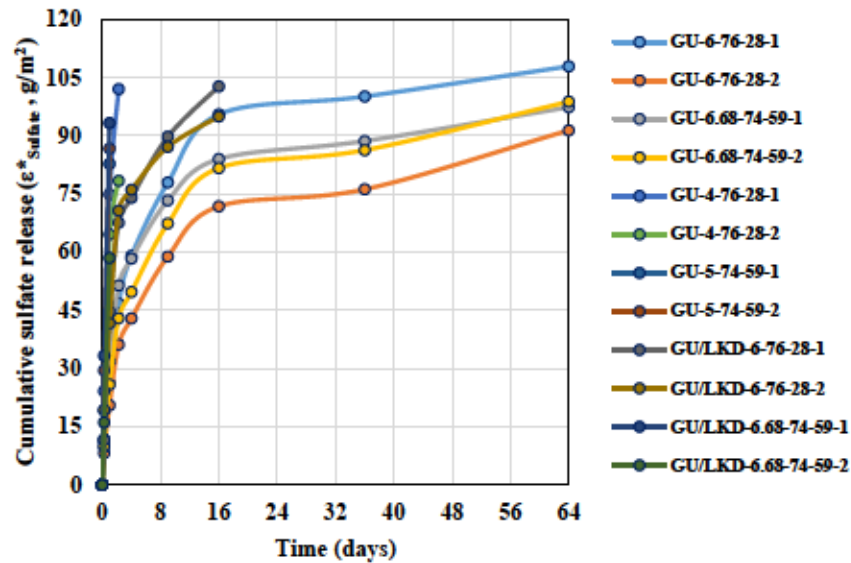
6-76-28-2 and lower than GU-6-76-28-1. These four samples displayed the same trend, and despite the small sulfate release between the 6th and 7th cycles, indicative of equilibrium conditions, an increase in sulfate release was observed in the last cycle of leachate renewal.



a



b



c

Figure D.3 Cumulative released contents of various components during TLT; a) arsenic, b) calcium, and c) sulfate

The lower leaching rates of As, Ca, and SO_4^{2-} in these four samples can be attributed to the formation of reaction gels. This favored the creation of a more compact matrix with higher compressive strength. The mechanical strength played a significant role in the immobilization effects; samples with high strength could maintain their integrity during leaching, reducing the release of As, Ca, and SO_4^{2-} . A higher amount of hydration products typically results in a reduction in pore volume and hydraulic conductivity (Yingliang Zhao, Gu, et al., 2022).

Figure D.4 depicts the depletion curves for two major elements (As and Ca) in the four main samples. For GU-6-76-28-1 samples, 40.8% of total arsenic was leached, followed by GU-6-76-28-2 with 35.4% (64.6% of total arsenic remaining in the sample). This graph confirms that the leached arsenic accounted for 32.8% and 31.6% of total arsenic for GU-6.68-74-59-1 and GU-6.68-74-59-2 samples, respectively, and these values were lower than those for GU-6-76-28 samples. Thus, it can be concluded that arsenic was less bound in GU-6-76-28 samples compared to GU-6.68-74-59 samples. This suggests that while GU-6-76-28 samples exhibited greater strength compared to GU-6.68-74-59 samples, the influence of higher binder content in GU-6.68-74-59 samples on arsenic stabilization was more pronounced than the effects of higher solid content in GU-6-76-28 samples. Furthermore, arsenic was not entirely depleted during the TLT test, suggesting that this contaminant may continue to be released over an extended period under

natural conditions. In terms of calcium depletion, almost all the samples exhibited nearly identical depletion values. The maximum depletion was attributed to GU-6-76-28-1 sample with 17.3% of Ca depletion after 64 days of leaching, followed by GU-6.68-74-59-1 (16.9%), GU-6.68-74-59-2 (16.6%), and GU-6-76-28-2 (15.6%). Typically, the release of calcium may occur due to the dissolution of cementitious calcium-bearing minerals, such as portlandite, calcium aluminates, or calcium-silicate-hydrates (C-S-H), in alkaline pH ranges (Coussy et al., 2011; Glass & Buenfeld, 1999; O Peyronnard et al., 2009). However, the low pH ranges of the current CPBs suggest that portlandite was not significantly present. Therefore, the phases primarily subject to dissolution would be mainly C-S-H. Additionally, the noticeable carbonate content (dolomite) of Giant Mine tailings could dissolve during the leaching test. Hence, the release of calcium is likely the result of both the dissolution of carbonates from the tailings and the cementitious minerals.

The cumulative derived leaching (ε_n) of arsenic, calcium, and sulfate was calculated using Equation D.1 to evaluate the leaching mechanism of these components from CPB samples. The slope (r_c) was calculated as the logarithm of the total mass of the component leached plotted against the logarithm of the time elapsed during the experiment. Slopes below 0.35 suggest either surface wash-off or depletion. In surface wash-off, elements that adhered to the surface are liberated from the CPB, while depletion entails the gradual extraction or removal of a component from the solid material by the percolating leachant. Conversely, a release controlled by diffusion due to concentration gradients should result in a linear plot with a slope ranging between 0.35 and 0.65. Slopes surpassing 0.65 suggest dissolution. The eluate fractions obtained and analysed in periods 1 to 8 were divided into increments that were long enough to establish the leaching mechanism. Table D.T.2 summarizes the calculations performed in accordance with the EA NEN 7375 (EA NEN 7375, 2004). The determination of the leaching mechanism and the quantification of the leaching per component only have meaning if the matrix of the material does not dissolve (EA NEN 7375, 2004). It was verified that the matrix of the samples was not dissolved in the mixtures and the leaching mechanisms of As, Ca, and SO_4^{2-} for each increment was defined. Based on the standard (EA NEN 7375, 2004), increment 2-7 (the first increment) is considered as a “total increment” for the entire leaching test. The first increment for a component is considered as the “leaching mechanism determining increment” for each component. For all the samples, the main mechanism of arsenic, calcium and sulfate leaching was surface wash-off. Moreover, if the increment analysis (Table D.T.2) reveals that in at least two of the increments 2-5 and/or 3-6 and/or

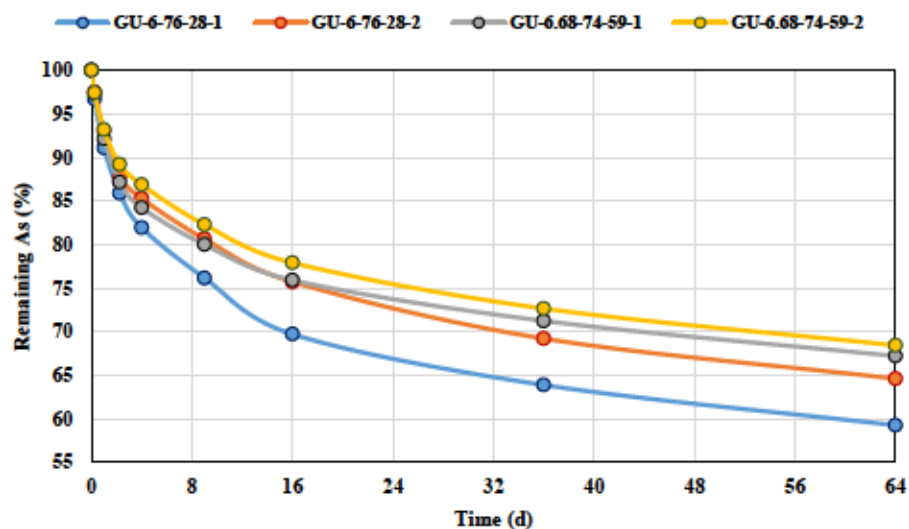
4-7 and/or 5-8, r_c is less than 0.35 and CF is greater than 1.5, then depletion of this component may have occurred. These criteria were validated for all the samples.

While the leaching of arsenic did not reach a plateau and could extend beyond the 64-day leaching period, the decreased amount of leached arsenic after 36 days (as shown in Figure D.2) for all CPB samples suggests that arsenic release slowed down due to the reduced availability of arsenic at the CPB matrix-leaching solution interface. This indicates that the elements available (arsenic, calcium, and other components) on the exposed surfaces were already transferred into solution. Therefore, the most effective strategy to limit arsenic release would be to minimize exposed surfaces to leaching by creating a dense paste with minimal porosity and cracks. One approach could involve increasing the binder content, as it has been observed that less than 1% (0.68%) of binder could decrease arsenic release (up to 9%, as illustrated in Figure 4), while CPBs with lower binder contents failed to stabilize arsenic and maintain their integrity during leaching. A previous experiment was performed to compare the leaching of ATRW alone and as part of CPB, using parallel extraction with 5 different reagents (Mohammadi, Demers, Benzaazoua, et al., 2023b). The results showed that ATRW leached significantly higher As than CPB for all reagents, illustrating the partial positive effect of cement on As stabilization. However, the financial cost of additional binder may limit the feasibility of adding more binders. Other alternatives to reduce arsenic release include lowering the solubility of arsenic by oxidizing As (III) in ATRW to As (V), converting arsenic trioxide to arsenic sulfide (which is 10,000 times less soluble), transforming ATRW into highly stable glass (vitrification), and converting ATRW into iron-arsenic solids ((GMOB), 2023). All these transformed materials could be incorporated into CPB to minimize exposure to the natural environment.

D.3.4 Thermogravimetric analysis

Two primary samples, designated as GU-6-76-28 and GU-6.68-74-59, were selected for thermogravimetric analysis. This analysis was carried out on portions of these samples that had not undergone leaching tests. The DTG and TG graphs presented in Figure D.5 illustrate four distinct temperature ranges characterized by significant weight reduction and noticeable phase changes. The initial peak is observed approximately between 90 and 140 °C, followed by a second peak occurring between 500 and 650 °C. The last two major peaks are noted between 660 and 770 °C. Similar findings can be observed in the literature, where researchers have investigated the thermal properties of both cemented paste backfills and tailings. Water loss from the interlayer and

dehydroxylation of C-S-H take place over a wide temperature range, typically ranging from 50 to 600 °C (Yingliang Zhao, Qiu, et al., 2022). The initial peak (around 90 - 140 °C) and its accompanying weight loss can be attributed to the evaporation of free water and the dehydration of C-(A)-S-H gels, along with potentially other hydrates (Q. Chen et al., 2022; Yingliang Zhao, Gu, et al., 2022; Yingliang Zhao, Qiu, et al., 2022). Such hydrates were significant factors influencing the strength of CPB (H. Jiang, Fall, et al., 2019). This conclusion is drawn from prior findings by the authors, which indicated negligible contents of ettringite and gypsum in these samples. The subsequent peak (500 - 650 °C) could be linked to the dehydroxylation and decomposition of portlandite (Q. Chen et al., 2022; H. Jiang, Fall, et al., 2019). However, unlike the CPBs studied previously (samples without arsenic trioxide), the paste samples containing As_2O_3 exhibited significantly lower pH values than 12 (the optimal pH value for portlandite formation in cementitious mixtures). Consequently, the quantity of portlandite in these samples, and hence the corresponding weight loss peak, is not substantial.



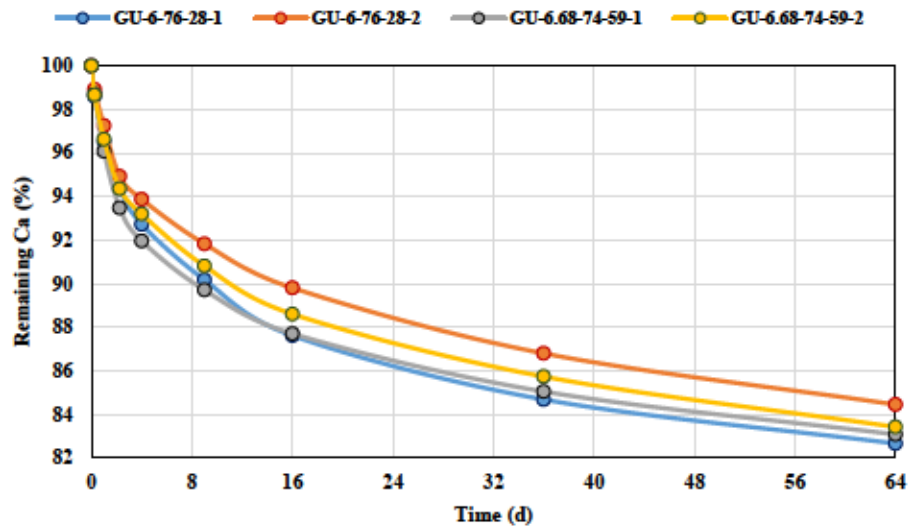


Figure D.4 Depletion curves of main chemical elements (As and Ca) from the leached samples

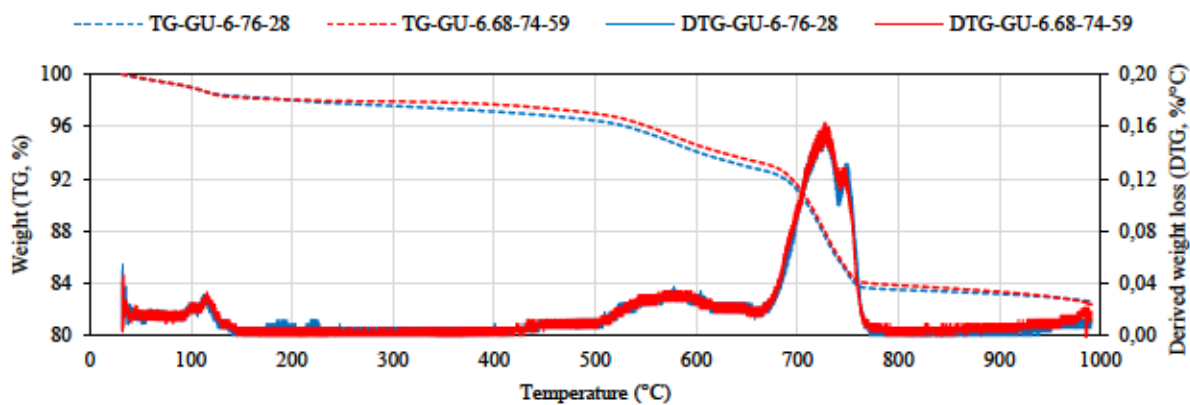


Figure D.5 TG and DTG curves of two main CPB samples

The third peak (and potentially the fourth peak, occurring between 660 and 770 °C) is likely due to the carbonization of calcite and the decomposition of carbonate phases, such as calcite, and other carbonate-based secondary minerals releasing CO_2 (Q. Chen et al., 2022; H. Jiang & Fall, 2017a; Yingliang Zhao, Qiu, et al., 2022). These peaks demonstrate the highest intensity compared to others in these samples. Previous literature has noted that the first peak (C-S-H) and the second peak (CH) demonstrate higher intensities in samples with greater strength, attributed to longer curing times and higher binder contents. It's important to emphasize that both C-S-H phases and portlandite contribute to the strength of CPB samples. The lower intensities of these peaks suggest that these phases were not extensively formed or consumed during the hydration process.

Additionally, in the current samples, there is no significant difference in the intensities of the second peak (CH decomposition), while the intensities of the third and fourth peaks are higher in the GU-6.68-74-59 sample. This indicates that increasing the binder content did not result in the formation of more portlandite, likely due to the presence of arsenic trioxide and the resulting lower pH conditions. The results of UCS tests (Mohammadi, Demers, Beier, et al., 2023) also indicate that the GU-6.68-74-59 sample (UCS = 472 kPa) exhibited slightly lower strength compared to the GU-6.76-28 sample (UCS = 491 kPa). Interestingly, longer curing times and higher binder contents did not yield higher strength in the GU-6.68-74-59 sample. The extra binding agent in GU-6.68-74-59 may have led to the formation of a greater amount of secondary minerals, possibly carbonate-based minerals, which decomposed within the temperature range of 660 to 770 °C. These secondary minerals bound the arsenic, resulting in a lower release of arsenic during the leaching period.

D.3.5 FTIR analysis

Figure D.6 shows the infrared spectra of two CPB samples with the highest strength prepared using GU binder. Both samples showed almost the same peaks; however, small differences in the normalized absorbance were observed. The observed peaks and their related wave numbers and normalized absorbances are shown in Table D.5.

These two CPB samples exhibited two primary spectral peaks, approximately at 459 cm^{-1} and 984 cm^{-1} . The former has been linked to the in-plane bending vibration of Si-O and Al-O (C. Wang et al., 2023), while the latter to Si-O(Al) asymmetric stretching vibration (Y. Feng et al., 2023; F. Zhang et al., 2022). Another peak at 795 cm^{-1} is also attributed to the asymmetric stretching vibration of Si-O(Al) in C-S-H gels (Y. Feng et al., 2023). Structural bonds appearing at 1161 cm^{-1} and 1431 cm^{-1} are attributed to the asymmetric stretching vibration of S-O in SO_4^{2-} and symmetrical vibration of O-C-O in CO_3^{2-} due to the carbonization of the sample in air (S. Chen, Du, Zhang, Yin, et al., 2020; F. Zhang et al., 2022), respectively. The broad band at approximately 3400 cm^{-1} is associated with the asymmetric stretching vibration of absorbed OH^- groups, characteristic of weakly chemically bound water molecules, either surface adsorbed or trapped (Álvarez-Ayuso et al., 2008; Yingliang Zhao, Qiu, et al., 2022). Apart from these bands, two additional peaks were detected at approximately 536 cm^{-1} and 880 cm^{-1} , possibly originating from the out-of-plane bending vibration of Si-O-Si and CO_3^{2-} , respectively (Y. Feng et al., 2023). Lastly,

the spectral peak identified at 675 cm^{-1} correlates with the stretching vibration of SiO_6 (Sun, Li, et al., 2020). The absence of the band wavelength around 1600 cm^{-1} proves the absence of portlandite (O-H vibrations) in these samples (Yingliang Zhao, Wu, et al., 2022). Furthermore, vibration bands associated with the As-O bond of arsenate molecules are situated within the ranges of $900\text{--}750\text{ cm}^{-1}$ and $500\text{--}400\text{ cm}^{-1}$ (Gomez et al., 2010). However, these interactions are relatively weak compared to other complexes, resulting only in modifications to the intensities of the FTIR bands (Perez Mora et al., 2019). Given the minimal disparities between the two samples, the observed normalized absorbances were also quite similar, with minor distinctions. The most significant variances occurred within the 459 cm^{-1} , 675 cm^{-1} , and 1431 cm^{-1} bands. Specifically, in the first two bands, the GU-6.68-74-59 sample exhibited higher normalized absorbance, while in the last band, it displayed lower normalized absorbance.

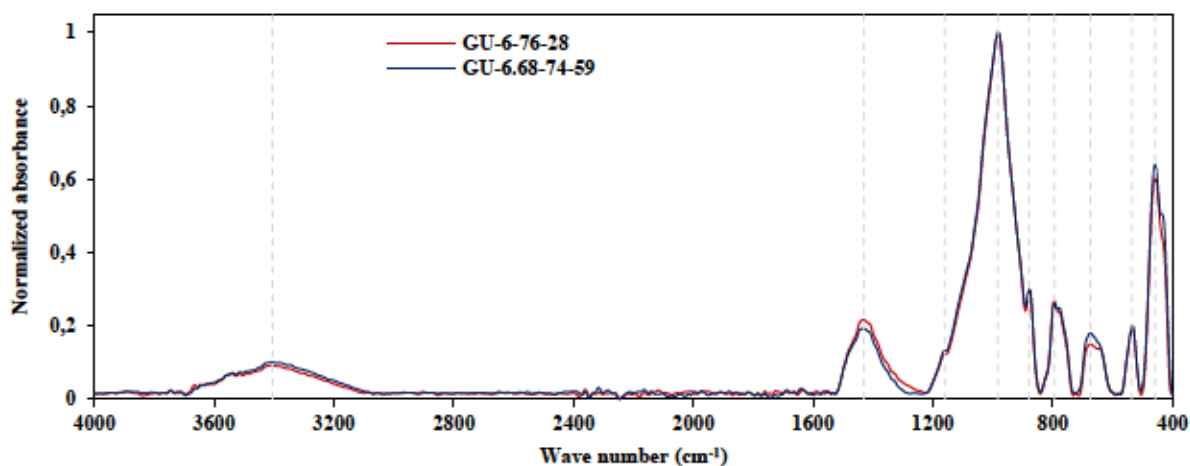


Figure D.6 FTIR spectra of two CPB samples (dashed lines indicate positions of the observed peaks)

Table D.5 The observed peaks and their corresponding normalized absorbances

Peak (cm^{-1})	459	536	675	795	880	984	1161	1431	3400
Normalized absorbance (GU-6-76-28)	0.601	0.199	0.150	0.269	0.295	1.000	0.123	0.217	0.092
Normalized absorbance (GU-6.68-74-59)	0.639	0.198	0.179	0.262	0.298	1.000	0.133	0.193	0.101

D.3.6 XAS analysis

Four samples with varying binder and solid contents—GU-4-76-28, GU-6-76-28, GU-6.68-74-59, and GU/LKD-6-76-28—were selected for XAS analysis. The XANES absorption spectra for all measured samples, including CPB samples and reference compounds, are presented in the left panel of Figure D.7. The white line (the peak with intense absorption in the near edge) position was found at 11870 eV for each sample, indicating As is predominantly found in the +3 oxidation state. However, a slight peak at 11874 eV suggests the presence of minor As^{5+} . Consequently, 3-4 reference materials were allowed during linear combination fitting that were refined or eliminated as needed according to the Hamilton test (Downward et al., 2006). The linear combination fitting (LCF) process revealed similarities between GU-6-76-28 and GU-6.68-74-59, and between GU/LKD-6-76-28 and GU-4-76-28. Overall, all spectra could be fit with the same reference spectra, however the proportions vary. Differences between E-space and $\chi(k)$ space LCF within each sample were also apparent, indicating potentially different local and extended structures.

The local structure of As in GU-6-76-28 and GU-6.68-74-59 could be fit with approximately 90% schneiderhohnite [$\text{Fe}^{2+}\text{Fe}^{3+}_3\text{As}^{3+}_5\text{O}_{13}$], while GU/LKD-6-76-28 and GU-4-76-28 were best fit with ~80% schneiderhohnite. The balance in all samples was best represented by arsenolite [$\text{As}^{3+}_2\text{O}_3$]. However, while these references provided the best fit, this method alone for identifying components can be inconclusive. Both arsenolite and schneiderhohnite contain arsenite, and together with the white line energy, indicate the majority of the As in the sample is in the +3 state. The inclusion of schneiderhohnite, suggests As-Fe bonding may play an important role in the local structure.

In contrast, $\chi(k)$ space details the EXAFS region, or the atomic neighbors beyond the central arsenic atom. Here, LCF detailed the inclusion of approximately 12-15 weight percent yukonite [$\text{Ca}_3\text{Fe}^{3+}(\text{AsO}_4)_2(\text{OH})_3 \cdot 5\text{H}_2\text{O}$] in all samples. GU-6-76-28 and GU-6.68-74-59 required approximately 20 and 45 weight percent arsenolite and schneiderhohnite, while samples GU-4-76-28 and GU/LKD-6-76-28 required approximately 40 weight percent each of arsenolite and schneiderhohnite. The addition of yukonite in the $\chi(k)$ LCF suggests that As-Ca bonding may also be important. Importantly, the included reference materials were select minerals and commercial compounds, and therefore do not represent all possible compounds in the cement field.

Consequently, additional EXAFS modeling was completed and illustrates more accurate and precise atomic interactions.

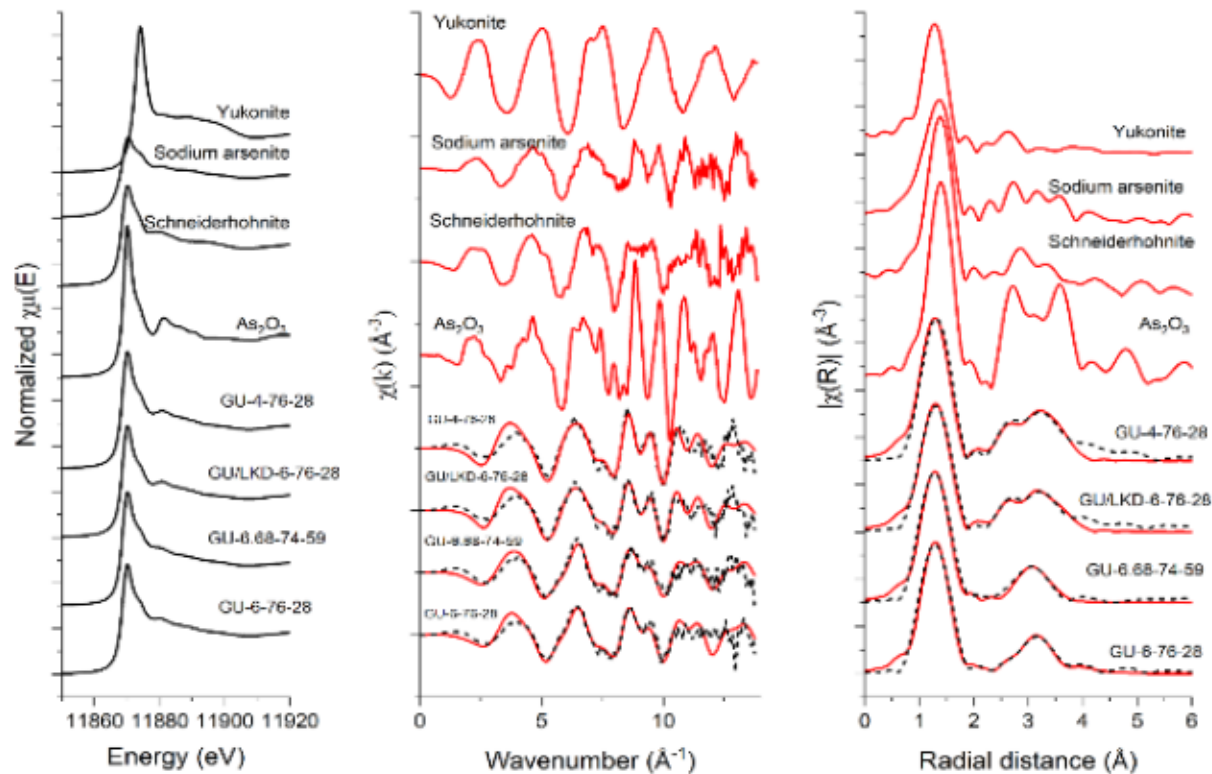


Figure D.7 (a) Normalized As K-edge XANES spectra for four CPB samples and reference compounds; (b) Measured (solid red lines) and modelled (black dashed lines) $\chi(k)$ EXAFS spectra (c) Measured (solid red lines) and modelled (black dashed lines) magnitudes of Fourier transformed EXAFS spectra

In the EXAFS region, all samples contained a first shell oxygen peak at approximately 1.78 Å, where the As is bound to ~3-4 oxygen atoms. Samples GU-6-76-28 and GU-6.68-74-59 contained an As-As bond at ~3.55 Å, however GU-6-76-28 required two additional As-Fe paths at distances of 3.37 Å and 4.65 Å for an accurate fit. This indicates that As in GU-6-76-28 remained bound to Fe, suggesting that the ATRW remained intact, did not dissociate, and As was not bound to other elements such as calcium. ATRW is known to contain substantial As-Fe compounds, with more than 30 g/kg of iron. The As in GU-6.68-74-59, however, may have dissolved out of the ATRW, but remained isolated from other elemental components as an As-O based compound. This suggests a partial breakdown of the ATRW, but no atomic incorporation into the paste mixtures. In these two samples, no chemical bond between As and Ca was observed; however, they exhibited the highest UCS. This indicates that the hydration products responsible for the strength gain may

not contain As-Ca compounds. Furthermore, these products might not stabilize the arsenic or reduce its leaching, despite providing the reasonable strength. The modelling of samples GU/LKD-6-76-28 and GU-4-76-28 (samples with lower strength) illustrate an As-Fe path at $\sim 3.34 \text{ \AA}$, As-Ca at $\sim 3.66 \text{ \AA}$, and an As-As path at 3.87 \AA . These models most likely suggest that there has been some As-Ca bonding in the CPB samples. While the initial ATRW does contain bulk Ca (5.36 gr/kg), As-Ca bonds were not observed in the initial ATRW, which suggests that new bonding between As and Ca may or may not be due to the hydration process. In other words, the bonding between As and Ca has not contributed to the strength gain or porosity evolution resulting from the formation of the hydration products.

D.3.7 CT scan analysis

Four samples were chosen for observation, namely GU-6-76-28 and GU/LKD-6-76-28, which had the highest UCS values, and GU-4-72-28 and GU/LKD-5-70.64-59, which exhibited the lowest UCS values. The objective was to examine the porosity and its effects on the differences in CPB strength. Each core segmented into three regions, representing the pore space, high-density (arsenic-containing) materials and the remaining sediment matrix. Based on this segmentation, 2D greyscale images were obtained along the center of each core in both longitudinal and transverse profiles (Figure D.8). In these figures, the locations of the ROI in the center of each core are also shown.

The information presented in the 2D slice image has limitations and may not adequately illustrate the initial pore and high-density materials development within the CPB structure (Fang et al., 2023). Additionally, while larger dimensions may capture greater variability, offering a more comprehensive depiction of the entire core, they can also result in reduced spatial resolution (Reedy & Reedy, 2022). Therefore, Dragonfly software was employed to reconstruct the 3D image of ROIs, as depicted in Figure 9, which displays the 3D representation of each ROI as well as the distinct 3D structures of pores and high-density materials.

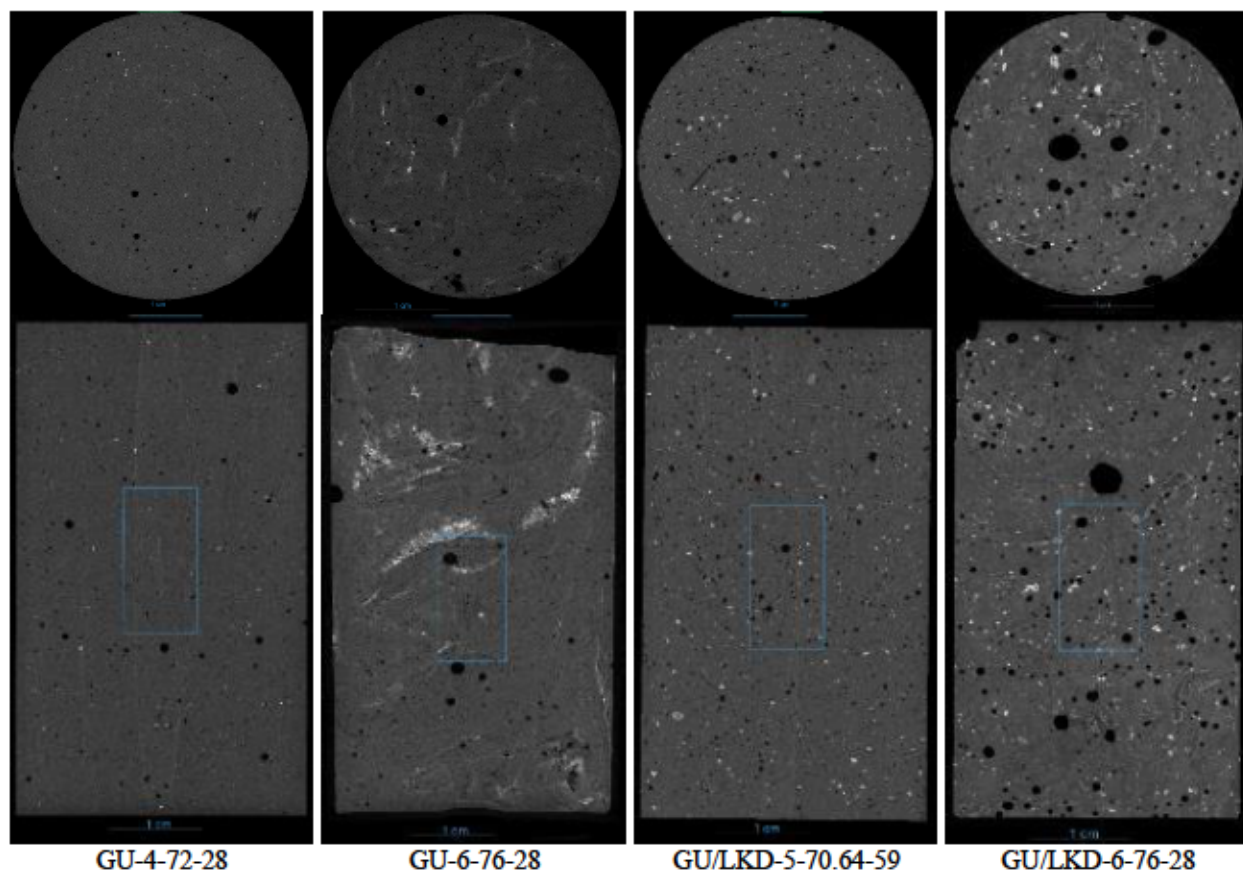
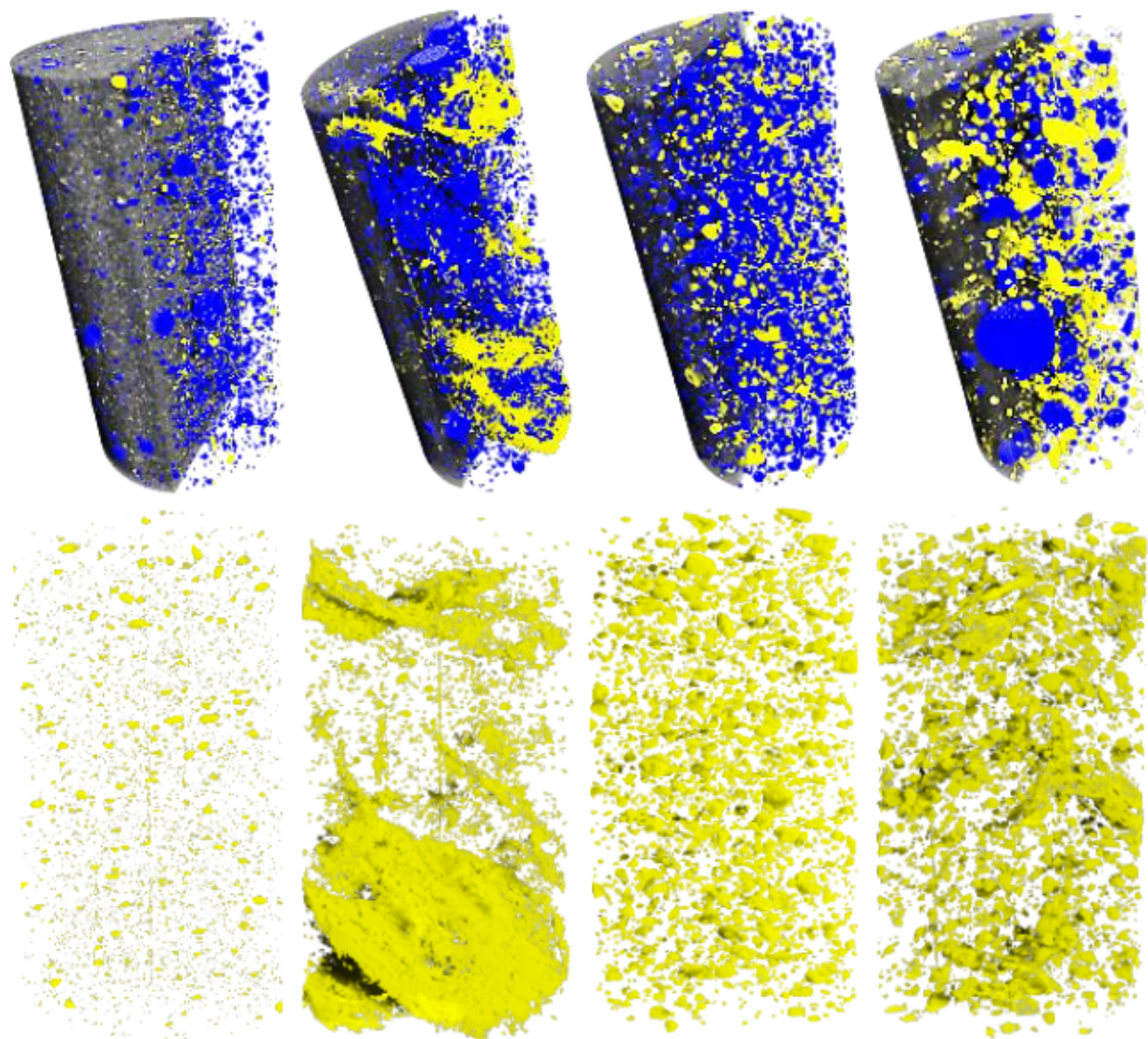


Figure D.8 2D greyscale images along the center of each core in both longitudinal and transverse profiles, with the location of ROIs

Pore structure in the ROIs of the studied CPBs were represented by some scalars such as pore volume, mean Feret diameter and sphericity. The main statistical parameters such as minimum, median, mean, and maximum values of these scalars are presented in Table D.6. The histograms that provide more information on the distribution of these scalars are presented in Figures D.F.1-D.F.3 (supplementary materials) for pore volume, mean Feret diameter and sphericity, respectively.



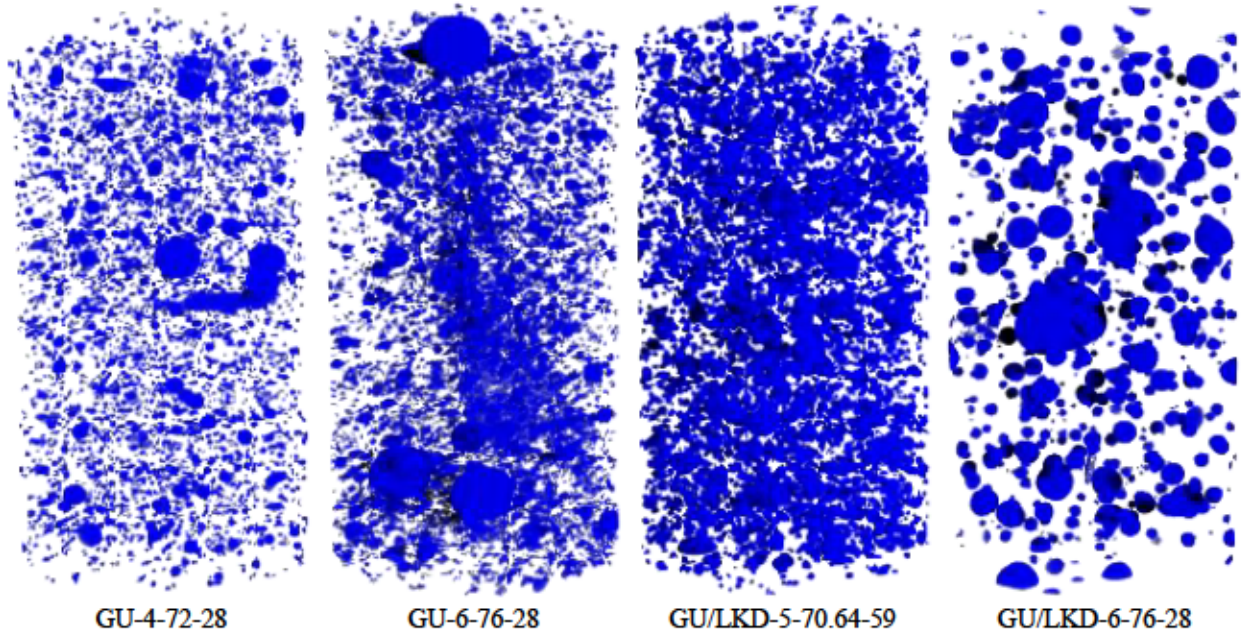


Figure D.9 3D model of each ROI cut in half lengthwise, displaying each segmented region individually (gray: sediment matrix, yellow: high-density materials, blue: pores)

In all samples, the median (as the middle value) and minimum volume of pores were the same. It proves that half of the pores had the minimum volume. Both GU-4-72-28 and GU/LKD-5-70.64-59 samples showed much lower pore volumes as the maximum pore volume for these samples (with the lowest strength) was much lower than two other samples with the highest strength. These observations could be visually approved considering the 3D ROIs of the samples as well as the longitudinal and transverse sections. Considering the statistical analysis of mean Feret diameter of the pores, the CPB samples with lower strength revealed smaller pores (i.e. mean values were lower). These results are in accordance with the pore volume of these samples. Quantification of pore shape properties in CPB samples was done by calculating the sphericity of the pores based on the Equation D.2. Although the samples with lower strength showed smaller pore structure, the sphericity of the pores in these samples was higher. The GU-6-76-28 with the highest UCS showed the lowest sphericity with a mean value of 0.72.

Table D.6 The statistical parameters related to the main scalars of the pores in ROI of the CPB samples

Scalar	Statistical parameter	GU-4-72-28 (UCS = 154 kPa)	GU-6-76-28 (UCS = 491 kPa)	GU/LKD-5-70.64-59 (UCS = 24 kPa)	GU/LKD-6-76-28 (UCS = 214 kPa)
Pore volume (mm ³)	Minimum	0.0003	0.001	0.0003	0.00001
	Median	0.0003	0.001	0.0003	0.00001
	Mean	0.005	0.02	0.01	0.07
	Maximum	0.81	2.68	0.87	8.38
Mean Feret diameter (mm)	Minimum	0.09	0.14	0.10	0.03
	Median	0.15	0.23	0.19	0.30
	Mean	0.18	0.28	0.23	0.34
	Maximum	1.57	6.08	3.97	2.79
Sphericity (-)	Minimum	0.22	0.11	0.30	0.28
	Median	0.89	0.74	0.88	0.81
	Mean	0.85	0.72	0.86	0.81
	Maximum	1.03	0.98	1.00	1.02

In this paper, the pores with volume $<0.001 \text{ mm}^3$ are defined as small pores, $0.001 \text{ mm}^3 \leq \text{volume} < 0.1 \text{ mm}^3$ as medium pores, and $0.1 \text{ mm}^3 \leq \text{volume} < 10 \text{ mm}^3$ as large pores. The variation in the number of different volumes of pores is shown in Figure 10. The distribution of pore numbers in the ROIs of the four CPB samples is not similar in pattern. Except for the GU-4-72-28 sample, most of the observed pores were in the range of medium pores (99.34% for GU-6-76-28, 67.57% for GU/LKD-5-70.64-59, and 61.72% for GU/LKD-6-76-28). More than 63% of the pores of GU-4-72-28 sample were in the range of small pores and less than 1% of the pores were in the range of large pores in all samples except GU/LKD-6-76-28 (9.47%). It's worth mentioning that the number of observed pores in the central ROIs of these four samples was as follows: GU-4-72-28 (4430 pores), GU-6-76-28 (2434 pores), GU/LKD-5-70.64-59 (5223 pores) and GU/LKD-6-76-28 (781 pores). To categorize the pores based on their shape, individual pores with varying sphericity were extracted from the histograms. Pores tend to shift from being spherical to acquiring irregular shapes. As the pore deviates from a perfect sphere (with a sphericity value of 1), its irregularity increases, approaching a value closer to 0 (J. Li et al., 2023). There are three main types of pores: spherical or quasi-spherical pores with a sphericity between 0.8 and 1. Semi-

spherical pores that have a sphericity of 0.5–0.8 and non-spherical pores with a sphericity less than 0.5. The distribution of the pores based on their sphericities is shown in Figure D.10. Except some relatively large pores in sample GU-6-76-28, the sphericity of the pores was in the range of 0.2-1 for all CPB samples.

Figure D.11 shows the relationship between pore volume and sphericity in the central ROIs of CPBs. For the case of GU samples, although the sphericity of the pores decreased with an increase in the pore volume, the results show that the dispersion of pore sphericity values increased with an increase in pore volume. For the GU/LKD-5-70.64-59 sample, the sphericity of the pores decreased as the pore volume increased; however, small changes were observable in the distribution of the sphericity of the pores with an increase in the pore volume. In GU/LKD-6-76-28 sample, the smallest and the largest pores showed the highest sphericities, whereas the mid-range pores (with volume between 0.001 and 0.1 mm³) revealed lower sphericities.

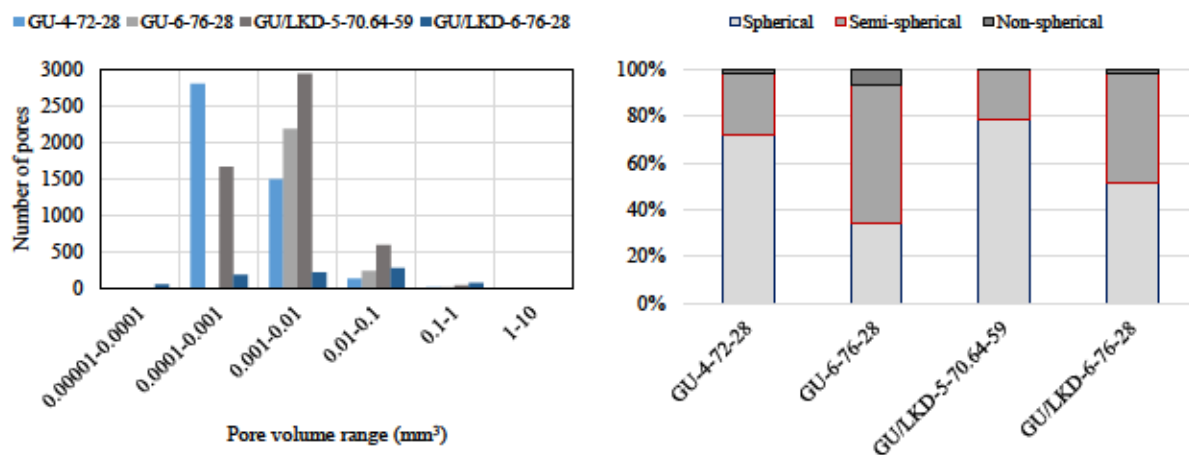


Figure D.10 The number of different volumes of pores (left) and the distribution of the sphericity of the pores (right)

Considering the visual disparities among the samples, a notable difference emerged in the distribution of high-density materials within the ROIs. Particularly in the case of GU-6-76-28, the sample with the highest UCS, the concentration of high-density materials appears notably higher compared to other samples. In samples with lower strength, most high-density materials were dispersed randomly as individual particles, whereas in high-strength samples (specifically the GU-6-76-28 sample), these materials were organized in a continuous manner. Hence, it can be deduced that the formation and random dispersion of these arsenic-containing high-density materials during

the preparation and curing process could be the primary factors contributing to the increased strength in these CPB samples. However, the unique pore characteristics of these samples (larger and more irregular pores) may have led to elevated arsenic release during the leaching process.

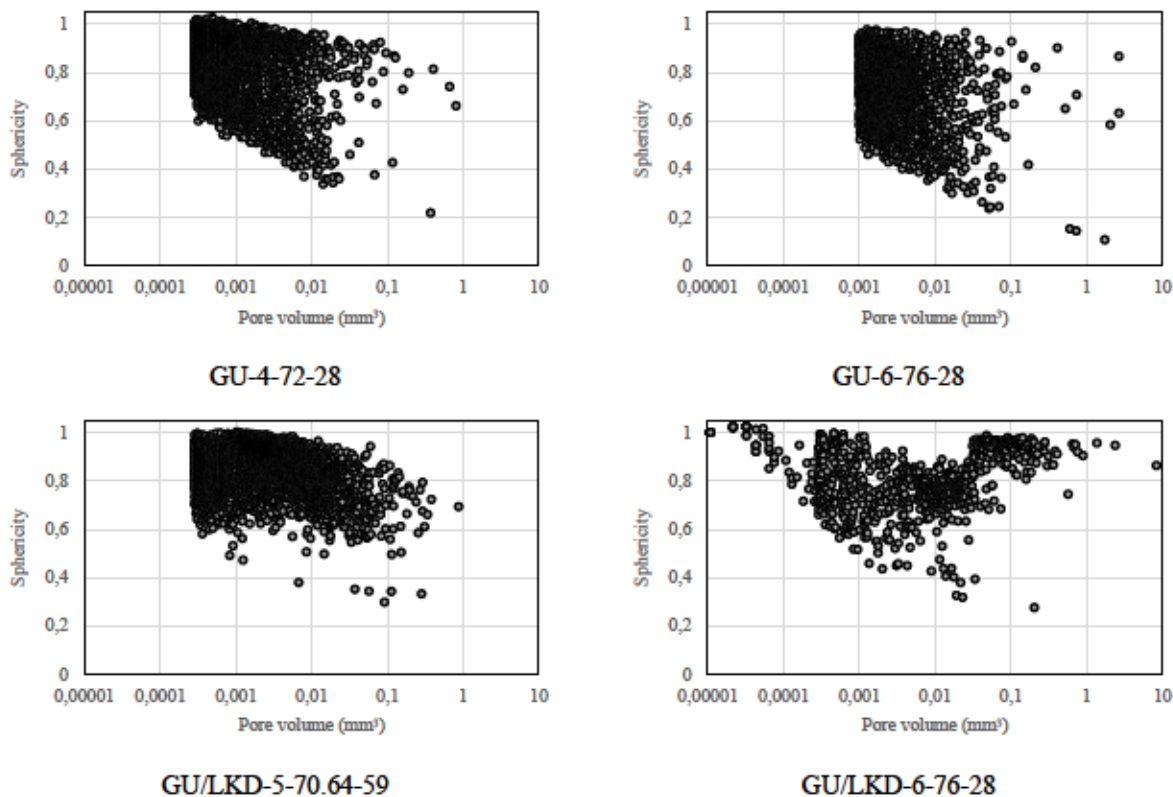


Figure D.11 The relationship between sphericity and pore volume

D.4 Conclusions

The primary goal of this study was to examine the stability of arsenic-bearing compounds formed within CPB cementitious matrices and to elucidate the mechanisms of arsenic release in CPB. To achieve this, CPB samples with various mix designs were prepared using ATRW and tailings from the Giant Mine. Based on UCS test results, certain samples were selected for monolithic tank leaching tests to assess the behavior and stability of arsenic in CPBs under dynamic conditions. Additionally, the microstructure of selected CPBs was analyzed using TGA, FTIR, XAS, and CT to investigate the relationship between microstructure and leachability. The findings and conclusions from this investigation are as follows:

- The selected samples for TLT included both high-strength and mid-strength samples. However, only the high-strength samples (GU-6-76-28 and GU-6.68-74-59) withstood the entire leaching process, while the others disintegrated before the process ended.
- The pH of the collected leachates during TLT was below 10, indicating that the dissolution of ATRW lowered the paste's pH and prevented the formation of some hydration products, such as portlandite, ettringite, and gypsum. For GU-6-76-28 samples, changes in As, Ca, and SO_4^{2-} levels appeared to be pH-dependent. However, for GU-6.68-74-59 samples, these changes did not align with pH variations. The EC of all leachates was very low due to the negligible concentrations of ions other than calcium.
- The leaching of arsenic, calcium, and sulfate did not reach a plateau and could extend beyond the 64-day leaching period. Moreover, the primary leaching mechanism of arsenic in the CPB samples studied was determined to be surface wash-off and, to some extent, depletion.
- Thermogravimetric analysis revealed that the formation of C-S-H gels and portlandite was not prominent in ATRW-containing CPBs. The primary weight loss observed was attributed to the carbonization of calcite and the decomposition of carbonate phases.
- The XAS analysis indicated that the high-strength samples exhibited consistent behavior, with no observed chemical bonding between arsenic and other elements, notably calcium. This suggests that the hydration process and subsequent strength gain in these samples did not lead to arsenic stabilization through the formation of As-Ca containing materials. However, in samples with lower strength, some As-Ca bonding was observed, although it did not result in strength gain or arsenic stabilization.
- The CT analysis results indicated that the higher the strength, the greater the pore volumes observed. Additionally, the presence of spherical and semi-spherical pores was significantly reduced in samples with the highest UCS.
- While incorporating ATRW as a partial replacement for tailings in CPBs may yield adequate strength and meet on-site requirements, the leaching of arsenic from CPBs containing ATRW could be significant and deemed unacceptable.

Declaration of competing interest

The authors declare that they do not have any identifiable financial conflicts of interest or personal associations that might have appeared to exert an influence on the research presented in this paper.

Acknowledgements

The authors would like to thank the “Giant Mine Oversight Board (GMOB)”, “NSERC (Alliance Grant)”, and the “Unité de Recherche et de Service en Technologie Minérale (URSTM)” for their financial and technical support. They also extend special thanks to the University of Alberta Permafrost Archives Science Laboratory for their assistance with CT scanning and image processing. This work was also supported by the Canadian Light Source, which is supported by the Canada Foundation for Innovation, the Natural Sciences and Engineering Research Council of Canada (NSERC), the University of Saskatchewan, the Government of Saskatchewan, Western Economic Diversification Canada, the National Research Council Canada, and the Canadian Institutes of Health Research.

Supplementary Tables

Table D.T.1 The calculated leached mass of each component (E^*_i) during each leaching period
(bolded values show the maximum leached mass)

Sample	Element/ion (g/m ²)	6h	24h	54h	4d	9d	16d	36d	64d	
GU-4-76-28-1	Arsenic	89.3	185.6	114.1						
GU-4-76-28-2		45.1	181.3	62.5						
GU-5-74-59-1		90.1	192.7							
GU-5-74-59-2		61.5	169.6							
GU-6-76-28-1		31.4	53.2	49.6	37.6	55.0	61.3	55.5	44.0	
GU-6-76-28-2		23.9	43.3	51.0	24.3	45.1	47.8	63.1	44.6	
GU-6.68-74-59-1		24.1	45.8	44.5	25.9	37.6	36.5	41.5	35.9	
GU-6.68-74-59-2		23.2	38.4	36.0	21.2	41.7	39.6	47.6	38.3	
GU/LKD-6-76-28-1		39.9	117.3	85.4	29.5	62.2	60.2			
GU/LKD-6-76-28-2		67.3	78.1	100.2	22.5	45.5	43.8			
GU/LKD-6.68-74-59-1		103.0	172.0							
GU/LKD-6.68-74-59-2		51.5	122.9							
GU-4-76-28-1		Calcium	24.4	46.1	31.3					
GU-4-76-28-2			12.8	44.6	18.9					
GU-5-74-59-1	27.7		54.4							
GU-5-74-59-2	19.3		50.2							
GU-6-76-28-1	11.8		17.6	18.3	14.0	21.6	21.7	24.8	17.1	
GU-6-76-28-2	9.4		14.3	20.1	9.1	17.7	17.5	26.0	20.3	
GU-6.68-74-59-1	10.3		20.8	20.6	12.0	17.8	15.9	21.1	15.6	
GU-6.68-74-59-2	10.8		16.4	18.3	9.4	19.2	17.8	23.2	18.7	
GU/LKD-6-76-28-1	12.2		33.1	27.4	10.1	19.9	19.4			
GU/LKD-6-76-28-2	21.4		21.3	32.2	7.7	14.9	14.0			
GU/LKD-6.68-74-59-1	32.6		49.7							
GU/LKD-6.68-74-59-2	15.2		33.6							
GU-4-76-28-1	Sulfate		24.2	50.7	27.2					
GU-4-76-28-2			11.8	52.8	13.8					
GU-5-74-59-1		19.2	63.6							
GU-5-74-59-2		29.5	57.2							
GU-6-76-28-1		11.3	15.1	20.4	12.3	18.9	17.6	4.6	7.8	
GU-6-76-28-2		8.2	12.3	15.6	6.8	15.9	12.9	4.4	15.2	
GU-6.68-74-59-1		9.7	22.1	19.6	6.9	15.0	10.6	4.6	8.7	
GU-6.68-74-59-2		10.1	15.7	17.1	6.8	17.6	14.3	4.6	12.5	
GU/LKD-6-76-28-1		11.6	33.2	22.8	6.4	15.8	13.0			
GU/LKD-6-76-28-2		19.3	22.3	29.0	5.4	11.1	7.8			
GU/LKD-6.68-74-59-1		33.3	59.9							
GU/LKD-6.68-74-59-2		16.1	42.4							

Table D.T.2 The calculated values include the slopes of the regression lines (r_c), their associated standard deviations (Sd_{rc}), concentration factors (CF) as well as the mechanisms of leaching for major components in four main samples based on EA NEN 7375 (EA NEN 7375, 2004)

Sample	Increment	Arsenic				Calcium				Sulfate			
		CF	r_c	Sd_{rc}	Mechanism	CF	r_c	Sd_{rc}	Mechanism	CF	r_c	Sd_{rc}	Mechanism
GU-6-76-28-1	Increment 2-7	19265.72	0.153	0.067	Surface wash-off	1787.93	0.214	0.051	Surface wash-off	148.07	-0.138	0.221	Surface wash-off
	Increment 5-8	19978.53	-0.041	0.151	Depletion	1937.75	-0.002	0.104	Depletion	122.09	-0.553	0.446	Depletion
	Increment 4-7	19180.72	0.087	0.153	Depletion	1825.77	0.154	0.093	Depletion	133.44	-0.516	0.422	Depletion
	Increment 3-6	18836.20	0.234	0.097	Depletion	1717.62	0.226	0.066	Depletion	172.88	0.085	0.105	Depletion
	Increment 2-5	18084.55	0.188	0.062	Depletion	1623.92	0.262	0.078	Depletion	166.63	0.244	0.170	Depletion
	Increment 1-4	15904.81	0.588	0.129	Diffusion	1402.36	0.589	0.102	Diffusion	147.62	0.594	0.140	Diffusion
GU-6-76-28-2	Increment 2-7	16956.29	0.202	0.076	Surface wash-off	1586.19	0.241	0.085	Surface wash-off	113.31	-0.091	0.196	Surface wash-off
	Increment 5-8	18579.91	0.119	0.102	Depletion	1850.69	0.204	0.059	Depletion	121.16	-0.141	0.564	Depletion
	Increment 4-7	16699.39	0.322	0.091	Depletion	1596.15	0.356	0.064	Diffusion	100.10	-0.295	0.433	Depletion
	Increment 3-6	15581.78	0.156	0.202	Depletion	1462.95	0.132	0.209	Depletion	128.10	0.146	0.220	Depletion
	Increment 2-5	15166.67	0.140	0.180	Depletion	1391.46	0.205	0.217	Depletion	126.62	0.221	0.218	Depletion
	Increment 1-4	13202.28	0.583	0.222	Diffusion	1203.29	0.578	0.215	Diffusion	107.28	0.518	0.223	Diffusion
GU-6.68-74-59-1	Increment 2-7	14311.96	0.078	0.052	Surface wash-off	1640.41	0.095	0.046	Surface wash-off	131.50	-0.252	0.149	Surface wash-off
	Increment 5-8	14028.78	0.077	0.084	Depletion	1600.41	0.066	0.049	Depletion	97.52	-0.312	0.387	Depletion
	Increment 4-7	13107.80	0.107	0.082	Depletion	1519.59	0.135	0.040	Depletion	93.03	-0.299	0.355	Depletion
	Increment 3-6	13383.25	0.053	0.121	Depletion	1510.14	0.031	0.104	Depletion	130.29	-0.052	0.251	Depletion
	Increment 2-5	14244.76	0.061	0.113	Depletion	1620.33	0.080	0.115	Depletion	159.02	-0.077	0.231	Depletion
	Increment 1-4	12996.50	0.576	0.194	Diffusion	1449.68	0.606	0.199	Diffusion	145.84	0.467	0.327	Diffusion
GU-6.68-74-59-2	Increment 2-7	13854.40	0.189	0.054	Surface wash-off	1580.87	0.205	0.066	Surface wash-off	126.94	-0.126	0.198	Surface wash-off
	Increment 5-8	15472.20	0.070	0.070	Depletion	1792.70	0.107	0.053	Depletion	122.61	-0.279	0.515	Depletion
	Increment 4-7	13887.77	0.248	0.113	Depletion	1582.50	0.285	0.101	Depletion	108.25	-0.276	0.466	Depletion
	Increment 3-6	12820.95	0.236	0.134	Depletion	1472.35	0.190	0.170	Depletion	139.56	0.167	0.257	Depletion
	Increment 2-5	12713.42	0.180	0.112	Depletion	1439.68	0.198	0.160	Depletion	143.10	0.149	0.238	Depletion
	Increment 1-4	11003.00	0.513	0.178	Diffusion	1248.35	0.517	0.188	Diffusion	124.34	0.443	0.250	Diffusion

Supplementary Figures

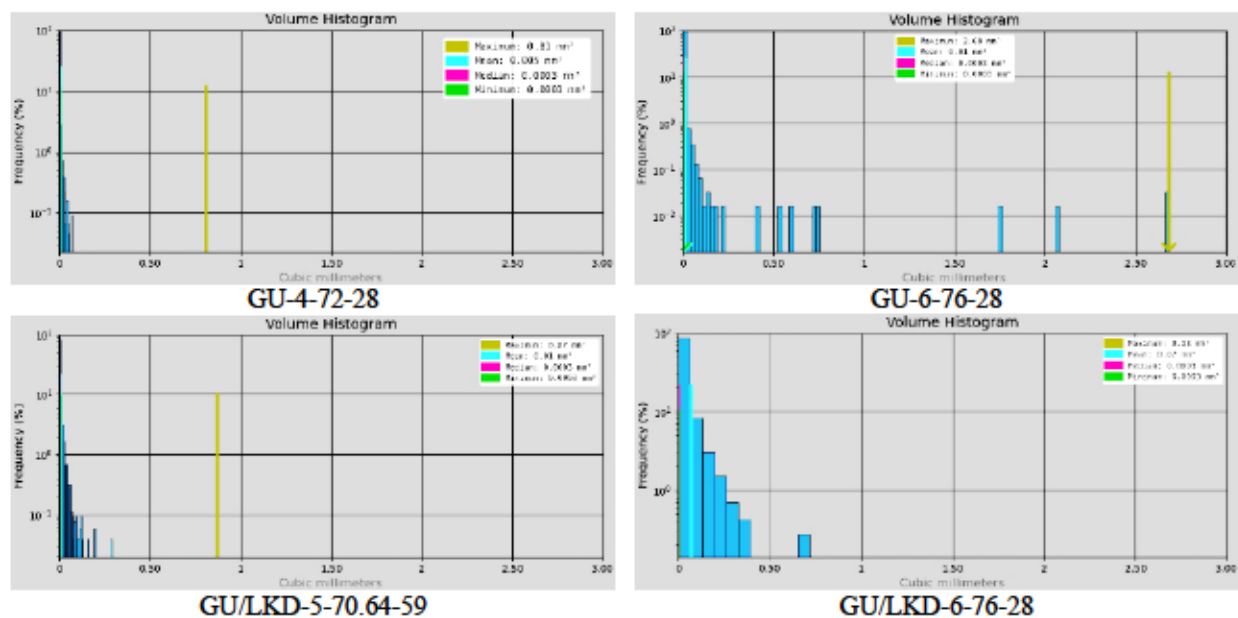


Figure D.F.1 Pore volume histograms of the ROIs of CPB samples

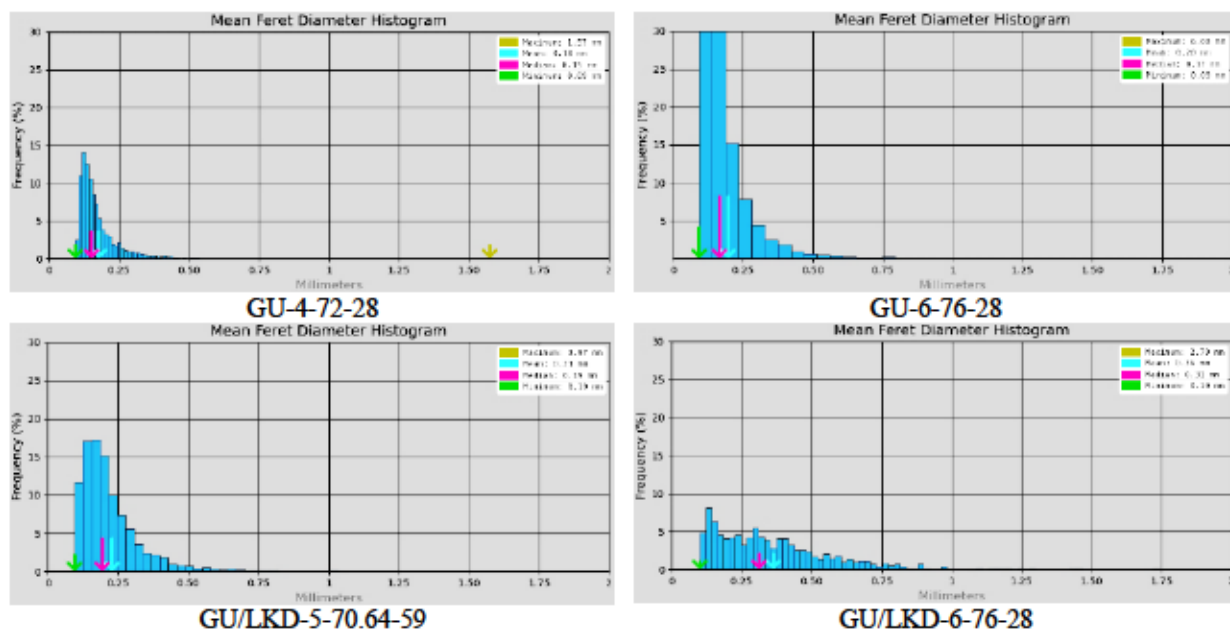


Figure D.F.2 Mean Feret diameter histograms of the ROIs of CPB samples

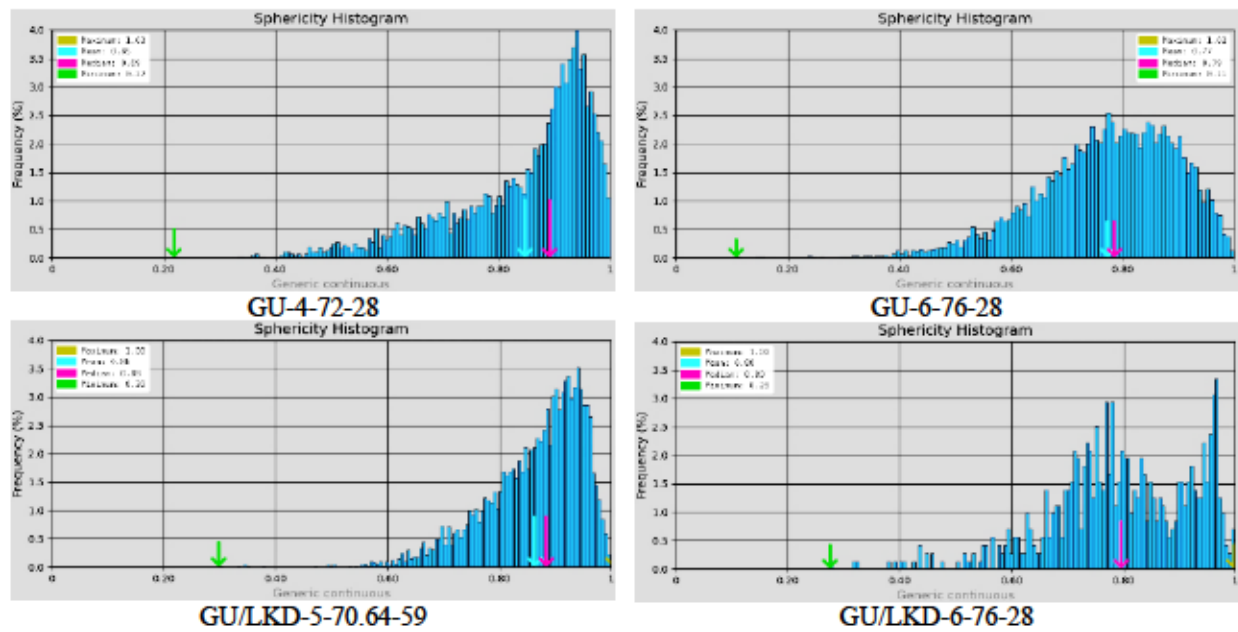


Figure D.F.3 Sphericity histograms of the ROIs of CPB samples

APPENDIX E ARTICLE 4: STUDY OF THE EFFECTS OF ARSENIC TRIOXIDE ROASTER WASTE DUSTS ON THE MECHANICAL BEHAVIOUR OF CEMENTED PASTE BACKFILLS

This article was presented and published in the proceedings of Paste 2023: 25th International Conference on Paste, Thickened and Filtered Tailings. This article was submitted on 12 February 2023 and presented on 29 April 2023. This appendix reproduces the full text.

Amirhossein Mohammadi^{1*}, Isabelle Demers^{1,2}, Nicholas Beier³, Mostafa Benzaazoua¹

1. UQAT-Polytechnique Research Institute on Mines and the Environment, Rouyn-Noranda, QC, Canada
2. Canada Research Chair on Integration of the Environment in the Mine Life Cycle, Rouyn-Noranda, QC, Canada
3. Department of Civil and Environmental Engineering, University of Alberta, Edmonton, AB, Canada

Keywords

Arsenic trioxide dusts, arsenic stabilization, cemented paste backfill (CPB), unconfined compressive strength (UCS), response surface methodology (RSM)

Abstract

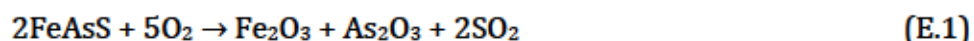
More than 237,000 metric tonnes of arsenic trioxide roaster waste dusts have been stored underground in the abandoned Giant Mine (Yellowknife, NWT). This waste arsenic trioxide material is approximately 60% arsenic, which is hazardous to both people and the environment. Long-term management of this waste is complex due to its large quantity, physical characteristics, and current storage conditions. Currently, the frozen block method was selected for the stabilization of the arsenic. However, because of climate change and decline in the permafrost as well as the current toxic form of dusts, there are some critical concerns about the long-term performance of this technology. Therefore, more permanent arsenic stabilization techniques must be considered. Among these techniques, cemented paste backfill (CPB) technology as a high-density slurry

* Corresponding author; amirhossein.mohammadi@uqat.ca

mixture of binding materials, dewatered tailings, roaster waste dusts, and mixing water, can be considered as a potential arsenic trioxide stabilization method. In this research, the effects of the addition of the arsenic trioxide dusts (10% wt.) within CPB on the mechanical strength of the cured pastes were evaluated. The CPB samples were prepared using general use (GU) cement and a mixture of GU cement and lime kiln dust (LKD) as binding agents based on the mix designs proposed by the response surface methodology (RSM). The solid content, binder type and dosage, and curing time were selected as the variables and the unconfined compressive strength (UCS) of the samples was chosen as the response of the modelling. The results of the experiments and analyses revealed that the incorporation of arsenic trioxide dusts within the CPB results in the reduction in the strength of the pastes. However, increasing binder dosage, as well as solid content, could compensate for this adverse effect. Moreover, the CPB prepared using GU cement showed higher strength than the ones incorporating GU cement/LKD.

E.1 Introduction

The former Giant Mine is located adjacent to Great Slave Lake, about five kilometres north of Yellowknife, in the Northwest Territories, Canada. This mine is an abandoned gold mine operated from 1948 until 1999. The Giant Mine ore had a complex mineralogy. Most of the gold occurred as extremely fine-grained particles that are “refractory,” i.e., mainly encased and hosted within the crystal structure of arsenopyrite (FeAsS) and to a lesser degree arsenian pyrite (Fe(As,S)₂). An oxidation process was required to convert the dense sulphide grains into porous structures and expose the gold to cyanide leaching solutions (Northwest Consulting Limited 2003). The roasting process in the Giant Mine produced SO₂ emissions, and As-rich vapours from arsenopyrite concentrates that precipitated as arsenic trioxide (As₂O₃)-rich dust from the oxidation of As (-I) to As (III) (Bromstad et al., 2017b):



The collected arsenic trioxide dust was pumped underground into ten purpose-built chambers and five mined-out stopes. Over 237,000 metric tonnes of arsenic trioxide were collected as a by-product of roasting and more than 17 million tonnes of tailings were also produced (Silke, 2009, 2013).

The arsenic trioxide dust is approximately 60% arsenic, hazardous to both people and the environment and can dissolve in water (SRK, 2002). Long-term management of the arsenic trioxide dust located at Giant Mine is complicated due to its large quantity, physical characteristics (dust-like), and current storage conditions (subsurface chambers and stopes). Because of this complexity, several different technologies, or methods, were assessed to determine the most promising stabilization option (Arcadis, 2017). The “Frozen Block” method was judged to be the most appropriate management approach available at the time. It is a remedial method currently being implemented at the Giant Mine that isolates the dust by freezing the ground surrounding the dust chambers and stopes. This method was considered as an interim solution for a maximum of 100 years; however, due to the climate change and decline in the permafrost, the current toxic form of the arsenic trioxide dust requires a more permanent solution (Arcadis, 2017; SRK, 2002).

Significant environmental impacts of the surface storage of hazardous and sulphide-rich wastes under atmospheric conditions (i.e., AMD formation and release of the heavy and toxic metals as well as contamination of the soils and groundwaters) may be significantly attenuated by safely placing such wastes underground (Yilmaz et al., 2013), the process being known as backfilling (Ercikdi, Kesimal, et al., 2009). Mine backfill refers to waste materials, such as waste rock, deslimed, and whole mill tailings, quarried and crushed aggregates placed into underground mined voids for either disposal and/or to perform some engineering function (Benzaazoua et al., 2002). Generally, there are three types of backfilling methods: hydraulic fill, rock fill, and cemented paste backfill (CPB). In recent years, the cemented paste backfill has gained worldwide acceptance, especially in Canada, to serve as an essential part of the underground mining operations (Ercikdi et al., 2014; Ercikdi, Kesimal, et al., 2009). CPB technology is known as a high-density slurry mixture of dewatered tailings, binding agents, and water, thickened to obtain a non-settling character for transport into mined cavities. CPB could provide environmental advantages by reducing the reactivity potential of sulphides and by stabilizing pollutants. The hydraulic binders can react during hydration with metals and metalloids to form stable compounds by precipitation (Coussy et al., 2011). Mechanical strength, workability, environmental performance, hydraulic conductivity, and durability are the most important design criteria of cemented paste backfills structures. These parameters depend on the physical, chemical, and mineralogical properties of the mine tailings and other wastes, mixing waters, additives, binder types, and their proportions (Benzaazoua et al., 2002; B. D. Thompson et al., 2012). Unconfined compressive strength (UCS)

can be considered the most common parameter used to determine the stability of the CPB structure due to the simplicity and low cost of the UCS test (Q. Chen, Zhang, Fourie, Chen, et al., 2017).

In previous studies, the cemented paste backfill technology has been successfully engaged to stabilise arsenic-bearing materials (Bull & Fall, 2020a, 2020b; Coussy et al., 2011; Coussy, Benzaazoua, et al., 2012; Hamberg et al., 2015a, 2015b; Y. Zhang et al., 2019a). However, there is a lack of experience in stabilizing arsenic trioxide using cemented paste backfills. Based on the available knowledge on stabilization mechanisms of arsenic in cemented paste backfills, it seems that the Giant Mine arsenic trioxide dust could be incorporated into cemented paste backfills for stabilizing this hazardous waste material as well as decreasing its long-term leaching potential. So, the object of the current research is to assess the feasibility of incorporating arsenic trioxide roaster waste dust into cemented paste backfill for arsenic stabilization. The mechanical behaviour of the CPB prepared with different binders at various binder and solid contents to obtain the most appropriate binder(s) and mixing ratios was assessed and response surface methodology (RSM) was used to define the mixing design and obtain the optimal recipes. Mechanical strength was used in this study as an indicator of cementation reactions that favour contaminant stabilization.

E.2 Materials and methods

E.2.1 Materials

The main materials for the preparation of the cemented paste backfills in this study consist of two binding agents, mine tailings, arsenic trioxide dusts, and deionized water. Tailings samples were taken from the north pond of the Giant Mine site. A trench was dug 1.8 – 2.1 m before taking the sample. After transferring the tailings to the laboratory, they were oven-dried at 40 °C for 48 hours before carrying out the preparation, homogenisation, and characterisation processes. GU Portland cement supplied by Bomix (Quebec, Canada) was used as the main binding agent for the preparation of the cemented paste backfill. A mixture of GU cement and lime kiln dust (LKD) with a 50/50 ratio was also used as the binding agent. Arsenic trioxide dusts from the Giant Mine were used as the arsenic source. The dust samples were sent to the laboratory in eight different samples from different stopes and chambers. After some preparation and homogenisation processes on the received samples, a mixed representative sample was obtained for the characterisation and utilisation in CPB samples. Deionised water was used for the preparation of cemented paste backfill samples to eliminate the effects water chemistry on CPB behaviour.

E.2.2 Methods

E.2.2.1 Initial characterisation

The specific gravity (G_s) of tailings and dust, GU cement, and LKD was measured using an automatic gas pycnometer (Ultracyc 1200e, Quantachrome Instruments). The particle size distribution (PSD) of tailings and dust was analysed by a laser diffraction particle size analyser (Malvern Mastersizer 3000) to obtain the size corresponding to 10%, 30%, and 60% by weight of passing (D_{10} , D_{30} , and D_{60} , respectively) and the coefficients of uniformity (C_u) and curvature (C_c). The specific surface of tailings and dust was analysed by Brunauer-Emmett-Teller (BET) method using liquid nitrogen (Gemini 2375, Micromeritics). The chemical composition of the GU cement and LKD as well as the dust and tailings were obtained by X-ray fluorescence spectrometry (S2 Ranger, Bruker AXS). Inductively Coupled Plasma Atomic Emission Spectroscopy (ICP-AES) was used to determine the concentrations of the elements such as Al, As, Ca, Cd, Fe, K, Mg, Mn, Na, and S. Inductively Coupled Plasma Mass Spectrometry (ICP-MS, Agilent 7800) was used to measure the concentration of antimony (Sb) and the chemical composition of the deionised water after acidification using a 2% v/v of HNO_3 . The solid samples were digested with HNO_3 , HF, and HCl by heating in the microwave with specific care to avoid arsenic volatilisation. Boric acid (H_3BO_3) was added after microwave digestion to neutralise the residual HF. Mineralogical analysis of the samples was done with X-Ray Diffractometry (XRD). XRD measurements were matched with reference databases using DIFFRAC.EVA software (version 5.2.0.3) and quantification are done by Rietveld-TOPAS software (version 4.2).

E.2.2.2 Preparation and curing of the cemented paste backfills

The mix designs (recipes) of the cemented paste backfill samples (amount of required water, tailings, binders, and arsenic trioxide dust) were prepared considering the specific gravity of the tailings, binders, arsenic trioxide dust, as well as the solids, dusts, and binder contents of the mixtures. The calculations of the required amount of each ingredient were based on the following equations:

$$\text{Solid content (\%)} = C_w = \frac{100 \times M_{\text{dry-solid}}}{M_{\text{dry-solid}} + M_{\text{water}}} \quad (\text{E.2})$$

$$\text{Binder content (\%)} = B_w = \frac{100 \times M_{\text{dry-binder}}}{M_{\text{dry-tailings}} + M_{\text{dry-As}_2\text{O}_3}} \quad (\text{E.3})$$

$$\text{As}_2\text{O}_3 \text{ dust content (\%)} = D_w = \frac{100 \times M_{\text{dry-As}_2\text{O}_3}}{M_{\text{dry-tailings}} + M_{\text{dry-As}_2\text{O}_3}} \quad (\text{E.4})$$

where: M_{water} = Mass of water in the paste, $M_{\text{dry-tailings}}$ = dry mass of tailings, $M_{\text{dry-binder}}$ = dry mass of binder, $M_{\text{dry-As}_2\text{O}_3}$ = dry mass of arsenic trioxide dusts, and $M_{\text{dry-solid}} = M_{\text{dry-tailings}} + M_{\text{dry-As}_2\text{O}_3} + M_{\text{dry-binder}}$. These calculations were based on the preparation of 3 cylindrical samples for each recipe (or run number) with the dimension of 2×4 inches (diameter × height, 50.8×101.6 mm) considering 20% additional materials to compensate for the possible losses during preparation and molding.

To decrease the number of samples, the response surface methodology (RSM) was used to define the appropriate recipes. RSM is a collection of mathematical and statistical methods that determine operating conditions and regression model equations using quantitative data obtained from relevant experiments. Central composite design (CCD) based RSM was used to optimise CPB recipes with the help of the Design-Expert software (version 13). Table E.1 shows the proposition of the RSM method by considering solid content, binder content, and curing time as the factors, and the strength (UCS) of the samples as the response. Considering two different binder combinations and three replicates for each recipe, at least 120 CPB samples were prepared and tested.

For the preparation of cemented paste backfills, a Hobart mixer with a capacity of 4.8 L was used. All the preparations were conducted in the laboratory. A half of the water was mixed with the binder in the bowl of the mixer using a hand spatula. Then, the tailings and the arsenic trioxide dust were added to the mixture, and they were mixed thoroughly in the bowl. The remaining water was added progressively to the mixture and mixing was continued for up to 5 minutes to achieve a homogenous paste; then it was cast into the three plastic molds in a single layer with minimum delay after mixing, because of the rapid initial setting of the samples. After molding, to expel the air bubbles from the pastes, the cylinders were rodded 25 times using a steel rod with a diameter of 9.53 mm (3/8 in). The prepared undrained cylindrical samples were labeled, sealed by a lid, and stored in a humidity chamber (approximately 90% relative humidity and 20 °C) to cure for up to 111 days before testing. The conditions remained unchanged over the curing period to ensure the comparability of tests and limit the number of influencing factors.

The strength evolution in the pastes was assessed by performing UCS tests on three separate specimens for each recipe (based on Table E.1). UCS tests were carried out based on the ASTM C39 standard by a computer-controlled mechanical press with a normal loading capacity of 50 kN and a 1 mm/min displacement rate, and the stress-strain data were recorded for each sample. The samples were taken out of molds after 7, 28, 59, 90, and 111 days of curing, according to the RSM (Table E.1). The base and top of the cylinders were flattened parallel to the plates of the mechanical press before the UCS tests. The UCS parameter corresponds to the maximum stress value before failure during the compression test. All the measurements were carried out in triplicate and the average values were taken as the final compressive strengths. The UCS test results were used to select the most appropriate binding agent and the mix designs with the highest strength.

Table E.1 The proposition of the CPB recipes by the RSM method

Run	Factor 1	Factor 2	Factor 3
	Solid content	Binder content	Curing time
	%	%	day
1	70.64	5	59
2	72	4	28
3	72	4	90
4	72	6	28
5	72	6	90
6	74	3.32	59
7	74	5	7
8	74	5	59
9	74	5	59
10	74	5	59
11	74	5	59
12	74	5	59
13	74	5	59
14	74	5	111
15	74	6.68	59
16	76	4	28
17	76	4	90
18	76	6	28
19	76	6	90
20	77.36	5	59

E.3 Results and discussions

Results of the initial characterisation of the materials and mechanical strength of the CPB samples are presented in this section.

E.3.1 Initial characterization

The specific gravity of the materials used for the preparation of the cemented paste backfill was 2.77, 3.45, 3.05, and 2.79 for the tailings, arsenic trioxide dusts, GU cement, and LKD, respectively. These values were used for the calculation of the required materials to obtain the CPB samples based on the mix design proposed in Table E.1. Figure E.1 depicts the cumulative PSD of the tailings and arsenic trioxide dust and Table E.2 presents some widely used indicators associated with PSD. The solid matrix of the CPB samples were made with 90% by mass of tailings and 10% by mass of dusts which is finer and more uniform than the tailings. The PSD results showed that more than 94% of the dusts and 53% of the tailings are less than 20 μm in diameter and most of the arsenic trioxide dusts grains are in the range of 1 to 20 μm . The specific surface (S_s) of the tailings and arsenic trioxide dusts are also shown in Table E.2. The specific surface area of the tailings was about half of the specific surface area of the dusts sample. Arsenic trioxide dusts are much finer than the tailings and their specific surface is also higher.

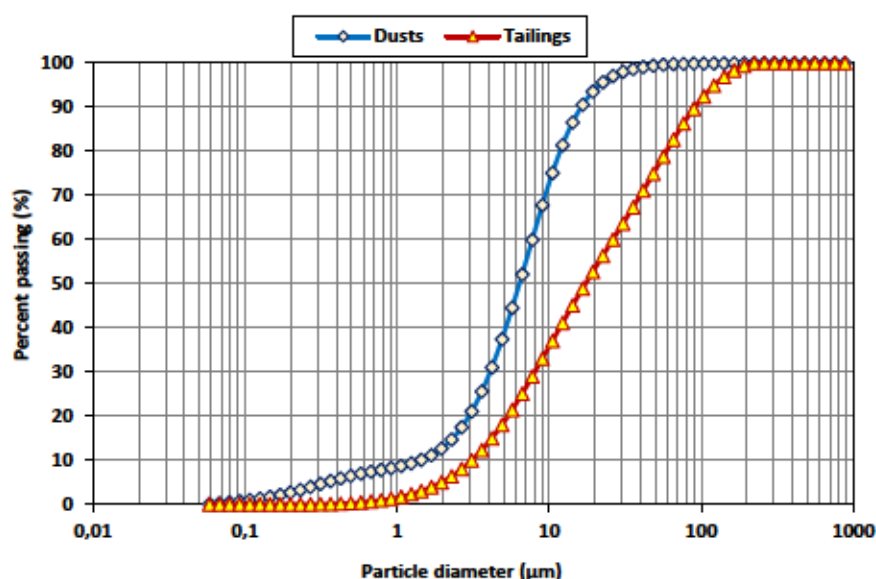


Figure E.1 Particle size distribution of the dusts and tailings samples

The results of the XRF analysis on the tailings, arsenic trioxide dusts, GU cement, and LKD are shown as oxides in Table E.3. Both GU cement and LKD contain high amounts of calcium oxide which is higher for the LKD (more than 75%), whereas GU has a higher amount of SiO_2 . The content of other oxides in these binders is in the same range. Table E.4 presents the results of the ICP analysis on the dusts and tailings sample. As can be seen, more than 57% of the dusts sample

was composed of arsenic. The amounts of neutralizing elements such as Ca and Mg in the tailings were significantly higher than the amount of the sulphur (about 0.5%), and the tailings can be suspected as non-acid generating tailings.

Table E.2 Results of the particle size analysis, specific gravity, and specific surface area of the representative dust and tailings samples

Parameter	Unit	Tailings sample	Dust sample
$C_u = D_{60}/D_{10}$	(-)	8.46	5.44
$C_c = D_{30}^2/(D_{60} * D_{10})$	(-)	0.80	1.51
$U = (D_{90}-D_{10})/D_{50}$	(-)	5.06	2.33
Specific surface area	m ² /g	3.59	7.04

Table E.3 The results of the XRF analysis of the dusts, tailings, and binders

Sample	SiO ₂	Al ₂ O ₃	Fe ₂ O ₃	MgO	CaO	Na ₂ O	K ₂ O	TiO ₂	P ₂ O ₅	MnO	SrO	SO ₃	ZnO	V ₂ O ₅	LOI	Sum
	%															
Dusts	4.67	1.91	3.99	8.59	0.66	0.25	0.33	0.15	0.02	0.05	<0.01	<0.01	<0.01	<0.01	79.4	100.1
Tailings	48.5	9.86	10.9	5.63	8.53	0.44	1.45	0.76	0.08	0.16	<0.01	<0.01	<0.01	0.03	12.4	98.8
GU	17.2	4.84	3.26	2.30	64.3	0.30	1.80	0.13	0.32	0.03	0.29	5.15	0.03	<0.01	<0.01	99.99
LKD	7.94	4.70	1.39	0.90	75.8	0.20	1.88	0.46	0.16	<0.01	0.07	6.16	<0.01	<0.01	<0.01	99.68

Table E.4 Chemical analysis results of the dusts and tailings samples by ICP-AES and ICP-MS method (mg/kg)

Element	Al	As	Ca	Cd	Fe	K	Mg	Mn	Na	S	Sb
Dusts	10730	571500	5360	7625	31720	2597	3756	128	541	2463	16782
Tailings	47000	2747	56260	25	72520	10550	29780	1092	3039	5192	118

The mineralogical analysis of the dust samples revealed that more than 86% of the dust sample was comprised of arsenolite (As₂O₃). The arsenic trioxide in the dust samples was formed during the roasting process, therefore, its mineralogical characterization is slightly different from naturally occurring arsenic trioxides. The tailings sample mainly includes quartz, chlorite, dolomite, and muscovite, and can be considered as a typical non-acid generating tailings.

E.3.2 CPB mechanical strength results

Table E.5 presents the results of UCS tests on the CPB samples prepared based on the proposed mix design using the GU and GU/LKD binders. Based on these results, it can be concluded that

the samples prepared using GU binder showed much higher strength than the samples prepared by the GU/LKD mixture. The samples with the highest solid content and highest binder content showed the highest UCS. For both GU and GU/LKD binders, the optimal recipe is the CPB sample with 6% of binder and 76% of solid content, which had the highest strength after 90 days and 28 days of curing for the GU and GU/LKD binders, respectively. Note that no specific UCS target was identified for this study. Indeed, the Giant Mine will not mine near backfilled stopes nor expose backfilled faces. Currently the backfill operation aims at filling the voids and storing tailings with no target strength. However, since chemical stabilization can be related to cementitious compounds formation, a higher UCS should hint at better contaminant stabilization. The results are further compared in the following sections.

E.3.2.1 Effects of solid content

Figure E.2 shows the effects of the solid content of the CPB samples on the strength of the samples for both GU and GU/LKD binders. All these samples were prepared using a 5% of binder and cured for 59 days. In this figure, the average of the six samples with 74% solid content, which were the replicates for assessing the repeatability of the results (based on the mix design proposed by the RSM), is presented. As observed, increasing the solid content increased the strength of the samples. Due to the inverse relationship between the solid content and water content of the CPB samples (the higher the solid content, the lower the water content), it is evident that increasing the solid content resulted in an improvement in the strength of the CPB samples. The differences between the strength of the CPB samples prepared by GU and GU/LKD at the same solid and binder content could be related to the difference between the physical, chemical, and mineralogical properties of the binders.

E.3.2.2 Effects of binder content

Figure E.3 depicts the influence of the binder content on the strength of the CPB samples. The effects of solid content on the strength of samples are also visible in this graph. Increasing the binder content increased the strength of the samples prepared by GU and GU/LKD mixtures both after 28 and 90 days. Increasing the binder content resulted in more cement hydration products, which led to the alteration of the pore structure (lower porosity), higher water consumption, and higher strength. Moreover, as expected, samples with higher solid content showed higher strength values. Changing from 4% to 6% of the binder had more effects on the strength at higher solid

content (76%). Except for the 6,76 GU samples, no improvement in the strength was visible from 28 to 90 days of curing.

Table E.5 Results of the UCS tests on the CPB samples prepared with GU cement and the mixture of GU and LKD

Run	Factor 1	Factor 2	Factor 3	Responses	
	Solid content	Binder content	Curing time	UCS-GU	UCS-GU/LKD
	%	%	day	kPa	kPa
1	70.64	5	59	154	24
2	72	4	28	154	42
3	72	4	90	154	42
4	72	6	28	296	100
5	72	6	90	278	105
6	74	3.32	59	155	27
7	74	5	7	174	108
8	74	5	59	268	76
9	74	5	59	282	87
10	74	5	59	264	67
11	74	5	59	268	48
12	74	5	59	276	81
13	74	5	59	296	90
14	74	5	111	232	109
15	74	6.68	59	472	175
16	76	4	28	276	92
17	76	4	90	249	90
18	76	6	28	491	214
19	76	6	90	531	213
20	77.36	5	59	478	178

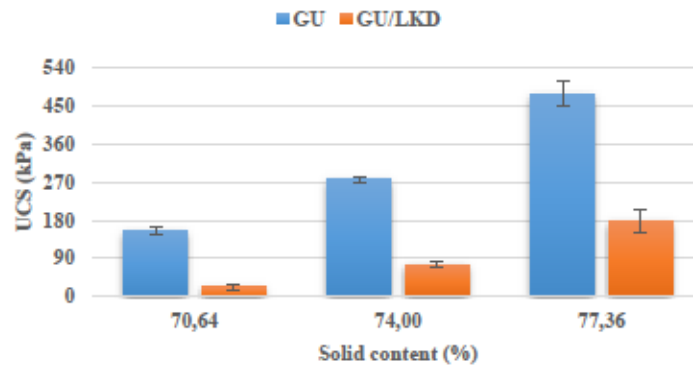


Figure E.2 The effects of solid content on the UCS of the CPB samples prepared with 5% of GU and GU/LKD binders and cured for 59 days

E.3.2.3 Effects of curing time

Figure E.4 presents the influence of the curing time on the strength gain of the CPB samples. These samples were prepared using 5% of GU and GU/LKD binders at 74% solid content and cured from 7 up to 111 days. Results showed that the effects of curing time are different on the GU and GU/LKD samples. For GU samples, increasing the curing time increased the strength of the samples up to 59 days and after that decreased their strength. For the GU/LKD samples, the strength was lowest at 59 days while UCS were similar at 7 and 111 days. Therefore, no trend is observable by changing the curing time. Generally, for the CPB samples without arsenic trioxide, increasing the curing time led to improvement in the strength since the binder hydration is an evolving process.

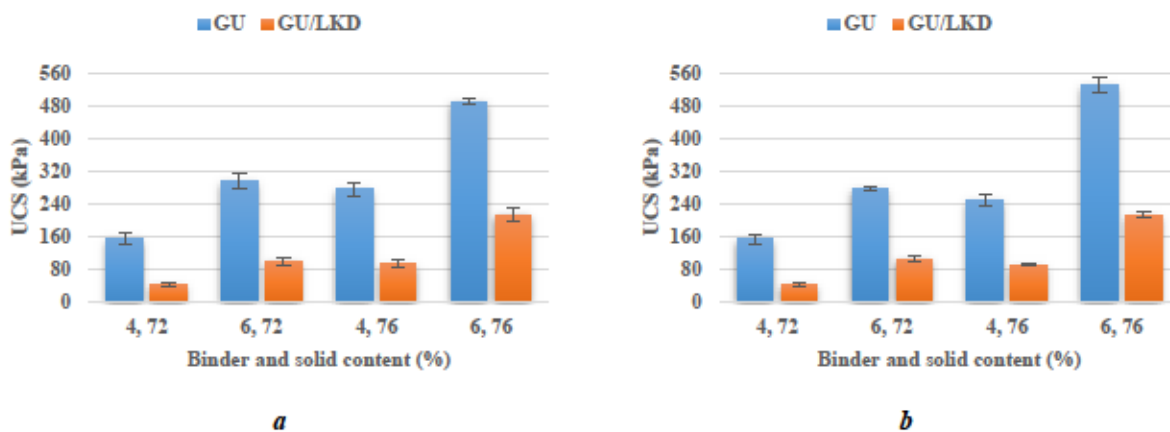


Figure E.3 The effects of binder content (as well as solid content) on the UCS of the CPB samples prepared with GU and GU/LKD after (a) 28 days and (b) 90 days of curing

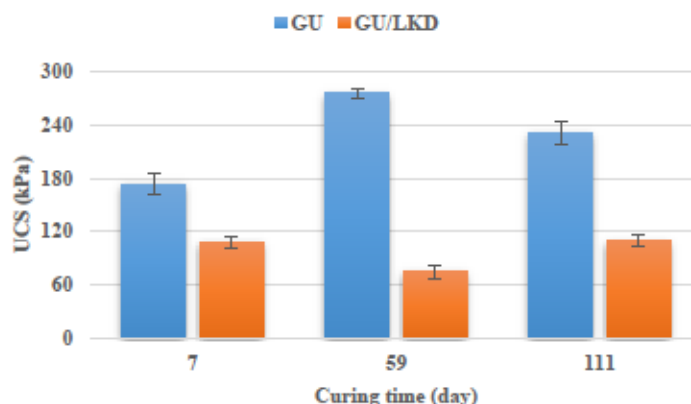


Figure E.4 The effects of curing time on the UCS of the CPB samples prepared with 5% of GU and GU/LKD binders and 74% solid content

To compare the obtained results with the UCS of CPB samples without arsenic trioxide, some samples were prepared using GU cement and tailings of the Giant Mine. For the samples that were prepared using 4% and 6% GU cement at 72% solid content and cured for 28 days, the average UCS was 274 kPa and 371 kPa, respectively. The strength of the samples prepared using 6% of GU and GU/LKD binders at 76% solid content and cured for 28 days was 678 and 301 kPa, respectively. This shows that the addition of the arsenic trioxide roaster waste dusts resulted in a substantial decrease in the CPB samples strength. However, the decision about the feasibility of the incorporation of the arsenic trioxide roaster waste dust in CPB will be drawn based on a combination of strength results and standardized leaching experiment results. Some investigations were undertaken to assess the effects of the incorporation of the arsenic trioxide roaster waste dusts in the cemented paste backfill on the strength of the samples. One of the suspected reasons for this significant reduction could be the modification of the geochemical conditions of the paste due to the high solubility of the arsenic trioxide at high pH values (typical condition of the cementitious matrices). The dissolution of the arsenic trioxide in the CPB structure and strength reduction may also affect the stabilisation of arsenic within CPB, and these effects are currently under further investigation.

E.4 Conclusion

Based on the results of this study, it can be concluded that:

- The addition of the arsenic trioxide dusts to the cemented paste backfills substantially decreased the strength of the pastes; however, increasing the binder content and solid content compensated for this negative effect.
- Paste samples prepared using GU cement showed higher strength than the samples prepared with GU cement and LKD.
- Both binder content and solid content had a direct positive impact on the strength of the paste samples, whereas the effect of curing time on the strength was not meaningful.
- The reasons for strength reduction in the CPB samples in the presence of the arsenic trioxide as well as the leaching characteristics of the optimal mix designs are under study; still, one possible reason could be the reduction in the pH of the paste due to the dissolution of arsenic trioxide in the paste at higher pH values.

Acknowledgement

The authors would like to acknowledge the “Giant Mine Oversight Board (GMOB)” and “NSERC Alliance” program for the financial support.

APPENDIX F ARTICLE 5: ARSENIC SPECIATION IN CEMENTED PASTE BACKFILL USING PARALLEL EXTRACTION

This extended abstract was presented and published in the proceedings of the 8th International Congress on Environment and Social Responsibility in Mining, Sustainable Mining 2023. This article was submitted on 19 December 2022 and presented on 10 May 2023. This appendix reproduces the full text.

Amirhossein Mohammadi^{1,5}, Isabelle Demers^{1,2}, Mostafa Benzaazoua¹ and Nicholas Beier³

1. UQAT-Polytechnique Research Institute on Mine and Environment, Rouyn-Noranda, QC, Canada

2. Canada Research Chair on Integration of the Environment in the Mine Life Cycle, Rouyn-Noranda, QC, Canada

3. Department of Civil and Environmental Engineering, University of Alberta, Edmonton, AB, Canada

ABSTRACT

Introduction: Cemented paste backfill technology has been widely used in hard rock underground mines for ground support purposes. This process consists of mixing tailings with a small proportion of binding agents and a relatively high proportion of mixing water. Although this process is mainly used to reduce tailings' surface impoundments and to fill the mined-out voids, it could also provide environmental advantages by stabilizing the pollutants. Arsenic is one of the metalloids which is commonly found in mine wastes and could be stabilized within cementitious matrices such as cemented paste backfills. The main objective of this study is to estimate the speciation of arsenic species in cemented paste backfill and evaluate the risk of arsenic leaching from the cured paste. The selected method to identify the arsenic species families was a parallel extraction procedure followed by geochemical modelling.

Methodology: Cemented paste backfill samples were prepared using pure silica as the tailings, general use (GU) cement (10% wt.) as the binder, reagent grade arsenic trioxide (15% wt.) and

⁵ Corresponding author: PhD candidate, UQAT-Polytechnique Research Institute on Mine and Environment, 445 Bd de l'Université, Rouyn-Noranda, QC J9X 5E4, Canada. Phone: +1 (819)880-1524. Email: amirhossein.mohammadi@uqat.ca

deionized water ($W/C = 3.37$). The samples were cured for 28 days, then dried and crushed using a pestle and mortar before performing the extractions. Arsenic trioxide roaster waste dusts as well as tailings from a gold mine site also were used for the arsenic extraction analysis as comparison. Five different reagents, shown in Table 1, were used to extract some specific target phases. The leachates were filtered using a $0.45 \mu\text{m}$ filter and analyzed using ICP-MS and the pH and Eh of the reagents were measured before and after each extraction process. The results of chemical analysis were used for the geochemical modeling using Visual MINTEQ 3.1 to differentiate arsenic species and their mobility for each condition.

Results and Conclusions: Figure F.1 shows the concentration of the extracted arsenic during each extraction period. The chemical and geochemical analysis showed that the arsenic in the extracted waters is in the form of various components such as aluminum, calcium, and ferro-arsenates as well as some secondary minerals such as arsenolite, claudetite, and realgar in significantly small concentrations. Geochemical modelling suggests that the incorporation of arsenic trioxide into cemented paste backfill enabled a significant reduction in the mobility of arsenic. The drop in arsenic concentration following the DI extraction step can be attributed to the insoluble iron oxide phases, which may have adsorbed part of As dissolved during the CPB mixing and hydration process. With the increase in aggressiveness of the leaching steps, the oxides became more soluble and released adsorbed As. Cemented past backfill is a promising process to stabilize arsenic from arsenic trioxide waste.

Table F.1 The list of conditions for the parallel extraction analysis

Target phases	Reagent	CPB sample mass (gr)	Solid/Reagent ratio	Extraction period (h)
Water-soluble phases	Deionized water	1	1:50	24 (room temp.)
Insoluble sulfates	0.3 M NaOH	1	1:30	16 (room temp.)
Amorphous oxyhydroxides	0.12 M Na-ascorbate, 0.6 M Na-bicarbonate & 0.17 M Na-citrate (pH \approx 8)	1	1:20	24 (in dark anaerobic glovebox)
Poorly crystalline phases & carbonates	0.5 M HCl	1	1:10	24 (room temp.)
Amorphous & crystalline oxyhydroxides	2.0 M $\text{NH}_2\text{OH}\cdot\text{HCl}$ in 25% (v-v-1) acetic acid	1	1:30	24 (at $95 \pm 4 \text{ }^\circ\text{C}$)

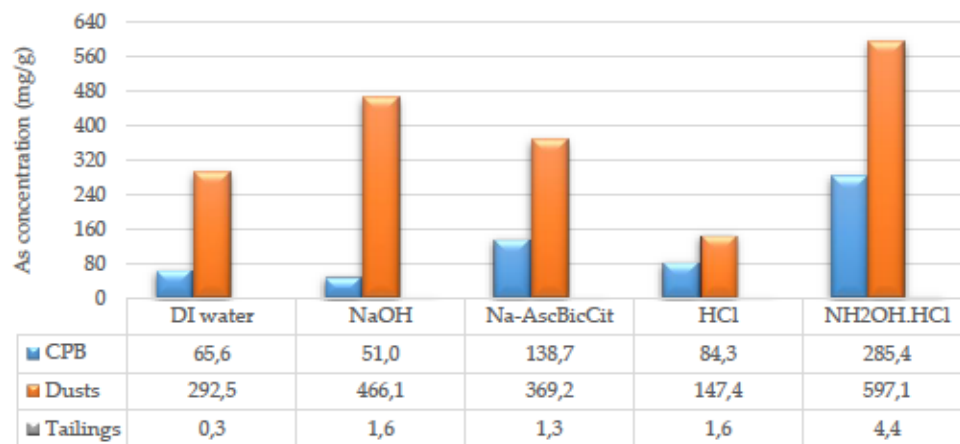


Figure F.1 The concentration of the extracted arsenic using various reagents for different samples

APPENDIX G XAS PARAMETERS

The following tables summarize the results obtained from the X-ray Absorption Spectroscopy (XAS) analyses conducted on the samples. The XANES (X-ray Absorption Near Edge Structure) peak parameters provide insights into the oxidation state and local chemical environment of arsenic, while the EXAFS (Extended X-ray Absorption Fine Structure) parameters detail the structural characteristics of the arsenic coordination environment, including bond distances, coordination numbers, and Debye-Waller factors. These results are critical for understanding the speciation and stabilization mechanisms of arsenic in the studied system.

Table G.1 Arsenic XANES peak parameters

Sample	Main peak (eV)	Formal oxidation state	Estimated oxidation state
CPB_GU-6-76-28	11870	-	3
CPB_GU-6.68-74-59	11870	-	3
CPB_GU/LKD-6-76-28	11869.9	-	3
CPB_GU-4-76-28	11869.9	-	3
HNa ₂ AsO ₄	11873.4	5	-
Hydrous Ferric Arsenate	11873.9	5	-
Sodium arsenite	11870.1	3	-
Arsenolite	11870	3	-
Arsenopyrite	11867.4	-1	-

Table G.2 Arsenic EXAFS parameters for the sample GU-6-76-28

Atom	N	R(Å)	σ^2 (Å ²)	ΔE_0 (eV)	R-factor
OFeCa					
O171	2.3	1.78	0.001	6.4	0.0409
Fe329	0.7	3.33	0.001		
Ca365	2.5	3.66	0.008		
OFeCaAs					
O171	2.3	1.78	0.001	6.4	0.0364
Fe329	0.6	3.31	0.001		
Ca365	2.2	3.65	0.010		
As393	0.5	3.94	0.002		
OFeFe					
O171	2.3	1.78	0.001	6.2	0.0365
Fe329	1.4	3.34	0.006		
Fe347	3.4	3.60	0.009		
OFeFeAs					
O171	2.3	1.78	0.001	6.6	0.0342
Fe329	0.7	3.29	0.001		
Fe347	9.0	3.62	0.029		
As393	0.7	3.92	0.003		

Table G.3 Arsenic EXAFS parameters for the sample GU-6.68-74-59

Atom	N	R(Å)	σ^2 (Å ²)	ΔE_0 (eV)	R-factor
OFeCa					
O179	2.2	1.77	0.002	5.8	0.0352
Fe329	1.7	3.31	0.010		
Ca365	2.6	3.66	0.007		
OFeCaFe					
O179	2.3	1.77	0.002	5.3	0.0343
Fe329	1.3	3.29	0.008		
Ca365	2.3	3.65	0.007		
Fe469	0.3	4.61	0.004		
OFeFe					
O179	2.3	1.77	0.002	5.2	0.0333
Fe329	1.6	3.29	0.008		
Fe347	5.3	3.59	0.016		
OFeFeFe					
O171	2.3	1.76	0.002	4.0	0.0364
Fe329	0.8	3.30	0.010		
Fe347	1.2	3.60	0.003		
Fe469	0.3	4.60	0.002		

Table G.4 Arsenic EXAFS parameters for the sample GU/LKD-6-76-28

Atom	N	R(Å)	σ^2 (Å ²)	ΔE_0 (eV)	R-factor
OFeCa					
O179	2.3	1.78	0.002	5.9	0.0558
Fe329	2.5	3.36	0.006		
Ca365	2.2	3.65	0.001		
OFeCaAsFe					
O179	2.4	1.77	0.002	4.7	0.0398
Fe329	1.4	3.31	0.002		
Ca365	7.0	3.68	0.022		
As393	8.1	3.90	0.015		
Fe469	6.1	4.65	0.018		
OFeFe					
O171	2.3	1.78	0.002	5.6	0.0504
Fe329	1.8	3.34	0.002		
Fe347	3.5	0.58	0.007		
OFeFeAsFe					
O171	2.2	1.78	0.001	5.3	0.0438
Fe329	1.5	3.31	0.002		
Fe347	1.0	3.55	0.003		
As393	1.5	3.94	0.003		
Fe469	4.8	4.70	0.016		

Table G.5 Arsenic EXAFS parameters for the sample GU-4-76-28

Atom	N	R(Å)	σ^2 (Å ²)	ΔE_0 (eV)	R-factor
OFeCa					
O179	2.7	1.78	0.002	6.1	0.0682
Fe329	2.9	3.36	0.007		
Ca365	2.6	3.65	0.001		
OFeCaAsFe					
O179	2.1	1.78	0.001	5.2	0.0386
Fe329	1.0	3.30	0.001		
Ca365	5.5	3.63	0.022		
As393	1.3	3.92	0.003		
Fe469	3.4	4.70	0.014		
OFeFe					
O171	2.1	1.78	0.000	5.8	0.0494
Fe329	2.1	3.34	0.003		
Fe347	3.9	3.58	0.007		
OFeFeAsFe					
O171	2.1	1.78	0.000	5.5	0.0331
Fe329	1.5	3.31	0.002		
Fe347	9.1	3.58	0.024		
As393	1.8	3.91	0.002		
Fe469	1.2	4.71	0.005		